What's in the brew?

A study of the molecular environment of methanol masers and UCHII regions.

by

Cormac R. Purcell

A thesis submitted in satisfaction of

the requirements for the degree of

Doctor of Philosophy

in the Faculty of Science.

31st of July, 2006

THE UNIVERSITY OF
NEW SOUTH WALES

SYDNEY • AUSTRALIA

Statement of Originality

I hereby declare that this submission is my own work and to the best of my knowledge it contains no materials previously published or written by another person, nor material which to a substantial extent has been accepted for the award of any other degree or diploma at UNSW or any other educational institution, except where due acknowledgement is made in the thesis. Any contribution made to the research by others, with whom I have worked at UNSW or elsewhere, is explicitly acknowledged in the thesis.

I also declare that the intellectual content of this thesis is the product of my own work, except to the extent that assistance from others in the project's design and conception or in style, presentation and linguistic expression is acknowledged.

(Signed) .....

Acknowledgements

First and foremost, my gratitude must go to my supervisor, Michael Burton, who has deftly steered me through the treacherous reefs of my PhD. Without Michael's keen scientific eye, this project would surely have floundered. Michael planted the seed of a stimulating and challenging PhD project and provided just the right amount of patronage for it to bear fruit.

I would also like to thank my co-supervisor, Maria Hunt, for her encouragement and support during my time in Australia. Maria's 'open door' policy and her alternative take on meetings stands to her credit.

I greatly appreciate the efforts both Michael and Maria made to secure funding support for me and their other PhD students. In that respect, Michael especially has a talent for 'pulling rabbits out of hats'. I am also most grateful to the School of Physics, who awarded me a 'School of Physics Scholarship'. This funding allowed me to pursue my research without having to worry about where the next meal was coming from. The School also provided me with many opportunities to engage in teaching and outreach, which I greatly appreciate, as such experiences are an essential aspect of any PhD.

Scientific learning builds on the knowledge of previous generations and I am no less 'standing on the shoulders of giants'. For many illuminating, sometimes baffling and always informative discussions, my thanks must go to Andrew Walsh, Vincent Minier, Steven Curran, Matthew Whiting, Indra Bains, Wilfred Walsh, Chris Blake, Tony Wong, Tamara Davis and Michael Murphy. Andrew in particular proof-read an early draft of this work, at what was a very busy time for him. Many thanks also to Ned Ladd, who's excellent mentoring helped shape my thesis project.

Staff at the ATNF deserve a special mention for their tireless support of Mopra and the Compact Array. Specifically, Stuart Robertson (aka Captain Mopra), Bob Sault, Robin Wark and Graeme Carrad, for supplying moments of light relief. I would like to thank also Paul Jones, Jim Caswell and Chris Philips with whom I have had many helpful discussions about radio astronomy.

My gratitude goes to Melinda Taylor for all her hard work suporting the computing environment for us demanding researchers.

Warm and heartfelt thanks go to my fellow PhD students and postdocs - my brothers (and sisters) in arms - for making the whole experience so much more enjoyable. To my office mates, Steven Longmore and Suzanne Kenyon: you have been the keepers of my sanity. Who else would listen to my rants in the morning? Many **yearr's!** go to the 'Pirate Crew' and their Scottish leader. May there be many more scurvy nights.

It is a pleasure for me to thank all the staff and students at the UNSW School of Physics for their friendship and company during the course of my stay in Australia. You shall all be sorely missed. Thanks especially to the members of the Theoretical Physics and Accoustic groups, especially, Julian, Clare and Claudia. A big thank-you to Ra Inta and Amy Winter, for the welcome breaks in Canberra and the best hospitality in Australia.

Thank you also to Damien Foley, my secondary school physics teacher, who always patiently answered my questions about astronomy and physics. Damien's yarns about the personalities behind the giants of science were always a reminder that science was far from a cold, clinical subject.

I am greatly indebted to the referees for taking the time to read and correct my thesis. It is clear from the quality of their comments that all parties gave careful consideration to each chapter and this has lead to a much improved the final version.

Finally, I would like to express my eternal gratitude and love to 'mo stór', Ciara, and to my parents, Pat and Veronica, who have supported me throughout my endeavours. Without you I could not have done this. Thank-you.

b

Abstract

In recent years the 6.67 GHz masing transition of CH_3OH has proven to be a superior tracer of massive star formation (see Minier et al. 2001). Maser sites often occur in proximity to UCHII regions, however, up to 75 per cent of sites have no detectable radio counterpart (Walsh et al. 1998) and are instead hypothesised to trace the less evolved 'hot molecular core' phase of stellar evolution. This has been confirmed for a only handful of well known sources (e.g., Cesaroni et al. 1994). Presented here are the results of multi-species molecular line observations towards warm, dusty clumps, undertaken with the goal of investigating the relationship between hot cores, UCHII regions and CH_3OH masers.

Data from the 22-m Mopra telescope is used extensively in this thesis and substantial efforts were made to calibrate the brightness temperature scale. Measurements conducted on SiO masers and planets show that the beam pattern is divided into a Gaussian main beam plus an inner error lobe, which in 2004 contained 1/3 of the power in the main beam. Full-width half-maximum beam sizes were measured from the data and the beam efficiencies were derived for the years 2000 – 2004.

A 3-mm wavelength molecular line survey was conducted, using Mopra, towards 83 massive star-forming clumps associated with CH_3OH masers. Emission from the transitions $^{13}CO\,(1-0)$, $N_2H^+\,(1-0)$, $HCO^+\,(1-0)$, $HCN\,(1-0)$ and $HNC\,(1-0)$ was detected towards 82 sources (99 per cent), while CH_3OH emission was detected towards 78 sources (94 per cent). The warm gas tracer CH_3CN was observed specifically to search for hot core chemistry, and was detected towards 58 sources (70 per cent), confirming that CH_3OH masers are excellent tracers of hot cores.

CH_3CN is found to be brighter and more commonly detected towards masers associated with UCHII regions compared to 'isolated' masers. That CH_3CN is detected towards isolated maser sources strongly suggests that these objects are internally heated.

The molecular line data have been used to derive rotational temperatures and

chemical abundances in the clumps and these properties have been compared between sub-samples associated with different indicators of evolution. In particular, CH_3OH is found to be brighter and more abundant in UCHII regions and in sources with detected CH_3CN, and may constitute a crude molecular clock in single dish observations.

Gas-kinematics were analysed via asymmetries in the HCO^+ line profiles. Approximately equal numbers of red and blue-skewed profiles, indicative of inward or outward motions, respectively, are found among all classes of object.

Bolometric luminosities were derived via greybody fits to the sub-millimetre and mid-infrared spectral energy distributions, and an empirical gas-mass to luminosity relation of $L \propto M^{0.68}$ was fit to the sample. This is a considerably shallower power law than $L \propto M^3$ for massive main-sequence stars.

In the mid-infrared, 12 sources were identified as 'infrared dark clouds' (IRDCs). Such objects have been hypothesised as precursors to the hot core phase of evolution, however, we find these sources have greater linewidths and rotational temperatures than the bulk of the sample, and one contains an embedded HII region

The filamentary star forming region NGC 3576 was also investigated via a molecular line and 23 GHz continuum mapping survey, utilising the ATCA, Mopra and Tidbinbilla telescopes. The results of these observations provide detailed information on the morphology, masses, kinematics, and physical and chemical conditions along the cloud.

Analysis of NH_3 data has revealed that the temperature and linewidth gradients exist in the western arm of the filament. Values are highest near to the central HII region, indicating that the embedded cluster of young stars is influencing the conditions in the bulk of the gas.

Six new H_2O masers were detected in the arms of the filament, all associated with clumps of NH_3 emission. Star formation is clearly underway, however, clump masses range from $1\,M_\odot$ to $128\,M_\odot$, possibly too low to harbour very massive stars. The lack of detected 23 GHz continuum emission in the arms supports this assertion.

Contents

List of Tables

List of Figures

Preface

The work presented herein is largely my own. Where previous work and/or contributions from other researchers have been included in the text, I have acknowledge these instances by referring to relevant papers or by referring explicitly to the researchers involved. I summarise the major contributions of others below. The content of Chapters 3, 4, 5 and 6 has been (or is to be) published in a series of papers.

- **Chapter 3:** The project to measure the beam-shape and efficiencies of the Mopra telescope was lead by Dr Ned Ladd. I was heavily involved in performing the beam mapping observations and measuring the calibration standards. At the time, software was not in place to reduce mapping data and an interim solution was developed by Dr Ladd and Dr Tony Wong. Code to fit the main beam with Gaussians and to measure the beam efficiencies was also written by Dr Ladd. I performed the analysis of the year-to-year efficiencies and compared the calibration standards to data from the SEST and IRAM 30-m observatories. The description of the beam analysis is my own summary of the methods used. The frequency rounding error was also investigated by Ned Ladd and Chris Phillips, who wrote the initial version of the 'moprafix.pl' script. I refined and modified later versions as the nature of the rounding error became clear.

  '*Beam size, shape and efficiencies for the ATNF Mopra radio telescope at 86-115 GHz*', – E. F. Ladd, **C. R. Purcell**, T. Wong, S. Robertson. 2004. *PASA 22*, 62-72.

- **Chapter 4:** Observations for the 'Hot Molecular Cores' project were conducted over four years by an army of observers. I was responsible for the design and management of the observations from the 2002 observing season onwards. Most of the data was taken after this time and over half of that personally by myself. All of the analysis and discussion in this chapter was developed by myself in close collaboration with my supervisors, Dr Michael Burton and Dr Maria Cunningham. Many helpful comments were kindly provided by the co-authors and observers.

'*A CH_3CN and HCO^+ survey towards methanol masers associated with star formation*', – **C. R. Purcell**, R. Balasubramanyam, M. G. Burton, A. J. Walsh, V. Minier, M. R. Hunt-Cunningham, + 29 others. 2006. *MNRAS 367*, 553-576.

- **Chapter 5:** As in the previous chapter, all of the analysis and discussion presented here was developed by myself in close collaboration Dr Michael Burton and Dr Maria Cunningham. This work is intended for publication in MNRAS as a follow-on paper to Purcell (2006).

  '*Physical and chemical conditions at methanol maser selected sites of massive star formation*', – **C. R. Purcell**, S. N. Longmore, V. Minier, P. Jones, M. G. Burton, M. Hunt-Cunningham, *MNRAS in prep.*

- **Chapter 6:** Compact array observations were performed by myself, with the assistance of Vincent Minier, Jim Caswell and Tracey Hill. I was responsible for all of the data reduction and analysis. This work is also intended for publication in MNRAS.

  '*A multi-wavelength study of the infrared dark filament associated with NGC 3576*', – **C. R. Purcell**, V. Minier, M. G. Burton, M. Hunt-Cunningham. *MNRAS in prep.*

Chapter 1

Introduction

1-1 Motivation

Massive ($> 8\,M_\odot$) stars play a pivotal role in astrophysics. In the early Universe, the first generation of stars were predominantly massive stars (Bromm et al. 1999). They produced copious amounts of UV photons, leading to the re-ionisation of the Universe, while their prodigious energy output had important effects on subsequent galaxy formation (Carr et al. 1984). Today, the only phenomena sufficiently bright to be seen from those times are due to massive stars (e.g. Salvaterra et al. 2006).

In the local Universe, massive stars are the powerhouses driving the cycles of matter and energy in the Milky Way. Formed from quiescent gas and dust, they evolve swiftly, develop energetic winds of charged particles and emit intense UV radiation. During their short lifetimes they actively reshape their environment, triggering the birth of new stars and possibly solar systems. They end their lives in violent supernova explosions that return much of their mass to interstellar space, where the cycle begins again. To understand the physics of the evolving Universe on both small and large scales, it is essential we first understand the nearest examples of massive star formation.

Despite decades of intensive research, the processes that give rise to the formation of massive stars within our Galaxy are still largely mysterious. This is because their

rapid evolution and many interacting phenomena make it difficult to disentangle cause and effect. In addition, most examples of massive star forming regions are thousands of light years away from us, buried at the heart of giant molecular clouds that obscure all visible radiation emitted. Unlike their low-mass cousins, whose formation via accretion is well established, a clear evolutionary sequence has yet to emerge for massive stars. The motivation for the work presented in this thesis is the quest for an empirical evolutionary sequence of massive star formation.

1-2 Star formation overview

Stars of all masses begin their lives as contracting clouds of dense gas and dust embedded in the interstellar medium. Low and high mass stars are distinguished from each other by the timescales over which they form. The timescale for collapse is given by the *free-fall* time (Shu et al. 1987)

$$t_{ff} = \left(\frac{3\pi}{32G\rho}\right)^{0.5} = 3.4 \times 10^7\, n^{-0.5} \quad \text{years}, \tag{1.1}$$

where $G = 6.673 \times 10^{-11}\,N.m^2.kg^{-2}$ is the gravitational constant, ρ is the average mass density in $kg.cm^{-3}$ and n is the number density in cm^{-3}. In typical molecular clouds $n \geq 50\,cm^{-3}$ and the free fall time is $t_{ff} \leq 5{\times}10^6$ yrs, which gives a lower limit on the timescale for stellar evolution.

Contraction of a mass of gas under self gravity results in gravitational potential energy being converted to heat. The timescale on which this process occurs is given by the Kelvin-Helmholtz time t_{KH}, which provides an estimate of the time taken for pre-fusion burning objects to evolve

$$t_{KH} \approx \frac{GM_*^2}{R_* L_*}. \tag{1.2}$$

In Equation 1.2 R_* is the stellar radius and L_* is the stellar luminosity. For a $1\,M_\odot$ star this time is relatively long at $t_{KH} \approx 3 \times 10^7$ yrs, but for a massive star of $50\,M_\odot$ ($L_* \approx 10^4\,L_\odot$) collapse takes place extremely rapidly and $t_{KH} \approx 10^4$ yrs. For stars with masses $> 8\,M_\odot$ we find $t_{KH} < t_{ff}$, implying that fusion ignites before the

collapse has ceased. This key fact has important implications for the process of forming a star via accretion.

1-2.1 Low mass star formation

Low mass stars are known to form in molecular clouds with masses greater than $\sim$0.3 $M_\odot$. Although they form in clusters with their more massive brethren, many examples also form in relative isolation where they can be studied without concern for the disruptive effects of surrounding stars. The closest complexes forming low mass stars are a mere few hundred parsecs away (e.g., Ophiuchus 150 pc, Bok 1956, Perseus 320 pc, de Zeeuw et al. 1999) facilitating the investigation of the physics and chemistry on scales down to a few hundred astronomical units (AU).

Theoretically, the process of low mass star formation is well understood and has a clear evolutionary scenario (e.g., Shu et al. 1987, 1991). The fundamental event leading to star formation is the collapse of a dense ($10^2 - 10^4$ cm^{-3}), cool ($\sim$10 K) knot of gas and dust within a molecular cloud. Initially the gravitational force acting towards the centre of the cloud is counterbalanced by rotation, thermal pressure and weak magnetic fields, or turbulence. Over time this support is lost as neutral particles slip through the ions (via ambipolar diffusion) and the central region increases in density. The core undergoes an 'inside-out' collapse and the collapse front expands outwards at the speed of sound in the gas. An accretion phase follows in which material from the extended envelope rains down onto the central condensation. The envelope, which was previously optically thin, becomes opaque to cooling radiation and the temperature of the central object increases. Residual angular momentum in the infalling material causes it to spin down into a dusty circumstellar disk as it contracts. Highly collimated jets and outflows are often detected at this stage as angular momentum is shed into the surrounding medium. After approximately 10^7 years the material in the vicinity of the protostar is exhausted and accretion ceases. By this time the pressure and temperature has increased enough to ignite fusion in the core and the young star begins life on the main sequence.

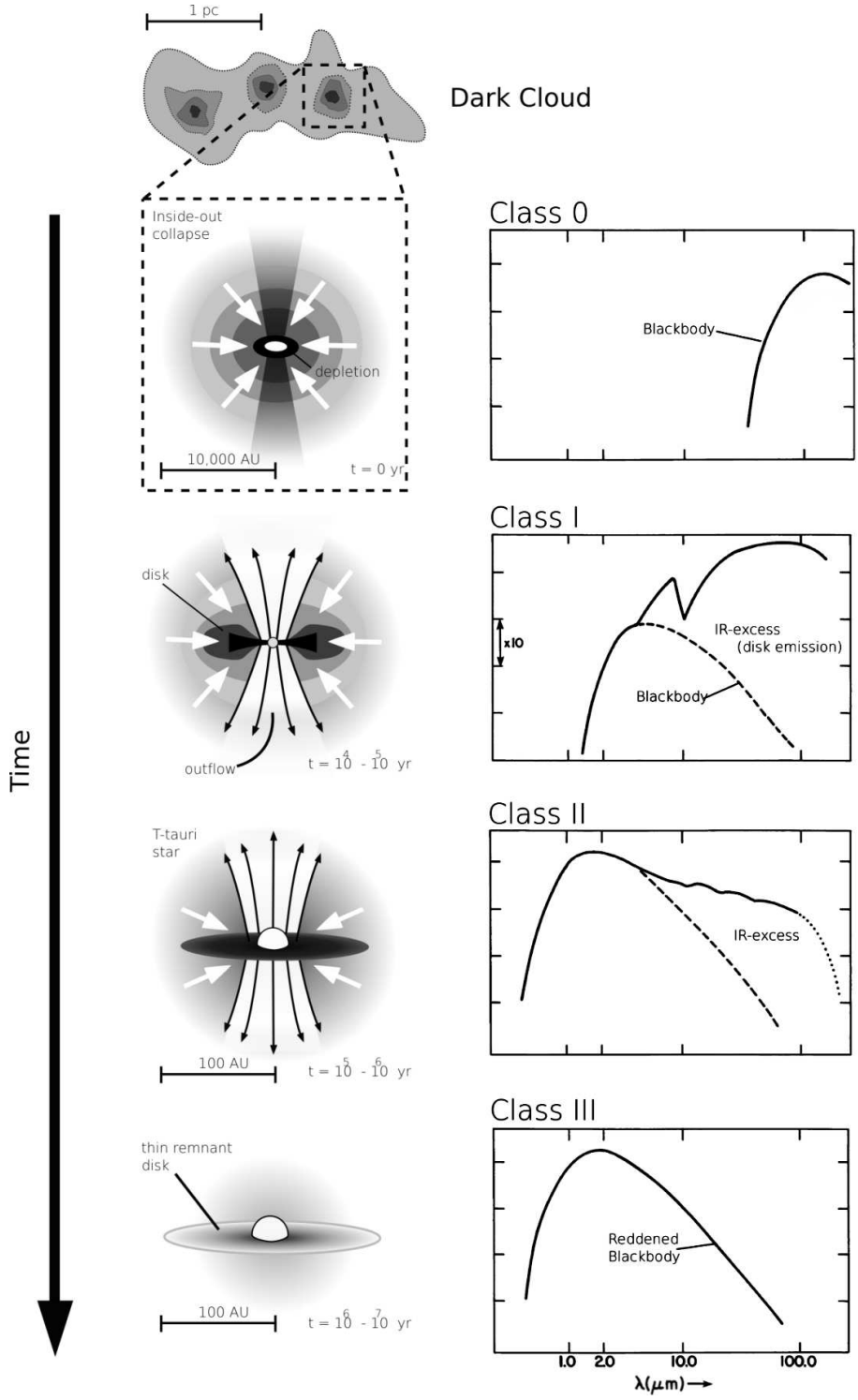

Figure 1.1. Schematic representation of the evolutionary sequence for low-mass stars (adapted from Lada & Wilking 1984 and van Dishoeck & Blake 1998). Initially a dense knot of gas undergoes inside-out collapse, forming a central protostellar core. Residual angular momentum causes the cloud to spin into a circumstellar disk. Accretion via the disk gives rise to bipolar outflows and collimated jets. After $> 10^7$ years the circumstellar material is exhausted and accretion ceases.

Observationally, low-mass young stellar objects have been divided into four distinct evolutionary classes on the basis of their spectral energy distributions (SEDs) (c.f. Lada & Wilking 1984; Andre et al. 1993). Radiation from the powering central source is scattered, absorbed and re-emitted by the dusty protostellar envelope before escaping to interstellar space. The variation in the shape of the resultant SED reflects the conditions in the envelope at each stage of evolution. Figure 1.1 represents the evolutionary sequence and the associated spectral energy distributions for the classes 0 to III.

Class 0: Collapse has commenced at this stage raising the temperature and luminosity of the core. The SED resembles a single blackbody, with a temperature between 20 and 30 K, and so peaks in the sub-millimetre band, at $\lambda > 150\,\mu$m. Many Class 0 sources drive energetic bipolar outflows (Lada 1999; Andre et al. 1993), implying that the infall is not spherical and disks-like structures have already formed.

Class I: As accretion proceeds the dust temperature rises and the peak of the SED moves to the far-IR ($\sim$100 μm). Residual rotation causes the infalling material to form an accretion disk around the central protostellar object. Bipolar outflows and jets are formed as momentum and energy is bled off into the surroundings. The SED profile corresponds to a 50–100 K blackbody, originating in the accreting envelope, plus additional 200–400 K components, originating in the disk. A silicate absorption feature is often present at 10 μm, indicating an optically thick envelope of dust. Observationally these sources are deeply embedded and invisible at wavelengths shortward of 1 μm.

Class II: After $\sim 10^6$ years, winds and molecular outflows have swept away much of the natal envelope, exposing the dusty disk. The peak of the SED falls in the near-infrared band, around 2 μm. Flux longward of 2 μm is dominated by excess emission from the disk. At this stage, the pre-main-sequence core is often visible in the optical and near-infrared, and is typically identified as a T-Tauri star.

Class III: These objects are visible as stars in the near-infrared and optical, where their SED peaks. Some circumstellar material may be present in the form of a thin disk, however, the SED is generally well fit by a reddened blackbody with little or

no IR excess emission. This is consistent with a reddened stellar photosphere of a star on the zero-age-main-sequence.

The evolution of the SED is due to gradual dissipation of gas and dust from the natal envelope. A quantitative classification scheme is based on the spectral index between $10\,\mu$m and $100\,\mu$m, according to (Lada 1987)

$$\mathrm{a} = \frac{\mathrm{dlog}(\lambda\,\mathrm{F}_\lambda)}{\mathrm{dlog}(\lambda)}. \tag{1.3}$$

For class I sources $0 < a \leq 3$, for class II sources $-2 \leq a \leq 0$, and for class III sources $-3 \leq a \leq -2$.

1-2.2 High mass star formation

High mass stars form within dense cores containing at least $10\,\mathrm{M}_\odot$ of gas concentrated in a region $\leq 0.05\,\mathrm{pc}$ (i.e., the mean separation between stars observed in clusters (Testi et al. 1997; Hillenbrand 1997; Kurtz et al. 2000).

The processes leading to the formation of massive stars are poorly understood for a number of reasons. Massive stars, due to the steep dependence on mass in the initial mass function (IMF), are much less common than their low mass cousins. Consequently, most examples of massive star forming regions are located at distances of several kiloparsecs and require interferometric techniques to resolve them. Obtaining a clear picture of the earliest stages is further confounded by the short timescales over which they evolve. Forming deep within molecular clouds, their birth is obscured by optically thick layers of dust and gas, from which they emerge only after having evolved onto the main sequence.

Massive stars are gregarious, that is they tend to form in clusters, giving rise to OB associations. A single region may contain several massive stars at varying stages of development. This means that energetic processes, such as outflows, from the more evolved massive young stellar objects (MYSOs) may disrupt the evolutionary sequence of the younger members. For observers it is nearly impossible to disentangle cause and effect in such a feedback loop.

If we try to apply the low-mass formation scenario to high mass stars we encounter a number of limiting problems which make the scenario implausible. As mentioned before, $t_{KH} < t_{ff}$ for massive protostellar objects, meaning that they begin emitting intense ultraviolet radiation and winds of energetic particles while still accreting material. Neglecting feedback from other members of protoclusters, the radiation pressure exerted by a single massive star later than B3 ($\sim$10 $M_\odot$) is capable of halting or reversing the accretion of material from a spherical envelope. This suggests there should be an upper limit to stars formed through this process, yet stars with masses up to 150 $M_\odot$ have been detected (e.g., Figer et al. 2002). Two solutions have been proposed to overcome the apparent limitations:

- **Enhanced accretion.** Recently 3-D hydrodynamic simulations have shown that massive stars can form via accretion if the accretion rate is significantly enhanced over the low-mass scenario. Enhanced accretion via a disk is capable of overcoming the extreme radiation pressure to build stars up to 100 $M_\odot$(e.g. Yorke & Sonnhalter 2002; Tan & McKee 2004; Krumholz et al. 2005; Krumholz 2006).

- **Dynamical interaction and mergers.** Massive stars may form through mergers of low-mass protostellar condensations at the heart of a cluster (e.g. Bonnell et al. 1998; Bonnell & Bate 2006). Support for this theory comes from the fact that massive stars tend to form in clusters. Simulations have shown that the merger must take place early on in the evolution of the cluster.

1-3 The star forming environment

All stars are born inside molecular clouds that vary in mass from a few to $\sim 10^6$ solar masses. At the high end of this mass scale, the basic unit of Galactic structure is the giant molecular cloud (GMC), formed as a result of interactions between the dusty interstellar medium and the propagating spiral density wave in the Galaxy (Elmegreen 1979). GMCs support a number of different environments related to star

formation. At the boundaries of the GMC the interstellar UV radiation field creates photon-dominated regions (PDRs) where the molecular gas is dissociated into its atomic components (Wannier et al. 1983). The shielded inner parts contain myriad clumps of molecular gas, some of which may collapse to form massive stellar clusters, resulting in embedded ultracompact HII regions, ionised by newborn OB-stars.

1-3.1 Clouds, clumps and cores

It is difficult to compartmentalise molecular clouds into sub-structures with similar properties because of the fractal nature of the interstellar medium. Solomon et al. (1987) found that the mass of molecular clouds follows a power law, implying there is no characteristic size. Nonetheless, the scales on which star formation takes place allow us to state typical values.

Traditionally, the star forming environment has been divided up into two components: 'dark clouds' which give birth only to isolated low mass stars, and GMCs, inside which multiple massive stars are formed. This distinction is somewhat artificial as the properties of the two cloud types are observed to overlap somewhat. Increasingly dense and warm sub-structures have been identified in both types of cloud. A consistent nomenclature has yet to emerge in the literature for this small scale structure, however, Table 1.1 presents the terms adopted in this work and typical values for size, mass, temperature and density.

1-3.2 UCHII Regions

Ultracompact HII (UCHII) regions are expanding bubbles of ionised gas, formed when a massive protostar at the centre of its cocoon begins emitting UV photons. It is thought that only stars of spectral type earlier than B3 are capable of producing the necessary ionising flux of Lyman continuum photons ($h\nu > 13.6\,eV$), e.g., Crowther & Conti (2003). For stars earlier later B0 the flux of UV photons emitted drops off rapidly (Panagia 1973). Initially the UCHII region expands rapidly outwards as the ionisation front moves through the ISM. The flux of photons decreases

Table 1.1. Typical physical parameters for structures in the ISM.

		Size (pc)	Mass $M_\odot$	Density (cm^{-3})	Temperature (K)
Giant Molecular Clouds	Complex	∼50	$\sim 2 \times 10^5$	100–300	10–15
	Cloud	3–20	10^3–10^4	10^3–10^4	15–40
	Clump	0.5–3	10–10^3	10^4–10^6	30–90
	Core	<0.5	10^3–10^6	$> 10^6$	30–200
	Hot Core	0.1–0.5	10^2	$> 10^7$	90–300
	UCHII Region	<0.1	–	$> 10^4$	$\sim 10^4$
Dark Clouds	Complex	6–10	10^3–10^4	10^2–10^4	∼10
	Cloud	0.2–4	5–500	10^2–10^4	8–15
	Core	0.1–0.4	0.3–10	10^4–10^5	∼10
	Hot Corino	<0.01	∼2	10^5–10^8	>90

Assembled from Cernicharo (1991), Garay & Lizano (1999), Ceccarelli et al. (2000) , (Kurtz et al. 2000) and (Fuente et al. 2005).

with distance and the rapid expansion phase comes to an end when the number of ionisations equals the number of recombinations. At this point the UCHII region fills a sphere with the Stromgren radius (Strömgren 1939). Temperatures in the ionised gas are typically 10^4 K and the resulting pressure gradient between the hot gas and the surrounding cool gas causes further expansion at the sound speed in the medium.

Observed UCHII regions rarely show the ideal spherical morphology one would expect from the above scenario. Wood & Churchwell (1989b) surveyed the Galactic Plane for UCHII regions and classified them by morphological type. They found that 20 per cent had spherical shapes, 16 per cent showed core-halo morphologies, 4 per cent had shell structures, 17 per cent were irregular and 46 percent were unresolved. It is thought that stellar winds have a major input of mechanical energy into the local environment from before a UCHII region develops. Winds are invoked to explain the rare spherical shell morphologies and, combined with unequal pressure gradients

in the natal gas, may also be able to explain cometary and irregular morphologies (Castor et al. 1975; Shull 1980). The motion of the powering star(s) through the ambient medium may also be responsible for cometary morphologies (Mac Low et al. 1991).

UCHII regions are best detected via observations in the infrared or at radio wavelengths because of their characteristic spectrum, illustrated in Figure 1.2. The dominant 'hump' is due to thermal emission from hot dust in a shell around the ionised gas. Radiation from the central source heats the dust, which re-emits in the infrared with a pseudo-blackbody spectrum peaking at $\sim$100 μm. At wavelengths longer than 3-mm the dust emission falls rapidly and the dominant emission is due to thermal 'free-free' radio emission from the ionised gas. At radio wavelengths the Rayleigh-Jeans distribution is a good approximation to the emission and the flux S_ν at a frequency ν is given by

$$S_\nu \approx \frac{2k}{c^2}\,\nu^2\,T_e\,\tau_\nu\,\Omega_s \qquad \text{when } \tau_\nu \ll 1 \tag{1.4}$$

$$S_\nu \approx \frac{2k}{c^2}\,\nu^2\,T_e\,\Omega_s \qquad \text{when } \tau_\nu \gg 1, \tag{1.5}$$

where T_e is the electron temperature, τ_ν is the optical depth and Ω_s is the source solid angle in steradians. The shape of the free-free portion of the spectrum is determined for the most part by the optical depth, τ_ν, derived using the expression given by Mezger & Henderson (1967)

$$\tau_\nu = 8.235 \times 10^2\, a_\nu \left(\frac{T_e}{K}\right)^{-1.35} \left(\frac{\nu}{GHz}\right)^{-2.1} \left(\frac{EM}{pc\,cm^{-6}}\right)^{-2.1}, \tag{1.6}$$

where a_ν is a frequency dependant correction factor approximately equal to unity and EM=$\int n_e^2\,dl$ is the emission measure. In the optically thin regime (Equation 1.4) $S_\nu \propto \nu^{-0.1}$, while in the optically thick regime (Equation 1.5) $S_\nu \propto \nu^2$.

In their seminal work, Wood & Churchwell (1989a) searched for UCHII regions using the Infrared Astronomical Satellite (IRAS) point source catalogue. The IRAS wavebands cover the spectrum in four windows centred on wavelengths of 12, 25, 60 and 100 μm, effectively sampling the blackbody component of the UCHII region's SED. Peaking at 100 μm, the SED of UCHII regions appear significantly reddened

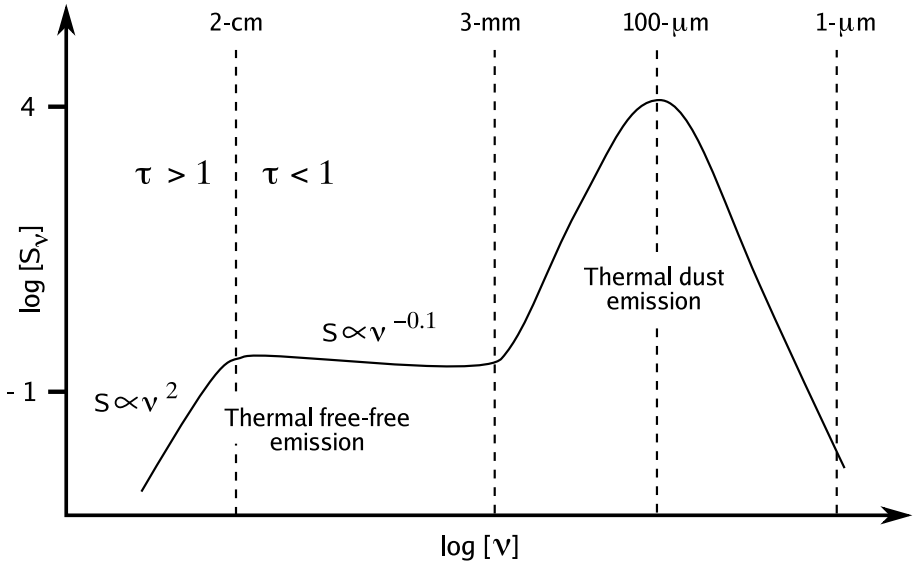

Figure 1.2. The spectral energy distribution of a UCHII region, after Churchwell (1999). At wavelengths longward of 3-mm the emission is dominated by thermal free-free emission (bremsstrahlung) from the ionised gas. Between 3-mm $\lesssim \lambda \lesssim$ 2-cm, this emission is optically thin and $S \propto \nu^{-0.1}$. At wavelengths longer than $\sim$2-cm the free-free emission is optically thick and $S \propto \nu^{2}$. At wavelengths shorter than $\sim$3-mm the spectrum is dominated by thermal blackbody emission from relatively warm ($\sim$30 K) dust, peaking at $\sim$100 μm (compared to $\sim$10 K dust in true 'cold clouds'). The wavelengths of these transition points are not fixed, but vary according to the pressure or confinement of the ionised gas (e.g., in hyper-compact HII regions) and the temperature of the thermal dust.

compared to other objects. Wood and Churchwell found that previously detected UCHII regions occupy a specific region of a colour-colour diagram defined by:

$$\log\left(\frac{f_{25}}{f_{12}}\right) > 0.57 \qquad \text{and} \qquad \log\left(\frac{f_{60}}{f_{12}}\right) > 1.3,$$

where f_x is the IRAS flux density in the waveband centred at x microns. Follow-up surveys for free-free radio continuum emission have confirmed the effectiveness of the selection criteria (e.g., Wood & Churchwell 1989b).

UCHII regions regions are obvious markers of sites of massive star-formation, as these are also the only phenomenon where a physical connection to the birth of massive stars has been firmly established. However, given the short timescales on which massive stars are formed and the propensity for massive stars to form

in clustered environments, molecular clouds containing UCHII regions are likely to harbour massive stellar objects at earlier stages of evolution (Kurtz et al. 2000).

1-3.3 Astrophysical masers

Masers are compact sites of molecular emission where certain transitions can be enormously amplified by the process of population inversion, giving rise to intense and narrow spectral lines. Physically, the emitting regions must be dense (10^6–$10^{11}\,\mathrm{cm}^{-3}$), be near an exciting source, and the masing transition must contain a high-excitation metastable level to facilitate population inversion. In a simplified 2-level case, population inversion occurs when the exciting source 'pumps' more molecules into the upper metastable state than there are in the ground state. Photons emitted due to a transition *upper*→*lower* stimulate further emission from nearby molecules and a cascade ensues. The intensity of a ray passing through the masing gas is amplified exponentially with distance travelled, until the pumping source cannot 're-stock' the metastable level fast enough and the maser saturates. Other factors which limit the amplification are the path length through the gas, the abundance of the molecule and the velocity dispersion of the gas. The requirement for a long column of gas means that the maser may operate efficiently in only one dimension and the emission will be beamed out over a very narrow opening angle. Alternatively, the structure of the maser sites may allow beaming in multiple directions, the so-called 'hedgehog' model (Sobolev et al. 1997). Determining which model applies is one of the major unanswered questions in maser research.

Masing transitions of H_2O and OH have been known to be associated with regions of massive star formation for some time (e.g. Mader et al. 1975; Reid et al. 1980; Brand et al. 1994). In the IRAS era these phenomenon were postulated to be physically connected to UCHII regions, but derived from different positions in relation to exciting sources. OH masers appeared to be confined close to the radio-continuum emission and the spread in velocity of the maser spectrum rarely exceeded $\sim$15 km s^{-1}. Proper motion observations by Bloemhof et al. (1989) clearly showed

that the general OH maser motion was expansion, lending support to an earlier theory by Elitzur & de Jong (1978) that the masers were located in the compressed shell between the shock and the ionisation fronts around HII regions. Unlike OH masers, H_2O masers are found at greater separations from the exciting source and their spectra have large velocity dispersions. The relatively high temperatures (>100 K) and densities ($\sim 10^9\,\mathrm{cm}^{-3}$) required for their excitation have been successfully modelled by highly supersonic mass outflows interacting with the clumpy ambient medium of the surrounding cloud (Genzel 1986). VLBI observations capable of resolving the maser spots lend credence to an origin in outflows, as the maser spots are often seen to form lines and arcs.

Maser emission from interstellar CH_3OH was first observed by Barrett et al. (1971) towards Orion-KL. This transition near 25 GHz was the only known CH_3OH maser transition until Wilson et al. (1984) discovered two new transitions, near 23 and 19 GHz, towards the star forming region W3(OH). Shortly after, new maser lines were discovered at 6.67 GHz Menten (1991b), 12 GHz (Batrla et al. 1987), 36 GHz and 44 GHz (Morimoto et al. 1985), prompting fresh interest in the field. In particular, the 6.67 GHz $J_K = 5_1 \rightarrow 6_0\,A^+$ transition of CH_3OH has proven to be comparable in strength to OH and is widespread towards massive star forming regions. For a review of the history of CH_3OH masers up until 1991 please see Menten (1991a).

OH and H_2O masers are not exclusive signposts of massive star formation – they are also found in the environments surrounding evolved stars. In contrast, the 6.67 GHz CH_3OH masers have been observed solely towards massive star forming regions. To test this transition's reliability as a tracer of massive stars Minier et al. (2003) conducted a sensitive survey of 13 low-mass young stellar objects. No detections were reported down to a 4-σ sensitivity of 400 mJy, supporting the hypothesis that 6.67 GHz CH_3OH masers are exclusively associated with high-mass star formation.

From an observational perspective methanol masers have been divided into two groups: Class I and Class II (see Menten 1991a).

Class I masers are found offset from the UCHII regions and luminous infrared

sources that trace young massive stars. Transitions in this class include the 25 GHz $J_2 \rightarrow J_1$ E lines, which have Orion-KL as their prototype, and the 36, 44, 84 and 95 GHz lines. The pumping mechanism for class I masers is thought to be related to shocks associated with mass outflows (Plambeck & Menten 1990), and they are frequently found coincident with H_2O masers.

Class II masers include the 6.67, 12, 19, 23, 37 and 38 GHz lines. They are typically found close to UCHII regions, at the same positions as OH maser emission (Norris et al. 1988). Unlike OH masers, individual maser spots sometimes appear to be distributed along lines or arcs suggesting origins in disks, jets or shock fronts.

Up until the mid 90s, 6.67 GHz CH_3OH masers were thought to be directly associated with UCHII regions and luminous infrared objects. Prior to that time most observations were conducted using single dish telescopes e.g., the unbiased surveys of Menten (1991b), MacLeod & Gaylard (1992), Caswell et al. (1995) and Ellingsen et al. (1996), and the surveys targeting colour-selected IRAS sources, e.g., Schutte et al. (1993), van der Walt et al. (1995) and Walsh et al. (1997). High resolution observations of these same sites were later conducted using VLBI instruments and the ATCA e.g., Caswell (1997), Norris et al. (1993) and Ellingsen et al. (1996). ATCA observations by Walsh et al. (1998, 1999) demonstrated that CH_3OH maser sites are in fact offset from the free-free radio continuum emission (marking UCHII regions) in over 80 per cent of sources. Follow-up observations have revealed that the maser sites are located on the peaks of compact millimetre and sub-millimetre thermal emission from dusty 'clumps' (Walsh et al. 2003; Hill et al. 2005). It has been postulated that these clumps represent an even earlier stage of massive star formation, prior to the UCHII phase. Independent observations have identified similar luminous and warm clumps of molecular gas as being excellent candidates for an earlier phase of massive star formation. Dubbed 'hot molecular cores', it is one of the goals of this work is to investigate the link between CH_3OH maser sites and the hot molecular core phenomenon.

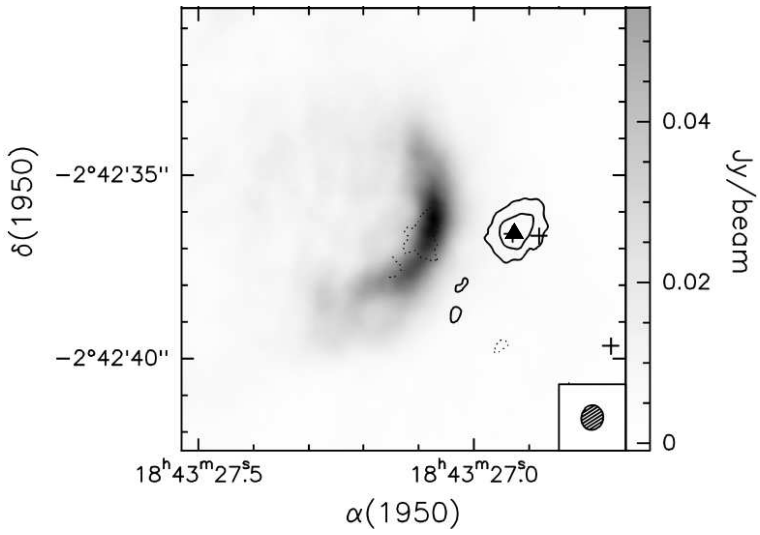

Figure 1.3. The UCHII region and hot core in G29.96−0.02, taken from Cesaroni et al. (1998). The hot core is traced by NH_3 (4,4) emission (contours), while the UCHII region is seen in via free-free continuum emission at 1.3-cm (grey-scale). The UCHII region and hot core are separated by only $\sim 5''$. Sites of 22 GHz water maser emission and 6.67 GHz methanol maser emission are marked by crosses and triangles, respectively.

1-3.4 Hot molecular cores

Hot molecular cores are knots of dense, compact and warm molecular gas detected towards massive star forming regions, and may represent an even earlier stage of evolution than UCHII regions.

Classification as a 'hot core' is done purely by observation. They are distinguished by the presence of molecular emission from high excitation lines (e.g. CS (7 – 6), Plume et al. 1992) and organic species rare in the quiescent interstellar medium. The emitting region is unresolved in single-dish observations (beam sizes $> 30''$), however, recent interferometric observations have shown the emitting regions to have diameters of < 0.1 pc and densities of $> 10^7\,\mathrm{cm}^{-3}$ (see Kurtz et al. 2000 for a summary). In addition, observations of high excitation transitions of NH_3 have shown that the average kinetic temperature of the gas ranges between 100 – 250 K (Cesaroni et al. 1992). Chemically, hot cores are abundant in complex organic molecules rare in the cold interstellar medium. This rich chemistry is attributed

to the evaporation of organic ices from dust grains heated above 90 K. We describe this chemistry in later sections.

Early single-dish observations had insufficient resolution to disentangle confused star forming environments and the link between hot cores and other tracers of massive stars, such as methanol masers and UCHII regions was far from clear. Today, only a handful of hot cores have been studied at high resolution and we do not know if they are the exception or the norm. One of the best studied regions, and an illustrative example, is G29.9−0.02 (Hofner et al. 1996; Cesaroni et al. 1998; Pratap et al. 1999; De Buizer et al. 2002; Olmi et al. 2003). Figure 1.3, taken from Olmi et al. (2003), illustrates the structure of the region. A cometary HII region, delineated by the free-free radio continuum emission (greyscale) is seen to the east, while the hot core, traced by NH_3 (contours) is the compact blob in the west. The offset between the two regions is $\sim 5''$, comparable to the scale of the hot core itself. On the image, crosses mark the positions of H_2O masers and triangles mark the position of methanol masers. Interestingly, both maser types are coincident with the hot core, rather than the UCHII region. The location of the hot core at the leading edge of the cometary UCHII region suggests that pressure from the expanding UCHII region may be responsible for compressing the gas in the hot core, meaning that the hot core is a younger object.

An important question to ask is: What and where is the heating source for hot cores? The cores may be externally heated, by nearby UCHII regions for example, and simply be by-products of the clumpy nature of giant molecular clouds. For this to be true the luminosity of the hot core must be less than the luminosity of the UCHII region by a factor of $\Omega/4\pi$, where Ω is the solid angle subtended by the hot core from the UCHII region (Garay & Lizano 1999). The hot cores in G32.80+0.19 and G61.48+0.09 are examples of such regions (Gomez et al. 1995). Alternatively, internally heated hot cores are excellent candidates for a phase of star formation prior to the onset of the UCHII phase. For example, the hot core G10.47+0.03 has been observed at sub-arcsecond resolution by Cesaroni et al. (1994) and Olmi et al. (1996) in the NH_3(4,4) line. These observations show that a temperature gradient exists,

peaking towards the centre, where two small UCHII regions are located, suggesting that the core is internally heated, perhaps by high mass stars. The temperature in G29.96−0.02 and G31.41+0.31, also mapped by Cesaroni et al. (1998), increases towards the centre adding weight to the case for internal heating.

If hot cores represent an early phase of massive star formation one might expect to see evidence of infalling motions and outflows, similar to the case of low mass stars. There is ample observational evidence to support this assertion. Line velocity shifts suggesting Keplerian rotation in accretion disks have been detected in molecular tracers such as NH_3 (4,4) and CH_3CN. In addition high resolution VLBI observation of maser sites show some maser spots may trace disks and others outflows. The line profiles of molecules observed towards hot cores also exhibit broad linewings suggestive of high velocity outflows. For example, maps of the massive star forming region G323.74−0.26 and G331.28−0.19 in H_2 emission by Lee et al. (2001) contain broad fan-shaped regions of red and blue-sifted gas diagonally opposed across the central sources. More recently Gibb et al. (2004) utilised the BIMA interferometer and the H_2S line to detect well collimated outflows towards four known hot cores: G9.62+0.19, G10.47+0.03, G29.26−0.02 and G31.41+0.31.

1-3.5 Cold cores and IR-dark clouds

The precursors to Class-0 young stellar objects (YSOs) have been identified as isolated and compact (0.1 – 0.2 pc) areas of extinction set against the optical background of the Galaxy (Bok & Reilly 1947). These 'Bok Globules' have been studied extensively at optical, infrared and radio wavelengths (e.g., Kandori et al. 2005). By measuring the reddening of stars behind the dark globules, or by comparing star counts with nearby unobscured fields, the visual extinction and hence the mass and density profile of the globules can be found. Typically, these objects have high densities ($10^5 - 10^6\,cm^{-3}$), low masses ($0.5 - 5\,M_\odot$) and kinetic temperatures of $\sim$10 K (e.g., Motte et al. 2003). Maps of the sub-millimetre continuum emission have confirmed the presence of cool and dense dust, which conforms closely to the

morphology of the extinction (e.g., Huard et al. 1999). Investigations of several Bok globules have revealed several deeply embedded YSOs emitting in the infrared (e.g., Lada & Wilking 1984) and driving collimated jets (e.g., Massi et al. 2005), confirming their star-forming nature.

We expect analogous dark clouds to exist as precursors to massive young stellar objects (MYSOs), except with correspondingly greater densities and masses. Excellent candidates have been discovered in the infrared dark clouds (IRDCs), first detected by ISO[1], and then in bulk by the MSX[2] satellite. IRDCs appear as regions of high extinction against the mid-infrared Galactic background at 8 μm. Rathborne et al. (2006) have conducted a recent study of 38 IRDCs which lie within the BU-FCRAO[3] Galactic Ring Survey (Simon et al. 2001; Jackson et al. 2006). They find that most IRDCs contain multiple compact cores, with similar sizes, masses and densities to hot cores associated with individual high mass stars. Because the detection of IRDCs require a bright background, the sample are biased towards nearby clouds. Clouds with similar physical properties almost certainly exist scattered throughout the galactic plane. Potentially the best way to detect and study these objects is at sub-millimetre wavelengths, where their spectral energy distribution peaks. Such a sample has been compiled by Hill et al. (2005), who mapped 1.2-mm thermal continuum emission towards a large sample of methanol masers and detected 41 confirmed IRDCs. It is interesting to note that the morphology of the 1.2-mm continuum emission matches the mid-infrared extinction extremely well. In Chapter 6 we investigate the infrared dark filament associated with the giant HII region NGC 3576, with the goal of assessing its star-forming state.

1-3.6 An evolutionary scenario

Considering the observational evidence cited in the previous sections, the following evolutionary sequence has been proposed by a number of authors (e.g. Walsh et al.

1. Infrared Space Observatory
2. Midcourse Space Experiment
3. Boston University-Five College Radio Astronomy Observatory

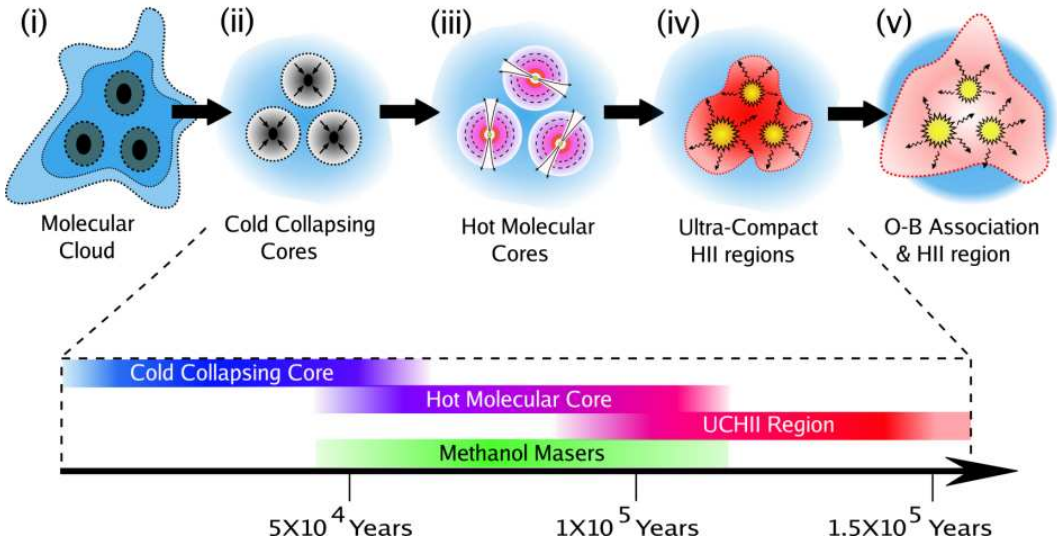

Figure 1.4. Illustration showing the proposed evolutionary scenario of a cluster of massive stars. (i) Massive stars are born in dense knots of cold gas and dust at the heart of giant molecular clouds. (ii) These knots collapse into cores under self gravity and increase in mass, via mergers or accretion. (iii) Heat and outflows from the central protostar evaporate simple ices from the dust grains, driving a rich time-dependent chemistry and leading to the production of complex hydrocarbons in a 'hot core'. (iv) UV-radiation from the young embedded stars creates a bubble of ionised gas, known as an ultra-compact HII (UCHII) region which subsequently expands, destroying the complex molecules.

1999; Minier et al. 2003):

1. Massive stars are born in dense knots of cold gas and dust at the heart of molecular clouds.

2. These knots collapse into cores under self gravity and increase in mass, via mergers or accretion.

3. Heat and outflows from the central object(s) evaporate simple ices from the dust grains, driving a rich time-dependent chemistry and leading to the production of complex hydrocarbons in a 'hot molecular core'. CH_3OH masers turn on early in this phase.

4. UV-radiation from the young embedded stars create a bubble of ionised gas,

known as an ultra-compact HII region, which subsequently expands, destroying the complex molecules and the methanol masers.

5. The continuing expansion of the hot ionised gas forms a giant HII region. Eventually, the gas is dissipated by the ionised winds, exposing the young cluster.

A representation of this scenario is shown in Figure 1.4. The timescales for each phase are uncertain, as are the times at which the CH_3OH masers turn on and off. That the Walsh et al. (1998, 1999) surveys detected CH_3OH masers towards only $\sim$20 per cent of UCHII regions suggests that the conditions leading to maser emission are disrupted shortly after a detectable UCHII region is formed. The turn-on time for masers is less certain and requires an investigation of the prevalence of hot core chemistry towards a large sample of masers. We present the results of such a survey in Chapters 4 and 5.

1-4 Chemical evolution

To date, the rotational spectra of over 120 molecules have been measured in the interstellar medium, primarily through emission at millimetre wavelengths[4]. The vast majority of these have been observed towards star forming environments and give access to the physics and chemistry on scales ranging from GMCs to low-mass prestellar cores.

Rotational spectral lines provide a useful probe of the physical conditions in molecular clouds. The intensity of the line is related to the density, temperature and pressure of the gas, while the shape of the line profile in addition reflects the velocity field and optical depth along the line of sight (see Chapter 2). However, the chemistry and physical conditions are intertwined. On the one hand, emission by molecules acts to cool molecular clouds by radiating away energy. Conversely, the chemical state of a cloud is dictated by the physical temperature and density.

4. The Cologne Database for Molecular Spectroscopy maintains an up-to-date list of the molecules detected in the interstellar medium at: http://www.ph1.uni-koeln.de/vorhersagen

Molecules do not exist in isolation, but are part of complex networks of reactions, which convert one species to another, and back again. A full understanding of the processes of star formation requires a combined model of the physical and chemical conditions.

The short time over which massive star forming regions evolve ($\sim 10^5$ yrs) mean that the reaction networks do not have time to establish equilibrium and settle down to a steady state. Thus, the relative abundances of molecules will be unique in time, and may act as a fingerprint for a particular evolutionary state. The 'holy grail' of astrochemistry is to develop accurate models of the chemical networks, so called 'chemical clocks', with which to determine the age of massive young stellar objects.

1-4.1 Basic ingredients in the interstellar medium

The interstellar medium is composed of tenuous gas and dust at widely varying densities, pressures, temperatures and compositions. In the broad picture, 70 per cent by mass is hydrogen, 29 per cent is helium and the other 1 per cent consists of trace elements scattered throughout as dust, ices and free molecules. Hydrogen and carbon dominate the chemistry in dense molecular clouds because of their high abundances, and their affinity for forming organic compounds with each other. Other abundant molecules are nitrogen, oxygen, iron and silicon, which form important radical groups. Here we consider the initial conditions in the clouds from which massive stars form.

Matter in the interstellar medium exists as either solid or gas and the division of elements between these two phases is important for the chemistry. Solid dust grains make up 1 per cent by mass and consist of a core of amorphous carbon, silicates or iron oxides, surrounded by a mantle of simple organic ices. Based on observations of the strong 9.7 and 18 μm absorption bands (Draine & Lee 1984), almost all of the Si and Fe is locked into the core and at least 25 per cent of the O is accounted for in grain mantles. Up to 60 per cent of the total carbon is bound into carbonaceous dust grains (Mathis 1996). H_2O and NH_3 ice constitute the bulk of the mantles,

with the abundance of NH_3 at only a few percent of H_2O. 5–25 per cent of the oxygen budget is locked into H_2O ice mantles in star forming regions (Whittet 1992; van Dishoeck & Blake 1998).

Apart from H_2, which forms the body of the gas, the most abundant molecule is CO. This molecule accounts for most of gas-phase carbon (40 per cent) and up to 20 per cent of the oxygen. Atomic C or C^+ account for only a few percent inside dense clouds, but are essential for forming compounds with large molecular weight.

O, O_2, N and N_2 are difficult to observe in the ISM as they have weak or no rotational or infrared transitions and the Earth's atmosphere absorbs those that do exist. Most models predict that bulk of the oxygen in cold clouds comprises of O or O_2, and nitrogen is mostly locked up in gas-phase N_2 and N atoms (van Dishoeck & Blake 1998).

1-4.2 UV radiation and cosmic rays

UV radiation and cosmic rays are essential sources of ions in the interstellar medium. Two distinct UV fields operate in molecular clouds. The first derives from naked OB-type stars and acts to destroy molecules, resulting in photon dominated regions on the boundaries of molecular clouds and HII regions in their interior. Molecular lifetimes in such regions can be as short as $10^2 - 10^3$ yrs, however, this 'external' uv-radiation does not penetrate the shielded depths of dense clouds (beyond Av $>$ 5, Draine 1978). The second field arises from ionisation of H_2 by cosmic rays and operates throughout dense clouds. Electrons released when cosmic-rays[5] ionise H_2 can collisionally excite other H_2 molecules, which decay by emitting a UV photon. The dissociation rate is 4-5 orders of magnitude lower than that caused by the interstellar UV field, and gives rise to the free radicals and ions which lie at the root of the reaction networks. In particular, this form of ionisation leads to the production of H_3^+, an important molecule at the start of many ion-molecule reaction

5. Cosmic rays are energetic particles consisting of mainly protons and alpha particles, and a small percentage of heavy nuclei, electrons and gamma rays.

Table 1.2. Formation and destruction reactions (from Hogerheijde 2005).

Radiative association	$X + Y \leftrightarrow XY^* \leftrightarrow XY + \nu$
Photodissociation	$XY + \nu \rightarrow X + Y$
Associative detachment	$\begin{cases} X + e \rightarrow X^- + \nu \\ X^- + Y \rightarrow XY + e \end{cases}$
Dissociative recombination	$X^+ + e \rightarrow X + \nu$
	$XY^+ + e \rightarrow \begin{cases} XY + \nu \\ X + Y \end{cases}$
Gas-phase neutral-neutral reaction	$X + YZ \rightarrow XY + Z$
Gas-phase ion-neutral reaction	$X^+ + YZ \rightarrow XY^+ + Z$
Charge transfer	$X^+ + YZ \rightarrow X + YZ^+$
Grain-surface reactions	$X + \mathcal{G}{:}Y \rightarrow X{:}\mathcal{G}{:}Y \rightarrow \mathcal{G}{:}XY \rightarrow \mathcal{G} + XY$

pathways (Hogerheijde 2005):

$$H_2 + \mathcal{CR} \rightarrow H_2^+ + e$$

$$H_2^+ + H_2 \rightarrow H_3^+ + H.$$

For example, H_3^+ reacts rapidly with CO or N_2 to form HCO^+ and N_2H^+. The primary cosmic-ray ionisation rate ζ_0 is thus an important parameter in chemical models.

1-4.3 Types of reaction

Two broad classes reaction are invoked to explain the chemistry in the dense clouds which form massive stars: gas-phase reactions and grain surface reactions. Chemical models, based on gas-phase ion-molecule reaction networks driven by cosmic ray ionisation, have been largely successful in explaining the abundances of simple hydrocarbons in cool (T<50 K) dense ($10^4\,\mathrm{cm}^{-3}$) clouds (van Dishoeck & Blake 1998 and references therein). However, gas-grain reactions are necessary to explain the abundance of ices on the dust grains and the enhanced abundances of certain species in higher temperature gas (Turner 1996; Boogert et al. 1996, 1997).

The rate of a reaction between two species A and B is proportional to the number densities, n_A and n_B, and to the rate coefficient k. Reactions can be endothermic

(require net energy input) or exothermic (release net energy), however, even exothermic reactions may require an initial input of 'activation energy' to break bonds, and will not take place at low temperatures. The types of reaction are given in Table 1.2.

Gas phase reactions

At the low densities typical of molecular clouds, reactions in the gas phase involve two bodies. Three-body reactions only play a role in shocks and in the inner regions of protoplanetary disks, where molecular densities exceed $\sim 10^{12}\,\mathrm{cm}^{-3}$ (Hogerheijde 2005).

At low temperatures the chemistry is dominated by gas phase ion-molecule reactions, as the activation energy for these is low, or zero. Typical reaction rates are $\sim 10^{-9}\ \mathrm{cm}^{-3}\,\mathrm{s}^{-1}$.

Dissociative-recombination reactions involving free electrons have large rate coefficients (typically $\sim 10^{-6}\ \mathrm{cm}^{-3}\,\mathrm{s}^{-1}$) due to Coulomb attraction. Despite the high rates, the efficiency in dense clouds is poor as low electron abundances ($\sim 10^{-8}\ \mathrm{cm}^{-3}$) limit the reaction rate (Hogerheijde 2005).

Neutral-neutral reactions have rates between 10^{-12} and $10^{-10}\,\mathrm{cm}^{-3}\,\mathrm{s}^{-1}$, and usually have large activation barriers, and so only take place efficiently in warm, dense gas (Hogerheijde 2005).

Grain surface reactions

Reactions with large activation energies can proceed on the grain because of the long time over which the species remain bound. The lightest atom, hydrogen, is extremely mobile on the grain surface and can 'hop' over the entire surface before evaporating. The grain surface thus acts as a catalyst for neutral-neutral reactions at low temperatures (van der Tak 2005). This leads to the production of hydrogenated species with saturated bonds (mainly single bonds), such as CH_4 and NH_3, and of course H_2.

At higher temperatures heavier radicals have sufficient energy to diffuse over the

surface, allowing a more complex reactions to proceed (e.g. Caselli et al. 1993). Above temperatures of $\sim 60\,\mathrm{K}$ polymerisation reactions involving H_2CO, NH_3 and CH_3OH ice can produce compounds of high molecular weight (Schutte et al. 1993). Further reactions involving thermal heating, cosmic rays and radiation facilitate the production of complex non-volatile organic compounds, and are referred to collectively as 'processing' in the literature.

1-4.4 Cold core chemistry

In cold ($< 10\,\mathrm{K}$), dense ($> 10^4\,\mathrm{cm}^{-3}$) cores prior to collapse the gas-phase chemistry is dominated by low-temperature, ion-molecule and neutral-neutral reactions. The principal products are small radicals and unsaturated molecules, primarily long carbon chains, formed through carbon insertion, condensation or radiative association (van Dishoeck & Blake 1998; Herbst & Leung 1989).

Carbon insertion	$C_2H_2 + C \rightarrow C_3H + H$
Condensation	$C_2H_2 + C_2H_2 \rightarrow C_4H_2 + H_2$
Radiative association	$C^+ + C_n \rightarrow C^+_{n+1} + \nu$

Carbon insertion is thought to be the dominant route and requires the presence of gas-phase atomic carbon as either C^+ or C. On the edges of clouds (Av<2) the buildup of long chain carbon molecules is limited by photodissociation. In the shielded interior the primary destruction routes are through reactions with C and O^+. Once the carbon and oxygen has been converted into the stable CO molecule the formation of complex hydrocarbons ceases (van Dishoeck & Blake 1998).

In an isothermal collapsing core, the resulting increase in density causes molecules to condense around dust grains on a timescale of $t_{acr} \approx 2 \times 10^9\,(n_H\,y_s)^{-1}$ sec, (Hogerheijde 2005) where $y_s = 0.1$–1.0 is the probability that a molecule sticks (Williams 1993). Modelling suggests that virtually all species will condense onto the dust grains over time, except H_3^+, whose main removal partners CO, H_2O, and O are depleted from the gas. Species formed from H_3^+, e.g. N_2H^+ and HCO^+ may remain as good tracers of early collapsing cores (Bergin & Langer 1997). In practise

depletion is difficult to observe because of the 'skin effect' (McMullin et al. 1994). In a centrally depleted cloud there will exist a shell, or skin, of molecules in which the abundances are normal. If the optical depth is high even relatively small abundances in the shell are capable of obscuring the depleted region.

The composition of the ices formed changes with increasing density. At densities lower than $10^4\,\mathrm{cm}^{-3}$, H is more abundant than O in the gas phase and the production of hydrogenated species is favoured (e.g., H_2O, NH_3, CH_4, H_2S, H_2CO and CH_3OH) (van der Tak 2004). At intermediate densities the gas phase carbon is locked into CO and this reacts on the grain surface with the small amount of H, produced by cosmic rays to form, H_2CO and CH_3OH ices. A small amount of the CO reacts with the O to form CO_2 also. At high densities non-polar[6] ices are formed by preference as most of the oxygen and nitrogen are in the form of O_2 and N_2. The polar ices condense first, leaving the non-polar ices to form a crust. Segregation of the ices may also depend on grain size. Spot heating by UV photons leads to higher effective temperatures on smaller grains and these ices may be processed to more complex non-volatile organics (Greenberg et al. 1993). Infrared absorption spectra of ice mantles in cold clouds can give the potential species in this group.

Ices will remain on the grain until a heating event (e.g cosmic ray spot heating, collisional heating or exothermic chemical reactions) raises the dust temperature (Leger et al. 1985; Dhendecourt et al. 1982). CO ice desorbs at approximately 20 K and H_2O ice at approximately 90 K. Molecules in mixed polar ices are expected to evaporate at the same temperature as H_2O (Sandford & Allamandola 1993).

1-4.5 Hot core chemistry

Observationally hot cores are distinguished by temperatures greater than 100 K and high abundances of 'exotic' organic molecules that cannot be explained solely

6. The distribution of electrons over a polar molecule is uneven resulting in a net electric field. Weak electromagnetic bonds form between adjacent molecules, making them more difficult to evaporate. H_2O is an example of a polar species.

Table 1.3. Species found in hot cores.

Primary species	H_2O, NH_3, CH_4, CO, CH_3OH. C_2H_2, H_2CO, O_2, N_2
First generation species	$HCOOCH_3$, HCN
Daughter species	CH_3OCH_3, HC_3N, C_2H_2CO, CH_2CHCN, CH_3CN

by ion-molecule gas-phase reactions. The enhanced abundances are attributed to evaporating grain mantles fuelling a rich chemistry in the warm gas. Three kinds of species are distinguishable in hot cores:

1. Primary species, present in the cold core phase, depleted onto the grains and subsequently released unaltered.

2. First generation species created by grain surface reactions, which subsequently desorb from the dust.

3. Daughter molecules produced from gas phase reactions in the hot core.

Table 1.3 presents examples of species falling into each category. Some uncertainty surrounds the classification of first generation and daughter species, as the exact composition of the ice mantles is still debated in the literature (e.g., is CH_3CN formed on the grain?).

Two species in particular, CH_3OH and NH_3, react to form large molecules. Both can form long carbon chains after acquiring a proton from H_3^+, H_3O^+ or HCO^+ (van der Tak 2004). Competition between these reaction paths for protons may have a defining effect on the chemistry, leading to either O-rich or N-rich cores. Above $\sim 300\,\mathrm{K}$ reactions of O and OH with H_2 operate very efficiently to convert all the available oxygen into H_2O (Charnley 1997). Cores at higher temperatures are expected to be rich in N-bearing species (Rodgers & Charnley 2001). Observational

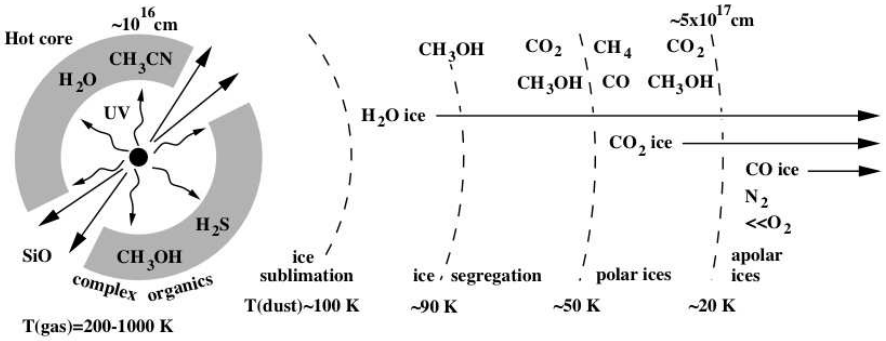

Figure 1.5. Schematic of the physical and chemical environment of a hot core (taken from van Dishoeck & Blake 1998). Dubbed the 'onion-layer effect', temperature and density gradients lead to distinct chemical shells at different radii. The diagram represents a snapshot of the chemistry at a single time. Changes in the temperature and density profiles as the hot core evolves would cause the shells to expand outward.

support comes from the work of Wyrowski et al. (1999) who measured the peak position of the N-bearing species to be at a higher temperature than the peak of the O-bearing species in the W3 star forming complex.

One major conclusion arising from this thesis is that most hot cores appear to be internally heated (see Chapter 4). The centrally peaked temperature and density profiles is predicted to lead to an 'onion layer' effect where different ice mantles evaporate at different radii from the powering source. Figure 1.5 is a schematic of the resulting structure. Volatile non-polar ices evaporate more readily than polar species leading to a distillation effect in the inner core as the temperature rises. All mixed polar ices are expected to evaporate above 90 K (Sandford & Allamandola 1993). If species were formed exclusively on the grain, or as daughter species, a radially averaged plot of the abundance will have a 'jump' profile (Figure 1.6 *left*). Inside the evaporation radius r_{evap} the species will be abundant, whereas at greater radii the abundance will negligible. Molecules present in the gas-phase of the primordial cold cloud will exhibit 'drop' profiles (Figure 1.6 *right*) caused by depletion onto the grains inside the accretion radius r_{acc}. Again at radii $<r_{evap}$ the abundance will be high, but at large radii $>r_{acc}$ the primordial abundances

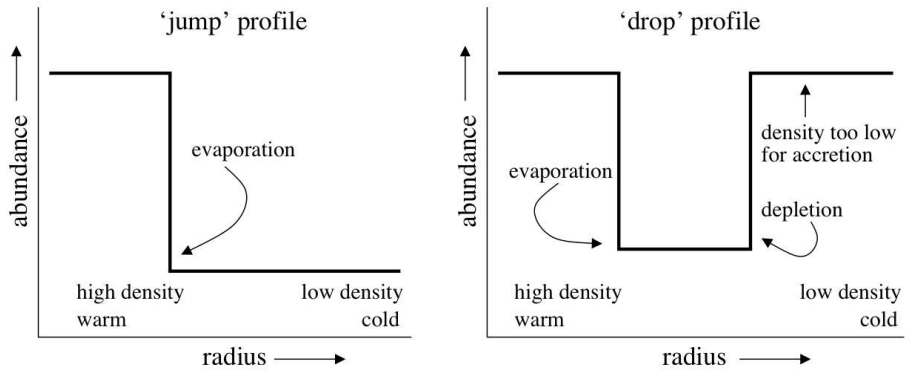

Figure 1.6. Jump (left) and drop (right) abundance profiles, taken from Hogerheijde (2005), after van der Tak et al. (2000) and Jørgensen et al. (2004). Jump profiles are predicted to occur for first generation or daughter species as the expanding evaporation front liberates molecules from the grains. Drop profiles are predicted to occur for cold core species, which are depleted in an annulus around the central heating source. In the central regions, heat from the powering source evaporates the molecules from the dust grains, while in the diffuse outer halo the density is too low for the molecules to deplete.

will not be affected by depletion within the lifetime of the core (Hogerheijde 2005). Observations of 'jump' profiles have been reported by van der Tak et al. (2000), Schöier et al. (2002) and van der Tak et al. (2003) for the molecules H_2CO, CH_3OH, SO, SO_2 and OCS at temperatures of T≈100 K. Drop profile have also recently been observed by van Dishoeck et al. (2005) in a single-dish survey of 18 deeply embedded young stellar objects.

1-4.6 Shock and outflow chemistry

The hot core environment is further enhanced as the powering source turns on outflows and jets, propelling shocks into the envelope. Two types of shock are identified in the literature: C (or continuous shocks) and J (or jump), (Hollenbach 1997).

C shocks propagate at speeds less than $\sim 40\,\mathrm{km\,s^{-1}}$ and have peak temperatures of 2000–3000 K, allowing gas phase reactions with substantial energy barriers to take

place. In particular, the reaction pathways

$$O + H_2 \rightarrow OH \rightarrow H_2O$$

$$S + H_2 \rightarrow SH \rightarrow H_2S$$

drive all the available oxygen and sulphur into OH, H_2O and H_2S (van Dishoeck & Blake 1998). In shocks with speeds $> 25\,\mathrm{km\,s^{-1}}$grain-grain collisions or sputtering leads to the release of large columns of refractory material like SiO (Schilke et al. 1997). Less violent shocks ($v_s < 10\,\mathrm{km\,s^{-1}}$) in the walls of outflow cavities can result in the evaporation of grain mantles, releasing large quantities of H_2O, and species such as CH_3OH and HCN. H_2O destroys N_2H^+, which is expected to be absent from shocked regions.

In faster J shocks the region heated by the shock front is thin compared to the cooling length. The temperature in the shocked gas reaches $10^5\,\mathrm{K}$, high enough to dissociate all molecules. Mechanical destruction of dust grains again releases large columns of SiO.

Chemical models by Viti et al. (2001) suggest that NS/CS, SO/CS and HCO/H_2CO abundance ratios may be useful tracers of the presence of shocked gas. OH is required to form NS, but is driven into H_2O in hot shocked gas, thus a low ratio (0.001–0.1) may indicate a shock has passed through the gas. However, the cool envelope chemistry models of Doty et al. (2002) also predict similar NS/CS ratio and this molecule cannot be used as an indicator of shocks (van der Tak 2004). Rawlings et al. (2004) predict the abundance of HCO^+ will be enhanced in outflows.

Enhancements to the molecular abundances due to shock processing will not affect the bulk of the gas, and so may be difficult to detect in single dish observations.

1-5 Molecules in this thesis

Here we briefly examine the molecules observed in this thesis as a knowledge of the conditions under which they exist and emit radiation are necessary for the correct interpretation of observations.

Carbon-monoxide: CO

CO has an abundance relative to H_2 of approximately 10^{-4} (van Dishoeck et al. 1992) and is often used to infer the gas-mass of molecular clouds. The 115 GHz J=1→0 transition is generally optically thick in Galactic clouds and is used as an indicator of gas temperature. The ^{13}CO isotopomer may also be moderately optically thick, while C^{18}O is almost always optically thin.

Methyl-cyanide: CH_3CN

CH_3CN, also known as acetonitrile, is a classical 'hot core' tracer, formed in the gas from evaporated grain mantles. Some dispute over the origin of CH_3CN exists, as there may be alternative formation routes available through grain-phase chemistry (Millar et al. 1997). The dominant gas-phase formation route is thought to be radiative association (Mackay 1999 and referenced therein):

$$CH_3^+ + HCN \rightarrow H_4C_2N^+ + h\nu,$$

followed by dissociative recombination

$$H_4C_2N^+ + e^- \rightarrow CH_3CN + H.$$

The precursor HCN is formed in the gas phase through the reaction of atomic N with HCO, CH_2, CH_3 or CH_3^+.

The spectrum of CH_3CN is useful as a temperature probe. Molecules with 'symmetric rotor' geometry have unique spectra, exhibiting multiple lines within a short frequency interval. The relative intensities of the lines can be used to estimate the kinetic temperature in the gas, with the assumption of optically thin conditions and that only collisions can excite the molecule (see Chapter 2 and Chapter 4).

Methanol: CH_3OH

The absorption bands of CH_3OH have been observed in ISO spectra towards star forming regions (Tielens & Allamandola 1987). It is thought to be formed on the grain surface and subsequently desorbed by a heating event into the gas phase.

The geometry of CH_3OH is slightly asymmetric and it consequently has an extraordinarily complex spectrum, with well over 200 lines in the frequency range between 834 MHz and 360 GHz (Elitzur 1992). Like CH_3CN, parts of its spectrum have closely spaced lines which can be used to derive a temperature. The derived temperature is less useful, however, as the excitation depends on factors other than collisions and is only weakly linked to the kinetic temperature of the gas (see Chapter 5 and Goldsmith & Langer 1999).

CH_3OH is a key ingredient in the early chemistry of a protostellar envelope as it lies at the root of most reaction networks. Many species can be seen as daughter molecules of either CH_3OH or NH_3 (Charnley et al. 1995). Its abundance is predicted to be enhanced in outflows and hot cores, where it evaporates from the dust grains.

Ammonia: NH_3

NH_3, the first polyatomic molecule detected in the interstellar medium, was found by Cheung et al. (1968), and has since been detected in a wide variety of environments, from cool dark clouds to hot molecular cores.

Abundances up to 10^{-8} compared to H_2 can be produced via ion-molecule gas-phase chemistry (Scott et al. 1997):

$$\begin{aligned} N + H_3^+ &\rightarrow NH_2^+ + H \\ NH_2^+ + H_2 &\rightarrow NH_3^+ + H \\ NH_3^+ + H_2 &\rightarrow NH_4^+ + H \\ NH_4^+ + e^- &\rightarrow NH_3 + H. \end{aligned}$$

Dissociation reactions compete to convert NH_3 back into NH_4^+, however, the reactions are temperature dependant so the synthesis of NH_3 may be enhanced at low temperatures (10-20 K) in dark clouds. In warm gas-grain chemistry desorption is likely important (Ho & Townes 1983).

NH_3 has an advantage over CH_3CN as a kinetic temperature probe. Individual

rotational-vibrational spectral lines are split into five hyperfine-components, the relative amplitudes of which can be used to derive the optical depth in the gas. In addition, the collisional rates with H_2 have been extensively modelled and the link between the excitation of NH_3 and the kinetic temperature is well understood. We examine the quantum origin of the NH_3 spectrum in Chapter 2 and explain the method for calculating kinetic temperatures.

The hyperfine lines of NH_3 (1,1) often exhibit anomalous intensity ratios towards star forming regions. Park (2001) investigated the effect using radiative transfer codes and concluded that the skewness of the spectrum could be a good probe of systematic motions inside dense cores with high optical depths. Caution much be be exercised, as skewed profiles may also be due to non-LTE excitation (Stutzki & Winnewisser 1985).

Formyl Ion: HCO^+

HCO^+ is a moderate density tracer ($n \approx 3\times10^5\,cm^{-3}$) and a useful probe of the kinematics in star formation regions. In a typical molecular cloud the J=1→0 transition is generally self absorbed (e.g., Hogerheijde et al. 1997 and this work), caused by layers of cool gas overlying a warmer core. Transitions of the isotopomer $H^{13}CO^+$ are usually optically thin and a comparison between the thick and thin line profiles yields information on bulk gas motions in the envelope (see Chapter 4). Models by Rawlings et al. (2000) predict enhanced HCO^+ abundances in outflows. Sublimation of CO and H_2O ices from the grain to the gas phase fuel the reactions in the shock-induced radiation field at the head of the outflow:

$$CO + h\nu \rightarrow C + O,$$
$$C + h\nu \rightarrow C^+ + e^-$$

followed by

$$C^+ + H_2O \rightarrow HCO^+ + H.$$

This is borne up by the common detection of strong high-velocity wings in the line profiles towards massive young stellar objects (e.g. Watson et al. 2002 and this

work).

Hydrogen-cyanide: HCN and Iso-hydrogen-cyanide: HNC

HCN is one of the best indicators of an N-rich chemistry. It forms in the gas phase through reaction of HCO and CH_3 with N_2 at low temperature ($< 100\,K$) and through reactions of C^+ with NH_3 and CN with H_2 at high temperature. HCN can be seen as a daughter molecule of both CH_3OH and NH_3, and is a precursor for the formation of CH_3CN and HC_3N.

The HCN/HNC ratio in gas phase chemical models is particularly sensitive to temperature. The following reactions become relevant at high temperatures:

$$HNC + O \rightarrow NH + CO$$
$$HNC + H \rightarrow HCN + H.$$

Steady state models (Schilke et al. 1992) predict the HCN abundance and the HNC/HCN ratio decline with increasing temperature and density. This trend is seen in observations by Goldsmith et al. (1981) towards four molecular clouds.

Diazenylium: N_2H^+

Initially detected by Turner (1974), N_2H^+ was one of the first molecular ions to be discovered in the interstellar medium. Because of its moderate critical density ($n_{crit} \approx 2 \times 10^5\,cm^{-3}$, Caselli et al. 2002), and its reluctance to deplete onto the grains surface, it has been used as the preferred tracer of high density gas in quiescent or collapsing molecular clouds. The spectrum of the $J = 1 \rightarrow 0$ transition is split into seven hyperfine components, whose ratios can be used as a reliable diagnostic of optical depth along the line of sight. The primary destruction mechanism for N_2H^+ is via proton transfer to CO, so it is under-abundant in dense and warm regions where CO is abundant.

1-6 Aim and outline of thesis

The broad aim of this work is to investigate the evolutionary sequence leading to the birth of a cluster of massive stars. In particular, the stages preceding the development of a UCHII region pose the most interesting questions. These include:

- How are 6.67 GHz methanol masers related to hot cores and UCHII regions?
- Are hot cores heated by an internal heating source (e.g., a massive young stellar object) or an external heating source (e.g., a nearby UCHII region)?
- Do we find differences in the chemistry between maser sites that can be correlated with indicators of age, such as radio emission and infrared colour?
- How does the proximity of a young HII region affect nearby molecular clouds, and do we see any evidence for sequential star formation?

To answer these questions we have conducted two observational studies of massive star forming regions using different approaches. In the first instance we searched for hot core chemistry in a sample of 83 methanol maser-selected star forming clumps and UCHII regions. The results of a statistical analysis of this project are reported in Chapters 4 and 5. Secondly, we conducted a high-resolution, multi-wavelength study of a single star forming complex, NGC 3576, with the goal of investigating the effect of a giant HII region on the surrounding molecular cloud. Chapter 6 present the results of this study.

The outline of this thesis is as follows. In Chapter 2 we begin by laying the theoretical foundations of the molecular analysis used throughout the thesis. In Chapter 3 we outline the calibration methodology and data reduction pathway developed for the Mopra single-dish telescope. This serves as an introduction to Chapter 4, which presents the first four lines in the Mopra 'Hot Molecular Cores' survey: $CH_3CN\,(5-4)$, $CH_3CN\,(6-5)$, $HCO^+\,(1-0)$ and $H^{13}CO^+$,$(1-0)$. Chapter 5 presents the remaining five lines in the survey and expands the analysis to cover abundance trends. We narrow our focus in Chapter 6, where we present and analyse

the results of a multi-wavelength study of NGC 3576. We conclude in Chapter 7 by summarising our main results and discussing potential future work.

Chapter 2

Radiation as a physical probe

Our sole window on the environment of molecular clouds is provided by radiation from astrophysical processes. Gas in star-forming environments may both emit and absorb spectral line and continuum radiation, whose properties can be used to derive physical and chemical conditions. This chapter begins with a description of how radiation and molecules interact to form rotational spectra in the millimetre regime. The statistical emission and absorption properties of the gas are then used to explain how radiation is transmitted through the interstellar medium, allowing the derivation of physical parameters from observations. Lastly, the spectrum of the versatile molecular thermometer NH_3 is described, and the analysis methodology presented as a case study. The following discussion borrows heavily from Townes & Schawlow (1955), Rohlfs & Wilson (2004) and Goldsmith & Langer (1999), whose formalisms have been adopted here. Unless specifically stated, all equations and quantities are presented in the SI (MKS) unit system.

2-1 Rotational spectral lines

In the gas phase, ensembles of molecules are in constant motion related to bulk motions, turbulence and their thermal kinetic energy. In addition, individual molecules have internal energy, a portion of which is stored as rotational energy. For an iso-

lated molecule, its angular momentum is quantised in multiples of $\hbar = h/2\pi$. The rotation of any molecule may be resolved into components about three perpendicular axes through the centre of mass. Classically, rotation is described in terms of the moment of inertia I about a particular axis. This is defined as

$$I = \sum m_i \, r_i^2, \tag{2.1}$$

where r_i is the perpendicular distance of the i^{th} atom from the axis of rotation, and m_i is its mass. A rotating body with three degrees of freedom has a total kinetic energy

$$E = \frac{1}{2} [\, I_a \, \omega_a^2 + I_b \, \omega_b^2 + I_c \, \omega_c^2 \,], \tag{2.2}$$

where ω_a is the angular velocity in radians/sec about an axis 'a'. Equation 2.2 may be written in terms of the classical angular momentum, $P_a = I_a \, \omega_a$:

$$E = \frac{P_a^2}{2I_a} + \frac{P_b^2}{2I_b} + \frac{P_c^2}{2I_c}, \tag{2.3}$$

with the magnitude of the total angular momentum given by $P^2 = P_a^2 + P_b^2 + P_c^2$.

Molecular rotors fall into four groups, according to the relative values of their three moments of inertia:

Spherical Rotors:	$I_a = I_b = I_c$,	e.g.: CH_4, SiH_4.
Linear Rotors:	$I_a = 0, I_b = I_c$,	e.g.: CO, HCO+, HCN, HNC, N_2H^+
Symmetric Rotors:	$I_a = I_b \neq I_c$,	e.g.: NH_3, CH_3CN, CH_3Cl.
Asymmetric Rotors:	$I_a \neq I_b \neq I_c$,	e.g.: H_2O, CH_3OH.

To emit or absorb radiation efficiently the molecule must have a permanent dipole moment, μ[1]. Usually the dipole is an electric moment due to the asymmetric distribution of positive and negative charges on a molecule. The electronic charge on spherical and homo-nuclear linear molecules is evenly distributed and these molecules do not exhibit rotational dipole transitions. Instead much weaker quadrupole lines are observed in the infrared, due to simple collisional excitation. The quadrupole

1. Molecules without a permanent dipole moment can couple to external radiation fields via higher moments, e.g., H_2 and N_2 exhibit quadrupole transitions, however these lines are usually weak.

arises from the interaction of external electromagnetic fields with the slightly asymmetric charge distribution in the nucleus.

In the following sections we will summarise the theory necessary to derive physical properties from the spectra of symmetric and linear rotors. One slightly asymmetric rotor, methanol (CH_3OH), is analysed in the thesis. For the purpose of calculating column densities and rotational temperatures, CH_3OH may be treated like a symmetric top.

2-1.1 Rotational energy levels

Symmetric rotors have one unique axis ($I_c \equiv I_\parallel$), called the principal axis, and two identical axes ($I_a = I_b \equiv I_\perp$) perpendicular to it. The energy of a symmetric rotor may be found from Equation 2.3

$$E = \frac{P^2}{2I_\perp} - \frac{P_c^2}{2I_\perp} + \frac{P_c^2}{2I_\parallel} = \frac{P^2}{2I_\perp} + \left(\frac{1}{2I_\parallel} - \frac{1}{2I_\perp}\right) P_c^2, \tag{2.4}$$

and the quantised expression for rotational energy levels can be obtained from the Correspondence Principle by substituting the angular momentum operator, $J^2 \rightarrow J(J+1)\hbar^2$, for P in Equation 2.4. We know that the projection of the total angular momentum onto the principal axis is restricted to values of $K\hbar$, with $K = 0, \pm1, \pm2, \ldots \pm J$, so J_c^2 is also replaced by $K^2\hbar^2$. The energy levels are then given by

$$E_{J,K} = hBJ(J+1) + h(A-B)K^2 \tag{2.5}$$

with

$$A = \frac{\hbar}{4\pi I_\parallel} \quad \text{and} \quad B = \frac{\hbar}{4\pi I_\perp} \tag{2.6}$$

defined as the rotational constants of the molecule. The units of the rotational constants are Hz.

Linear rotors can be considered a special case of symmetric top, which only rotate perpendicular to the principal axis, therefore the projection of the total angular momentum onto this axis is zero, i.e., K=0. In this case Equation 2.5 reduces to

$$E_J = hBJ(J+1) \tag{2.7}$$

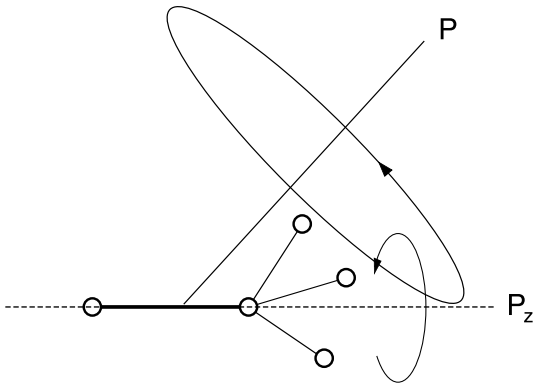

Figure 2.1. Classical motion of a symmetric rotor (adapted from Townes & Schawlow 1955). The dipole moment is parallel to the unique principal axis P_z, which itself precesses about the total angular momentum vector P.

for linear molecules and $A \equiv 0$.

2-1.2 Form of the rotational spectrum

Even simple molecules can have complicated spectra. The wavelength of a spectral line and its intensity are related to the intrinsic properties of the molecule and transition, but the physical and chemical conditions of the gas determine the final intensity and shape of the spectral lines. Quantum selection rules and centripetal distortion determine the frequencies of allowed spectral lines and the intensity is governed by the intrinsic permanent dipole moment, the degeneracy of the energy level, and the temperature, density and abundance of the gas. The following sections present the basic molecular theory from which we can derive physical properties from observed spectral lines.

2-1.2.1 Selection rules

Selection rules imposed by quantum mechanics and conservation principles mean that not all transitions between energy levels are allowed. Symmetric rotors have no dipole moment perpendicular to the axis of symmetry, hence radiation cannot change the rotational state around the principal axis, and $\Delta K = 0$. The dipole mo-

ment lies along the principal axis of the rotor P_z, as shown in Figure 2.1, which itself precesses about the total angular momentum, P. Conservation of angular momentum dictates that the change in J when a photon is emitted or absorbed must be ± 1. In the absence of other factors it can be shown that there is equal probability of any particular transition with $\Delta J = \pm 1$. If distortion of the molecule through centrifugal stretching is neglected, the frequencies observed for any $\Delta J = \pm 1$ transition do not depend on the value of K and are given by

$$\nu = 2B(J+1). \tag{2.8}$$

2-1.2.2 Centripetal distortion

Molecules are not rigid rotors. Atoms feel the effect of centripetal forces which tend to distort the geometry of the molecule. The effect is to stretch the bonds, leading to a change in the value of I and therefore a change in the value of the rotation constant B. The resultant change in the energy levels is empirically modelled by centripetal distortion constants (D_J, D_K, D_{JK}), and Equation 2.5 becomes

$$E_{J,K} = h[BJ(J+1) + (A-B)K^2 - D_J J^2(J+1)^2 - D_{JK}J(J+1)K^2 - D_K K^4]. \tag{2.9}$$

The frequency of a rotational transition $J \rightarrow J+1, \Delta K=0$ is then

$$\nu = 2(J+1)(B - D_{JK}K^2) - 4D_J(J+1)^3. \tag{2.10}$$

For a particular $J+1 \rightarrow J$ transition, spectral lines due to different K values will be shifted in frequency with respect to each other, giving rise to a 'K-ladder' spectrum. The distortion constants, D_J, D_K and D_{JK}, are very small compared to the rotational constants, A and B, so the shift is on the order of a few MHz at 110 GHz. It is this property which makes symmetric tops a good observational probe, as several K-components may be observed in the same bandpass, and relative calibration is assured. Figure 2.2 shows the energy level diagram for the symmetric rotor CH_3CN and the observed spectrum of the $J=(5 \rightarrow 4)$ K-ladder in the source G0.55−0.85.

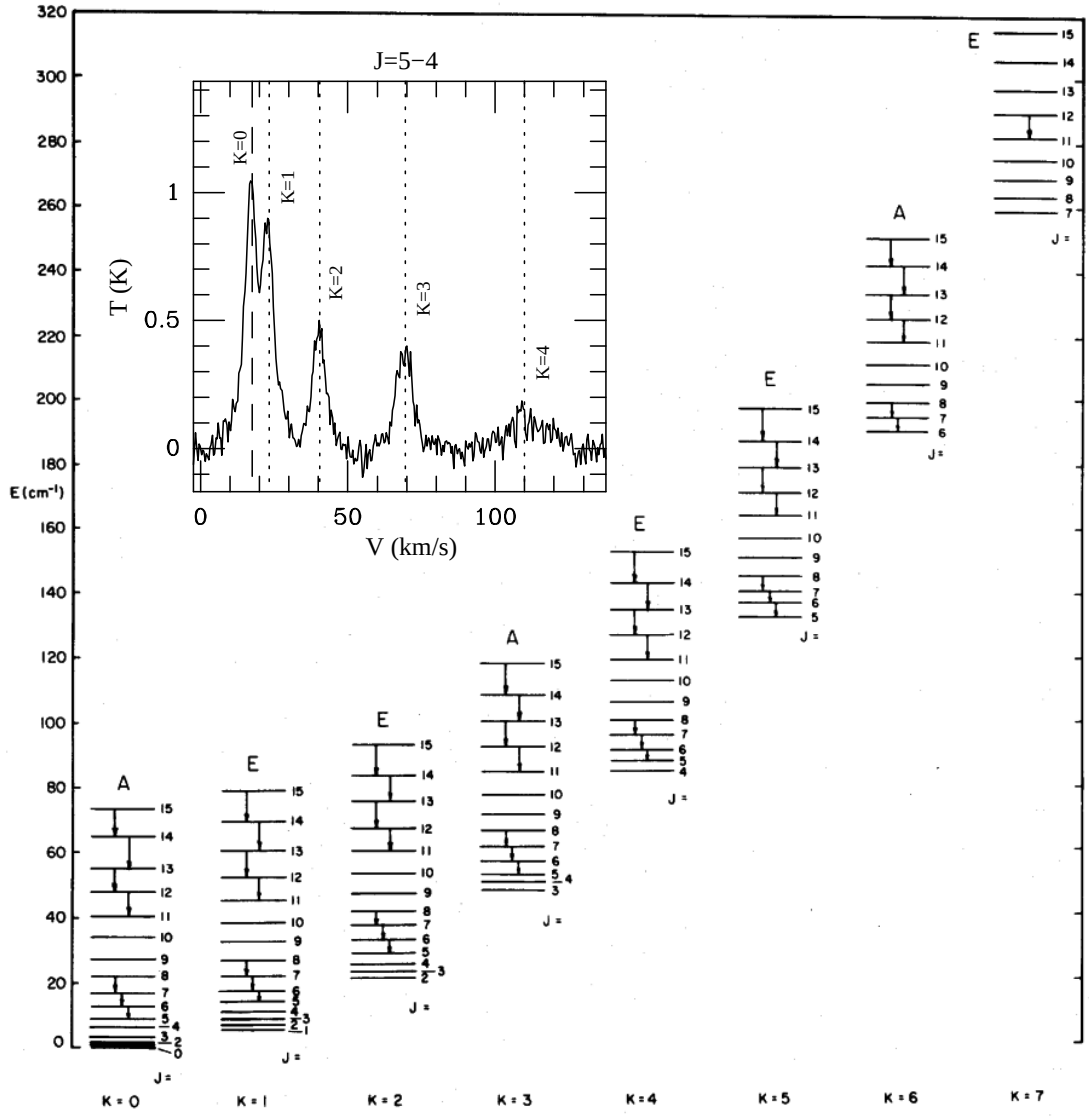

Figure 2.2. Energy level diagram for the symmetric rotor CH_3CN (taken from Loren & Mundy 1984). Energy levels with the same value for K are grouped into 'K-ladders' terminating in the J = K level. Radiative transitions are forbidden between K-ladders so collisions alone are responsible for excitation and under LTE conditions the relative level populations are governed by a Boltzmann distribution. *Inset*: The resultant spectrum in the J = 5→4 K-ladder in the source G0.55−0.85 (this work).

2-1.2.3 Permanent dipole moment

The value of the permanent dipole moment μ determines the effectiveness of an electric field in exerting a torque on a rotating molecule, or in inducing a transition between states J,M and J′,M′, where M = M′ is the magnetic quantum number. If the electric is field polarised along a particular axis (e.g. z) the intensity of the emission or absorption of radiation is proportional to $|\mu_z|^2$, where μ_z is the projection of the electric dipole moment onto that axis. μ_z is known as a dipole moment matrix element. For unpolarised radiation

$$\mathrm{I_{peak}} \propto |\mu_{\mathrm{ij}}|^2 = \sum_{\mathrm{M'}} |\mu_{\mathrm{c}}(\mathrm{JMJ'M'})|^2 + |\mu_{\mathrm{y}}(\mathrm{JMJ'M'})|^2 + |\mu_{\mathrm{z}}(\mathrm{JMJ'M'})|^2. \tag{2.11}$$

For any initial state J,K,M it can be shown (see Townes & Schawlow 1955) that

$$|\mu_{\mathrm{ij}}|^2 = \mu^2 \frac{(\mathrm{J}+1)^2 - \mathrm{K}^2}{(\mathrm{J}+1)(2\mathrm{J}+1)} \quad \text{for the transition J} + 1 \leftarrow \mathrm{J},\ \mathrm{K} \leftarrow \mathrm{K}, \tag{2.12}$$

$$|\mu_{\mathrm{ij}}|^2 = \mu^2 \frac{(\mathrm{J}+1)^2 - \mathrm{K}^2}{(\mathrm{J}+1)(2\mathrm{J}+3)} \quad \text{for the transition J} + 1 \rightarrow \mathrm{J},\ \mathrm{K} \rightarrow \mathrm{K}, \tag{2.13}$$

$$|\mu_{\mathrm{ij}}|^2 = \mu^2 \frac{\mathrm{K}^2}{\mathrm{J}(2\mathrm{J}+1)} \quad \text{for the transition J} \leftarrow \mathrm{J},\ \mathrm{K} \leftarrow \mathrm{K}. \tag{2.14}$$

The value of μ above is the permanent dipole moment of the molecule, usually quoted in Debyes. In SI units, one Debye = $3.2225641 \times 10^{-30}$ coulomb metres.

2-1.2.4 Degeneracy of rotational levels

If two or more levels coincide in energy, transitions involving these levels will give rise to overlapping spectral lines. The total angular momentum J may be oriented in space $2\mathrm{J}+1$ different ways, corresponding to the different values of the magnetic quantum number $\mathrm{M} = 0, \ldots \pm\mathrm{J}$. Thus the energy of any J level is degenerate by a factor $\mathrm{g_u} = 2\mathrm{J}+1$. For symmetric tops, K levels greater than zero are doubly degenerate, as the −K and +K levels have the same energy. Symmetric tops with tri-fold symmetry (e.g., CH_3CN, NH_3) also have a degeneracy due to quantum mechanical symmetry considerations associated with the spins on the three identical

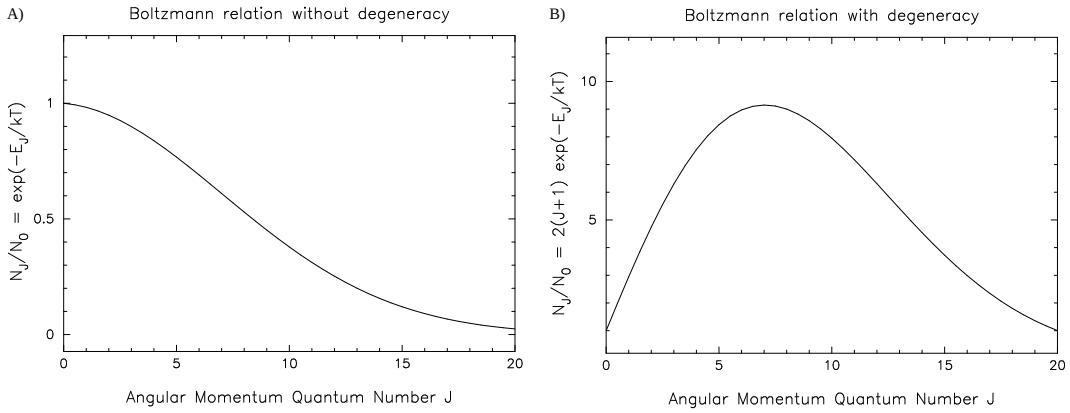

Figure 2.3. The relative population as a function of J for a linear molecule, in this case HCO^+ at 50 K. Panel A shows the Boltzmann distribution without taking into account degeneracy. The number density of molecules in higher J levels decreases exponentially. Panel B shows the Boltzmann distribution including a factor of 2J+1 degeneracy. The J = 7 level contains the highest population of molecules. As the temperature increases the peak of the curve moves to higher J values.

atoms. The degeneracy, $S(\mathrm{I},\mathrm{K})$ due to spin and K degeneracy is given by:

$$S(\mathrm{I},\mathrm{K}) = 2(4\mathrm{I}^2 + 4\mathrm{I} + 3) \qquad \text{For K} = 3\mathrm{n},\ \mathrm{n} = 1, 2, \ldots \tag{2.15}$$

$$S(\mathrm{I},\mathrm{K}) = (4\mathrm{I}^2 + 4\mathrm{I} + 3) \qquad \text{For K} = 0 \tag{2.16}$$

$$S(\mathrm{I},\mathrm{K}) = 2(4\mathrm{I}^2 + 4\mathrm{I}) \qquad \text{For K} \neq 3\mathrm{n},\ \mathrm{n} = 1, 2, \ldots \tag{2.17}$$

where I is the spin of the identical atoms, which in the case of hydrogen is $\frac{1}{2}$. The total degeneracy of any J,K level is then given by $\mathrm{g_u}\, S(\mathrm{I},\mathrm{K})$.

2-1.2.5 Population in energy levels

In an ensemble of molecules, the number of molecules at a particular rotational energy will be governed by the Boltzmann Distribution

$$\frac{\mathrm{n_J}}{\mathrm{n_0}} = \frac{\mathrm{g_J}}{\mathrm{g_0}}\, \mathrm{e}^{-(\mathrm{E_J}-\mathrm{E_0})/\mathrm{kT_{ex}}} \tag{2.18}$$

where $\mathrm{n_0}$ is the number density of molecules in the lowest rotational state (J = 0) and $\mathrm{n_J}$ is the number density of molecules in the $\mathrm{J^{th}}$ level. $\mathrm{T_{ex}}$ is defined as the

excitation temperature, and will be equal to the kinetic temperature under conditions of local thermal equilibrium (LTE). For a given temperature the number of molecules decreases exponentially with increasing J (Figure 2.3-A). As the temperature is increased the curve becomes shallower and the higher J levels are populated with greater numbers of molecules. However, as the total degeneracy increases with J, the population curve has the form of Figure 2.3-B.

The parameter of interest to astronomers is often the total number density of molecules, n, which is given by the sum of the number density of molecules in all states

$$\mathrm{n} = \sum_{\mathrm{i}=0}^{\infty} \mathrm{n_i}. \tag{2.19}$$

If the energy levels are populated according to the Boltzmann Distribution the total number density of molecules may be inferred from the population in one energy level. By combining Equations 2.18 and 2.19 we find

$$\mathrm{n} = \mathrm{n_0} \sum_{\mathrm{i}=0}^{\infty} \frac{\mathrm{n_i}}{\mathrm{n_0}} = \mathrm{n_0} \sum_{\mathrm{i}=0}^{\infty} \frac{\mathrm{g_i}}{\mathrm{g_0}} \, \mathrm{e}^{-\mathrm{E_i}/\mathrm{kT}} = \frac{\mathrm{n_0}}{\mathrm{g_0}} \, \mathrm{e}^{\mathrm{E_0}/\mathrm{kT}} \mathrm{Q(T)} \tag{2.20}$$

where $\mathrm{Q(T_{ex})}$ is the partition function, a sum over all energy states that normalises the distribution, and is given by

$$\mathrm{Q(T_{ex})} = \sum_{\mathrm{i}} \mathrm{g_i} \, \mathrm{e}^{-\mathrm{E_i}/\mathrm{kT_{ex}}}. \tag{2.21}$$

2-1.2.6 Total intensity in a rotational molecular transition

In summary, the intensity of a $\mathrm{J}\rightarrow\mathrm{J}-1, \mathrm{K}$ rotational transition is proportional to the permanent dipole moment μ, the degeneracy of the upper energy level $\mathrm{g_u}$, the number density of emitting molecules n and the excitation temperature of the gas T_{ex} as follows:

$$\text{Intensity} \propto \frac{|\mu^2| \, \mathrm{n} \, \mathrm{g_u} \, S(\mathrm{I}, \mathrm{K}) \, \mathrm{e}^{-(\mathrm{E_u}-\mathrm{E_l})/\mathrm{kT_{ex}}}}{\mathrm{Q(T_{ex})}}. \tag{2.22}$$

Derivation of the full formula requires a consideration of radiation transport through a medium, which will be presented in Section 2-2.

2-1.2.7 Spectral line profiles

Spectral lines are not discrete and are spread out over a finite frequency space. The following mechanisms account for the broadening of a line profile.

Natural broadening is the term given to the intrinsic width of the line, described by a Lorentzian profile. In an ensemble of emitting molecules the Uncertainty principle ($\Delta \mathrm{E}\, \Delta \mathrm{t} \approx \hbar$) causes variations in the lifetime of an excited state. The effect introduces an uncertainty in the energy level, leading to a spread in the frequency of the emitted or absorbed radiation.

The proximity of other molecules affects the radiation emitted by an individual molecule. **Pressure broadening** occurs when collisions interrupt the emission process, or when the energy levels in the emitting molecule are modified by the presence of other nearby molecules. The magnitude of the effects depend on both the temperature and the density of the gas.

Doppler broadening occurs due to the chaotic motion of the observed molecules in random directions. The resultant Doppler shifts produce a further spread in the frequency of the observed line.

Thermal Doppler broadening is the specific Doppler broadening due to the thermal motions of the molecules. Pure thermal broadening results in a Gaussian line shape with a full-width half-maximum (FWHM) given by

$$\Delta \nu_{\mathrm{FWHM}} = 2 \sqrt{\ln(2)}\, \frac{\nu_0}{\mathrm{c}} \sqrt{\frac{2\mathrm{kT_{kin}}}{\mathrm{m}}}, \tag{2.23}$$

where ν_0 is the central frequency and m is the mass of the molecule in kilogrammes.

Large scale collective motions of groups of molecules can also contribute significantly to the broadening of the line profile. This **turbulent Doppler broadening** is described by

$$\Delta \nu_{\mathrm{FWHM}} = 2 \sqrt{\ln(2)}\, \frac{\nu_0}{\mathrm{c}} \sqrt{\frac{2\mathrm{kT_{kin}}}{\mathrm{m}} + \mathrm{V_t^2}}, \tag{2.24}$$

where $\mathrm{V_t^2}$ is a constant called the micro-turbulent velocity.

The gas in cold (<15 K) quiescent clouds is usually not affected by turbulent motions. In such regions the line profile is dominated by thermal broadening and Equa-

tion 2.23 predicts FWHM linewidths of $\lesssim 0.5\,\mathrm{km\,s^{-1}}$. In molecular clouds forming massive stars linewidths of $> 3\,\mathrm{km\,s^{-1}}$ are common and turbulence is the dominant broadening mechanism.

During the analysis of spectral line data Gaussian line profiles are often assumed. The normalised Gaussian line profile is given by:

$$\phi(\nu) = \frac{\sqrt{4\,\ln\,2}}{\Delta\nu\sqrt{\pi}}\,\mathrm{e}^{-4\ln 2\,(\frac{\nu}{\Delta\nu})^2}, \tag{2.25}$$

where ν is the frequency and $\Delta\nu$ is the 1-σ linewidth in frequency units. $\Delta\nu$ is related to the FWHM linewidth via $\Delta\nu = \Delta\,\nu_{\mathrm{FWHM}}/(2\sqrt{2\,ln\,2})$ and the area under a Gaussian curve (i.e., the integrated intensity) may be found from

$$\mathrm{Area} = \frac{2\sqrt{\ln 2}}{\sqrt{\pi}} \times \Delta\,\nu_{\mathrm{FWHM}} \times \mathrm{Height}. \tag{2.26}$$

2-1.3 Molecular excitation and Einstein coefficients

Consider an ensemble of molecules with only two energy levels $\mathrm{E_u}$ and $\mathrm{E_l}$, bathed in a radiation field of specific intensity I_ν. The population in both levels is governed by the interaction of the system with external radiation and particles. Radiative transitions between the levels are conveniently described by the Einstein coefficients, which are defined as:

- $\mathrm{A_{ul}}$ = Probability of spontaneous radiative decay from the upper to the lower energy level ($\mathrm{s^{-1}}$).
- $\bar{\mathrm{I}}\,\mathrm{B_{ul}}$ = Probability of stimulated emission from the upper to the lower energy level.
- $\bar{\mathrm{I}}\,\mathrm{B_{lu}}$ = Probability of photon absorption leading to a transition from the lower to upper energy level.

$\bar{\mathrm{I}}$ is the average intensity of the external radiation field. The Einstein coefficients are intrinsic properties of the particular transition, and are related to the molecular properties via

$$\mathrm{A_{ul}} = \frac{16\,\pi^3\,\nu^3}{3\,\epsilon_0\,\mathrm{h\,c^3}}\,|\mu^2| \tag{2.27}$$

where $|\mu^2|$ is the dipole matrix element for the transition given by one of Equations 2.12 – 2.14, ϵ_0 is the permittivity of free space, and ν is the frequency of the transition. The Einstein A and B coefficients are related through

$$\mathrm{B_{ul}} = \frac{\mathrm{c}^2}{2\mathrm{h}\nu^3}\,\mathrm{A_{ul}} \qquad \text{and} \qquad \mathrm{B_{lu}\,g_l} = \mathrm{B_{ul}\,g_u}. \tag{2.28}$$

The Einstein coefficients describe interactions between the system and external radiation, however, collisions can also cause excitation and de-excitation. Collisional coefficients are defined according to:

- $\mathrm{C_{ul}} = \mathrm{n_{H_2}}\,\gamma_{\mathrm{ul}}$ = Rate of collision induced transitions from upper to lower level (in molecules $\mathrm{s^{-1}}$).
- $\mathrm{C_{lu}} = \mathrm{n_{H_2}}\,\gamma_{\mathrm{lu}}$ = Rate of collision induced transitions from lower to upper level (in molecules $\mathrm{s^{-1}}$).

where $\mathrm{n_{H_2}}$ is the H_2 number density and γ_{ul} and γ_{lu} are the coefficients for downward and upward collisions, respectively (in molecules $\mathrm{s^{-1}}$ $\mathrm{H_2\text{-}molecules^{-1}}$). We assume here that H_2 molecules are the dominant collisional partner and $\gamma = \gamma_{\mathrm{H_2}}$. In the steady state the number of molecules in upper and lower levels remain constant, therefore:

$$\mathrm{n_u}\,[\mathrm{A_{ul}} + \mathrm{B_{ul}}\,\bar{\mathrm{I}}_\nu + \mathrm{C_{ul}}] = \mathrm{n_l}\,[\mathrm{B_{lu}}\,\bar{\mathrm{I}}_\nu + \mathrm{C_{lu}}], \tag{2.29}$$

where $\mathrm{n_u}$ is the number density of molecules in the upper state and $\mathrm{n_l}$ is the number density of molecules in the lower state. Assuming LTE conditions, (and therefore a Boltzmann population distribution), an excitation temperature, $\mathrm{T_{ex}}$, describing the ratio of the level populations is defined from Equation 2.18 (repeated here):

$$\frac{\mathrm{n_u}}{\mathrm{n_l}} = \frac{\mathrm{g_u}}{\mathrm{g_l}}\,\mathrm{e}^{-(\mathrm{E_u}-\mathrm{E_l})/\mathrm{k\,T_{ex}}}.$$

Considering only collisions, ($\mathrm{n_l\,C_{lu}} = \mathrm{n_u\,C_{ul}}$), and applying Equation 2.18 we find a Boltzmann relation for the ratio of the collision rates:

$$\frac{\mathrm{C_{lu}}}{\mathrm{C_{ul}}} = \frac{\mathrm{g_u}}{\mathrm{g_l}}\,\mathrm{e}^{-(\mathrm{E_u}-\mathrm{E_l})/\mathrm{k\,T_{kin}}}, \tag{2.30}$$

called the 'detailed balance' condition. Although we derived this relation assuming the radiation field was negligible, it must always hold since it depends only on molecular parameters. By combining Equations 2.29 and 2.18 we arrive at an expression for the excitation temperature:

$$\frac{n_u}{n_l} = \frac{g_u}{g_l} e^{-(E_u - E_l)/k\,T_{ex}} = \frac{B_{lu}\,\bar{I}_\nu + C_{lu}}{A_{ul} + B_{ul}\,\bar{I}_\nu + C_{ul}} \tag{2.31}$$

If the radiation originates from a blackbody (e.g. the Cosmic Microwave Background) with a temperature T_{bg}, then $\bar{I}_\nu$ will be given by the Planck radiation law

$$\bar{I}_\nu = B_\nu(T_{bg}) = \frac{2h\nu^3}{c^2} J_\nu(T), \tag{2.32}$$

with $J_\nu(T) = (e^{(E_u - E_l)/kT_{bg}} - 1)^{-1}$. Using Equation 2.30 and substituting for $\bar{I}_\nu$ in Equation 2.31 we find

$$e^{(E_u - E_l)/k\,T_{ex}} = \frac{A_{ul}[1 + J_\nu(T_{bg})] + C_{ul}}{A_{ul}J_\nu(T_{bg}) + C_{ul}\,e^{-E_u/k\,T_{kin}}}, \tag{2.33}$$

which relates the excitation temperature to the kinetic temperature in a gas bathed in a radiation field. Consider two limiting cases:

Collisions Unimportant: Radiation dominates the excitation, collisional terms are negligible and may be discarded. The population is in equilibrium with the background radiation field and

$$T_{ex} = T_{bg}. \tag{2.34}$$

Collisions Dominate: Excitation takes place mainly due to collisions and the radiative terms may be discarded. The population is in thermal equilibrium and

$$T_{ex} = T_{kin}. \tag{2.35}$$

A useful quantity to define is the *critical density* of H_2 at which downward collisional processes equal downward radiative processes. It is taken to be a measure of the density necessary for collisional excitation to be effective. In the steady state equation the downward terms are:

$$A_{ul} + A_{ul}J_\nu(T_{bg}) = n_{H_2}\gamma_{ul}$$

and the critical density is defined as:

$$n_{crit} = \frac{A_{ul}(1 + J(T_{bg}))}{\gamma_{ul}} \approx \frac{A_{ul}}{\gamma_{ul}} \tag{2.36}$$

At densities lower than n_{crit}, collisions are too infrequent to excite the gas and under LTE conditions a spectral line will not be visible against the background radiation. The value of A_{ul} increases with ν_{ul}^3 (Equation 2.27), so higher frequency transitions trace increasingly dense gas.

2-2 Radiative transfer in an isothermal medium

Having laid the ground rules governing molecular excitation in an ensemble of molecules, we must now consider how the spectral lines are processed as they pass through the intervening gas and dust to reach the observer. The following description is equally valid for continuum radiation, such as thermal radiation due to warm dust, or free-free emission from a HII region.

2-2.1 The equation of radiative transfer

The change in the intensity of radiation as it passes through an isothermal medium (e.g. a molecular cloud, Figure 2.4) is described by the radiative transfer equation:

$$\frac{dI_\nu}{ds} = -\kappa_\nu I_\nu + \epsilon_\nu, \tag{2.37}$$

where I_ν is the specific intensity of the radiation, κ_ν is the absorption coefficient and ϵ_ν is the specific intensity of radiation emitted by the medium. The absorption and emission coefficients in the radiative transfer equation can be expressed in terms of the Einstein coefficients:

$$\epsilon_\nu = \frac{h\nu_{ul}}{4\pi} n_u A_{ul} \phi(\nu), \tag{2.38}$$

$$\kappa_\nu = \frac{h\nu_{ul}}{4\pi} (n_l B_{lu} - n_u B_{ul}) \phi(\nu), \tag{2.39}$$

where $\phi(\nu)$ is a normalised line profile, usually taken to be Gaussian in form. Equation 2.37 may also be expressed in terms of optical depth τ_ν, defined as $\tau_\nu = -\kappa_\nu ds$,

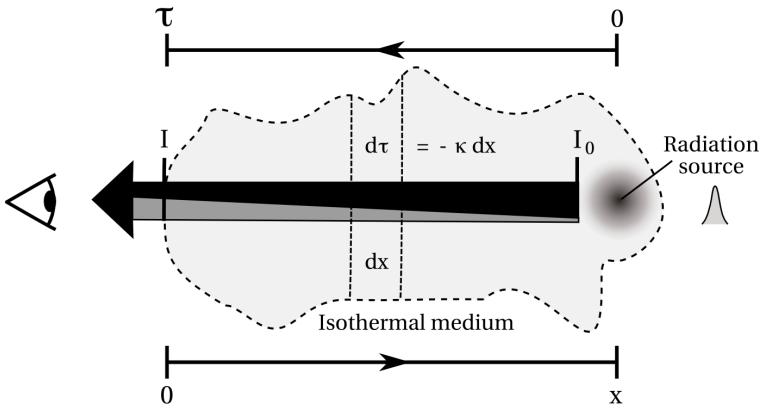

Figure 2.4. For a radiating source embedded in a molecular cloud the intensity measured by an external observer will be the sum of the initial intensity I_0, attenuated by the intervening medium (black bar), and the self-attenuated emission from the medium (grey bar). The change in intensity over any interval dx is described by the radiative transfer equation (Equation 2.37) in terms of κ and ϵ, the absorption and emission coefficients of the medium.

giving

$$\frac{dI_\nu}{d\tau_\nu} = I_\nu - \frac{\epsilon_\nu}{\kappa_\nu} = I_\nu - S_\nu, \tag{2.40}$$

where ϵ_ν/κ_ν completely describes the properties of the medium and is known as the source function, S_ν.

The radiative transfer equation may be solved to obtain an expression for observed intensity, I_ν, as a function of distance s:

$$I_{\nu,s} = I_{\nu,0}e^{-\tau_\nu} + S_\nu(1 - e^{-\tau_\nu}). \tag{2.41}$$

This is the general solution to the radiative transfer equation assuming an isothermal, homogeneous medium. The intensity of the detected radiation is the sum of the attenuated radiation from the source, $I_{\nu,0}e^{-\tau_\nu}$, and the self attenuated radiation emitted by the medium, $S_\nu(1 - e^{-\tau_\nu})$.

2-2.2 Brightness temperature and the detection equation

If the source of radiation is assumed to be a blackbody then the source function S_ν will be described by Equation 2.32, Planck's radiation law. At low frequencies when $h\nu \ll kT$ the Planck function is well approximated by the Rayleigh-Jeans Law:

$$S_\nu = B_\nu(T_R) \approx \frac{2k\nu^2 T_R}{c^2}, \tag{2.42}$$

where T_R is the radiation temperature of the source. A brightness temperature T_b is defined such that

$$T_b = \frac{c^2}{2k\nu^2} B_\nu(T_R) = \frac{h\,\nu}{k}\, J_\nu(T_R), \tag{2.43}$$

with $J_\nu(T) = (e^{(E_u - El)/kT} - 1)^{-1}$ as before. Equation 2.41 may be expressed in terms of brightness temperatures:

$$T_b = \frac{h\,\nu}{k}\, J_\nu(T_{bg})\, e^{-\tau_\nu} + \frac{h\,\nu}{k}\, J_\nu(T_s)\,(1 - e^{-\tau_\nu}), \tag{2.44}$$

where T_{bg} is the temperature of the background radiation field and T_s is the radiation temperature of the source. During position or frequency switched observations the excess brightness temperature above a background (e.g., the cosmic microwave background) is measured and Equation 2.44 becomes

$$T_b = \frac{h\,\nu}{k}\,[J_\nu(T_s) - J_\nu(T_{bg})]\;(1 - e^{-\tau_\nu}). \tag{2.45}$$

This is known as the detection equation as it relates the brightness temperature measured at the telescope to the thermodynamic temperature of the source. Two special cases occur when the medium is optically thin ($\tau \ll 1$) or optically thick ($\tau \gg 1$):

Optically Thin Emission:

$$T_b = \frac{h\,\nu}{k}\,[J_\nu(T_s) - J_\nu(T_{bg})]\tau_\nu \tag{2.46}$$

Optically Thick Emission:

$$T_b = \frac{h\,\nu}{k}\,[J_\nu(T_s) - J_\nu(T_{bg})] \tag{2.47}$$

2-3 Physical parameters from observations

Of primary interest to the astronomer are the physical conditions such as kinetic temperature, density and abundance which give rise to the spectral lines. Under optically thick conditions the brightness of a spectral line saturates at the excitation temperature, which under LTE conditions is proportional to the kinetic temperature (Equation 2.35). Under optically thin conditions the intensity under a spectral line is proportional to the number of molecules emitting and their excitation temperature (Equation 2.22). In this case the total number density of molecules emitting in the beam (the column density) may be found if the excitation temperature is known. Traditionally, the excitation temperature is found from observations of generally optically thick transitions (e.g. CO (1 – 0)) and the column density is found from a generally optically thin isotopomer (e.g. $C^{18}O$ (1 – 0)), assuming the same excitation temperature.

2-3.1 Kinetic temperature from optically thick transitions

If the emission is optically thick then Equation 2.47 and the Planck functions allows us to determine the source temperature as follows

$$\frac{1}{\mathrm{J}_\nu(\mathrm{T_s})} = \mathrm{e}^{\mathrm{h}\nu/\mathrm{kT_{kin}}} - 1 = \frac{(\mathrm{h}\nu/\mathrm{k})}{\mathrm{T_b} + \frac{\mathrm{h}\nu}{\mathrm{k}}\mathrm{J}_\nu(\mathrm{T_{bg}})}.$$

If local thermal equilibrium conditions apply then $\mathrm{T_s} = \mathrm{T_{kin}}$ so

$$\mathrm{T_{kin}} = \mathrm{T_s} = \frac{\mathrm{h}\nu}{\mathrm{k}} \left[\ln\left(1 + \frac{(\mathrm{h}\nu/\mathrm{k})}{\mathrm{T_b} + \frac{\mathrm{h}\nu}{\mathrm{k}}\,\mathrm{J}_\nu(\mathrm{T_{bg}})} \right) \right]^{-1}. \tag{2.48}$$

This equation gives the kinetic temperature of the gas if the line is optically thick.

2-3.2 Column density from optically thin transitions

Expanding the definition of optical depth, τ_ν, using Equations 2.39 and 2.28:

$$\tau_\nu = -\kappa_\nu \, \mathrm{ds} \quad = \quad \frac{\mathrm{c}^2}{8\pi\nu^2} \, \mathrm{A_{ul}} \, (\mathrm{n_l} \, \frac{\mathrm{g_u}}{\mathrm{g_l}} - \mathrm{n_u}) \, \phi(\nu) \, \mathrm{ds},$$

and substituting the Boltzmann Equation (2.18) for g_u/g_l we find:

$$\tau_\nu = \frac{c^2}{8\pi\nu^2}\, A_{ul}\, n_u\, (e^{h\nu_{ul}/kT_{ul}} - 1)\, \phi(\nu)\, ds. \tag{2.49}$$

Now integrate along the line of sight to obtain

$$\tau_\nu = \frac{c^2}{8\pi\nu^2}\, A_{ul}\, N_u\, (e^{h\nu_{ul}/kT_{ul}} - 1)\, \phi(\nu), \tag{2.50}$$

where $N_u = \int n_u ds$ is the column density of molecules in the upper state and $\phi(\nu)$ is the normalised line profile, usually taken to be a Gaussian.

Returning to the detection equation (2.45), and assuming emission from background is negligible, we find

$$T_b = \frac{h\nu}{k}\, J_\nu(T_{ex})\, (1 - e^{-\tau_\nu}). \tag{2.51}$$

As a convenience we will multiply by τ/τ and substitute the full expression for optical depth (Equation 2.50):

$$T_b = \left(\frac{h\nu}{k}\, J_\nu(T_{ex})\right) \left(\frac{1 - e^{-\tau_\nu}}{\tau_\nu}\right) \left(\frac{c^2}{8\pi\nu^2}\, A_{ul}\, N_u\, (e^{E_{ul}/kT_{ul}} - 1)\, \phi(\nu)\right)$$

$$= \frac{hc^2}{8k\pi\nu} A_{ul}\, N_u \left(\frac{1 - e^{-\tau_\nu}}{\tau_\nu}\right) \phi(\nu).$$

Then integrate over the full width of the line (normalised to 1):

$$\int_{-\infty}^{\infty} T_b\, d\nu = \frac{\nu}{c} \int_{-\infty}^{\infty} T_b\, dv = \frac{hc^3}{8k\pi\nu^2}\, A_{ul}\, N_u \left(\frac{1 - e^{-\tau_\nu}}{\tau_\nu}\right) \int_{-\infty}^{\infty} \phi(\nu)\, d\nu$$

to find the general relation for the column density of molecules in the upper energy level:

$$N_u = \frac{8k\pi\nu^2}{A_{ul}hc^3} \int_{-\infty}^{\infty} T_b\, dv \left(\frac{\tau_\nu}{1 - e^{-\tau_\nu}}\right). \tag{2.52}$$

Here $\int T_b\, dv$ is the integrated intensity of the spectral line in $km\, s^{-1}$. In the optically thin case the term $(1 - e^{-\tau_\nu})/\tau_\nu$ is approximately equal to one and

$$N_u = \frac{8k\pi\nu^2}{A_{ul}hc^3} \int_{-\infty}^{\infty} T_b\, dv. \tag{2.53}$$

This equation gives the column density in the *upper state* assuming optically thin conditions. To find the total column density from Equations 2.52 or 2.53 we must assume all the energy levels are populated according to a Boltzmann distribution

characterised by a single temperature, T_{ex}. The total column density may then be found from Equations 2.20 and 2.21, repeated here:

$$N = \frac{N_u}{g_u} e^{E_u/kT} Q(T_{ex}) \qquad \text{and} \qquad Q(T_{ex}) = \sum_i g_i e^{-E_i/kT_{ex}}.$$

2-3.3 The rotational diagram

In many instances it is not practical or possible to find an optically thick tracer to measure the excitation temperature and an optically thin tracer to measure the column density. Fortunately, there is a better way to measure both simultaneously through the analysis of the excitation of asymmetric molecules. The *rotation diagram* method simultaneously yields the excitation temperature T_{ex} and total column density N, assuming LTE and optically thin transitions.

Equation 2.20 relates the upper state column density to the total column density, assuming Boltzmann statistics. Rearranging and taking the natural log of both sides we find

$$\ln\left(\frac{N_u}{g_u}\right) = \ln\left(\frac{N}{Q(T)}\right) - \frac{E_u}{kT_{ex}}. \tag{2.54}$$

The column density in the upper level, N_u may be found from the integrated intensity under the spectral line, ($\int_{-\infty}^{\infty} T_b \, dv$), through Equation 2.53. If several transitions have been measured, a straight line through a plot of $\ln(N_u/g_u)$ versus E_u/k will have a slope of $1/T_{ex}$ and a y-intercept of $\ln[N/Q(T)]$. Temperatures found through this method are referred to as rotational temperatures ($T_{ex} = T_{rot}$).

Symmetric tops lend themselves well to this approach as multiple (J+1→J, K) transitions may be observed in a single bandpass. Radiative transitions are forbidden between K levels, therefore the relative population in the K levels is determined only by collisions and T_{rot} will be equal to the kinetic temperature.

2-4 Case study: NH_3, the molecular thermometer

Ammonia (NH_3) is a symmetric rotor that constitutes an ideal probe of the temperatures and densities in molecular clouds. The spectrum of NH_3 is distinguished from

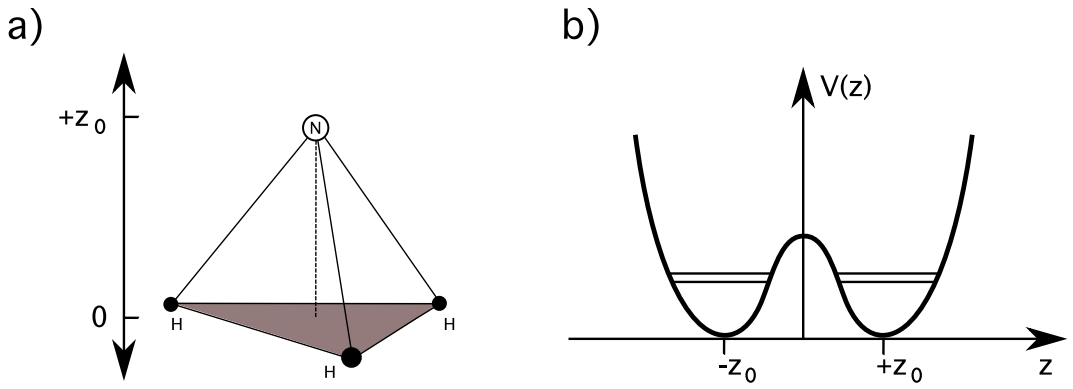

Figure 2.5. a) The trigonal-pyramid structure of NH_3. The Nitrogen atom can quantum mechanically 'tunnel' through the plane of the Hydrogen atoms, giving rise to the inversion transitions. b) The double-well potential experienced by the nitrogen atom due to Coulomb repulsion by the three hydrogen atoms.

other symmetric tops as it is split into five 'hyperfine groups' - a main group and two pairs of satellite lines. The optical depth may be determined directly from the intensity ratios of the satellite lines, facilitating the calculation of rotational temperatures and column densities without making the assumption of optically thin conditions. In addition, the collisional excitation of NH_3 has been extensively modelled allowing the accurate conversion of rotational temperatures to kinetic temperatures. In the following sections we outline the theory necessary to understand the form of the NH_3 inversion spectrum and describe the modified rotational diagram analysis used to calculate kinetic temperatures and column densities.

2-4.1 The spectrum of NH_3

The rich spectrum of NH_3 is a result of interactions between vibrational and rotational modes, and the internal electronic structure of the molecule. We will examine the contribution from each mode in turn, leading to an explanation for the form of the observed spectrum.

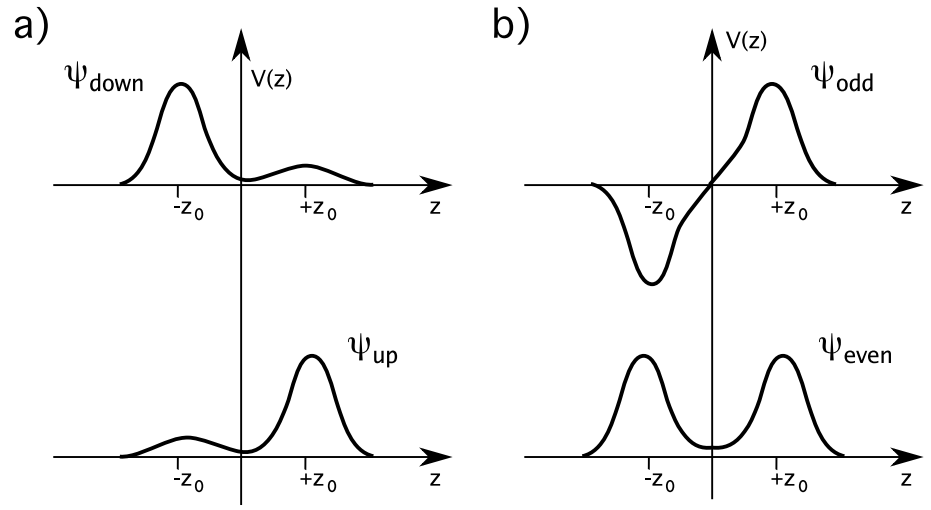

Figure 2.6. a) Individual solutions to the Schroedinger equation for a double well potential. b) Eigenfunctions for the double well potential with a finite barrier.

Inversion

NH_3 is a trigonal pyramid with three identical N–H bonds. It is a member of a unique class of molecules which vibrate in an 'inversion' mode (Kukolich 1967). Figure 2.5-a illustrates the structure of NH_3. The potential experienced by the nitrogen atom is that of a double well, with one well on either side of the plane defined by the three hydrogen atoms (Figure 2.5-b). Classically, the nitrogen atom is confined to a single well, as in the ground state it does not have enough energy to overcome the central barrier. However, quantum theory allows the nitrogen to 'tunnel' through the barrier and it has a non-zero probability of being found in the opposite well after a finite time.

Inversion energies

The wavefunctions describing the solution to the Schroedinger equation for a double well are illustrated in Figure 2.6a. $\psi_{\rm up}$ and $\psi_{\rm down}$ represent the wavefunctions when the nitrogen atom is predominantly localised to the +z and −z sides of the plane, respectively. The full solution is formed from linear combinations of $\psi_{\rm up}$ and $\psi_{\rm down}$ satisfying the requirement $\psi(\mathrm{z}) = \pm\psi(-\mathrm{z})$. This is necessary because the wave-

function must have identical forms in both wells under transformation in Cartesian coordinates. Two solutions are defined:

$$\psi_{\rm odd} = \left(\frac{1}{\sqrt{2}}\right)(\psi_{\rm up} - \psi_{\rm down}) \qquad \text{and} \qquad \psi_{\rm even} = \left(\frac{1}{\sqrt{2}}\right)(\psi_{\rm up} + \psi_{\rm down}).$$

These wavefunctions are illustrated in Figure 2.6b. The complete expressions for ψ_{odd} and ψ_{even} in the steady state are given by

$$\psi_{\rm odd}({\rm z},{\rm t}) = \psi_{\rm odd}({\rm z})\,{\rm e}^{-{\rm i}{\rm E}_1{\rm t}/\hbar} \qquad \text{and} \qquad \psi_{\rm even}({\rm z},{\rm t}) = \psi_{\rm even}({\rm z})\,{\rm e}^{-{\rm i}{\rm E}_2{\rm t}/\hbar},$$

where $\rm E_1$ and $\rm E_2$ are the energies of the ψ_{odd} and ψ_{even} wavefunctions. $\rm E_1 > E_2$ as can be seen by decreasing the height of the potential barrier. As the shape of the potential approaches that of a single well the ψ_{odd} and ψ_{even} wavefunctions approach the first and second vibrational states, respectively, of a linear molecule. For NH_3 in the ground vibrational state, the inversion transition between $\rm E_1$ and $\rm E_2$ corresponds to a frequency $\nu_0 = 23.8\,$GHz.

Rotation

Centripetal distortion of the molecule leads to a splitting of the inversion transition into multiple lines. The shape of the potential barrier is determined by the separation between the nitrogen atom and the hydrogen atoms. This spacing in turn is dependent on the quantised rotational state of the molecule. Rotation about the principal axis (J>0, K=J) tends to flatten out the pyramid, increasing the distance between the hydrogen atoms. Hence, the potential barrier lowers and the inversion frequency increases. If there is significant angular momentum perpendicular to the principal axis (J>0, K$\ll$J) then rotation tends to elongate the pyramid, leading to a higher potential barrier and a decrease in the inversion frequency. The inversion frequency of a J,K level is given by (Townes & Schawlow 1955)

$$\nu_{\rm inversion} = \nu_0 - {\rm c}_1[{\rm J}({\rm J}+1) - {\rm K}^2] + {\rm c}_2{\rm K}^2, \tag{2.55}$$

where $\rm c_1$ and $\rm c_1$ are positive constants. Quantum symmetry considerations forbid the splitting of any state where K=0.

Quadrupole splitting

The nitrogen nucleus has a quadrupole moment resulting from the non-spherical distributions of charge within the nucleus. This quadrupole moment interacts with the electric field of the electrons giving rise to further splitting. Each J,K inversion energy level splits into three levels characterised by the quantised nuclear spin of the nitrogen, I=1, and the total angular momentum, F=I+J. The following selection rules apply:

$$\mathrm{F} = \mathrm{J}+1, \mathrm{J}, \mathrm{J}-1 \qquad \Delta\mathrm{F} = 0, \pm 1 \qquad \Delta\mathrm{J} = 0, \pm 1 \qquad \Delta\mathrm{I} = 0,$$

leading to seven transitions between the ψ_{odd} and ψ_{even} inversion levels. Figure 2.7 (*top*) illustrates the resultant energy levels for the case of the J,K=(1,1) transition. These transitions lead to the distinctive 5-finger spectrum of NH_3, illustrated in Figure 2.7 (*bottom*). The central (or main) group is comprised of the transitions with $\Delta\mathrm{F} = 0$ and the $\Delta\mathrm{F} = \pm 1$ transitions appear as pairs of satellite lines on either side of the main line. The relative intensities of these transitions may be calculated from

$$\mathrm{F}-1 \rightarrow \mathrm{F}: \qquad -\frac{\mathrm{A}(\mathrm{J}+\mathrm{F}+\mathrm{I}+1)(\mathrm{J}+\mathrm{F}-\mathrm{I})(\mathrm{J}-\mathrm{F}+\mathrm{I}+1)(\mathrm{J}-\mathrm{F}-\mathrm{I})}{\mathrm{F}} \tag{2.56}$$

$$\mathrm{F} \rightarrow \mathrm{F}: \qquad \frac{\mathrm{A}[\mathrm{J}(\mathrm{J}+1)+\mathrm{F}(\mathrm{F}+1)-\mathrm{I}(\mathrm{I}+1)]^2(2\mathrm{F}+\mathrm{I})}{\mathrm{F}(\mathrm{F}+1)} \tag{2.57}$$

$$\mathrm{F}+1 \rightarrow \mathrm{F}: \quad -\frac{\mathrm{A}(\mathrm{J}+\mathrm{F}+\mathrm{I}+2)(\mathrm{J}+\mathrm{F}-\mathrm{I}+1)(\mathrm{J}-\mathrm{F}+\mathrm{I})(\mathrm{J}-\mathrm{F}-\mathrm{I}-1)}{\mathrm{F}+1} \tag{2.58}$$

Values for the J,K=(1,1) and (2,2) transitions are tabulated in Table 2.1.

Magnetic hyperfine splitting.

Both the nitrogen and hydrogen nuclei have magnetic moments which interact with the magnetic field generated by the rotating molecule. This results in energy shifts much smaller than the quadrupole splitting and the main line and satellites are

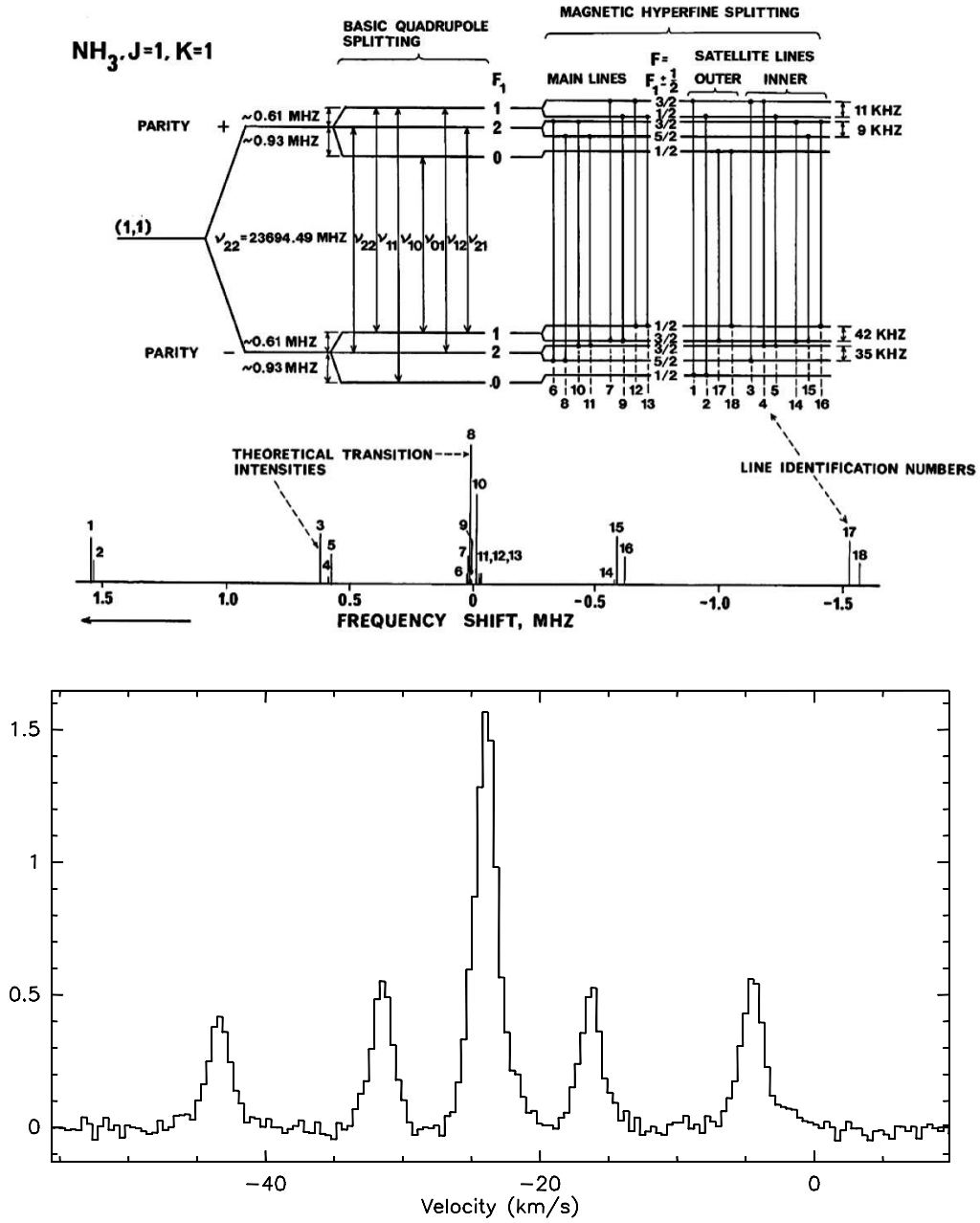

Figure 2.7. (*Top*) Schematic showing the quadrupole and magnetic hyperfine splitting of the NH_3 (1,1) inversion spectrum (taken from Rydbeck et al. 1977). (*Bottom*) Typical example of a NH_3 (1,1) spectrum showing the main group (centre) and the pairs of satellite lines on either side.

Table 2.1. Relative intensities of the quadrupole hyperfine lines in the NH_3 spectrum.

Rotational Transition	F-Transition		Relative[α] Intensity	Hyperfine Group	f[β]
J, K=(1,1)	ΔF=0	F=0 → 0	$0.0A_1$	Main	0.502
		F=1 → 1	$6.0A_1$	Main	
		F=2 → 2	$30.0A_1$	Main	
	ΔF=±1	F=1 ↔ 0	$8.0A_1$	Outer Satellites	0.111
		F=1 ↔ 2	$10.0A_1$	Inner Satellites	0.139
J, K=(2,2)	ΔF=0	F=1 → 1	$54.0A_2$	Main	0.796
		F=2 → 2	$83.3A_2$	Main	
		F=3 → 3	$149.7A_2$	Main	
	ΔF=±1	F=2 ↔ 1	$18.0A_2$	Outer Satellites	0.050
		F=2 ↔ 3	$10.7A_2$	Inner Satellites	0.052

[α] The relative intensities tabulated here have been calculated from Equations 2.56, 2.57 and 2.58. A_1 and A_2 are normalisation factors chosen so that the total intensity across all hyperfine components is equal to 1. A_1=0.0139 for J, K=(1,1) and A_2=0.0360 for J, K=(2,2).

[β] Fractional intensity of the line, i.e., the fraction of the total intensity present in the main line or individual satellite lines under optically thin conditions.

further split into a total of 18 components. Observations presented here are not capable of resolving these lines (see Figure 2.7).

Inversion-rotation energy levels

Figure 2.8 is the energy level diagram for the inversion-rotation states of NH_3 showing the quadrupole hyperfine splitting (from Ho & Townes 1983). Radiative transitions between the K-ladders are normally forbidden by the selection rule ΔK=0, however, interactions between vibrational and rotational motions induce a small dipole moment perpendicular to the rotation axis giving rise to very slow $\Delta k = \pm 3$, $K = |k|$ transitions between K-ladders. Within each K-ladder the upper states ($J > K$) are called non-metastable because they can decay rapidly down to the lowest

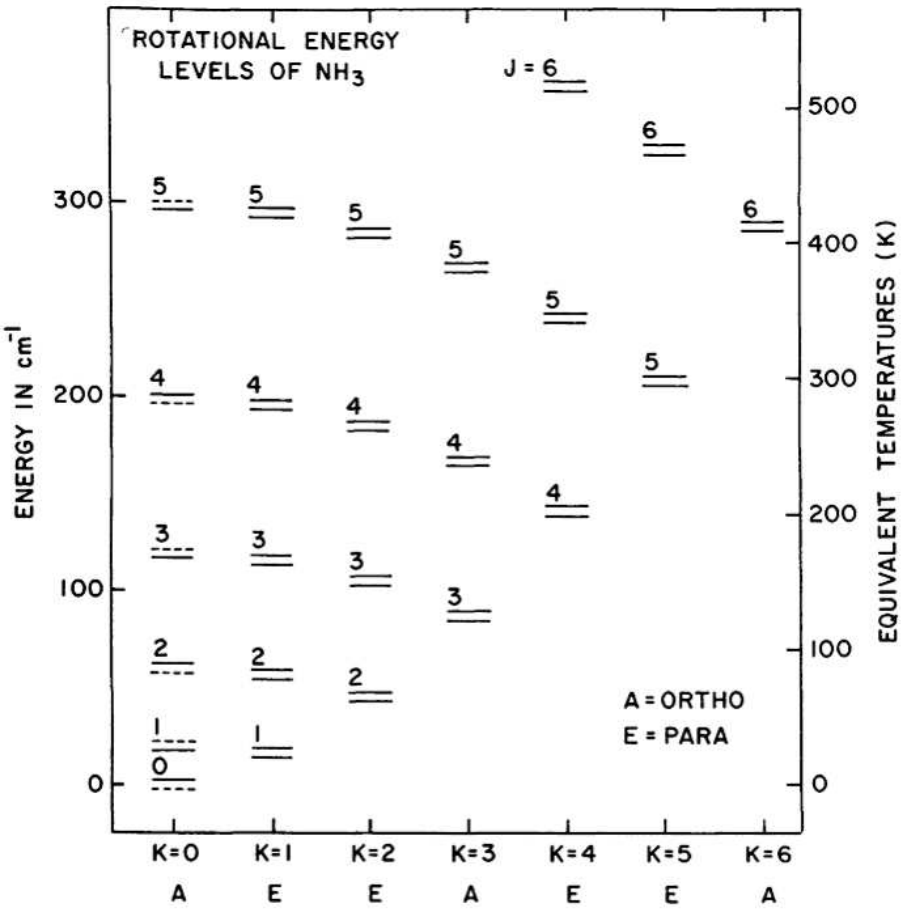

Figure 2.8. The energy levels for NH_3(taken from Ho & Townes 1983).

'metastable' states via the $\Delta J = 1$ transitions in the far-infrared (Oka et al. 1971). The lowest states in each ladder (J = K) are called the metastable states as they can only decay via the much slower (10^9 s) $\Delta k = \pm 3$ transitions (Ho & Townes 1983). The population in the metastable states thus excited mostly by collisions and should reflect the kinetic temperature of the gas via a Boltzmann distribution.

NH_3 is divided into two distinct species based on the orientation of the hydrogen spins. Ortho-NH_3 has all H-spins parallel, and gives rise to (K=3n, n=1,2,3,...) levels while Para-NH_3 has some H-spins anti-parallel and gives rise to (K≠3n, n=1,2,3,...) levels. Under normal conditions these species do not inter-convert. Ortho-NH_3 has twice the statistical weight of para-NH_3.

2-4.2 Modified rotational diagram method

Here we present the modified rotational diagram method used to calculate kinetic temperatures and column densities via a comparison of the NH_3(1,1) and (2,2) spectra. This method follows closely to that presented in Ungerechts et al. (1986), who consolidated the methods of Ho et al. (1977), Ungerechts et al. (1980) and Townes et al. (1983).

1: Determine optical depth of the J,K=(1,1) transition

Optical depth as a function of frequency over the NH_3 spectrum may be modelled by a sum of five individual Gaussian line profiles

$$\tau(\nu) = \tau^{\rm total} \times \phi(\nu) \quad = \quad \tau^{\rm total} \times \sum_{\rm i=1}^{5} \, {\rm f_i} \left[\exp \, - \left(\frac{\nu - \nu_0 - \Delta\nu_{\rm i}}{\Delta\nu} \right) \right], \qquad (2.59)$$

where f_i is the fraction of the total intensity the i^{th} component (see Table 2.1), $\Delta\nu_i$ is the frequency offset between i^{th} component and the central component, ν_0 is the frequency of the central component, and $\Delta\nu$ is the common linewidth. The total optical depth is related to the physical conditions in the gas via Equation 2.50,

$$\tau^{\rm total} = \tau^{\rm peak} = \frac{\rm c^2}{8\pi\nu^2} \, {\rm A_{ul} N_u} ({\rm e}^{\rm h\nu/kT_{ex}} - 1) \, \phi^{\rm peak},$$

where the $\phi^{\rm peak}$ is the peak height of an unsplit J,K line profile. Assuming a normalised Gaussian profile, this is given by

$$\phi^{\rm peak} = \frac{\sqrt{4 \ln 2}}{\Delta\nu\sqrt{\pi}}. \qquad (2.60)$$

Intensity as a function of frequency may then be modelled by applying $\tau(\nu)$ calculated from Equation 2.59 to the detection equation (Equation 2.45):

$$\rm T_b(\nu) = \frac{h\,\nu}{k} \left[J_\nu(T_{ex}) - J_\nu(T_{bg}) \right] \left(1 - e^{-\tau(\nu)} \right).$$

A fit of this model profile to the observed spectrum will yield the total optical depth, excitation temperature and linewidth. The NH_3(1,1) and NH_3(2,2) hyperfine fitting routines in the CLASS[2]. analysis package performs this fit automatically.

2. CLASS is a spectral line analysis package within the GILDAS suite of radio-astronomy processing software, which is available at: http://www.iram.fr/IRAMFR/GILDAS/

Alternatively, optical depth may be found by comparing the peak intensities of the satellites and the main line. From the detection equation we see that

$$\frac{\mathrm{T_{B,main}}}{\mathrm{T_{B,sat}}} = \frac{1-\mathrm{e}^{-\tau_{\mathrm{main}}}}{1-\mathrm{e}^{-\tau_{\mathrm{sat}}}} = \frac{1-\mathrm{e}^{-\tau_{\mathrm{main}}}}{1-\mathrm{e}^{-\mathrm{a_{ms}}\,\tau_{\mathrm{main}}}}, \tag{2.61}$$

where '$\mathrm{a_{ms}}$' is the expected ratio of $\mathrm{T_{main}/T_{sat}}$ under optically thin conditions. Theoretically, this ratio is found from $\mathrm{a_{ms}} = \mathrm{f_{main}/f_{sat}}$ whose values are presented in column four of Table 2.1. Equation 2.61 must be solved numerically for τ_{main}. The total optical depth of the transition is then found from

$$\tau^{\mathrm{total}} = \frac{\tau_{\mathrm{main}}}{\mathrm{f_{main}}}. \tag{2.62}$$

This method is equally valid for any J→J,K=±1, … ±J transition of the NH_3 inversion spectrum.

2: Determine optical depth of the J,K=(2,2) transition

In practise, for transitions with J > 1 it is often difficult to calculate the optical depth directly from the brightness temperature ratio of satellite to main lines as the signal-to-noise on the weak satellite lines is usually poor. For any (J,K) transition, $\tau_{\mathrm{J,K}}$ may be calculated from the ratio of the NH_3(J,K) and NH_3(1,1) main lines instead, assuming the emission comes from the same gas and the level populations are described by the same excitation temperature. Considering only the main line in each spectrum, Equations 2.62 and 2.45 give

$$\tau_{\mathrm{J,K\,main}} = \tau^{\mathrm{total}}_{\mathrm{J,K}} \times \mathrm{f_{J,K\,main}} = -\ln\left(1 - \frac{\mathrm{T_{B_{J,K\,main}}}}{\mathrm{A_{J,K\,main}}}\right), \tag{2.63}$$

where $\mathrm{A_{J,K\,main}} = [\mathrm{J(T_{ex})} - \mathrm{J(T_{bg})}]$. In the case of the NH_3 (2,2) line we have

$$\tau^{\mathrm{total}}_{2,2} = -\frac{1}{\mathrm{f_{2,2\,main}}} \ln\left(1 - \frac{\mathrm{T_{B_{2,2\,main}}}}{\mathrm{A_{1,1\,main}}}\left[\frac{\mathrm{A_{1,1\,main}}}{\mathrm{A_{2,2\,main}}}\right]\right). \tag{2.64}$$

For equal excitation temperatures the factor $[\mathrm{A_{1,1,main}/A_{2,2\,main}}]$ is approximately 1. From the detection equation we see that $\mathrm{A_{1,1\,main}} = \mathrm{T_{B_{1,1,main}}}/(1-\mathrm{e}^{-\tau_{1,1\,\mathrm{main}}})$ and Equation 2.64 becomes

$$\tau^{\mathrm{total}}_{2,2} = -\frac{1}{\mathrm{f_{2,2\,main}}} \ln\left[1 - \frac{\mathrm{T_{B_{2,2\,main}}}}{\mathrm{T_{B_{1,1\,main}}}}\left(1-\mathrm{e}^{-\tau_{1,1\,\mathrm{main}}}\right)\right]. \tag{2.65}$$

3: Calculate the rotational temperature

A rotational temperature may be defined from Equation 2.54:

$$\ln\left(\frac{N_u}{g_u}\right) = \ln\left(\frac{N}{Q(T)}\right) - \frac{E_u}{kT_{rot}},$$

where N_u is the column density of molecules in the upper state. In the analysis performed in this thesis we utilise only the NH_3 (1,1) and (2,2) transitions so an explicit formula may be stated for the rotational temperature defined by these lines:

$$\frac{N_{2,2}}{N_{1,1}} = \frac{g_{2,2}}{g_{1,1}}\left(\, e^{-(E_{2,2}-E_{1,1})/kT_{rot}}\right).$$

Rearranging in terms of T_{rot} and inserting values for the constants we find

$$T_{rot} = -41\,K/\ln\left(\frac{3}{5}\frac{N_{2,2}}{N_{1,1}}\right), \tag{2.66}$$

where $g_{1,1}=3$, $g_{2,2}=5$ and $(E_{2,2}-E_{1,1})/k$=41 K. The column density in a particular state is proportional to $(\tau\,\Delta v)/A_{ul}$ via Equation 2.50, so Equation 2.66 may be written in terms of the optical depths of the NH_3 (1,1) and (2,2) lines:

$$T_{rot} = -41\,K/\ln\left(\frac{5}{3}\frac{A_{1,1}}{A_{2,2}}\frac{\tau_{2,2}}{\tau_{1,1}}\left[\frac{\Delta\nu_{2,2}}{\Delta\nu_{1,1}}\right]\right) = -41\,K/\ln\left(\frac{9}{20}\frac{\tau_{2,2}}{\tau_{1,1}}\left[\frac{\Delta\nu_{2,2}}{\Delta\nu_{1,1}}\right]\right), \tag{2.67}$$

Assuming the NH_3 (1,1) and (2,2) emission arises in the same gas then the linewidths should have the same value and $[\Delta\nu_{2,2}/\Delta\nu_{1,1}] \approx 1$. A comparison of the optical depths in the NH_3 (2,2) and (1,1) lines yields the rotation temperature from

$$T_{rot} = -41\,K/\ln\left(\frac{9}{20}\frac{\tau_{2,2}}{\tau_{1,1}}\right). \tag{2.68}$$

4: Calculate the kinetic temperature

In a simple two-level system in the steady state $n_u\,C_u = n_l\,C_l$, (Equation 2.29), if radiative transitions are negligible. Assuming LTE conditions, and therefore a Boltzmann distribution of populations (Equation 2.18), and applying detailed-balance (Equation 2.30) we find that $T_{rot} = T_{kin}$. However in the case of NH_3 the population in the non-metastable levels may be non-negligible. Hence the approximation of a Boltzmann distribution between the NH_3(1,1) and (2,2) levels may not be valid.

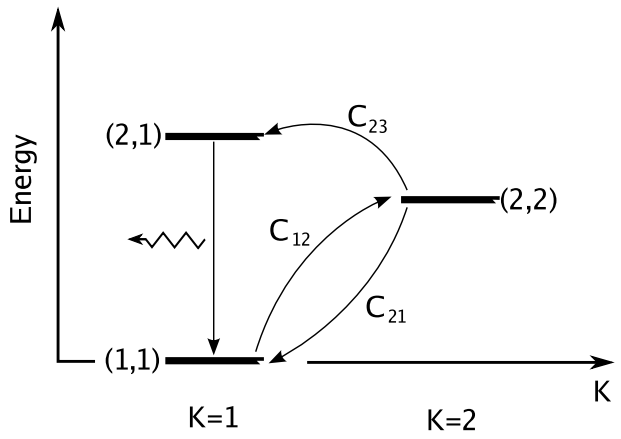

Figure 2.9. Energy level diagram showing the collisional transitions between the J,K=(2,2), (2,1) and (1,1) energy levels of NH_3. Quadrupole splitting is not shown. C_{xy} are the collisional coefficients between levels. When calculating kinetic temperatures from the NH_3 (1,1) and (2,2) lines we must also take into account the non-metastable levels as they can still contain significant numbers of molecules. For temperatures under $\sim$50 K it is sufficient to include only the J,K=(2,1) level.

If the excitation temperature is below $\sim$50 K, we can improve our estimate of the kinetic temperature by considering collisions between the (1,1), (1,2) and (2,2) states (see Figure 2.9). The steady state equation for collisional transitions between these three states is

$$\frac{n_{22}}{n_{11}} = \frac{C_{12}}{(C_{21}+C_{23})} = \frac{C_{12}}{C_{21}}\frac{1}{(1+C_{23}/C_{21})}, \tag{2.69}$$

where C_{23}, C_{21} and C_{12} are the collisional rate coefficients between the J,K=(2,2→2,1), J,K=(2,2→1,1) and J,K=(1,1→2,2) levels, respectively. Substitution of the Boltzmann and detail balance relations for the factors n_{22}/n_{11} and C_{12}/C_{21} yields a new relationship between the rotational and kinetic temperatures:

$$T_{rot} = \frac{T_{kin}}{[1+(T_{kin}/41\,K)\ln(1+C_{23}/C_{21})]}. \tag{2.70}$$

Collisional rates have been modelled by Danby et al. (1988) and are given in Table 2.2.

Table 2.2. Collisional rates between the NH_3 (2,2), (1,1) and (2,1) rotational levels, from Danby et al. (1988).

	Collisional rates ($cm^3.s^{-1}$)			
Transition[a]	15 K	25 K	50 K	75 K
C_{23}	0.6×10^{-11}	1.0×10^{-11}	1.5×10^{-11}	1.7×10^{-11}
C_{21}	3.0×10^{-11}	2.8×10^{-11}	2.7×10^{-11}	2.8×10^{-11}
C_{23}/C_{21}	0.19	0.34	0.54	0.63

[a] C_{23}=C(22→21) is calculated from C(21→22) tabulated in Danby et al. (1988) via the detail balance equation ($C_{lu}/C_{ul} = e^{-(\Delta E)/T_{kin}}$), where ΔE is the energy difference between the energy levels ≈ 17.1 K.

5: Calculate the column density

Given the total integrated intensity ($\int_{-\infty}^{\infty} T_b\,dv$) in the NH_3 (1,1) spectrum, the column density in the J,K = 1,1 level may be found using Equation 2.52,

$$N_{1,1} = \frac{8k\pi\nu_{1,1}^2}{A_{ul}hc^3}\int_{-\infty}^{\infty} T_b\,dv\,\left(\frac{\tau}{1-e^{-\tau}}\right),$$

where τ is the total optical depth in the NH_3 (1,1) spectrum. The total column density, N, may then be found from Equations 2.20 and 2.21, as before

$$N = \frac{N_{1,1}}{g_{1,1}}\,e^{(E_{1,1})/kT}\,Q(T_{rot}) \qquad\qquad Q(T_{rot}) = \sum_i g_i\,e^{-E_i/kT_{rot}},$$

where $Q(T_{rot})$ is the partition function. If only data for the (1,1) and (2,2) transitions are available then it is reasonable to approximate the partition function by a sum over the first few J,K energy levels. The total column density is then given by

$$N = N_{1,1}\left[\frac{1}{3}e^{+23.26/T_{rot}} + 1 + \frac{5}{3}e^{-41.18/T_{rot}} + \frac{14}{3}e^{-100.25/T_{rot}} + \frac{9}{3}e^{-177.21/T_{rot}} + \frac{11}{3}e^{-272.02/T_{rot}} + \frac{26}{3}e^{-284.67/T_{rot}} \ldots\right], \quad (2.71)$$

which assumes that the relative population of all metastable levels of both ortho- and para-NH_3 are in thermal equilibrium at a temperature T_{rot}. Note that states with J = 3n have statistical weights of **2**×(2J+1).

Chapter 3

The Mopra millimetre-wave telescope

Two millimetre-wave facilities provided the bulk of the data underpinning this thesis: the Australia Telescope Compact Array (ATCA) and the single-dish Mopra telescope. The ATCA is a interferometer consisting of six 22-m antennas, operating at wavelengths down to 3-mm. With a maximum baseline length of six kilometres, the ATCA is ideally suited to imaging a small number of sources at resolutions of a few arcseconds (e.g., Chapter 6). The Mopra telescope with its $\sim$35$''$ beam is more suited to conducting surveys of a large number of sources (e.g., Chapters 4 and 5).

While the Compact Array is fully supported by the Australia Telescope National Facility (ATNF), Mopra is run in partnership with the University of New South Wales (UNSW) and is utilised as a 'teaching telescope' for new millimetre astronomers. Between June 1999 and September 2004 astronomers from UNSW played a significant role in commissioning the telescope for full operations at 3-mm wavelengths. The author was heavily involved in measuring the beam-shape and efficiencies, and in developing a data reduction package for position switched data. In this chapter we introduce the Mopra telescope, present the characterisation work and describe the data reduction methodology.

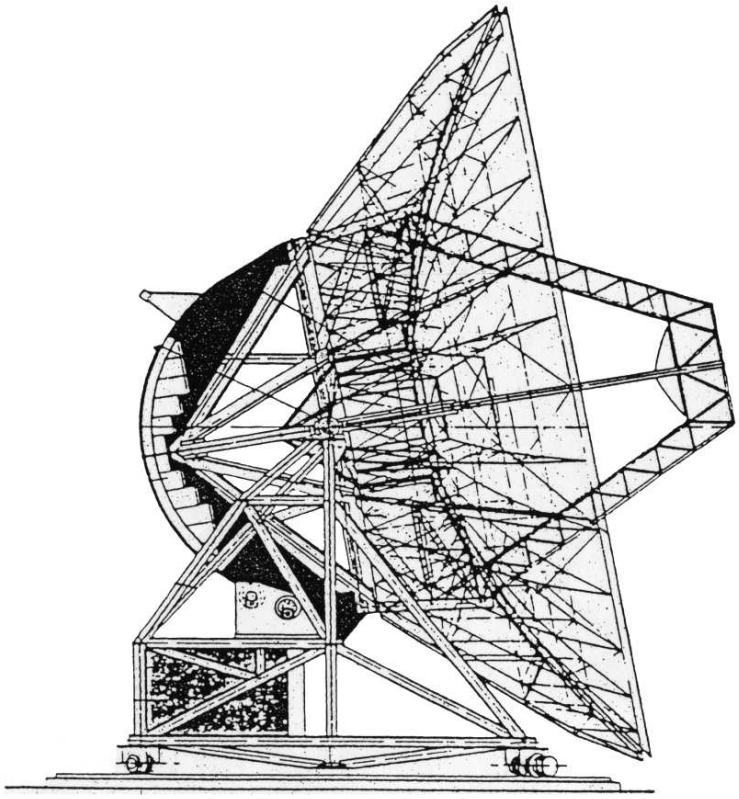

Figure 3.1. Sketch of the Mopra antenna showing the A-frame mount and cassegrain optical design.

3-1 Construction

The Mopra antenna is a 22-m single-dish telescope, located 26 km outside the town of Coonabarabaran, in northern New South Wales. The observatory is located at an elevation of 866.4 metres above sea-level and at coordinates $-31^\circ\,16'\,04.127''$ (S), $+149^\circ\,05'\,58.706''$ (E). A sketch of the antenna structure is presented in Figure 3.1. The optical system is a cassegrain design, with a 4-m secondary and a pseudo-parabolic primary reflector, shaped to maximise the gain for single-feed receivers. The dish, receiver cabin and support structure are mounted on a wheeled A-frame, which rotates in azimuth on a circular ground rail. The wide aspect ratio of the mount means it is exceptionally stable, leading to greater pointing accuracy compared to the similar dishes of the Compact Array. The telescope is free to pivot from 0° to 90° in elevation, however, objects cannot be tracked through the zenith

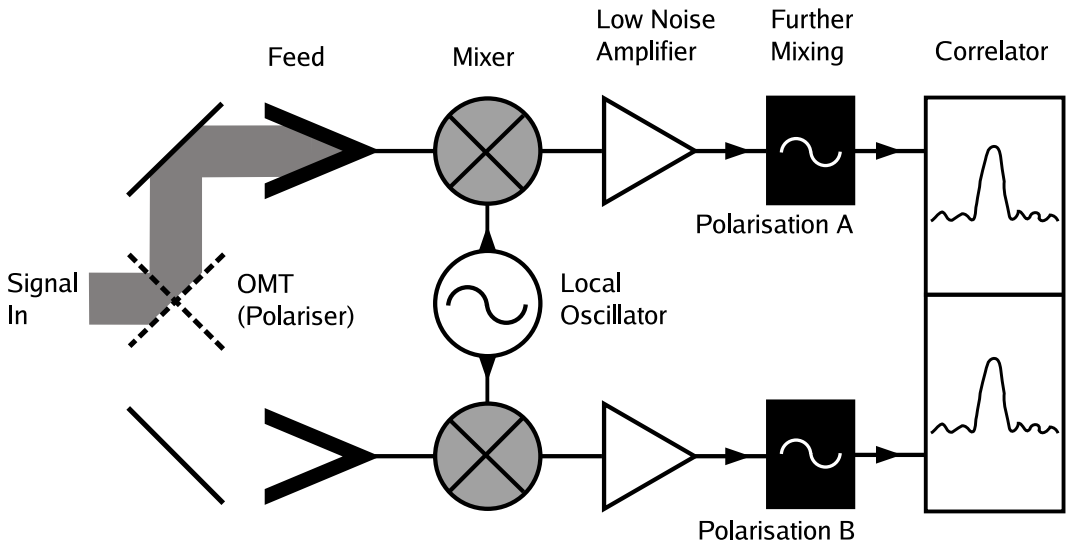

Figure 3.2. A block diagram of the Mopra SIS receiver. Radiation is split into orthogonal linear polarisations by the ortho-mode transducer (OMT) before entering separate receiver chains, via the feed horns. The signal is mixed with a 'local oscillator' reference, resulting in a lower frequency signal suitable for processing. The signal is then amplified by a low noise amplifier, mixed further, digitised and finally passed to a digital auto-correlator, where a spectrum is produced.

as the telescope must swivel 180° in azimuth, leading to a true elevation limit of 85°. Pointing accuracy has been estimated to be better than 9″ (RMS) between elevations of 45° and 80°.

3-2 The 3-mm receiver and correlator

The 3-mm receiver is based around a superconductor-insulator-superconductor (SIS) diode, which must be cooled to temperatures below 4 K in order to remain operational. This is achieved by a three-stage closed-cycle cryogenic system utilising liquid helium as the working fluid. The low thermal noise leads to correspondingly low system temperatures and a high sensitivity. At a frequency of 86 GHz, and in good conditions, the typical receiver and system noise temperatures are 80 K and 200 K, respectively.

Radiation entering the receiver package is split into orthogonal linear polarisations by crossed wire polarisers mounted at 45 ° to the optical axis. Each polarisation is reflected into a separate feed-horn and fed into one of two independently tunable receiver chains. Figure 3.2 shows a block diagram of the principal receiver components. Incident radiation is conveyed from the feed-horn, via a waveguide, into the mixer cavity, where it is mixed with a reference signal called the *local oscillator*. The local oscillator is tuned to be exactly 80 MHz offset from the desired sky frequency resulting in two components at frequencies given by the relation

$$\mathrm{Cos}(\nu_{\mathrm{sig}})\,\mathrm{Cos}(\nu_{\mathrm{lo}}) = 1/2\ [\mathrm{Cos}(\nu_{\mathrm{sig}} - \nu_{\mathrm{lo}}) + \mathrm{Cos}(\nu_{\mathrm{sig}} + \nu_{\mathrm{lo}})], \tag{3.1}$$

where ν_{sig} is the frequency of the signal and ν_{lo} is the frequency of the local oscillator. The cavity shape is tuned to reject the high frequency component and the low frequency component is converted into an electrical signal by the SIS junction. Finally the signal is amplified by a low noise amplifier (LNA) and further mixed to lower frequencies, before being digitised by a 2-bit sampler and sent to the correlator.

The signal is processed into a spectrum by a digital auto-correlator and written to disk. The correlator may be configured to have a bandwidths between 8 and 256 MHz, split into 32 – 2048 spectral channels. Data is written to the output file at the clock cycle time of the correlator, usually set at two seconds.

3-3 Observing modes

3-3.1 Position switching

The principal observing mode offered on the Mopra antenna is *position switching*. In this mode the antenna alternately points at the target (or ON) position and an emission free region of 'blank' sky (or OFF). The contribution due to instrumental and atmospheric emission is removed by subtracting the OFF signal from the ON signal, resulting in a flat spectrum containing only emission due to the target source. Because the atmospheric transmission varies on timescales shorter than ∼15 minutes

the antenna performs several short (2 minute) position-switched observations, which are then averaged together to produce the final spectrum. The ideal RMS sensitivity is given by the radiometer equation

$$\Delta T^*_{A,RMS} = \frac{2\,f\,T_{sys}}{\sqrt{n_p\,\Delta\nu\,t_{on}}} \quad \ldots \text{(in K)}, \tag{3.2}$$

where $f = (1/\text{Transmission})$ describes the losses of the spectrometer (at Mopra $f \approx 1.3$), T_{sys} is the system temperature (see Section 3-4), n_p is the number of polarisations observed, $\Delta\nu$ is the bandwidth in Hz and t_{on} is the total time spent observing the target source. The sensitivity calculated using Equation 3.2 must be corrected for further losses due to the efficiency of the telescope (see Section 3-4.1).

3-3.2 On-the-fly mapping

The antenna is also capable of on-the-fly (OTF) mapping. In this mode the beam is scanned along a line on the sky at a constant rate, recording spectra every clock cycle (2 sec). An image is built up by combining multiple scans. Before commencing each scan an OFF spectrum is recorded, which is then used to remove the sky and atmospheric contribution. The scanning rate and the offset between the scan lines depends on the beam-size and hence the observation frequency. To fully sample the spatial scales in the scan direction, the scan rate must be slow enough so that the beam position does not change by more than half the beam FWHM every clock cycle. To fully sample in the orthogonal direction adjacent scan lines must be spaced by half of the beam FWHM.

The RMS sensitivity in an image is given by the more general form of the radiometer equation

$$\Delta T^*_{A,RMS} = \frac{(1 + 1/\sqrt{n_{dumps}})\,f\,T_{sys}}{\sqrt{n_p\,n_{Sp}\,\Delta\nu\,t_{int}}}\sqrt{1 + \frac{t_{on}}{t_{off}}}, \tag{3.3}$$

where n_{dumps} is the number of times the spectra are written to the file per second (in the case of a 2-s clock time $n_{dumps} = 0.5\,s^{-1}$) and n_{sp} is the number of spectra contributing to each pixel in the final map, if the map is oversampled.

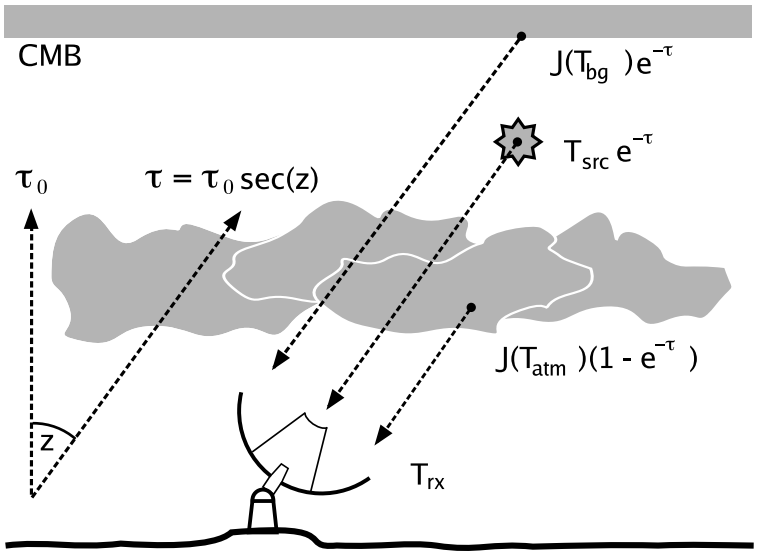

Figure 3.3. Graphical representation of the main components contributing to total measured power in the receiver. The measured power is the sum of contributions from the cosmic microwave background (T_{bg}), source (T_{src}), atmosphere (T_{atm}) and noise in the receiver (T_{rx}). The measured total power also varies with the optical depth of the atmosphere (τ) and the pointing angle with respect to the zenith (z).

3-4 Calibrating single dish data

At wavelengths shorter than 1-cm it becomes increasingly difficult to accurately calibrate a telescope flux scale. Water vapour, and to a lesser extent oxygen, in the atmosphere attenuates the signal from space. The level of attenuation is variable and depends on the weather conditions. To preserve the telescope flux scale the level of attenuation must be measured and corrected for on timescales less than ∼15 minutes. In the discussion which follows we assume that the emission from a radio source can be characterised by an effective source radiation temperature $J(T_B)$, related to a blackbody brightness temperature, T_B, by

$$J(T_B) \equiv \frac{h\nu}{k} \frac{1}{e^{h\nu/kT_B} - 1}.$$

Figure 3.3 is a graphical representation of the major components which contribute to the signal measured in the receiver. The raw voltage when pointed on-source is

given by

$$V_{source} = C\ [\ T_{src}\ e^{-\tau} + J(T_{atm})\ (1 - e^{-\tau}) + J(T_{bg})\ e^{-\tau} + T_{rx}\ ], \tag{3.4}$$

and when pointed off-source is given by

$$V_{sky} = C\ [\ J(T_{atm})\ (1 - e^{-\tau}) + J(T_{bg})\ e^{-\tau} + T_{rx}\ ], \tag{3.5}$$

where C is the constant conversion factor between brightness temperature and voltage, T_{src} is the brightness temperature of the source, T_{atm} is the ambient temperature of the atmosphere, T_{bg} is the temperature of the background radiation field, and T_{rx} is the noise temperature of the receiver. The brightness temperature of the source is then given by

$$T_{src} = (V_{source} - V_{sky})\ \frac{e^{\tau}}{C}. \tag{3.6}$$

A convenient definition is that of the system temperature, T_{sys}

$$T_{sys} = V_{sky}\ \frac{e^{\tau}}{C} = J(T_{atm})\ (e^{\tau} - 1) + J(T_{bg}) + T_{rx}\ e^{\tau}, \tag{3.7}$$

which is in fact a measurement of the total noise in the system. Equation 3.6 then becomes

$$T_{src} = T_A^* = \left(\frac{V_{source} - V_{sky}}{V_{sky}}\right) T_{sys}, \tag{3.8}$$

and a measurement of T_{sys} will enable the calibration of the brightness temperature scale.

3-4.1 Telescope efficiencies and temperature scales

The variation in sensitivity as a function of offset angle is known as the telescope 'beam pattern'. For an ideal circular aperture this is given by an airy pattern, however, mm-wave telescopes usually operate close to the diffraction limit and have obscuring secondary reflectors, leading to a more extended beam pattern. Figure 3.4 is a 1-D polar plot of sensitivity versus angle for a typical parabolic antenna. The beam pattern can be divided into two distinct zones: the main beam and the error pattern, which includes near side lobes, far side lobes and rear lobes. Some fraction of

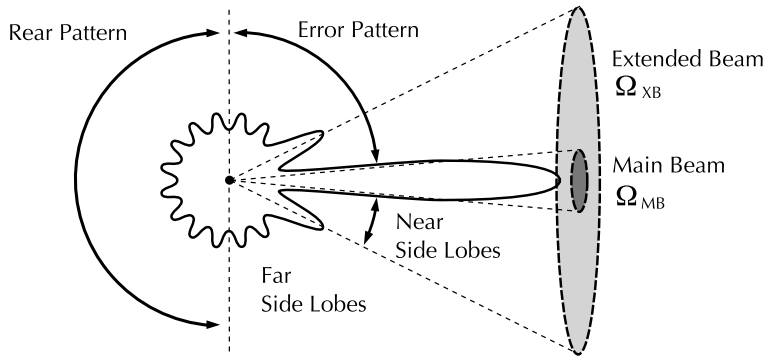

Figure 3.4. Polar plot of the response or 'beam pattern' of a single dish telescope (adapted from Rohlfs & Wilson 2004). The beam pattern is divided into a main beam plus an error pattern. While the main beam is relatively sensitive compared to the error pattern, a significant fraction of the power entering the receiver comes from the error pattern due to the large solid angle it covers.

the received power comes from the error pattern, effectively diluting the signal from the main lobe. We can define a main beam efficiency $\eta_{\rm mb}$, indicating the fraction of power concentrated in the main lobe compared to the total power received from the forward hemisphere

$$\eta_{\rm mb} = \frac{\iint \mathrm{P_{mb}}(\Omega)\,\mathrm{d}\Omega}{\iint_{2\pi} \mathrm{P_b}(\Omega)\,\mathrm{d}\Omega}. \tag{3.9}$$

In Equation 3.9 $\mathrm{P_{mb}}(\Omega)$ is the main lobe power pattern covering a solid angle $\Omega_{\rm MB}$, $\mathrm{P_b}(\Omega)$ is the normalised antenna power pattern and Ω is the solid angle on the sky. For a source with an intensity distribution $\mathrm{T_R}(\phi)$ as a function of offset angle ϕ, the measured brightness temperature will be given by

$$\mathrm{T_A^*} = \eta_{\rm mb} \frac{\iint \mathrm{P_{mb}}(\phi)\,\mathrm{T_R}(\phi)\,\mathrm{d}\phi}{\iint \mathrm{P_{mb}}(\Omega)\,\mathrm{d}\Omega}. \tag{3.10}$$

The main beam efficiency can be broken up into more specific terms and at different stages in the calibration different temperature scales are used to denote what efficiency factors have been taken into account. The following temperature scales have been defined:

$\mathrm{T_R}$ Source radiation temperature.

$\mathrm{T_A}$ Observed source antenna temperature.

T'_A $= T_A\ e^{\tau}$

Observed source antenna temperature corrected for atmospheric attenuation (e^{τ}).

T^*_A $= T'_A/\eta_r\eta_{rss}$

Observed source antenna temperature corrected for atmospheric attenuation, radiative loss (η_r) and rearward scattering (η_{rss}).

T_{MB} $= T'_A/(\eta_r\eta_{rss}\eta_{mb})$

Observed source antenna temperature corrected for atmospheric attenuation, radiative loss, rearward and forward scattering (η_{mb}).

In the notation used in this work $T_{MB} \equiv T^*_R$ and $\eta_{mb} \equiv \eta_{fss}$, where T^*_R and η_{fss} are defined in Kutner & Ulich (1981). T_{MB} is the source brightness temperature measured by the main lobe of the telescope beam, and will be equal to the source brightness temperature T_R if the source just fills the main beam.

3-4.2 Online calibration: the chopper wheel method

Calibration to the telescope dependent T^*_A scale is achieved by measuring a noise source of known amplitude during observations. At centimetre wavelengths this usually takes the form of a thermal diode coupled directly to the feed. Historically, these noise-diodes have proven problematic to use at millimetre-wavelengths as their time, frequency and polarisation dependent output made them unreliable[1]. As an alternative, Penzias & Burrus (1973) developed the chopper wheel technique, where a blackbody emitter of known physical properties is alternately introduced and removed from the signal path. The voltage measured when the emitter is in place is given by

$$V_{load} = C\ [\ J(T_{load}) + T_{rx}], \tag{3.11}$$

1. A new generation of noise diodes suitable for use at 3-mm wavelengths were installed at Mopra in 2006, however, all data in this thesis was calibrated using the chopper-wheel technique.

where T_{load} is the temperature of the blackbody emitter. Comparing the signal from blank sky to the known load allows the determination of T_{sys} as follows. Using Equations 3.5 and 3.11 we find

$$\frac{V_{sky}}{V_{load} - V_{sky}} = \frac{J(T_{atm})\ (1 - e^{-\tau}) + J(T_{bg})\ e^{-\tau} + T_{rx}}{J(T_{load}) - J(T_{atm})\ (1 - e^{-\tau}) - J(T_{bg})\ e^{-\tau}}.$$

This expression can be simplified considerably by assuming $T_{atm} = T_{load}$, i.e., the ambient atmospheric temperature is the same as the temperature of the absorbing load, therefore

$$\frac{V_{sky}}{V_{load} - V_{sky}} = \frac{J(T_{atm})\ (1 - e^{-\tau}) + J(T_{bg})\ e^{-\tau} + T_{rx}}{J(T_{atm})\ e^{-\tau} - J(T_{bg})\ e^{-\tau}}.$$

Multiplying across by e^{τ} and substituting in Equation 3.7 we get

$$\frac{V_{sky}}{V_{load} - V_{sky}} = \frac{T_{sys}}{J(T_{atm}) - J(T_{bg})},$$

and

$$T_{sys} = \frac{V_{sky}\ [J(T_{atm}) - J(T_{bg})]}{V_{load} - V_{sky}}. \tag{3.12}$$

In Equation 3.12, T_{atm} is assumed to be 300 K and T_{bg} is 2.7 K, the temperature of the cosmic microwave background. Given a value for T_{sys} the radiation temperature of the source, $T_R = T_{src}$, may then be found from Equation 3.8.

3-5 Characterising the Mopra beam

The beam shape and efficiencies of the Mopra telescope were characterised for the first time during the 2003 and 2004 observing seasons. The response of the beam was measured from on the fly maps (see Section 3-3) of strong SiO masers and continuum emission from the planets Mercury, Mars and Jupiter. Full details of the results are published in Ladd et al. (2005), from which the following discussion is adapted.

3-5.1 Measuring the beam shape

The 86.243 GHz $J = 2 \rightarrow 1, v = 1$ masing transition of SiO is an ideal probe of the Mopra beam shape in the 3-mm waveband. Originating in the atmosphere of

Table 3.1. Details of the SiO masers mapped.

Source	R.A. (hms) (J2000.0)	Dec (dms) (J2000.0)	Date Observed (UT)	Frequency (GHz)	Map Extent (″)
O Ceti (Mira)	02 : 19 : 20.7	−02 : 58 : 38	2003 Aug 18 17:18	86.2	110″ × 120″
O Ceti (Mira)	02 : 19 : 20.7	−02 : 58 : 38	2003 Aug 18 18:33	86.2	110″ × 120″
O Ceti (Mira)	02 : 19 : 20.7	−02 : 58 : 38	2003 Aug 19 17:34	86.2	110″ × 120″
O Ceti (Mira)	02 : 19 : 20.7	−02 : 58 : 38	2003 Aug 19 19:02	86.2	110″ × 120″
O Ceti (Mira)	02 : 19 : 20.7	−02 : 58 : 38	2003 Aug 20 17:11	86.2	110″ × 120″
O Ceti (Mira)	02 : 19 : 20.7	−02 : 58 : 38	2003 Aug 20 18:23	86.2	110″ × 120″
W Hya	13 : 49 : 29.4	−28 : 22 : 03	2004 Oct 21 03:36	86.2	110″ × 120″
W Hya	13 : 49 : 29.4	−28 : 22 : 03	2004 Oct 21 05:25	86.2	110″ × 120″
IK Tau	03 : 53 : 53.2	11 : 24 : 23	2004 Oct 22 15:15	86.2	110″ × 120″
Orion	05 : 35 : 38.6	−05 : 22 : 30	2004 Oct 22 16:56	86.2	110″ × 120″
Orion	05 : 35 : 38.6	−05 : 22 : 30	2004 Oct 22 18:08	86.2	110″ × 120″
AH Sco	17 : 12 : 04.2	−32 : 19 : 32	2004 Oct 23 07:02	86.2	170″ × 180″
VY CMa	07 : 23 : 42.5	−25 : 46 : 02	2004 Oct 23 20:21	86.2	170″ × 180″
R Leo	09 : 48 : 14.3	11 : 25 : 44	2004 Oct 23 21:44	86.2	170″ × 180″
W Hya	13 : 49 : 29.4	−28 : 22 : 03	2004 Oct 24 00:11	86.2	170″ × 180″
R Leo	09 : 48 : 14.3	11 : 25 : 44	2004 Oct 24 19:18	86.2	170″ × 180″
R Leo	09 : 48 : 14.3	11 : 25 : 44	2004 Oct 24 21:41	86.2	170″ × 180″

evolved stars, SiO maser sites have angular spreads typically less than 1″ (e.g., Soria-Ruiz et al. 2004) and are effectively point sources within the ∼37″ Mopra beam. The brightest examples reach brightness temperatures of tens of Kelvin (e.g., the SiO maser in Orion) allowing the production of very high signal-to-noise maps of the beam structure.

Several OTF maps were made of SiO masers in August 2003 and October 2004. The coordinates of the masers, observation dates and extents of the maps are recorded in Table 3.1. During the data reduction process individual maps were re-gridded to an altitude-azimuth rest frame centred on the maser position and several maps were co-added to produce the final image. The resultant 86 GHz beam maps for 2003 and 2004 are presented in Figure 3.5. In both years the main lobe was symmetric and round to the 20 per cent level. The most distinctive feature in the 2003 beam is the inner error lobe, which peaks at an azimuth offset of +60″ and has maximum response of approximately 10 per cent. Analysis of the asymmetry revealed that the cause was a misalignment of the sub-reflector with the optical axis of the telescope. In May 2004 a translational shift was applied to the position of

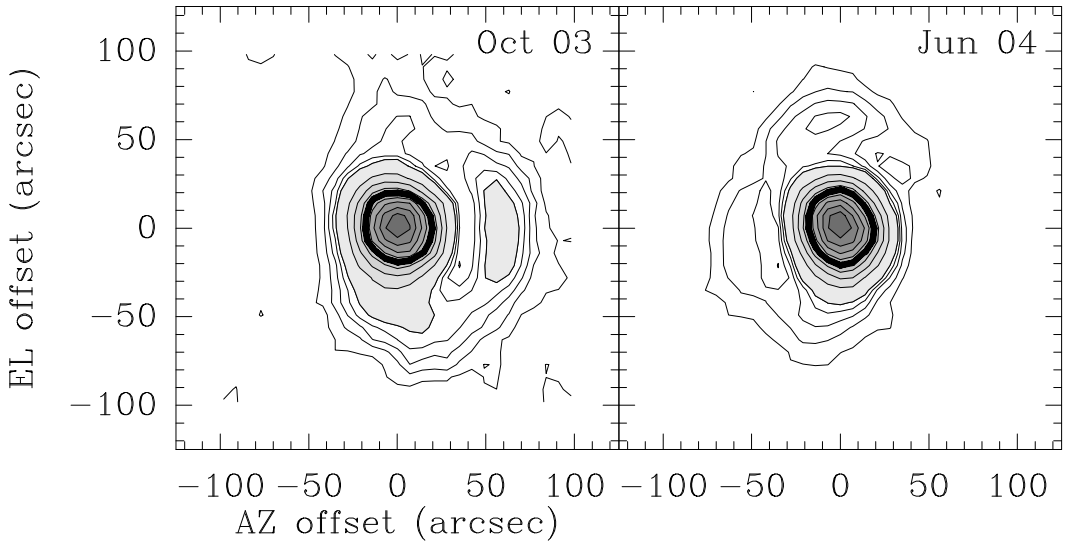

Figure 3.5. Maps of the telescope beam constructed from 86 GHz SiO maser emission data taken in October 2003 (left panel) and June 2004 (right panel). Contours first increment from 1% to 10% of peak intensity in 1% intervals, and then from 10% to 90% in 10% intervals (with greyscales). The 50% contour is plotted in bold. The substantial change in the beam response at low levels is due to a translational shift in the position of the telescope's sub-reflector accomplished in May 2004.

the sub-reflector, resulting in a substantial decrease in the error lobe as shown in Figure 3.5, *right*.

3-5.2 Beam size versus frequency

At frequencies above 86 GHz there are no convenient masers bright enough to produce high signal-to-noise maps of the beam. Instead, the response of the beam at other frequencies was measured by mapping thermal continuum emission from planets. The sensitivity to continuum emission is limited at Mopra by the 600 MHz maximum bandwidth available through the SIS receiver, consequently the maps have lower signal to noise than the SiO maser data. By averaging several maps together it is possible to improve the signal-to-noise ratio considerably.

Maps of the continuum emission from planets were made at a range of frequencies from 86 – 110 GHz and these data show how the shape of the beam changes

Table 3.2. Details of the planetary observations.

Source	Date Observed (UT)	Angular Size (″)	Frequency 1 (GHz)	Frequency 2 (GHz)	Map Extent (″)
Mars	2003 October 20 1110	16.9	100	86	$110'' \times 70''$
Mars	2003 October 22 1230	16.5	100	86	$130'' \times 120''$
Mars	2003 October 22 1405	16.5	100	86	$90'' \times 80''$
Mars	2003 October 23 1015	16.4	100	86	$200'' \times 180''$
Mars	2003 October 23 1205	16.4	100	86	$200'' \times 180''$
Mars	2003 October 23 1335	16.4	100	86	$200'' \times 180''$
Mercury	2004 June 4 2308	5.7	110	86	$130'' \times 120''$
Mercury	2004 June 4 2345	5.7	110	86	$130'' \times 120''$
Mercury	2004 June 5 2245	5.7	99	99	$130'' \times 120''$
Mercury	2004 June 5 2315	5.6	99	99	$130'' \times 120''$
Mercury	2004 June 6 0028	5.6	115	115	$130'' \times 120''$
Mercury	2004 June 6 0058	5.6	115	115	$130'' \times 120''$
Mercury	2004 June 6 0200	5.6	99	86	$130'' \times 120''$
Mercury	2004 June 6 0230	5.6	99	86	$130'' \times 120''$
Jupiter	2004 June 5 0836	36.4	115	86	$130'' \times 120''$
Jupiter	2004 June 5 0913	36.4	115	86	$130'' \times 120''$
Jupiter	2004 June 5 1007	36.4	86	86	$130'' \times 120''$
Jupiter	2004 June 6 0523	36.3	99	99	$130'' \times 120''$
Jupiter	2004 June 6 0551	36.3	99	99	$130'' \times 120''$
Jupiter	2004 June 6 0704	36.3	99	99	$130'' \times 120''$
Jupiter	2004 June 6 0802	36.3	115	115	$130'' \times 120''$
Jupiter	2004 June 6 0833	36.3	115	86	$130'' \times 120''$

with frequency. In 2003 the only suitably bright planet visible from the southern hemisphere was Mars, which we mapped at frequencies of 86 and 100 GHz. We observed the continuum emission from the planets Mercury and Jupiter in 2004, at frequencies of 86, 100 and 115 GHz. Table 3.2 presents the details of the planet mapping observations, including the observation date, frequency and angular size of the planets at that time.

Unlike SiO masers, planets may have large angular diameters and fill a significant fraction of the telescope's beam. Strictly speaking, maps of planets show the beam structure convolved with the disk of the planet. This was the case for Jupiter, which in June 2004 had an angular diameter of 37″, comparable to the FWHM size of the Mopra beam. Mars had an angular size of $< 17''$ in October 2004, resulting in a broadening of the measured beam FWHM of less than 10 per cent. Similarly, Mercury had an angular size of $< 6''$ and maps of these planets represent the true

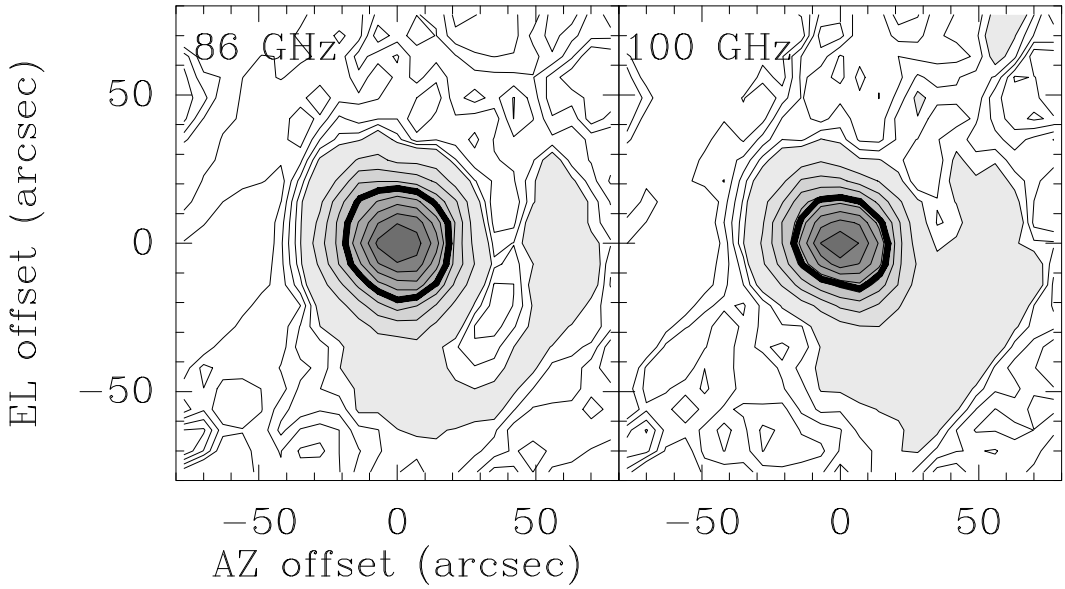

Figure 3.6. Maps of the telescope beam constructed from continuum observations of Mars taken in 2003 October at 86 GHz (left panel) and 100 GHz (right panel). Contours first increment from 1% to 10% of peak intensity in 1% intervals, and then from 10% to 90% in 10% intervals (with greyscales). The 50% contour is plotted in bold.

structure of the Mopra beam.

Maps of the 2003 beam at 86 GHz and 100 GHz are presented in Figure 3.6. The FWHM of main lobe (thick contour) is clearly seen to be smaller in the 100 GHz map. Figure 3.7 presents maps of Mercury (left panels) and Jupiter (right panels) made in June 2004 from data at frequencies of 86, 99, 110 and 115 GHz. Again, the decrease in the FWHM size of the beam is visible in the Mercury maps. The change in the FWHM size is less obvious in the Jupiter maps, however, Jupiter is much brighter than Mercury and the low level structure is easier to see.

To measure the FWHM beam size at each frequency we modelled the main beam as a two dimensional Gaussian. The SiO maser maps were fitted with a Gaussian function, while the planetary maps were fitted with a Gaussian convolved with a disk of the appropriate angular size. The 2004 Mercury data suffered from low signal to noise and the resulting fits are poorly constrained, however, the 2004 Jupiter maps are well-fitted by a Gaussian-plus-disk model. Final values for the FWHM beam

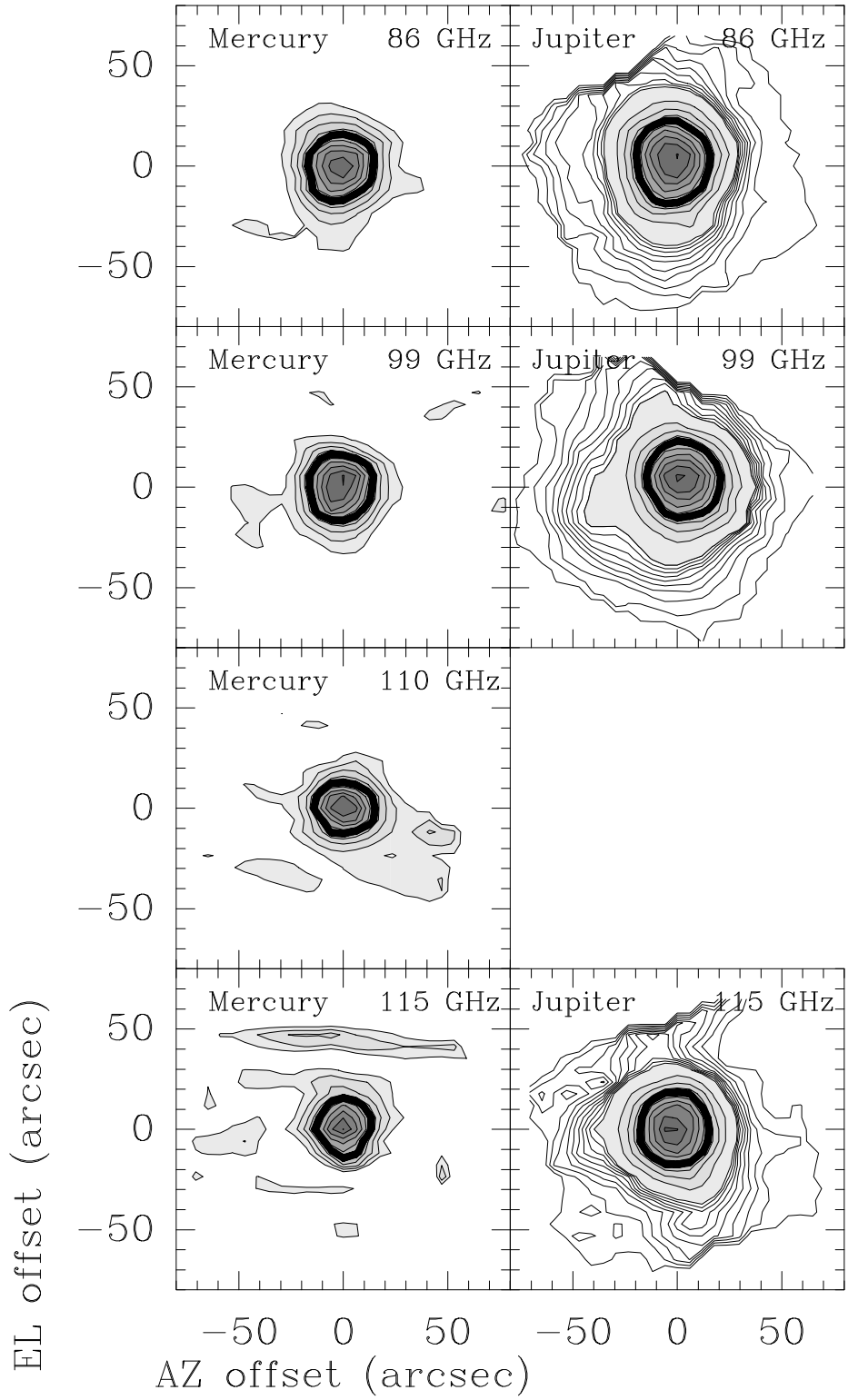

Figure 3.7. Maps of the telescope beam constructed from continuum observations of Mercury (left panels) and Jupiter (right panels) taken in June 2004. Contours are as per Figure 3.6.

Table 3.3. FWHM beam sizes from SiO maser and planetary observations.

Frequency	FWHM (″)	
(GHz)	2003 Data	2004 Data
86	37 ± 1	36 ± 3
100	35 ± 4	36 ± 3
115	–	33 ± 2

sizes were calculated from a weighted average of the fits to the 2003 Mars data and 2004 Jupiter data, and are presented in Table 3.3.

3-5.3 The beam efficiencies

3-5.3.1 The main and inner error-beams

Figure 3.8 presents an azimuthally averaged beam profile obtained in June 2004 from SiO maser observations. The top two panels plot the normalised intensity versus angular offset, clearly showing the separation between main beam and extended error pattern. We divide the beam response into three zones: 1) a Gaussian main beam extending to angular offsets of $\sim 40''$, 2) an 'extended beam' encompassing the main beam and near side lobes, which extend out to $80''$ and 3) an outer error beam of low intensity, but which may extend to large angular offsets. The main beam is well fit with a Gaussian of FWHM $37''$ out to angular offsets of $\sim 40''$, where the response falls to $\sim$5 per cent. The bottom panel of Figure 3.8 plots the normalised encircled power as a function of angular offset. We find that the main beam contains $\sim$75 per cent of the total measured power, while the remaining 25 per cent lies in the error beam. The outer error beam may also contain a significant fraction of the total power but we are unable to measure this quantity directly as the observations presented here are referenced to positions only $5-15'$ from the map centre.

Sources with angular sizes between 80 and $160''$ will couple to the main beam, but not to the error pattern. In this case the measured intensity of a source will depend on the source intensity distribution $T_R(\phi)$ as a function of offset angle ϕ,

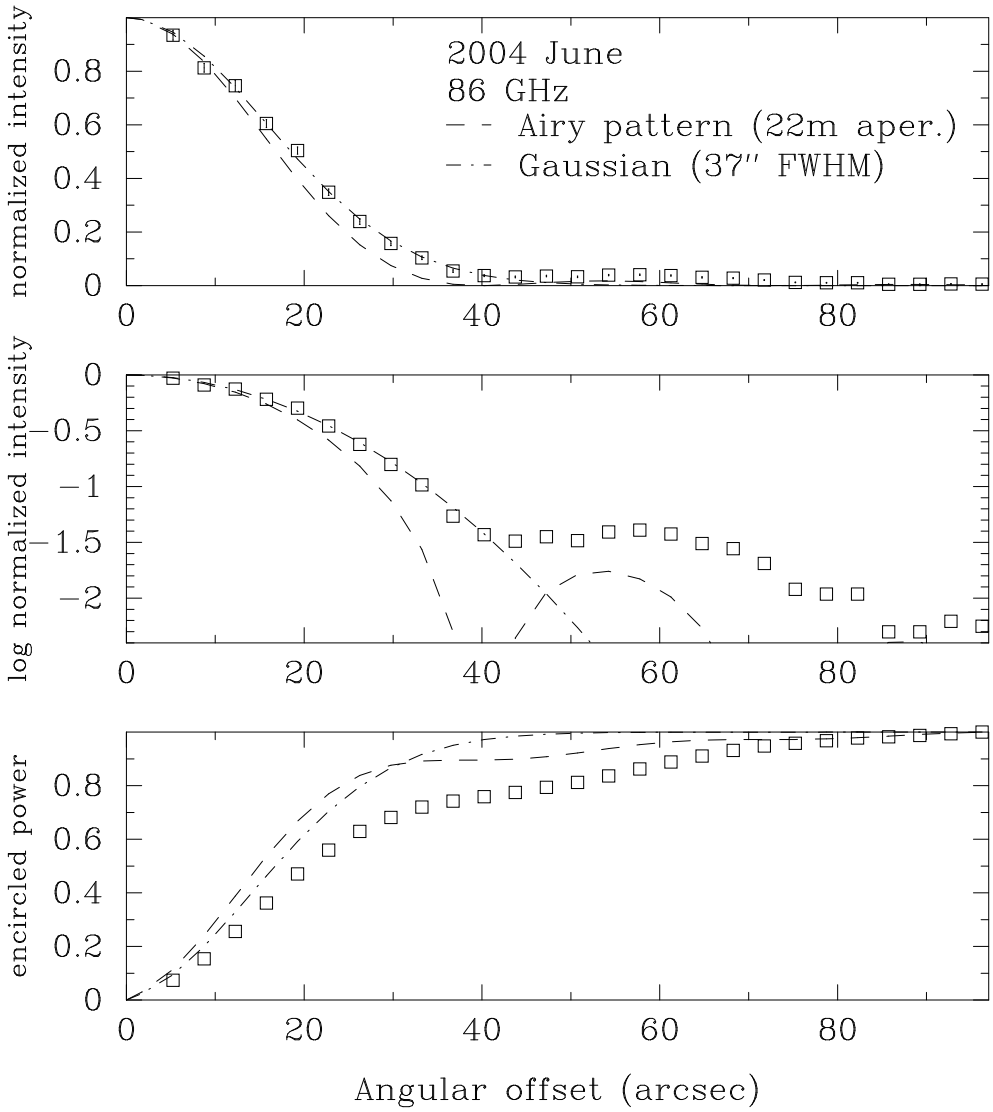

Figure 3.8. The azimuthally averaged radial beam profiles obtained in June 2004 from SiO maser observations. The top panel plots the normalised intensity as a function of offset angle in arcseconds. The bottom panel plots the log of the normalised intensity as a function of offset angle. In both panels the dashed line is the intensity expected from an unobstructed 22-m diameter aperture (i.e., the Airy pattern), and the dot-dashed line is the intensity expected from a Gaussian beam of FWHM 37″. The bottom panel plots the encircled power as a function of offset angle for the measured profile, Gaussian profile and Airy profile. The encircled power is normalised to the power at an offset of 96″.

and its coupling to the Gaussian main beam $\mathrm{P_{mb}}(\Omega)$ via Equation 3.10,

$$\mathrm{T_A^*} = \eta_{\mathrm{mb}} \frac{\iint \mathrm{P_{mb}}(\phi)\,\mathrm{T_R}(\phi)\,\mathrm{d}\phi}{\iint \mathrm{P_{mb}}(\Omega)\,\mathrm{d}\Omega},$$

where η_{mb} is the fraction of total measured power contained in the main beam, as defined by Equation 3.9

$$\eta_{\mathrm{mb}} = \frac{\iint \mathrm{P_{mb}}(\Omega)\,\mathrm{d}\Omega}{\iint_{2\pi} \mathrm{P_b}(\Omega)\,\mathrm{d}\Omega}.$$

Sources with angular diameters larger than $\sim 80''$ will couple well to the extended beam. The measured brightness temperature will be a function of the source intensity distribution $\mathrm{T_R}(\phi)$ and its coupling to the extended beam $\mathrm{P_{xb}}(\Omega)$

$$\mathrm{T_A^*} = \eta_{\mathrm{xb}} \frac{\iint \mathrm{P_{xb}}(\phi)\,\mathrm{T_R}(\phi)\,\mathrm{d}\phi}{\iint \mathrm{P_{xb}}(\Omega)\,\mathrm{d}\Omega}, \tag{3.13}$$

where η_{xb} is the beam efficiency which quantifies the fraction of the total measured power contained in the extended beam

$$\eta_{\mathrm{xb}} = \frac{\iint \mathrm{P_{xb}}(\Omega)\,\mathrm{d}\Omega}{\iint_{2\pi} \mathrm{P_b}(\Omega)\,\mathrm{d}\Omega}. \tag{3.14}$$

In Equation 3.14, $\mathrm{P_b}$ is the response of the telescope beam integrated over the forward hemisphere only.

3-5.3.2 Setting an absolute flux scale

An absolute measurement of the main beam efficiency η_{mb} may be obtained from a measurement of a source with a known intensity distribution, e.g. a planet. By measuring $\mathrm{T_A^*}$ on a planet the main beam efficiency η_{mb} may be derived from

$$\eta_{\mathrm{mb}} = \frac{\frac{1}{2}\,\mathrm{T_A^*(Planet)}}{\mathrm{J(T_{source})} - \mathrm{J(T_{bg})}} \left[1 - \exp\left(-\ln 2\,\frac{\Theta_{\mathrm{eq}}\Theta_{\mathrm{pol}}}{\Theta_{\mathrm{mb}}^2}\right)\right]^{-1}, \tag{3.15}$$

which is the convolution of a Gaussian telescope beam with a uniform disk source (Mangum 1993). In Equation 3.15 $\mathrm{T_{source}}$ is the brightness temperature of the planet, $\mathrm{T_{bg}} = 2.78\,\mathrm{K}$ is the temperature of the cosmic microwave background, Θ_{eq} is the equatorial diameter of the planet, Θ_{pol} is the poloidal diameter of the planet and Θ_{mb} is the FWHM of the main beam. The brightness temperature of Mercury, Mars and Jupiter have been modelled by Ulich (1981) based on careful observations at

Table 3.4. The main and extended beam efficiencies.

Frequency	2003		2004	
(GHz)	$\eta_{\rm mb}$	$\eta_{\rm xb}$	$\eta_{\rm mb}$	$\eta_{\rm xb}$
86	0.39 ± 0.02	0.58 ± 0.03	0.49 ± 0.03	0.65 ± 0.04
100	0.37 ± 0.02	0.55 ± 0.03	0.44 ± 0.03	0.58 ± 0.04
115	–	–	0.42 ± 0.02	0.56 ± 0.03

radio, millimetre and sub-millimetre wavelengths. Jupiter has a constant brightness temperature of 179.4 ± 4.7 K at 3-mm wavelengths, but because the orbit of Mars is eccentric, its brightness temperature $\mathrm{T_B}$ varies as the inverse square root of the its heliocentric distance, $\mathrm{R_\odot}$. To facilitate a direct comparison of data taken at different times, measurements may be corrected to an equivalent brightness temperature scale given by the following equation (Ulich 1981):

$$\mathrm{T'_B} = \mathrm{T_B} \sqrt{\frac{\mathrm{R_\odot}}{\langle \mathrm{R_\odot} \rangle}}. \tag{3.16}$$

In Equation 3.16, $\mathrm{T'_B} = 206.8 \pm 5.6$ K is the equivalent temperature of Mars at its mean solar distance $\langle \mathrm{R_\odot} \rangle = 1.524$ AU. Determining the disk-averaged brightness temperature of Mercury is more complicated as its sun-facing side is considerably warmer than its night side. Because it is an inner planet, the brightness temperature depends not only on its distance from the sun, but also on the phase angle as seen from the Earth. For this reason we use only the Jupiter data to determine $\eta_{\rm mb}$ for 2004. Using the Equation 3.15, we find the efficiencies presented in Table 3.4 for the 2003 and 2004 observing seasons. Values for $\eta_{\rm xb}$ were calculated by scaling the values of $\eta_{\rm mb}$, i.e., in 2004 the inner error-beam contained one-third the power in the main beam, so the efficiencies when observing objects with angular scales greater than $80''$ are better by one-third. Our measurements of the encircled power in 2003 indicate that the inner error-beam contained half the power in the main beam. This results in 2003 values for $\eta_{\rm xb}$ similar to the 2004 values.

Table 3.5. Telescope adjustments 2000 – 2004.

Date	Adjustment
Jan 2000	Subreflector Adjustment
May 2000	Collimation & Focusing
May 2001	Collimation & Focusing
Jun 2002	Subreflector Adjustment
	Collimation & Focusing
May 2003	Subreflector Adjustment
	Panel Adjustment
	Collimation & Focusing
May 2004	Subreflector Adjustment

3-5.4 The gain history

In an effort to improve system sensitivity and beam shape, the dish surface and sub-reflector position were adjusted several times between 1999 and 2004. Successive rounds of panel settings based on holography at 30 GHz have reduced the r.m.s. error on the surface from 270 μm in 1999 to 180 μm in 2004 (*B. Sault, private communication*). The telescope was also collimated by moving the sub-reflector with respect to the optical axis, leading to a more symmetrical beam shape and an increase in the fraction of the total power present in the main beam.

The telescope focus was set at the start of each observing season by scanning the beam across a bright SiO maser and measuring the beam profile at 86 GHz. Several focus positions were evaluated in this manner and the position of highest received power and smallest angular profile was taken to be the optimum focus point. The beam size and therefore the gain depend on the accuracy of the focus achieved.

Table 3.5 lists the changes made to the telescope in chronological order from 2000 to 2004. All changes, except for one panel setting during 2003 August, occurred outside of the normal 3-mm observing season. Our data show that the 2003 August panel setting had a negligible effect on the gain during that period, allowing us to assign a single constant efficiency for each observing season.

We measured the beam efficiency for the 2003 and 2004 seasons directly from

planetary observations, but no similar dataset exists for previous seasons. Therefore, we have attempted to determine the beam efficiency for the 2000 – 2004 seasons by comparing the intensities of spectral line observations of molecular cloud cores taken during different seasons. Table 3.6 shows the intensity ratios of the sources observed and the periods which they cover. We define the relative seasonal beam efficiency $\eta_{\rm yr}$ to be:

$$\eta_{\rm yr} \equiv \frac{\rm T^*_{A,yr}}{\rm T^*_{A,2004}}, \tag{3.17}$$

where $\rm T^*_{A,yr}$ is the antenna temperature measured in a given year and $\rm T^*_{A,2004}$ is the antenna temperature that would have been measured had the observation been done during the 2004 season.

Table 3.6: Details of the cross period observations.

Source	Line	Period 1	Period 2	P1 / P2
Orion KL	HCO^+	Sep 2000	Oct 2001	0.912 ± 0.011
	HCO^+	Sep 2000	Jun 2004	0.630 ± 0.003
	HCO^+	Oct 2001	Jun 2004	0.691 ± 0.008
M17SW	HCN	Oct 2000	Aug 2001	0.943 ± 0.009
	HCN	Oct 2000	Aug 2001	0.937 ± 0.005
	HCN	Oct 2000	Aug 2001	0.858 ± 0.005
	HCN	Oct 2000	Jul 2004	0.630 ± 0.003
	HCN	Aug 2001	Jul 2004	0.669 ± 0.006
	HCN	Aug 2001	Jul 2004	0.673 ± 0.004
	HCN	Aug 2001	Jul 2004	0.735 ± 0.004
	HCO^+	Oct 2000	Aug 2001	0.747 ± 0.003
	HCO^+	Oct 2000	Jul 2004	0.516 ± 0.003
	HCO^+	Aug 2001	Jul 2004	0.691 ± 0.003
OPH-EL21	$C^{18}O$	Jul 2002	Aug 2003	0.635 ± 0.029
CHA-B18	$C^{18}O$	Jul 2002	Aug 2003	1.057 ± 0.234
CHA-B35	$C^{18}O$	Jul 2002	Aug 2003	0.826 ± 0.077
CHA-C1-6	$C^{18}O$	Jul 2002	Aug 2003	1.096 ± 0.120
CHA-INA2	$C^{18}O$	Jul 2002	Aug 2003	1.067 ± 0.103
CHA-IRAS1107	$C^{18}O$	Jul 2002	Aug 2003	0.979 ± 0.143
CHA-IRAS1303	$C^{18}O$	Jul 2002	Aug 2003	0.838 ± 0.243
CHA-IRASF125	$C^{18}O$	Jul 2002	Aug 2003	2.098 ± 0.833
CHA-IRS11	$C^{18}O$	Jul 2002	Aug 2003	0.875 ± 0.093
CHA-IRS4	$C^{18}O$	Jul 2002	Aug 2003	0.757 ± 0.077

Details of the cross period observations – *continued.*

Source	Line	Period 1	Period 2	P1 / P2
CHA-PERSI91	$C^{18}O$	Jul 2002	Aug 2003	0.775 ± 0.079
CRA-W97-1-26	$C^{18}O$	Jul 2002	Aug 2003	0.926 ± 0.067
L1527	$C^{18}O$	Jul 2002	Aug 2003	0.934 ± 0.059
G0.55-0.85	CH_3CN	Sep 2000	Oct 2003	0.788 ± 0.017
G5.90-0.43	HCN	Oct 2003	Jun 2004	0.834 ± 0.019
	HCN	Oct 2003	Jun 2004	0.802 ± 0.012
G10.32-0.16	HCN	Oct 2000	Oct 2003	0.895 ± 0.022
	HCN	Oct 2000	Jun 2004	0.641 ± 0.015
	HCN	Oct 2003	Jun 2004	0.717 ± 0.014
G10.47+0.03	CH_3CN	Oct 2002	Oct 2003	0.885 ± 0.013
G11.94-0.15	HCO^+	Jul 2001	Oct 2003	0.768 ± 0.029
G11.94-0.62	HCO^+	Sep 2000	Oct 2003	0.878 ± 0.021
G12.18-0.12	HCO^+	Jul 2001	Oct 2003	0.637 ± 0.017
	HCO^+	Jul 2001	Jun 2004	0.634 ± 0.026
	HCO^+	Jul 2001	Jun 2004	0.636 ± 0.037
	HCO^+	Oct 2003	Jun 2004	0.996 ± 0.040
	HCO^+	Oct 2003	Jun 2004	0.998 ± 0.056
G15.03-0.68	HCO^+	Aug 2001	Jun 2004	0.690 ± 0.005
	HCO^+	Aug 2001	Jun 2004	0.732 ± 0.011
	HCN^+	Oct 2000	Oct 2003	0.531 ± 0.003
G29.87-0.04	HCN	Oct 2000	Jun 2004	0.780 ± 0.014
	HCN	Oct 2000	Jun 2004	0.869 ± 0.015
G30.82-0.05	CH_3CN	Aug 2001	Oct 2003	0.688 ± 0.015

Since most of the observed sources are molecular cloud cores with extents $\geq 2'$, we assume that emission from these sources encompasses both the main beam and inner error beam at the frequencies observed. Hence, we believe that $\eta_{\rm yr}$ quantifies how $\eta_{\rm xb}$ varies as a function of observing season. Equation 3.13 can then be written as follows:

$$\mathrm{T}^{*}_{\mathrm{A,yr}} = \eta_{\mathrm{xb,2004}}\,\eta_{\mathrm{yr}}\,\frac{\int \mathrm{T_R}(\phi)\,\mathrm{P_{xb}}(\phi)\,\mathrm{d}\Omega}{\int \mathrm{P_{xb}}(\phi)\,\mathrm{d}\Omega}, \tag{3.18}$$

where $\eta_{\rm xb,2004}$ is the extended beam efficiency during the 2004 season, and ($\eta_{\rm xb,2004}\,\eta_{\rm yr}$) = $\eta_{\rm xb,yr}$ is the extended beam efficiency for a given season.

Table 3.7. Mopra seasonal efficiencies.

Period	η_{yr}	η_{xb}[86 GHz]	η_{xb}[115 GHz]
2004	1.00	0.65	0.55
2003	0.95	0.62	0.52
2002	0.80	0.52	0.44
2001	0.70	0.46	0.39
2000	0.63	0.41	0.35

Using the measured year-to-year intensity ratios, we estimated the beam efficiency for each year, normalised to the 2004 observing season values. No source was observed during every observing season, so we adopted an indirect method for determining the relative gains that made use of each pair of observations. The relative efficiencies of all the observing seasons can be expressed as a five element vector, $[\eta_{2000}, \eta_{2001}, \eta_{2002}, \eta_{2003}, \eta_{2004}]$, with η_{2004} set to 1. Starting from an initial guess, the parameter space of potential model vectors was generated by numerically incrementing each element in steps of ± 0.05 over a suitable range. Each model was evaluated by comparing the model's predicted intensity ratios with the observed values. The reduced χ^2 value was calculated from each model based on this comparison. As our final vector of efficiencies we took the χ^2-weighted average of the models with χ^2 values from the minimum value ($\chi^2_{\rm min}$) to $\chi^2_{\rm min}+1$. The results for the years 2000 to 2004 are shown in Table 3.7. An estimate of the error associated with the results was obtained from the standard deviation of the raw intensity ratios for each period and was approximately 30 per cent.

3-5.5 Comparisons with other observatories

We compare efficiency-corrected Mopra observations with measurements of the same sources made at other facilities, namely the Five College Radio Astronomy Observatory (FCRAO) 14-m telescope in New Salem, Massachusetts, USA, the Swedish-ESO Sub-millimetre Telescope (SEST), at La Silla, Chile and the Institut de Radioastronomie Millimétrique (IRAM) 30-m telescope near Granada, Spain. These tele-

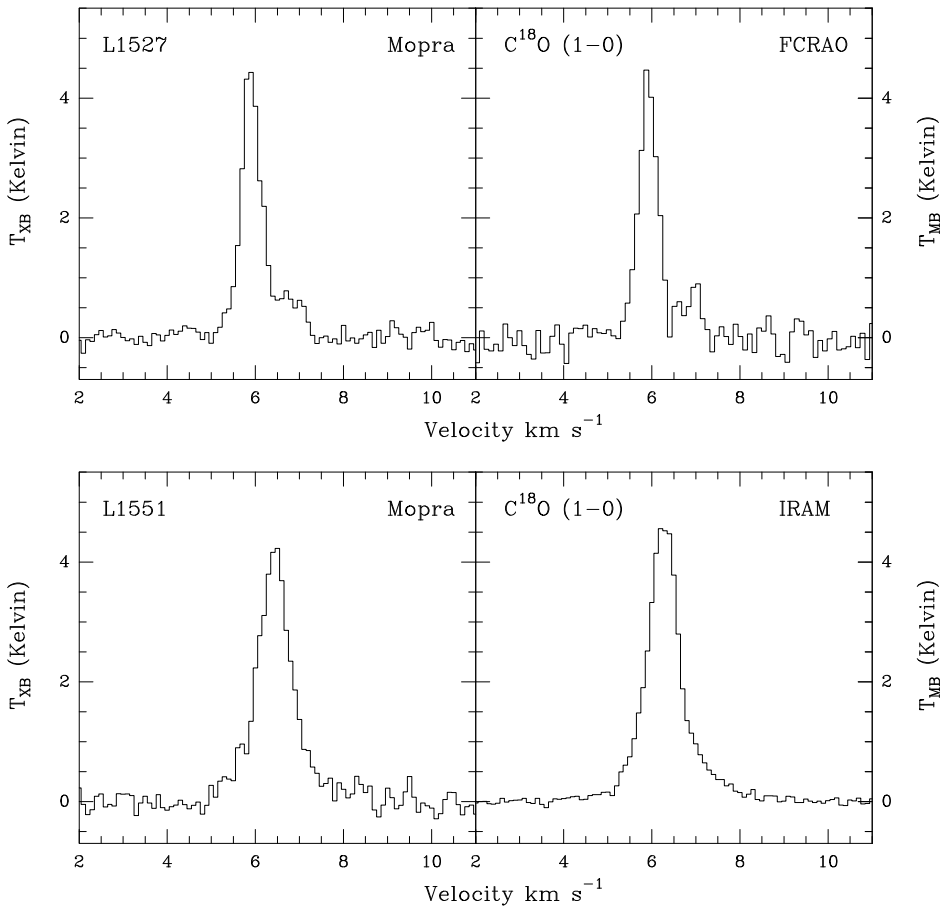

Figure 3.9. Efficiency-corrected $C^{18}O$ spectra of the molecular cores L1527 and L1551 acquired with the Mopra telescope (left panels) and the FCRAO and IRAM telescopes (right panels). The Mopra L1527 data have been calibrated onto an extended beam temperature scale using $\eta_{\rm xb}$ and the analogous FCRAO value for the FCRAO spectrum while the Mopra L1551 data have been calibrated onto a main beam temperature scale using $\eta_{\rm mb}$.

scopes vary from two thirds the size of Mopra to 50 per cent larger, and so the FWHM size of their main beams differ from that of the Mopra main beam. The FWHM sizes of the 14-m FCRAO and 15-m SEST telescope main beams are 48″ and 45″ respectively, while the FWHM size of the IRAM 30-m telescope main beam is 24″ at the frequencies observed. The choice of filter banks lead to a similar velocity resolution of ~ 0.1–$0.2\,{\rm km\,s^{-1}}$ for all telescopes.

The spectra from the Mopra telescope and from the other facilities are shown in

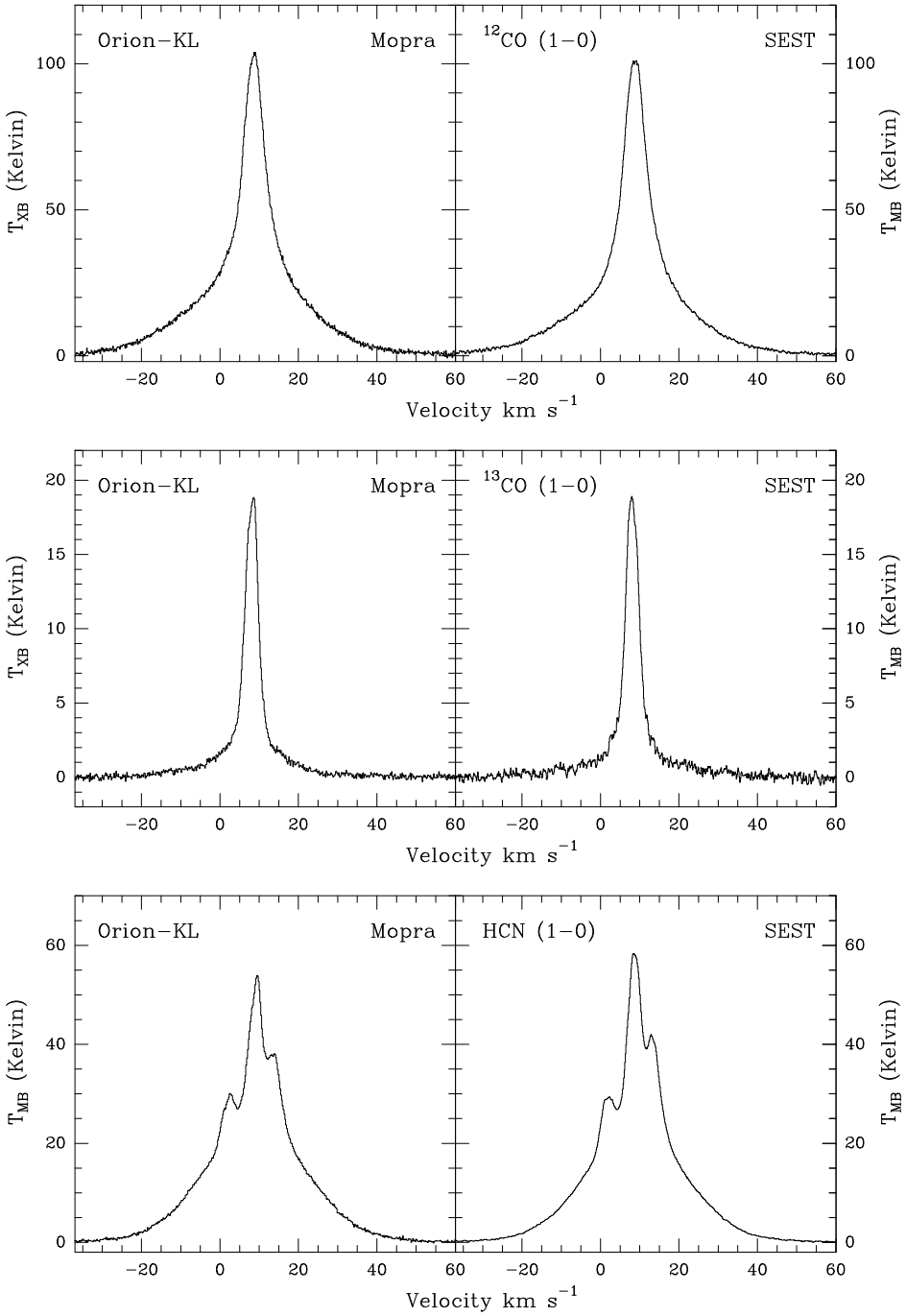

Figure 3.10. Efficiency-corrected ^{12}CO, ^{13}CO and HCN spectra of the molecular core Orion-KL taken with the Mopra telescope (left panels) and the SEST 15-m telescope (right panels). The CO data have been calibrated onto an extended beam temperature scale using $\eta_{\rm xb}$ and the analogous SEST value for the SEST spectrum while the Mopra HCN data have been calibrated onto a main beam temperature scale using $\eta_{\rm mb}$. Integration times have not been matched across line-pairs.

Figures 3.9 and 3.10. The sources observed with the FCRAO and IRAM telescopes consist of circumstellar material surrounding forming stars deeply embedded in the Taurus Molecular cloud, measured in the 110 GHz line of $C^{18}O$. The Mopra observations were acquired in 2003, while the FCRAO spectrum of L1527 was obtained in 1995, and the IRAM spectrum of L1551 was obtained in 1999. Observations of the nearby Orion-KL hot core with the SEST were acquired in as part of the calibration program in 1997[2], while the Mopra observations were acquired during June 2004.

The $C^{18}O$ emission in the region around L1527 is extended on scales larger than $2'$, and so the Mopra data were calibrated with the extended beam efficiency, $\eta_{\rm xb}$. The FCRAO spectrum was calibrated onto a comparable temperature scale using the forward scattering efficiency measured by Ladd & Heyer (1996).

The $C^{18}O$ emission in the region around L1551 is more localised, and so calibration with the main beam efficiency, $\eta_{\rm mb}$ is more appropriate. The IRAM data for this source were calibrated onto the main beam temperature scale using the efficiencies quoted on the IRAM website (http://www.iram.es/).

In both cases, the correspondence between the Mopra data and the spectra from other facilities is quite good. The line shape, line centre velocity[3], and peak intensity correspond well. The calibrated IRAM spectrum has a slightly higher peak temperature which probably results from the smaller FWHM beam size, and the fact that the intensity distribution is somewhat centrally-peaked around this source.

Both the ^{12}CO and ^{13}CO emission in the Orion-KL region are extended on scales larger than an arcminute with the narrow spike feature of the spectrum attributed to the central source and the broad linewings to the associated bipolar outflow (e.g. Gillespie & White 1980). Both features are assumed to couple well to the extended beam and are calibrated onto the $T_{\rm XB}$ temperature scale. The SEST beam at $45''$

2. SEST calibration data was provided courtesy of the Onsala Space Observatory and Chalmers University of Technology.
3. During and before the 2003 observing season, some Mopra data suffered from a frequency calculation error that resulted in spectra which appeared shifted in frequency by as much at 500 kHz. The source of this error has been identified, and all data can be corrected to a proper frequency scale with a simple algorithm. See Section 3-6 for details.

FWHM is calibrated onto the equivalent SEST T_{MB} using the efficiencies quoted in the SEST observers manual[4].

Maps of Orion KL in the 89 GHz transition of HCN (c.f. Rydbeck et al. 1981) show the emission to be localised to the central 20″, so calibration of the Mopra HCN data with the main beam efficiency is more appropriate. The spectra from both facilities have similar shapes and intensities. Peak intensities agree to within 10%, well within the expected calibration uncertainty of the single load calibration method employed at Mopra.

3-5.6 Standard spectra

M17-SW and Orion-KL are commonly used as calibrators in mm-line spectroscopy due to the high intensity of observed molecular transitions and their relatively large angular extent compared to modern telescope beams at 3-mm wavelengths. We present high signal-to-noise spectra toward both sources in Figure 3.11, taken in a number of abundant molecular species. The coordinates used are the same as those quoted by other millimetre and sub-millimetre telescopes, such as the SEST, so a direct comparison may be made. A digital auto-correlator having a bandwidth of 64 MHz divided into 1024 channels formed the back-end, delivering a velocity resolution of less than 0.3 km s^{-1}. Care was taken to reduce the pointing error while observing to $< 5''$ by reference pointing on a nearby bright SiO maser, or in the case of Orion its own associated maser.

3-6 Telescope software problems

Several software problems affecting the Telescope Control System (TCS) were discovered during the commissioning work in 2003 and 2004.

4. The SEST observers manual, maintained by Markus Nielbock, is available online from the SEST web site: http://www.ls.eso.org/lasilla/Telescopes/SEST/SEST.html

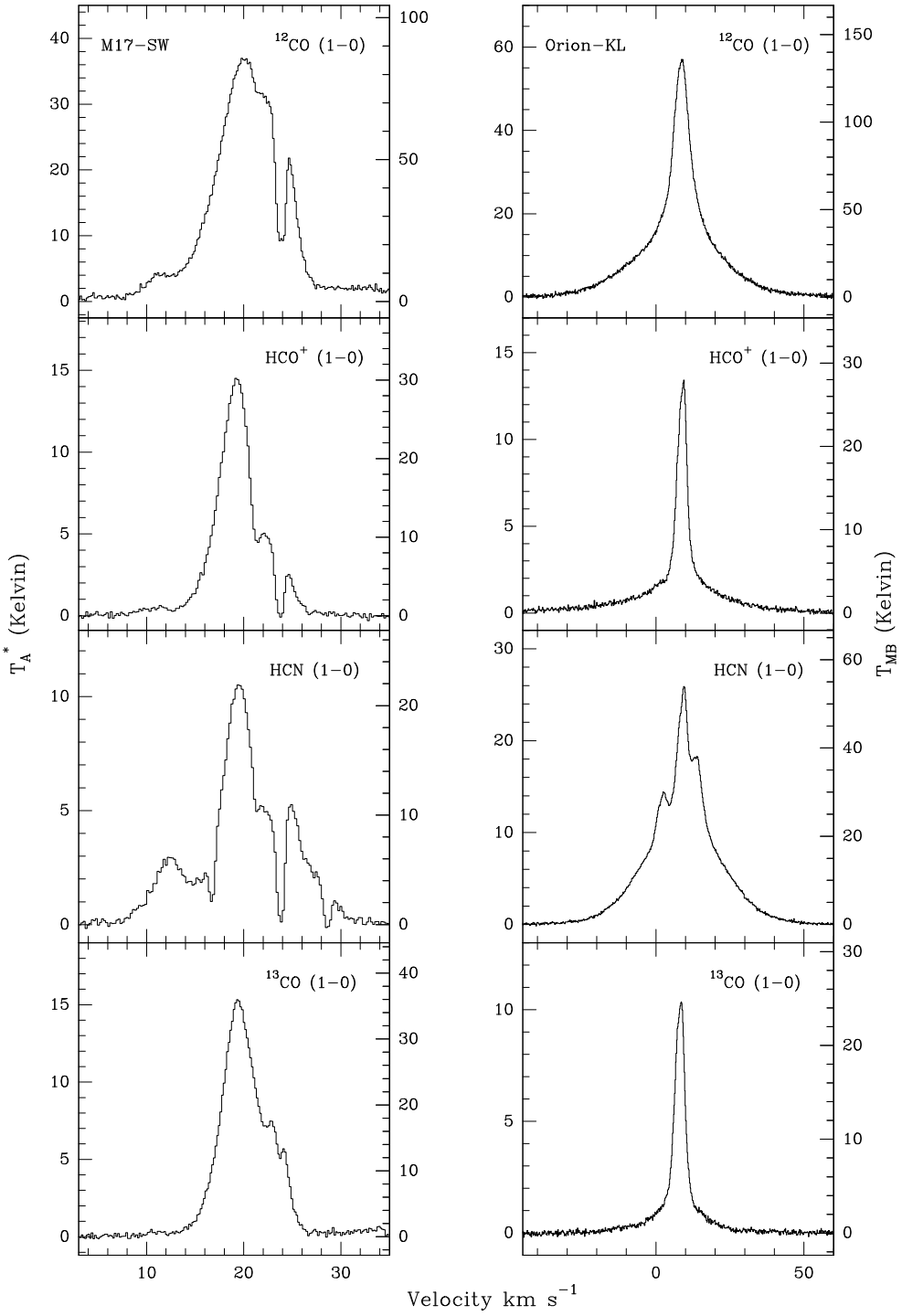

Figure 3.11. Standard spectra towards M17-SW and Orion-KL. The following coordinates were used in all observations: Orion-KL – $05^h\ 35^m\ 14.5^s$, $-05^\circ\ 22'\ 29.6''$ (J200.0), and M17-SW – $18^h\ 20^m\ 23.1^s$, $-16^\circ\ 11'\ 37.2''$ (J2000.0). The left y-axis displays T_A^* and the right y-axis T_{mb}, corrected for the main beam efficiency at the frequency of the line.

3-6.1 The TCS scaling error

Mopra data taken on certain dates in 2001 and 2002 is affected by a scaling error introduced by TCS. The system temperatures of the polarisation A and B data were erroneously multiplied by 1.51 and 1.73, respectively, causing the scaling of the spectra by the same amounts. These factors are believed to have originated in the version of TCS used on the Parkes telescope. Data taken between the following dates were affected by the error:

- 15^{th} May 2001, 01:15 UT $\rightarrow$ 05^{th} September 2002, 14:18 UT
- 06^{th} September 2002, 14:02 UT $\rightarrow$ 17^{th} September 2002, 21:10 UT

The data may be corrected onto the T_A^* scale by dividing by the above factors.

3-6.2 The frequency rounding error

Prior to 2003 data was also affected by a frequency error in the TCS software. The receiver and frequency synthesiser chain contain components which are quantised in 1 MHz steps. As a result the *actual* sky frequency to which the receiver is tuned will not usually match the *requested* sky frequency, but instead be rounded to the nearest MHz. In normal operation the actual sky frequency is written to the raw data-file and processing software, such as SPC, is designed to reconstruct the frequency and velocity scales matching the requested rest-frame. Unfortunately, when observing in dual-frequency mode (i.e., both polarisations tuned to the same rest frequency) a software bug meant that the *requested* sky frequency was written to the header and this may have been incorrect by up to ± 0.5 MHz. At 100 GHz ± 0.5 MHz equates to a $\pm 1.5\,\mathrm{km\,s^{-1}}$ shift in velocity, or ± 4 channels in the 64 MHz/1024 channel correlator configuration commonly used.

The problem is compounded if Doppler tracking has been turned on as the requested frequency shifts by up to 30 kHz every hour. Over the course of long observations these small corrections are rounded to the nearest MHz and the line appears

to move in velocity. A special case occurs when the requested sky frequency is near to a 0.5 MHz rounding boundary in the receiver. Small Doppler corrections may result in the actual sky frequency jumping by 1 MHz, leading to a corresponding shift in the centre of the bandpass, which will go unrecorded in the data-file.

Fortunately, it is possible to address the problem before reducing the data by simply replacing the incorrect sky frequency in the header of the data file with the correct value. The value of the actual sky frequency, $F_{\mathrm{sky,\,actual}}$ may be calculated from:

$$F_{\mathrm{sky,\,actual}} = F_{\mathrm{rest}} + \mathrm{round}[F_{\mathrm{sky,\,requested}} - F_{\mathrm{rest}}], \tag{3.19}$$

where $F_{\mathrm{sky,\,requested}}$ is the incorrect sky frequency, recorded in the header, and F_{rest} is the rest frequency of the line, as stored in a lookup table on the receiver Tuning PC. Full details of the error are recorded in an ATNF memo (Ladd et al. 2005) available at http://narribri.atnf.csiro.au/mopra. A pre-processing script, called 'moprafix.pl' (written by Chris Phillips), that will automatically repair the data-files is also available from the same web site.

3-7 Reducing Mopra data

Raw spectra from the Mopra correlator are written to a data-file in the *rpfits* format. *rpfits* files are similar to standard *fits* files, that is they consist of plain text (ASCII) headers describing the observations, and a set of binary tables containing the raw data. However, the file format[5] is sufficiently different that proprietary software is required to read and process the data. Prior to 2005 the SPC[6] package from the ATNF was used to reduce simple position-switched data. In 2005 a new single-dish reduction package, called ASAP[7], replaced SPC. On-the-fly mapping data are reduced using the LIVEDATA and GRIDZILLA packages, which are part of the AIPS++[8]

5. See http://www.atnf.csiro.au/computing/software/rpfits.html for a description of the *rpfits* file format.
6. http://www.atnf.csiro.au/computing/software/spc.html
7. http://www.atnf.csiro.au/computing/software/asap/
8. http://aips2.nrao.edu

software suite.

3-7.1 Position-switched data

While position-switching, the telescope alternates between observing the science object (source or ON position) and a nearby emission-free region of sky (reference or OFF position). The reference spectra are used to subtract the atmospheric and sky-background emission from the source spectra by forming a 'quotient' according to the formula:

$$Q_i = (S_i\, T_{sys}) \,/\, R_i - T_{sys}. \tag{3.20}$$

In Equation 3.20 Q_i, S_i and R_i are the i^{th} channel values of the quotient, source and reference spectra, respectively, and T_{sys} is the system temperature. Figure 3.12 illustrates typical reference and signal spectra, and the resultant quotient spectrum. The characteristic 'Indian elephant' shape of the bandpass is due to the response of the receiver electronics.

During the Hot Molecular Cores survey (Chapters 4 and 5) over 700 individual files of data were collected, each of which contained multiple reference and source spectra. The data was reduced in SPC using the following methodology:

1. Correct for the frequency rounding error (see Section 3-6.2) using the 'mo-prafix.pl' pre-processing script.

2. Shift the velocity scale of each spectrum to the LSR-K reference frame and re-sample onto a common channelisation. Any Doppler corrections due to the Earth's rotation are applied in this step.

3. Form the quotient spectra from adjacent source-reference pairs. A quotient is formed between each source spectrum and the nearest (in time) reference spectrum according to Equation 3.20.

4. Flag any bad data and average all good scans together. Individual velocity channels are averaged weighted by [Integration time/T_{sys}^2]. If two linear polarisations have been observed these data are reduced separately.

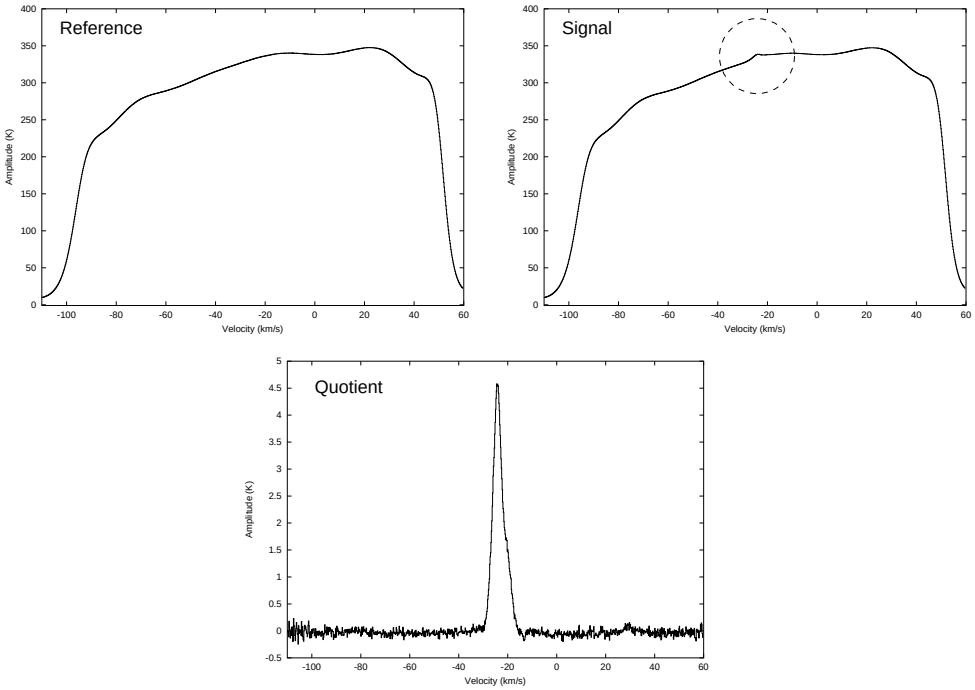

Figure 3.12. Plot of the reference, signal and quotient spectra for a position-switched observation. The dashed circle marks the position of the spectral line in the signal spectrum.

5. If both polarisations have been tuned to the same rest frequency then polarisations A and B are also averaged together to form the final spectrum.

6. Identify the line-free channels in the spectrum and fit a low order (3 – 5) polynomial to the continuum level. Subtract this polynomial from the spectrum, leaving only line emission on a flat baseline.

7. Divide the T_{sys} value by the correct year-to-year efficiency η_{yr} to place the spectrum on the 2004 T_A^* scale.

8. Save the final spectrum as a *fits* file.

Further processing was done using the GILDAS/CLASS[9] or XS software packages. The following additional steps were taken to convert the *fits* data to the GILDAS format

9. GILDAS is a suite of radio-astronomy processing and analysis software available at http://www.iram.fr/IRAMFR/GILDAS/. CLASS is a package within GILDAS, used to analyse spectral-line data.

and finally place the data onto the Mopra T_{MB} brightness temperature scale.

9. Change the *fits* header keyword from CRDELTn to CDELTn. This was necessary for the *fits* reader in CLASS to function correctly.

10. Use the CFITS routine to convert the Mopra *fits* data to the GILDAS format.

11. Using the original *rpfits* file as a template, re-populate missing header information (telescope name, rest-frequency, date and time).

12. Correct any rounding errors introduced by SPC and divide by the frequency-dependent main beam efficiency, η_{MB}.

All observations at this stage are on the main beam brightness scale (T_{MB}). This the true brightness temperature of a source that exactly fills the main beam.

3-7.1.1 SPC and the 'DFM' script

The SPC package was used to reduce all position switched data used in this thesis. Upon loading the data, SPC stores information on individual spectra in unique internal memory-registers. Each register contains an array, used to record the spectrum, and a set of variables (called headers) which store information on the observation (e.g., RA, Dec, T_{sys}, integration time, rest-frequency etc.). The data-processing commands in SPC operate directly on values in the memory registers.

During the telescope commissioning a number of bugs and internal inconsistencies were discovered in SPC, which may result in errors in the data if the user is not wary. Fortunately, it is possible to manually correct for these problems by using the low level 'Ed' command to modify the memory registers. Table 3.8 details the problems and solutions for each command.

To facilitate data reduction process, and to allow automatic correction of the above errors, a front-end to SPC was written called 'Data from Mopra' (DFM)[10]. DFM is a graphical interface to SPC, designed to enable the user to quickly and easily

10. The DFM source code is available from http://www.phys.unsw.edu.au/mopra/

Table 3.8. Problems and solutions in the SPC program

Problem	Solution
Headers not transfered from between quadrants 1 and 2 when copying	Use the 'EDIT' routine to copy the relevant variables
Frequency scale not shifted simultaneously with the velocity scale when assigning the rest frame	Read the header variables and calculate the frequency shift to be applied
FITS writer does not fill the header keys with correct information	FITS writer reads from redundant header variables, which must be filled before writing out to file.

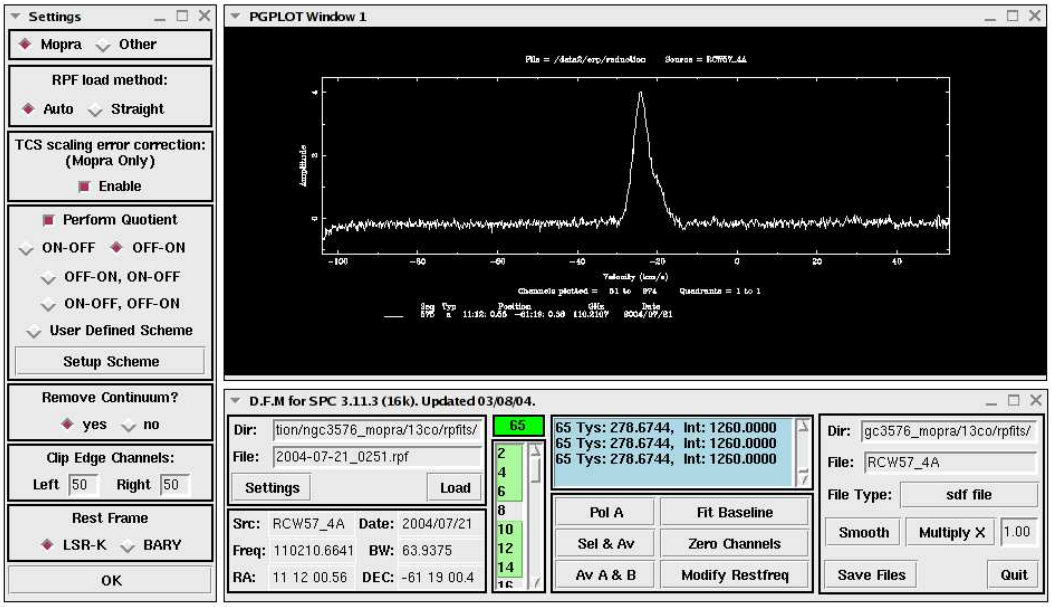

Figure 3.13. Screen-shot of DFM, the graphical user interface to SPC.

reduce dual-polarisation position-switched data. Figure 3.13 is a screen-capture of the interface showing the main control panel and settings dialogue. The data-reduction methodology outlined earlier is implemented as a series of 'events' linked to buttons on the DFM interface. A schematic representation of reduction pathway showing how the data-reduction procedure is linked to the buttons is presented in Figure 3.14.

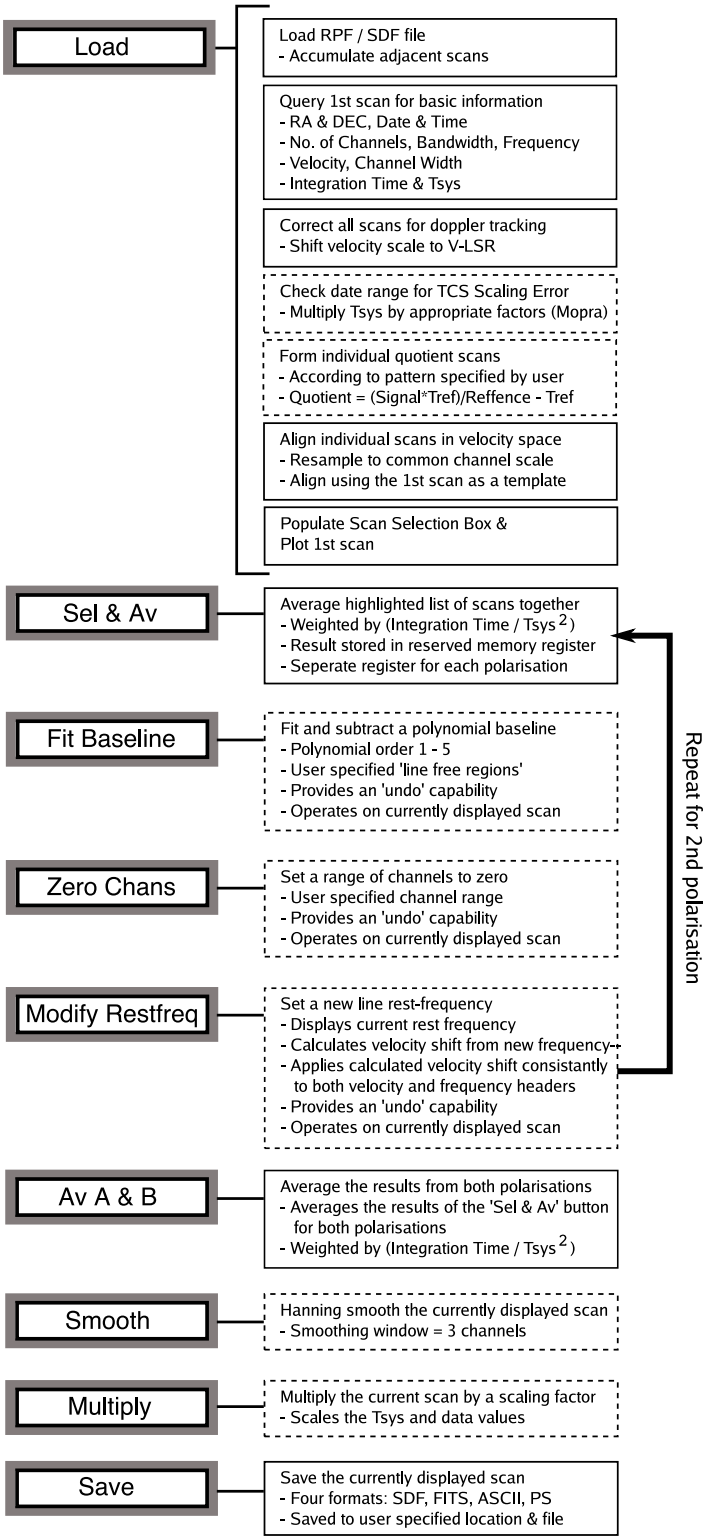

Figure 3.14. Schematic representation of the data reduction path for dual-polarisation position switched data. Buttons on the user interface are represented by grey boxes and the events linked to these buttons are listed in the white boxes. Boxes with dashed lines represent optional steps.

3-7.2 On the fly mapping

Like position-switched data, the raw output from the telescope when utilising the OTF-mode is simply a *rpfits* file containing a list of spectra. Reduction of OTF-mapping data is done in two steps.

Firstly, the LIVEDATA package is used to automatically perform bandpass calibration and baseline fitting. The package assumes the format of the data will be a repeating pattern of OFF – SCAN – OFF – SCAN ... and it uses the OFF spectra preceding each SCAN to form the quotient. An algorithm is then used to find the line-free channels in the data and a low order polynomial fit is used to baseline the spectra. LIVEDATA also assigns each spectrum a position stamp based on data in the header. The result is a *sdfits* file with a list of calibrated spectra.

This *sdfits* file is then loaded into the GRIDZILLA package. Here the spectra from multiple files may be resampled onto common pixel scales (x, y and z) and averaged or joined to form a data-cube. The final resolution of the image is dependent on the choice sampling function. Further details are presented in the Mopra User Manual, available from the ATNF Mopra pages at: http://www.atnf.csiro.au/mopra.

Chapter 4

The Hot Molecular Core Survey I

Identifying young massive stars ($> 8\,M_{\odot}$) in their early evolutionary phases is an important step in attempting to understand massive star formation and its effect on the Galactic ecology.

To recap, massive stars begin their lives at the centre of dense contracting cores, embedded in giant molecular clouds (GMCs). At the earliest stages of their evolution they heat the surrounding dust and are visible as luminous sub-millimetre (mm) and far-infrared sources (Kurtz et al. 2000). High densities existing prior to the final collapse cause simple organic molecules present in the interstellar medium to freeze onto the dust mantles. Grain surface chemistry leads to the production of heavy ices such as methanol (CH_3OH). As the protostar evolves, heat and radiation evaporate these species, expelling them into gas phase where they fuel a rich 'hot core' chemistry (van Dishoeck & Blake 1998). Eventually, the embedded protostar ionises the surrounding environment, forming an ultra-compact HII (UCHII) region. During this phase it is thought that complex molecules are destroyed owing to continued exposure to heat and radiation, although the timescales are far from clear.

Targeted surveys towards known star forming regions have implied a close relationship between class II methanol masers, hot cores and UCHII regions (Menten 1991b; Minier et al. 2001). Parkes 64-m and Australia Telescope Compact Array

(ATCA) observations by Walsh et al. (1997, 1998) have shown that only 25 % of methanol masers are directly associated with radio continuum emission, tracing UCHII regions. Subsequent follow-up observations towards the *isolated* masers confirm that all maser sites are associated with luminous sub-mm continuum emission (Walsh et al. 2003).

In this chapter we investigate the link between methanol masers, UCHII regions and the chemically active 'hot molecular core' (HMC) phase of massive star formation. We present the initial results of a single-dish molecular line survey of 83 methanol maser selected massive star forming regions.

4-1 Introduction

4-1.1 CH_3CN spectroscopy

The primary chemical tracer in this survey is methyl cyanide (CH_3CN). CH_3CN is a good tracer of the conditions found in HMCs owing to its favourable abundance and excitation in warm ($> 100\,K$) and dense ($> 10^5\,cm^{-3}$) regions. It is thought to form through reactions between species evaporated from dust grain mantles (e.g. Millar, MacDonald & Gibb 1997) or through gas phase chemistry in the envelope around massive young stars (see Mackay 1999). Grain-surface chemistry has also been invoked to explain the enhanced abundances observed in HMCs, however, in all formation scenarios CH_3CN is evident in observations after the core temperature rises past $\sim 90\,K$.

CH_3CN is a member of the c_{3v} group of symmetric tops, whose rotational energy levels may be described by two quantum numbers: J, the total angular momentum and K, the projection of J along the axis of symmetry. Individual $J \rightarrow (J-1)$ transitions are grouped into 'rotational ladders' labelled by their K values (see Loren & Mundy (1984) and Chapter 2 for a detailed description). For each $J \rightarrow (J-1)$ transition, selection rules prohibit radiative transitions between the K ladders and their relative populations are determined exclusively by collisional excitation.

Assuming local thermal equilibrium (LTE) and optically thin lines, the relative intensities of the K components yield a direct measure of the kinetic temperature and column density.

The energy spacings between individual J levels are almost independent of K ladder, however, increasing centrifugal distortion causes successive K components to shift to progressively lower frequencies. The offset in frequency is slight, and the K components of a particular $J \rightarrow (J-1)$ transition may be observed simultaneously in a single bandpass, minimising errors in their relative calibration.

Spin statistics of the hydrogen nuclei divide CH_3CN into two spin states, dubbed A and E. Energy levels with $K = 3n,\ n = 0, 1, 2 \ldots$ belong to the A state, while those with $K \neq 3n,\ n = 0, 1, 2 \ldots$ belong to the E state. The A states have twice the statistical weight of the E states. Neither radiation nor collisions convert between states; if formed in equilibrium conditions the A / E abundance ratio is expected to be ~ 1 (Minh et al. 1993).

4-1.2 HCO^+ spectroscopy

HCO^+ and its isotopomer, $H^{13}CO^+$, were also observed in order to probe the kinematics of the extended envelopes and as a diagnostic of the optical depth towards the cores. A comparison between the generally optically thick HCO^+ line and the optically thin $H^{13}CO^+$ line yields information on the bulk motions of gas in the regions.

HCO^+ has a large dipole moment and is a highly abundant molecule, with abundance especially enhanced around regions of higher fractional ionisation. HCO^+ is also enhanced by the presence of outflows where shock generated radiation fields are present (Rawlings, Taylor & Williams 2000; Rawlings et al. 2004). It shows saturated and self absorbed line profiles around massive star-forming regions and is a good tracer of the dynamics in the vicinity of young protostellar objects (e.g. De Vries & Myers 2005). The emission from its isotopomer, $H^{13}CO^+$, is generally optically thin and traces similar gas densities to HCO^+ at $n \approx 3 \times 10^5\,cm^{-3}$.

Table 4.1. Details of observed transitions.

Species	Transition [α]	Frequency (GHz)	E_u/k (K)	A_{ul} [β] ($\times 10^{-5}\,s^{-1}$)	g_{JK} [γ]
CH_3CN	$5_0 \rightarrow 4_0$	91.987054	13.24	6.121	44
	$5_1 \rightarrow 4_1$	91.985284	20.39	5.875	44
	$5_2 \rightarrow 4_2$	91.980000	41.82	5.139	44
	$5_3 \rightarrow 4_3$	91.971374	77.53	3.913	88
	$5_4 \rightarrow 4_4$	91.959206	127.51	2.200	44
	$6_0 \rightarrow 5_0$	110.383494	18.54	10.895	52
	$6_1 \rightarrow 5_1$	110.381376	25.68	10.592	52
	$6_2 \rightarrow 5_2$	110.374968	47.11	9.681	52
	$6_3 \rightarrow 5_3$	110.364470	82.82	8.166	104
	$6_4 \rightarrow 5_4$	110.349760	134.25	6.045	52
HCO^+	$1 \rightarrow 0$	89.188526	4.28	3.02	3
$H^{13}CO^+$	$1 \rightarrow 0$	86.754330	4.16	2.80	3

[α] J_K quantum numbers.

[β] Einstein A coefficients for symmetric tops and linear rotors are given by $(16\pi^3\nu^3\mu^2 S)/(3\epsilon_0 hc^3 g_u)$ where $g_u = (2J+1)$ and μ is the electric dipole moment for the molecule. Other constants take their usual values and are in SI units.

[γ] $g_{jk} = g_u\,S(I,J)$ is the degeneracy of the J_K rotational level as given by Araya et al. (2005), matched with the partition function quoted in the same paper. $S(I,J) = (J^2 - K^2)/J$ is the intrinsic line strength.

Table 4.1 presents the details of the observed transitions. All molecular constants are in SI units and come from the catalogue of Pickett, et al. (1998).

We justify the source selection criteria and derive the distances and luminosities in the following section. In Section 4-3 we describe the observations and data reduction methodology. In Section 4-4, we present the initial results of the line survey and describe the data. We outline the analysis techniques used and present derived physical parameters in Section 4-5, and in Section 4-6 we analyse and discuss general trends in the data and test the validity of our results. Finally, in Section 4-7 we conclude with a summary of our investigations. The full set of spectra, MSX images and related plots are presented in the Appendix.

4-2 Source selection

77 sources were drawn from the methanol maser, radio and sub-millimetre surveys conducted by Walsh et al. (1997, 1998, 2003). The original sources were chosen for their red IRAS colours using the colour selection criteria of Wood & Churchwell (1989a), to be indicative of UCHII regions. Our sub-sample of 6.67 GHz methanol maser sites are all associated with warm, dusty clumps, traced by sub-millimetre continuum emission (Walsh et al. 2003). The final selection was also constrained by the latitude of the Mopra antenna at -31°. We required that the sources remain above an elevation of $\sim 30°$ for at least three hours, so allowed declinations were restricted between 0 and $-60\,°$. The sample are split into two main categories: eighteen maser sites are within a Mopra beam ($\sim 33''$) of UCHII regions. The remaining 59 maser-sites have no detectable radio emission and are associated only with thermal emission in the sub-mm and infrared. An additional six 'maserless cores', only detected in thermal emission, were added to the list, bringing the total sample to 83. These cool dusty clumps were selected from recent 1.2-mm continuum observations by Hill et al. (2005) and are found in the same fields but offset from the masers and radio emission. One such core was subsequently found to be coincident with an UCHII region but the others are not directly associated with other tracers of massive star formation. We investigate the remaining five as potential precursors to the hot core phase.

Table 4.2 presents the source details and their associations. The first column is the abbreviated Galactic name, columns two and three are the J2000 equatorial coordinates of the pointing centre (usually coincident with the maser site). Column five presents the adopted kinematic distances in kpc. The approximate bolometric luminosity and single-star spectral type are noted in columns six and seven and any associated methanol maser, radio-continuum or mid-infrared thermal emission is noted in column eight. Alternative names used in the literature are presented in the final column.

Table 4.2: Details of the 83 sources observed.

Galactic Name	Right Ascension (J2000)	Declination (J2000)	Velocity (LSR) ($km\,s^{-1}$)	Adopted Distance[α] (kpc)	Luminosity[β] ($\times 10^4 L_\odot$)	Single Star Type[γ]	Other Associations[δ]			Molecular Cloud Name
G0.21+0.00	17:46:07.7	−28:45:20	44.6	8.4[t]	11.9	O8	M	R	MIR	
G0.26+0.01	17:46:11.3	−28:42:48	26.0	8.4[t]	–	–	M	–	DRK	
G0.32−0.20	17:47:09.1	−28:46:16	18.9	8.5[t]	39.9	O6	M	R	MIR	
G0.50+0.19	17:46:04.0	−28:24:51	−6.1	2.6[p]	0.9	B1	M	–	MIR	
G0.55−0.85	17:50:14.5	−28:54:31	17.5	8.5[t]	85.5	O5	M	R	MIR	RCW142
G0.84+0.18	17:46:52.8	−28:07:35	5.9	5.6	3.7	O9.5	M	–	MIR	
G1.15−0.12	17:48:48.5	−28:01:12	−17.2	8.5	10.9	08	M	–	MIR	
G2.54+0.20	17:50:46.5	−26:39:45	10.1	4.4[r]	–	–	M	–	DRK	
G5.89−0.39	18:00:31.0	−24:03:59	9.3	2.0[a]	14.7	O7.5	M	R	MIR	W28
G5.90−0.43	18:00:40.9	−24:04:21	7.0	2.0[d]	6.8	O9.5	M	–	MIR	W28
G5.90−0.44	18:00:43.9	−24:04:47	9.5	2.5[d]	3.7	B0	M	–	MIR	W28
G6.54−0.11	18:00:50.9	−23:21:29	0.0	14.9[w]	37.2	06	M	–	MIR	
G6.61−0.08	18:00:54.0	−23:17:02	7.7	14.9	5.7	O9.5	M	–	MIR	
G8.14+0.23	18:03:00.8	−21:48:10	19.2	3.3[w]	8.5	O8.5	M	R	MIR	W30
G8.67−0.36	18:06:19.0	−21:37:32	34.8	4.5[d]	7.4	O9	M	R	MIR	
G8.68−0.37	18:06:23.5	−21:37:11	37.2	4.8[d]	–	–	M	–	DRK	
G9.62+0.19	18:06:14.8	−20:31:37	4.4	5.7[ho]	28.0	O6.5	M	R	MIR	
G9.99−0.03	18:07:50.1	−20:18:57	48.9	5.0	2.0	BO.5	M	–	MIR	
G10.10−0.72	18:05:18.2	−19:51:14	-4.0	16	–	–	M	–	–	
G10.29−0.13	18:08:49.4	−20:05:59	13.7	2.2[d]	1.1	B1	M	–	MIR	
G10.30−0.15	18:08:55.5	−20:05:58	13.0	2.1[d]	6.6	O9.5	M	R	MIR	W31

Details of the 83 sources observed – *continued.*

Galactic Name	Right Ascension (J2000)	Declination (J2000)	Velocity (LSR) ($\mathrm{km\,s^{-1}}$)	Adopted [α] Distance (kpc)	Luminosity [β] ($\times 10^4 L_\odot$)	Single [γ] Star Type	Other [δ] Associations			Molecular Cloud Name
G10.32−0.16	18:09:01.5	−20:05:08	12.2	2.2[d]	8.1	09	M	–	MIR	W31
G10.34−0.14	18:09:00.0	−20:03:36	12.2	2.2[d]	1.7	B0.5	M	–	MIR	
G10.44−0.02	18:08:44.9	−19:54:38	75.4	6.0[r]	–	–	M	–	DRK	
G10.47+0.03	18:08:38.2	−19:51:50	67.0	5.7[ce]	23.0	O6.5	M	R	MIR	
G10.48+0.03	18:08:37.9	−19:51:15	66.2	5.7[ce]	–	–	M	–	DRK	
G10.63−0.33	18:10:18.0	−19:54:05	−4.1	6.0[d]	56.8	05.5	M	–	MIR	W31
G10.63−0.38	18:10:29.2	−19:55:41	−3.1	6.0[d]	26.4	O6.5	M	R	MIR	
G11.50−1.49	18:16:22.1	−19:41:28	10.3	1.6	0.5	B2	M	–	MIR	
G11.94−0.15	18:12:17.3	−18:40:03	42.6	4.4	0.6	B2	M	–	MIR	
G11.94−0.62	18:14:00.9	−18:53:27	37.9	4.1[ch]	7.6	O9	M	R	MIR	
G11.99−0.27	18:12:51.2	−18:40:40	59.7	5.2	1.2	B1	M	–	MIR	
G12.03−0.03	18:12:01.9	−18:31:56	110.5	6.7	1.3	B0.5	M	–	MIR	
G12.18−0.12	18:12:41.0	−18:26:22	26.5	13.4[d]	–	–	M	–	MIR	
G12.21−0.09	18:12:37.5	−18:24:08	23.8	13.6[d]	–	–	M	–	MIR	
G12.68−0.18	18:13:54.7	−18:01:41	56.5	4.9[s]	1.5	B0.5	M	–	MIR	W33
G12.72−0.22	18:14:07.0	−18:00:37	34.2	3.7[s]	4.7	B0	M	–	MIR	W33
G12.89+0.49	18:11:51.4	−17:31:30	33.3	3.6[m]	3.4	B0	M	–	MIR	
G12.91−0.26	18:14:39.5	−17:52:00	37.0	3.9[s]	7.3	O9.5	M	–	MIR	W33
G14.60+0.02	18:17:01.1	−16:14:39	24.7	2.8[d]	1.0	B1	M	R	MIR	
G14.99−0.70	18:20:23.1	−16:14:43	18.7	1.6[h]	–	–	M	–	DRK	M17
G15.03−0.68	18:20:24.8	−16:11:35	19.5	1.6[h]	16.3	O7	M	–	MIR	M17
G15.03−0.71	18:20:30.3	−16:12:43	21.0	1.6[h]	3.1	B0	M	–	MIR	M17

Details of the 83 sources observed – *continued.*

Galactic Name	Right Ascension (J2000)	Declination (J2000)	Velocity (LSR) ($km\,s^{-1}$)	Adopted Distance[α] (kpc)	Luminosity[β] ($\times 10^4 L_\odot$)	Single Star Type[γ]	Other Associations[δ]			Molecular Cloud Name
G16.59−0.05	18:21:09.1	−14:31:49	59.9	4.6[co]	2.5	B0.5	M	–	MIR	
G16.86−2.16	18:29:24.4	−15:16:04	17.8	1.9	0.4	B2	M	–	MIR	
G19.36−0.03	18:26:25.2	−12:03:53	26.7	2.5	0.5	B2	M	–	MIR	
G19.47+0.17	18:25:54.7	−11:52:34	19.7	1.9	1.3	B0.5	M	–	MIR	
G19.49+0.15	18:26:00.4	−11:52:22	23.0	2.2	0.6	B2	M	–	MIR	
G19.61−0.13	18:27:16.4	−11:53:38	56.9	4.2[d]	2.1	B0.5	M	–	MIR	
G19.70−0.27	18:27:55.9	−11:52:39	43.0	3.5	0.6	B2	M	–	MIR	
G21.88+0.01	18:31:01.7	−09:49:01	23.3	2.0	–	–	M	–	–	
G22.36+0.07	18:31:44.1	−09:22:13	84.1	10.5[s]	7.9	O9	M	–	MIR	
G23.26−0.24	18:34:31.8	−08:42:47	61.5	4.2	2.6	B0.5	M	–	MIR	
G23.44−0.18	18:34:39.2	−08:31:32	101.6	5.9[d]	–	–	M	–	DRK	
G23.71−0.20	18:35:12.4	−08:17:40	69.0	4.5	1.6	B0.5	M	–	MIR	
G24.79+0.08	18:36:12.3	−07:12:11	110.5	7.7[be]	20.4	O6.5	M	–	MIR	
G24.85+0.09	18:36:18.4	−07:08:52	108.9	6.3[co]	10.8	O8	M	–	MIR	
G25.65+1.05	18:34:20.9	−05:59:40	42.4	3.1[m]	2.5	B0.5	M	R	MIR	
G25.71+0.04	18:38:03.1	−06:24:15	98.7	9.5[d]	8.9	O8.5	M	–	MIR	
G25.83−0.18	18:39:03.6	−06:24:10	93.4	5.6[r]	–	–	M	–	DRK	
G28.15+0.00	18:42:42.2	−04:15:32	98.6	5.9	2.0	B0.5	M	–	MIR	
G28.20−0.05	18:42:58.1	−04:13:56	95.6	6.8[r]	17.1	O7	M	R	MIR	
G28.28−0.36	18:44:13.3	−04:18:03	48.9	3.3[so]	–	–	M	R	–	
G28.31−0.39	18:44:22.0	−04:17:38	86.2	5.2[so]	4.0	B0	M	–	MIR	
G28.83−0.25	18:44:51.1	−03:45:48	87.1	5.3[so]	3.5	B0	M	–	MIR	

Details of the 83 sources observed – *continued.*

Galactic Name	Right Ascension (J2000)	Declination (J2000)	Velocity (LSR) ($\mathrm{km\,s^{-1}}$)	Adopted [α] Distance (kpc)	Luminosity [β] ($\times 10^4 L_\odot$)	Single [γ] Star Type	Other [δ] Associations			Molecular Cloud Name
G29.87−0.04	18:46:00.0	−02:44:58	100.9	6.3	5.3	B0	M	–	MIR	
G29.96−0.02	18:46:04.8	−02:39:20	97.6	6.0[p]	74.0	O5	M	R	MIR	W43S
G29.98−0.04	18:46:12.1	−02:38:58	101.6	6.3[r]	–	–	M	–	DRK	
G30.59−0.04	18:47:18.6	−02:06:07	41.8	11.8[so]	32.6	O6	M	–	MIR	
G30.71−0.06	18:47:36.5	−02:00:31	92.8	5.8[r]	–	–	M	R	DRK	W43
G30.76−0.05	18:47:39.7	−01:57:22	93.0	5.8[r]	12.1	O8	M	–	MIR	W43
G30.78+0.23	18:46:41.5	−01:48:32	41.8	2.9	–	–	M	–	MIR	
G30.79+0.20	18:46:48.1	−01:48:46	81.6	5.1[r]	2.3	B0.5	M	–	DRK	
G30.82−0.05	18:47:46.5	−01:54:17	96.6	6.0[r]	2.7	B0.5	M	–	DRK	W43
G30.82+0.28	18:46:36.1	−01:45:18	97.8	8.5[l]	–	–	M	–	MIR	
G30.90+0.16	18:47:09.2	−01:44:09	106.2	7.3[t]	4.8	B0	M	–	MIR	
G31.28+0.06	18:48:12.4	−01:26:23	109.4	7.2[t]	12.0	O8	M	R	MIR	
G31.41+0.31	18:47:34.3	−01:12:47	96.7	7.9[ce]	17.0	O7	M	R	MIR	
G316.81−0.06	14:45:26.9	−59:49:16	−38.7	2.7	13.2	O7.5	M	–	MIR	
G318.95−0.20	15:00:55.3	−58:58:54	−34.5	2.4	2.9	B0.5	M	–	MIR	
G323.74−0.26	15:31:45.8	−56:30:50	−49.6	3.3	5.3	B0	M	–	MIR	
G331.28−0.19	16:11:26.9	−51:41:57	−88.1	5.4	23.0	O6.5	M	–	MIR	
G332.73−0.62	16:20:02.7	−51:00:32	−50.2	3.5	–	–	M	–	DRK	

[a] The distance given in column 5 is the assumed kinematic distance, in kpc, based on the rotation curve of Brand & Blitz (1993). We have resolved the kinematic distance ambiguity for 58 sources, mainly using the work of the following authors: [a] Acord et al. (1998), [ho] Hofner et al. (1994), [be] Beltrán et al. (2005), [p] Pratap et al. (1999), [d] Downes et al. (1980), [w] Wink et al. (1982), [ch] Churchwell et al. (1990), [ce] Cesaroni et al.

(1998), [m] Molinari et al. (1996), [so] Solomon et al. (1987), [co] Codella et al. (1997), [l] Larionov et al. (1999), [h] Hanson et al. (1997), [s] Stier et al. (1984). Also, the near and far distances for sources marked with a 't' were within 1 kpc and they were placed at the middle distance. Sources marked with a 'r' were seen in absorption at 8μm (dark clouds) and were placed at the near distance. The remaining 25 sources were assumed to lie at the near distance except for G10.10−0.72.

[b] Bolometric luminosities were calculated from a two component greybody fit to the SED containing SCUBA and MSX fluxes (Walsh et al. 2003). The IRAS fluxes were included in the fit only if known with confidence. Sources without a quoted luminosity had insufficient data to constrain a fit.

[c] Approximate spectral types for a given luminosity were read from Table 1 of Panagia (1973).

[d] 'M' indicates a 6.7 GHz methanol-maser at the position. 'R' indicates a UCHII region lies within the Mopra beam. 'MIR' indicates a detection of mid-infrared MSX emission near the source, 'DRK' indicates the source is associated with a MSX dark cloud.

4-2.1 Kinematic distances

The majority of sources are in the first quadrant of the Galactic plane, between longitude $l = 0°$ and 35°. Five sources are located between l = 316° and 335°. We used the rotation curve of Brand & Blitz (1993) to calculate the kinematic distance, assuming a distance to the Galactic centre of 8.5 kpc and a solar angular velocity $\Theta = 220\,\mathrm{km\,s^{-1}}$. In most cases the V_{LSR} was determined from Gaussian fits to the $H^{13}CO^+$ line. The method is described in detail in Appendix A.

All sources lie inside the solar circle and thus have a near / far distance ambiguity. We were able to resolve the ambiguity for 58 sources, mainly referencing the work of Downes et al. (1980), Solomon et al. (1987) and Wink, Altenhoff & Mezger (1982). These authors have distinguished between the near and far distances of our common sources by looking for molecular absorbsion (e.g., H_2CO formaldehide) against continuum sources (HII regions) within the same cloud. Also, where the near and far kinematic distances are within ~ 1 kpc we have assigned the distance of the tangent point to the source. We favoured the near distance when a source was seen in absorption in 8 μm images. Several sources have been identified in the literature as being part of the same complex and we have placed them at a common distance. The remaining 25 sources are assumed to lie at the near kinematic distance, except for G10.10+0.72, which was not convincingly detected in any molecular tracer and was placed at the far distance.

Assuming peculiar velocities $\pm 10\,\mathrm{km\,s^{-1}}$ from the model Galactic rotation curve, we estimate the error in the distance is 0.65 ± 0.29 kpc, or 20 ± 9 per cent of the near kinematic distance. Eighteen sources in our sample lie between $l = 0°$ and $l = 10°$. Over these longitudes the Galactic rotation curve is not well determined and large peculiar velocities will lead to correspondingly greater errors in the distance determination.

4-2.2 Bolometric luminosities

If we assume the millimetre, sub-millimetre, far and near infrared emission is associated with the same object, we can estimate a bolometric luminosity by fitting a two-component greybody to the spectral energy distribution (SED) (e.g. Faúndez et al. 2004; Minier et al. 2005 and references therein, also see Appendix B). The model greybody SED is a summation of two blackbodies, with separate temperatures and amplitudes, modified by a common dust emissivity index, β. Typical values for β range between one and two, with the Kramers-Kroing theorem constraining the lower limit at one (Emerson 1988). In the literature a value of two is generally assumed (Dunne et al. 2000; James et al. 2002; Kramer et al. 2003) and recent results by Hill et al. (in preparation) suggest an emissivity of two for a sample of massive star forming regions. Accordingly we limit β between values of one and two for our fits, while all other parameters are free. No attempt was made to interpret the greybody fits, except to measure the total intensity by integrating under the curve between 10^6 and 10^{16} Hz.

Sub-millimetre data for 78 maser sites comes from the observations of Walsh et al. (2003) using the SCUBA bolometer on the James Clerk Maxwell Telescope (JCMT). 1.2-mm flux densities were taken from the work of Hill et al. (2005). Far and mid-infrared flux densities are drawn from the Infrared Astronomy Satellite (IRAS) point source catalogue[1] and measured directly from the Midcourse Space Experiment (MSX) images. We have assumed 30 per cent errors on all flux densities.

High source multiplicity in the Galactic plane means quoted IRAS flux densities may contain contributions from several sources within the $\sim 1'$ IRAS beam. We include IRAS data in the SED if the source appears isolated in the higher resolution MSX image, or if the MSX and IRAS flux densities match at 14 μm. In some cases the 60 and 100 μm points are included as upper limits to the fit. Without data points at $\sim 100\,\mu$m, the peak of the SED is not well constrained. In an attempt to measure the effect of missing data, we fit fifteen SEDs with the IRAS data removed

1. IRAS images and photometry data are available online at http://www.ipac.gov.com

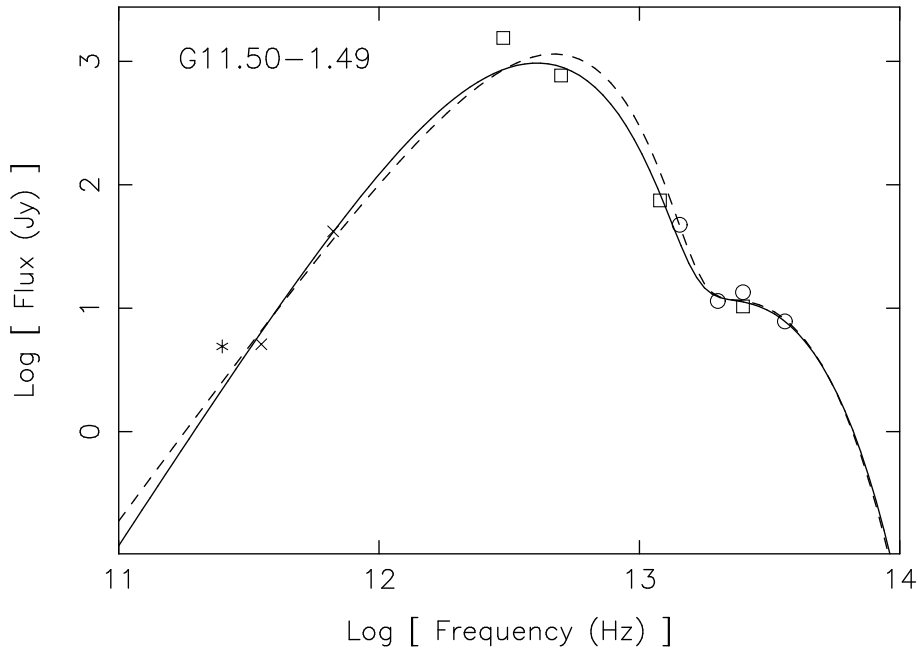

Figure 4.1. Greybody fits to the SED of source G11.50−1.49. MSX data points are plotted as circles, IRAS data points are plotted as squares, SCUBA data points are plotted as crosses and SIMBA data points are plotted stars. The solid line represents a two-component fit to all data points, while the dashed line represents a fit to the SIMBA, SCUBA and MSX data only. Without the IRAS points the fit overestimates the integrated intensity by a factor of 1.5 ± 0.8. The bolometric luminosity is estimated to be accurate to a within a factor of two.

and compared the results to fits utilising the IRAS data. We find that the integrated intensity is, on average, overestimated by a factor of 1.3 ± 0.6 when the IRAS data is absent. An inspection of the fits reveals that when IRAS data is not present the height of the peak depends most strongly on the SCUBA 450 and 850 μm data and tends to be exaggerated. Figure 4.1 shows a typical SED. The solid line is a two-component greybody fit to all points, while the dashed line represents a fit to the data with the IRAS points removed. Plots of the greybody fits to all sources are available in Appendix B.

The percentage error in the fit adds in quadrature to twice the error in the distance, leading to a luminosity determined to within a factor of ~ 2 in most cases.

4-3 Observations and data reduction

4-3.1 The Mopra mm-wave observatory

The Australia Telescope National Facility (ATNF) 'Mopra' telescope is a 22-m antenna located 26 km outside the town of Coonabarabran in New South Wales, Australia. At an elevation of 850 metres above sea level and a latitude of 31° south, it is ideally placed for observations of the southern Galactic plane.

Details of the design and operation of the Mopra antenna and receiver systems can be found in Chapter 3 and in the Special Edition of the Journal for Electrical and Electronic Engineering, Australia, Vol 12, No 2, 1992.

4-3.2 The MSX satellite

The MSX satellite was launched in 1995 by the US Ballistic Missile Defence Organisation with the principal aim of performing a census of the mid-infrared sky. The telescope has a 35-cm clear aperture feeding the SPIRIT-III infrared camera, which has a spatial resolution of 18.3″. Four wavebands dubbed A, C, D and E are useful for astronomical research and lie at 8, 12, 14 and 21 μm, respectively. Band-A (6.8 – 10.8 μm) is the most sensitive of the four filters but is contaminated by emission from the strong silicate band at 9.7 μm and the polycyclic aromatic hydrocarbon (PAH) band at 8.6 μm. Band-E (17.2 – 27.1 μm) is less sensitive by a factor of $\sim$20 than A, and is directly analogous to the broad IRAS 25 μm filter. The instrumentation and survey is described in detail by Egan & Price (1996). Calibrated images of the Galactic plane on a common grid are freely available from the on-line MSX image server at the IPAC archive website at: http://irsa.ipac.caltech.edu/.

4-3.3 Observations

We observed our sample using the 92 GHz J = 5 – 4 and 110 GHz J = 6 – 5 transitions of CH_3CN, as well as the 89 and 86 GHz J = 1 – 0 transitions of HCO^+ and $H^{13}CO^+$.

The observations reported here were performed as part of a larger survey using the Mopra antenna, conducted over 5 years, from 2000 – 2004, and between the months May – September. We observed primarily in the dual-polarisation mode. Each polarisation spanned an identical bandwidth of 64 MHz split into 1024 channels, resulting in a velocity resolution of $\sim 0.2\,\mathrm{km\,s^{-1}}$ over a range of $\sim 180\,\mathrm{km\,s^{-1}}$. Typical system temperatures ranged from 150 K to 350 K over the course of the observations. Position switching was employed to subtract the sky contribution and bandpass, with emission-free reference positions chosen at declination offsets greater than $10'$. In the few cases where evidence of emission was seen at the reference position, new coordinates were selected greater than 1° away from the Galactic plane. The pointing accuracy was checked at hourly intervals by observing bright SiO masers of known position and is estimated to be better than $10''$. The pointings towards four sources were consistently off by between 5 and $15''$, due to an error in the observing schedule file. G5.89−0.39 and G19.70−0.27 are offset by $5''$, G29.98−0.04 is offset by $10''$ and G29.96−0.02 is offset by $15''$. The measured brightness temperature will be diminished by an unknown factor in these sources.

A single-load chopper wheel was used to calibrate the data onto a T_A^* scale (see Chapter 3). At Mopra this was implemented by means of a single ambient temperature blackbody paddle placed in front of the beam every few minutes. The data were further calibrated onto a main beam temperature scale (T_{MB}) by dividing by the main beam efficiencies quoted in Chapter 3.

The typical RMS noise on the T_{MB} calibrated CH_3CN spectra is 80 mK for integrations on-source of approximately 30 minutes. Integration times of 5 and 15 minutes lead to a RMS noise of ~ 200 mK and ~ 100 mK in the HCO^+ and $H^{13}CO^+$ spectra, respectively.

4-3.4 Data reduction

4-3.4.1 Mopra spectral line data

Raw data in *rpfits* format were initially reduced using the SPC [2, 3] package developed by the ATNF and custom routines used to correct for errors in the headers [4]. During the reduction, the spectra were sky-subtracted and the two polarisations averaged together, before a low order polynomial was subtracted from the baseline. The reduced data were then read in to the XS [5] package where higher order polynomials or sine waves were subtracted if necessary. Finally all the data were converted into the CLASS format and the spectra were divided by the year-to-year efficiency, $\eta_{\rm yr}$, before calibrating onto the main beam brightness temperature ($T_{\rm MB}$) scale. The general data reduction methodology is described in more detail in Chapter 3.

4-3.4.2 Mid-infrared data

Individual 8 and 21μm images centred on the methanol maser position were acquired from the MSX image server. The MSX images have a stated positional accuracy of 10″. In an effort to improve registration between datasets, we have utilised the 2MASS near-IR images, which have a pointing accuracy generally better than 1″. If a constant offset was observed between two or more bright sources present in both data sets, we shifted the MSX coordinates to match those of the 2MASS images. We considered a maser site or UCHII region to be associated with a MSX source if it fell within 9″ (half of the FWHM of the MSX point spread function) of the peak of the infrared source. The MSX fields often suffered from confusion and blending,

2. http://www.atnf.csiro.au/software/
3. A tcl/tk user interface to SPC known as Data From Mopra (DFM) is available from http://www.phys.unsw.edu.au/mopra/software/
4. During 2000 – 2003 Mopra suffered from a rounding error in the receiver control software which lead to an incorrect velocity scale in the data. A pre-processing script for correcting the data is available from the ATNF Mopra website: http://www.mopra.atnf.csiro.au
5. XS is written by Per Bergman at the Onsala Space Observatory and is available via FTP on request.

especially at 8 μm. Where possible, we measured the integrated intensity by drawing a polygon around the source and summing the pixel values. A pixel-averaged sky value was measured from an emission-free region and subtracted from the resulting figure to find the net integrated flux denisty in units of $\mathrm{Wm^{-2}\,sr^{-1}}$. Conversion to Janskys ($\mathrm{W\,m^{-2}\,Hz^{-1}} \times 10^{26}$) was achieved by dividing by the bandwidth of the filter, and multiplying by the $6 \times 6''$ pixel area in steradians ($8.4615{\times}10^{-10}$ Sr). An additional multiplicative factor of 1.113 was required to correct for the Gaussian response of the individual pixels (Egan & Price 1996). The final scaling factors to convert flux densities in $\mathrm{W\,m^{-2}\,sr^{-1}}$ to Jy were: $6.84{\times}10^{3}$, $2.74{\times}10^{4}$, $3.08{\times}10^{4}$ and $2.37{\times}10^{4}$ for the four bands A, C, D and E respectively. On inspection of the 8 μm images we suspect much of the extended emission seen is due to PAHs. If a clear distinction was evident between the source and the extended emission, we measured the sky value from average level of the extended emission close to the source.

4-4 Results

4-4.1 Spectral line detections

We present a summary of the lines detected towards our sources in Table 4.3. $CH_3CN\,(5-4)$ emission was detected towards 58 sources (70 per cent), 43 of which are new detections. We followed up the $CH_3CN\,(5-4)$ detections in 33 sources by searching for the 110 GHz $CH_3CN\,(6-5)$ transition and detected the line in 24. HCO^+ was detected towards 82 sources (99 per cent), and $H^{13}CO^+$ was detected towards 80 sources (98 per cent). Detected spectral lines peak at least 2-σ above the baseline and in most cases have a signal to noise ratio greater than four.

Table 4.3: Summary of detections towards observed sources.

Source	CH_3CN [α]	HCO^+	$H^{13}CO^+$	21μm [β]	8μm [β]
G0.21+0.00	n –	y	n	y	y
G0.26+0.01	y –	y	y	d	d
G0.32-0.20	y –	y	y	y	y
G0.50+0.19	n –	y	y	y	y

Summary of detections towards observed sources. – *continued.*

Source	CH_3CN [α]		HCO^+	$H^{13}CO^+$	21μm [β]	8μm [β]
G0.55-0.85	y	y	y	y	y	y
G0.84+0.18	y	n	y	y	y	y
G1.15-0.12	y	n	y	y	y	y
G2.54+0.20	n	–	y	y	n	d
G5.89-0.39	y	–	y	y	y	y
G5.90-0.43	y	y	y	y	y	y
G5.90-0.44	y	–	y	y	y	y
G6.54-0.11	n	–	y	n	y	y
G6.61-0.08	n	–	y	y	y	y
G8.14+0.23	y	–	y	y	y	y
G8.67-0.36	y	–	y	y	y	y
G8.68-0.37	y	–	y	y	n	d
G9.62+0.19	y	n	y	y	y	y
G9.99-0.03	y	–	y	y	y	y
G10.10+0.72	n	–	n	n	n	n
G10.29-0.13	y	n	y	y	y	y
G10.30-0.15	y	y	y	y	y	y
G10.32-0.16	y	y	y	y	y	y
G10.34-0.14	y	y	y	y	n	y
G10.44-0.02	y	y	y	y	n	d
G10.47+0.03	y	–	y	y	y	y
G10.48+0.03	y	–	y	y	n	d
G10.63-0.33	n	–	y	y	y	y
G10.63-0.38	y	y	y	y	y	y
G11.50-1.49	n	–	y	y	y	y
G11.94-0.15	n	–	y	y	y	y
G11.94-0.62	y	y	y	y	y	y
G11.99-0.27	n	–	y	y	y	y
G12.03-0.03	n	–	y	y	y	y
G12.18-0.12	n	–	y	y	y	n
G12.21-0.09	n	–	y	y	y	n
G12.68-0.18	y	y	y	y	y	y
G12.72-0.22	y	–	y	y	y	y
G12.89+0.49	y	n	y	y	y	y
G12.91-0.26	y	y	y	y	y	y
G14.60+0.02	y	–	y	y	y	n
G14.99-0.70	y	–	y	y	n	d
G15.03-0.68	y	–	y	y	y	y

Summary of detections towards observed sources. – *continued.*

Source	CH_3CN [α]		HCO^+	$H^{13}CO^+$	21μm [β]	8μm [β]
G15.03-0.71	n	–	y	y	y	y
G16.59-0.05	y	–	y	y	y	y
G16.86-2.16	y	y	y	y	y	y
G19.36-0.03	y	–	y	y	y	y
G19.47+0.17	y	n	y	y	y	y
G19.49+0.15	n	–	y	y	y	y
G19.61-0.13	y	–	y	y	y	y
G19.70-0.27	n	–	y	y	y	y
G21.88+0.01	n	–	y	y	n	n
G22.36+0.07	y	–	y	y	y	y
G23.26-0.24	n	–	y	y	n	y
G23.44-0.18	y	y	y	y	n	d
G23.71-0.20	n	–	y	y	y	y
G24.79+0.08	y	y	y	y	y	n
G24.85+0.09	n	–	y	y	y	y
G25.65+1.05	y	–	y	y	y	y
G25.71+0.04	y	–	y	y	y	n
G25.83-0.18	y	y	y	y	n	d
G28.15+0.00	y	–	y	y	y	y
G28.20-0.05	y	–	y	y	y	y
G28.28-0.36	y	–	y	y	n	n
G28.31-0.39	n	–	y	y	y	y
G28.83-0.25	y	–	y	y	y	n
G29.87-0.04	n	–	y	y	y	y
G29.96-0.02	y	y	y	y	y	y
G29.98-0.04	y	y	y	y	n	d
G30.59-0.04	n	–	y	y	y	y
G30.71-0.06	y	y	y	y	d	d
G30.76-0.05	y	y	y	y	y	y
G30.78+0.23	n	–	y	y	n	y
G30.79+0.20	y	–	y	y	y	d
G30.82-0.05	y	y	y	y	n	d
G30.82+0.28	n	–	y	y	y	y
G30.90+0.16	y	–	y	y	y	y
G31.28+0.06	y	y	y	y	y	y
G31.41+0.31	y	y	y	y	y	y
G316.81-0.06	y	y	y	y	y	y
G318.95-0.20	y	n	y	y	y	y

Summary of detections towards observed sources. – *continued.*

Source	CH_3CN [α]		HCO^+	$H^{13}CO^+$	21 μm [β]	8 μm [β]
G323.74-0.26	y	y	y	y	y	n
G331.28-0.19	y	n	y	y	y	y
G332.73-0.62	y	n	y	y	d	d
% Detections[γ]	70		99	98	78	72

[α] 33 sources were searched for both $CH_3CN\,(5-4)$ (first entry), and $CH_3CN\,(6-5)$ (second entry).

[β] MSX dark clouds seen in absorption against background radiation at 8 or 21 μm are marked with a 'd'.

[γ] If dark clouds are counted then the detection rate rises to 82 % and 88 % for the 21 and 8 μm MSX bands respectively.

Figure 4.2 presents example spectra for the bright source G0.55+0.85 alongside the 21 μm MSX image. Annotated on the MSX image are the positions of the methanol masers (crosses) and the 36″ FWHM size of the Mopra beam at ∼90 GHz (circle). Squares mark the peaks of the compact 8 GHz continuum emission detected by Walsh et al. (1998). Spectra and MSX images for all sources are presented in Appendix C.

Individual components within the CH_3CN K-ladder were fit simultaneously with multiple Gaussians. The separations were fixed to their theoretical values and the linewidths constrained to have the same value in the fit. Table D.1 in Appendix D lists the Gaussian parameters of the fits to both the $CH_3CN\,(5-4)$ and $(6-5)$ lines. Column one is the Galactic source name, columns two and three are the V_{LSR} and FWHM, columns four to eight contain the flux densities, in $K\,km\,s^{-1}$, of the $K=0$ to $K=4$ rotational ladder components. Quoted 1-σ uncertainties in the fits are those reported by the CLASS analysis package used to fit the data. The 1-σ noise on the spectra of sources without detected $CH_3CN\,(5–4)$ are given in Table 4.4.

Absolute calibration errors were estimated from multiple observations of individual sources and are generally on the order of 30 per cent. The low signal to noise ratios in many spectra made identification of asymmetries or line wings difficult and we assume the individual K-lines were well fit by Gaussians. During our analysis

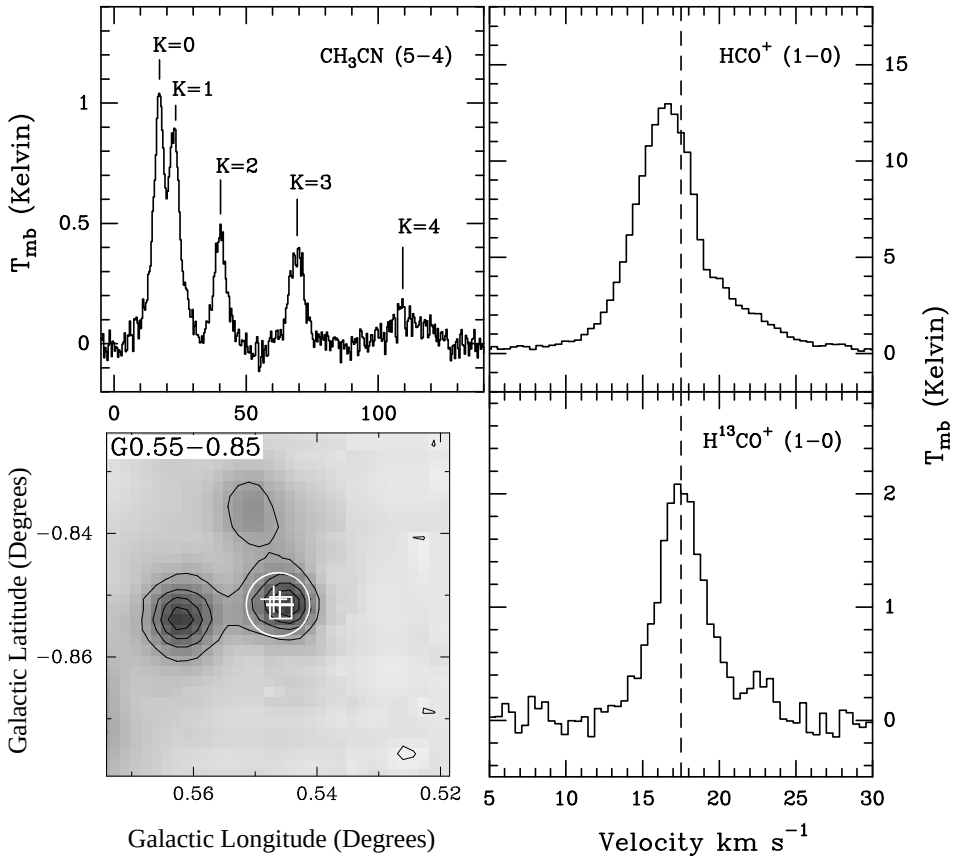

Figure 4.2. CH_3CN, HCO^+ and $H^{13}CO^+$ spectra for the bright source G0.55+0.85 alongside the 21μm MSX image (grey-scale and contours). On the image, squares mark known UCHII regions and crosses mark 6.67 GHz methanol-maser sites. The circle shows the 36″ Mopra beam, centred on the maser position. The CH_3CN K-components are well fit by Gaussians, except for the K = 4 line, which may be affected by baseline instabilities. The dashed line marks the V_{LSR}, taken from a Gaussian fit to the $H^{13}CO^+$ line. The HCO^+ line profile is asymmetric and blue-shifted with respect to the $H^{13}CO^+$ line, possibly indicating inward gas motions.

we found that the K = 4 component of the CH_3CN (5–4) spectrum was almost always anomalously strong and sometimes appeared shifted lower in frequency with respect to the other components. It is possible we are beginning to see excitation by higher temperature gas within the hot core, however, the signal to noise ratio for almost all the K = 4 detections is very low and in many cases broad features are seen which have no counterpart in the other K-components, indicating possible baseline

Table 4.4. Sources without detected CH_3CN.

Source	rms-noise [α] (mK)	Source	rms-noise [α] (mK)	Source	rms-noise [α] (mK)
G0.21+0.00	0.101	G11.99−0.27	0.080	G23.71−0.20	0.088
G0.50+0.19	0.060	G12.03−0.03	0.083	G24.85+0.09	0.098
G2.54+0.20	0.149	G12.18−0.12	0.096	G28.31−0.39	0.079
G6.54−0.11	0.075	G12.21−0.09	0.099	G29.87−0.04	0.106
G6.61−0.08	0.108	G15.03−0.71	0.064	G30.59−0.04	0.093
G10.10+0.72	0.054	G19.49+0.15	0.082	G30.78+0.23	0.089
G10.63−0.33	0.087	G19.70−0.27	0.074	G30.82+0.28	0.064
G11.50−1.49	0.143	G21.88+0.01	0.036		
G11.94−0.15	0.082	G23.26−0.24	0.093		

[α] 1-σ noise in the $CH_3CN\,(5-4)$ spectrum.

problems.

In most cases the detected $H^{13}CO^+$ lines are well fit with a single Gaussian line, show little evidence of self absorption or line wings, and are assumed to be optically thin. In contrast, the HCO^+ profiles are complex, often exhibiting two or more components (e.g. G8.68−0.37). These profiles may be interpreted as either multiple clouds along the line of sight or a single broad emission line with a self-absorption dip. In an attempt to distinguish between these two cases we examined the optically thin $H^{13}CO^+$ profiles for evidence of multiple components. Where a single $H^{13}CO^+$ component was visible at the velocity of the dip in the HCO^+ line, we attempted to fit the double-peaked profile with a single Gaussian, based on the assumption that the line was strongly self-absorbed. In practise, we blanked the absorption dip from the fitting routine so that the Gaussian fit was constrained only by the sides of the line. At best this gives an upper limit to the intensity of the line. As a lower limit we measured the integrated intensity under the line-profile, after subtracting Gaussian fits to any line wings. Figure 4.3 illustrates this method using the extreme case of G16.86−2.16. The results of these measurements are reported in Table D.2, in Appendix D.

Twenty sources detected in HCO^+ have residual line wings distinct from the main line, pointing to the possible existence of molecular outflows. We fitted and

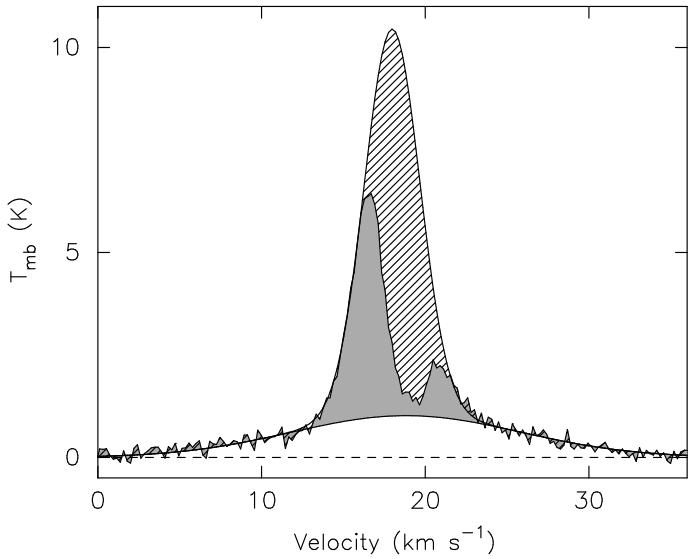

Figure 4.3. An illustration showing the different methods of measuring the self-absorbed HCO^+ line profiles. We measure the line intensity by integrating under the profile (grey area) and by fitting a Gaussian, constrained by the sides of the line and the velocity of the optically thin $H^{13}CO^+$ (hatched + grey area). The contribution from high velocity outflow-wings are omitted from both measurements.

subtracted detected line wings with a single broad Gaussian *before* attempting to analyse the main line. Fourteen sources are found to contain blends of two or more HCO^+ lines, which we attempted to fit with individual Gaussians in order to separate the main line from the blend. Quoted intensities for the main lines in Table D.2 do *not* contain contributions from line wings or blended lines. The Gaussian fit parameters to the line wings and blended lines are recorded in the same table, marked with either a 'b' or a 'w' in the last column.

4-4.2 Mid-infrared associations

We present the association between the maser-selected sample and mid-infrared MSX sources in Table 4.3. Sixty-eight positions observed have mid-IR emission peaking within $10''$. Of these, 3 are detected at $8\,\mu$m but not at $21\,\mu$m, and 7 are detected at $21\,\mu$m but not at $8\,\mu$m. 15 positions show no evidence of a mid-infrared

emission, however 12 of these are identified as MSX 'dark-clouds', seen in absorption against the Galactic plane at 8 μm. A single source, G30.79+0.20, is detected as a point-source at 21 μm but is embedded within a dark cloud at 8 μm.

Of the 80 sources detected in emission or absorption in the mid-IR, 57 have 'compact' or unresolved morphologies, 17 are extended and the remainder are confused.

4-5 Derived physical parameters

4-5.1 The rotational diagram analysis

To estimate the temperature and column density of CH_3CN, we have used the rotational diagram (RD) analysis first introduced by Hollis (1982). The method has been developed and expanded on by a number of authors (Loren & Mundy 1984, Turner 1991, Goldsmith & Langer 1999). The method is fully explained in Chapter 2, however, we provide a brief summary here for convenience.

By solving the radiative transfer equation, assuming low optical depth (i.e. $\tau \ll 1$), we arrive at the well known relation between upper state column density, N_u, and line intensity, $\int_{-\infty}^{\infty} T_b \, dv$

$$N_u = \frac{8\pi k \nu_{ul}^2}{hc^3 A_{ul}} \int_{-\infty}^{\infty} T_b \, dv, \tag{4.1}$$

where ν_{ul} is the frequency of the transition in Hz and A_{ul} is the Einstein A coefficient in s^{-1}. The line intensity is in units of K and is related to the *measured* line intensity T_{mb} via $T_b = T_{mb}/\eta_b$, where η_b is the beam filling factor. All other constants take their usual values in SI units. Assuming local thermal equilibrium (LTE) (i.e. the energy levels are populated according to a Boltzmann distribution characterised by a single temperature, T), the upper state column density is related to the total column density, N, by

$$N_u = \frac{N g_u}{Q(T)} e^{-E_u/kT}, \tag{4.2}$$

where g_u is the degeneracy of the upper state, E_u is the energy of the upper state in joules and Q(T) is the partition function. Rearranging and taking the natural log

of both sides we find

$$\ln\left(\frac{\mathrm{N_u}}{\mathrm{g_u}}\right) = \ln\left(\frac{\mathrm{N}}{\mathrm{Q(T)}}\right) - \frac{\mathrm{E_u}}{\mathrm{kT}}. \tag{4.3}$$

A straight line fitted to a plot of $\ln(\mathrm{N_u}/\mathrm{g_u})$ versus $\mathrm{E_u}/\mathrm{k}$ will have a slope of $1/\mathrm{T}$ and an intercept of $\ln(\mathrm{N}/\mathrm{Q(T)})$. Temperatures found from this method are referred to as rotational temperatures ($\mathrm{T_{rot}}$) in the literature. In our analysis we used the partition function for CH_3CN quoted in Araya et al. (2005)

$$\mathrm{Q(T)} = \frac{3.89\mathrm{T_{rot}^{1.5}}}{(1-\mathrm{e}^{-524.8/\mathrm{T_{rot}}})^2}. \tag{4.4}$$

Inherent in the RD method are some formal assumptions which may effect the interpretation of the results. Firstly, the emitting region is assumed to be optically thin. If optical depths are high the measured line intensities will not reflect the column densities of the levels. Optical depth effects will be evident in the rotational diagram as deviations of the intensities from a straight line and a flattening of the slope (Goldsmith & Langer 1999), leading to anomalously large values for $\mathrm{T_{rot}}$.

We have attempted to iteratively correct individual $\mathrm{N_u}/\mathrm{g_u}$ values by multiplying by the optical depth correction factor, $\mathrm{C}_\tau = \tau/(1-\mathrm{e}^{-\tau})$, after the method of Remijan et al. (2004). Assuming Gaussian line profiles, the line-centre optical depth is given by

$$\tau = \frac{\mathrm{c}^3\sqrt{4\ \ln\ 2}}{8\pi\nu^3\sqrt{\pi}\Delta\mathrm{v}}\mathrm{N_u A_{ul}}\left(\mathrm{e}^{\mathrm{h}\nu/\mathrm{kT_{rot}}}-1\right), \tag{4.5}$$

where Δv is the FWHM of the line profile in $\mathrm{m.s^{-1}}$ (see Goldsmith & Langer 1999 and Remijan et al. 2004 for a formal description). In our calculations we initially assumed the source fills the beam. We find that the corrected optical depth is always $\ll 1$, even in the $\mathrm{K}=0$ transitions, and the correction factors are less than 1 per cent. The FWHM of the Mopra beam at 92 GHz is $\sim 36''$. If previous high-resolution surveys (e.g. Remijan et al. 2004, Wilner, Wright & Plambeck 1994) are indicative, the angular size of CH_3CN emission will be $< 10''$. Our measurements of CH_3CN intensity are thus likely to be affected by a dilution factor of > 13 and the measured optical depth, and therefore the correction factors, are anomalously low because of this.

If we then assume a 7″ source size and determine the correction factor, we find that the rotational temperature is corrected down by ∼10 per cent and the total column density is corrected up by ∼6 per cent, on average. In their analysis of Sagittarius B2 Nummelin et al. (2000) chose a source size which minimises the χ^2 value on their RD fits. They find that for some molecules the best fit to the data is obtained for beam filling factors $\ll 1$. We find that in most cases the quality of our fits *deteriorate* as the beam filling factor is decreased, most likely because our fits our not well constrained due to low signal-to-noise data. Thus, we use a beam filling factor of 1 in our final calculations, and beam-averaged column densities stemming from this analysis should be considered a lower limit.

Secondly, the emitting region is assumed to be in LTE where the population within a K ladder is characterised by a single excitation temperature, described by a Boltzmann distribution. For the non-LTE case the temperature and column density will be underestimated.

Figure 4.4 shows a typical example of a rotational diagram made using the J = 6 – 5 and J = 5 – 4 transitions. Calibration errors between the J transitions are approximately 30 per cent and manifest themselves as a vertical offset between the two sets of points in the graph. The change in the FWHM of the Mopra beam between 92 and 110 GHz has been measured in Chapter 3, and the intensities of the J = 6 – 5 lines have been divided by the relative beam filling factor, given by $(\theta_{110\,\mathrm{GHz}}/\theta_{93\,\mathrm{GHz}})^2 = (34''/36'')^2$. As the K components within a single J transition were observed simultaneously, the relative errors are smaller and arise from the quality of the detection and stability of the bandpass. Error bars mark the 1-σ error in the column density of individual K components, as determined by Gaussian fitting. In the analysis we fit the J = 6 – 5 and J = 5 – 4 data separately, shown in Figure 4.4 as dashed lines. We took as our final result the weighted average of the derived T_{rot} and N, plotted on the diagram as a solid line. The rotational diagrams for the remaining sources are available in Appendix E.

The results of our rotational diagram analysis are presented in Table 4.5. In general, the observed intensities were well fit by a straight line, except for G10.47+0.03,

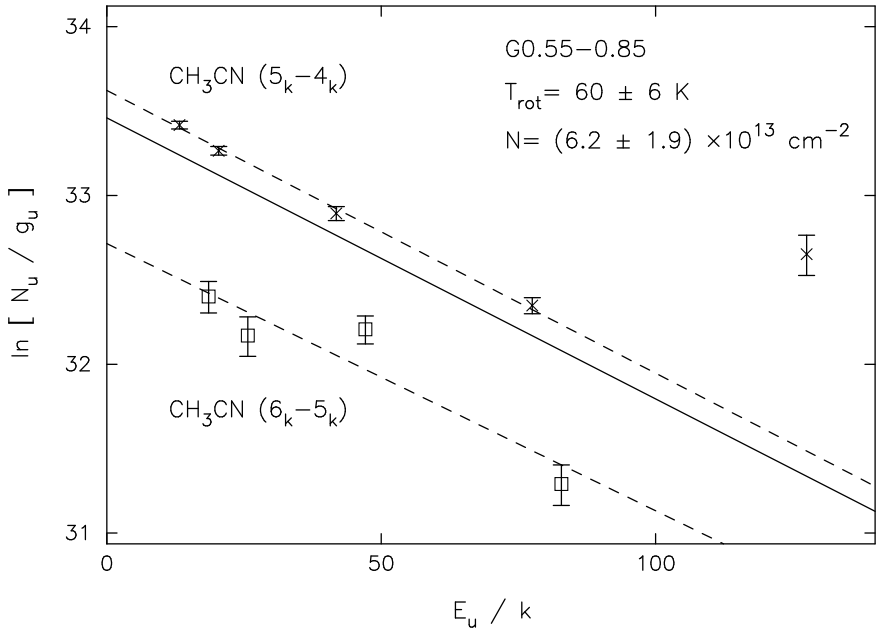

Figure 4.4. CH_3CN rotational diagram of $\ln(N_u/g_u)$ vs E_u/k for the source G0.55−0.85. The J = 5 – 4 K-components are plotted with crosses and the J = 6 – 5 K-components are plotted with squares. Error bars denote the 1-σ errors in the Gaussian fit to individual lines. The rotational temperature, T_{rot}, and total column density, N, may be found from the slope and y-axis intercept of a straight line fit to the data points. We fit the K-ladders separately (dashed lines) and in most cases took the weighted mean of the results as our final values for T_{rot} and N (solid line). The error in T_{rot} is dependant only on the relative calibration between lines in a single spectrum. The error in N is dependant on the absolute calibration, and is approximately 30 per cent.

which exhibited anomalous line ratios and for which a meaningful temperature

Table 4.5: Parameters derived from CH_3CN.

Source	T_{rot} [α] (K)	Column Density [β] ($\times 10^{13}$ m^{-2})	Notes [γ]		
G0.55−0.85	60 ± 3	7.2 ± 2.2	5	M	R
	63 ± 8	3.2 ± 1.0	6		
	60 ± 6	6.2 ± 1.9	b		
G5.89−0.39	56 ± 4	3.5 ± 1.1	5	–	R
G5.90−0.43	46 ± 8	3.3 ± 1.0	5	M	–
	45 ± 6	2.1 ± 0.6	6		
	45 ± 7	2.5 ± 0.8	b		

Parameters derived from CH_3CN – *continued.*

Source	T_{rot} [α] (K)	Column Density [β] ($\times 10^{13}$ m^{-2})	Notes [γ]		
G5.90−0.44	32 ± 5	0.6 ± 0.2	5	–	–
G8.14+0.23	42 ± 10	0.7 ± 0.2	5	M	R
G8.67−0.36	43 ± 3	2.6 ± 0.8	5	M	R
G8.68−0.37	44 ± 3	2.2 ± 0.7	5	M	–
G9.62+0.19	60 ± 9	4.1 ± 1.2	5	M	R
G9.99−0.03	38 ± 29	0.3 ± 0.1	5	M	–
G10.29−0.13	30 ± 8	1.2 ± 0.4	5	M	–
G10.30−0.15	32 ± 8	1.8 ± 0.5	5	M	R
G10.32−0.16	56 ± 19	1.6 ± 0.5	5	M	–
	53 ± 24	0.5 ± 0.1	6		
	55 ± 22	0.6 ± 0.2	b		
G10.34−0.14	30 ± 12	0.7 ± 0.2	5	M	–
	28 ± 7	0.8 ± 0.2	6		
	28 ± 10	0.8 ± 0.2	b		
G10.48+0.03	64 ± 13	3.3 ± 1.0	5	M	–
G10.63−0.38	52 ± 5	4.8 ± 1.4	5	M	R
	55 ± 7	3.1 ± 0.9	6		
	53 ± 6	3.9 ± 1.2	b		
G11.94−0.62	32 ± 9	1.1 ± 0.3	5	M	R
G12.68−0.18	44 ± 18	0.8 ± 0.2	5	M	–
	84 ± 35	1.6 ± 0.5	6		
	52 ± 28	0.9 ± 0.3	b		
G12.72−0.22	28 ± 17	0.4 ± 0.1	5	–	–
G12.89+0.49	131 ± 53	5.2 ± 1.6	5	M	–
G12.91−0.26	28 ± 18	0.6 ± 0.2	5	M	–
	94 ± 15	5.0 ± 1.5	6		
	68 ± 16	2.0 ± 0.6	b		
G14.60+0.02	63 ± 12	0.8 ± 0.2	5	M	R
G15.03−0.68	78 ± 16	1.2 ± 0.4	6	M	–
G16.86−2.16	36 ± 16	1.1 ± 0.3	5	M	–
	43 ± 9	1.1 ± 0.3	6		
	41 ± 13	1.1 ± 0.3	b		
G19.47+0.17	55 ± 13	2.5 ± 0.8	5	M	–

Parameters derived from CH_3CN – *continued.*

Source	T_{rot} [α] (K)	Column Density [β] ($\times 10^{13}$ m^{-2})	Notes [γ]		
G23.44−0.18	47 ± 7	2.2 ± 0.7	5	M	–
	47 ± 6	2.0 ± 0.6	6		
	47 ± 7	2.1 ± 0.6	b		
G24.79+0.08	74 ± 9	6.7 ± 2.0	5	M	–
	81 ± 9	6.3 ± 1.9	6		
	77 ± 9	6.5 ± 1.9	b		
G25.83−0.18	53 ± 8	2.5 ± 0.8	5	M	–
	55 ± 19	2.0 ± 0.6	6		
	53 ± 15	2.3 ± 0.7	b		
G28.20−0.05	74 ± 26	2.6 ± 0.8	5	M	R
G29.96−0.02	75 ± 23	3.5 ± 1.1	5	M	R
	116 ± 39	4.8 ± 1.4	6		
	86 ± 32	3.9 ± 1.2	b		
G30.71−0.06	51 ± 9	3.7 ± 1.1	5	M	R
	75 ± 16	3.3 ± 1.0	6		
	57 ± 13	3.5 ± 1.1	b		
G30.76−0.05	29 ± 14	0.4 ± 0.1	5	M	–
G30.82−0.05	52 ± 6	6.6 ± 2.0	5	M	–
	78 ± 9	7.7 ± 2.3	6		
	61 ± 8	7.1 ± 2.1	b		
G31.41+0.31	98 ± 13	8.3 ± 2.5	6	M	R
G316.81−0.06	73 ± 24	1.7 ± 0.5	5	M	–
G318.95−0.20	55 ± 9	1.8 ± 0.5	5	M	–
G323.74−0.26	67 ± 12	2.3 ± 0.7	5	M	–
G331.28−0.19	74 ± 16	2.7 ± 0.8	5	M	–

[α] Quoted errors in T_{rot} are the $1\,\sigma$ uncertainties arising from the least-squares straight line fit to the rotational diagram.

[β] Quoted errors in N are $\sim$30 %, arising from the relative calibration error between observations.

[γ] Results marked with a '6' or a '5' were derived from individual J = (6 – 5) or J = (5 – 4) rotational ladders respectively. Where we could derive T_{rot} and N from both J-transitions we calculated the weighted average, marked with a 'b' in the notes column. 'R' denotes associated 8.6 GHz radio emission and 'M' marks a methanol maser site.

could not be derived. Rotational temperatures range from 28 K to 166 K with an average value of 57 K. Temperatures derived from sources where we detected less than four CH_3CN K-components are not well constrained, but are still useful for comparative purposes.

We compared distributions of T_{rot} for UCHII regions and isolated masers, but a KS-test did not find any significant difference in rotational temperature between them.

It is interesting to compare our derived rotational temperatures and column densities to previously published results. Eleven sources reported here overlap with previous studies by Pankonin et al. (2001), Hatchell et al. (1998), Olmi et al. (1993) and Churchwell, Walmsley & Wood (1992). Table 4.6 is a reproduction of Table 6 from Pankonin et al. (2001), expanded to include this work. In it we compare values of derived rotational temperature and column density. Our values for T_{rot} are generally lower, typically by a factor of ~ 2, except when compared to values derived by Olmi et al. (1993), who also employ the CH_3CN (5–4) transition in their analysis. The other studies have included data from the $J = 12 - 11$ transitions or higher. The $J = 5 - 4$ and $J = 6 - 5$ transitions have upper-state energies spanning $\sim 8 - 130$ K compared to $\sim 68 - 500$ K for the $J = 12 - 11$ transition. It is likely our survey is sensitive to cooler gas, as evidenced by our lower derived temperatures, whereas the surveys utilising higher energy transitions in their analysis are sensitive to hotter gas. These assertions are supported by recent observations by Araya et al. (2005) who found it necessary to fit two temperatures to their observations of the $J = 5 - 4$, $6 - 5$, $8 - 7$ and $12 - 11$ transitions of CH_3CN. The lower energy lines yield typical temperatures of 35 K whereas the higher energy lines are well fit by temperatures above 90 K, suggesting the existence of a hot molecular clump embedded in a cooler envelope, or simply a temperature gradient. Further evidence of a temperature gradient in hot cores is presented by Olmi et al. (2003), who observed $CH_3CN\,(6 - 5)$ in G29.96−0.02. An analysis of the angular diameter of the emission measured in each K component shows that higher energy transitions are excited closer to the centre of the hot core.

Table 4.6. Comparison of CH_3CN parameters to previous surveys.

	This thesis	Pankonin (2001)	Hatchell (1998)	Olmi (1993)	Churchwell (1992)
Antenna Diameter:	22-m	10-m	15-m	30-m	30-m
Beam Size:	$35''$	$35''$	$21'', 14''$	$21'', 17'', 12''$	$25'', 11''$
(Assumed) source size:	$35''$	$35''$	$< 1.5''$	$5''$	$10''$
	Rotational Temperature, T_{rot} (K)				
Transitions used:	$J_u = 5,6$	$J_u = 12$	$J_u = 12,19$	$J_u = 6,8,12$	$J_u = 6,12$
G5.89-0.39	56	75	d	–	84
G9.62+0.19	60	135	119 and 65	123	–
G10.30-0.15	32	n	n	34	–
G10.47+0.03	d	196	87 and 134	d	–
G10.63-0.38	53	103	–	–	102
G11.94-0.62	32	n	–	–	d
G12.21-0.09	n	d	d	72	–
G15.03-0.68	78	n	–	52	–
G25.65+1.05	166	197	–	–	–
G29.96-0.02	86	150	114 and 141	–	144
G31.41+0.31	98	292	149 and 142	–	372
	Column Density, N_{col} ($\times 10^{13}$ cm^{-2})				
Transitions Used:	$J_u = 5,6$	$J_u = 12$	$J_u = 13$	$J_u = 6,8,12$	$J_u = 6,12$
G5.89-0.39	3.5	2.3	d	–	13
G9.62+0.19	4.1	1.8	2	10.6	–
G10.30-0.15	1.8	n	n	11.9	–
G10.47+0.03	d	8	13	d	–
G10.63-0.38	3.9	2.2	–	–	11
G11.94-0.62	1.2	n	–	–	d
G12.21-0.09	n	d	d	7.1	–
G15.03-0.68	0.8	n	–	2.6	–
G25.65+1.05	d	0.74	–	–	–
G29.96-0.02	3.9	1.8	3	–	6
G31.41+0.31	8.3	8	5	–	17

d = CH_3CN detected but no meaningful rotational temperature or column-density could be derived.

n = CH_3CN was not detected.

– = Source not observed.

Column densities derived here are comparable to those reported in other work. They are higher by factors of $\sim 1.5-2$ compared to the work of Pankonin et al. (2001), but significantly lower than earlier surveys by Olmi, Cesaroni & Walmsley (1993) and Churchwell, Walmsley & Wood (1992). Caution is needed, however, in making a direct comparison of column-densities between surveys, as the beam-sizes and excitation conditions of different observations are not well matched. There is also confusion in the literature with regard to the correct partition function for CH_3CN, which may lead to the column-densities being miscalculated by as much as a factor of 5 (see Araya et al. 2005). The high figures derived in this work compared to Pankonin et al. (2001) probably reflect the greater volume of lower temperature gas probed by the $36''$ Mopra beam compared to more compact, warmer gas probed by other surveys.

4-5.2 HCO^+ column density and abundance

We derive HCO^+ column densities assuming optically thick HCO^+ and optically thin $H^{13}CO^+$ lines.

Assuming the HCO^+ line is optically thick, $(1 - e^{-\tau} \approx 1)$, we can calculate an excitation temperature according to Equation 2.48

$$\mathrm{T_{ex}} = \mathrm{T_s} = \frac{\mathrm{h}\nu_\mathrm{u}}{\mathrm{k}} \left[\ln \left(1 + \frac{(\mathrm{h}\nu_\mathrm{u}/\mathrm{k})}{\mathrm{T_{thick}} + \mathrm{J}_\nu(\mathrm{T_{bg}})} \right) \right]^{-1},$$

where $\mathrm{T_{thick}} = \mathrm{T_r}$ is the beam corrected brightness temperature of the HCO^+ line. We assume the HCO^+ and $H^{13}CO^+$ emission arises from the same gas and shares a common excitation temperature. Given the excitation temperature, the optical depth of the $H^{13}CO^+$ line may be found from

$$\tau_\mathrm{thin} = -\ln \left[1 - \frac{\mathrm{T_{thin}}}{[\mathrm{T_{ex}} - \mathrm{J}_\nu(\mathrm{T_{bg}})]} \right], \tag{4.6}$$

where $\mathrm{T_{thin}} = \mathrm{T_r}$ is the beam corrected brightness temperature of the $H^{13}CO^+$ line.

Equations 4.2 and 4.5 may then be applied to find the total $H^{13}CO^+$ column column density, again assuming LTE conditions. The partition function for linear

rotors is well approximated by $Q(T) = (kT_{ex})/(hB)$, where B is the rotational constant in Hz (43377 MHz for $H^{13}CO^+$). The HCO^+ and $H^{13}CO^+$ column densities are related through their relative abundance ratio,

$$X = \frac{[HCO^+]}{[H^{13}CO^+]} = \frac{N_{HCO^+}}{N_{H^{13}CO^+}}, \tag{4.7}$$

which is partially dependant on the fraction of ^{13}C present in the interstellar medium. A Galactic gradient in the $^{12}C\,/\,^{13}C$ ratio, ranging from ~ 20 to ~ 70, has been measured using several methods (see Savage et al. 2002 and references therein). The measurement uncertainties are large, however, and the ratio of $[HCO^+]\,/\,[H^{13}CO^+]$ may also be affected by chemistry. Thus, we have assumed a constant $X = 50$ for all our calculations.

A major source of error in this analysis stems from the assumption that the HCO^+ lines provide a meaningful estimate of the excitation temperature. In many cases the line profiles show evidence of self absorption and are poorly fit by simple Gaussians. As outlined in Section 4-4 we used two methods to estimate the HCO^+ brightness temperature. In the first method we measure the brightness temperature from a Gaussian fit to the profile, by masking off the absorption dip. In the second method we took as the value for brightness temperature the highest peak in the profile (see Figure 4.3). If the emission is smaller than the beam, the filling factor, η_{bf}, will be less than one and the excitation temperature will be underestimated. Using the above methods we find average excitation temperatures of ~ 7.5 K and ~ 6.1 K, respectively. These values are considerably lower than the ~ 15 K temperatures quoted in previous work (e.g. Girart et al. 2000) and we conclude that the emission is beam diluted in a significant fraction of our observations. In our final analysis we have assumed an excitation temperature of 15 K and the column densities are calculated solely from the $H^{13}CO^+$ lines. The $H^{13}CO^+$ lines were well fit with Gaussians and are consistent with being optically thin in most cases. The results of the analysis are presented in Table 4.7. As the source size is unknown the values quoted are beam-averaged, assuming a filling factor of one.

Table 4.7: Parameters derived from analysis of the HCO^+ and $H^{13}CO^+$ lines.

Source	$\tau\,(H^{13}CO^+)$ [α]	$N\,(H^{13}CO^+)$ ($\times 10^{13}\,cm^{-2}$)	$N\,(HCO^+)$ [β] ($\times 10^{14}\,cm^{-2}$)
G0.32−0.20	0.050	2.0	10.1
G0.50+0.19	0.040	2.4	12.1
G0.55−0.85	0.190	10.2	50.8
G0.84+0.18	0.010	0.6	3.0
G1.15−0.12	0.020	1.3	6.7
G2.54+0.20	0.100	4.1	20.4
G5.89−0.39	0.150	9.4	47.1
G5.90−0.43	0.100	5.1	25.7
G5.90−0.44	0.070	2.0	10.2
G6.61−0.08	0.020	0.7	3.5
G8.14+0.23	0.030	1.9	9.3
G8.67−0.36	0.120	7.4	37.2
G8.68−0.37	0.090	7.0	34.8
G9.62+0.19	0.060	4.5	22.3
G9.99−0.03	0.030	1.0	4.8
G10.29−0.13	0.050	3.0	14.7
G10.30−0.15	0.100	6.7	33.5
G10.32−0.16	0.060	2.3	11.7
G10.34−0.14	0.060	2.8	14.2
G10.44−0.02	0.030	2.0	10.0
G10.47+0.03	0.060	6.1	30.4
G10.48+0.03	0.040	4.2	20.8
G10.63−0.33	0.060	2.7	13.4
G10.63−0.38	0.160	14.3	71.4
G11.50−1.49	0.050	1.4	7.1
G11.94−0.15	0.030	1.9	9.3
G11.94−0.62	0.070	4.4	22.2
G11.99−0.27	0.010	0.8	3.9
G12.03−0.03	0.020	0.8	4.2
G12.18−0.12	0.010	1.5	7.5
G12.21−0.09	0.030	1.2	6.2
G12.68−0.18	0.030	1.4	7.0
G12.72−0.22	0.080	3.3	16.3
G12.89+0.49	0.060	2.8	13.7

Parameters derived HCO^+ and $H^{13}CO^+$ – *continued*.

Source	$\tau\,(H^{13}CO^+)$ [α]	N $(H^{13}CO^+)$ $(\times 10^{13}\,cm^{-2})$	N (HCO^+) [β] $(\times 10^{14}\,cm^{-2})$
G12.91−0.26	0.110	6.1	30.4
G14.60+0.02	0.040	3.8	19.2
G14.99−0.70	0.040	2.7	13.3
G15.03−0.68	0.160	6.8	34.1
G15.03−0.71	0.010	0.8	3.8
G16.59−0.05	0.060	2.8	13.9
G16.86−2.16	0.130	7.0	34.9
G19.36−0.03	0.040	1.9	9.6
G19.47+0.17	0.070	4.9	24.5
G19.49+0.15	0.020	0.9	4.5
G19.61−0.13	0.010	0.5	2.5
G19.70−0.27	0.030	1.1	5.4
G21.88+0.01	0.020	1.1	5.3
G22.36+0.07	0.030	1.0	4.9
G23.26−0.24	0.030	1.2	6.2
G23.44−0.18	0.070	4.3	21.7
G23.71−0.20	0.020	1.1	5.7
G24.79+0.08	0.090	5.5	27.6
G24.85+0.09	0.010	0.5	2.6
G25.65+1.05	0.090	5.1	25.3
G25.71+0.04	0.030	1.3	6.5
G25.83−0.18	0.050	2.3	11.6
G28.15+0.00	0.040	1.4	6.8
G28.20−0.05	0.060	3.3	16.6
G28.28−0.36	0.020	1.1	5.4
G28.31−0.39	0.030	1.8	9.1
G28.83−0.25	0.050	2.6	13.2
G29.87−0.04	0.040	1.8	9.0
G29.96−0.02	0.080	3.6	17.9
G29.98−0.04	0.060	2.2	11.1
G30.59−0.04	0.040	2.1	10.6
G30.71−0.06	0.100	8.0	40.1
G30.76−0.05	0.040	3.6	17.8
G30.78+0.23	0.050	1.1	5.5

Parameters derived HCO^+ and $H^{13}CO^+$ – *continued*.

Source	$\tau\,(H^{13}CO^+)^{\,\alpha}$	$N\,(H^{13}CO^+)$ $(\times 10^{13}\,cm^{-2})$	$N\,(HCO^+)^{\,\beta}$ $(\times 10^{14}\,cm^{-2})$
G30.79+0.20	0.030	1.3	6.7
G30.82−0.05	0.080	5.1	25.5
G30.82+0.28	0.020	0.5	2.6
G30.90+0.16	0.040	1.8	8.9
G31.28+0.06	0.060	4.0	19.9
G31.41+0.31	0.030	1.8	8.9
G316.81−0.06	0.050	3.3	16.7
G318.95−0.20	0.110	4.5	22.5
G323.74−0.26	0.080	3.2	15.9
G331.28−0.19	0.050	2.9	14.7
G332.73−0.62	0.040	0.9	4.4

$^{\alpha}$ We assumed an excitation temperature of 15 K when calculating the optical depth of the $H^{13}CO^+$ (1 – 0) line. Excitation temparatures derived from the HCO^+ (1 – 0) line were anomalously low, most likely as a result of beam dilution.

$^{\beta}$ A Galactic gradient in the $^{12}C\,/\,^{13}C$ isotope ratio has been observed, ranging from 20 to 70, however, there is considerable uncertainty in these results. The $[HCO^+]\,/\,[H^{13}CO^+]$ ratio may also be affected by chemistry. We prefer to use an average value of 50 when calculating the column density of HCO^+.

4-6 Analysis and discussion

We detect CH_3CN towards all classes of sources: UCHII regions, isolated masers and maserless cores. This result confirms a direct link between each of these objects and massive star formation. In the following analysis we will discuss the implications for a possible evolutionary sequence.

4-6.1 The presence of an UCHII region

The CH_3CN detection rate towards maser sources associated with an UCHII region (radio-loud), compared to isolated maser sources (radio-quiet) is strikingly different. Figure 4.5-A shows the distributions of integrated $CH_3CN\,(5-4)$ intensity for the two classes of source, including non-detections, which are summed in the shaded bar. CH_3CN was detected towards 18 out of the 19 radio-loud sources (94 per cent) compared to only 40 out of 64 radio-quiet sources (63 per cent). Furthermore, the average integrated $CH_3CN\,(5-4)$ intensity measured towards the radio-loud sources is $7.4\,\mathrm{K\,km\,s^{-1}}$, stronger than the average value measured towards the radio-quiet sources, which is 3.5 $\mathrm{K\,km\,s^{-1}}$. We use a Kolomogorov-Smirnov (KS) test to measure the difference between the distributions of the two classes. Non-detections are included as upper limits, measured from the RMS noise in the spectra, and by assuming $\mathrm{K}=0$ and $\mathrm{K}=1$ CH_3CN components of linewidth $4\,\mathrm{km\,s^{-1}}$ are present at a 3-σ level. Using this conservative estimate, a KS-test indicates there is only a 0.13 per cent probability of the samples being drawn from the same population. Probabilities below ~ 2 per cent indicate that the distributions are significantly different.

A similar result applies for $H^{13}CO^+$. Figure 4.5-B shows the distributions of $H^{13}CO^+$ intensity for the two classes of objects. The mean intensity for the radio-loud sources is 4.3 $\mathrm{K\,km\,s^{-1}}$, compared to 1.9 $\mathrm{K\,km\,s^{-1}}$ for the radio-quiet sources. A KS-test returns a probability of 0.02 per cent that the distributions are similar.

We find the HCO^+ lines are also brighter towards radio-loud sources, however, we do not consider them in this analysis as they show evidence of optical depth effects

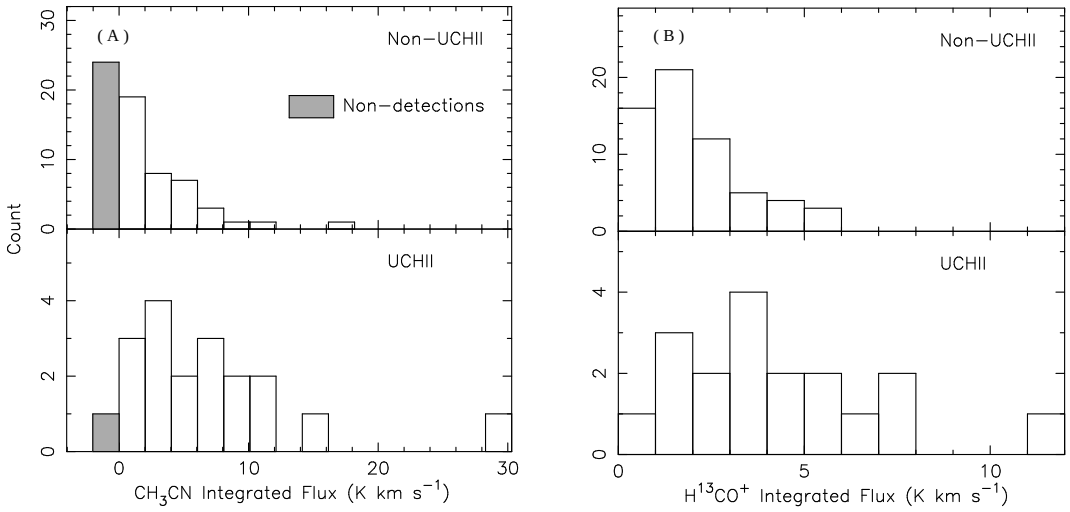

Figure 4.5. A) Distributions of integrated CH_3CN $(5-4)$ flux denisties, summed over all detected K-components, for sources with UCHII regions within the Mopra beam (bottom) and those without (top). The shaded bar represents the number of CH_3CN non-detections for each population. A KS-test yields a maximum difference of 0.48 between the distributions, with a probability of 0.13 per cent of being drawn from the same parent distribution. B) Distributions of integrated $H^{13}CO^+$ $(1-0)$ flux density for the same populations. Lines associated with UCHII regions are markedly brighter than those without. A KS-test yields a difference of 0.55 between the distributions, with an associated probability of 0.02 per cent of being drawn from the same parent distribution. A similar result has been found for the HCO^+ lines.

which may confuse their interpretation.

4-6.1.1 The effect of distance on the results

A higher CH_3CN detection rate towards UCHII regions is consistent with a fall-off in flux denisty with distance in the original radio survey. Our classification of sources into radio-loud and radio-quiet regions may be artificial, and undetected UCHII regions may simply be a result of the sources being further away. Closer examination shows this is not likely to be the case. The distribution of distances to the two populations is shown in Figure 4.6. No UCHII regions have been detected further than 9 kpc away, however only 9 out of 83 sources lie at greater distances.

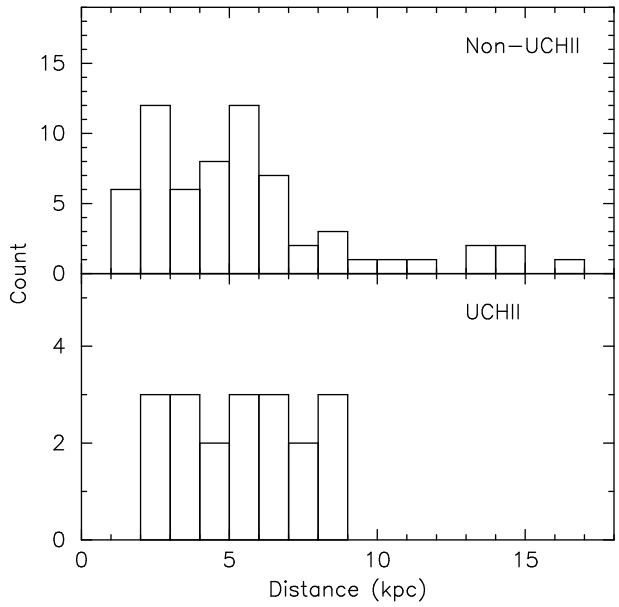

Figure 4.6. Distributions of distances in kiloparsecs for sources with and without associated UCHII regions. A KS-test yields a probability of 53 per cent that samples are consistent with being drawn from the same population and thus probe the same distances.

A comparison yields a 53 per cent probability that the classes are consistent with being drawn from the same population and thus they likely probe the same distance range.

It is possible that greater incidence of CH_3CN detections towards UCHII regions could be a luminosity effect. To test this assertion sources below $6 \times 10^4\,L_\odot$ were omitted from the sample and the CH_3CN detection rates compared again. The resulting luminosity distributions are similar for the remaining isolated masers and UCHII regions (KS-test probability = 89 per cent) in this luminosity-matched sample. We find the CH_3CN detection rate is 73 per cent (11/15) for the isolated masers versus 93 per cent (14/15) for the UCHII regions, and the original result stands.

We further examine the detection limits on the Walsh et al. (1998) 8.64 GHz radio survey from which our sample was drawn. The quoted 1-σ sensitivity is ~ 1 mJy/beam. Assuming a 3-σ detection limit, the limiting distance, D, in kpc at which free-free radio emission from a UCHII region is detectable, may be calcu-

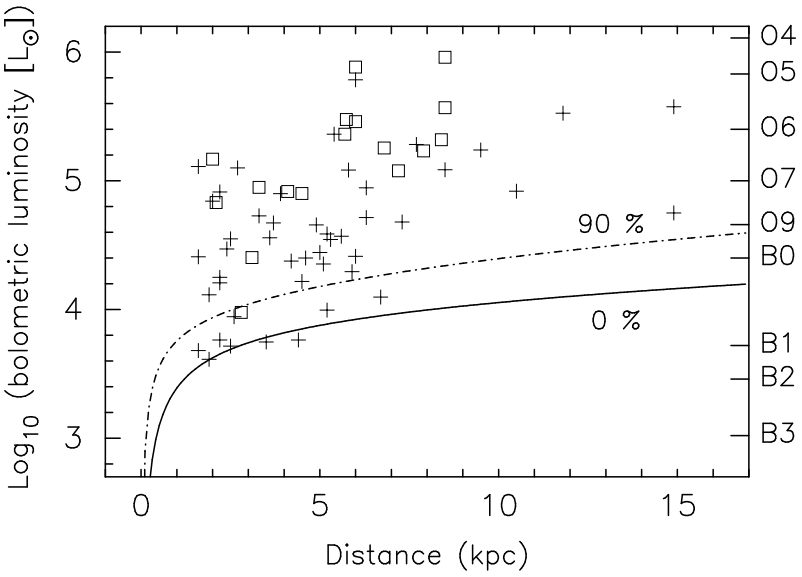

Figure 4.7. A plot of distance versus bolometric luminosity for the sample. The solid line shows the 3-σ detection limit for 8.67 GHz radio continuum emission, assuming all the Lyman-continuum flux contributes to creating an UCHII region. The dashed line shows how the detection limit changes if 90 per cent of the ionising photons are absorbed by dust. UCHII regions are represented by squares, and isolated maser sources by crosses.

lated from Kurtz, Churchwell & Wood (1994):

$$\left(\frac{S_\nu}{Jy}\right) = 1.32 \times 10^{-49}\, N_L \left(\frac{D}{kpc}\right)^{-2} a(\nu, T_e) \left(\frac{\nu}{GHz}\right)^{-0.1} \left(\frac{T_e}{K}\right), \qquad (4.8)$$

where $\nu = 8.64$ GHz is the frequency, $T_e \approx 10^4$ K is the electron temperature, $a(\nu, T_e)$ is a factor of order unity tabulated by Mezger & Henderson (1967) and N_L is the number of Lyman-continuum photons. Values of N_L for early-type stars are tabulated by Panagia (1973), however, in practise some fraction of the emitted photons will be absorbed by dust before ionising the surrounding medium. In a study of UCHII regions, Kurtz et al. (1994) found that between 50 per cent and 90 per cent of the ionising photons are absorbed for the majority of their sample. Figure 4.7 is a plot of luminosity against distance, in kpc, for all the sources whose luminosity could be determined. The solid line marks the 3-σ sensitivity limit to 8.64 GHz radio continuum, assuming no Lyman-continuum photons are absorbed, while the dotted line shows the sensitivity limit assuming 90 per cent of all ionising photons are absorbed. The luminosities of our sources were determined by fitting a 2-component

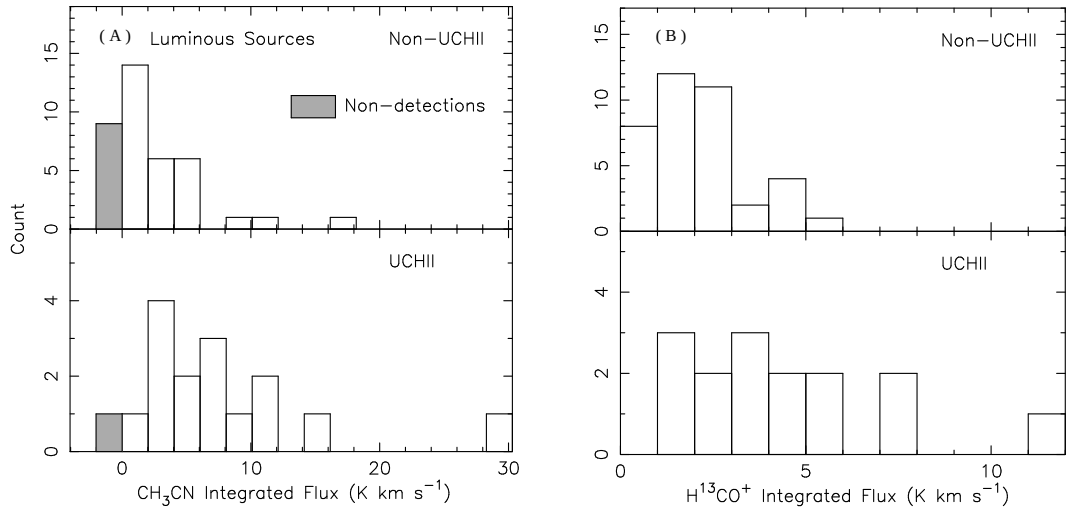

Figure 4.8. As for Figure 4.5 but limited to sources which are luminous enough to have detectable UCHII regions, assuming no less than 90 per cent of the ionising photons are attenuated. A) A KS-test yields a maximum difference of 0.50 between the CH_3CN distributions, with an associated probability of 0.93 per cent of being drawn from the same parent distribution. B) Similarly the maximum difference between the $H^{13}CO^+$ populations is 0.56, with an associated probability of 0.12 per cent.

greybody to available MSX, SCUBA and IRAS flux densities, as discussed earlier, and are accurate to a factor of ~ 2. For those sources above the 90 per cent absorption limit, UCHII regions would have been detected if they existed, and it is unlikely that the comparison between CH_3CN detected for UCHII regions and isolated maser sources is biased. We plot Figure 4.8-A as per Figure 4.5, but include only sources luminous enough to have detectable radio-continuum emission, assuming 90 per cent attenuation of ionising photons. We find that the CH_3CN distributions are still significantly different, with only a 0.9 per cent probability of being drawn from the same population. The $H^{13}CO^+$ intensity distribution for the two classes, filtered to the same luminosity limit, is shown in Figure 4.8-B. A KS-test returns a 0.1 per cent probability of them being drawn from the same population.

The apparent enhancement in *line brightness* towards UCHII regions could be mimicked by the effect of beam dilution. A previous high resolution survey for CH_3CN has found the typical size of the emitting region to be $< 10''$ (Remijan et al.

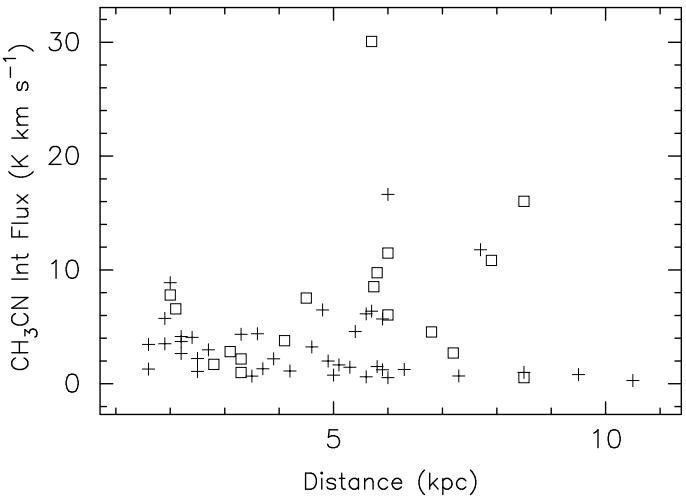

Figure 4.9. Plot of integrated CH_3CN $(5-4)$ flux density vs kinematic distance, in kpc. UCHII regions are marked with squares and isolated maser sources are marked with crosses. No correlation is evident.

2004). Assuming a constant spatial size, the effect of beam dilution on the CH_3CN brightness temperature will depend on the angular size and hence distance to the source. We have shown that the radio-loud and radio-quiet samples probe the same distance range and thus neither class is biased towards being nearer.

Figure 4.9 plots measured CH_3CN $(5-4)$ flux density against kinematic distance and we do not find any correlation. As an additional test we can recover the line-luminosity by multiplying by the square of the distance. This has the effect of increasing the spread in the brightness distribution for both samples, however a KS-test returns a 1.5 per cent probability in the case of CH_3CN and a 1.0 per cent probability in the case of $H^{13}CO^+$ that the radio-quiet and radio loud line-luminosity distributions are drawn from the same population. The average line-luminosity remain higher for the radio-loud class of objects.

4-6.1.2 Interpretation.

Previous work on hot cores suggests CH_3CN is the tracer of choice for massive protostellar objects in the hot core phase (e.g. Kurtz et al. 2000), however we find

CH_3CN is preferentially associated with UCHII regions. Pankonin et al. (2001) conducted a $CH_3CN\,(12-11)$ survey for hot cores and also found a correlation between the presence of CH_3CN and UCHII regions. In one of the few high resolution studies Remijan et al. (2004) used the BIMA array to image the hot core regions W51e1 and W51e2 and found that the CH_3CN emission was centred on known UCHII regions.

That we detect CH_3CN towards isolated methanol masers, for which there are no other tracers indicative of star-formation, clearly suggests that these objects are internally heated. The lack of CH_3CN towards some isolated maser sources is consistent with them being at a less advanced stage of evolution compared to UCHII regions. In young hot cores we would expect any emission to be concentrated in the central regions, where the protostar has heated the dust sufficiently for icy mantles to evaporate and for CH_3CN to form. As the temperature rises, icy mantles continue to evaporate and the emitting region expands outwards and becomes easier to detect. UCHII regions represent the most advanced evolutionary stage before the young star emerges from its natal cocoon. It is reasonable to assume a relatively extended envelope of CH_3CN may exist around the UCHII region, which is less beam diluted and easier for a single-dish survey to detect. Such a scenario is lent weight by high resolutions ($\sim 1''$) observations of the hot core in G29.96−0.02. Olmi et al. (2003) derive a kinetic temperature of $\sim 150\,\mathrm{K}$ from vibrationally excited CH_3CN, significantly higher than the $\sim 90\,\mathrm{K}$ found by Pratap et al. (1999), using ground-state lines. Olmi et al. (2003) also find evidence for a temperature gradient, as the emission from higher energy transitions is confined to increasingly compact regions.

Alternatively, the dominant CH_3CN emission may emanate from an unresolved hot core within the same beam. G29.96−0.02 is the classic example of a hot core on the edge of a cometary UCHII region (c.f. Cesaroni et al. 1998). We note that in the present survey the CH_3CN emission in this object is classified as being associated with the UCHII region, as at 3-mm wavelengths, Mopra does not have the resolution to disentangle the hot core from the nearby ($\sim 5''$) radio emission. Conclusions drawn from this work refer to the properties of "clumps", which may contain more than one core. We speculate that clumps containing UCHII regions are more likely

to contain an evolved hot core and thus have greater abundances of daughter species, like CH_3CN.

Further enhancements come from the work of Mackay (1999) who developed a chemical model of the hot core G34.3+0.15. The model predicts an enhanced abundance of CH_3CN in the presence of a far-ultraviolet radiation field. MacKay assumed a spherically symmetric core surrounded by a photon dominated region (PDR), created by the ultraviolet radiation from a nearby OB association. It is more likely that the cores are inhomogeneous and have clumpy density distributions, in which case the incident radiation will penetrate deeper and the CH_3CN abundance will be further enhanced. Seven out of the nineteen UCHII regions in our sample are exactly coincident with methanol maser sites, however the remaining twelve are offset by less than a beam and it is likely that these sources have a complex clumpy structure.

4-6.2 V_{LSR} and linewidths

The difference between the CH_3CN and $H^{13}CO^+$ V_{LSR} is plotted in Figure 4.10. The velocity offsets are all less than $2\,km\,s^{-1}$, indicating that the molecules are probably within the same star forming region. 92 per cent of the sources have velocity offsets less than the fitting errors ($\pm\,0.4\,km\,s^{-1}$), suggesting that they trace the same clump or core within the beam.

Figure 4.11 displays the distributions of linewidth from the Gaussian fits to the CH_3CN and $H^{13}CO^+$ lines. Both distributions are roughly symmetrical about means of 4.9 and $3.5\,km\,s^{-1}$respectively, higher than typical linewidths of $< 2\,km\,s^{-1}$ measured in low-mass star-forming regions. At 100 K the thermal linewidths of CH_3CN (5 – 4) and $H^{13}CO^+$ (1 – 0) are $0.20\,km\,s^{-1}$ and $0.24\,km\,s^{-1}$, respectively, with turbulence or bulk gas motions accounting for most of the broadening. The CH_3CN linewidth is broader than the $H^{13}CO^+$ linewidth, which suggests that the two species trace different spatial scales. This is consistent with CH_3CN being concentrated around a dynamic core and the $H^{13}CO^+$ tracing a more extended quiescent envelope.

We also note that sources with associated radio continuum emission have larger

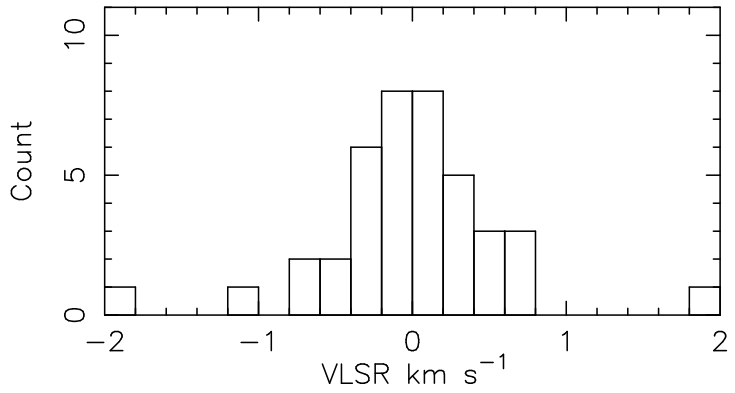

Figure 4.10. V_{LSR} (CH_3CN – $H^{13}CO^+$). The difference in velocity between the CH_3CN and $H^{13}CO^+$ lines is within the errors, making it likely that the emission arises from the same source. Velocity errors are derived from Gaussian fits and are typically $\pm 0.4\,\mathrm{km\,s^{-1}}$.

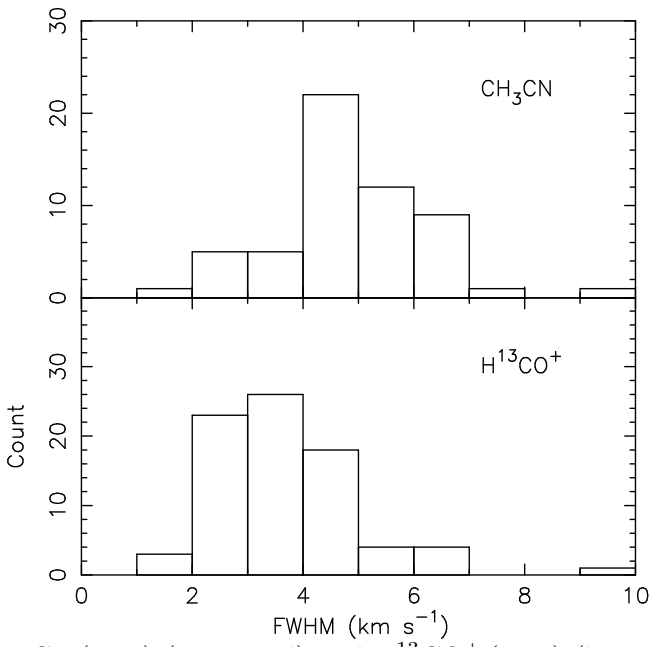

Figure 4.11. CH_3CN (5 – 4) (top panel) and $H^{13}CO^+$ (1 – 0) (bottom panel) linewidth distributions. Both distributions are roughly symmetrical about means of 4.9 and $3.5\,\mathrm{km\,s^{-1}}$ respectively.

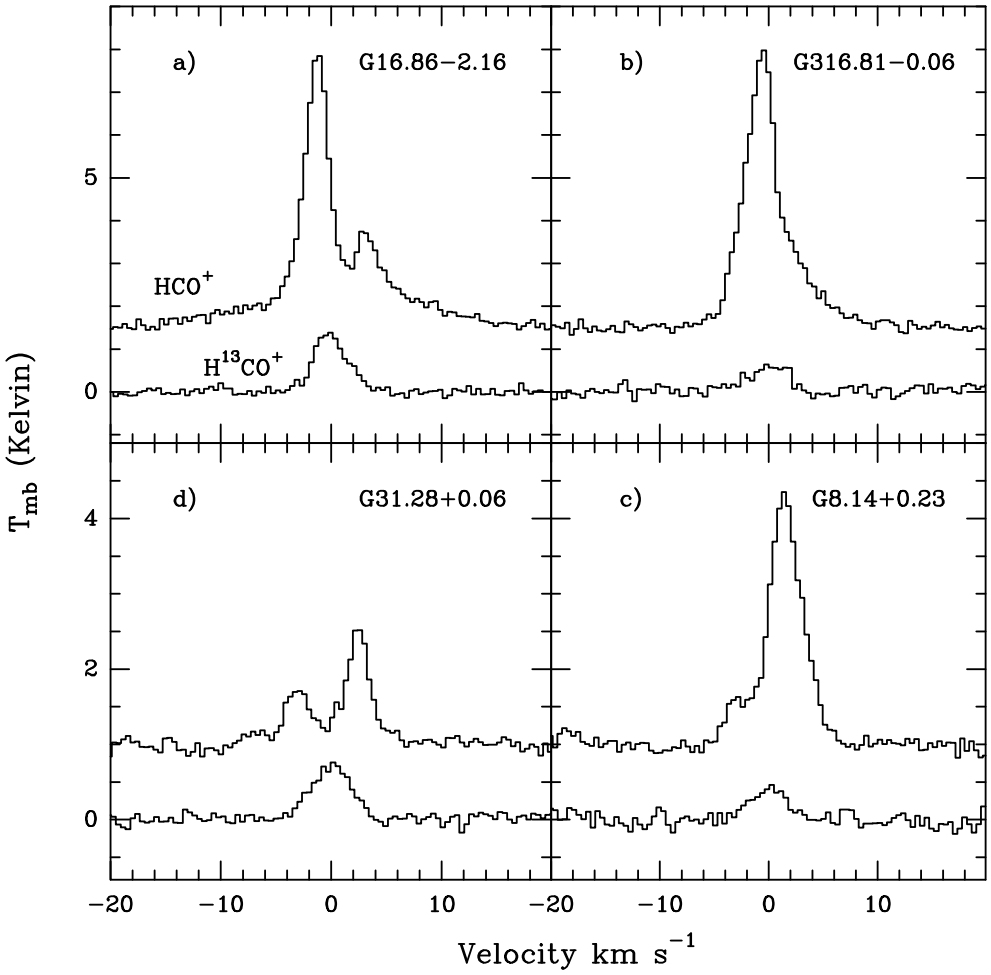

Figure 4.12. Example HCO^+ line profiles. **a**) Blue double-peaked profile, **b**) blue skewed profile, **c**) red skewed profile, **d**) red double-peaked profile.

linewidths than sources without (i.e. isolated maser sources). The mean CH_3CN (5 – 4) linewidths are $6.2\,\mathrm{km\,s^{-1}}$ for UCHII regions versus $4.7\,\mathrm{km\,s^{-1}}$ for isolated masers, while the mean $H^{13}CO^+$ (1 – 0) linewidths are $4.0\,\mathrm{km\,s^{-1}}$ for UCHII regions versus $3.4\,\mathrm{km\,s^{-1}}$ for isolated masers. Linewidths are a rough indicator of star-formation activity: we expect to see greater linewidths towards more active regions. The greater linewidths reported for UCHII regions are certainly consistent with a scenario where the isolated maser sources are precursors to the UCHII phase.

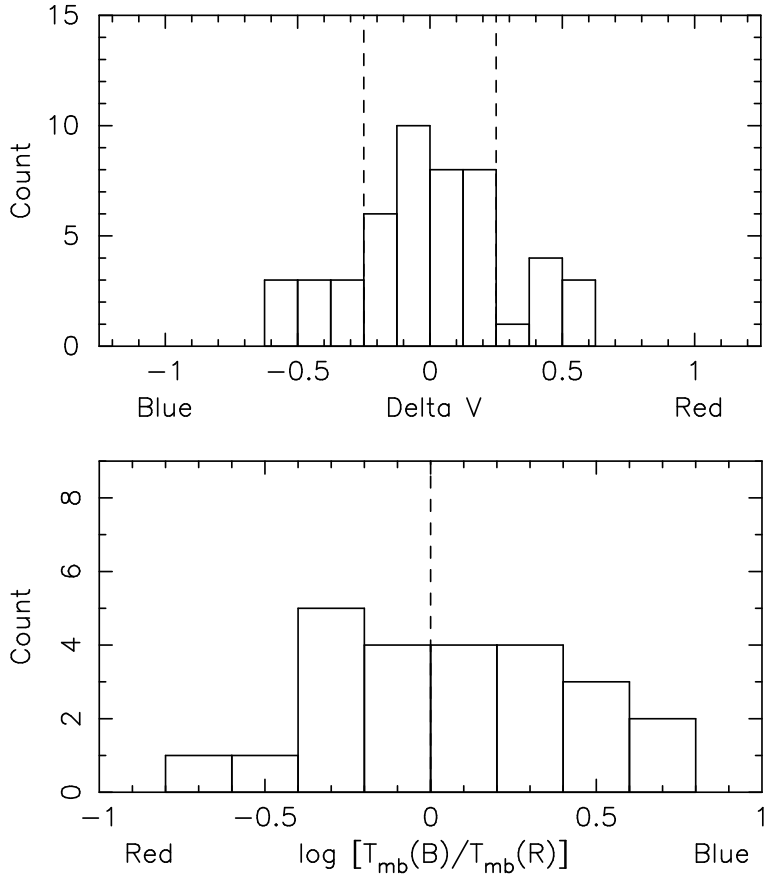

Figure 4.13. Distributions of red and blue profiles measured by $(v_{thick} - v_{thin})/v_{thin}$ (upper panel) and $[T_{MB}(B)/T_{MB}(R)]$ (lower panel). In the top panel the vertical dashed lines mark the absolute velocity difference beyond which profiles are considered to be blue or red skewed. In the lower panel the line divides red and blue profiles. One red and one blue source were discarded as the difference in peak height was within the 1-σ noise on the spectrum.

4-6.3 HCO^+ line profiles

Almost all HCO^+ lines exhibit asymmetric line profiles or high-velocity line wings. Complex profiles may be interpreted as either multiple emitting regions along the same line of sight, or as a single emitting region with cold absorbing gas intervening. By examining the line profiles of optically thin $H^{13}CO^+$ we attempt to distinguish between these two causes, and find that most sources are composed of a single broad line with a self absorption dip. Depending on the shape of the profile, we can infer inward or outward motions. Blue-skewed profiles are predicted by collapse

models of star formation, however, rotation or outflow-blobs can also produce similar line shapes. The presence of a statistical excess of blue profiles in a survey can indicate that inflow is a likely explanation (Wu & Evans 2003). Two methods of characterising line profiles appear in the literature. Where the opacity is high and the line takes on a double-peaked form, Wu & Evans (2003) measure the ratio of the blue to the red peak $[T_{MB}(B)/T_{MB}(R)]$. A blue profile fulfils the criterion: $[T_{MB}(B)/T_{MB}(R)] > 1$ by a statistically significant amount. At lower optical depths the absorption will be less severe and the line will appear as a skewed peak with a red or blue shoulder. Mardones et al. (1997) suggest an alternative measurement: the line may be classed as blue if the difference between the peak velocity of the optically-thick and optically-thin lines is greater than 1/4 the line width of the optically thin line: $\delta v = (v_{thick} - v_{thin})/v_{thin} < -0.25$. Similarly for a red profile: $\delta v = (v_{thick} - v_{thin})/v_{thin} > 0.25$. Figure 4.12 displays a range of HCO^+ profiles from blue to red. We have classed all detected HCO^+ lines using one of the two schemes above.

The results are displayed in Figure 4.13. We identify 9 blue and 8 red profiles using the δv measurement, and 12 blue and 10 red profiles using the brightness method. To effect a comparison with other surveys we adopt the concept of "excess" introduced by Mardones et al. (1997) and later used by Wu & Evans (2003): $E = (N_{blue} - N_{red})/N_{total}$, where N_{total} is the number of sources in the sample. The excesses using the δv and brightness methods are E = 0.02 and 0.08, respectively. By comparison, Wu & Evans (2003) measure excesses of 0.29 and 0.21 in a sample of 28 low-mass star-forming regions.

We also split our sample into radio-strong and radio-weak population, searching for differences in the incidence of blue or red profiles; however we do not find any convincing difference between the populations.

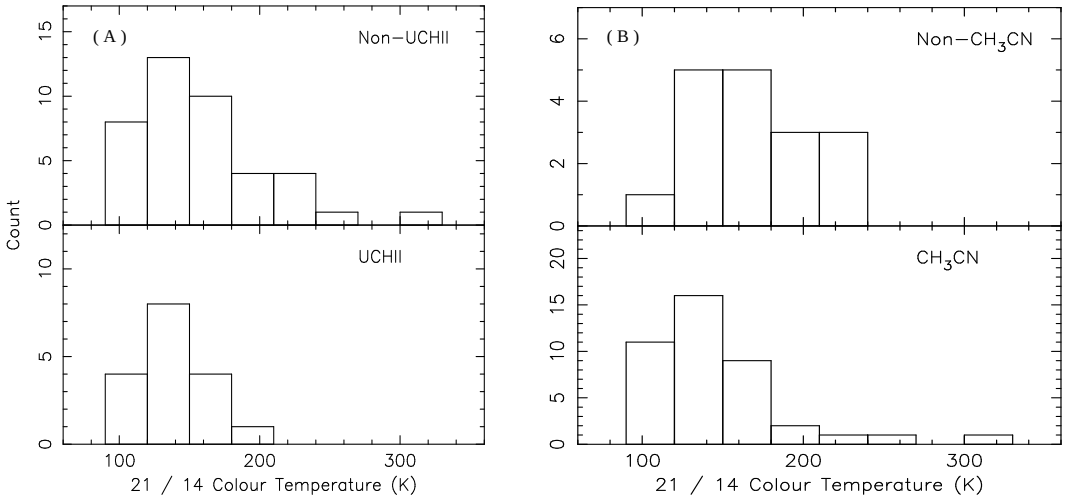

Figure 4.14. Colour temperature distributions derived from the 21 / 14 μm ratio, for sources with and without associated UCHII regions, (A), and CH_3CN emission, (B). A KS-test cannot distinguish between the distributions with confidence.

4-6.4 MSX colours

The MSX colours of our sample are primarily determined by the temperature and optical depth of the dust in which they are embedded. As a first attempt to distinguish between classes of source we have derived the colour temperature from the 21/14 μm ratio, assuming blackbody emission. Larger ratios are equivalent to lower temperatures and increasingly reddened colours. We have avoided using the 21/8 μm or 21/12 μm ratios because of possible contamination from PAHs emission at 7.7, 8.6 and 13.3 μm, and silicate features at 9.7 and 11.3 μm. Distributions of derived temperatures for sources split into classes with and without UCHII regions and CH_3CN emission are displayed in Figure 4.14. A KS-test fails to find any significant difference between the classes.

Figure 4.15 shows a plot of colour temperature against T_{rot}, however no correlation is evident, most likely because the thermal infrared and CH_3CN emission arise in different regions. Although optical depth effects render colour ratios a poor indicator of kinetic temperature, we note that the rotational temperatures are on average three times lower than the colour temperatures.

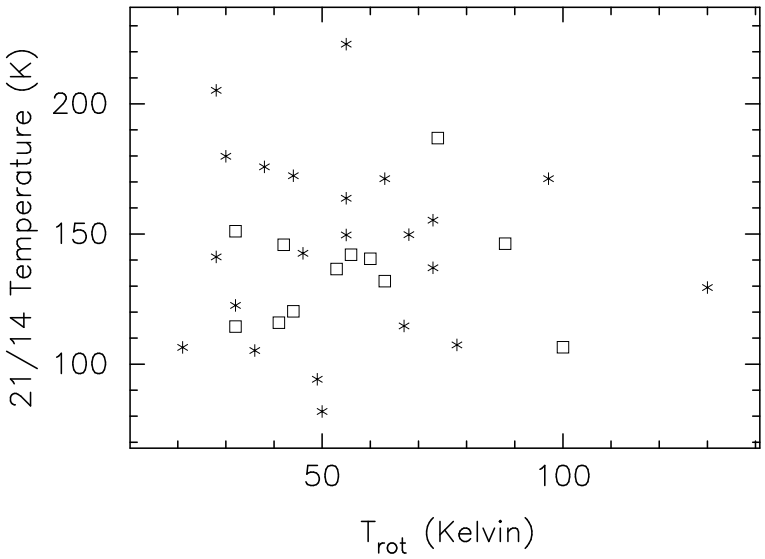

Figure 4.15. 21 / 14 μm ratio vs T_{rot}. Squares represent sources containing UCHII regions. The 21 / 14 μm ratio does not appear to be correlated with the temperature obtained from the rotational analysis of the CH_3CN. Note also that the distribution of T_{rot} is nearly identical for the UCHII regions and isolated masers.

Lumsden et al. (2002) have made a study of sources in the MSX catalogue in an effort to perform a census of massive protostars in the Galactic plane. They have arrived at a set of mid-infrared colour criteria forming the first step in a selection process designed to find the majority of massive protostars present in the Galaxy. As most massive protostars have a featureless red continuum rising between 1 and 100 μm, they require that $F_8 < F_{14} < F_{21}$. Known massive protostars, when plotted on a mid-infrared colour-colour diagram, have an infrared excess such that $F_{21}/F_8 > 2$. In the absence of other selection criteria, sources which satisfy these colour-cuts will include massive protostars, evolved stars, planetary nebula and UCHII regions. Applying these criteria to our data-set we initially discard 28 sources which have incomplete data. Figure 4.16 shows the mid-infrared colour-colour diagrams for the remaining 55 sources. Associations with UCHII regions and CH_3CN are noted by way of different symbols and the selection limits are marked as horizontal and vertical dashed lines. Five sources fail the selection criteria: G23.26−0.24 fails both colour-cuts, G30.90+0.16 fails because $F_{21}/F_8 < 2$ and the remaining three

(G6.54−0.11, G12.72−0.22, G16.59−0.05) fail because $F_{14} < F_8$. All sources are radio-quiet and three have detected CH_3CN emission, but are unremarkable in other ways. No clustering is seen on the colour-colour plots that would distinguish the classes of source, except perhaps a slight enhancement of the 14/12 μm ratio for UCHII regions. UCHII regions are on average also a factor of two brighter in all bands than radio-quiet sources. To further separate young massive stars from planetary nebula and evolved stars Lumsden et al. (2002) resorted to near-infrared JHK colour selection criteria. 6.67 GHz methanol-masers have not, to date, been found towards low-mass star forming regions and we believe that all of our maser sources represent massive stars (Minier et al. 2005).

Potentially the most interesting sources are 'MSX-dark clouds', seen in absorption against the Galactic plane, and the 'MSX-red' sources, detected only at 21 μm. It has been suggested that these sources harbour massive protostars at earlier, more obscured phases of massive star-formation, characterised by low temperatures (T$\sim$30 K) and spectral energy distributions which peak in the sub-millimetre and far-infrared. Table 4.8 summarises the properties of the sources which fall into these categories. The 'MSX-dark' category contains thirteen sources, one of which (G30.71−0.06) is within 30″ of a UCHII region. The 'MSX-red' category contains seven sources, one of which (G30.79+0.20) is also seen in absorption at 8 μm but is detected in emission at 21 μm.

We find that the 'MSX-red' sources are indistinguishable from the bulk of the sample, having approximately the same molecular detection rates and brightness. Four out of eight sources exhibit asymmetric HCO^+ profiles, three of which are skewed to the red, suggestive of outflowing motions.

'MSX-dark' sources exhibit distinct differences from the bulk of the sample. 91 per cent were detected in CH_3CN, and the CH_3CN and $H^{13}CO^+$ brightness temperatures tend to be higher. However, by their nature dark-clouds are located nearby making it easier to detect weak lines. Seven of twelve sources exhibit asymmetric HCO^+ profiles, six of which are skewed to the blue, indicative of inward motions, and consistent with a scenario of cloud collapse. Further analysis is required to

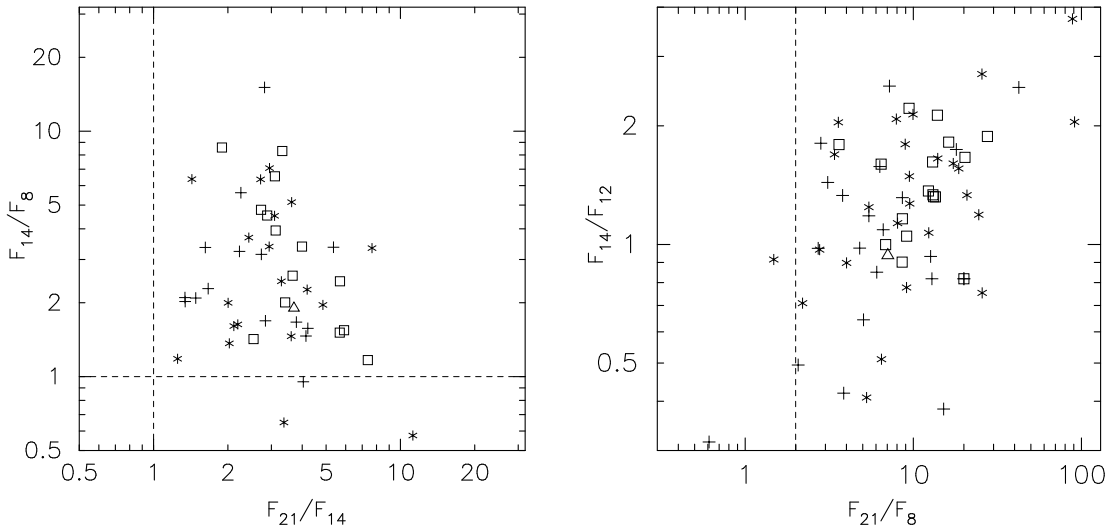

Figure 4.16. Mid-infrared colour-colour diagrams for sources detected in all bands. The following symbols mark classes of source: Square = UCHII region with CH_3CN, Triangle = UCHII without CH_3CN, Star = Non-UCHII region with CH_3CN, Cross = Non-UCHII region without CH_3CN. The dashed lines mark the selection criteria proposed by Lumsden et al. (2002): $F_8 < F_{14} < F_{21}$ and $F_{21}/F_8 < 2$. Sources which fulfil these criteria include MYSOs, UCHII regions, evolved stars and planetary nebula.

judge if these cores will collapse to form massive stars.

4-6.5 Maserless sources

Six maserless sources, identified by thermal emission at 1.2-mm from the work of Hill et al. (2005), were included in the source list as potential precursors to the hot core phase. One of these, G5.89−0.39, was subsequently identified as an UCHII region. The remaining five are spread among the classes of source identified in the previous section: G0.26+0.01 and G14.99−0.70 are MSX-dark clouds, G5.90−0.44 and G12.72−0.22 are bright and partially resolved MSX sources, and G15.03−0.71 is embedded in confused region of extended emission near the M17 molecular cloud. All lie at distances nearer than 4 kpc, except for G0.26+0.01 which we place at the distance of the Galactic centre. CH_3CN is moderately detected towards all sources, except G15.03-0.71. HCO^+ and $H^{13}CO^+$ are found towards all sources while the

Table 4.8. Parameters of the MSX red and MSX dark sources.

Source	CH_3CN	HCO^+	$H^{13}CO^+$	21 μm	8 μm	Maser	Radio	Profile	Wings	T_{rot} (K)
	MSX-red [α]									
G12.18-0.12	n	y	y	y	n	y	n	–	–	–
G12.21-0.09	n	y	y	y	n	y	n	blue	–	–
G14.60+0.02	y	y	y	y	n	y	n	–	–	63
G24.79+0.08	y	y	y	y	n	y	n	red	y	77
G25.71+0.04	y	y	y	y	n	y	n	–	–	–
G28.83-0.25	y	y	y	y	n	y	n	red	y	–
G30.79+0.20	y	y	y	y	d	y	n	–	–	–
G323.74-0.26	y	y	y	y	n	y	n	red	y	67
	MSX-dark [α]									
G0.26+0.01	y	y	y	d	d	n	n	–	–	–
G2.54+0.20	n	y	y	n	d	y	n	blue	y	–
G8.68-0.37	y	y	y	n	d	y	n	blue	–	43
G10.44-0.02	y	y	y	n	d	y	n	blue	–	–
G10.48+0.03	y	y	y	n	d	y	n	–	y	64
G14.99-0.70	y	y	y	n	d	n	n	–	–	–
G23.44-0.18	y	y	y	n	d	y	n	red	–	47
G25.83-0.18	y	y	y	n	d	y	n	blue	y	53
G29.98-0.04	y	y	y	n	d	y	n	–	y	–
G30.71-0.06	y	y	y	d	d	y	b	blue	y	57
G30.82-0.05	y	y	y	n	d	y	n	blue	–	61
G332.73-0.62	y	y	y	d	d	y	n	–	–	–

[α] MSX-dark sources are seen in absorption against the bright 8 μm background emission from the plane of the Galaxy. MSX-red sources have very red mid-infrared colours and are detected only at 21 μm by MSX.

$H^{13}CO^+$ linewidths vary from $2-4.5\,\mathrm{km\,s^{-1}}$ without any obvious relation to MSX brightness or class. The absence of a further link between these maserless sources and the spread in observed properties suggests a range of evolutionary phases; i.e. the absence of maser emission towards these sources does not necessarily indicate an early phase star-formation, even with the presence of CH_3CN.

4-7 Summary and conclusions

We have detected 58 candidate hot molecular cores, including 43 new detections, through the presence of CH_3CN emission in a sample of 83 methanol maser selected star-forming regions, . All sites are associated with mm-continuum thermal emission, seen at 1.2-mm, 450 μm and 850 μm. Six sites are not directly associated with maser

emission but are within the same star-forming region. Our major findings are as follows:

1. CH_3CN is commonly detected towards methanol maser sites, but is more prevalent and brighter in the presence of a UCHII region, independent of the distance to the source.

2. CH_3CN is detected towards isolated methanol maser sites, where no nearby external heating sources exist. This strongly suggests that these sources are internally heated. Conversely, the lack of CH_3CN towards some isolated maser sites is consistent with them being at a less advanced stage of evolution than UCHII regions.

3. We report the CH_3CN rotational temperatures for 38 sources where at least three K components were detected. Values range from 28 to 166 K. These values are generally lower than those found in previous studies utilising higher energy transitions. Derived column densities are poorly constrained but are comparable to previous studies. There is no significant difference between the isolated maser and UCHII populations.

4. HCO^+ and $H^{13}CO^+$ are detected towards 99 per cent and 98 per cent of the sample, respectively. Low excitation temperatures derived from HCO^+ lead us to believe that the emission is generally beam diluted in our 36″ beam, however, self absorption in the HCO^+ line profile may also cause us to underestimate the line brightness. We derived beam averaged column densities assuming a $[HCO^+]\,/\,[H^{13}CO^+]$ ratio of 50 and an excitation temperature of 15 K.

5. Most HCO^+ line profiles exhibit asymmetries due to self-absorption, which may be interpreted as inward or outward motions. Approximately equal numbers of red and blue profiles are found towards UCHII regions, isolated masers and maserless sources.

6. The majority of sources with multi-colour MSX flux densities pass the MYSO colour selection criteria of Lumsden et al. (2002). Five maser sources fail the

colour cuts and are likely very young massive star-forming cores. Sources with very red MSX colours are indistinguishable from the bulk of the sample in terms of CH_3CN detections and brightness. MSX-dark clouds are notable as CH_3CN is generally brighter than in sources detected in emission with MSX; however this may be as a result of their near distances. Where asymmetric HCO^+ profiles are seen towards MSX-dark clouds they tend to be blue-skewed, indicative of inward motions.

In continuation of this work we will report on the detection of other molecules in the next chapter. We have surveyed the same sources for $CH_3OH\,(2-1)$, $^{13}CO\,(1-0)$, $N_2H^+\,(1-0)$, $HCN\,(1-0)$ and $HNC\,(1-0)$, also using the Mopra antenna at 3-mm.

Chapter 5

The Hot Molecular Core Survey II

5-1 Introduction

Molecular emission is a powerful tool when used to investigate the physical and chemical conditions in hot cores. Transitions requiring different temperatures and densities for excitation constitute an excellent probe of physical structure. Because the chemical properties of hot cores vary with time, the relative molecular abundances can also be used as indicators of evolution.

In the preceding decades, representative line surveys of a limited sample of cores have begun to identify the molecules most suited to investigating the process of massive star formation. To date these have been restricted to a few objects: Orion-KL (Blake et al. 1986; Turner 1989; Ziurys & McGonagle 1993; Schilke et al. 1997), Sgr-B2 (Cummins et al. 1986; Turner 1989; Sutton et al. 1991), G34.3+0.15 (MacDonald et al. 1996; Kim et al. 2000, 2001), IRAS 17470−2853 (also known as G5.89−0.39, Kim et al. 2002).

Chemical models, including both gas-phase and grain-surface reactions have been developed for specific objects whose physical structure and conditions are well known, e.g. G34.3+0.15 (Millar et al. 1997; Thompson et al. 1999), as well as for general cases, e.g. Rodgers & Charnley (2003). These and earlier models were limited by the computational power available at the time and considered either time-

dependent chemistry at a test position, or a 'snapshot' of spatial abundances at a single time. Advances in computational power have recently allowed the development of models which consider both time- *and* space-dependent chemistry simultaneously, e.g., the model of AFGL 2591 by Doty et al. (2002). Today it is the lack of observational constraints which restrict our understanding of chemistry in young massive stellar objects. The priority in the coming years must be to assemble a large sample of molecular abundance measurements towards a broad range of massive star forming regions, at different stages of evolution and with luminosities and masses from B3 to O9 type massive stars.

In this chapter we present the remaining results of the Mopra Hot Molecular Cores survey towards CH_3OH maser selected targets. The initial results were presented in Chapter 4, where we reported the detection of the hot-core species methyl-cyanide (CH_3CN) and the observations of the formyl ion (HCO^+), and its isotopomer ($H^{13}CO^+$). Here we expand the analysis to cover transitions of methanol (CH_3OH), carbon-monoxide (^{13}CO), diazenylium (N_2H^+) hydrocyanic acid (HCN) and hydroisocyanic acid (HNC). We analyse the full complement of molecules for evidence of evolution.

5-2 Observations

Observations were conducted on the Mopra millimetre wave telescope over five years 2000 – 2004, and during the winter observing season, June – September. We observed the following transitions, CH_3OH (2–1), ^{13}CO (1–0), N_2H^+ (1–0), HCN (1–0) and HNC (1–0) as single pointings, targeted at the maser sites. Electronic properties of the molecules and transitions are presented in Table 5.1. Five sources did not contain methanol masers and in these cases we targeted the peak of the 450 μm continuum emission detected by Walsh et al. (2003). The signal from the receiver was processed in an autocorrelator backend configured to have a bandwidth of 64 MHz, split into 1024 channels. At 3-mm wavelengths this delivers a velocity resolution of $\sim$0.2 km s^{-1} over a usable velocity interval of $\sim$130 km s^{-1}.

Table 5.1. Details of observed transitions.

Species	Transition	Frequency (GHz)	E_u/k [κ] (K)	A_{ul} (s^{-1})	g_u
CH_3OH [α]	$2_{(-1,2)} \rightarrow 1_{(-1,1)}$ E	96.739390	4.642	2.495×10^{-6}	5
	$2_{(0,2)} \rightarrow 1_{(0,1)}$ A+	96.741420	6.963	3.327×10^{-6}	5
	$2_{(0,2)} \rightarrow 1_{(0,1)}$ E	96.744580	12.188	3.327×10^{-6}	5
	$2_{(1,1)} \rightarrow 1_{(1,0)}$ E	96.755510	20.108	2.496×10^{-6}	5
^{13}CO [β]	$1 \rightarrow 0$	110.210353	5.288	6.389×10^{-8}	3
HNC [β]	$1 \rightarrow 0$	90.663593	4.350	2.709×10^{-5}	3
HCN [γ]	$1_1 \rightarrow 0_1$	88.630416	4.253	2.444×10^{-5}	3
	$1_2 \rightarrow 0_1$	88.631847	–	–	5
	$1_0 \rightarrow 0_1$	88.633936	–	–	1
N_2H^+ [γ]	$1_1 \rightarrow 0_1$	93.171880	4.471	3.654×10^{-5}	9
	$1_2 \rightarrow 0_1$	93.173700	–	–	15
	$1_0 \rightarrow 0_1$	93.176130	–	–	3

[α] $J_{K,K_1} \rightarrow J'_{K',K'_1}$ quantum numbers.

[β] J→J′ quantum numbers.

[γ] $J_F \rightarrow J'_{F'}$ quantum numbers.

[κ] Energies of the upper levels relative to the $J_K = 1_{-1}$ level for E-type CH_3OH, and relative to the $J_K = 0_0$ level for A-type CH_3OH.

All observations were performed in position switching mode by integrating for equal times on the science object and an emission-free reference position. Initial reduction of the raw data was performed using the SPC package. The CLASS spectral line analysis software was used for all further processing and analysis, including baseline subtraction and fitting Gaussian line profiles. For further details on the observing setup and data analysis please refer back to section 4-3.

5-3 Results

Molecular emission was detected in almost all of the targets, with the exception being the source G10.10−0.72, which has an assumed far kinematic distance of 16 kpc. The detection rate for all transitions was close to 100 per cent. Emission from ^{13}CO(1–

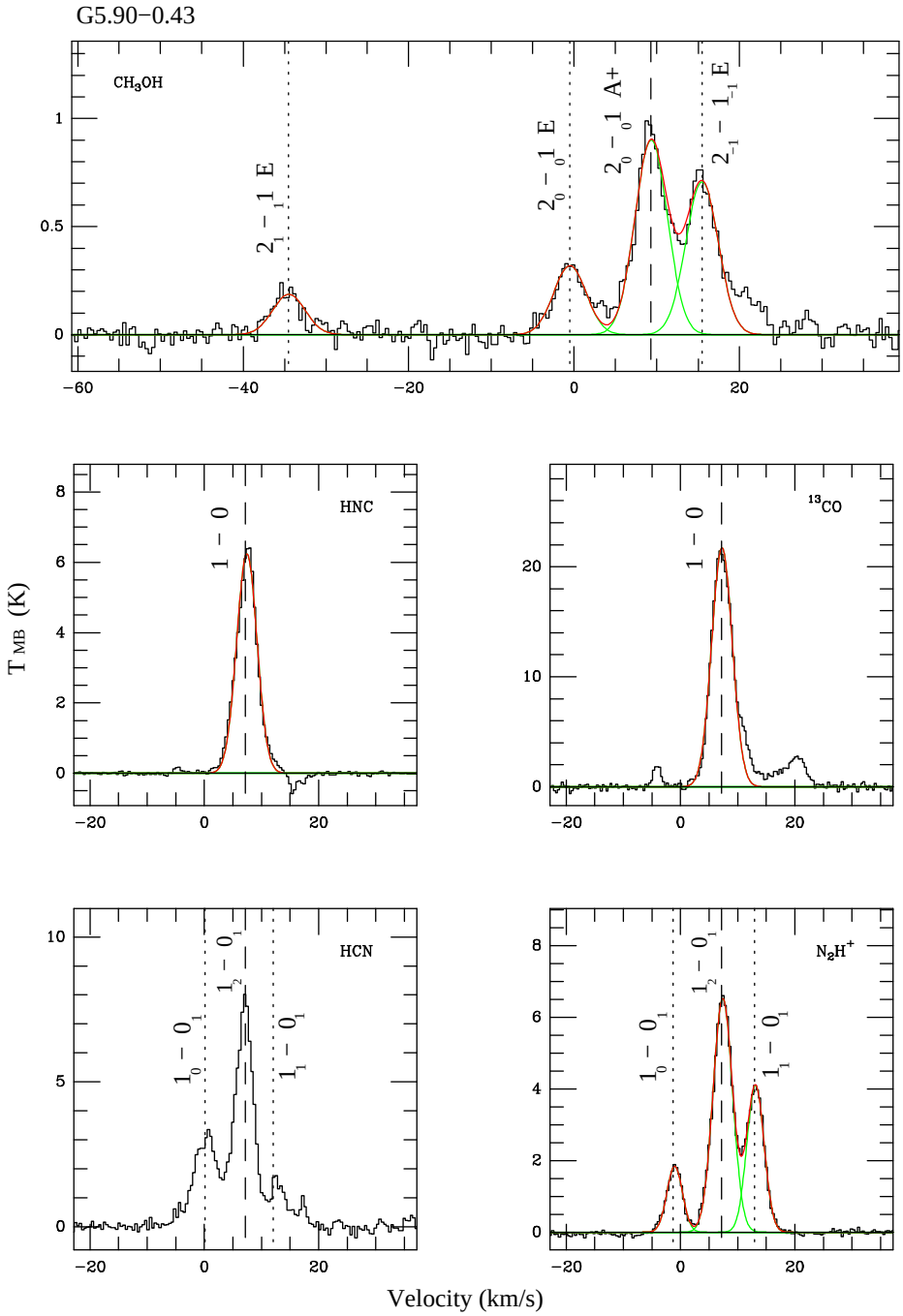

Figure 5.1. Sample spectra for the maser site associated with G5.90−0.43. The vertical dashed line marks the systemic velocity of the source, measured from the peak of the optically thin $H^{13}CO^+$ line profile (see Chapter 4). Vertical dotted lines mark the expected velocity of other transitions of the same molecule. Individual Gaussian fits to the line profiles are plotted by a solid green line and the cumulative fit by a solid red line. We did not attempt to fit Gaussians to HCN lines as the majority of profiles have complex shapes.

Table 5.2. Noise detection limit on the spectra with no emission.

Source	T_{MB} 3-σ detection limit (mK)				
	CH_3OH	^{13}CO	N_2H^+	HNC	HCN
G0.32−0.20	230	–	–	–	–
G6.61−0.08	104	–	–	–	–
G10.10−0.72	69	414	142	127	163
G30.78+0.23	95	–	–	–	–

0), N_2H^+ (1–0), HNC (1–0) and HCN (1–0) was detected towards all other sources (99 per cent), however, CH_3OH (2–1) emission was not detected towards the sources G0.32−0.20, G6.61−0.08 and G30.78+0.23. The 3-σ noise limit on the spectra where no lines were detected is recorded in Table 5.2. Figure 5.1 presents sample spectra for the well known source G5.90−0.43. The vertical dashed line marks the systemic velocity of the source, measured from the $H^{13}CO^+$ line. In the case of CH_3OH, the rest-frame is centred on the A+ transition, and for N_2H^+ and HCN the rest-frame is centred on the $J_K = 1_2 \rightarrow 0_1$ transition. Plots of all molecular spectra for each source are presented Appendix C.

5-3.1 Line profile parameters

As with CH_3CN in Chapter 4 we fit the CH_3OH spectra simultaneously with four Gaussian lines having equal full-width half-maximum (FWHM) linewidths and whose line-centre separations were fixed to the expected values. The weakest component in the spectrum, the $J_{K,K'} = 2_{1,1} \rightarrow 1_{1,0}$ line, was detected towards 50 per cent of sources. Individual line profiles are generally well fit by single Gaussians, and the average linewidth is $4.7\,\mathrm{km\,s^{-1}}$. The parameters of the Gaussian fits are presented in Table D.3 in Appendix D.

The N_2H^+ (1–0) transition is split into seven hyperfine lines, as illustrated in Figure 5.2 (adapted from Caselli et al. 1995). The typical linewidths of greater than $2\,\mathrm{km\,s^{-1}}$ observed towards massive star forming regions result in the seven components blending into three groups with roughly Gaussian shapes. Consequently, we

characterised the profiles using two analysis schemes. In the first instance we used the hyperfine structure fitting (HFS) routine in the CLASS software to simultaneously fit the N_2H^+ profiles with seven Gaussians. Free parameters were the velocity (V_{LSR}), common linewidth, excitation temperature, and optical depth. In the case of severely blended lines (as presented in this work) the fits are not well constrained and values for the optical depth and excitation temperature contain substantial uncertainties. Using this method we find the mean N_2H^+ linewidth of the sample is $3.0\,\mathrm{km\,s^{-1}}$. Because of the uncertainty introduced by the blending, CLASS assigned an erroneous value of $\tau = 0.1$ to all sources, rendering the resultant excitation temperatures meaningless. As an alternative measure of optical depth and integrated intensity, we also fit the three blended groups individually with single Gaussians. We discuss the optical depth and column densities derived from the N_2H^+ spectra in Sections 5-4.4. The results of the CLASS HFS fits and the parameters of the Gaussian fits are presented in Table D.4, in Appendix D.

Line profiles of HNC are observed to be similar to HCO^+. The critical densities of the two molecules are approximately the same at $\sim 3\times10^5\,\mathrm{cm^{-3}}$ and it is likely that they trace the same gas. Self-absorbed HNC line profiles are common in the sample and we referred to the low optical depth $H^{13}CO^+$ and N_2H^+ line profiles when attempting to distinguish between self-absorption and multiple clouds along the line of sight. As in Chapter 4 we fit self-absorbed profiles with a single Gaussian by masking off the absorption dip (see Figure 4.3). We also measured the line intensity by integrating under the line between suitable velocity limits and we calculated an equivalent linewidth from

$$\Delta V_{\mathrm{equiv}} = \frac{\int T_b\,dv}{(T_b - T_{\mathrm{rms}})}. \tag{5.1}$$

In Equation 5.1 $\int T_b\,dv$ is the integrated intensity, T_b is the peak brightness temperature and T_{rms} is the root-mean-square noise on the line-free region of the spectrum. The results of the fits are presented in Table D.5, in Appendix D.

The ^{13}CO line profile often exhibits multiple components spread over the 64 MHz bandpass. Usually a single bright component is present at the systemic velocity of

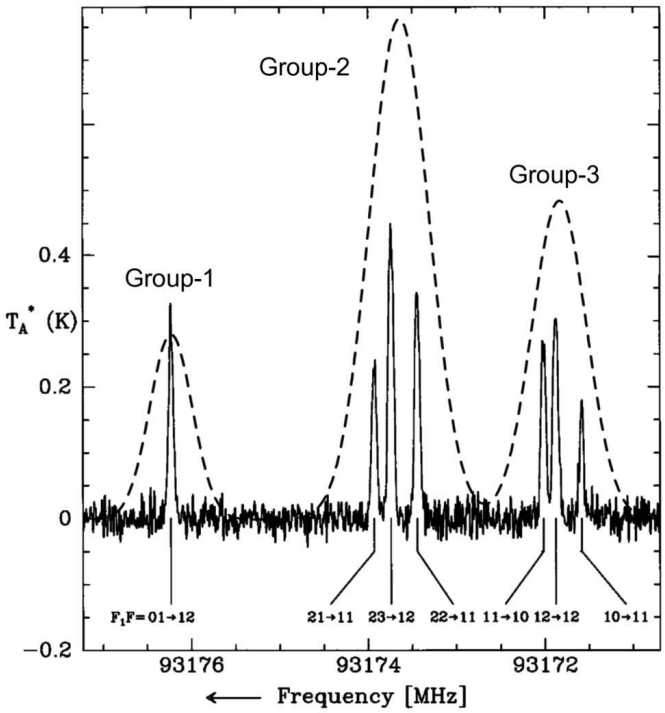

Figure 5.2. Spectrum of N_2H^+ (1–0) towards a dark cloud showing the seven hyperfine components (Caselli et al. 1995). Linewidths towards massive star-forming regions are 4 – 5 times greater resulting in the hyperfine components blending into three groups, designated 1 – 3 in this work (dashed lines).

the source, which was easily fit with a single Gaussian. Occasionally several smaller components are crowded around the main line and these were fit as blended Gaussian lines. In general, the ^{13}CO profile appears moderately optically thick but exhibits less self-absorption than HNC or HCO^+. We again measured the integrated intensity and peak brightness temperature directly from the line profile. The parameters of the fits are presented in Table D.6, in Appendix D.

HCN exhibited highly confused line profiles, with few sources exhibiting the expected 3-component hyperfine structure. We attribute the complex profiles to a combination of high optical depths, multiple clouds along the line of sight and low level emission from broad line-wings tracing outflows. It is possible that some spectra may be contaminated by emission from the reference position, as HCN appears

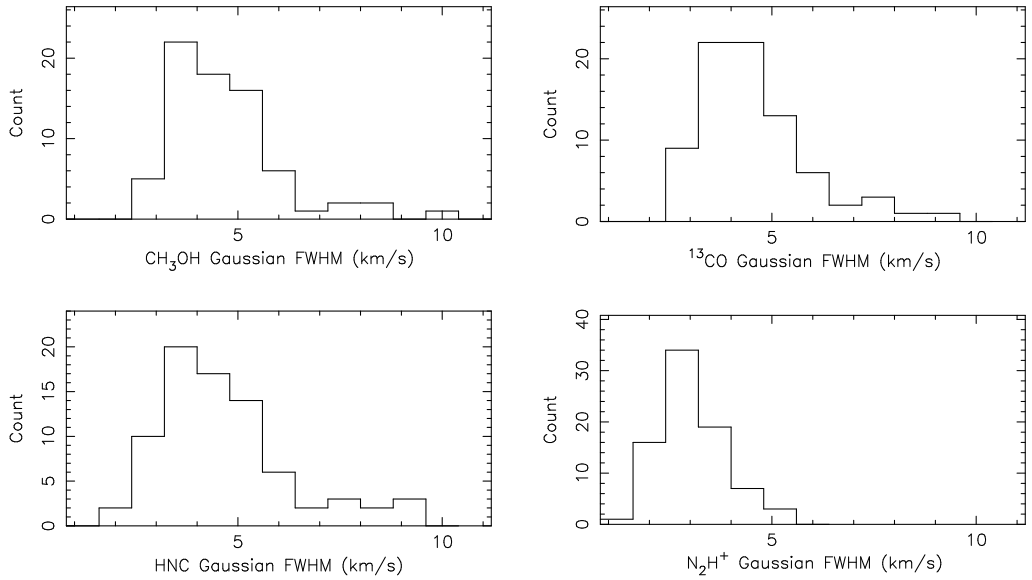

Figure 5.3. Distributions of full-width half-maximum linewidths from the Gaussian fits to the spectra. The HNC and ^{13}CO line profiles were fit with single Gaussian components. CH_3OH was fit with multiple Gaussians, where the linewidths were constrained to have the same value. The N_2H^+ spectrum was fit using the HFS method in CLASS. Seven Gaussian components with a common linewidth were fit to the three groups of blended lines. The value plotted here is the linewidth of an individual component. The mean CH_3OH, HNC and ^{13}CO linewidth are all at approximately $4.5\,\mathrm{km\,s^{-1}}$, while the mean N_2H^+ linewidth is at $3.0\,\mathrm{km\,s^{-1}}$.

to be ubiquitous near the Galactic plane.

Like HCO^+, high velocity outflows wings were common in the spectra of HNC and, to a lesser extent, ^{13}CO. We fit broad Gaussians to these wings simultaneously with the main component, and their parameters are presented in Tables D.5 and D.6 marked with a 'w'. The Gaussian parameters for blended lines are marked with a 'b' in the same tables.

5-3.2 Linewidths

Figure 5.3 show the distributions of full-width half-maximum linewidths for the four molecules which were fit with Gaussians. The mean CH_3OH, HNC and ^{13}CO

linewidth are all at approximately $4.5\,\mathrm{km\,s^{-1}}$, in contrast to the mean N_2H^+ linewidth, which is $3.0\,\mathrm{km\,s^{-1}}$. The shape of the distributions is similar in each case.

5-4 Derived parameters

We present the physical parameters of the sources and the excitation temperatures, column densities and optical depths derived from the line profiles. The frequencies and electronic constants used in the calculations are collected in Table 5.1.

5-4.1 Gas mass and virial mass

Gas masses have been calculated from the 1.2-mm continuum flux density, taken from the work of Hill et al. (2005). For a 1.2-mm integrated continuum flux density S_ν the mass of gas is given by (Hildebrand 1983)

$$M_{\mathrm{gas}} = \frac{S_\nu\, D^2}{\kappa_{\mathrm{d}}\, R_{\mathrm{d}}\, B_{\mathrm{v}}(T_{\mathrm{dust}})}, \tag{5.2}$$

where D is the distance to the source in metres, κ_d is the mass absorption coefficient per unit mass of dust, B_ν is the Planck function for a blackbody of temperature T_{dust}, and R_{d} is the dust to gas mass ratio. We have adopted a value of $0.1\ \mathrm{m^2\,kg^{-1}}$ for κ_{d} and have assumed a dust to gas mass ratio of 0.01 (Ossenkopf & Henning 1994). The distance has been estimated from the V_{LSR} of the source using the Galactic rotation curve of Brand & Blitz (1993) (see Chapter 4 and Appendix A). Values for T_{dust} were taken from the cold component of the greybody-fit to the spectral energy distribution (SED) performed in Chapter 4. For sources where we had insufficient data to perform a fit we adopted the average value of $T_{\mathrm{dust}} = 58\,\mathrm{K}$. We note that these temperatures are not well constrained by the sparsely sampled SED and are generally higher than the values of $20-30\,\mathrm{K}$ adopted in the literature. For dust temperatures of 20 K and 30 K the gas-mass derived here will be under-estimated on average by factors of 3.6 and 2.1, respectively. Values for M_{gas} were derived for 66 sources and are recored in column six of Table 5.3.

We estimated virial masses from the CH_3OH, N_2H^+, ^{13}CO and HNC line-profiles following the approach by MacLaren et al. (1988). In the simplest case, neglecting support by magnetic fields or internal heating sources, the total mass of a simple spherical system is given by

$$M_{vir} = \frac{\sigma^2\, r}{G} = 126\, r\, \Delta v^2 \qquad \ldots \qquad \text{in } (M_\odot), \tag{5.3}$$

where σ is the full 3-dimensional velocity dispersion, r is the dust-radius of the cloud in pc, Δv is the FWHM linewidth of the molecular line in $km\,s^{-1}$ and G is the gravitational constant in $N\,m^2\,kg^{-2}$. The virial mass is the minimum mass required in order for a cloud to be gravitationally bound, i.e. the cloud is bound if $M_{gas}/M_{vir} > 1$. If magnetic field support is important the virial mass may be overestimated by up to a factor of two (MacLaren et al. 1988). Observationally, the linewidths may be artificially broadened due to blending of multiple components along the line of sight, or in optically thick lines, due to radiative transfer effects. Enhanced linewidths will cause us to overestimate the virial mass by an unknown amount and the values quoted here should be considered upper limits. Columns 7 – 10 of Table 5.3 presents the virial masses derived from the four molecules.

The distributions of M_{gas} and M_{vir} are illustrated in Figure 5.4. Optically thin N_2H^+ and $H^{13}CO^+$ produce similar estimates of the mean virial mass at $573\,M_\odot$ and $905\,M_\odot$, respectively. ^{13}CO and CH_3OH have the broadest linewidths, most likely due to optical depth effects, leading to mean mass estimates of $1293\,M_\odot$ and $1305\,M_\odot$, respectively. The values derived for M_{gas} and M_{vir} are consistent with having the same magnitude in the majority of clumps. The large uncertainties associated with the calculations prevent the interpretation of individual objects as gravitationally bound.

5-4.2 H_2 column and volume density

We estimated the H_2 column density, N_{H_2}, from the gas-mass using the following relation:

$$N_{H_2} = \frac{M_{gas}}{2\, M_p\, f_{He}\, A}, \tag{5.4}$$

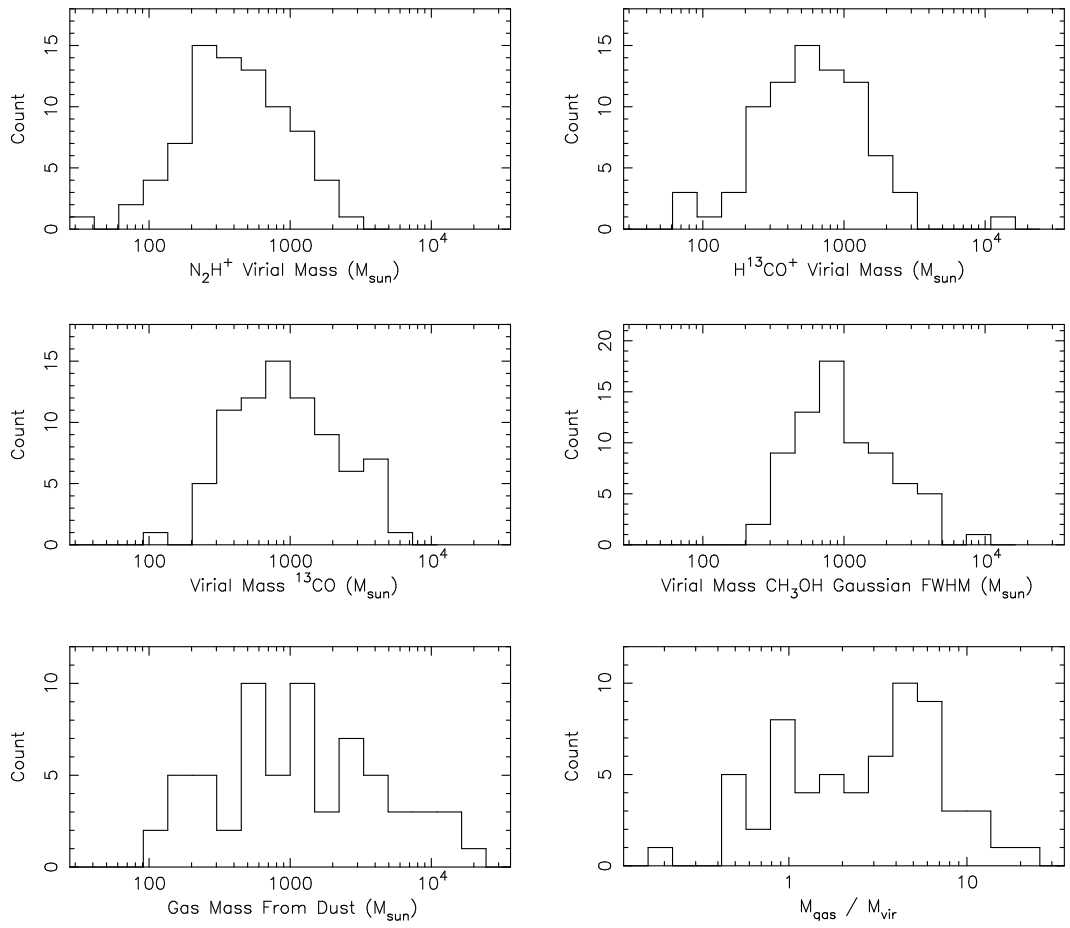

Figure 5.4. Histograms showing the distributions of the virial masses derived from N_2H^+, $H^{13}CO^+$, ^{13}CO and CH_3OH, and the gas masses derived from the 1.2-mm continuum emission from the work of Hill et al. (2005). Virial masses should be considered upper limits. The plot on the bottom right shows the distribution of the M_{gas}/M_{vir} ratio derived from N_2H^+. The values of M_{gas} and M_{vir} are consistent with having the same order of magnitude.

where $M_p = 1.673 \times 10^{-27}$ kg is the mass of a proton, $f_{He} = 1.36$ is a correction factor to account for Helium present in the interstellar medium (Allen 1973) and A is the projected surface area of the mm-continuum emission. Assuming a cylindrical source with uniform density, the projected area is given by

$$A = \pi\, r^2\, D^2, \tag{5.5}$$

where r is the angular radius of the source in radians ($1\,\mathrm{deg}^2 = \pi/180$ radians) and D is the distance to the source in metres ($1\,\mathrm{pc} = 3.08568 \times 10^{16}$ m). In a similar manner

Table 5.3: H_2 densities, mass of gas from dust continuum, and virial masses.

Source	θ_{dust}	T_{cold}	N_{H_2}	n_{H_2}	M_{gas}	M_{vir} (10^2 $M_\odot$)			
	($''$)	(K)	(10^{22} cm^{-2})	(10^4 cm^{-3})	(10^2 $M_\odot$)	N_2H^+	$H^{13}CO^+$	^{13}CO	CH_3OH
G0.32−0.20	40	70	3.5	1.0	16.4	3.3	6.7	11.6	–
G0.50+0.19	30	47	2.0	2.5	0.5	2.3	5.2	6.1	4.0
G0.55−0.85	30	59	20.5	8.1	53.7	11.0	11.8	22.8	27.2
G0.84+0.18	27	61	1.8	1.2	1.7	2.7	4.6	9.9	10.0
G1.15−0.12	24	42	0.6	0.3	1.0	5.7	15.8	16.8	16.3
G2.54+0.20	45	58	1.2	0.6	1.9	2.3	3.9	4.0	4.0
G5.89−0.39	30	69	25.1	42.0	3.6	1.7	3.7	2.8	4.7
G5.90−0.43	31	71	8.0	12.9	1.2	2.2	2.5	3.9	3.6
G5.90−0.44	30	72	5.2	6.9	1.2	0.8	1.1	3.8	4.1
G6.61−0.08	24	50	0.7	0.2	3.7	24.7	8.2	29.2	–
G8.14+0.23	41	71	4.5	3.3	3.3	3.7	4.7	7.0	4.0
G8.67−0.36	30	47	22.9	17.0	16.8	7.2	8.4	6.2	15.0
G8.68−0.37	26	58	5.9	4.8	3.7	8.9	15.1	18.9	19.2
G9.62+0.19	31	62	9.7	5.5	12.3	7.5	13.0	16.2	25.4
G9.99−0.03	26	39	3.3	2.5	2.2	3.1	2.9	8.4	14.4
G10.29−0.13	28	56	4.1	6.6	0.6	2.0	3.1	6.9	3.3
G10.30−0.15	36	71	5.7	7.5	1.3	2.8	4.4	3.5	–
G10.32−0.16	38	42	6.6	7.9	1.8	0.8	1.7	5.4	4.7
G10.34−0.14	26	45	4.0	7.0	0.5	1.4	2.2	3.7	5.0
G10.44−0.02	31	58	2.0	1.1	2.7	9.5	13.9	22.3	14.7
G10.47+0.03	26	48	52.2	35.3	46.1	14.4	29.1	37.2	42.3

H_2 densities and masses – *continued.*

Source	θ_{dust}	T_{cold}	N_{H_2}	n_{H_2}	M_{gas}	M_{vir} ($10^2\,M_\odot$)			
	($''$)	(K)	($10^{22}\,cm^{-2}$)	($10^4\,cm^{-3}$)	($10^2\,M_\odot$)	N_2H^+	$H^{13}CO^+$	^{13}CO	CH_3OH
G10.48+0.03	–	–	–	–	–	18.0	24.6	32.8	23.7
G10.63−0.33	35	44	4.8	2.3	8.5	4.5	5.4	9.5	6.0
G10.63−0.38	–	–	–	–	–	5.3	24.0	27.2	36.1
G11.50−1.49	38	66	3.5	5.8	0.5	0.4	0.7	1.1	2.1
G11.94−0.15	24	50	1.4	1.4	0.6	4.3	9.6	9.5	12.0
G11.94−0.62	32	64	6.1	4.7	4.2	6.0	7.2	10.9	5.4
G11.99−0.27	35	50	0.3	0.2	0.5	7.3	11.4	11.3	8.1
G12.03−0.03	34	64	0.5	0.2	1.1	5.5	9.4	10.7	9.5
G12.18−0.12	–	–	–	–	–	12.3	122.5	36.3	32.9
G12.21−0.09	–	–	–	–	–	17.4	14.3	36.1	43.6
G12.68−0.18	49	80	1.9	0.8	4.5	3.6	3.9	3.9	9.1
G12.72−0.22	31	54	2.5	2.2	1.3	3.4	2.8	4.5	10.5
G12.89+0.49	29	54	10.5	10.0	4.6	3.6	3.8	5.6	4.8
G12.91−0.26	41	69	5.0	3.1	5.1	4.6	5.4	19.8	12.0
G14.60+0.02	–	–	–	–	–	4.1	12.1	9.6	7.6
G14.99−0.70	53	58	1.5	1.8	0.4	1.7	4.0	5.0	7.4
G15.03−0.68	–	–	–	–	–	1.4	1.5	2.6	3.4
G15.03−0.71	52	103	1.5	1.8	0.4	2.0	5.2	4.7	–
G16.59−0.05	27	63	4.4	3.6	2.7	3.6	5.4	5.7	5.1
G16.86−2.16	50	70	6.5	6.9	2.4	2.1	2.6	2.5	5.1
G19.36−0.03	–	–	–	–	–	1.1	2.3	3.1	3.7

H_2 densities and masses – *continued.*

Source	θ_{dust}	T_{cold}	N_{H_2}	n_{H_2}	M_{gas}	M_{vir} (10^2 $M_\odot$)			
	($''$)	(K)	(10^{22} cm^{-2})	(10^4 cm^{-3})	(10^2 $M_\odot$)	N_2H^+	$H^{13}CO^+$	^{13}CO	CH_3OH
G19.47+0.17	–	–	–	–	–	5.8	4.2	7.0	8.4
G19.49+0.15	–	–	–	–	–	1.2	2.3	3.9	2.6
G19.61−0.13	35	56	1.3	0.9	1.1	6.9	6.6	8.5	13.6
G19.70−0.27	32	45	1.7	1.5	0.9	3.0	2.6	8.5	8.4
G21.88+0.01	–	–	–	–	–	2.1	3.8	4.6	7.6
G22.36+0.07	41	52	1.3	0.3	9.5	5.6	7.5	11.3	15.1
G23.26−0.24	31	58	0.5	0.4	0.3	2.2	3.7	9.3	4.9
G23.44−0.18	33	58	4.3	2.2	6.6	12.4	11.7	17.8	36.0
G23.71−0.20	–	–	–	–	–	3.9	7.4	9.1	8.0
G24.79+0.08	34	47	17.5	6.7	48.3	10.3	15.2	11.7	18.0
G24.85+0.09	39	85	0.5	0.2	1.2	2.6	6.3	5.7	9.1
G25.65+1.05	31	72	6.3	6.5	2.3	3.0	4.5	2.9	10.5
G25.71+0.04	29	53	3.0	1.1	9.1	6.4	10.6	16.8	9.9
G25.83−0.18	30	58	7.1	4.2	8.1	4.6	6.8	10.8	8.2
G28.15+0.00	30	55	1.1	0.6	1.4	3.0	3.9	13.2	8.5
G28.20−0.05	34	59	7.1	3.1	15.2	9.3	11.5	28.1	80.2
G28.28−0.36	–	–	–	–	–	2.2	3.0	4.5	4.3
G28.31−0.39	32	80	0.9	0.5	1.0	3.8	8.8	4.8	19.3
G28.83−0.25	–	–	–	–	–	5.1	6.6	8.4	8.9
G29.87−0.04	24	65	1.8	1.2	1.7	5.4	7.1	8.3	6.8
G29.96−0.02	34	71	7.7	3.8	12.8	4.8	5.3	13.5	8.9

H_2 densities and masses – *continued.*

Source	θ_{dust}	T_{cold}	N_{H_2}	n_{H_2}	M_{gas}	M_{vir} ($10^2\,M_\odot$)			
	($''$)	(K)	($10^{22}\,cm^{-2}$)	($10^4\,cm^{-3}$)	($10^2\,M_\odot$)	N_2H^+	$H^{13}CO^+$	^{13}CO	CH_3OH
G29.98−0.04	43	58	1.2	0.5	3.6	6.4	4.8	11.9	–
G30.59−0.04	31	50	4.7	1.3	25.2	14.0	19.6	34.8	25.1
G30.71−0.06	30	58	11.0	6.4	13.4	14.0	19.5	34.4	19.1
G30.76−0.05	52	60	1.0	0.3	3.5	15.9	18.5	50.1	46.2
G30.78+0.23	–	–	–	–	–	1.2	0.8	2.8	–
G30.79+0.20	–	–	–	–	–	4.1	5.6	16.9	9.3
G30.82−0.05	31	58	20.8	11.2	28.9	12.7	11.0	47.5	13.6
G30.82+0.28	–	–	–	–	–	4.3	3.7	13.0	13.8
G30.90+0.16	24	47	2.1	1.2	2.6	7.6	8.2	13.0	18.1
G31.28+0.06	35	65	4.5	1.8	11.6	9.0	13.8	15.4	18.5
G31.41+0.31	26	59	26.2	12.8	44.4	16.0	10.6	34.0	22.7
G316.81−0.06	–	–	–	–	–	2.8	5.3	7.1	5.7
G318.95−0.20	33	56	5.4	6.8	1.4	1.5	2.0	3.7	6.1
G323.74−0.26	30	64	7.0	7.1	2.8	2.2	2.5	4.2	4.7
G331.28−0.19	41	42	7.0	3.2	13.8	6.9	9.6	21.4	14.2
G332.73−0.62	24	58	1.2	1.5	0.3	1.3	0.8	3.6	5.0

θ_{dust} has been measured by fitting a Gaussian function to the azimuthally averaged intensity profile of the SIMBA source. T_{cold} is the temperature used to estimate the gas-mass (M_{gas}) through Equation 5.2, and is taken from the cold component of the fit to the SED. n_{H_2} has been estimated from the gas-mass by assuming a uniformly filled spherical source. Estimates of the virial mass have been made assuming a $1/r^2$ density profile.

the volume density n_{H_2} can be estimated by replacing A in Equation 5.4 by V the projected volume of emitting gas

$$V = \frac{4}{3}\,\pi\, r^3\, D^3. \tag{5.6}$$

Equation 5.6 assumes emission from a uniformly dense sphere of angular radius r. The radius of the dust continuum emission was measured directly from the 1.2-mm continuum images (provided courtesy of Hill et al. 2005) by fitting a Gaussian to the azimuthally averaged source profiles. We find values for the full-width half-maximum vary between 99″ and 24″ (the limiting resolution of the SIMBA bolometer), and have a mean value of 34″. Derived values of N_{H_2} and n_{H_2} are presented in columns four and five of Table 5.3 and have means of $6.1\times 10^{22}\,cm^{-2}$ and $4.8\times 10^{4}\,cm^{-3}$, respectively.

We urge caution in interpreting any value of the H_2 column density derived in this manner as the assumptions introduce large unknown errors. Firstly, the mass absorption coefficient and dust to gas ratio used to calculate M_{gas} in Equation 5.2 may vary considerably from source to source, leading to a corresponding error in the H_2 column density. The spatial distribution of H_2 is a further unknown and additional errors are introduced by assuming a uniform column density over a spherical projected volume.

5-4.3 CH_3OH rotational temperature and column density

CH_3OH is a slightly asymmetric rotor, resembling a symmetric top except for the O-H group, which is angled with respect to the principal axis. Internal hindered motion coupled with the rotation of the molecule results in a complicated rotational spectrum, organised into non-degenerate A and two-fold degenerate E levels, corresponding to different torsional symmetry (Bockelee-Morvan et al. 1994). The A and E states have nuclear statistical weights of 2 and 1, respectively, thus their overall degeneracy is the same.

A rotational temperature T_{rot} and column density N may be estimated from the ratios of the CH_3OH lines based on the assumptions of low optical depths and

that the background temperature ($T_b \approx 2.7\,K$) is small compared to the brightness temperature of the line. For the rotation temperature to be equal to the kinetic temperature of the gas the population of *all* the observed energy levels must be described by a single excitation temperature T_{ex}, defined by the Boltzmann relation (Equation 2.18). Using the relation for rotational temperature derived in Chapter 2,

$$\ln\left(\frac{N_u}{g_u}\right) = \ln\left(\frac{N}{Q(T)}\right) - \frac{E_u}{k\,T_{rot}}$$

a rotation diagram may be drawn by plotting $\ln(N_u/g_u)$ versus E_u/k and rotation temperature and column density in the upper level N_u found from the slope and y-axis intercept, respectively, of a straight line fit to the data. The total column density N may then be found assuming local thermal equilibrium and a partition function $Q(T_{rot})$, which for CH_3OH is given by

$$Q(T) = \sum_{J=0}^{\infty}(2J+1)\,e^{-E_J/kT} \;\approx\; 1.2327\,T_{rot}^{1.5}. \tag{5.7}$$

In Equation 5.7 we have approximated the partition function by a fit to the discrete values in the Pickett, et al. (1998) spectral line catalogue. We note that values for E_u are referenced to different ground state energy levels for A and E-type CH_3OH. The ground state for A-type is the $J_K = 0_0$ level, while for E-type CH_3OH is the $J_K = 1_{-1}$ level (Menten et al. 1988). This is commonly overlooked in the literature as all values quoted in Pickett, et al. (1998) are referenced to the $J_K = 0_0$ level, resulting in incorrect rotation diagrams. The correct values of E_u/k are cited in Table 5.1. An example of a CH_3OH rotation diagram is shown in Figure 5.5 (*left*). The data point at $E_u/k \approx 7k$ corresponds to the A+ line, while the other three points correspond to E transitions. In general, where we detect three E-type lines, they are well fit with a straight line, implying that our assumption of optically thin conditions is valid.

A and E type methanol are equivalent to oblate and prolate NH_3 and only interconvert on timescales of ∼10,000 years. The A/E ratio is effectively 'frozen in' and may provide useful information on the conditions when the CH_3OH was formed. It is not clear that the A/E ratio can be assumed equal to one, and a rotation diagram

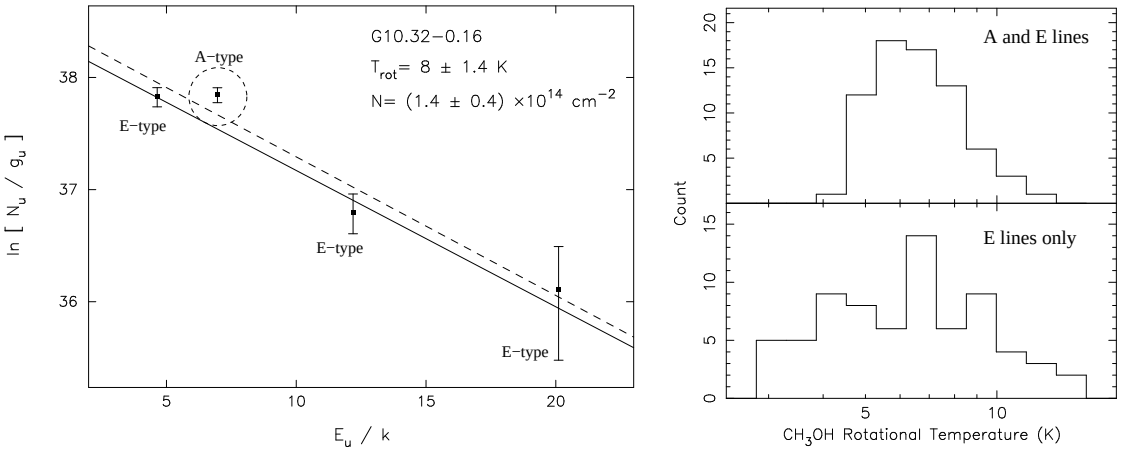

Figure 5.5. (*left*) Rotational diagram of CH_3OH for the source G10.32−0.16, made using the 96.7 GHz lines. The point at $E_u \approx 7$ K corresponds to the $2_0 \rightarrow 1_0$ A+ transition. The three other points are due to transitions of E-type methanol. The solid line and values for T_{rot} and N correspond to a fit through the E transitions only. The dashed line represents a fit to all transitions. (*right*) Distributions of rotational temperatures derived from CH_3OH using both A and E-type transitions (top), and E-type transitions only (bottom).

including both A and E type transitions may not be valid. In Figure 5.5 (*left*) the solid line indicates a fit to the E-type transitions only, while the dotted line is a fit to both the A and E-type. Rotation temperatures derived from only the E-transitions have a mean value of 6.7 K, similar to the mean temperature derived from all four transitions, which is 6.8 K. Rotational temperatures and column densities derived using both fitting methods are presented in Table 5.4 and the distributions of rotational temperatures are illustrated in Figure 5.5 (*right*).

Column densities are averaged over the telescope beam and are likely underestimated. If the bulk of the CH_3OH emission stems from within a hot cores then the typical size of the emitting region will be 0.1 pc ($\approx 20,000$ AU, Kurtz et al. 2000). Columns three and four of Table 5.4 present the angular size and beam dilution factor calculated using this assumption. Columns seven and ten present the column densities corrected for this assumed dilution factor.

On inspection of the bulk of the rotation diagrams (presented in Appendix E) we

Table 5.4: Rotational temperature and column densities derived from CH_3OH.

Source	No. of lines	θ ($''$)	$\left(\frac{\Omega_s}{\Omega_b}\right)^{\alpha}$	A+ and E lines			E lines only			A/E ratio
				T_{rot} (K)	$N_{CH_3OH}\,(10^{15}\,cm^{-2})^{\beta}$		T_{rot} (K)	$N_{CH_3OH}\,(10^{15}\,cm^{-2})^{\beta}$		
					$36''$	0.1 pc		$36''$	0.1 pc	
G0.50+0.19	3	7.9	0.049	7 ± 0.7	0.10 ± 0.03	1.96 ± 0.59	6 ± 1.0	0.07 ± 0.02	1.48 ± 0.44	1.56
G0.55−0.85	4	2.4	0.005	8 ± 0.3	1.00 ± 0.30	220.00 ± 66.00	9 ± 0.3	1.02 ± 0.31	224.00 ± 67.20	1.19
G0.84+0.18	3	3.7	0.010	7 ± 1.7	0.05 ± 0.02	4.89 ± 1.47	5 ± 2.2	0.03 ± 0.01	3.31 ± 0.99	1.83
G1.15−0.12	3	2.4	0.005	6 ± 0.3	0.12 ± 0.04	27.00 ± 8.10	5 ± 0.5	0.09 ± 0.03	19.20 ± 5.76	1.75
G2.54+0.20	3	4.7	0.017	5 ± 0.5	0.08 ± 0.02	4.88 ± 1.46	3 ± 0.9	0.06 ± 0.02	3.80 ± 1.14	1.75
G5.89−0.39	4	10.3	0.082	8 ± 0.3	0.29 ± 0.09	3.52 ± 1.06	10 ± 0.4	0.30 ± 0.09	3.62 ± 1.09	1.23
G5.90−0.43	4	10.3	0.082	9 ± 0.4	0.40 ± 0.12	4.93 ± 1.48	9 ± 0.5	0.36 ± 0.11	4.37 ± 1.31	1.27
G5.90−0.44	4	8.3	0.053	7 ± 0.3	0.17 ± 0.05	3.17 ± 0.95	7 ± 0.3	0.14 ± 0.04	2.59 ± 0.78	1.62
G8.14+0.23	3	6.3	0.030	5 ± 0.9	0.06 ± 0.02	1.91 ± 0.57	4 ± 1.5	0.04 ± 0.01	1.39 ± 0.42	1.86
G8.67−0.36	4	4.6	0.016	8 ± 0.3	1.13 ± 0.34	69.50 ± 20.85	8 ± 0.3	1.05 ± 0.32	64.70 ± 19.41	1.19
G8.68−0.37	4	4.3	0.014	7 ± 0.2	1.11 ± 0.33	77.90 ± 23.37	6 ± 0.3	0.93 ± 0.28	65.60 ± 19.68	1.39
G9.62+0.19	4	3.6	0.010	10 ± 0.7	0.80 ± 0.24	80.20 ± 24.06	14 ± 1.0	0.97 ± 0.29	97.30 ± 29.19	1.31
G9.99−0.03	3	4.1	0.013	6 ± 0.7	0.08 ± 0.02	6.09 ± 1.83	5 ± 1.0	0.07 ± 0.02	5.35 ± 1.60	1.24
G10.29−0.13	4	9.4	0.068	6 ± 0.3	0.37 ± 0.11	5.43 ± 1.63	6 ± 0.4	0.32 ± 0.10	4.77 ± 1.43	1.41
G10.32−0.16	4	9.4	0.068	8 ± 1.2	0.15 ± 0.05	2.26 ± 0.68	8 ± 1.4	0.14 ± 0.04	2.01 ± 0.60	1.36
G10.34−0.14	4	9.4	0.068	6 ± 0.4	0.33 ± 0.10	4.92 ± 1.48	5 ± 0.6	0.28 ± 0.08	4.06 ± 1.22	1.45
G10.44−0.02	3	3.4	0.009	11 ± 5.1	0.08 ± 0.03	9.31 ± 2.79	11 ± 7.4	0.06 ± 0.02	6.47 ± 1.94	1.92
G10.47+0.03	4	3.6	0.010	12 ± 0.2	1.47 ± 0.44	145.00 ± 43.50	15 ± 0.2	2.01 ± 0.60	199.00 ± 59.70	0.90
G10.48+0.03	4	3.6	0.010	6 ± 0.1	0.55 ± 0.17	54.70 ± 16.41	7 ± 0.2	0.53 ± 0.16	52.40 ± 15.72	1.24
G10.63−0.33	3	3.4	0.009	5 ± 0.3	0.18 ± 0.05	19.90 ± 5.97	4 ± 0.5	0.14 ± 0.04	15.10 ± 4.53	1.66
G10.63−0.38	4	3.4	0.009	10 ± 0.4	0.97 ± 0.29	107.00 ± 32.10	14 ± 0.6	1.20 ± 0.36	132.00 ± 39.60	1.31

Rotational temperature and column densities derived from CH_3OH – *continued.*

Source	No. of lines	θ ($''$)	$\left(\frac{\Omega_s}{\Omega_b}\right)^{\alpha}$	A+ and E lines			E lines only			A/E ratio
				T_{rot} (K)	$N_{CH_3OH}\,(10^{15}\,cm^{-2})^{\beta}$		T_{rot} (K)	$N_{CH_3OH}\,(10^{15}\,cm^{-2})^{\beta}$		
					$36''$	0.1 pc		$36''$	0.1 pc	
G11.50−1.49	3	12.9	0.128	8 ± 1.0	0.09 ± 0.03	0.71 ± 0.21	7 ± 1.3	0.07 ± 0.02	0.57 ± 0.17	1.45
G11.94−0.15	3	4.7	0.017	6 ± 0.6	0.17 ± 0.05	10.10 ± 3.03	5 ± 0.9	0.12 ± 0.04	7.30 ± 2.19	1.70
G11.94−0.62	4	5.0	0.020	6 ± 0.3	0.32 ± 0.10	16.50 ± 4.95	7 ± 0.4	0.29 ± 0.09	14.80 ± 4.44	1.41
G11.99−0.27	3	4.0	0.012	5 ± 1.1	0.05 ± 0.01	3.71 ± 1.11	4 ± 1.6	0.04 ± 0.01	3.26 ± 0.98	1.28
G12.03−0.03	3	3.1	0.007	6 ± 1.6	0.05 ± 0.02	6.93 ± 2.08	5 ± 2.4	0.04 ± 0.01	5.32 ± 1.60	1.57
G12.18−0.12	3	1.5	0.002	7 ± 2.8	0.06 ± 0.02	31.80 ± 9.54	6 ± 5.0	0.04 ± 0.01	22.80 ± 6.84	1.81
G12.21−0.09	4	1.5	0.002	7 ± 0.4	0.16 ± 0.05	88.10 ± 26.43	7 ± 0.5	0.14 ± 0.04	81.40 ± 24.42	1.30
G12.68−0.18	4	4.2	0.014	6 ± 0.3	0.24 ± 0.07	17.60 ± 5.28	5 ± 0.4	0.21 ± 0.06	15.70 ± 4.71	1.29
G12.72−0.22	3	5.6	0.024	6 ± 0.9	0.06 ± 0.02	2.58 ± 0.77	3 ± 1.5	0.04 ± 0.01	1.53 ± 0.46	2.79
G12.89+0.49	3	5.7	0.025	5 ± 0.8	0.09 ± 0.03	3.38 ± 1.01	4 ± 1.2	0.06 ± 0.02	2.49 ± 0.75	1.76
G12.91−0.26	4	5.3	0.022	7 ± 0.2	0.81 ± 0.24	37.60 ± 11.28	7 ± 0.3	0.79 ± 0.24	36.50 ± 10.95	1.20
G14.60+0.02	3	7.4	0.042	5 ± 0.3	0.20 ± 0.06	4.83 ± 1.45	3 ± 0.4	0.15 ± 0.04	3.59 ± 1.08	1.96
G14.99−0.70	3	12.9	0.128	7 ± 0.4	0.27 ± 0.08	2.12 ± 0.64	6 ± 0.7	0.21 ± 0.06	1.64 ± 0.49	1.66
G15.03−0.68	4	12.9	0.128	8 ± 0.5	0.26 ± 0.08	1.99 ± 0.60	9 ± 0.6	0.23 ± 0.07	1.80 ± 0.54	1.37
G16.59−0.05	4	4.5	0.016	7 ± 0.4	0.17 ± 0.05	11.30 ± 3.39	7 ± 0.5	0.17 ± 0.05	10.80 ± 3.24	1.26
G16.86−2.16	4	10.9	0.091	6 ± 0.1	0.56 ± 0.17	6.19 ± 1.86	6 ± 0.1	0.46 ± 0.14	5.07 ± 1.52	1.42
G19.36−0.03	3	8.3	0.053	6 ± 0.2	0.31 ± 0.09	5.89 ± 1.77	5 ± 0.3	0.23 ± 0.07	4.48 ± 1.34	1.58
G19.47+0.17	4	10.9	0.091	9 ± 0.3	0.57 ± 0.17	6.26 ± 1.88	11 ± 0.4	0.57 ± 0.17	6.24 ± 1.87	1.39
G19.49+0.15	3	9.4	0.068	5 ± 1.0	0.04 ± 0.01	0.53 ± 0.16	3 ± 1.7	0.03 ± 0.01	0.40 ± 0.12	2.04
G19.61−0.13	4	4.9	0.019	5 ± 0.3	0.13 ± 0.04	7.23 ± 2.17	4 ± 0.4	0.10 ± 0.03	5.34 ± 1.60	1.80
G19.70−0.27	3	5.9	0.027	7 ± 0.9	0.09 ± 0.03	3.30 ± 0.99	7 ± 1.1	0.07 ± 0.02	2.76 ± 0.83	1.32

Rotational temperature and column densities derived from CH_3OH – *continued.*

Source	No. of lines	θ ($''$)	$\left(\frac{\Omega_s}{\Omega_b}\right)^{\alpha}$	A+ and E lines			E lines only			A/E ratio
				T_{rot} (K)	$N_{CH_3OH}\,(10^{15}\,cm^{-2})^{\beta}$		T_{rot} (K)	$N_{CH_3OH}\,(10^{15}\,cm^{-2})^{\beta}$		
					$36''$	0.1 pc		$36''$	0.1 pc	
G21.88+0.01	3	10.3	0.082	6 ± 0.7	0.07 ± 0.02	0.85 ± 0.26	5 ± 1.1	0.07 ± 0.02	0.80 ± 0.24	1.13
G22.36+0.07	3	2.0	0.003	5 ± 0.6	0.08 ± 0.02	27.30 ± 8.19	3 ± 1.0	0.07 ± 0.02	21.90 ± 6.57	1.66
G23.26−0.24	3	4.9	0.019	5 ± 0.7	0.07 ± 0.02	3.68 ± 1.10	4 ± 1.1	0.06 ± 0.02	3.00 ± 0.90	1.47
G23.44−0.18	4	3.5	0.009	8 ± 0.3	1.37 ± 0.41	145.00 ± 43.50	9 ± 0.4	1.40 ± 0.42	148.00 ± 44.40	1.19
G24.79+0.08	4	2.7	0.006	8 ± 0.2	0.52 ± 0.16	93.90 ± 28.17	9 ± 0.2	0.53 ± 0.16	94.90 ± 28.47	1.21
G25.65+1.05	4	6.7	0.034	8 ± 0.3	0.69 ± 0.21	20.10 ± 6.03	8 ± 0.3	0.59 ± 0.18	17.30 ± 5.19	1.23
G25.71+0.04	3	2.2	0.004	5 ± 0.4	0.07 ± 0.02	19.90 ± 5.97	4 ± 0.6	0.05 ± 0.02	14.80 ± 4.44	1.75
G25.83−0.18	4	3.7	0.010	7 ± 0.8	0.17 ± 0.05	16.50 ± 4.95	7 ± 0.9	0.15 ± 0.04	14.40 ± 4.32	1.43
G28.15+0.00	3	3.5	0.009	6 ± 1.1	0.07 ± 0.02	7.88 ± 2.36	4 ± 1.5	0.05 ± 0.01	5.13 ± 1.54	2.02
G28.20−0.05	4	3.0	0.007	5 ± 0.3	0.36 ± 0.11	50.70 ± 15.21	7 ± 0.6	0.43 ± 0.13	60.50 ± 18.15	1.24
G28.28−0.36	3	6.3	0.030	5 ± 0.5	0.10 ± 0.03	3.46 ± 1.04	4 ± 0.8	0.07 ± 0.02	2.47 ± 0.74	1.94
G28.31−0.39	3	4.0	0.012	9 ± 4.0	0.09 ± 0.03	7.66 ± 2.30	10 ± 6.7	0.08 ± 0.02	6.63 ± 1.99	1.52
G28.83−0.25	3	3.9	0.012	5 ± 0.9	0.15 ± 0.05	13.30 ± 3.99	4 ± 1.3	0.12 ± 0.03	9.87 ± 2.96	1.70
G29.87−0.04	4	3.3	0.008	7 ± 1.1	0.07 ± 0.02	8.96 ± 2.69	10 ± 1.7	0.09 ± 0.03	10.90 ± 3.27	1.30
G29.96−0.02	4	3.4	0.009	8 ± 0.9	0.21 ± 0.06	22.90 ± 6.87	12 ± 1.5	0.25 ± 0.08	27.50 ± 8.25	1.40
G29.98−0.04	3	3.3	0.008	4 ± 0.7	0.33 ± 0.10	39.80 ± 11.94	4 ± 3.4	0.25 ± 0.08	30.40 ± 9.12	2.07
G30.59−0.04	3	1.7	0.002	6 ± 0.7	0.13 ± 0.04	55.50 ± 16.65	5 ± 0.9	0.10 ± 0.03	44.40 ± 13.32	1.42
G30.71−0.06	4	3.6	0.010	7 ± 0.1	0.91 ± 0.27	93.10 ± 27.93	6 ± 0.1	0.82 ± 0.24	83.60 ± 25.08	1.30
G30.76−0.05	3	3.6	0.010	6 ± 1.1	0.08 ± 0.02	8.38 ± 2.51	6 ± 3.1	0.07 ± 0.02	7.36 ± 2.21	1.43
G30.79+0.20	3	4.0	0.013	6 ± 0.4	0.31 ± 0.09	24.30 ± 7.29	5 ± 0.5	0.24 ± 0.07	18.70 ± 5.61	1.51
G30.82−0.05	4	3.4	0.009	10 ± 0.2	1.52 ± 0.46	167.00 ± 50.10	9 ± 0.1	1.82 ± 0.55	200.00 ± 60.00	0.47

Rotational temperature and column densities derived from CH_3OH – *continued.*

Source	No. of lines	θ ($''$)	$\left(\frac{\Omega_s}{\Omega_b}\right)^{\alpha}$	A+ and E lines			E lines only			A/E ratio
				T_{rot} (K)	N_{CH_3OH} (10^{15} cm^{-2})$^{\beta}$		T_{rot} (K)	N_{CH_3OH} (10^{15} cm^{-2})$^{\beta}$		
					36$''$	0.1 pc		36$''$	0.1 pc	
G30.90+0.16	3	2.8	0.006	5 ± 0.3	0.17 ± 0.05	28.20 ± 8.46	3 ± 0.6	0.13 ± 0.04	21.30 ± 6.39	1.87
G31.28+0.06	4	2.9	0.006	8 ± 0.2	0.57 ± 0.17	90.50 ± 27.15	8 ± 0.2	0.52 ± 0.16	82.70 ± 24.81	1.28
G31.41+0.31	4	2.6	0.005	8 ± 0.3	0.32 ± 0.10	60.50 ± 18.15	10 ± 0.4	0.39 ± 0.12	74.80 ± 22.44	1.11
G316.81−0.06	3	7.6	0.045	5 ± 0.8	0.06 ± 0.02	1.37 ± 0.41	3 ± 1.3	0.04 ± 0.01	0.97 ± 0.29	2.16
G318.95−0.20	3	8.6	0.057	5 ± 0.2	0.20 ± 0.06	3.54 ± 1.06	5 ± 0.4	0.18 ± 0.05	3.20 ± 0.96	1.20
G323.74−0.26	4	6.3	0.030	7 ± 0.3	0.23 ± 0.07	7.58 ± 2.27	7 ± 0.4	0.21 ± 0.06	6.91 ± 2.07	1.32
G331.28−0.19	4	3.8	0.011	9 ± 0.7	0.31 ± 0.09	27.20 ± 8.16	9 ± 0.8	0.28 ± 0.08	24.80 ± 7.44	1.37
G332.73−0.62	4	5.9	0.027	10 ± 1.9	0.06 ± 0.02	2.09 ± 0.63	13 ± 2.8	0.06 ± 0.02	2.23 ± 0.67	1.46

$^{\alpha}$ Beam filling factor assuming the CH_3OH emission subtends an angle θ equivalent to ∼20,000 AU at the distance of the source.

$^{\beta}$ Two values for column density are presented: the beam-averaged column density in a 36$''$ beam, and a column density corrected for beam dilution, assuming the size of the emitting region is ∼20,000 AU.

see a pattern emerge. The A-type transition has a consistently higher N_u/g_u compared to a straight line fit through the E-type transitions. This indicates a greater abundance of A-type CH_3OH and an A/E ratio >1. Considering only sources in which all three E-type lines were detected, and assuming equal excitation temperatures in A and E lines, we derive A/E abundance ratios ranging from 0.47 to 1.80, with a mean of 1.30. These values are comparable to values previously derived in the literature, e.g., Menten et al. (1988) who calculated A/E ratios between 1.3 and 2.0, using the same transitions, towards cores in Orion KL.

5-4.4 N_2H^+ optical depth and column density

Optical depths were derived directly from the hyperfine components of N_2H^+, which assume set ratios under optically thin conditions. Figure 5.2 is taken from Caselli et al. (1995) and illustrates the hyperfine structure of N_2H^+ $(1-0)$ seen in a quiescent dark cloud. In massive star forming regions, where the linewidths are typically greater than $2\,\mathrm{km\,s^{-1}}$, the seven components are blended into three groups. Attempting to fit seven Gaussians to the data using the HFS routine in CLASS results in a value of $\tau = 0.1$ for all sources, indicating that the program cannot constrain the optical depth sufficiently well using this method. Instead, we try to estimate the optical depth from the integrated intensity ratios of the three blended groups. Assuming the linewidths of the individual hyperfine components are all equal, the integrated intensities of the three groups should be in the ratio of $3:15:9$ under optically thin conditions. The optical depth is calculated from the ratio of integrated intensities ($\int T_B\,dv$) of any two groups using the following equation:

$$\frac{\int T_{B,1}\,dv}{\int T_{B,2}\,dv} = \frac{1-e^{-\tau_1}}{1-e^{-\tau_2}} = \frac{1-e^{-\tau_1}}{1-e^{-a\,\tau_1}}, \tag{5.8}$$

where 'a' is the expected ratio of τ_2/τ_1 under optically thin conditions. Caselli et al. (1995) report anomalous excitation of the $F_1, F = 1,0 \rightarrow 1,1$ and $1,2 \rightarrow 1,2$ components (in our group-3), so we determine the optical depth solely from the intensity ratio of group-1/group-2. We find that 97 percent of sources have optical depths below 1. Figure 5.6 plots the distribution of the derived optical depths, which range

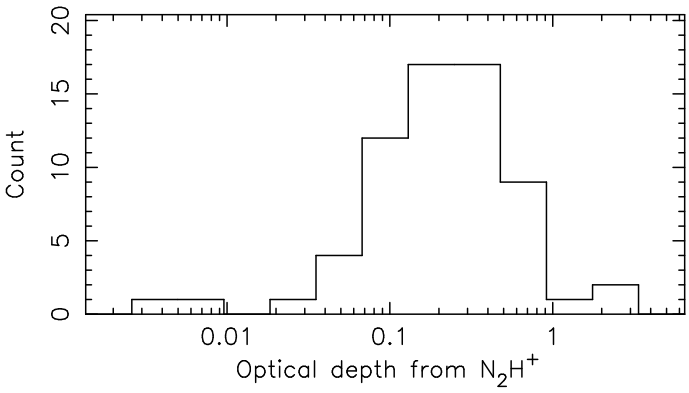

Figure 5.6. Distribution of optical-depths derived from the ratios of the hyperfine groups of N_2H^+. The mean is 0.35 ± 0.42.

from 0.035 to 2.43, with a mean of 0.35 and a standard-deviation of 0.42. Values for the optical depth towards individual sources are presented in column two of Table 5.5. That the N_2H^+ emission is optically thin in the majority of sources implies low column or volume-densities in the Mopra beam.

Column densities of N_2H^+ can be found from the following formula,

$$N = \frac{8k\pi\nu^2}{A_{ul}hc^3} \frac{\int T_b \, dv}{\left(\frac{\tau_\nu}{1 - e^{-\tau_\nu}}\right)} \frac{Q(T_{ex})}{g_u} e^{E_u/kT} \tag{5.9}$$

where $Q(T_{ex})$ is the partition function, extrapolated from a fit to the values given by the (Pickett, et al. 1998) spectral line catalogue:

$$Q(T) = 4.198 \, T_{ex}. \tag{5.10}$$

Equation 5.9 requires an estimate of the excitation temperature T_{ex}. Unfortunately, under optically thin conditions, the excitation temperature cannot be determined from the N_2H^+ line profiles, so we assume a constant value of 10 K. For excitation temperatures of 5 K and 20 K the total column density should be multiplied by 0.8 and 1.6, respectively. Beam averaged column densities derived using Equation 5.9 are presented in column five of Table 5.5. In the literature, high-resolution maps show that N_2H^+ traces the spatial extent of the dust closely (e.g. Caselli et al. 2002; Pirogov et al. 2003). We have estimated the average FWHM of the dust emission for all sources observed by Hill et al. (2005) (see section 5-4.2) and use these

Table 5.5: Optical depths and column densities derived from N_2H^+.

Source	$\theta_{\rm dust}$ ($''$)	$\left(\frac{\Omega_s}{\Omega_b}\right)^{\alpha}$	τ	$N_{N_2H^+}\,(10^{14}\,{\rm cm}^{-2})^{\beta}$	
				$36''$	$\Theta_{\rm dust}$
G0.32−0.20	126	1.0	0.046 ± 0.026	1.10 ± 0.33	1.10 ± 0.33
G0.50+0.19	30	0.7	–	0.61 ± 0.18	0.88 ± 0.26
G0.55−0.85	24	0.5	0.040 ± 0.044	1.87 ± 0.56	4.22 ± 1.27
G0.84+0.18	29	0.6	–	0.22 ± 0.07	0.33 ± 0.10
G1.15−0.12	47	1.0	–	1.04 ± 0.31	1.04 ± 0.31
G2.54+0.20	63	1.0	0.084 ± 0.026	0.78 ± 0.23	0.78 ± 0.23
G5.89−0.39	90	1.0	0.002 ± 0.013	2.20 ± 0.66	2.20 ± 0.66
G5.90−0.43	62	1.0	0.059 ± 0.010	3.19 ± 0.96	3.19 ± 0.96
G5.90−0.44	69	1.0	0.153 ± 0.017	1.56 ± 0.47	1.56 ± 0.47
G6.54−0.11	24	0.5	–	0.21 ± 0.06	0.47 ± 0.14
G6.61−0.08	24	0.5	–	0.12 ± 0.04	0.27 ± 0.08
G8.14+0.23	69	1.0	0.076 ± 0.033	1.45 ± 0.43	1.45 ± 0.43
G8.67−0.36	81	1.0	0.449 ± 0.029	5.07 ± 1.52	5.07 ± 1.52
G8.68−0.37	55	1.0	0.045 ± 0.013	2.26 ± 0.68	2.26 ± 0.68
G9.62+0.19	94	1.0	0.078 ± 0.037	1.57 ± 0.47	1.57 ± 0.47
G9.99−0.03	45	1.0	0.156 ± 0.064	0.62 ± 0.19	0.62 ± 0.19
G10.29−0.13	46	1.0	0.020 ± 0.015	2.36 ± 0.71	2.36 ± 0.71
G10.30−0.15	73	1.0	0.142 ± 0.016	2.52 ± 0.76	2.52 ± 0.76
G10.32−0.16	53	1.0	0.087 ± 0.017	1.43 ± 0.43	1.43 ± 0.43
G10.34−0.14	26	0.5	0.013 ± 0.014	1.96 ± 0.59	3.77 ± 1.13
G10.44−0.02	51	1.0	0.436 ± 0.057	0.97 ± 0.29	0.97 ± 0.29
G10.47+0.03	122	1.0	0.164 ± 0.032	3.34 ± 1.00	3.34 ± 1.00
G10.48+0.03	24	0.5	0.466 ± 0.200	4.29 ± 1.29	9.64 ± 2.89
G10.63−0.33	63	1.0	0.056 ± 0.013	1.74 ± 0.52	1.74 ± 0.52
G10.63−0.38	24	0.5	–	1.85 ± 0.56	4.17 ± 1.25
G11.50−1.49	97	1.0	0.093 ± 0.039	0.75 ± 0.23	0.75 ± 0.23
G11.94−0.15	31	0.8	0.165 ± 0.037	1.03 ± 0.31	1.39 ± 0.42
G11.94−0.62	67	1.0	0.087 ± 0.014	2.64 ± 0.79	2.64 ± 0.79
G11.99−0.27	28	0.6	0.431 ± 0.147	0.45 ± 0.13	0.74 ± 0.22
G12.03−0.03	28	0.6	0.444 ± 0.099	0.61 ± 0.18	1.01 ± 0.30
G12.18−0.12	24	0.5	–	0.56 ± 0.17	1.27 ± 0.38
G12.21−0.09	24	0.5	0.177 ± 0.073	0.79 ± 0.24	1.78 ± 0.53
G12.68−0.18	102	1.0	0.502 ± 0.043	1.79 ± 0.54	1.79 ± 0.54
G12.72−0.22	50	1.0	0.138 ± 0.076	0.50 ± 0.15	0.50 ± 0.15
G12.89+0.49	87	1.0	0.150 ± 0.050	1.34 ± 0.40	1.34 ± 0.40
G12.91−0.26	90	1.0	0.121 ± 0.013	3.87 ± 1.16	3.87 ± 1.16

Optical depths and column densities – *continued.*

Source	$\theta_{\rm dust}$ ($''$)	$\left(\frac{\Omega_s}{\Omega_b}\right)^{\alpha}$	τ	$N_{N_2H^+}\,(10^{14}\,{\rm cm}^{-2})^{\beta}$	
				$36''$	$\Theta_{\rm dust}$
G14.60+0.02	24	0.5	0.066 ± 0.035	1.50 ± 0.45	3.38 ± 1.01
G14.99−0.70	43	1.0	0.186 ± 0.021	1.50 ± 0.45	1.50 ± 0.45
G15.03−0.68	24	0.5	0.106 ± 0.049	1.00 ± 0.30	2.26 ± 0.68
G15.03−0.71	52	1.0	–	0.17 ± 0.05	0.17 ± 0.05
G16.59−0.05	58	1.0	0.118 ± 0.063	1.36 ± 0.41	1.36 ± 0.41
G16.86−2.16	109	1.0	0.329 ± 0.032	1.87 ± 0.56	1.87 ± 0.56
G19.36−0.03	24	0.5	0.135 ± 0.033	1.03 ± 0.31	2.31 ± 0.69
G19.47+0.17	24	0.5	0.053 ± 0.043	1.67 ± 0.50	3.76 ± 1.13
G19.49+0.15	24	0.5	0.131 ± 0.083	0.46 ± 0.14	1.04 ± 0.31
G19.61−0.13	43	1.0	–	0.76 ± 0.23	0.76 ± 0.23
G19.70−0.27	35	1.1	0.198 ± 0.142	0.82 ± 0.25	0.87 ± 0.26
G21.88+0.01	24	0.5	0.259 ± 0.145	0.33 ± 0.10	0.74 ± 0.22
G22.36+0.07	39	1.0	0.098 ± 0.024	1.24 ± 0.37	1.24 ± 0.37
G23.26−0.24	24	0.5	–	0.96 ± 0.29	2.16 ± 0.65
G23.44−0.18	55	1.0	0.031 ± 0.022	1.97 ± 0.59	1.97 ± 0.59
G23.71−0.20	24	0.5	0.071 ± 0.042	0.64 ± 0.19	1.43 ± 0.43
G24.79+0.08	73	1.0	0.130 ± 0.014	2.89 ± 0.87	2.89 ± 0.87
G24.85+0.09	24	0.5	–	0.09 ± 0.03	0.20 ± 0.06
G25.65+1.05	63	1.0	0.166 ± 0.027	2.02 ± 0.61	2.02 ± 0.61
G25.71+0.04	46	1.0	–	0.72 ± 0.22	0.72 ± 0.22
G25.83−0.18	60	1.0	0.139 ± 0.027	0.93 ± 0.28	0.93 ± 0.28
G28.15+0.00	40	1.0	–	0.53 ± 0.16	0.53 ± 0.16
G28.20−0.05	70	1.0	0.092 ± 0.027	1.73 ± 0.52	1.73 ± 0.52
G28.28−0.36	24	0.5	0.160 ± 0.033	1.04 ± 0.31	2.35 ± 0.70
G28.31−0.39	39	1.0	0.032 ± 0.057	0.31 ± 0.09	0.31 ± 0.09
G28.83−0.25	24	0.5	0.045 ± 0.023	1.56 ± 0.47	3.51 ± 1.05
G29.87−0.04	32	0.8	0.188 ± 0.051	0.84 ± 0.25	1.06 ± 0.32
G29.96−0.02	80	1.0	0.143 ± 0.154	0.84 ± 0.25	0.84 ± 0.25
G29.98−0.04	55	1.0	0.544 ± 0.133	2.02 ± 0.61	2.02 ± 0.61
G30.59−0.04	51	1.0	0.058 ± 0.041	0.81 ± 0.24	0.81 ± 0.24
G30.71−0.06	70	1.0	0.210 ± 0.011	4.46 ± 1.34	4.46 ± 1.34
G30.76−0.05	52	1.0	–	0.35 ± 0.11	0.35 ± 0.11
G30.78+0.23	24	0.5	0.502 ± 0.321	0.12 ± 0.04	0.28 ± 0.08
G30.79+0.20	24	0.5	0.091 ± 0.025	0.91 ± 0.27	2.05 ± 0.61
G30.82−0.05	75	1.0	0.447 ± 0.026	5.93 ± 1.78	5.93 ± 1.78
G30.82+0.28	24	0.5	–	0.46 ± 0.14	1.03 ± 0.31
G30.90+0.16	28	0.6	–	1.25 ± 0.38	2.07 ± 0.62

Optical depths and column densities – *continued.*

Source	$\theta_{\rm dust}$ ($''$)	$\left(\frac{\Omega_s}{\Omega_b}\right)$ $^{\alpha}$	τ	$N_{N_2H^+}$ (10^{14} cm^{-2}) $^{\beta}$	
				$36''$	$\Theta_{\rm dust}$
G31.28+0.06	91	1.0	0.058 ± 0.022	1.76 ± 0.53	1.76 ± 0.53
G31.41+0.31	67	1.0	1.351 ± 0.288	2.99 ± 0.90	2.99 ± 0.90
G316.81−0.06	24	0.5	0.190 ± 0.020	2.43 ± 0.73	5.47 ± 1.64
G318.95−0.20	36	1.0	0.077 ± 0.030	1.68 ± 0.50	1.68 ± 0.50
G323.74−0.26	36	1.0	0.027 ± 0.027	1.54 ± 0.46	1.54 ± 0.46
G331.28−0.19	38	1.0	0.061 ± 0.055	0.71 ± 0.21	0.71 ± 0.21
G332.73−0.62	24	0.5	0.004 ± 0.051	0.24 ± 0.07	0.54 ± 0.16

$^{\alpha}$ Beam filling factor assuming the CH_3OH emission subtends an angle $\theta_{\rm dust}$.

$^{\beta}$ $36''$: the beam-averaged column density in a $36''$ beam. $\theta_{\rm dust}$: the column density corrected by the beam dilution factor.

values to correct for beam dilution. Total column densities corrected by a factor $(\Theta_{\rm dust}/\Theta_{\rm beam})^2$ are presented in column six of Table 5.5.

5-4.5 ^{13}CO, HNC and HCN column density

The HNC HCN and ^{13}CO profiles frequently display asymmetries which may indicate that they are optically thick in general. Lacking an estimate for both the excitation temperature and the optical depth we are unable to calculate reliable column densities.

5-4.6 Abundances

The relative abundance X between two species may be found directly from the ratio of their volume densities. Assuming both molecules occupy the same volume of space, this is simply equivalent to the ratio of their column densities.

$$X = \frac{n_1}{n_2} \approx \frac{N_1}{N_2}. \tag{5.11}$$

If, however, one or both species subtend angles smaller than the beam, we must correct for their *relative* volume filling factor and Equation 5.11 becomes

$$X = \frac{N_1}{N_2}\left(\frac{\Theta_2}{\Theta_1}\right)^3, \tag{5.12}$$

assuming spherically symmetric emission with characteristic sizes Θ_1 and Θ_2. For the single-position observations presented here, the volume filling factors are complete unknowns and constitute the greatest source of errors in the abundance. Additional errors stem from calibration of the brightness scale and the pointing accuracy of the telescope. Abundances relative to H_2 depend also on the assumptions made in calculating the gas mass from the 1.2-mm continuum emission and cannot be determined reliably.

5-5 Analysis and discussion

5-5.1 Luminosities and masses

The relationship between mass and luminosity provides clues to the star formation efficiency, stellar content and evolutionary state of the clumps. Figure 5.7 (*left*) is an expanded version of Fig. 2 in Cesaroni (2005), showing the relationship between luminosity and gas mass for the 55 clumps whose properties could be determined. The luminosity has been measured from a two-component greybody fit to the spectral energy distribution (see Chapter 4 and Appendix B) and is directly related to the stellar content of the clump. Sub-millimetre emission from assumed optically thin dust (Hill et al. 2005) has been used to derive the total gas-mass of the clumps. In the plot, the thick line marks the expected luminosity from a minimum number of stars of mass $M_* \leq 100\,M_\odot$, assuming $M_{gas} \equiv M_{stars}$. Cesaroni (2005) divide a sample of 21 known hot cores[1] into 'light' and 'heavy' categories, based on their position above or below this division. 'Light' cores have gas masses below $\sim 100\,M_\odot$ and fall above the thick line. Their high luminosity-to-mass ratio implies that the mass of their stellar content is greater than that of the gas. 'Heavy' cores have gas masses above $\sim 100\,M_\odot$ and fall below the thick line. The mass of their stellar content is comparable to, or less than, the mass of the gas. Cesaroni (2005) have

1. We have the following sources in common with Cesaroni: G5.89−0.39, G9.62+0.19, G10.47+0.03, G10.62−0.38, G29.96−0.02 and G31.41+0.31.

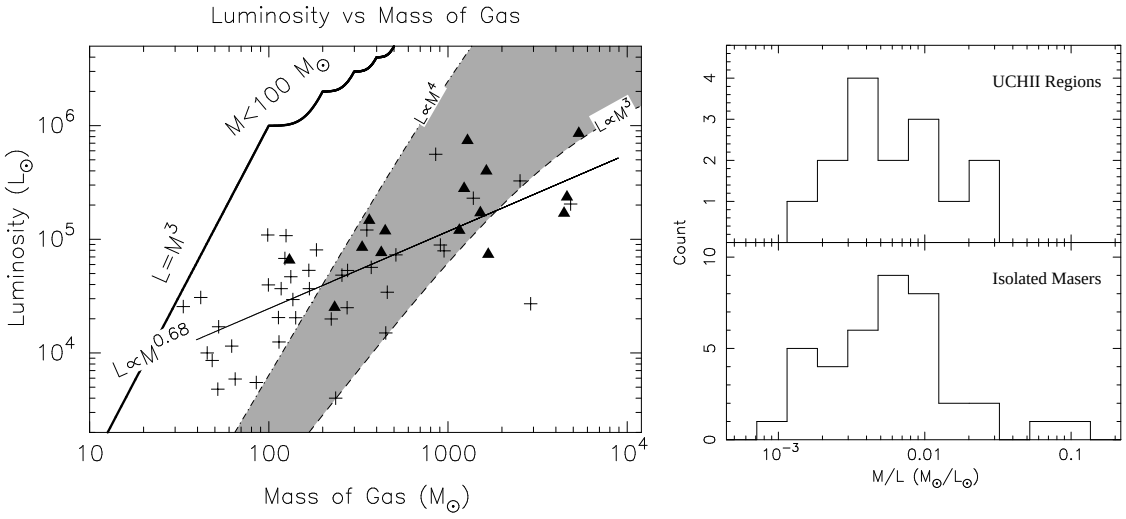

Figure 5.7. (*left*) Plot of luminosity versus dust + gas mass for 55 sources whose properties could be determined (after Fig. 2, Cesaroni 2005). UCHII regions are represented by solid triangles and isolated masers by crosses. The thick solid line traces the luminosity expected if $M_{gas} \equiv M_{stars}$ in the clumps, and the stellar population is concentrated in a minimum number of stars with masses $\leq 100\,M_{\odot}$. The dashed line is the luminosity expected from the most massive star in a M_{gas} cluster with stellar masses distributed according a Salpeter IMF ($\alpha = 2.35$), and a fundamental upper stellar mass limit of $150\,M_{\odot}$ (Weidner & Kroupa 2004). We have assumed a mass-luminosity relation of $L \propto M^3$. The dash-dot line traces the expected luminosity from the same IMF assuming $L \propto M^4$ and the shaded region indicates intermediate values. The observed mass-luminosity relation is fit with a single power law of index 0.68 ± 0.09 (thin solid line). (*right*) Histograms of the distribution in the M_{gas}/L_{stars} values for UCHII regions and isolated masers. A KS-test cannot distinguish between them.

interpreted the L_{stars}/M_{gas} ratio in the 'light' cores as suggesting only a single embedded massive star exists in these clumps. Conversely the 'heavy' clumps are likely to contain multiple massive stars which have formed in clustered mode. We do not find any 'light' cores in our sample.

An alternative explanation for high L_{stars}/M_{gas} ratios in the 'light' sources might derive from the age of the star forming regions. A massive young stellar object at a late stage of evolution could be expected to have dispersed a large fraction

of its molecular gas, through the action of stellar winds, intense UV-radiation and outflows from young OB stars. This would result in a decrease in the measured gas-mass without a corresponding decrease in the luminosity. In Figure 5.7 the points would move horizontally into the 'light' portion of the plot. We note that Cesaroni's light cores include Orion-KL, and IRAS 20126+4014, neither of which are believed to be at a late stage of evolution. Orion is not considered to be representative of massive star-forming regions, while the mass of IRAS 20126+4014 ($7 \pm 3 M_{\odot}$) has been measured assuming Keplerian rotation of a molecular disk (Cesaroni et al. 2005) and relates to the inner object only. On larger scales the gas-mass has been measured to be several hundred solar masses (e.g. Estalella et al. 1993), putting IRAS 20126+4014 in the 'heavy' category. We find that all of our maser selected sample have gas masses above $\sim 30\,M_{\odot}$ and *all* fall into the 'heavy' category. If the division between 'light' and 'heavy' cores is an indication of age, then all of our sample are at a relatively early stage of evolution, i.e., the powering massive young stellar objects have not yet dispersed their natal molecular clouds.

In Figure 5.7 the shaded region between the dashed lines represents the range of luminosities expected from the *most massive* star in a cluster where $M_{\rm stars} = M_{\rm gas}$, if the initial mass function (IMF) follows a Salpeter power law ($\alpha = 2.35$) and assuming a fundamental upper stellar mass limit of $M_{*} = 150\,M_{\odot}$ (Weidner & Kroupa 2004). The luminosity of the cluster will be dominated by the most massive star so this is a good approximation to the expected total luminosity. The range in expected luminosities derives from the uncertainty in the mass-luminosity relation for massive young stellar objects. This may be represented by a power law of the form $L_{*} \propto M_{*}^{\gamma}$, where γ ranges between 3 and 4 in the literature for OB-stars (e.g., Lada 1999; Churchwell 2002). Our maser selected sample exhibit a rough correlation between mass and luminosity, which may be fit with a single power law with index $\gamma = 0.68 \pm 0.08$. This is a much shallower rise than observed in evolved stars, however, the luminosities of the most massive clusters are consistent with the $150\,M_{\odot}$ stellar cutoff (Weidner & Kroupa 2004), even in the more conservative limit of $L_{*} \propto M_{*}^{3}$.

The derived gas-mass is highly dependant on the temperature in Equation 5.2.

The shallow power law might be explained if the average dust temperature increases with luminosity and this change is not reflected in the sparsely sampled greybody fits to the SED, from which we take our temperature estimates. If we assume the mass estimates are correct to within a factor of a few, then the main result is that the lower mass clumps are over-luminous and the higher mass clumps are under-luminous. This result is not unexpected: stars forming in lower mass clumps must consume a larger fraction of the gas.

5-5.1.1 UCHII regions: Luminosity or Age?

UCHII region (triangles) are in general more luminous *and* more massive than the isolated masers (crosses) in the sample. Individual power law fits to the isolated masers and UCHII sub-samples yield mass-luminosity relations of $L_{masers} \propto M^{0.59\pm0.13}$ and $L_{UCHII} \propto M^{0.64\pm0.177}$, respectively. These fits are consistent with the fit to the combined sample, within the errors, and a single power law can describe both distributions. Figure 5.7 (*right*) is a histogram of the M_{gas}/L_{stars} ratio for UCHII regions (top) and isolated masers (bottom). As expected from the mass-luminosity plot, the distributions are similar and a Kolmogorov-Smirnov (KS) test cannot distinguish between them, yielding a 76 per cent probability of the two sub-samples being drawn from the same population. This result implies that for the same masses, the two samples have the same luminosities. Early in the evolution of a massive young stellar object we would expect its luminosity to increase as it accretes matter and more mass is transfered from the envelope to the star. At the same time the overall mass of gas and dust in the clump is expected to remain relatively constant, or indeed decrease, as winds from the young OB-cluster break up the cloud. By this rationale, if our sample of UCHII regions are older and more evolved, we would expect them to have a lower M_{gas}/L_{stars} ratio than the isolated masers. There are several possible reasons why we do not see a difference between the mass-luminosity distributions.

It is possible that systematic errors associated with our assumptions cause us to overestimate the mass of the UCHII regions relative to the isolated masers. For there

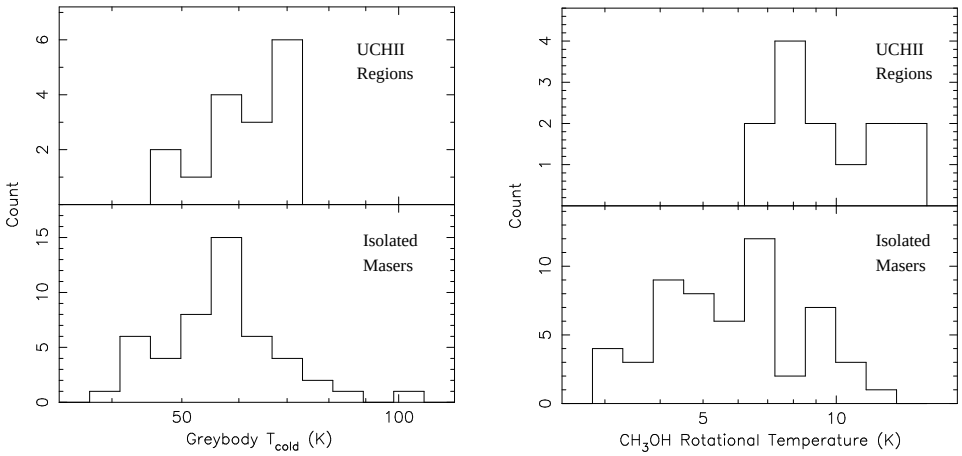

Figure 5.8. (*left*) Histograms showing the distributions of dust temperature taken from the cold component of the greybody fit to the SED. The top panel is UCHII regions, which have a mean T_{cold} of 62.4 K, while the bottom panel is isolated masers, which have a mean T_{cold} of 58.1 K. (*right*) Histograms showing the distributions of CH_3OH rotational temperature for UCHII regions (top) and isolated masers (bottom). The mean values are 9.9 K for UCHII regions and 6.1 K for isolated masers. A KS-test establishes that the distributions are significantly different, returning a probability of 0.002 per cent.

to be no difference between the mean masses of the sub-samples, the isolated masers would need to have a dust temperature on average 36 K lower than the UCHII regions. Figure 5.8 (*left*) illustrates the distributions of T_{cold} from the SED fits, for UCHII regions (top) and isolated masers (bottom). While the UCHII regions clearly have temperatures which are skewed to the high end, the difference in the means is only 4.2 K. The rotational temperatures calculated from CH_3CN are likewise similar, however, we cannot rule out different average dust temperatures on the basis that CH_3CN emission likely probes only the embedded 'hot core' and does not reflect the conditions in the extended clump. CH_3OH emission is thought to derive from a more extended envelope and rotational temperatures calculated from this molecule appear to support very different temperatures in the two groups. Figure 5.8 (*right*) shows histograms of the CH_3OH rotational temperature for the UCHII regions (top) and isolated masers (bottom). A KS-test returns a probability of 0.002 per cent of the distributions deriving from the same parent. We note that the mean values of 9.9 K

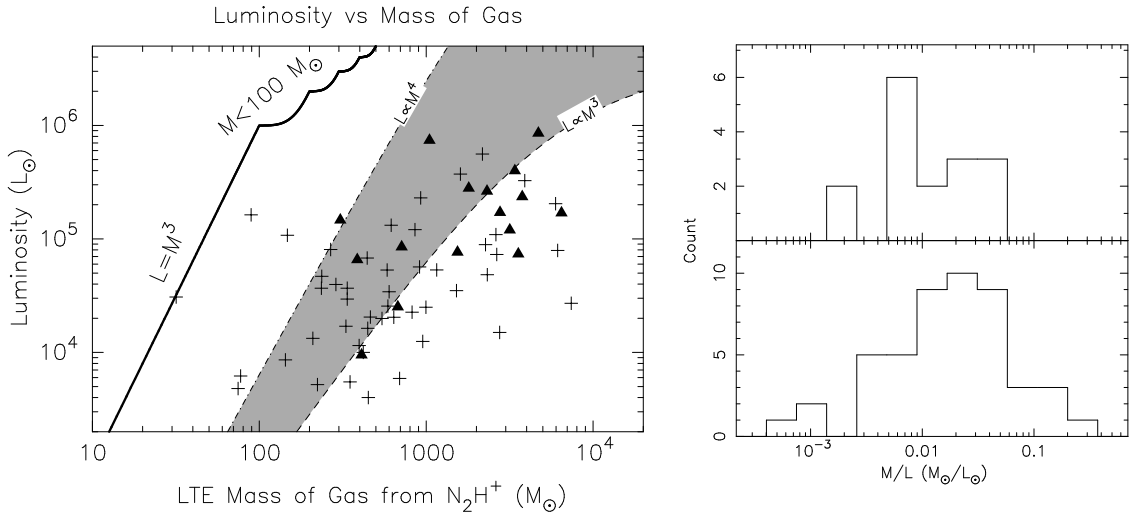

Figure 5.9. As Figure 5.7, except in this case the mass is the LTE-mass derived from the column density of N_2H^+ assuming a fixed abundance ratio of 1.7×10^{-10} and that the N_2H^+ emission closely follows the spacial distribution of the 1.2-mm continuum emission.

for the UCHII regions and 6.1 K for the isolated masers do not reflect the kinetic temperature as the CH_3OH is likely sub-thermally excited (see Goldsmith & Langer 1999).

As an alternate estimate of the mass we derived a 'LTE-mass' from the column density of N_2H^+. In our calculations we assume (i) the N_2H^+ emission closely traces the 1.2-mm dust continuum and has a uniform density, (ii) a fixed $[H_2] \,/\, [N_2H^+]$ abundance ratio of 1.7×10^{-10} (Pirogov et al. 2003). The mass of gas may then be estimated from the column density using Equation 5.4. Figure 5.9 (*left*) is is a mass-luminosity plot similar to Figure 5.7, except that the mass plotted on the x-axis is the LTE-mass calculated from N_2H^+. Although the scatter is greater, we clearly see the masses of the UCHII regions and isolated masers are offset, with the UCHII regions having greater masses on average, as in Figure 5.7. The distributions of the M_{gas}/L_{stars} ratios are illustrated in Figure 5.9 (*right*). A KS-test for returns a probability of 50 per cent that the both distributions are derived from the same parent, confirming the original result.

Another explanation for the offset in the masses derives from the sensitivity limit on the radio-survey. In Chapter 4 we assumed the UCHII regions were older and

more evolved than the isolated masers. We argued that the original radio continuum survey was sensitive enough to detect UCHII regions associated with isolated masers (see section 4-6.1.1). However, assuming the mass of gas derived from the 1.2-mm continuum flux denisty is correct, is difficult to explain why sources with radio-continuum emission are *more massive and more luminous* than the isolated masers, without invoking sensitivity arguments. In other words, some of the lower L_{stars} isolated masers may be associated with UCHII regions which fall below our detection limit. In Chapter 4 we showed that most sources are luminous enough to have detectable UCHII regions, assuming up to 90 per cent of the Lyman continuum photons are absorbed by dust (Kurtz et al. 1994). If the disparity in luminosity is due to a real sensitivity limit, this would imply that, on average, at least 99 per cent of the ionising photons are absorbed by dust before contributing to the creation of a UCHII region. If a sensitivity limit exists on the original radio-survey then we cannot tell if the isolated masers are in fact younger than the UCHII regions, or simply intrinsically more luminous.

Some of the isolated maser sites may also be associated with hyper-compact HII (HCHII) regions. This recently discovered class of HII region is typically less than 0.01 pc across (Avalos et al. 2006) and exhibits a free-free emission spectrum with a turnover frequency at higher frequencies than UCHII regions, typically 20 GHz. HCHII regions are expected to be optically thick at 8.6 GHz and due to the squared dependace of the flux density with frequency and will be difficult to detect.

Differences between the radio-bright and radio-quiet samples may be attributed to either evolution or luminosity. We cannot separate the two effects with confidence using this limited sample.

5-5.2 Detailed comparison between sub-samples

The aim of this molecular survey is to investigate the utility of molecular lines in the 3-mm band to act as 'molecular clocks'. In this section we consider the differences between sub-samples divided from the source list based on associations with tracers

of potentially different evolutionary states. We separate the source list into sub-samples based on the following criteria:

- Presence or absence of radio emission from a UCHII region.
- CH_3CN detected versus no CH_3CN detected.
- MSX-dark (seen in absorption at 8 μm) versus MSX-bright.
- Presence or absence of high velocity line-wings in HCO^+, HNC or ^{13}CO.
- Presence or absence of blue-skewed HCO^+ line profiles, indicating infall.

In the following analysis we contrast the sub-samples by looking for differences in the median properties. A KS-test is used to assess the similarity of the two distributions and trends are found based on large differences in the median values, coupled with a low probability that the sub-populations are drawn from the same parent distribution.

Initially, we compare the spectral line luminosities calculated from the integrated line intensity multiplied by the square of the distance to the source. If the distance is well known then comparisons of line luminosities will potentially reveal intrinsic differences between the sub-samples. However, the error in the distance for this sample is relatively large (± 0.65 kpc ≈ 20 per cent), and increases towards Galactic longitudes $< 5°$, where the Galactic rotation curve begins to break down. Only the strongest trends will be seen using such a comparison.

We also compare the distance-independent linewidths. Linewidths in massive star forming regions are generally much greater than the thermal width and are indicators of the level of turbulence present in the gas. Turbulence arises from bulk motions of gas, is often associated with energetic phenomena, such as outflows, and is correlated with star formation activity (e.g. Dobbs et al. 2005).

The ratio of two spectral line intensities is unaffected by the distance and constitutes a much better probe of the physical and chemical conditions. The dominant errors are due to the absolute accuracy with which the data has been calibrated and

the unknown relative beam-filling factors. The results presented here are based on data taken over four years and the calibration error in the data has been determined to be better than 30 per cent in most cases. The uncertainty due to the beam filling factors is given by the ratio of the solid angles over which the two molecules emit, (Ω_1/Ω_2), and may be large for dense-gas tracers which subtend angles smaller than the beam. The trends underlying the data should still be visible given the sample size.

Ideally, in a search for molecular clocks the abundances should be compared directly. Unfortunately, the small number of transitions observed in this work make it difficult to constrain the column densities accurately. Two or more transitions of a single molecule are needed to solve for the optical depth, excitation temperature and column density. We have been able to determine the column densities of CH_3CN and CH_3OH through the rotational diagram method, and by assuming an excitation temperature or $[^{12}C/^{13}C]$ abundance ratio, we have calculated the column densities of N_2H^+ and HCO^+. Here we compare the beam-averaged column densities of these molecules directly to find the abundance ratios.

Lastly, we contrast the differences in a suite of measured physical parameters such as bolometric luminosity, gas-mass, rotational-temperature and mid-infrared flux density, drawn from this and other work.

The important differences are summarised in section 5-5.2.7.

5-5.2.1 Radio-loud versus radio-quiet sources

Figure 5.12 illustrates the difference in line luminosity between sources with and without UCHII regions in the Mopra beam (the radio-loud and radio-quiet sub-samples, respectively). As with CH_3CN and HCO^+ in Chapter 4, we find that the luminosity the remaining transitions is enhanced towards the radio-loud sub-sample. The median line luminosity is greater by 0.65-σ, on average, where σ is the standard deviation of the combined sample. CH_3OH stands out as having the most significantly different distribution and the largest difference in line-luminosity,

followed by $H^{13}CO^+$, CH_3CN, HNC and N_2H^+.

We find the median linewidths of all species are broader towards the radio-loud sub-sample (see Figure 5.13). CH_3OH exhibits the greatest differences, closely followed by $N_2H^+$and $H^{13}CO^+$, all of which have statistically different distributions according to the KS-test. HCO^+, HCN, HNC and CH_3CN have broader lines on average, however the distributions are not significantly different. The differences in the median linewidth range from $0.37\,\mathrm{km\,s^{-1}}$ to $1.62\,\mathrm{km\,s^{-1}}$, greater than can be attributed to thermal broadening and most likely due to the greater turbulent energy in the gas associated with UCHII regions.

The differences found between the linewidths and line-luminosities are echoed in a comparison of the raw integrated line intensities. Figure 5.14 (*left*) shows the difference in the median values of the 28 intensity ratios between eight molecules. The median intensity of CH_3OH and, to a much lesser extent, CH_3CN, are clearly enhanced with respect to all other molecules. Statistically, the most significant difference in intensity ratio occurs between CH_3OH and other molecules, specifically N_2H^+ and ^{13}CO. The $[CH_3CN/^{13}CO]$ and $[H^{13}CO^+/^{13}CO]$ ratios also stand out as being significantly greater towards the radio-loud sub-sample.

Figure 5.14 (*right*) illustrates a comparison of the median beam-averaged column densities of four molecules: CH_3CN, CH_3OH, HCO^+ and N_2H^+. Again, CH_3OH stands out as having greater a column density, and hence a higher abundance, towards the radio-loud sub-sample.

The median differences between other measured and calculated properties are shown in Figure 5.15. The median bolometric luminosity and median mass of the radio-loud sub-sample is significantly greater than for the isolated masers (see section 5-5.1). The rotational temperature derived from CH_3CN is similar in both groups, however, the CH_3OH rotational temperature is significantly greater in the radio-bright group (also see Figure 5.8).

5-5.2.2 Sources with and without CH_3CN

CH_3CN was detected towards 58 sources (70 per cent), however the detection rate towards the radio-loud sub-sample (19 sources) was 90 per cent. The enhanced luminosities and masses of our UCHII regions may bias the results of a comparison between CH_3CN-bright and CH_3CN-dark groups. We therefore exclude any regions with radio emission from the comparison. In practise, we find that the major results are robust to the presence of UCHII regions.

The differences in median line luminosity between the two groups presented in Figure 5.16 are not as pronounced as in the previous section, however, all lines are marginally (0.07-σ) more luminous towards the CH_3CN-bright sub-sample. HCO^+ and HCN have the most significantly different distributions. We note that the HCO^+ and HCN profiles are affected by self absorption, with the CH_3CN-bright group containing the most extreme examples. The significant difference in the HCO^+ luminosity is also not reflected in the optically thin $H^{13}CO^+$ isotopomer, suggesting that an abundance difference is unlikely. The greatest difference in the median values occurs in ^{13}CO, followed by CH_3OH and CH_3CN.

Linewidths are also biased towards being greater in the sample with detected CH_3CN (see Figure 5.17). HCO^+ exhibits the most significant difference, followed by CH_3OH, although a KS-test cannot distinguish between the populations with confidence.

When we examine the line intensity ratios in Figure 5.18 (*left*) a similar picture emerges to the case of the UCHII regions. CH_3OH stands out, as its intensity relative to all other lines is enhanced in the CH_3CN-bright sub-sample. We also see evidence for enhanced N_2H^+ emission. In contrast, ^{13}CO emission is relatively weak towards the CH_3CN-bright sub-sample. These ratios are highly suggestive of higher excitation conditions in the dense gas (traced by N_2H^+ and CH_3OH) compared to the more extended gas (traced by ^{13}CO), and correlate well with the line luminosities.

Figure 5.18 (*right*) shows the differences in the median column densities of CH_3OH, HCO^+ and N_2H^+. Again, the CH_3OH column is seen to be significantly enhanced

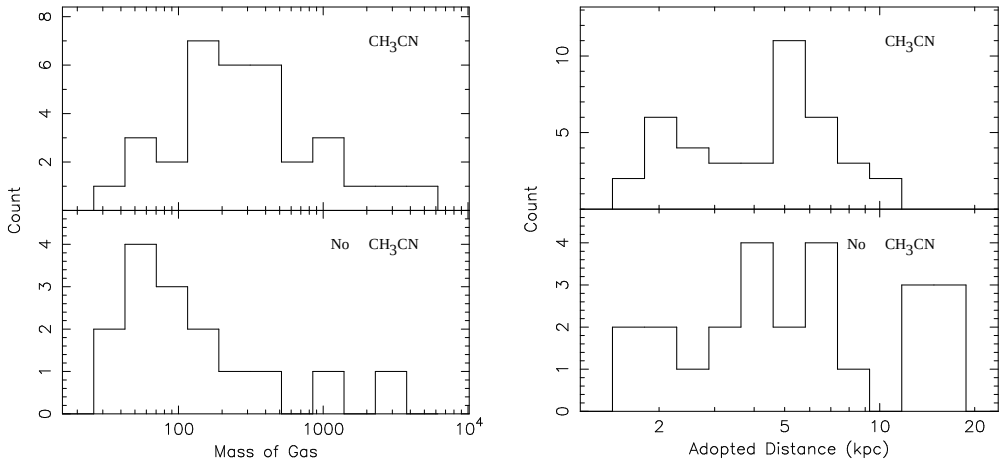

Figure 5.10. (*left*) Histograms showing the distributions of gas masses derived from 1.2-mm continuum flux density for sources with (top) and without (bottom) detected CH_3CN. Sources with in which CH_3CN has been detected tend to be more massive. (*right*) The distribution of distances for sources with (top) and without (bottom) detected CH_3CN. A tail of more distant objects exists in the CH_3CN-dark sample, suggesting that a small fraction of non-detections may be due to sensitivity limits.

towards the CH_3CN bright group, echoing the result from comparing the raw line ratios.

The difference in the median values of other derived parameters are displayed in Figure 5.19. Sources with detected CH_3CN have significantly brighter thermal continuum emission at 1.2-mm wavelengths. This translates into a mean mass higher by $\sim$300 $M_\odot$, omitting UCHII regions or $\sim$600 $M_\odot$, including UCHII regions. Histograms of the mass distributions for the two groups are plotted in Figure 5.10 (*left*), and show significant differences. All other parameters presented in Figure 5.19 are similar for both sub-samples.

The division of the sample into populations with and without detected CH_3CN may be a somewhat artificial distinction. While CH_3CN emission may be present in more distant sources, it may fall below our 2-σ detection threshold of 80 mK. Emission over a small solid angle will suffer from high beam-dilution factors, further compounding the problem. The distributions of distance in the two samples, plotted in Figure 5.10 (*right*), are similar, except for a tail of more distant objects without

CH_3CN. This difference suggests that a small fraction of non-detections may be attributable to sensitivity limits.

5-5.2.3 MSX-dark and MSX-bright clumps

Twelve 'dark' clouds were detected in MSX 8 μm maps as regions of extinction superimposed against background emission from the Galactic plane. Despite the small sample size these 'MSX dark' clumps were associated with a variety of tracers: G30.71−0.06 contained both a methanol maser site and an embedded UCHII region, G30.79+20 was dark at 8 μm, but faint 21 μm emission was detectable at the maser site. Eight others contained embedded masers and two were seen only by their thermal continuum emission at 1.2-mm (see section 4-6.4 for further details). When comparing the dark and bright sample we excluded G30.71−0.06 as the extreme properties of the UCHII region may eclipse faint trends in the data. In most instances the MSX-dark group contains only 9 or 10 members.

The median line luminosity for all lines tends to be greater towards the MSX-dark sample (see Figure 5.20), however, only HCO^+ and $H^{13}CO^+$ have close to significantly different distributions in the sub-samples.

Linewidths follow a similar pattern in Figure 5.21; all species have marginally greater linewidths towards the dark clouds. ^{13}CO and HNC have the most significantly different linewidth distributions, with the median ^{13}CO linewidth greater in the MSX-dark sample by 1.8 km s^{-1}.

Figure 5.22 (*left*) shows the difference in the median intensity ratios for the MSX dark and bright groups. The relative median intensities of HCO^+, and to a lesser extent CH_3OH, are biased towards being marginally greater in the MSX-dark sample. None of the differences have KS-probability statistics less than 5.9 per cent, and are not judged to be significant.

The comparison of column densities is similarly inconclusive, as shown in Figure 5.22 (*right*). In the case of the [CH_3CN/CH_3OH] ratio, the MSX-dark subsample contains only four sources and a KS-test does not return a meaningful value.

Figure 5.23 shows there are no significant differences in the measured physical parameters of the two sub-samples. The greatest difference occurs between median values of the CH_3OH rotational temperature, which is greater in the MSX-dark sub-sample.

5-5.2.4 The presence of high velocity linewings

Doppler shifted line-wings, signifying high-velocity gas along the line of sight, were identified by eye in the HCO^+, HNC and ^{13}CO line profiles and fit with a single broad (FWHM $> 6\,\mathrm{km\,s^{-1}}$) Gaussian. Here we divide the sample into sources with and without detected line-wings and compare the properties of the two groups. As before we have excluded sources with known UCHII regions, so the sample consists of 59 isolated masers and five mm-only clumps.

Figure 5.24 shows that there are no significant differences in line-luminosity between the samples with and without linewings.

Figure 5.25 presents the difference in the median linewidths between the two sub-samples. HCO^+ exhibits the most significant differences, according to a KS-test. This difference takes the form of a tail of sources with broader than average line-profiles in the sub-sample without linewings, as shown in Figure 5.11. We suspect that these broad profiles are due to undetected low-velocity line wings from rotating gas or outflows nearly perpendicular to the line of sight. The median CH_3CN linewidth is also greater towards sources with detected linewings, however this difference is not significant. All other species, including $H^{13}CO^+$, have similar linewidths in both groups.

Figure 5.26 (*left*) presents the median line intensity ratios for the sub-samples. The most significant differences arise from ratios to ^{13}CO, which is relatively weak in objects with linewings. We also note that CH_3CN and CH_3OH tend to be relatively bright in the objects with linewings, however, only CH_3CN exhibits abundance differences (illustrated in Figure 5.26 *right*) and these are not significant according to a KS test.

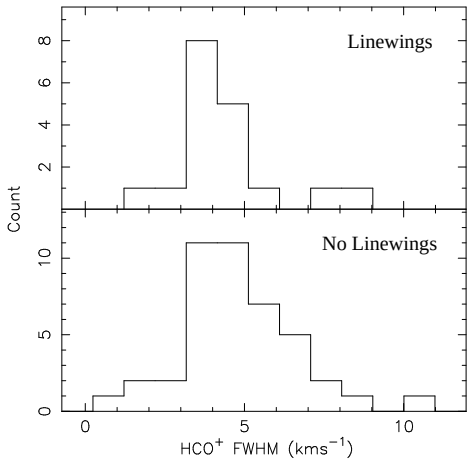

Figure 5.11. Histograms showing the distributions of HCO^+ FWHM linewidths from Gaussian fitting. The top panel includes only sources where broad linewings have been detected and the bottom panel includes only sources where no linewings have been detected.

The median differences in computed and measured physical parameters are presented in Figure 5.27. We see the sub-sample with linewings is significantly brighter at 1.2-mm, however, when distance and dust temperature are factored in this translates to a similar gas-mass in the two sub-samples. The distance-independent bolometric intensity is likewise greater towards the sub-sample with linewings, however, the bolometric luminosity, which includes the distance, shows little difference between the two groups. No other significant differences exist.

5-5.2.5 Infall Profiles vs No Infall Profiles

'Infall profiles' were identified through a comparison of the shape of the optically thick HCO^+ line to the optically thin $H^{13}CO^+$ line (see Section 4-6.3). A bright wing or shoulder in the HCO^+ profile on the blue side of the $H^{13}CO^+$ line centre may be interpreted as being due to inward gas motions. We compare the properties of the sources with infall profiles to the remainder of the population. As in the previous comparisons, we exclude sources with radio-continuum emission.

Figure 5.28 presents the difference in the line luminosity between sources with

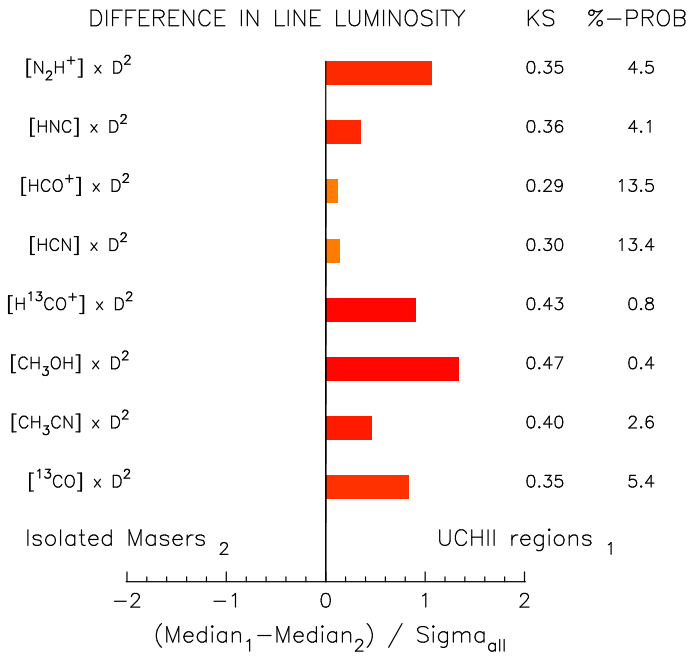

Figure 5.12. The bars in this horizontal histogram represent the difference between the median values of two distributions. Here, we compare *spectral line luminosity* in sources with and without UCHII regions. A positive value means the line is more luminous towards UCHII regions. To asses the significance of the differences, we compute the KS-statistic (left column) and associated percentage probability (right column). As a visual aid, the colour of the bars is scaled to the probability. Probabilities smaller than approximately two per cent (red bars) indicate significant differences.

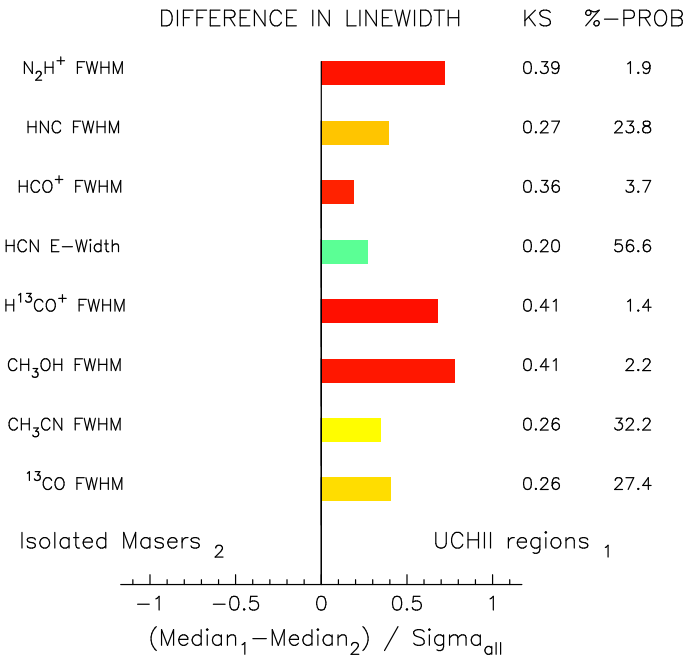

Figure 5.13. Differences in the median linewidth, for sources with and without an associated UCHII region. The linewidths were measured in two ways: by fitting a Gaussian to the line profile and measuring the full-width at half-maximum, or by integrating under the line and computing the equivalent width.

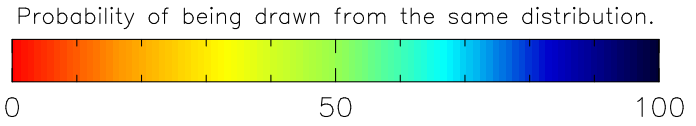

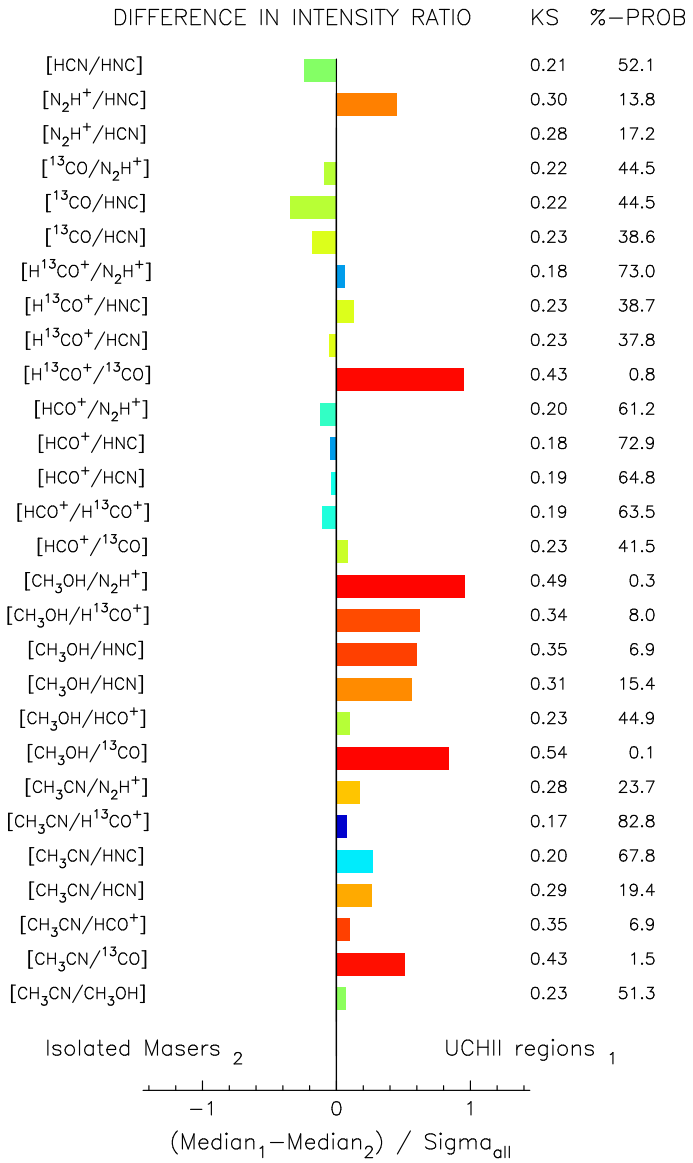

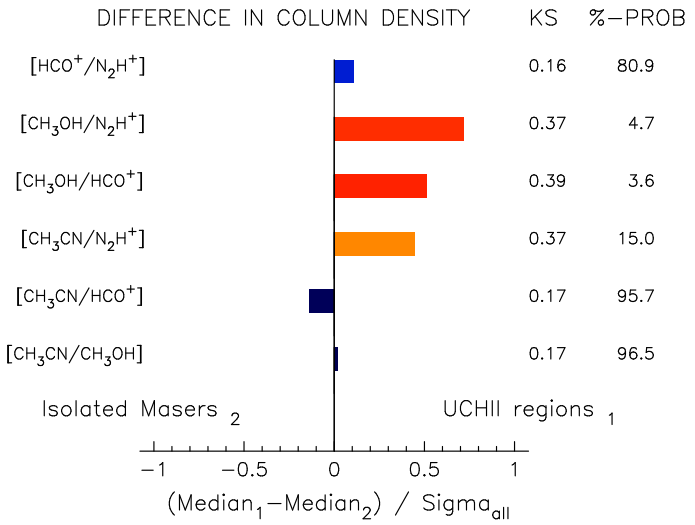

Figure 5.14. Differences in the median line-line intensity ratio (*left*) and column density (*right*), for sources with and without an associated UCHII region.

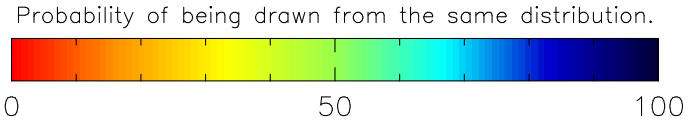

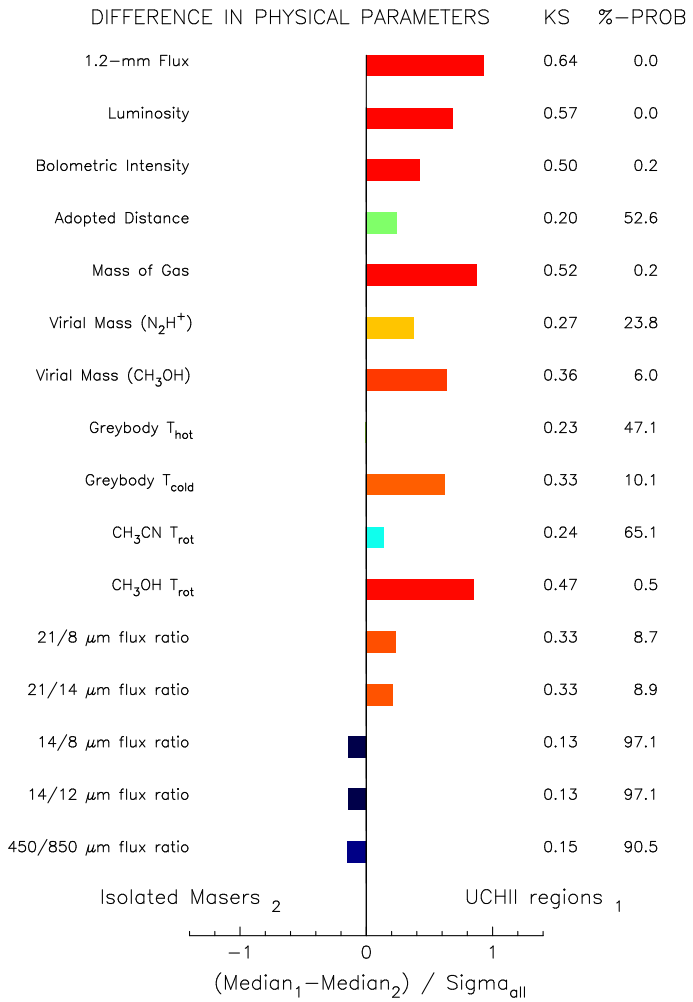

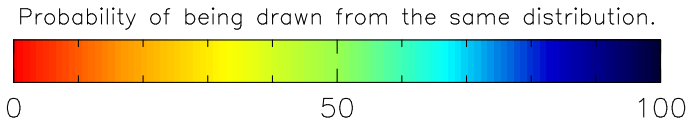

Figure 5.15. Differences in other computed and measured parameters, for sources with and without an associated UCHII region.

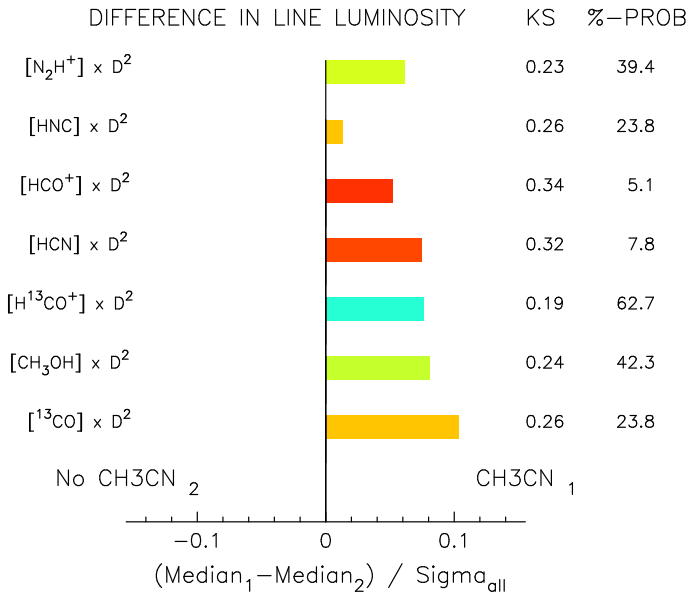

Figure 5.16. Differences in the median line luminosity, for sources with and without CH_3CN.

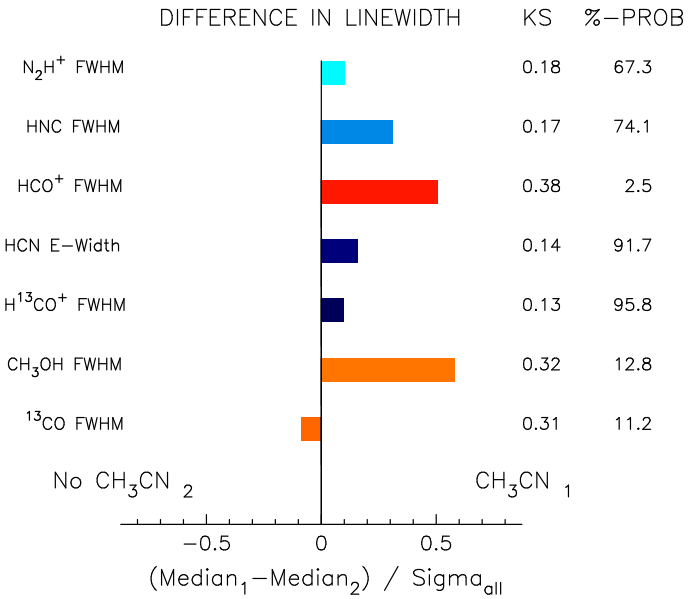

Figure 5.17. Differences in the median linewidth, for sources with and without CH_3CN.

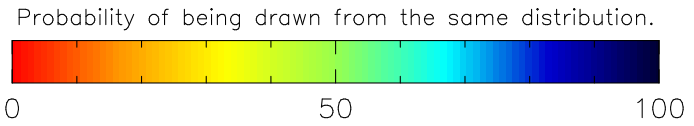

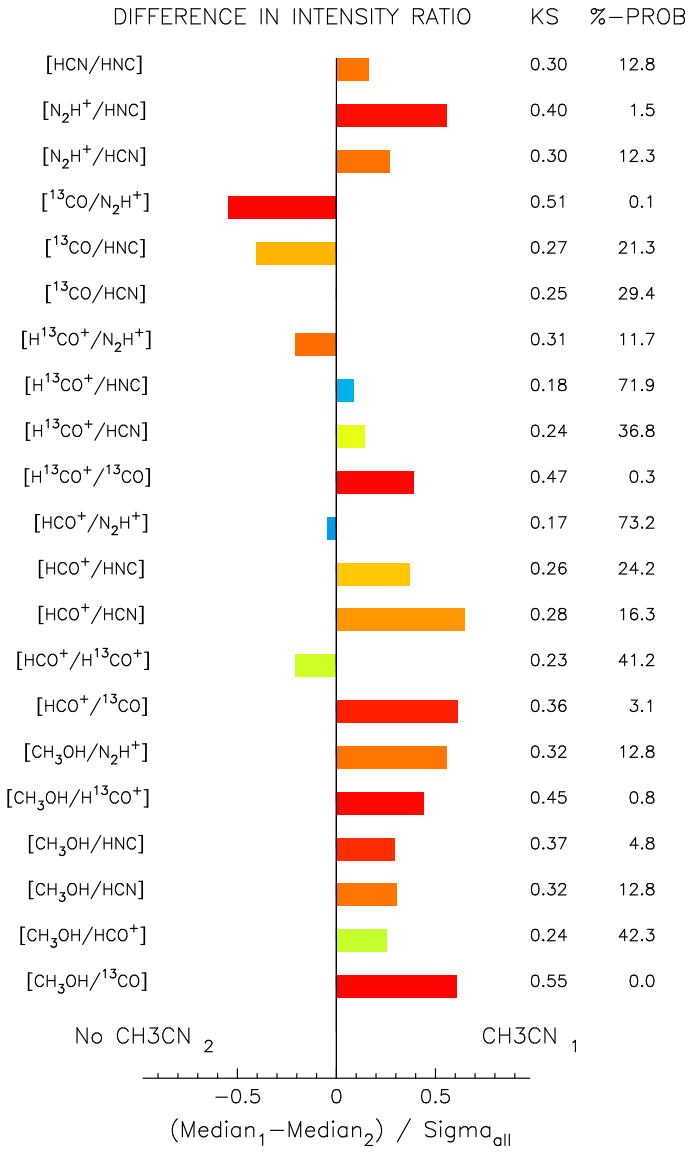

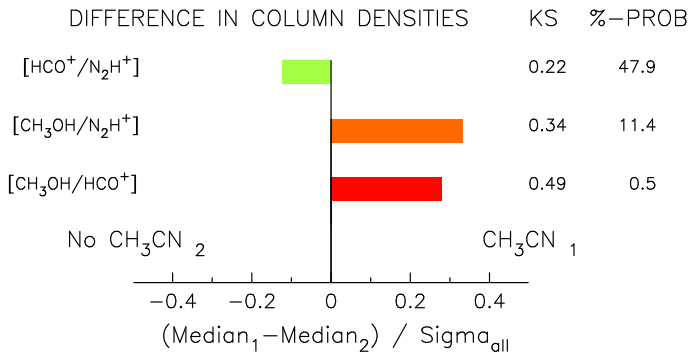

Figure 5.18. Differences in the median line-line intensity ratios (*left*) and column densities (*right*), for sources with and without CH_3CN.

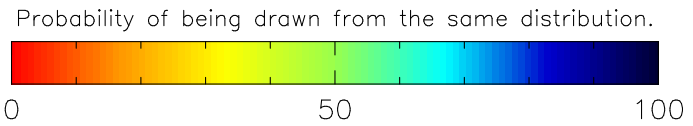

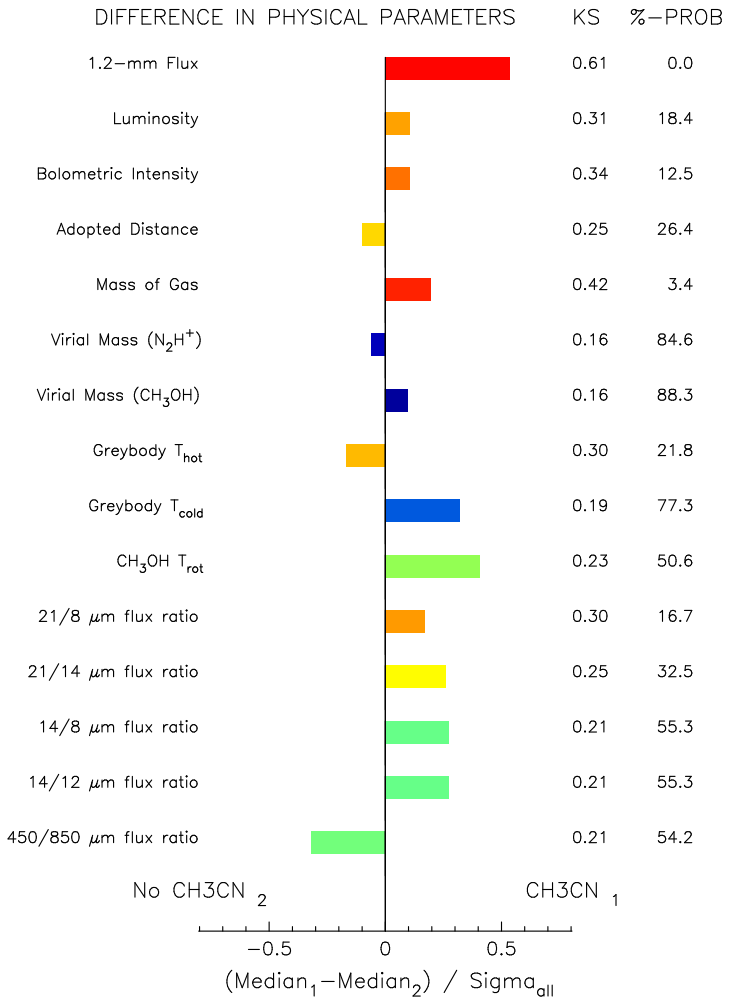

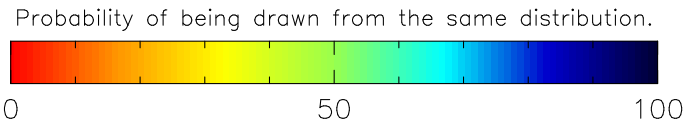

Figure 5.19. Differences in other computed and measured parameters, for sources with and without CH_3CN.

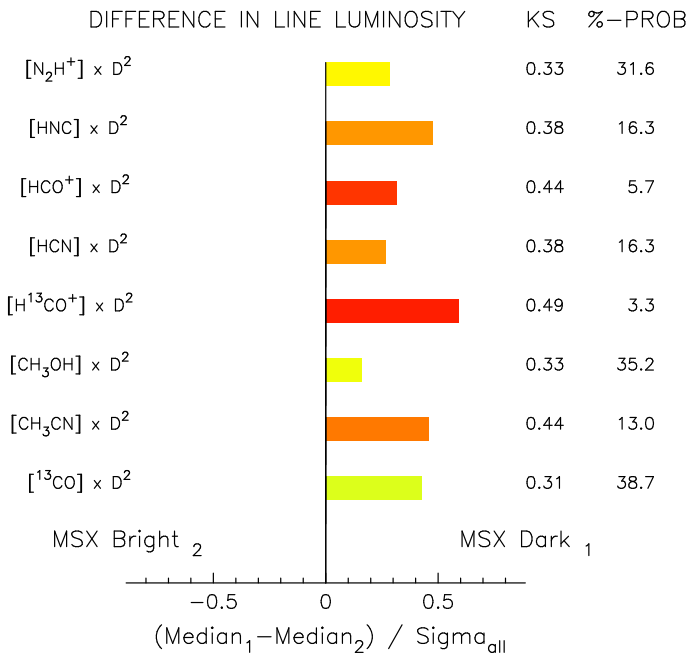

Figure 5.20. Differences in the median line luminosity, for sources seen in absorption in the 8 μm MSX band (MSX-dark) versus those seen in emission (MSX-bright).

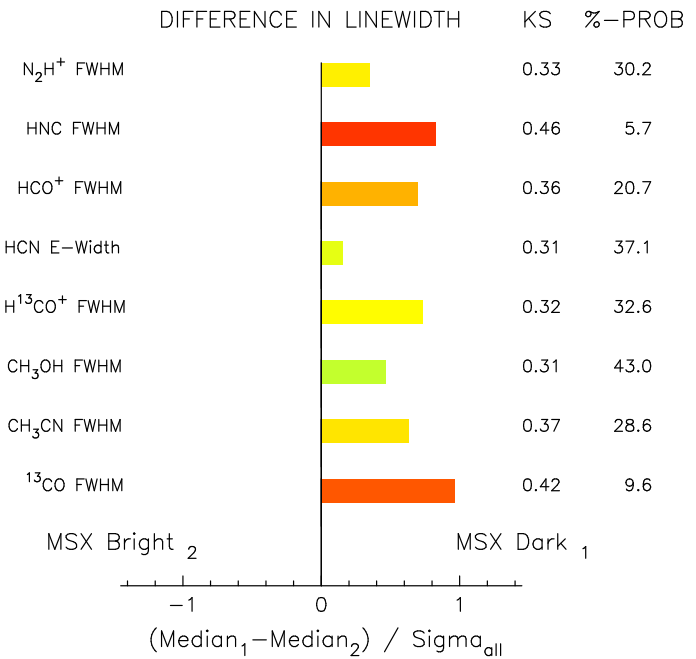

Figure 5.21. Differences in the median linewidth, for sources in the MSX-dark and MSX bright sub-samples.

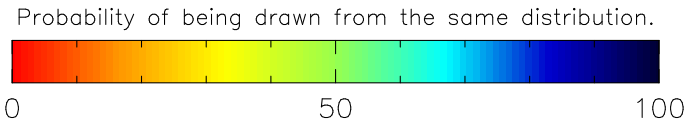

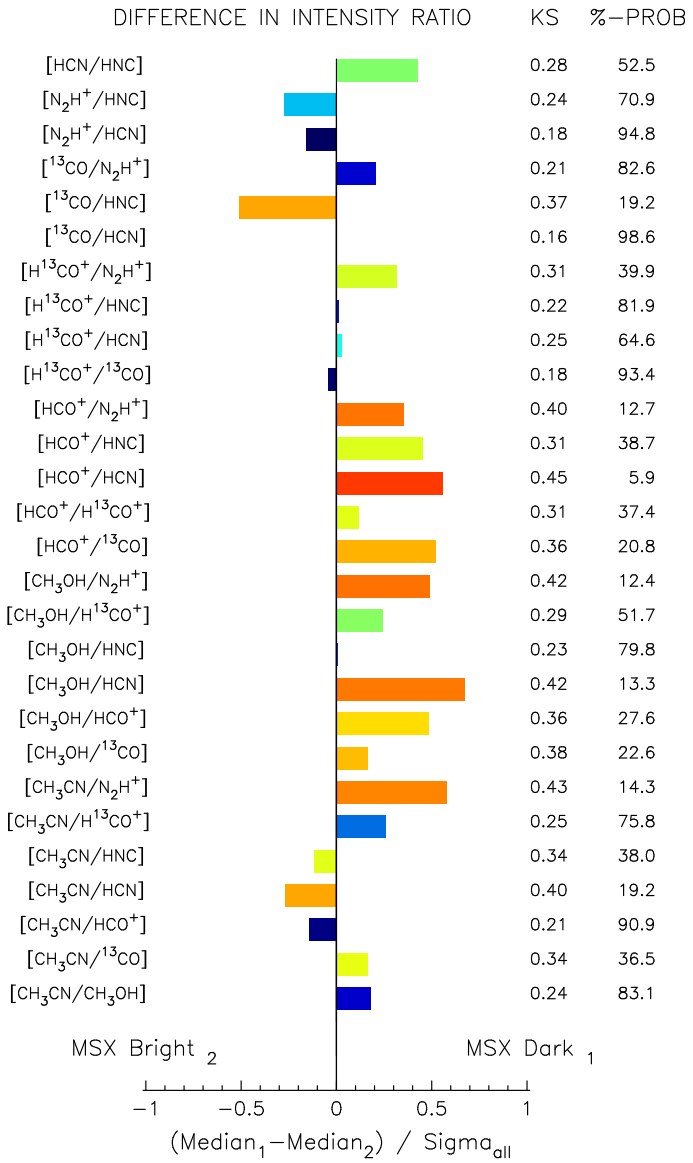

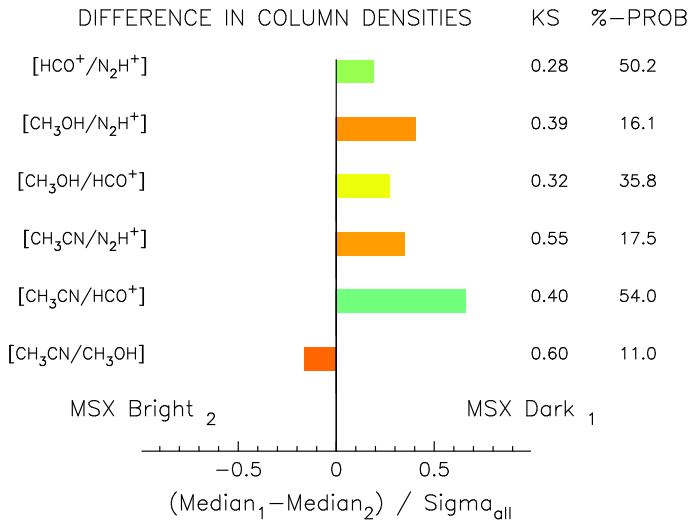

Figure 5.22. Differences in the median line-line intensity ratios (*left*) and column densities (*right*), for sources in the MSX-dark and MSX-bright sub-samples.

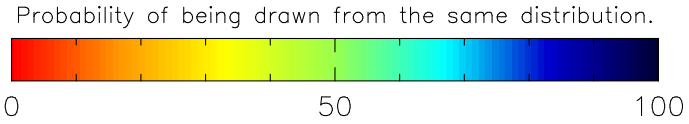

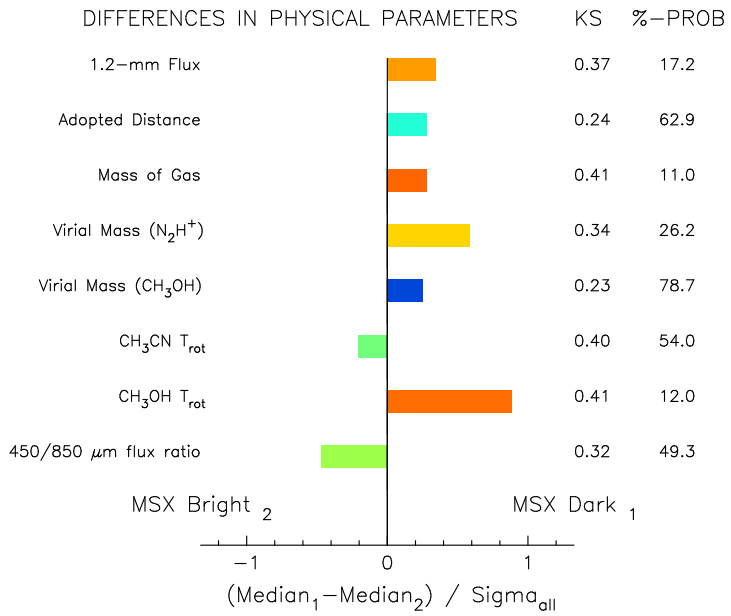

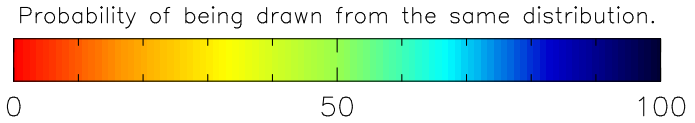

Figure 5.23. Differences in other computed and measured parameters, for sources in the MSX-dark and MSX-bright subsamples.

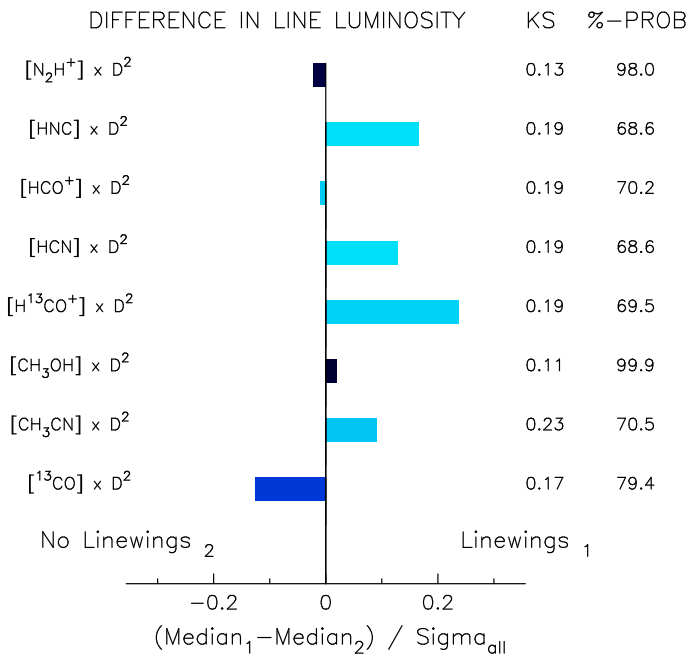

Figure 5.24. Differences in the median line luminosity, for sources with and without emission from high velocity line wings.

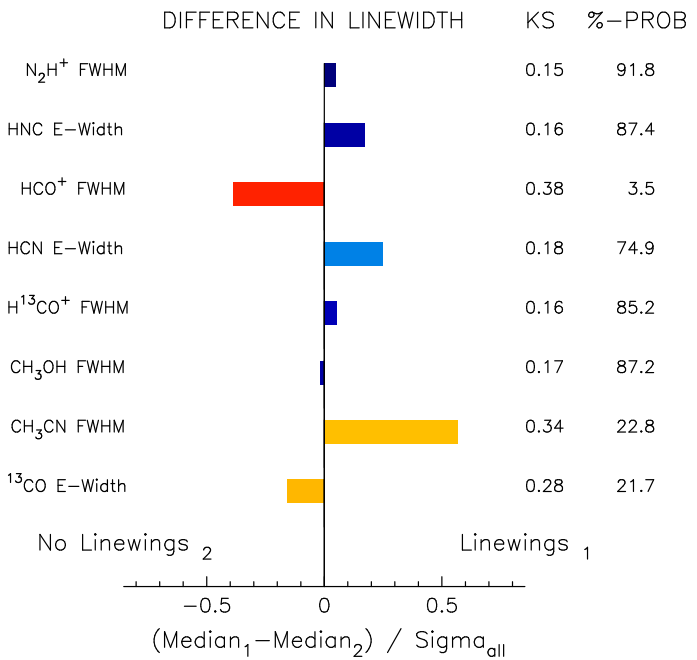

Figure 5.25. Differences in the median linewidth, for sources with and without high velocity line wings.

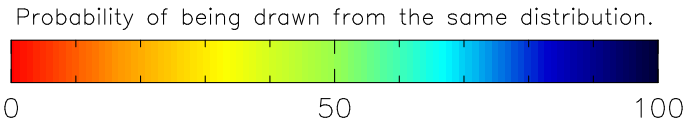

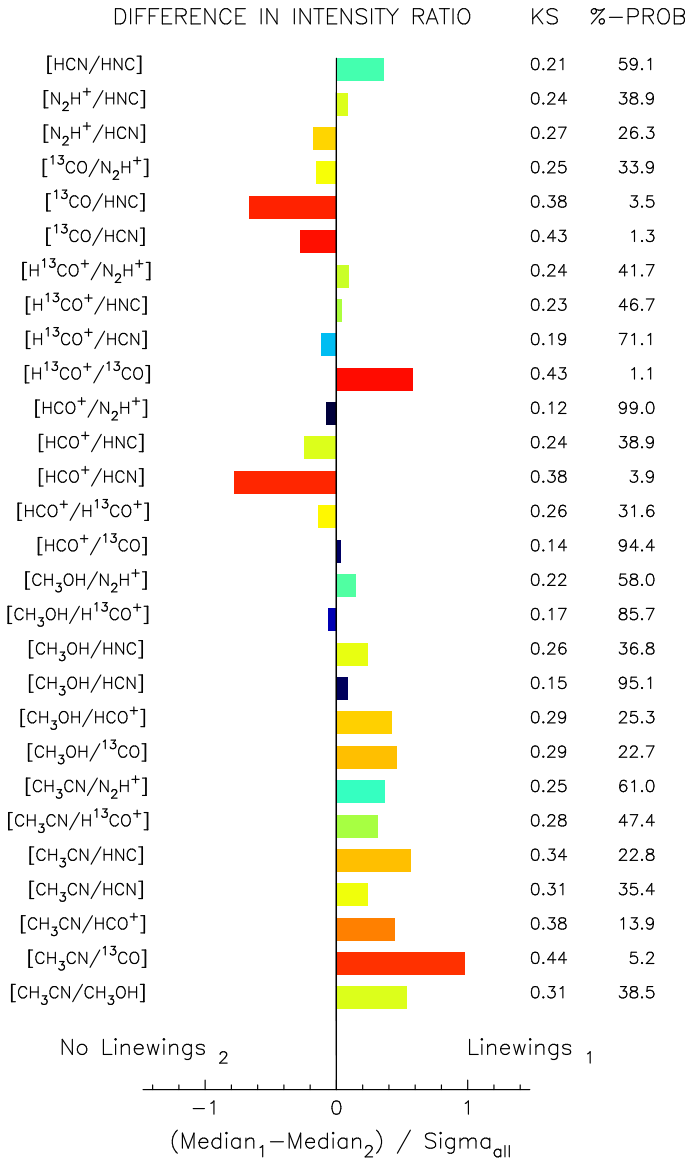

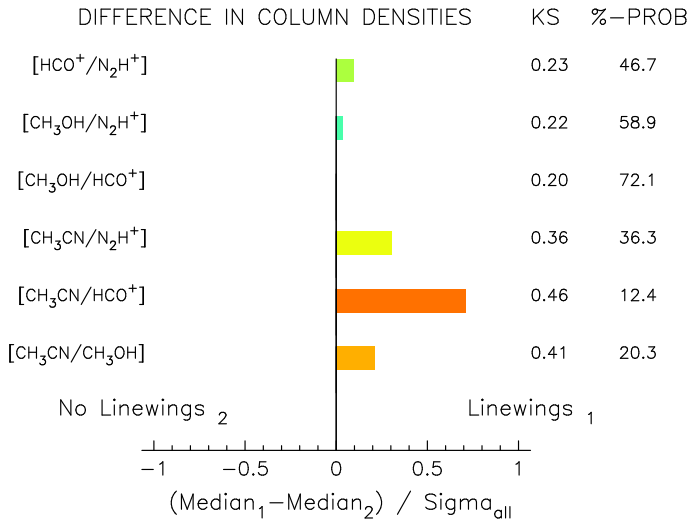

Figure 5.26. Differences in the median line-line intensity ratios (*left*) and column densities (*right*), for sources with and without high velocity line wings.

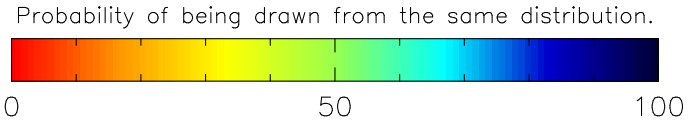

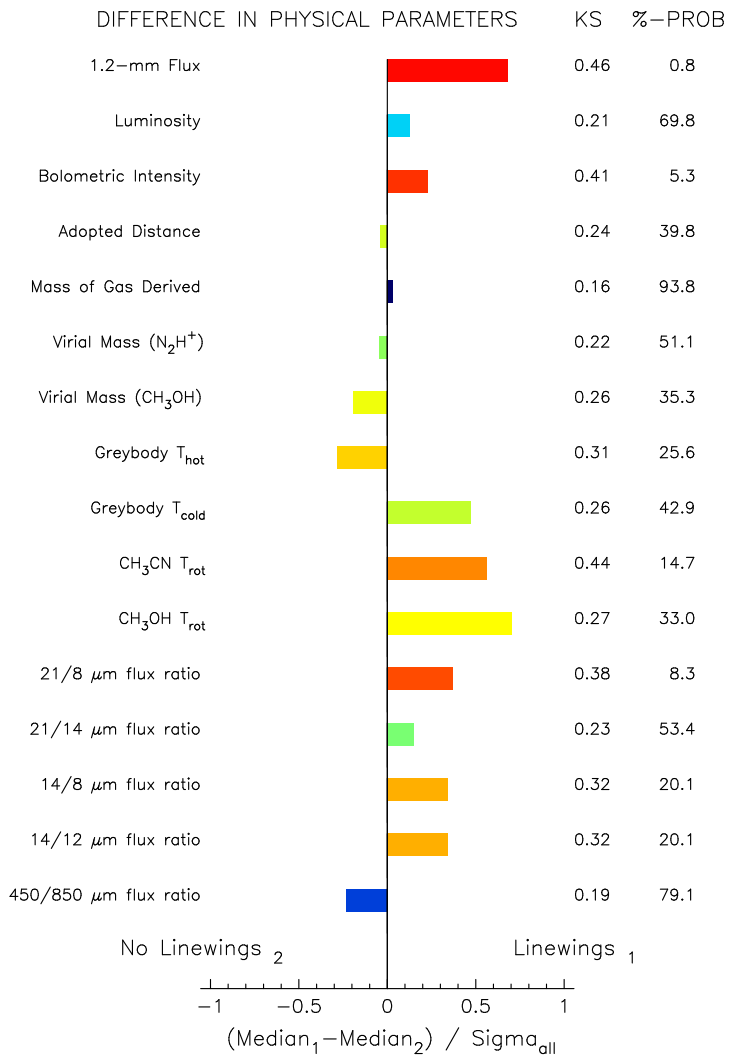

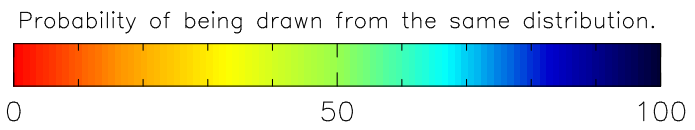

Figure 5.27. Differences in other computed and measured parameters, for sources with and without high velocity linewings.

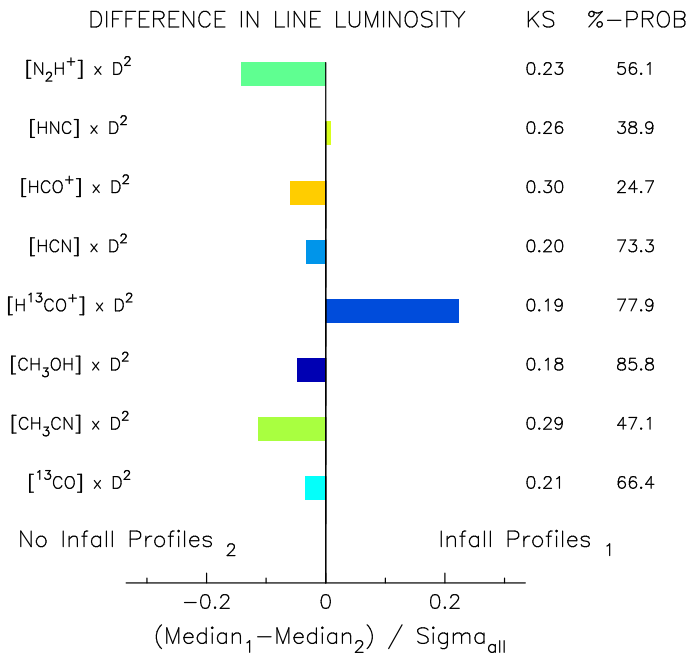

Figure 5.28. Differences in the median line luminosity, for sources with blue shifted HCO^+ line profiles (indicating inward motions) and those without.

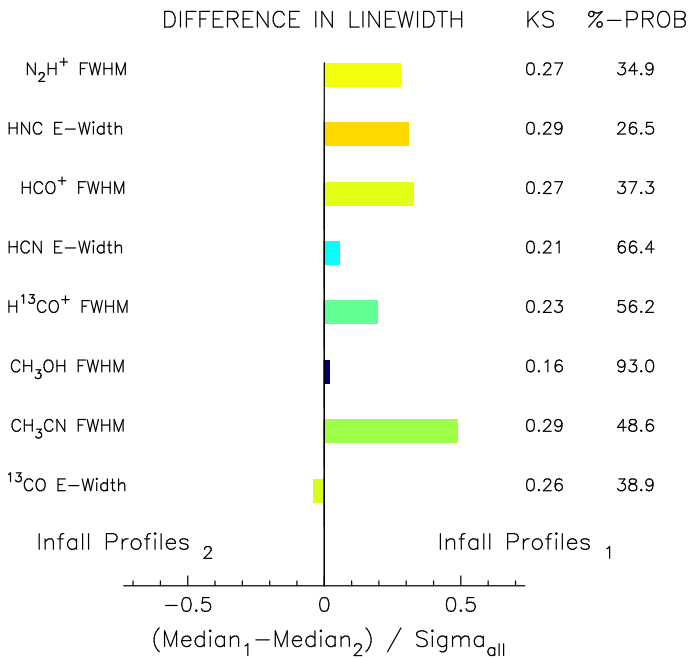

Figure 5.29. Differences in the median linewidth, for sources with and without 'infall profiles'.

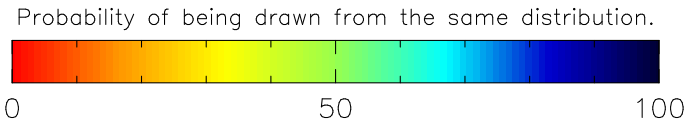

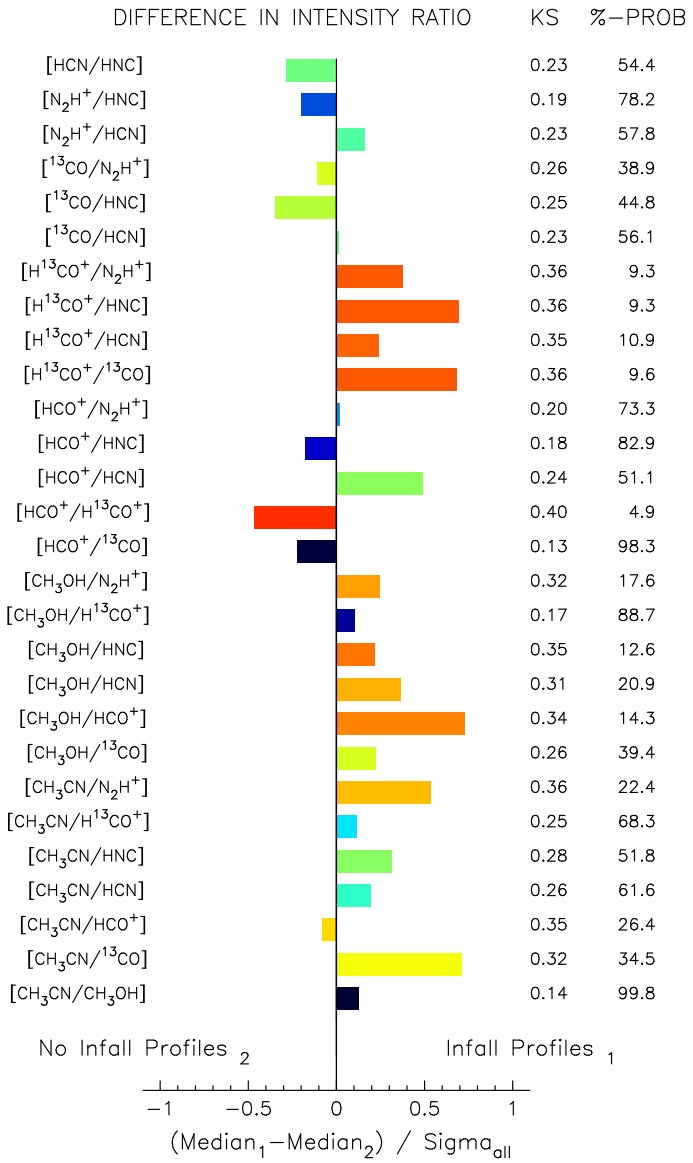

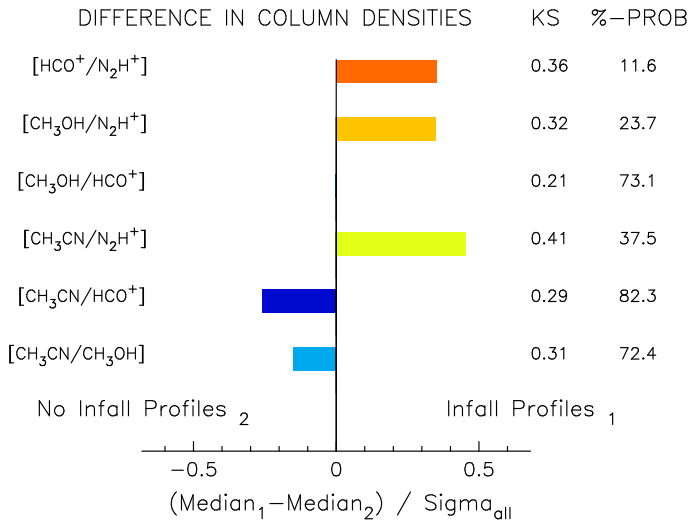

Figure 5.30. Differences in the median line-line intensity ratios (*left*) and column densities (*right*), for sources with and without 'infall profiles'.

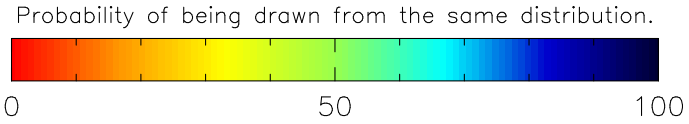

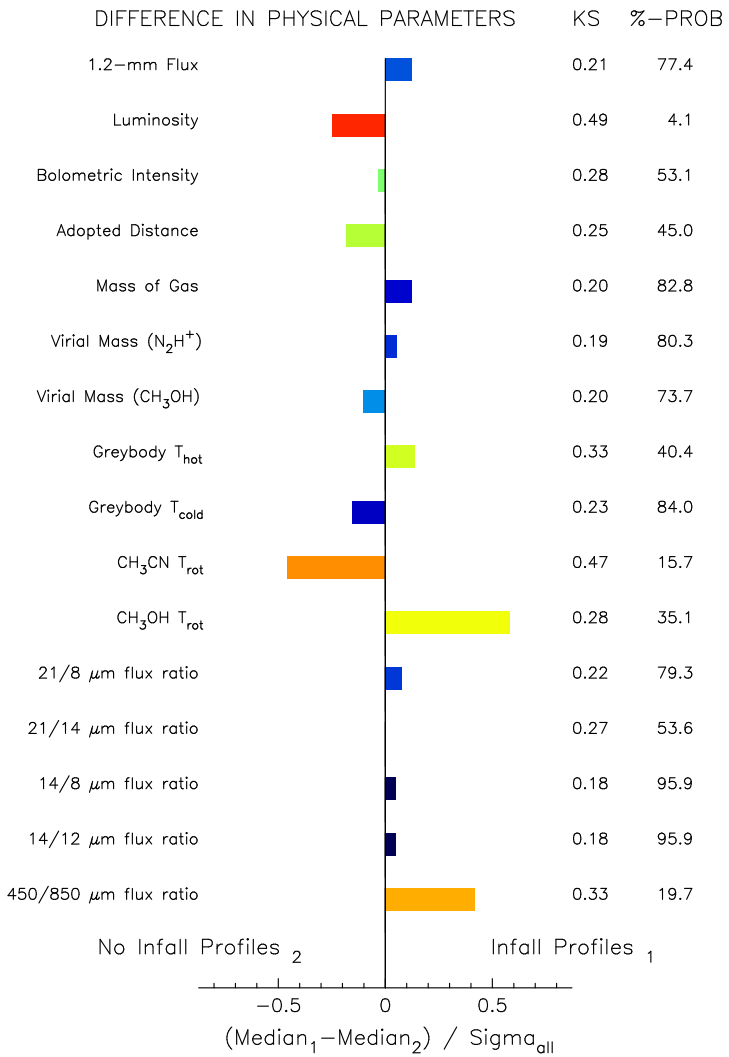

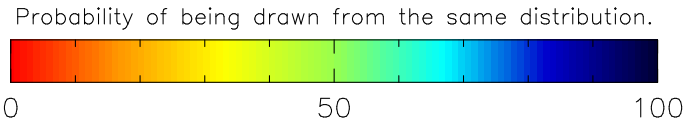

Figure 5.31. Differences in other computed and measured parameters, for sources with and without 'infall profiles'.

and without infall profiles. $H^{13}CO^+$ is biased towards greater luminosity in the sources with infall profiles while all other molecules have similar or lower luminosities. None of the differences are significant.

The linewidths of most species in the 'in-falling' group are biased towards being marginally wider (see Figure 5.29), however difference in the median values is slight for all species, with CH_3CN exhibiting the greatest difference at 0.5-σ. A KS-test does not distinguish between the two populations.

A comparison of line intensity ratios is also inconclusive (Figure 5.30 *left*). HCO^+ is biased weaker and $H^{13}CO^+$ is biased brighter in the 'infall' group. This is almost certainly a selection effect, as a high signal-to-noise ratio was needed on the $H^{13}CO^+$ profile to identify infall, and the HCO^+ suffer from extreme optical depth effects. CH_3OH is biased towards being marginally more intense in the objects with infall profiles, but again a KS-test cannot distinguish between the distributions with confidence. A comparison of the median column-densities, shown in Figure 5.30 (*right*) is similarly inconclusive.

Figure 5.31 presents the median differences between other measured parameters. The most significant difference between the two groups lies in the luminosity, which is marginally lower in the sub-sample with infall profiles. The mean rotational temperatures derived from CH_3CN and CH_3OH are marginally lower and higher, respectively, towards the infall-profile group. In all other respects the sample are close to identical.

5-5.2.6 The effect of beam dilution

As mentioned in section 5-4.6 the beam filling factors constitute an unknown source of error when comparing the intensities or column densities of two molecules. If both emitting regions subtend angles (Θ) smaller than the beam, then we must correct for the relative volume filling factor, given by $(\Theta_1/\Theta_2)^2$. Assuming the emitting regions have similar characteristic sizes in all sources, the relative beam filling factors will average to ~ 1 over the entire sample. However, if one species

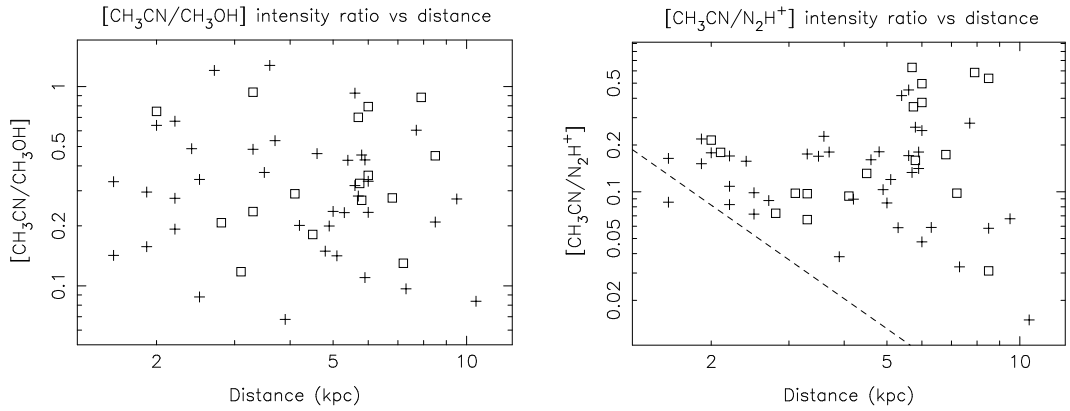

Figure 5.32. Plots of line-line intensity ratio versus distance. (*left*) $[CH_3CN/CH_3OH]$ ratio vs distance. (*right*) $[CH_3CN/N_2H^+]$ ratio vs distance. Crosses mark isolated masers, while squares mark UCHII regions. The dotted line show how the $[CH_3CN/N_2H^+]$ ratio is expected to decrease with distance if the CH_3CN emission has a fixed physical size and the N_2H^+ emission always fills the beam.

generally fills the beam while the other species is generally beam-diluted (i.e., one has constant angular size while the other doesn't, then we would expect a $1/\text{distance}^2$ dependence in the line intensity ratios. Figure 5.32 presents two plots of line intensity ratio versus distance. The left panel plots the CH_3CN/CH_3OH ratio versus distance. The emission from both molecules is expected to derive from regions smaller than the $36''$ Mopra beam, even for nearby sources. We see the line-ratios are not correlated with distance, consistent with a constant ratio between the angular sizes of the species. The right panel plots the CH_3CN/N_2H^+ ratio versus distance. Assuming N_2H^+ emission closely follows the dust morphology, we have shown in Table 5.5 that the beam-dilution factor is generally close to 1. In Figure 5.32 (*right*) the dashed line plots the expected effect of CH_3CN beam dilution as a source is moved further away. We see the scatter in measured line-ratio increases with distance making it difficult to interpret the data and, in addition to beam dilution, chemical and physical differences in the sources affect the line intensity ratios. Omitting the UCHII regions (squares) and considering only isolated masers (crosses), we see a possible trend towards decreasing CH_3CN/N_2H^+ ratio with increasing distance. This trend does not approach the $1/\text{distance}^2$ dependence expected, but it may

indicate that some of our comparisons will include beam dilution effects for CH_3CN.

5-5.2.7 Interpretation and discussion

It is clear we are seeing significant differences between sources associated with different tracers. In this section we summarise the differences between the sub-samples and suggest some possible interpretations of the results.

UCHII regions vs isolated masers

The clearest distinctions exist between isolated CH_3OH masers and UCHII regions. The result found in Chapter 4, where the CH_3CN and HCO^+ lines were shown to be more luminous and have greater linewidths in the presence of a UCHII region, has been extended to the other observed species. When we examine the raw line intensity ratios, CH_3OH distinguishes itself as being relatively intense towards the radio loud sources. This is reflected in both the higher median column density and CH_3OH rotational temperature. We interpret this result as evidence for an enhanced abundance of CH_3OH in relatively warm gas nearby the UCHII regions. Significant differences are also found between other tracers of high and low density gas. The $[CH_3CN/^{13}CO]$, $[N_2H^+/^{13}CO]$ and $[H^{13}CO^+/^{13}CO]$ ratios are enhanced in the radio-loud sub-sample, possibly indicating different excitation conditions or abundances in the 'core' compared to the 'envelope' gas. Interestingly, when compared to all other lines, the relative brightness of the hot-core tracer CH_3CN is *not* significantly greater, yet we detect it towards 95 per cent of UCHII regions and only 63 per cent of the isolated masers.

A potential explanation for the median offset in line-luminosity and linewidths may be found in the significantly greater bolometric luminosity and gas-mass of the radio-loud sample. Simply put, more luminous clumps will likely have a greater flux of IR-photons and higher gas temperatures. Under these conditions one would expect to see more luminous spectral lines. Linewidth is commonly used as a proxy for star formation activity, and hence evolutionary state, as it is largely dependant on turbulence in massive star forming regions. However, on the scale of molecular

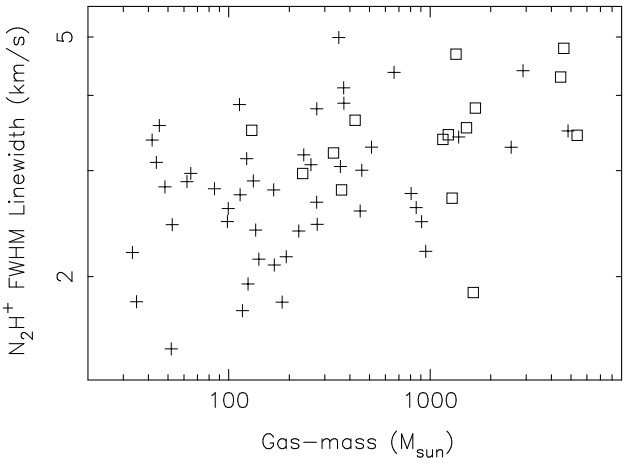

Figure 5.33. Plot of N_2H^+ FWHM linewidth versus gas-mass. Squares represent UCHII regions and crosses represent isolated masers.

clouds (3-20 pc) the linewidth has also been empirically correlated with the cloud mass (Solomon et al. 1987), possibly due to multiple (sub)-clumps with different velocities within the beam. It is unclear which effect dominates in our sample. Figure 5.33 plots the linewidth of a representative molecule, N_2H^+, versus the gas-mass. A weak correlation is observed which may account for some of the linewidth differences between the groups, however we cannot rule out an evolutionary effect.

That the relative intensity and abundance of CH_3OH is greater towards the radio-loud sources likely reflects real chemical differences between the sub-samples. This may be interpreted as evidence for the more advanced evolutionary state of the radio-loud sample. CH_3OH abundance is predicted to be enhanced by a number of mechanisms as a massive young stellar object evolves. In the hot-core phase it is known to be evaporated from the dust grains as the heating source evolves (Charnley et al. 1995). The abundance of CH_3OH is also predicted to be enhanced in the walls of outflow cavities, where it is sputtered from the grains by low-velocity shocks (Hogerheijde 2005).

CH_3CN-bright vs CH_3CN-dark

We find sources with detected CH_3CN are also biased towards having greater line-luminosities and linewidths, although these differences are not as pronounced as with

the radio-loud versus radio-quiet division. The most striking result is the significant tendency for CH_3OH to be brighter and have a greater column-density in the CH_3CN bright group. This is not unexpected as the CH_3CN and CH_3OH abundances are predicted to increase with time in hot cores (Charnley et al. 1995). We also see evidence for higher excitation conditions in the dense gas (traced by N_2H^+ and CH_3OH) compared to more extended and diffuse gas (traced by ^{13}CO), implying a more advanced evolutionary state in the CH_3CN-bright sub-sample. Interestingly, the CH_3CN-bright sub-sample also has a significantly greater median mass, which may bias this result. CH_3CN is also not detected in sources with distances greater than 10 kpc, suggesting that a small number of sources may contain CH_3CN below the sensitivity limit of our survey.

MSX-bright vs MSX-dark

All species in the MSX-dark sample have marginally greater line-luminosities and linewidths compared to their MSX-bright counterparts, with the ^{13}CO linewidth being especially notable. This is unexpected, as infrared dark clouds have been postulated to be the young and quiescent precursors to hot cores and UCHII regions (Rathborne et al. 2006). HCO^+ and CH_3OH tend to be brighter and CH_3OH marginally more abundant in the MSX-dark sub-sample, although this is not judged to be significant. Other parameters are similar in both sub-samples. Given the small number of sources in the MSX-bright subsample (9 – 11 sources), none of the observed differences are large enough to draw any definite conclusions from the data.

Line-wings vs no line-wings

There are no significant differences between the median line-luminosities when the sources are divided into sub-samples with and without high-velocity line-wings. Differences between the HCO^+ linewidth distributions can be attributed to unidentified low-velocity linewings. ^{13}CO is significantly brighter (relative to other lines) in the sources without linewings and CH_3CN is biased towards being brighter and more abundant in the sub-sample with linewings. No distinguishing differences are seen

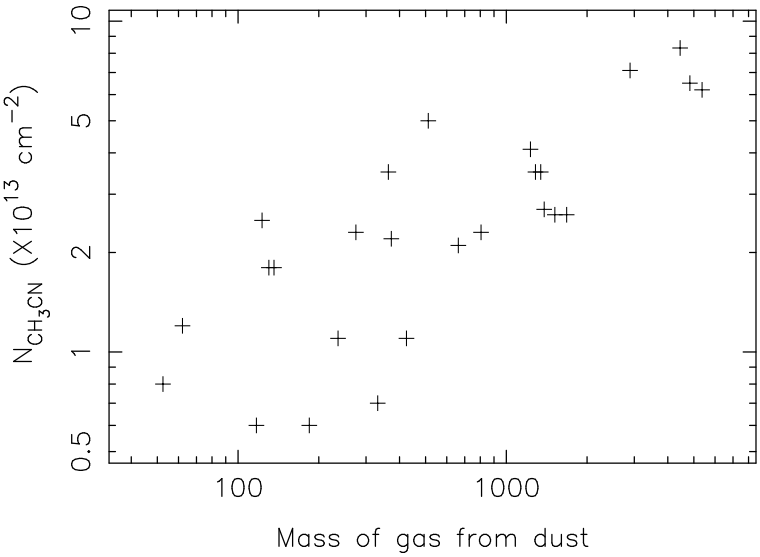

Figure 5.34. Plot of CH_3CN column density versus gas-mass derived from 1.2-mm continuum flux density.

in the physical parameters or IR-colour ratios.

Infall profiles vs no infall profiles

The properties of sources with and without HCO^+ 'infall-profiles' are close to identical. Little difference is seen between the median line-luminosities, linewidths or line intensity ratios. Biases in the $H^{13}CO^+$ and HCO^+ line ratios can be attributed to selection effects.

5-5.3 Further discussion

Is the mass of the hot core related to the dust mass? Figure 5.34 shows a plot of CH_3CN beam averaged column density versus mass of gas derived from 1.2-mm continuum emission. A clear positive correlation is seen between the two. If we assume the column of CH_3CN is a proxy for the size of the hot core, then it follows that the size of the hot core increases with the mass of the extended clump. This is consistent with the results of Cesaroni (2005) who found that the hot core is an extension of the clump, and there is no break in the approximately $1/r^2$ density power law. Rather, the hot core is differentiated by temperature and excitation

conditions influenced by the central heating source.

5-6 Summary and conclusions

In continuation of the Hot Molecular Cores survey we used the Mopra telescope to search for 3-mm transitions of CH_3OH (2 – 1), N_2H^+ (1 – 0), ^{13}CO (1 – 0), HCN (1 – 0) and HNC (1,– 0). Molecular emission was detected in all but one source (G10.10−0.72), with N_2H^+, ^{13}CO, HNC and HCN detected towards all of the remaining 82 targets. CH_3OH emission was detected in 88 sources (95 per cent). The following conclusions have been drawn from the data:

1. Virial masses estimated from N_2H^+ are comparable to or lower than the gas masses of the sample. Values for M_{gas} have been calculated from the 1.2-mm dust emission and range from $30\,M_\odot$ to $5\times10^3\,M_\odot$, while values for M_{virial} range from ~40 to $2.5\times10^3\,M_\odot$. We have assumed a $1/r^2$ spherical density profile and that the N_2H^+ emission follows the 1.2-mm dust emission closely.

2. H_2 volume densities have also been estimated from the surface brightness and extent of 1.2-mm emission. The mean value is $5\times10^4\,cm^{-3}$, however, we note that the assumptions inherent in the calculation introduce large unknown uncertainties in values for individual sources.

3. Rotational temperatures derived from CH_3OH range from 3.0 K to 14.0 K, with a mean value of 6.7 K. These anomalously low temperatures strongly suggest that the CH_3OH is sub-thermally excited. Assuming the same excitation temperature, we find the abundance ratio of A to E-type CH_3OH ranges from 0.5 to 2.8, with a mean of 1.5, consistent with previously published values.

4. N_2H^+ is found to be optically thin towards most of the sample, implying low column or volume densities in the 36″ Mopra beam. Likewise the CH_3OH rotational diagrams are consistent with low optical depths in the J = 2 – 1 transitions. ^{13}CO, HCN and HNC all exhibit line profile asymmetries and may be significantly optically thick.

5. The *luminosity/gas-mass* relationship for the sample is found to follow a rough power law of the form $L \propto M^{0.68}$, meaning that the lower mass clumps are over-luminous and the higher mass clumps are under-luminous. We find that the gas-mass of the clumps is comparable to or greater than the mass of the stellar content (implied by the luminosity). We interpret this as an indicator of young ages, as the newborn massive stars still retain their natal molecular clouds.

6. The radio loud sub-sample (UCHII regions) are on average more massive *and* more luminous than the radio-quiet sub-sample (isolated masers). We argued in Chapter 4 that UCHII regions are detectable in the majority of our sample, however, it now appears that the most likely explanation is a sensitivity limit in the original Walsh et al. 1999 radio survey. It is also possible that the isolated maser sample contains undetected hyper-compact HII regions and so the effect may be due in part to evolution.

7. We separated the source list into sub-samples associated with different tracers of evolution and compared their median physical and chemical properties. Our findings are as follows:

   - *All* spectral lines are brighter and more luminous towards the radio loud sample, extending the result found in Chapter 4.
   - The CH_3OH brightness and abundance is found to be enhanced (compared to other species) in radio-loud and CH_3CN-bright sources. We suggest that in single-dish observations CH_3OH may be used as a crude molecular clock to indicate the evolutionary state of a clump.
   - Given the small sample size, conclusions drawn from a comparison of MSX-bright and MSX-dark sources are not significant. It is worth noting, however, that linewidths and line-luminosities are generally greater in the infrared dark clouds, indicating perhaps that when selected using CH_3OH masers, dark-clouds conceal objects at later stages of evolution.
   - We divided the source list into sub-samples with and without high velocity

linewings and HCO^+-infall-profiles, but found no significant differences in chemical or physical properties.

8. We find that the beam-averaged column density is correlated with the gas-mass derived from 1.2-mm emission. This suggests that the mass of the hot-core is dependant on the mass of the clump in which it is embedded.

Chapter 6

Dissecting the star-forming region NGC 3576

A necessary precursor to massive star formation is the existence of dense clumps of self-gravitating gas. Elmegreen (1998) developed the first coherent picture of sequential star formation, in which the formation and collapse of these clumps within giant molecular clouds is triggered by an external event. Three distinct triggering mechanism are considered:

1. Globule squeezing: compression of pre-existing clumps, e.g. due to a propagating shock-wave from a supernova.

2. Cloud-cloud collisions: two molecular clouds collide resulting in gravitational instabilities.

3. Collect and collapse: accumulation of gas into a shell or ridge, and subsequent fragmentation and collapse.

Examples of the latter mechanism are observed to occur on the edges of HII regions. Created by the far-UV radiation from a young OB-cluster, the hot ionised gas expands rapidly, sweeping up a shell of dense molecular material before it. A photon dominated region (PDR) is created at the interface between the HII region and the molecular cloud (see Hollenbach & Tielens 1999 for a review of PDRs).

If the PDR is over-pressured compared to the bulk of the molecular gas, shocks are driven into the dense neutral medium of the cloud, potentially leading to its fragmentation into clumps (c.f. Urquhart et al. 2006 and references therein). Subsequent disturbances may then trigger collapse and hence star formation. Material swept into a core shields the column of molecular material behind it, forming giant pillars, the best known example of which are the 'elephant trunks' in the Eagle Nebula (White et al. 1999; Allen et al. 1999). Recently observed examples of swept-up shells around HII regions include W5 (Karr & Martin 2003), RCW 49 (Whitney et al. 2004), RCW 79 and (Zavagno et al. 2006).

It is important to note that energy injected into molecular clouds by newly formed stars may instead quench the star formation process. Supersonic particle-winds from massive stars account for ∼0.1 - 1.0 per cent of the stellar luminosity and act to disperse molecular material and dust (Genzel 1991). The two most important feedback mechanisms, photonisation and the cluster winds, compete with each other to disrupt the cloud. On the scale of giant molecular clouds, feedback from newly formed stars is responsible for regulating the star-formation rate and hence the evolution of Galactic structure.

In this chapter we present new multi-wavelength observations of the giant HII region NGC 3576, which is claimed to be undergoing sequential star formation. We examine the evidence for star formation in the nearby molecular environment.

6-1 Introduction

The environment of the giant HII region NGC 3576 (also known as RCW 57, G291.3−0.7 and IRAS 11097−6102) has been extensively studied at infrared and radio wavelengths. Figure 6.1-A presents a 3-colour composite image of the region made using 2MASS[1] near-infrared data. In the image, blue is 1.2 μm (J-band), green is 1.65 μm (H-band) and red is 2.17 μm (K-band). The HII region can be

1. 2MASS data is available online from the 2MASS image server at: http://www.ipac.caltech.edu/2mass/

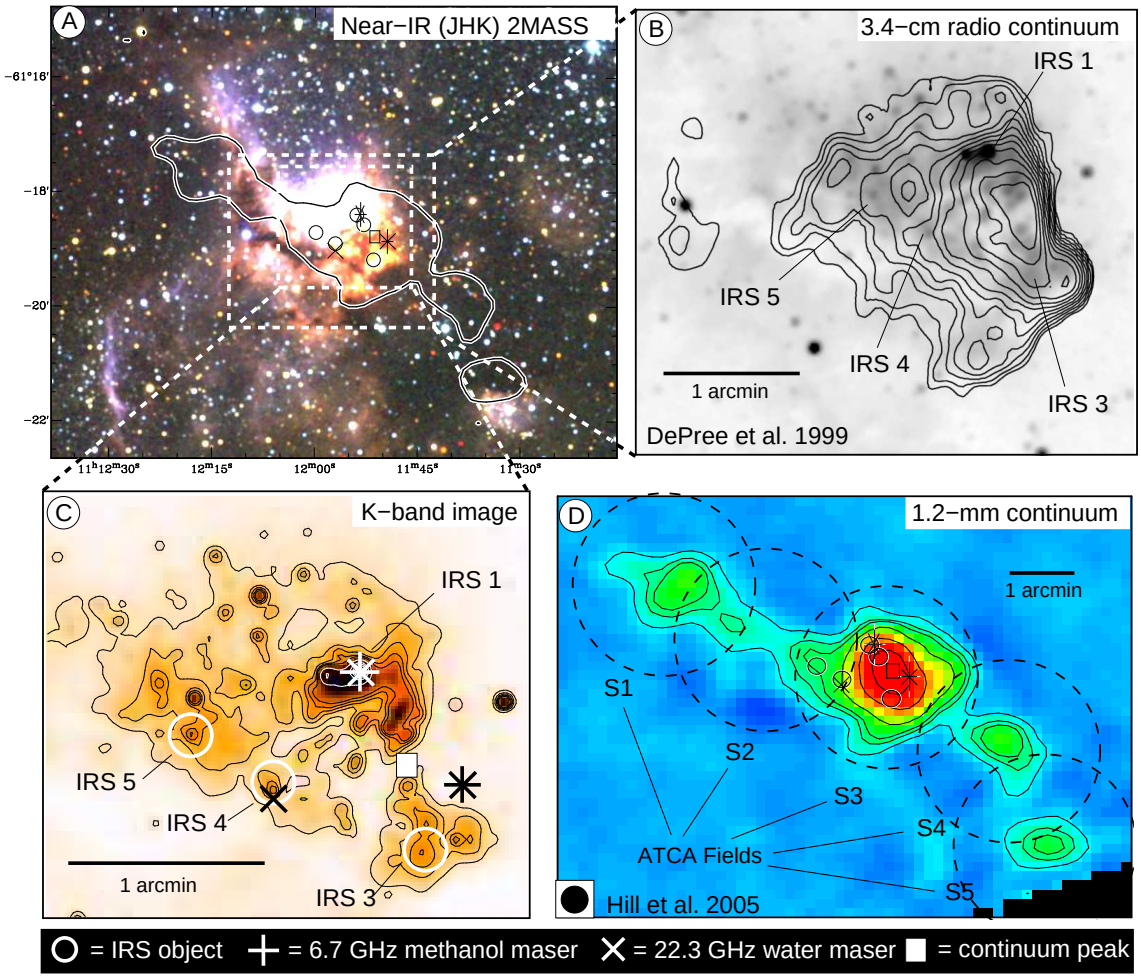

Figure 6.1. Overview of the NGC 3576 star forming region. (**A**) 3-colour near-infrared image of the region, made from 2MASS data. B = 1.2 μm, G = 1.65 μm, R = 2.17 μm. (**B**) Contours of the 3.4-cm free-free emission from ionised gas in the giant HII region at the heart of the complex (de Pree et al. 1999) plotted over the 2.2 μm K-band image. (**C**) 2MASS K-band image showing the positions assigned to the original infrared sources (IRS) discovered by Frogel & Persson (1974) and the positions of CH_3OH and H_2O masers. Contours are set at 1 per cent intervals from 1–5 percent of peak to highlight the extended emission, and at 10 percent intervals from 10 – 90 percent thereafter. (**D**) 1.2-mm continuum image of the complex (Hill et al. 2005) showing the dusty filament running across the HII region. The 5 percent contour of the dust emission is also drawn on the 3-colour near-infrared image. In panels A, C and D, '+' marks methanol maser positions, '×' marks water maser positions, circles mark the IRS objects and '□' marks the peak of the radio-continuum emission.

seen via the bright nebulosity in the centre of the field. Figure 6.1-B illustrates the 3.4-cm free-free emission mapped by de Pree et al. (1999). The ionised gas covers the brightest infrared emission, peaking sharply in the west and extending $\sim 2'$ to the north-east and south. Frogel & Persson (1974) discovered five near- and mid-infrared sources in the ionised gas, with the brightest source (IRS 1) located adjacent to the main peak of the radio emission (see Figure 6.1-C). Further high resolution photometric observations by Persi et al. (1994) have revealed the presence of a very young, deeply embedded cluster with 130 members in the same region. Spectra of these sources exhibit deep 9.7 μm silicate absorption features (Moorwood & Salinari 1981), leading to their interpretation as pre-main-sequence objects.

There is controversial evidence for sequential star formation in NGC 3576. Persi et al. (1994) showed that a steep near-IR colour gradient exists in the embedded cluster, implying that star-formation began in the east, gradually moving to the location of the strong radio peak in the west. This is supported by the existence of an electron temperature gradient in the ionised gas (de Pree et al. 1999) indicating that the youngest and hottest stars are located near the sharp western edge of the HII region (Hjellming 1966). High helium abundance in the east may also indicate the presence of a population of older stars and their mass loss (Hanson & Conti 1993). Bright 22 GHz water masers, commonly found in outflows, have been found adjacent to the main radio peak (Caswell 2004), while Norris et al. (1993) also detected two 6.67 GHz methanol maser sites near IRS 1 and IRS 3. Shocked molecular hydrogen emission was measured peaking towards IRS 1 by Oliva & Moorwood (1986), also pointing to the existence of outflows. IRS 1 was later resolved into three components by Moneti (1992) and Barbosa et al. (2003), one of which is seen through scattered light from a cavity or a dusty disk (Moneti 1992). None of the detected infrared sources contributes significantly to the ionisation of the HII region, (Barbosa et al. 2003) and it is thought that the main ionising source of NGC 3576 lies behind the dark lane seen in 2.2 μm (K-band) images.

The HII region was mapped at 1-mm wavelengths for continuum emission, with a resolution of $1'$, by Cheung et al. (1980), who found that the flux density ratio

compared to 40-350 μm was consistent with optically thin thermal dust emission. More recently, Hill et al. (2005) used the SIMBA bolometer to map 1.2-mm continuum emission at a resolution of $\sim$24″, as shown in Figure 6.1-D. The SIMBA field covers an area of $4' \times 6'$, centred on the radio peak and reveals that the HII region is embedded in a filamentary structure of cool dust, running north-east to south-west. The dusty HII region is prominent in the centre, however, several bright knots are apparent along the length of the filament. These clumps, designated S1 – S5, fall along the dark lane traversing the nebulosity in the near-infrared image, and are coincident with infrared-dark clouds (IRDCs) in the mid-infrared (e.g., the 8 μm MSX images). IRDCs have been found throughout the Galactic plane with masses in excess of 30 $M_\odot$ and it has been suggested they are the cold precursors to massive star clusters (e.g., Pillai et al. 2006).

NGC 3576 constitutes an ideal laboratory in which to study the process of massive star formation. In particular, we want to investigate if the HII region is interacting with the dusty filament and if star-formation has been triggered in the dense knots along its length. In this chapter we present new observations of the whole filament, in several molecular tracers, with the goal of constraining the star-forming properties of these new cores, and determining the effect of the HII region on the complex.

6-2 Observations and data reduction

Data from three telescopes, the Australia Telescope Compact Array (ATCA), the 22-m Mopra telescope and the 70-m Tidbinbilla telescope, were combined to build up a picture NGC 3576. The ATCA was used to obtain high resolution NH_3 maps as a probe of the density and temperature structure of the filament. We simultaneously searched for UCHII regions via their 23 GHz free-free continuum emission. The ATCA interferometer filters out low spatial frequencies, so we used the Tidbinbilla telescope to map the extended NH_3 emission, providing a measure of the total column of NH_3 in the filament. We utilised the Mopra telescope to map the complex in the 3-mm lines of $^{13}CO\,(1-0)$, $C^{18}O\,(1-0)$, $HCO^+\,(1-0)$, $H^{13}CO^+\,(1-$

Table 6.1. Details of the Australia Telescope Compact Array observing runs.

UT Date	Array Config.	Beam [α] Size (″)	Transitions	Frequency (GHz)	Bandwidth (MHz)	No. Channels
2003 Aug 28	EW367	7.6×6.2	NH_3 (1,1)	23.694480	8	512
			Continuum	23.694500	128	32
			H_2O (6–5)	22.235120	16	16
2004 Jul 02	750D	6.6×2.4	NH_3 (4,4)	24.139417	8	512
			Continuum	22.000000	128	32
2005 Jul 17	H75	26.8×20.9	NH_3 (1,1)	23.694480	8	512
			NH_3 (2,2)	23.722630	8	128

[α] Beam size excluding the 3 km+ baselines to Antenna 6.

0), N_2H^+ (1 – 0) and CS (2 – 1), with the goal of probing the physical and chemical conditions in each of the dusty clumps.

6-2.1 ATCA observations

Observations were made with the ATCA in three blocks during the years 2003 – 2005. Table 6.1 summarises details of the dates, array-configurations and frequencies used. NH_3 (1,1) data was obtained using the EW367 and H75 array configurations in August 2003 and July 2005, respectively. Two orthogonal circular polarisations were observed at each frequency. The raw data was processed in a digital correlator, which was configured to deliver a bandwidth of $\sim 101\,\mathrm{km\,s^{-1}}$ split into $\sim 0.2\,\mathrm{km\,s^{-1}}$ wide channels. NH_3 (2,2) was observed simultaneously with NH_3 (1,1) on the H75 array in June 2005. Due to engineering constraints only 128 channels were available on the correlator, yielding a spectral resolution of $\sim 0.8\,\mathrm{km\,s^{-1}}$ over the $101\,\mathrm{km\,s^{-1}}$ bandwidth. In August 2003 the region was also mapped for 23 GHz continuum and 22 GHz water masers using the EW367 array. Finally, in July 2004, the 750D array was used to simultaneously map the NH_3 (4,4) transition and 23 GHz continuum. The correlator configuration was identical to that used to obtain the NH_3 (1,1) data.

The primary beam of the ATCA at 23 GHz has a full width half maximum of 2.5′. To cover the filament we observed five overlapping fields, marked by dashed lines in Figure 6.1-D and centred on the coordinates of the dusty SIMBA cores. Table 6.2

Table 6.2. Centre coordinates of the ATCA fields.

Field	RA (J2000)	DEC (J2000)
S1	$11^h12^m17.00^s$	$-61^d17^m40.0^s$
S2	$11^h12^m04.90^s$	$-61^d18^m20.0^s$
S3	$11^h11^m51.50^s$	$-61^d18^m52.0^s$
S4	$11^h11^m38.33^s$	$-61^d19^m53.9^s$
S5	$11^h11^m33.86^s$	$-61^d21^m20.9^s$

lists the coordinates of the pointing centres. Each of the five fields was observed for 10 minutes in turn, over the course of one hour. In order to correct for fluctuations in the phase and amplitude caused by atmospheric and instrumental effects, a strong phase calibrator was observed for two minutes before and after changing fields. The instrumental contribution to the bandpass shape was measured by integrating on a strong continuum source (e.g., 0420-014) and was subsequently subtracted from all spectra. A primary flux calibrator (1934-638 or Uranus) was observed once daily, to allow the absolute calibration of the flux scale.

The data were reduced using the MIRIAD package (Sault et al. 1995) following standard procedures. During the data reduction the sources were assumed to be unpolarised and both polarisations were averaged together. Continuum emission was subtracted from the spectral line data by using the task *uvlin* to fit a polynomial to the line free-channels. An image of the continuum emission was produced by combining the line-free channels in the NH_3 data with the dedicated 22 and 23 GHz continuum observations. The *invert* task was used to form images of the five fields and natural weighting was used to minimise the noise in the image-plane. At this stage the $\sim$3 km baselines to antenna CA06 were discarded as the phases were found to be decorrelated, degrading the image quality. All images were deconvolved using the standard *clean* algorithm and, if a sufficiently bright source was present, several iterations of the *selfcal* task were applied. The above procedure was performed on all fields, before using the task *linmos* to mosaic the data into a single map.

6-2.2 Mopra observations

Mopra observations were conducted using the new 'on the fly' (OTF) mapping mode, between the months June – September, during 2004 and 2005. In this mode the telescope alternates between scanning in right-ascension and integrating on an emission-free 'OFF' position. An image is built up by combining overlapping scan rows, each containing 30 – 40 spectra. The OFF positions are later used to subtract the contribution due to sky and atmospheric emission (see section 3-3.2). Scan rows were offset by half of the beam-FWHM and the scanning speed was slow enough to ensure Nyquist sampling in the scan direction.

The need to check pointing accuracy at hourly intervals limits the time devoted to a single OTF map. For observations longer than ~ 1.5 hours the usual procedure is to map several small fields, which are then sewn together to produce the final image. NGC 3576 was divided into an overlapping mosaic of three or more $5' \times 5'$ fields, positioned to cover the 1.2-mm continuum emission. The pointing centres of individual fields varied, depending on where molecular emission was detected, and the final maps were assembled by co-adding the fields together. Each field took ~ 80 minutes to complete, plus a further ~ 10 minutes for pointing checks and calibration measurements.

The signal from the receiver was processed in a digital auto-correlator, configured to have a bandwidth of 64 MHz divided into 1024 channels, which provided a velocity resolution of $\sim 0.2\,\mathrm{km\,s^{-1}}$ over a usable bandwidth of $\sim 120\,\mathrm{km\,s^{-1}}$. The central frequency was chosen so that the channel 512 was centred on the systemic velocity of NGC 3576 at $-24\,\mathrm{km\,s^{-1}}$. Observations were made in dual orthogonal linear polarisation mode and the polarisations were averaged together during the reduction procedure. The pointing accuracy was checked on a nearby SiO maser before observing each field and is estimated to be better than $8''$. Calibration to the T_A^* scale was achieved by measuring the emission from a single hot load, placed in front of the receiver every 20 minutes (see Chapter 3 and Kutner & Ulich 1981). The maps were further calibrated onto the main-beam brightness temperature scale

(T_{MB}) by dividing the T_A^* pixel values by the main beam efficiency η_{mb} at the observing frequency (see Table 3.4).

The data was reduced using the LIVEDATA and GRIDZILLA packages, available from the ATNF. LIVEDATA performs bandpass calibration by subtracting the preceding OFF spectrum from the SCAN spectra in each row. A low-order polynomial is then fit to line-free channels and subtracted, resulting in a smooth baseline at zero Kelvin. The spectra are assigned individual position stamps and regridded to the LSR-K reference frame, before being written to disk. The GRIDZILLA package is then used to resample the maps to a regular pixel scale, weighted according to the system temperature (T_{sys}). To grid the data we used a pixel-size of 6×6 arcsec^2 and a Gaussian smoothing kernel with a FWHM of 18″, truncated at an angular offset of 36″. This resulted in a final resolution of ∼40″.

6-2.3 Tidbinbilla observations

The 70-m antenna located at the NASA Tidbinbilla Deep Space Communications Complex near Canberra has a limited time devoted to radio astronomy. When Mars is above the horizon the 70-m telescope is almost entirely utilised supporting the various NASA missions to that planet and as such has been little used by the radio astronomy community. In 2005 we performed the first frequency-switched spectral line mapping observations using the 23 GHz K-band receiver.

Frequency-switching is an observation mode during which the telescope spends 100 per cent of the time pointed on-source, i.e., no emission-free OFF position is observed. Bandpass subtraction is performed by forming a quotient between alternate spectra. To avoid cancelling out the desired spectral lines, the sky-frequency in each spectrum is shifted by an amount $\Delta\nu$ corresponding to an integral number of channels. The resultant quotient spectra contains two copies of the targeted lines, one positive and one negative, separated by $2\Delta\nu$. The value of $\Delta\nu$ must be chosen carefully so that lines of interest fall into an emission-free region of the bandpass when shifted. During the reduction procedure the spectrum is split into two and

the negative spectral line is made positive. Finally, both lines are shifted back to the same rest-frequency and averaged together.

The frequency-switching technique has a number of advantages over position switching: There are no time overheads associated with observing an OFF position, leading to a $\sqrt{2}$ improvement in sensitivity for the same observing time. Fast frequency switching also provides better cancellation of atmospheric emission fluctuations, however, the response of the receiver may vary considerably with frequency, resulting in poor spectroscopic baselines.

We targeted the same five fields in NGC 3576 as were observed with the ATCA. The OTF method had not yet been implemented on the 70-m antenna so we observed each field as a square grid of 5×5 positions, spaced by half the 45″ beam-FWHM. Each position was observed for 10 minutes and the pointing accuracy was checked by observing a planet every hour. Pointing errors were usually below 10″, or 1/4 beam. Individual maps took 5 – 6 hours to complete, including 15 minutes spent measuring the atmospheric opacity using the 'skydip' method. During the observations the data were calibrated against an ambient load (a noise diode) and the zenith system temperature at 23 GHz was typically 40 – 50 K during the observations. We estimate the T_A^* flux scale is uncertain by ≤ 10 per cent. The 2003 beam efficiency was measured as 0.48 Greenhill et al. (2003), however, the value may have changed in the interim period resulting in a larger error on the main beam brightness temperature T_{MB} flux scale.

The K-band receiver on the 70-m antenna measured only the left circular polarisation, but provided two IFs which could be tuned to separate frequencies. The first frequency was centred mid-way between the NH_3 (1,1) and (2,2) transitions and the correlator was configured to have a 64 MHz wide bandpass divided into 2048 channels. Both the NH_3(1,1) and (2,2) spectra, including satellite lines, fell well inside the 850 km s^{-1} usable range and were observed at a velocity resolution of ~ 0.4 km s^{-1}. The second frequency was tuned to the NH_3 (3,3) line which was centred in the bandpass and the correlator setup was the same as for the first frequency. While NH_3 (3,3) was detected, we do not utilise the data in this work.

The experimental mapping data were reduced in an ad-hoc pipeline built using the SPC, GILDAS and MIRIAD packages. SPC was used initially to load the raw *rpfits* data. The spectra were resampled to the V_{LSR} rest-frame, quotients were formed between adjacent spectra and the results written to disk as *fits* files. These quotient spectra were read into the CLASS package, where the positive and negative spectra were separated, inverted (if necessary), frequency-shifted and averaged together. As the spectral baselines were poor, a polynomials of order 5 – 9 (in extreme cases) was fit to the line-free channels before spectra from individual integrations were averaged together. The result was a list of 25 spectra, one for each position in the field. The data were then assembled into a 3-D data-cube using the *cube* command in the GREG package and resampled onto a finer spatial pixel grid using the *make_cube* command. Finally, the data were output as *fits* cubes and MIRIAD was used to restore missing header information, such as the beam-size and data-unit.

6-3 Results

Molecular emission was detected from all of the clumps identified in the SIMBA map. The following sections describe the results from the ATCA, Mopra and Tidbinbilla telescopes.

6-3.1 ATCA results

We detected NH_3 (1,1), and NH_3 (2,2) from across the whole filament. NH_3 (4,4) was not detected down to a sensitivity limit of ~ 5 mJy/beam, constraining the temperature of the gas below 200 K. Figure 6.2-A and -B present the NH_3 (1,1) and (2,2) integrated intensity maps of the region. The NH_3 (1,1) map utilises data from both the H75 and EW367 array configurations and has a resolution of $\sim 11''$. Only H75 data exist for NH_3 (2,2) transition and the resulting map has a resolution of $\sim 24''$. For reference, the 3 per cent contour of the SIMBA 1.2-mm emission is plotted in white. The thick black line is the 5 per cent contour of the 23-GHz continuum

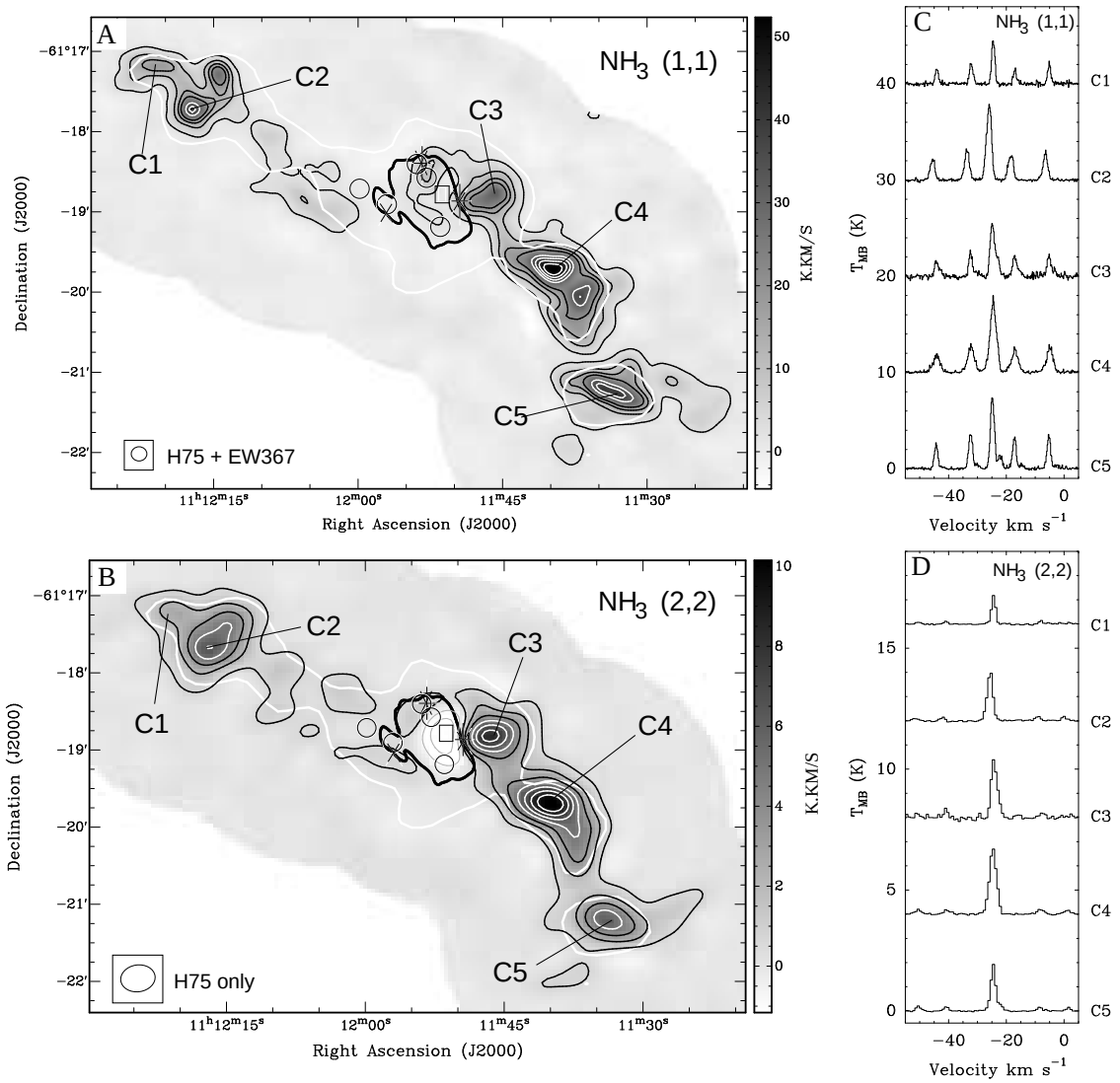

Figure 6.2. **A**) Integrated intensity map of the NH_3 (1,1) emission (thin black and white contours, and greyscale) made using the combined ATCA H75 and EW367 data. **B**) Integrated intensity map of the NH_3 (2,2) emission made using data from the ATCA H75 array. The extent of the 23 GHz continuum emission from the central HII region is marked by the thick black contour. A cross marks the 6.67 GHz methanol maser sites and '+' marks the positions of water masers. The 1.2-mm dust emission is outlined by a single white contour ($\sim$3 per cent, courtesy of Hill et al. 2005) and matches the NH_3 emission closely, except in the central clump. **C**) Sample NH_3 (1,1) spectra measured from the peaks of the clumps labelled C1 – C5. **D**) Sample NH_3 (2,2) spectra measured from the same positions. The brightness temperature ratios between the main and satellite lines indicate that the clumps have low to moderate optical depths.

emission from the central HII region. We see the NH_3 emission has approximately the same morphology in both transitions and closely follows the structure of the 1.2-mm emission, except immediately to the east of the central HII region. Sample NH_3 (1,1) and (2,2) spectra from the peak pixels of five clumps (labelled C1 – C5) are presented in Figure 6.2-C and -D. Both of the NH_3 transitions exhibit the classic 'five-finger' profiles at all positions. Some slight asymmetries are visible in the NH_3 (1,1) profiles towards the C1 and C2 clumps, however, for the most part the spectra appear optically thin. Linewidths vary between 1 and 2.5 $\mathrm{km\,s^{-1}}$, and peak brightness temperatures range between 4.4 and 8 K for the (1,1) line and between 1.2 and 2.6 K for the (2,2) lines.

23 GHz continuum was imaged simultaneously with all the NH_3 lines. To make the final map we combined data from the EW367, H75 and 750D arrays, including the continuum visibilities from the narrow-band spectral line windows. No 23 GHz continuum emission was detected away from the central HII region, down to a sensitivity limit of ~ 10 mJy/beam. Figure 6.3 presents the final image of the HII region at 23 GHz. Crosses mark the positions of 6.67 GHz methanol masers and '$\times$'s marks the sites of 22 GHz water masers. The contours are similar to the central part of the 3.4-cm map made by de Pree et al. (1999), with a single strong peak at $11^h11^m51.08^s$, $-61^d18^m50.0^s$ (J2000) and diffuse emission extending to the east. The flux density at the peak is 3.6 Jy/beam and we measure an integrated intensity of approximately 42.6 Jy. These values are lower than the 4.1 Jy/beam and 71 Jy/beam, respectively, measured by de Pree et al. (1999) at 3.4-cm, however, our observations sample the UV-plane less well and we likely filter out a significant fraction of the extended emission. Our values are consistent with emission from optically-thin ionised gas, assuming we are missing ~ 34 percent of the flux detected by de Pree et al. (1999).

We also searched for 22 GHz water maser emission across the filament. New masers were detected at six positions, as well as at the three previously known sites adjacent to IRS 1, IRS 3 and IRS 4. Figure 6.4 presents a sample spectrum from a single baseline showing the majority of the maser lines detected. Two groupings of lines are observed, centred at approximately $-115\,\mathrm{km\,s^{-1}}$ and $-30\,\mathrm{km\,s^{-1}}$. The intense

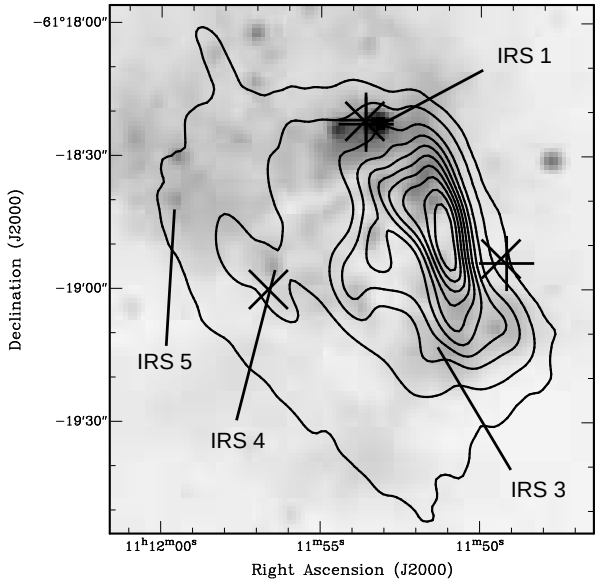

Figure 6.3. 23-GHz continuum emission from the HII region at the centre of the NGC 3576 complex. The image was made by combining multi-frequency data from the ATCA H75, 750D and EW367 arrays, including the line-free channels from the NH_3 observations. Contours are at values of 0.01, 0.11 0.45, 0.85, 1.35, 1.65, 2.00, 2.48, 2.82, and 3.25 Jy/beam. '×' mark H_2O masers, while '+' marks CH_3OH masers. The total integrated flux density is ∼42.6 Jy.

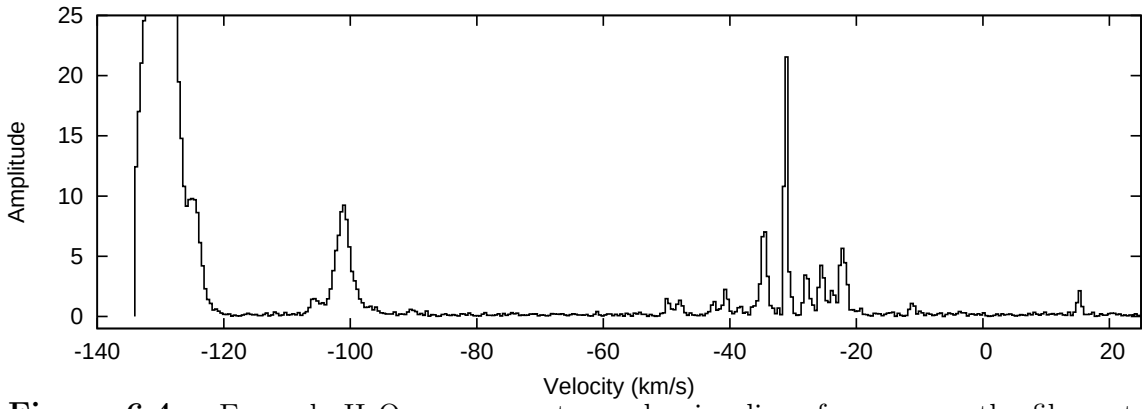

Figure 6.4. Example H_2O maser spectrum showing lines from across the filament. The two broad maser lines at $-130\,\mathrm{km\,s^{-1}}$ and $-102\,\mathrm{km\,s^{-1}}$ derive from positions M9 and M5, respectively, within the central HII region, while the bulk of the maser lines are concentrated near the systemic velocity of the system at $-24\,\mathrm{km\,s^{-1}}$ and are scattered across the filament. The units of amplitude are arbitrary.

lines at -100 and $-130\,\mathrm{km\,s^{-1}}$ have peak amplitudes of $\sim$900 and $\sim$70 Jy/beam, respectively, and derive from maser sites within the central HII region. Maser sites scattered across the filament contribute to the group of lines between -60 and $-10\,\mathrm{km\,s^{-1}}$. Figure 6.5 presents the maser spectra and illustrates the positions of individual maser sites superimposed on the NH_3 (1,1) image. Precise coordinates, intensities and velocities are noted in Table 6.3. The three well-known sites in the central region (labelled M4, M5 and M9 in Figure 6.5) have been investigated by Caswell (2004), who summarises their properties. At the M4 site (*291.274−0.709*) the H_2O maser coexists with 6.67 GHz CH_3OH and 1.67 GHz OH masers. In the H_2O maser spectrum we detect bright maser features ranging from $-37\,\mathrm{km\,s^{-1}}$ to $23\,\mathrm{km\,s^{-1}}$, as reported by Caswell, however, we also detect weak (< 5 Jy) lines out to velocities of $-51\,\mathrm{km\,s^{-1}}$ and $+20\,\mathrm{km\,s^{-1}}$ on either side. The M5 site (*291.270−0.719*) hosts a weak CH_3OH maser at $-26\,\mathrm{km\,s^{-1}}$ and a bright H_2O maser at a velocity of $-102\,\mathrm{km\,s^{-1}}$. First reported by Caswell et al. (1989) we find this H_2O maser has an unusually broad linewidth ($2.9\,\mathrm{km\,s^{-1}}$) and a peak flux density of 69 Jy, the same as in the original observations. The V_{LSR} of this maser feature is reported to have become increasingly negative since its discovery in 1989 when it had a velocity of $-88\,\mathrm{km\,s^{-1}}$. This has been interpreted as being due to acceleration of the emitting gas, perhaps in a high velocity outflow (Caswell 2004). Alternatively, we suggest the $-102\,\mathrm{km\,s^{-1}}$ line may be a new maser feature not associated with the component seen at $-88\,\mathrm{km\,s^{-1}}$, which may have been quenched in the intervening time. The final known site, M9 (*291.284-0.716*), exhibits a single intense maser at a velocity of $-130\,\mathrm{km\,s^{-1}}$ and with a linewidth of $4.8\,\mathrm{km\,s^{-1}}$. We measure an intensity of 670 Jy in contrast to the earlier value of 945 Jy (Caswell et al. 1989), perhaps reflecting a real decrease in the intensity over the intervening time. We note that this maser feature falls on the edge of our bandpass, which may make the flux density measurement unreliable.

The six new maser sites reported here (M1, M2, M3, M6, M7 and M8) are located in the 'arms' of the filament. As can be seen from Figure 6.5 all sites are within a few arc-seconds of the peaks of NH_3 cores. With the exception of M8, it is notable

Table 6.3. 22 GHz H_2O masers in NGC 3576.

Maser	RA (J2000)	Dec (J2000)	Velocity Range ($km\,s^{-1}$)	Peak V_{LSR} ($km\,s^{-1}$)	Peak (Jy)	Ref
M1	$11^h12^m16.72^s$	$-61^d17^m47.0^s$	−27 to −19	−24.3	5.1	new
M2	$11^h12^m13.95^s$	$-61^d17^m30.0^s$	−22 to −18	−20.7	3.3	new
M3	$11^h12^m00.76^s$	$-61^d18^m31.0^s$	−41 to +15	−25.5	6.5	new
M4	$11^h11^m53.40^s$	$-61^d18^m24.0^s$	−51 to +17	−31.4	46.5	Caswell
M5	$11^h11^m50.07^s$	$-61^d18^m51.0^s$	−110 to +12	−101.5	69.3	Caswell
M6	$11^h11^m39.80^s$	$-61^d19^m41.0^s$	−27 to −20	−20.9	7.8	new
M7	$11^h11^m39.52^s$	$-61^d20^m17.0^s$	−25 to −17	−18.4	1.3	new
M8	$11^h11^m34.52^s$	$-61^d21^m16.0^s$	−31 to −3	−27.7	24.8	new
M9	$11^h11^m56.64^s$	$-61^d19^m01.0^s$	< −134 to −121	−129.9	5.1	Caswell

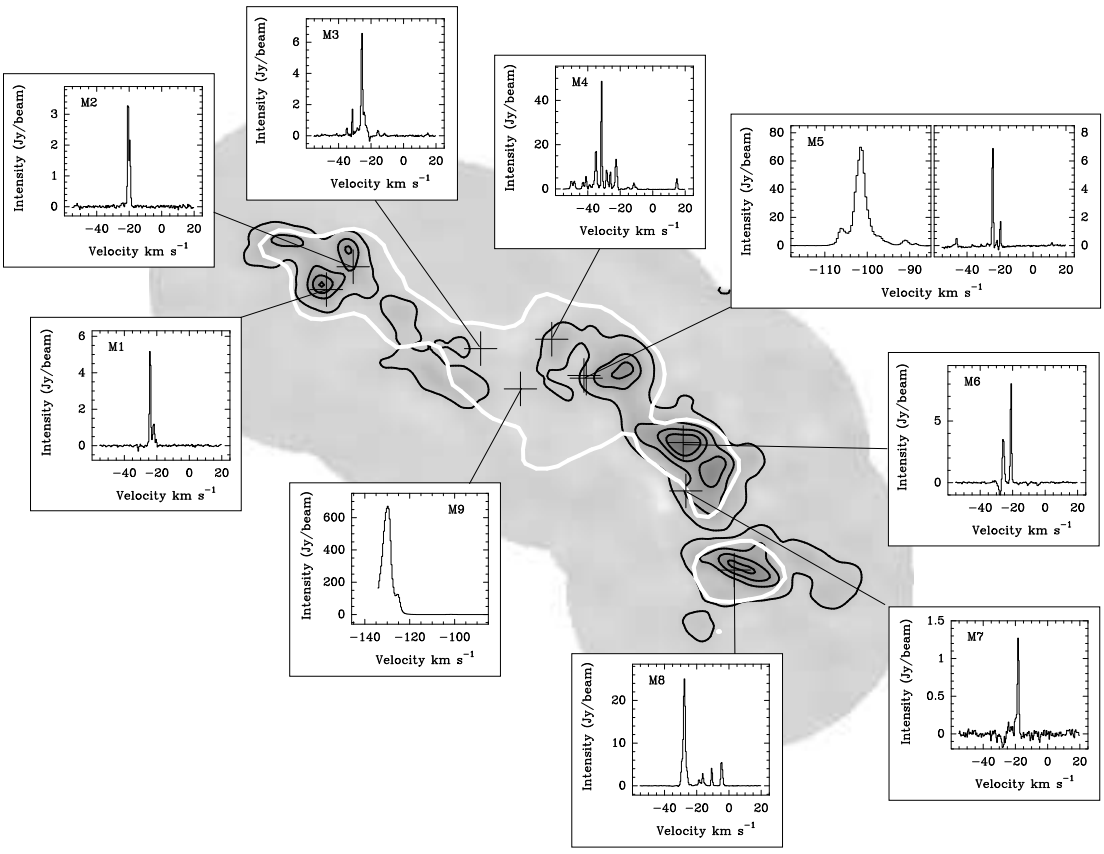

Figure 6.5. Positions and spectra for the 22 GHz H_2O masers in NGC 3576. Six masers (M1, M2, M3, M6, M7 and M8) are new detections. Greyscale and black contours are the NH_3 (1,1) integrated intensity map. The white line is the ∼5 per cent emission contour from of the 1.2-mm continuum map. Individual spectra are sampled from the peak maser pixel and from *clean*ed images of five fields.

that the spectra of these new masers exhibit, at most, two bright features. These features have velocities close to the systemic velocity and intensities below 10 Jy. In contrast, the maser spectrum of M8 has four strong peaks spread over $\sim 35\,\mathrm{km\,s^{-1}}$, the brightest of which has an intensity of 25 Jy.

6-3.2 Tidbinbilla results

NH_3 (1,1) and (2,2) integrated intensity maps made using the Tidbinbilla 70-m telescope are presented in Figure 6.6. Individual maps are centred on the same position as the ATCA fields, however, technical difficulties meant that we were unable to finish one column of field S3, covering the HII region. Each field is composed of an array of 25 pointings in a square grid, as illustrated in the case of clump S5. These fields were re-sampled to a smaller pixel scale and sewn together to make the final data-cube. It is immediately evident that the morphology of the emission is similar to the maps made using the ATCA data.

We initially intended to use data from the 70-m antenna to 'fill in' the missing short-spacings in our ATCA data. For the merging to be successful, the emission in the single-dish dataset must be imaged out to its extremes. Unfortunately, there is still considerable flux at the edge of all fields and, due to time constraints and the experimental nature of the observations, we were unable to enlarge the maps. Instead, the Tidbinbilla data is used to estimate the fraction of missing flux due to extended emission in each of the fields. To do this we smoothed the final ATCA maps to the same resolution and pixel scale as the Tidbinbilla maps and compared the integrated intensities measured under the same aperture. The following are the ATCA/Tidbinbilla integrated intensity ratios:

$$\mathrm{S1} = 0.72, \quad \mathrm{S2} = 0.50, \quad \mathrm{S3} = 0.42, \quad \mathrm{S4} = 0.35, \quad \mathrm{S5} = 0.31$$

The above figures assume a beam-efficiency of 48 per cent for the 70-m telescope, as measured by Greenhill et al. (2003). We note that these are preliminary results. Conclusive figures will be derived when the beam-shape and efficiencies of the 70-m

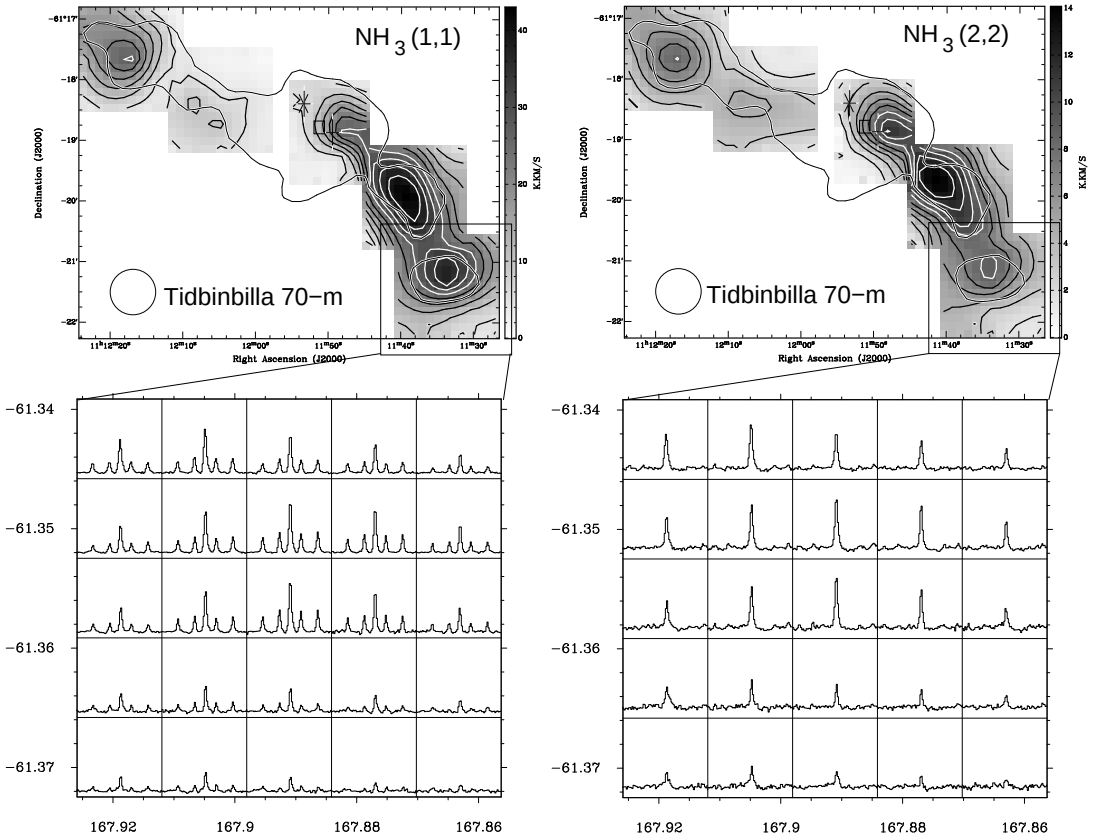

Figure 6.6. NH_3 (1,1) and (2,2) integrated intensity maps made using the 70-m Tidbinbilla telescope. The lower panels present final spectra which formed the maps of the S5 field.

telescope have been fully characterised.

6-3.3 Mopra results

Figure 6.7 presents integrated intensity maps and sample spectra for all molecules detected by Mopra towards the NGC 3576. The data have been hanning-smoothed to a velocity resolution of $0.4\,\mathrm{km\,s^{-1}}$. Sample spectra presented alongside each map have been extracted from the data-cubes at the peak positions of clumps (labelled C1 – C5) identified in the 1.2-mm continuum map and marked by filled circles in the integrated intensity map.

As in the NH_3 maps, the distribution of the gas closely follows the 1.2-mm emis-

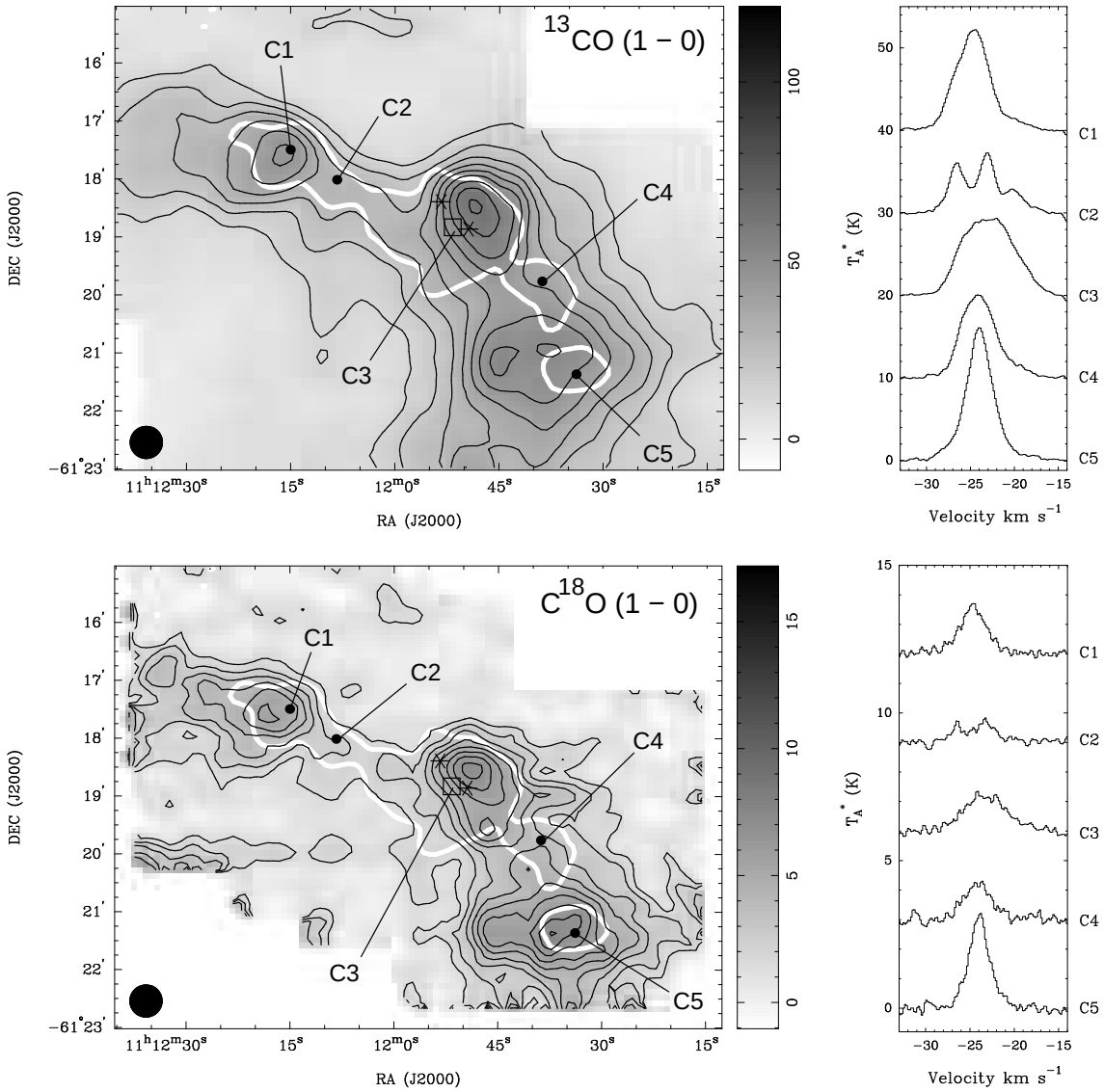

Figure 6.7. Integrated intensity (zeroth-moment) maps of NGC 3576 in the six molecular transitions observed with the Mopra telescope (left panels). Sample spectra, extracted from the data cube at the positions C1 – C5, are presented in the right panels. ^{13}CO is generally optically thick and is a good tracer of the extended molecular envelope. Although the C^{18}O map is noisy it has a lower optical depth and we begin to see clumpy substructure in the cloud. *Continued over ...*

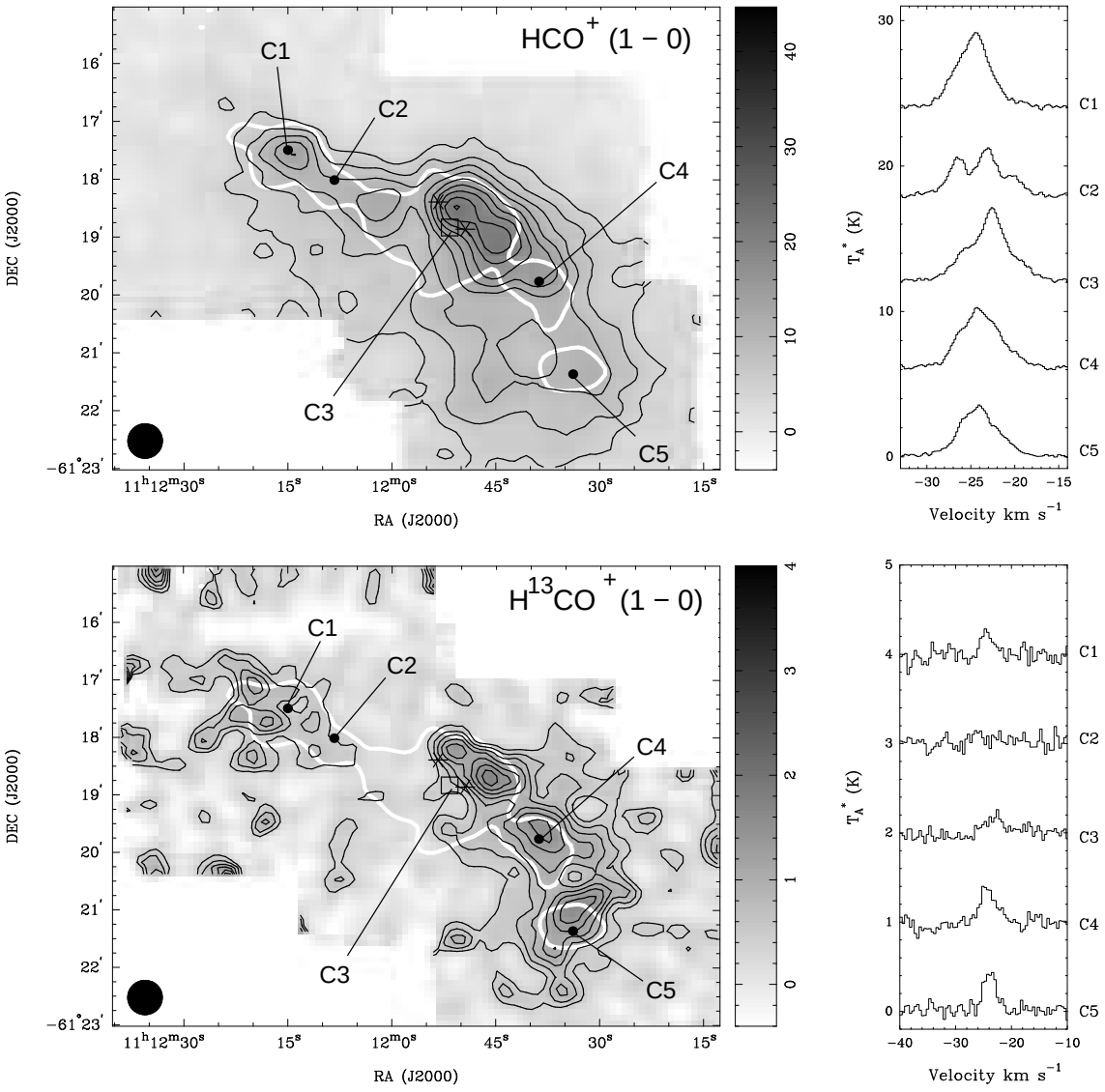

Figure 6.7. – *continued.* Maps of the integrated HCO^+ and $H^{13}CO^+$ molecular emission in NGC 3576. The side panels presents sample spectra extracted from the positions marked C1 – C5.

sion, except in the central HII region. $^{13}CO\,(1-0)$ and $HCO^+\,(1-0)$ trace more extended gas than the other lines, and their spectra appear moderately optically thick compared to their isotopomers, $C^{18}O\,(1-0)$ and $H^{13}CO^+\,(1-0)$. N_2H^+ both trace dense gas, however N_2H^+ exhibits optically thin line profiles while CS appears optically thick in places. The full-width half-maximum N_2H^+ linewidth varies between approximately 1 and 3 km s^{-1} across the filament. At position C2 the spectra of all species display three line components, offset in velocity by $\sim$4 km s^{-1}. Spectra

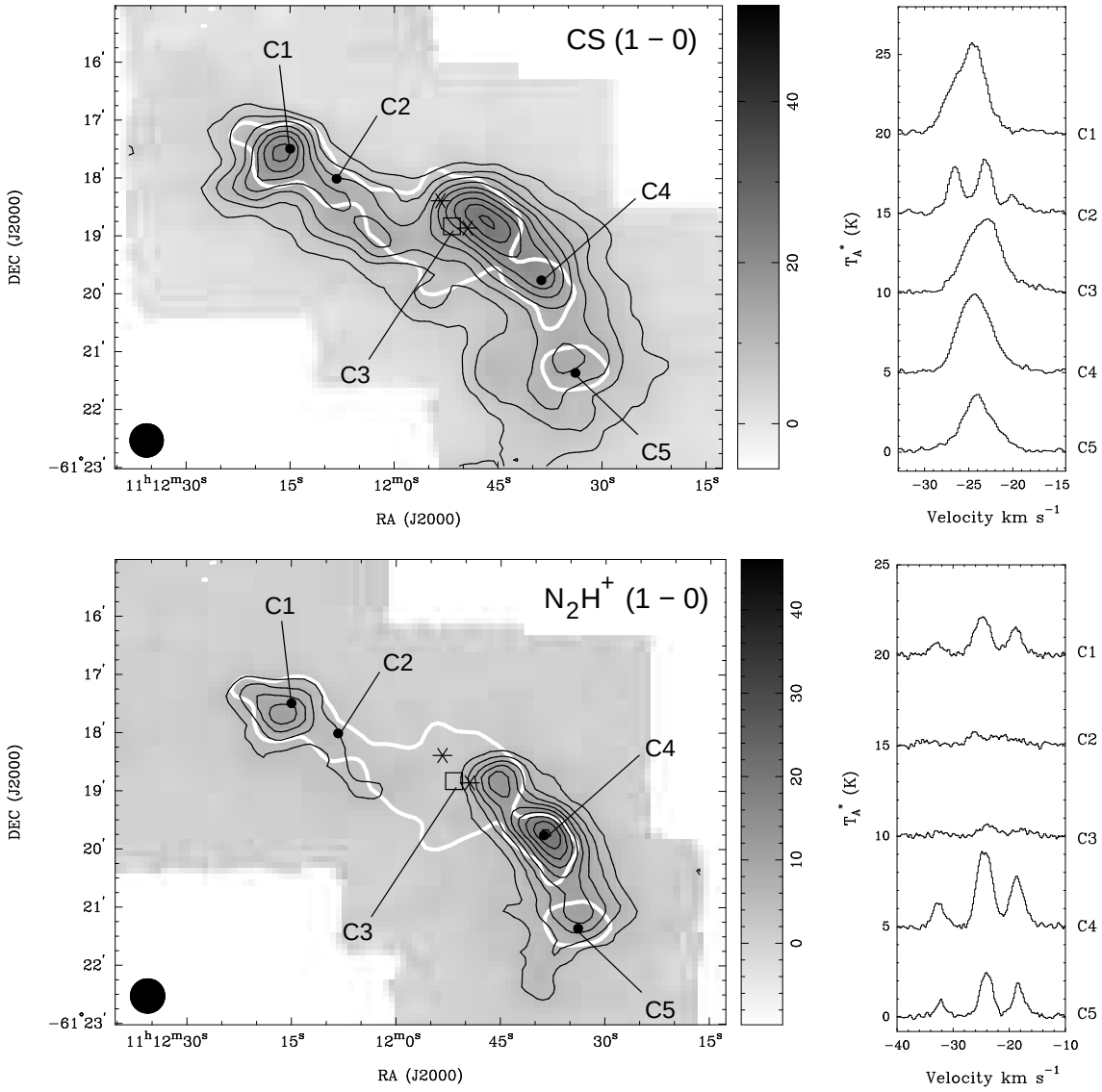

Figure 6.7. – *continued.* Maps of the integrated CS and N_2H^+ molecular emission in NGC 3576. The side panels presents sample spectra extracted from the positions marked C1 – C5.

sampled at the other positions appear as a single line profile, however, except at position C5 these lines are not well fit by single Gaussians and are possibly composed of several blended features. Taking the optically thin N_2H^+ as an example, the peak V_{lsr} of the emission varies over $\sim 5\,\mathrm{km\,s^{-1}}$ across the field, with velocity gradient evident east to west.

The most striking differences lie in the relative brightness and morphology of different species. By comparing the integrated intensity maps we see N_2H^+ (1 – 0)

is clearly enhanced near position C4, while CS (1 – 0) and HCO^+ (1 – 0) are brightest near the HII region. In the following sections we will analyse the morphology, kinematics and relative abundances in detail.

6-4 Analysis and Discussion

6-4.1 Physical properties from NH_3

The rotation-inversion transitions of NH_3 have been used extensively in the literature to derive the kinetic temperature and column densities in molecular clouds (e.g., Ungerechts et al. 1986; Cesaroni et al. 1992; Bourke et al. 1995). Due to its electronic properties, the NH_3 inversion spectrum is split into multiple hyperfine components from which the optical depth may be derived directly, hence removing a major assumption from the calculation of rotational temperatures.

6-4.1.1 Kinetic Temperature

The modified rotational diagram method used to calculate rotational temperatures (T_{rot}) from NH_3 has been described in detail in section 2-4. We provide a brief summary of the procedure here, specifically for the NH_3 (1,1) and (2,2) transitions.

Firstly, Equation 2.61 is used to calculate the optical depth of the NH_3 (1,1) transition via a comparison of brightness temperature T_B in the main and satellite lines:

$$\frac{T_{B,m}}{T_{B,s}} = \frac{1 - e^{-\tau_m}}{1 - e^{-a\tau_m}}.$$

The subscripts 'm' and 's' indicate the main and satellite groups, respectively, and 'a' is the theoretical $T_{B,s}/T_{B,m}$ ratio under optically thin conditions (see Table 2.1). In the case of NH_3 (2,2) is often difficult to measure the optical depth directly, as the signal-to-noise on the satellites is usually poor. Instead, $\tau_{2,2}$ may be calculated from the brightness temperatures of the (2,2) and (1,1) main groups via Equation 2.65:

$$\tau_{2,2} = -\frac{1}{f_{2,2}} \ln \left[1 - \frac{T_{B_{2,2}\,\mathrm{main}}}{T_{B_{1,1}\,\mathrm{main}}} \left(1 - e^{-\tau_{1,1}^{tot} f_{1,1}} \right) \right],$$

where $f_{1,1} = 0.502$ and $f_{1,1} = 0.796$ are the fractional intensities in the (1,1) and (2,2) main groups respectively. The rotational temperature is found from the optical depth ratio $\tau_{2,2}/\tau_{1,1}$ via Equation 2.66:

$$T_{rot} = -41\,K/\ln\left(\frac{9}{20}\,\frac{\tau_{2,2}}{\tau_{1,1}}\,\frac{\Delta\,\nu_{2,2}}{\Delta\,\nu_{1,1}}\right),$$

where $\tau_{J,K}$ and $\Delta\nu_{J,K}$ are the total optical depth and the FWHM linewidth of the NH_3 (J,K) transition. Finally, the rotational temperature may be converted directly to a kinetic temperature T_{kin} via Equation 2.70

$$T_{rot} = \frac{T_{kin}}{[1 + (T_{kin}/41\,K)\ln(1 + C_{23}/C_{21})]}.$$

Danby et al. (1988) have used large velocity gradient (LVG) models to calculate the collisional coefficients C_{23} and C_{21}, for kinetic temperatures ranging from 5 – 300 K. Assumptions made in the LVG technique mean that above $T_{rot} \sim 30$ K the kinetic temperature found via comparison of the NH_3 (1,1) and (2,2) lines becomes unreliable.

Figure 6.8-A presents a kinetic temperature map of NGC 3576 made using the NH_3 (1,1) and (2,2) data from our H75 observations. At a resolution of $\sim 23''$, the map reflects the *average* temperature of gas above a density of $n \approx 2\times10^4$ cm^{-3} (Swade 1989). Higher resolution observations would doubtlessly reveal regions with hotter or cooler temperatures than average. An obvious temperature gradient exists across parts of the filament. Figure 6.8-B plots kinetic temperature as a function of angular offset from the peak of the ionised emission. The data was sampled at 12 positions, corresponding roughly to the peaks of the NH_3 clumps. We find that the kinetic temperature is higher towards regions adjacent to the HII region. In the outlying positions the kinetic temperature is ~ 12 K, and it increases to ~ 30 K towards the centre. Some hot spots with temperatures above 40 K exist to the east of the HII region (between RAs of $11^h12^m00^s$ and $11^d12^m15^s$), but the signal-to-noise ratio in this part of the map is poor, hence the derived temperatures are more uncertain.

It is clear that the central star-forming complex is heating the gas in its immediate surroundings. The heating is gradual on the western side of the filament and the

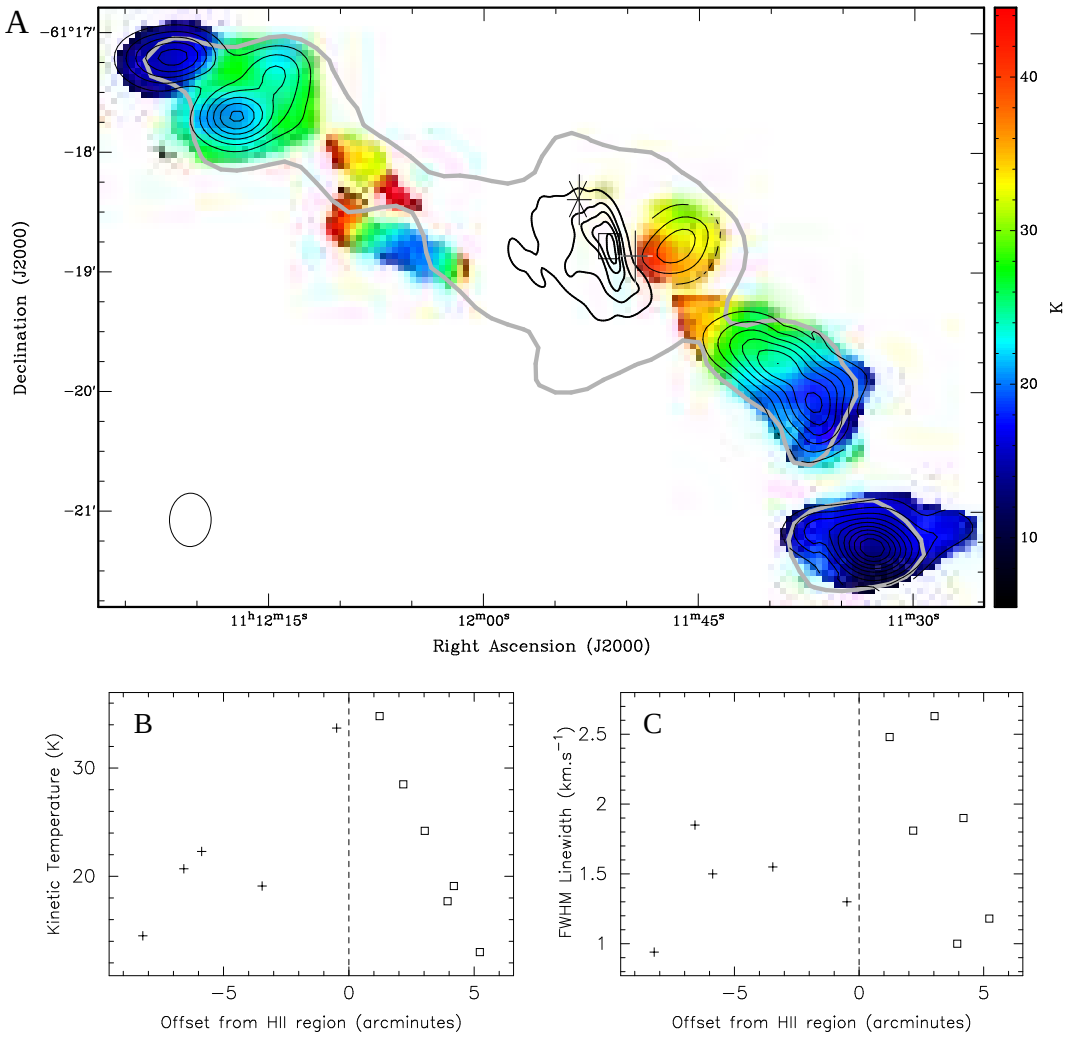

Figure 6.8. (*top*) Map of the kinetic temperature derived from the ratio of the NH_3 (1,1) and (2,2) lines. The beam size is $10.6'' \times 11.9''$. Kinetic temperatures range from > 40 K, in the centre of the map, to 10 K at the extremes. (*bottom*) Kinetic temperature (left) and NH_3 (1,1) linewidth (right) as a function of angular offset from the peak of the HII region. Crosses represent positions eastwards of the HII region and squares positions to the west.

temperature decreases linearly towards the extremes. The gradient in temperature strongly suggest that the HII region is embedded within the filament and is not merely a line of sight projection. The temperature fluctuates between ~ 15 and ~ 30 K in the region immediately east of the HII region. Heating here is less even, perhaps because the gas is less dense and has a more clumpy distribution, or because it cools more efficiently. It is interesting to note that there is a weak linewidth

gradient in the western arm also, as plotted in Figure 6.8-C . This may reflect the turbulent energy injected into the cloud via shocks driven by the expanding ionised gas in the HII region.

6-4.1.2 Column density and clump mass

If the optical depth and excitation temperature in any NH_3 (J,K) transition are known, the total column density of emitting molecules may be calculated assuming local thermal equilibrium (LTE). Combining Equations 2.52 and 2.20 we find

$$N_{J,K} = \frac{8k\pi\nu_{J,K}^2}{A_{ul}hc^3} \int_{-\infty}^{\infty} T_b \, dv \left(\frac{\tau}{1 - e^{-\tau}} \right) \frac{e^{(E_{J,K})/kT}}{g_{J,K} \, Q(T_{rot})}, \tag{6.1}$$

where $Q(T_{rot})$ is the partition function. The exact partition function is the sum over the all levels (Equation 2.71), however, this can be approximated by an exponential fit to the discrete values in the Pickett, et al. (1998) spectral line catalogue. For NH_3 this is:

$$Q(T) = 0.1266 \, T^{1.48}. \tag{6.2}$$

An estimate of the total mass of gas may be determined from the column density of NH_3, assuming a constant relative abundance to H_2. In the $\sim 11''$ resolution NH_3 (1,1) map we begin to resolve substructure within the 1.2-mm clumps spied by SIMBA. We have attempted to decompose the emission using the CLUMPFIND routine (Williams et al. 1994) as a starting point.

CLUMPFIND attempts to divide regions of emission into clumps based on a set of contour levels chosen by the user. Starting at the highest contour level, the routine searches for pixels with emission and assigns them to clumps based on their proximity to other emission at similar velocities. The signal/noise ratio was not constant across the mosaiced NH_3 (1,1) map, so the CLUMPFIND routine was run on the five ATCA fields individually, using the same base contour level of 50 mK, but slightly different contour increments. The results were inspected by eye and compared to the original data-cube for consistency. In some instances we found that the CLUMPFIND routine had merged what were clearly two clumps in the original data-cube. These were

broken apart manually by editing the output cube. Clumps with fewer pixels than the area of the synthesised beam were omitted as unreliable detections. Thirty-seven believable clumps were found, whose positions are plotted in Figure 6.9. The mass of NH_3 in each clump was calculated from the sum of the integrated intensities of the individual pixels in the clump, assuming an average excitation temperature corresponding to that derived from the 23″ H75 data. The total mass of gas was derived assuming an abundance ratio $[NH_3] / [H_2]$ of $1{\times}10^{-8}$ (Ott et al. 2005), and a correction factor of 1.38 for the abundance of helium and heavier elements in the interstellar medium (Allen 1973). Table 6.4 presents the properties of the detected clumps and the distribution of clump masses is illustrated in the histogram inset into Figure 6.9.

We compare clump masses from this work to the masses derived from the 1.2-mm dust emission (Hill et al. 2005) in Table 6.5. Column five contains the total mass of the NH_3 clumps summed over the equivalent SIMBA clump. We see that LTE-mass is always lower than the corresponding mass derived using the 1.2-mm emission (column four). This is likely because the LTE-masses should be considered a lower limit. There are several reasons for this: Firstly, the lower CLUMPFIND sensitivity limit was set at 30 mJy/beam ($\sim 2\,\sigma$) to avoid spurious detections, therefore some fraction of the emission will be absent from the CLUMPFIND result. Secondly, our Tidbinbilla data indicates a significant fraction of the NH_3 flux is missing from the ATCA maps due to spatial filtering of extended emission. In this case a comparison to the SIMBA-masses yields a lower limit on the abundance of NH_3, as presented in column six of Table 6.5. Estimates of the true mass of individual NH_3 clumps may be found by scaling the LTE masses to the dust + gas mass derived from the 1.2-mm data (column 7 of Table 6.5). Figure 6.10 compares this scaled dust-mass with the virial masses derived using Equation 5.3 and the NH_3 data. We find that in most cases, values of M_{Dust} and M_{virial} are within a factor of $\sim$3 of each other, and that at least two-thirds of the clumps are consistent with being gravitationally bound (i.e., $M_{Dust} > M_{virial}$). Given the assumptions made in calculating the masses these results should be viewed with caution.

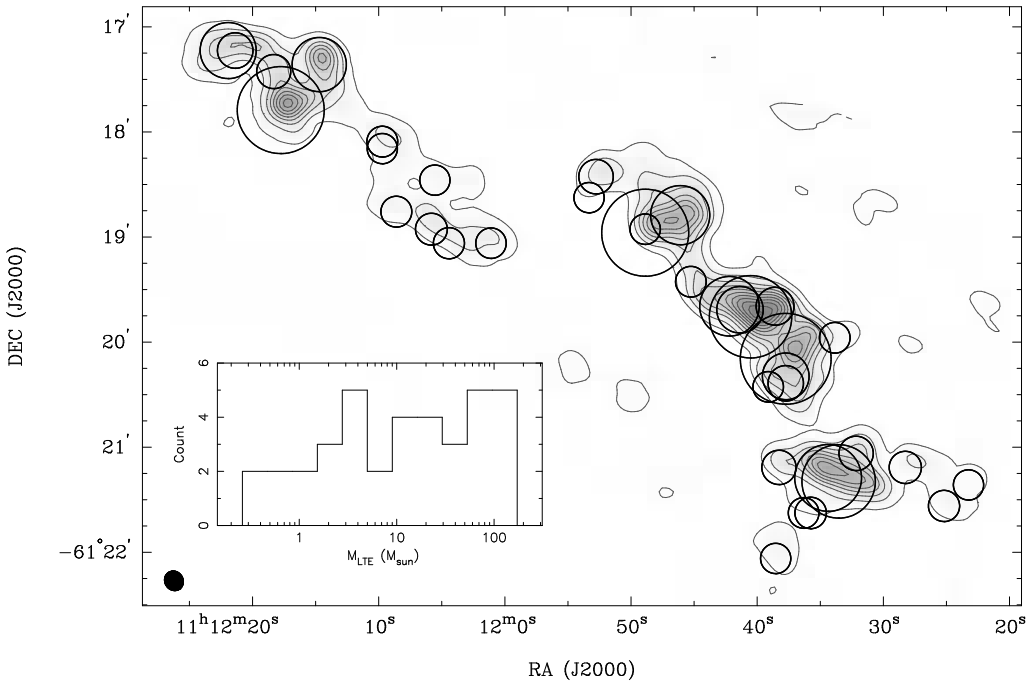

Figure 6.9. The spatial distribution of clumps detected in the NH_3 (1,1) map using CLUMPFIND. Circles mark the positions of the clumps and the radii are scaled to the clump mass, as reported in Table 6.4.

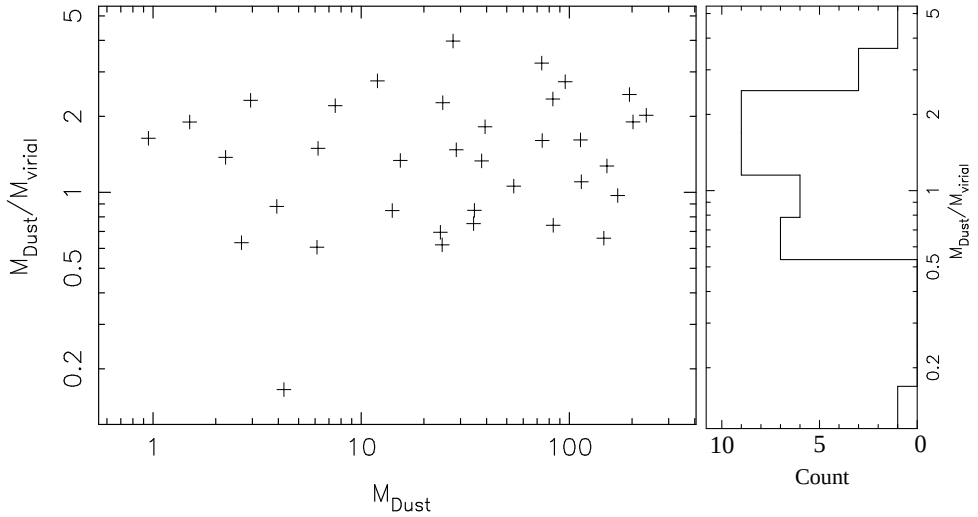

Figure 6.10. Plot of the (M_{Dust}/M_{vir}) ratio versus M_{LTE}. In this case we have subdivided the dust masses of each of the SIMBA clump into the ratios of the clump masses derived from NH_3.

Table 6.4. Properties of the NH_3 (1,1) clumps found using the CLUMPFIND routine.

RA (J2000)	Dec (J2000)	Radius ($''$)	$V_{LSR,FWHM}$ ($km\,s^{-1}$)	$\sum T_{MB}\,dv$ ($K\,km\,s^{-1}$)	M_{LTE}-1 $^{\alpha}$ ($M_\odot$)	M_{LTE}-2 $^{\beta}$ ($M_\odot$)	M_{virial} ($M_\odot$)
11:12:17.8	-61:17:49	20.2	1.8	3244.1	99.9	151.4	119.0
11:12:14.7	-61:17:22	18.2	1.8	1910.5	55.2	83.6	112.8
11:12:21.9	-61:17:14	17.4	1.0	1381.8	63.0	95.5	34.8
11:12:21.4	-61:17:16	12.9	1.3	777.2	23.1	35.0	41.2
11:12:18.9	-61:17:38	13.1	1.3	524.4	16.1	24.5	39.5
11:12:05.8	-61:18:56	11.2	1.1	334.5	10.3	73.6	22.6
11:12:09.7	-61:18:10	5.6	0.3	15.2	0.4	2.9	1.3
11:12:09.7	-61:18:06	10.8	0.6	142.7	3.9	27.6	7.0
11:12:07.8	-61:18:48	11.6	0.7	127.1	3.5	24.6	10.9
11:12:04.4	-61:19:04	11.2	1.0	178.8	5.5	39.3	21.6
11:12:05.5	-61:18:28	7.1	0.0	12.9	0.3	2.5	>0.1
11:12:03.0	-61:18:59	9.4	1.0	64.0	2.0	14.1	16.6
11:11:46.1	-61:18:48	19.2	1.7	2075.7	57.0	114.1	103.5
11:11:48.9	-61:18:58	22.2	2.3	2698.2	73.2	146.4	222.4
11:11:52.8	-61:18:26	15.2	1.1	442.7	12.0	24.0	34.5
11:11:53.3	-61:18:34	7.9	0.2	27.7	0.8	1.5	0.8
11:11:48.8	-61:18:56	10.1	0.5	49.0	1.3	2.7	4.2
11:11:37.7	-61:20:10	18.9	1.8	4179.5	128.7	234.0	115.9
11:11:40.5	-61:19:46	18.8	1.8	3743.5	111.2	202.1	106.3
11:11:41.4	-61:19:42	16.5	1.1	1620.5	45.8	83.2	35.5
11:11:41.4	-61:19:42	19.0	1.4	2294.3	62.2	113.1	70.1
11:11:38.6	-61:19:40	14.0	1.4	1030.1	29.7	54.1	51.1
11:11:37.7	-61:20:24	13.8	1.1	676.1	20.8	37.9	28.4
11:11:34.4	-61:20:00	10.1	1.2	68.4	2.3	4.2	25.7
11:11:39.1	-61:20:28	9.0	0.5	120.8	3.4	6.2	4.2
11:11:45.3	-61:19:26	9.7	0.8	124.3	3.4	6.1	10.1
11:11:37.5	-61:20:20	18.2	1.2	1261.5	40.7	74.0	46.1
11:11:34.4	-61:21:18	15.8	2.5	2529.6	102.3	170.5	175.4
11:11:38.3	-61:21:12	12.8	0.9	466.3	17.2	28.6	19.4
11:11:28.0	-61:21:10	11.8	0.7	251.1	9.2	15.4	11.5
11:11:32.2	-61:21:02	11.8	1.5	564.7	20.8	34.6	46.1
11:11:34.1	-61:21:32	10.2	0.4	84.6	4.5	7.5	3.4
11:11:36.9	-61:21:34	9.5	0.5	68.9	2.4	3.9	4.5
11:11:33.3	-61:21:22	16.4	1.6	2882.8	116.6	194.3	79.6
11:11:24.9	-61:21:34	10.5	0.5	135.0	7.2	12.0	4.3
11:11:23.3	-61:21:22	7.0	0.2	10.7	0.6	0.9	0.6
11:11:38.3	-61:22:02	6.2	0.4	25.1	1.3	2.2	1.6

$^{\alpha}$ Mass derived from the integrated intensity of NH_3 (1,1) assuming an abundance of 1×10^{-8}.

$^{\beta}$ Individual clump masses scaled so as to be consistent with the masses derived from the 1.2-mm emission. In the case of clump S3 the molecular emission does not trace the 1.2-mm emission and we scaled by a factor of 2, the average of the other scaling factors. Table 6.5 presents the NH_3 abundance derived from these factors.

Table 6.5. Comparision of SIMBA 1.2-mm mass and LTE mass from NH_3 (1,1).

SIMBA Clump	RA (J2000)	Dec (J2000)	Gas + Dust Mass ($M_\odot$)	LTE Mass ($M_\odot$)	NH_3 (1,1) [α] Abundance ($\times 10^{-8}$)
S1	11:12:09.4	-61:18:10	390	257	0.7
S2	11:12:00.6	-61:18:34	190	26	0.1
S3	11:11:54.8	-61:18:26	10000	144	–[β]
S4	11:11:38.3	-61:19:54	810	448	0.6
S5	11:11:33.9	-61:21:22	470	282	0.6

[α] Relative abundance of NH_3 to H_2 derived from a direct comparision of LTE-mass and the Gass + Dust-mass. These values should be considered lower limits.

[β] The morphology of the gas and 22 GHz continuum emission compared to the 1.2-mm SIMBA emission suggests that much of the molecular gas has been destroyed or dispersed by the HII region. The NH_3 emission in this field may not reflect the mass of dust in the clump. Alternatively, some of the 1.2-mm emission may be due to free-free emission from ionized gas.

6-4.2 Physical properties from Mopra maps

The molecules observed with Mopra towards NGC 3576 were chosen specifically to probe the physical conditions in different parts of the cloud. ^{13}CO and $C^{18}O$ emission derives from the more tenuous gas ($n_{crit} \approx 6 \times 10^2\,cm^{-3}$) in the envelope surrounding the dense filament. HCO^+ and $H^{13}CO^+$ have higher critical densities ($n_{crit} \approx 3 \times 10^5\,cm^{-3}$) and so probe conditions at greater depths, but are also proven tracers of outflows and bulk gas motions (see section 4-6.3). CS ($n_{crit} \approx 2 \times 10^5\,cm^{-3}$) and N_2H^+ ($n_{crit} \approx 2 \times 10^5\,cm^{-3}$) have comparable critical densities but exclusively trace dense gas. N_2H^+ especially, is considered to be useful indicator of the coldest (≤ 10 K) and most dense regions, where it is predicted to be the most abundant gas-phase ion (Caselli et al. 1995). This is due to the depletion of its main destruction partner, CO, onto the dust grains. In the following sub-sections we derive optical depths, excitation temperatures and column densities for these molecules.

6-4.2.1 CO and HCO^+

Through a comparison of the ^{13}CO and C^{18}O maps we independently solved for the optical depth, excitation temperature and total column density of CO. The following procedure assumes LTE conditions:

Using the *regrid* task in MIRIAD, the CO data-cubes were first resampled to the same pixel-scale in RA, Dec and velocity. For each spatial pixel we calculated the optical depth as a function of frequency using a modified version of Equation 2.61 (Bourke et al. 1997)

$$\frac{\mathrm{T_{MB}\,(C^{18}O)}}{\mathrm{T_{MB}\,(^{13}CO)}} = \frac{1-\mathrm{e}^{-(\tau_{13}/\mathrm{X})}}{1-\mathrm{e}^{-\tau_{13}}}, \tag{6.3}$$

In the above equation, $\mathrm{T_{MB}}$ is the main beam brightness temperature and X is the abundance ratio of [^{13}CO/C^{18}O], assumed to be constant. During the calculation pixels with insufficient emission were blanked, resulting in a data-cube of ^{13}CO optical depth with real values wherever C^{18}O emission was detected. The expected [^{13}CO/C^{18}O] ratio in giant molecular clouds is ~ 11.5 (see Goldsmith et al. 1997 and references therein), however, we found that this value resulted in negative optical depths in some parts of the cube. The *lowest* abundance ratio that did not result in negative optical depths was $\sim$16. This value was used in our calculations and should be considered a lower limit. Optical depths ranged from $\tau \approx 0.1$ to $\tau \approx 4$. Using the ^{13}CO optical depth and intensity data-cubes as input, we then constructed an excitation temperature cube via Equation 2.48

$$\mathrm{T_{ex}} = \frac{\mathrm{h}\nu_\mathrm{u}}{\mathrm{k}} \left[\ln\left(1 + \frac{(\mathrm{h}\nu_\mathrm{u}/\mathrm{k})}{\mathrm{T_{13}}/\mathrm{C}_\tau + \mathrm{J}_\nu(\mathrm{T_{bg}})}\right)\right]^{-1},$$

where $\mathrm{C}_\tau = (1-\mathrm{e}^{-\tau_{13}})$. At this stage we blanked pixels with spuriously excitation temperatures ($\mathrm{T_{ex}}$ <4 K and $\mathrm{T_{ex}}$ >40 K) due to noisy C^{18}O data which had passed our initial signal-to-noise cutoff. Assuming a thermalised population with $\mathrm{T_{kin}} = \mathrm{T_{ex}}$, a column density cube may be produced via Equation 6.1. The partition function Q(T) for ^{13}CO has been approximated by a fit to the values in the Pickett, et al. (1998) spectral line catalogue and for CO is

$$\mathrm{Q(T_{kin})} = 0.3968\,\mathrm{T_{kin}}. \tag{6.4}$$

The resultant column density cube is then integrated in velocity to obtain the total column density map. Figure 6.11-A presents the final CO column density map towards NGC 3576. The column-density peaks at $\sim 1.7\times 10^{17}\,\mathrm{cm}^{-2}$, equivalent to a peak H_2 column of $\sim 1.2\times 10^{23}\,\mathrm{cm}^{-2}$, assuming an relative abundance [CO/H_2] of 1.4×10^{-4}.

We calculated the column-density of HCO^+ using the same procedure, except due to the low signal-to-noise ratio on the $H^{13}CO^+$ map we operated on the peak brightness-temperature and integrated intensity cubes at each step. The partition function for HCO^+ was approximated by

$$Q(T_{kin}) = 0.4798\,T_{kin}. \tag{6.5}$$

Figure 6.11-B presents the final HCO^+ column density map towards NGC 3576, unfortunately, there are large uncertainties associated with the very low signal-to-noise ratio on the $H^{13}CO^+$ map and the unknown [$^{13}C/^{12}C$] abundance ratio, which is set at 40 for these calculations.

6-4.2.2 N_2H^+ and CS

A slightly different approach is taken for the N_2H^+ data. Like NH_3, the hyperfine structure in the spectrum of $N_2H^+\,(1-0)$ allows the direct determination of optical depth (see section 5-4.4). We fit all spectra in the N_2H^+ data-cube using the HFS method in CLASS and found that the N_2H^+ emission is consistent with being optically thin ($\tau \ll 0.1$) over the entire filament. Hence, no independent estimate could be made of the excitation temperature. N_2H^+ and NH_3 have similar critical densities and, being nitrogen bearing molecules, are often detected under similar conditions. We calculated the column density of N_2H^+ assuming excitation temperatures equal to the NH_3 rotational temperatures. In practise, we smoothed the $T_{rot}(NH_3)$ map to the same resolution as the Mopra N_2H^+ data. We then produced a column density map by combining this T_{ex} map with the N_2H^+ integrated map via Equation 6.1 in the limit that $\tau \ll 0$. The partition function for N_2H^+ was again interpolated from

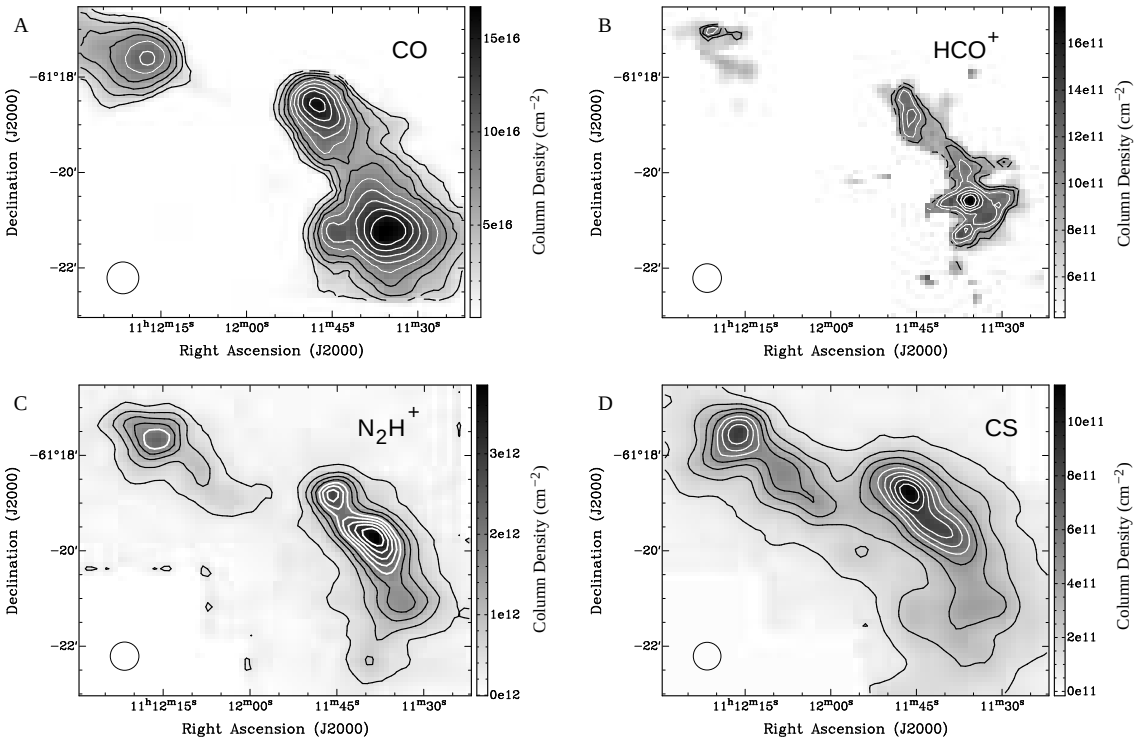

Figure 6.11. Column density maps of the four species targeted by the Mopra telescope. Contours are set at 10 per cent intervals, beginning at 10 per cent, except in the HCO^+ column density map, where they start at 30 per cent of peak.

the values in the Pickett, et al. (1998) catalogue:

$$Q(T_{kin}) = 4.198\, T_{kin}. \tag{6.6}$$

A column density map of CS was prepared in a similar manner, although we note that our assumption of optically thin emission may not be valid. Judging by the non-Gaussian shapes of some line profiles, regions with strong emission may have significant optical depths. The final N_2H^+ and CS column-density maps are presented in Figure 6.11-C and -D, respectively.

6-4.3 Relative molecular abundances.

Once the physical conditions of temperature, density and optical-depth have been determined, we can begin to examine chemistry in NGC 3576. Ratios of column density provide beam-averaged measures of the relative abundances between two

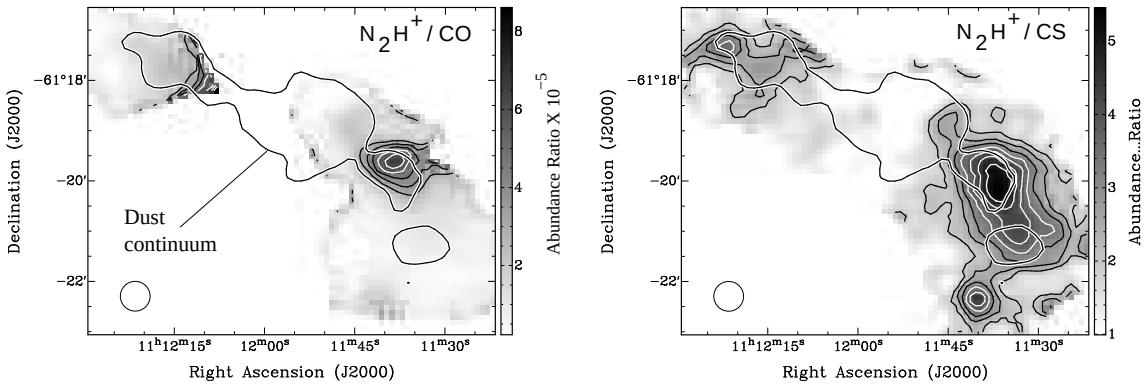

Figure 6.12. Maps of the relative abundance of $[N_2H^+/CO]$ (*left*) and $[N_2H^+/CS]$ (*right*) made from individual column density maps. Greyscale + contours are set at 10 per cent intervals, starting at 30 per cent of peak. The N_2H^+ abundance is significantly enhanced towards clump S4. This difference is especially pronounced in the $[N_2H^+/CO]$ map but is not as clear when comparing N_2H^+ and CS. We note that the column density of CS is the least well known of the three species.

species. For key molecules this ratio is tied directly to the physical conditions and hence to the embedded star formation activity (see Chapter 1).

Figure 6.12 presents maps of the relative abundance of $[N_2H^+/CO]$ and $[N_2H^+/CS]$ made by taking the ratios of the column densities. The abundance ratio is beam-averaged and assumes all of the gas is above the critical density for each species. Immediately clump S4 stands out in the $[N_2H^+/CO]$ map, as it has an over-abundance of N_2H^+ compared to the other SIMBA dust-clumps. The difference is not as pronounced in the $[N_2H^+/CS]$ map, however, we note the optical depth of CS is not known and hence there are significant uncertainties its column density across the map. A comparison between the N_2H^+ and $H^{13}CO^+$ column densities also reveals the same enhancement in clump S4, which we believe to be a real chemical difference.

The abundance of N_2H^+ is predicted to be enhanced in cold ($\leq 10\,\mathrm{K}$) or dense cores as it is one of the last species to freeze onto dust grains and survives in the gas phase, at least for densities in the range $10^5 - 10^6$ cm^{-3}. In such environments CO, its main destruction partner, depletes onto the grains and the abundance of N_2H^+ consequently increases (e.g., Bergin et al. 2002). Interestingly, ^{13}CO and $C^{18}O$ emission

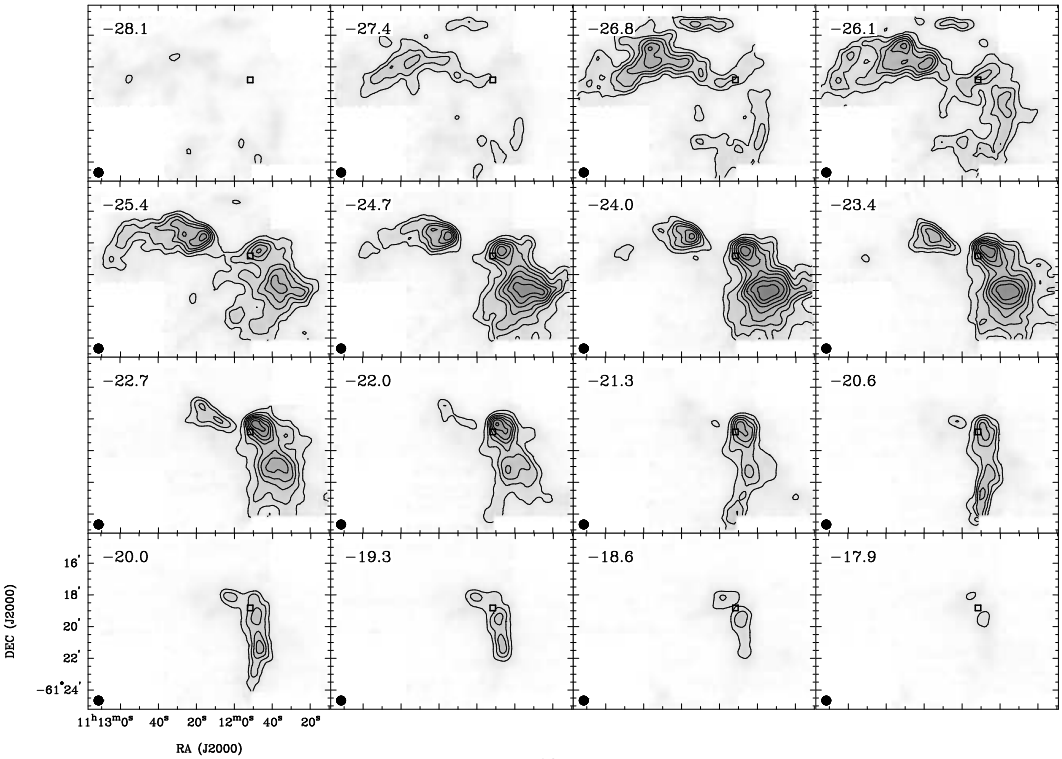

Figure 6.13. Channel maps of the Mopra ^{13}CO data in NGC 3576 from $V_{LSR} = -28$ to $-18\,\mathrm{km\,s^{-1}}$, at velocity intervals of $\sim 0.7\,\mathrm{km\,s^{-1}}$.

are noticeably absent from this position, giving us further confidence in this interpretation. Conditions such as these are found in starless cores, but particularly in cold collapsing cores on the way to forming stars. Core S4 has an average kinetic temperature of ∼25 K according to our analysis of NH_3 data. This seems high for a IRDC undergoing collapse, however, CO depletion may still occur at these temperatures if the density is high enough (Aikawa et al. 2001). In the following section we will examine the evidence for inflowing gas motions in this clump.

6-4.4 Morphology and kinematics

We have examined the molecular emission for evidence of velocity gradients, indicating bulk motions or rotation. Figure 6.13 presents a channel map of NGC 3576 in ^{13}CO, which traces the extended envelope of the molecular cloud. Individual velocity planes are separated by $\sim 0.7\,\mathrm{km\,s^{-1}}$, beginning at $-28\,\mathrm{km\,s^{-1}}$and ending at $-18\,\mathrm{km\,s^{-1}}$. A rough velocity gradient exists across the map: emission moves

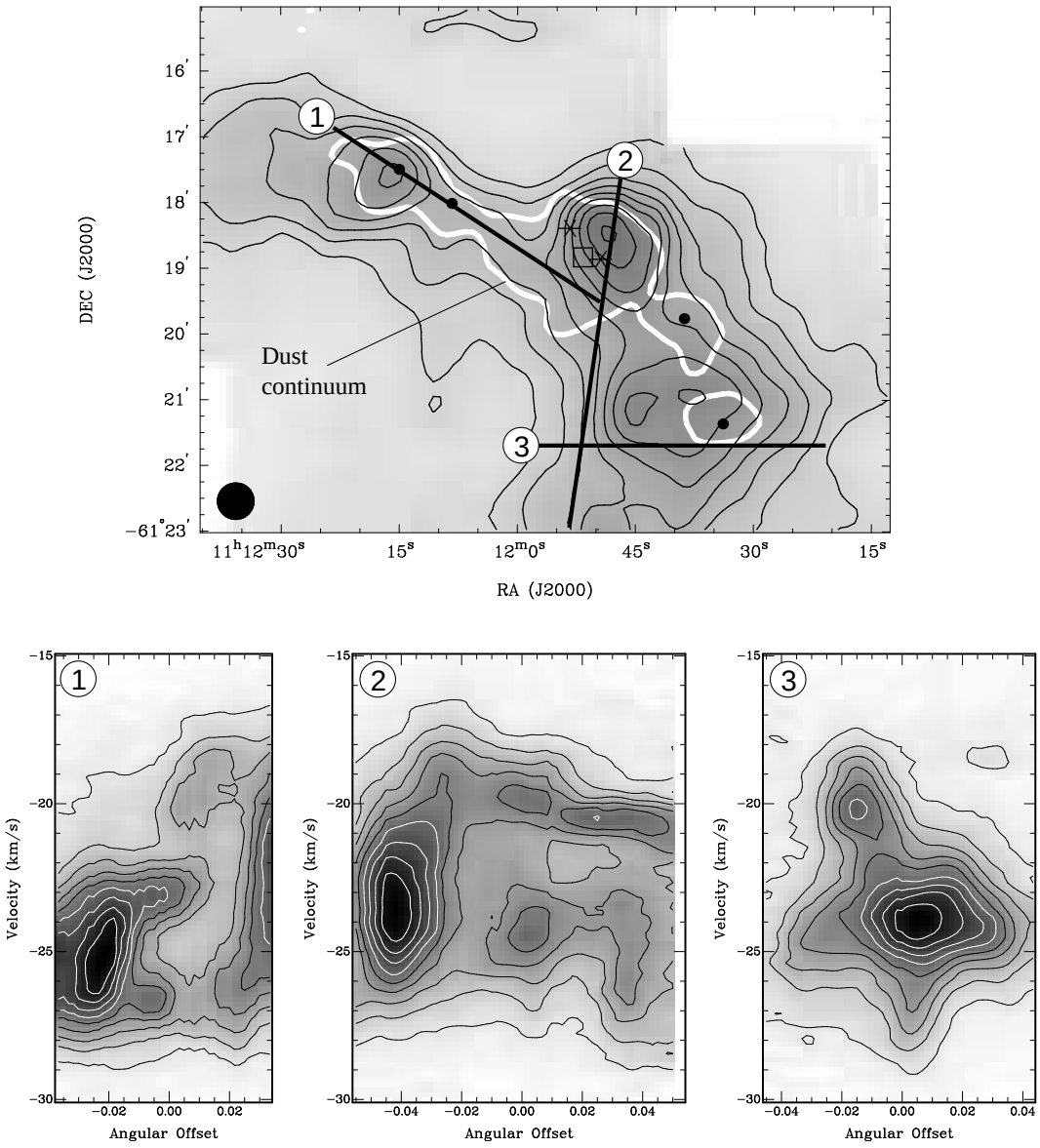

Figure 6.14. Position-velocity cuts through the ^{13}CO data-cube along three directions (shown above). See text for details.

from east to west as the velocity becomes less negative. On closer examination the velocity sub-structure of the cloud is more complex than a simple gradient and the filament contains multiple velocity components. Figure 6.14 shows position-velocity (PV) diagrams taken along the three cuts marked on the inset integrated intensity map. The first cut, (centred at 11:11:09.9, -61:15:45.6 J2000 and at a position angle $\Theta = 244.5°$) is a longitudinal slice through the eastern arm of the filament and reveals

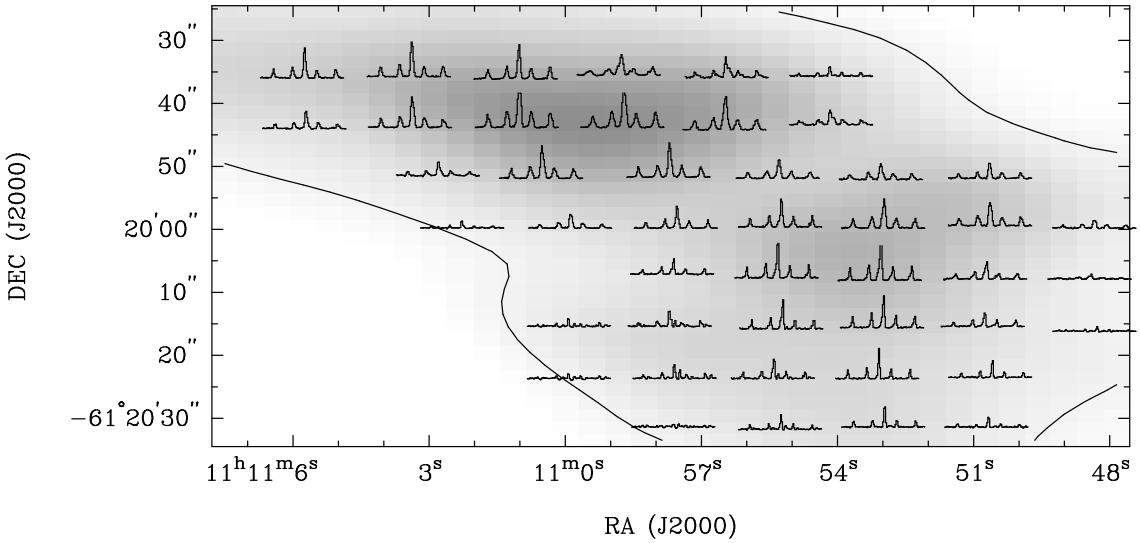

Figure 6.15. Sample spectra overlaid on the NH_3 (1,1) integrated intensity map of SIMBA-clump S4.

a forked cross-section: two tenuous tentacles of emission merge into the eastern-most SIMBA clump (S1). We suspect the HII region has played a significant role in sculpting these features. The second cut (11:11:48.6, -61:20:57.6, $\Theta = 174°$) follows the line of emission evident in Figure 6.13 at $-20.6\,\mathrm{km\,s^{-1}}$. It is clear from the PV-diagram that two velocity components exist, separated by $\sim 4\,\mathrm{km\,s^{-1}}$. Both appear to merge into the strong emission immediately west of the HII region. These two velocity features are clearly visible in the third cut (11:11:39.50, −61:21:46.85, $\Theta = 268°$), which presents the velocity structure of the western arm in cross-section. The bulk of the emission in the arm comes from the velocity component at $-24\,\mathrm{km\,s^{-1}}$. The small velocity differences of $4-5\,\mathrm{km\,s^{-1}}$ between the two components make it likely that all the emission derives from the same cloud and is not merely a projection or line-of-sight effect. It is interesting that the two most intense tentacles of emission merge at the HII region, perhaps indicating that star formation in the region was initiated by a collision between two flows of gas, or two clouds. Likewise, in the eastern arm where the two tentacles merge we find two sites of water maser emission.

The $\sim 10''$ NH_3 (1,1) data gives access to the velocity structure of the dense cores in the cloud. In particular, we are interested in probing for bulk gas motions in clump S4, where we find an over-abundance of N_2H^+. Asymmetric spectra towards

star forming regions are often interpreted as indicators of inward or outward motions. In the case of NH_3 (1,1) asymmetries may be produced by a combination of non-LTE effects and bulk motions. Park (2001) has modelled NH_3 (1,1) spectra over a wide range of physical conditions and predicted that asymmetries between the *inner* satellite lines may indicate inward or outward flows of gas. On the other hand, asymmetries between the outer satellites are indicative of selective radiative trapping and non-LTE excitation (Stutzki & Winnewisser 1985). The amount by which both effects skew the profiles increases with optical depth. Figure 6.15 presents sample spectra towards positions in the S4 SIMBA clump. Although asymmetries on the order of $\sim$15 per cent are observed between the outer satellites, the ratios of the inner satellites remain relatively constant throughout the map. We caution that the optical depth in the clump ranges between $\tau \approx 0.1$ and $\tau \approx 1.0$ and we do not expect large asymmetries under these conditions.

6-4.5 Infrared excess stars

Previous studies have focused on the infrared properties of embedded stars in the region. Emission in the K and L bands, which cannot be accounted for by interstellar reddening, has been interpreted as the signature of thermal emission from a dusty disk. Maercker et al. (2006) imaged the region in J, H, K and L, and found 113 stars with infrared excess. Their distribution is plotted in Figure 6.16 over the ^{13}CO (1 – 0) integrated intensity map. Foreground stars have been filtered from the list. A dense cluster of IR-excess stars is centred on the Giant HII region, as reported in work by Persi et al. (1994) using Las Campanas Observatory. It is clear that there are few IR-excess stars associated with the molecular gas in the bulk of the filament. This suggests that the clumps are not associated with star-formation in an advanced stage of development. If young stars are present in the filament, they are likely so young that they are still deeply embedded and not yet visible in the near-infrared.

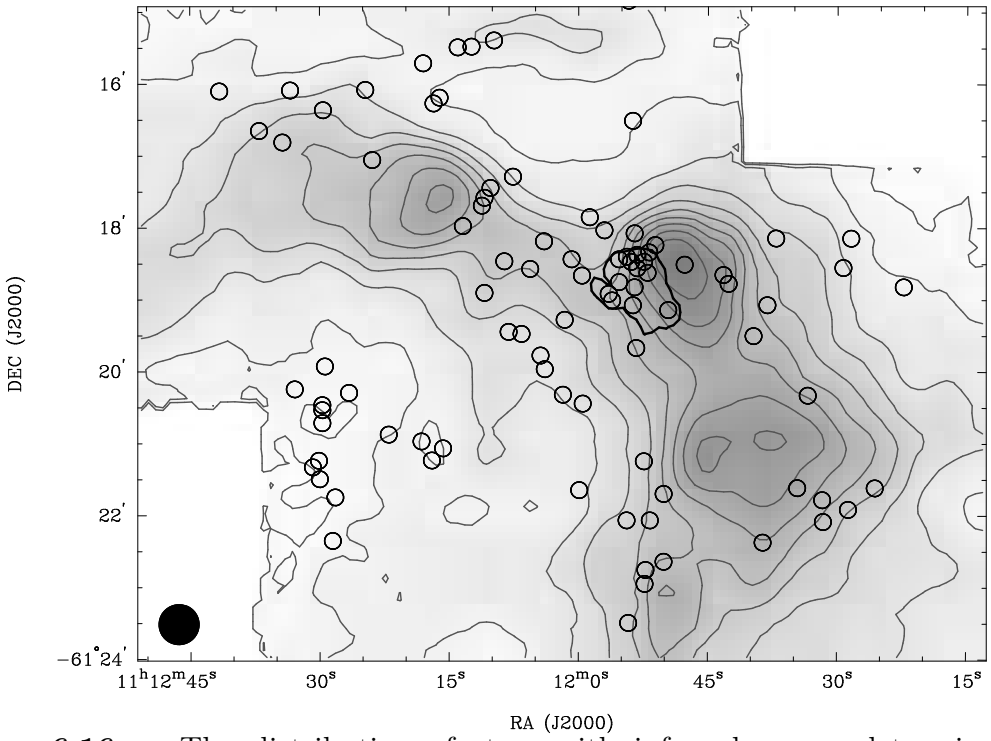

Figure 6.16. The distribution of stars with infrared excess determined by Maercker et al. (2006), plotted over the molecular gas traced by ^{13}CO (1 – 0) emission.

6-5 Star formation in NGC 3576

Our observations provide an interesting glimpse into star formation activity within NGC 3576. It is clear that the HII region is embedded within the dusty filament and is exerting a powerful influence on its immediate surroundings. By comparing the morphology of the 23 GHz continuum emission to the dense molecular gas (traced by NH_3) and the thermal dust (traced by 1.2-mm continuum), we see that the young cluster at the heart of the complex has destroyed or dispersed much of the gas in the central clump. To the east of the 23 GHz peak, molecular gas is sparse and does not follow the morphology of the dust, while at 3.4-cm wavelengths the ionised gas is observed to extend throughout most of field S2 (see Figure 6.1-D). In contrast, the western edge of the free-free continuum emission is observed to have a very well defined boundary. We find from our molecular-line observations that this edge coincides with a dense molecular cloud, implying that the HII region is pressure-

confined on this side. At the same time, the HII region appears to be heating the arms of the filament and the western arm exhibits a clear temperature gradient, peaking adjacent to the HII region. In the eastern arm, the clumpy nature of the gas gives rise to 'hot spots' with higher temperatures, consistent with our 'dispersal' interpretation. Some of the structures visible in the eastern arm are reminiscent of the 'elephant's trunks' pillars in the Eagle Nebula (White et al. 1999).

Water masers have always been associated with star formation (see Beuther et al. 2002 for a summary). That we detect water-maser emission towards the arms of the filament confirms the presence of shocks and hence that stars are forming within the molecular gas. However, unlike 6.67 GHz CH_3OH masers, 22 GHz water masers are not a clear confirmation of high-mass ($> 8 M_\odot$) star formation as they are also found towards sites where intermediate mass ($4-8 M_\odot$) stars are forming. Water masers are thought to originate in the shocked gas associated with outflows and are collisionally pumped (e.g., Kylafis & Pavlakis 1992). The three water masers within the HII region each have maximum flux densities of $40-700$ Jy, compared to a few tens of Janskys for the masers in the arms. If maser intensity reflects outflow activity, then perhaps outflow activity in the arms is less energetic than in the HII region. This may indicate stars forming within the arms are at an early stage of evolution, or will eventually be less massive than those in the central clump. Lower limits on clump masses derived from NH_3 range from less than $1 M_\odot$ to $\sim 130 M_\odot$, with a median value of $\sim 10 M_\odot$. For a typical star formation efficiency of up to 0.3 (c.f. Lada & Lada 2003) very few stars greater than $8 M_\odot$ will be formed.

Four merging velocity components are identified within the western and eastern arms of the filament, providing a clue to the trigger behind the star formation in the complex. The two components in the western arm merge adjacent to the HII region and we suggest that this may be the archaeological remains of a cloud-cloud collision. Similarly, two components are seen to merge at SIMBA clump S1, although this forked morphology may also have been sculpted by winds from the HII region.

On examination of the relative abundances, SIMBA clump S4 stands out as it

has an over-abundance of N_2H^+ and an under-abundance of CO. Such a chemical signature is typical of dense and cold regions and is often found towards collapsing cores. We looked for signatures of inflowing motions in the NH_3 line profiles but found none. However, we note that our data may be too optically thin to exhibit the expected line asymmetries.

We have confirmed that the stars are likely forming in the arms of the filament, however, it is not clear from our data if sequential star formation is taking place. The HII region is clearly influencing the conditions in the bulk of the cloud, as evidenced by the temperature gradients and gas-morphology. Confirmation of sequential star formation requires evidence of an 'age gradient', which is not present in the data. Further observations are needed to determine the spectral types and ages of the stars forming in each of the clumps.

6-6 Conclusions

We have mapped the molecular environment of the giant HII region NGC 3576 in lines of NH_3, CO, HCO^+, CS and N_2H^+. Additionally, we have also searched for 22 GHz water masers and UCHII regions via 23 GHz free-free emission. Our main conclusions are as follows:

1. We have detected molecular emission from all clumps identified in the 1.2-mm SIMBA map. Dense gas tracers (NH_3, N_2H^+, and CS) follow the morphology of the thermal dust emission, except within the HII region (traced by free-free continuum emission). Molecules with low and intermediate critical densities or with high abundances (CO, HCO^+) trace the extended envelope well.

2. We searched for UCHII regions in the arms of the filament via their 23 GHz emission, but found none down to a detection limit of 10 mJy/beam. The central HII region was mapped and exhibited a similar morphology to the earlier 3.4-cm image by de Pree et al. 1999.

3. Six new sites of 22 GHz water maser emission were detected, all of which lie

adjacent to discrete NH_3 clumps in the arms of the filament. All new masers have flux densities in the tens of Janskys, compared to the three known sites in the HII region, which have flux densities between $40-700$ Jy. The maser site in clump S5 has the greatest range of velocities and warrants further investigation.

4. NH_3 (1,1) and (2,2) were used to derive the kinetic temperature across the region. We find a temperature gradient exists in the western arm, with temperatures ranging from ~ 30 K near the HII region to ~ 11 K at the extremes. Clearly, the HII region is responsible for the heating.

5. The $\sim 10''$ resolution NH_3 (1,1) emission was decomposed into thirty-seven individual clumps, ranging in mass from $0.1\,M_\odot$ to $128\,M_\odot$, assuming a relative abundance of 1×10^{-8}. Results from the Tidbinbilla 70-m dish suggest these values are a lower limit because of missing flux in the ATCA data.

6. Virial masses are comparable to the LTE- and dust-masses, within the errors. LTE masses range from $1\,M_\odot$ to $128\,M_\odot$.

7. Clump S4 in Figure 6.1 is over-abundant in N_2H^+ and shows evidence for depletion of CO, consistent with chemistry in a cold, dense core. We examined our NH_3 data for line-profile asymmetries indicating inflowing motions, but none are apparent. We note that the emission has a low optical depth and line asymmetries, if present, are expected to be weak.

8. The filament displays a complex velocity structure, with two main components in each arm. The two components in the western arm appear to merge in the clump adjacent to the HII region. Such a morphology is consistent with a collision between molecular clouds.

9. The positions of stars with infrared-excess, indicating circumstellar disks, are anti-correlated with the dense molecular gas, implying star formation has not yet advanced far enough to be visible in the near-infrared.

10. From the above evidence it is clear that star formation is underway across the whole of the NGC 3576 filament and that the HII region is influencing the physical

conditions in the bulk of the molecular gas. Further observations are necessary to determine the nature of the stars being formed and whether the HII region is is the trigger.

Chapter 7

Conclusions and future work

This thesis presents a major investigation into the relationship between methanol (CH_3OH) masers, hot molecular cores and UCHII regions. Molecular line data spanning four years of observations are used to investigate the physical and chemical conditions at sites of 6.67 GHz CH_3OH masers.

In the 'Hot Molecular Cores' (HMC) project (Chapters 4 and 5) the properties of a large sample of sources are measured and conclusions are drawn from a statistical analysis of the data. The overall goal is to identify molecular signatures of evolution at methanol maser sites.

Using a different approach, Chapter 6 presents a detailed study of a single star forming complex: the molecular cloud surrounding the giant HII region NGC 3576. A clear picture is built up of how the emerging massive cluster influences its natal environment as it evolves.

Data from the Mopra telescope is used extensively throughout this thesis and collaborative work undertaken to calibrate its beam-shape and efficiencies is presented in Chapter 3.

In the following sections the results from the calibration of Mopra, the HMC project and the investigation of NGC 3576 are summarised and recommendations are made for future work.

7-1 Characterisation of the Mopra telescope

7-1.1 Summary

For the first time in 2004, the beam-shape and efficiencies of the 22-m Mopra telescope have been measured at frequencies ranging from 86 to 115 GHz. Beam-mapping observations were conducted in the winter of 2003 and 2004 only, however, the likely beam efficiencies for the years 2000 – 2003 have also been estimated from archived data.

The beam profile is found to be composed of two principal components: a Gaussian main beam extending out to angular offsets of $\sim 40''$ and an inner error beam, extending to offsets of $\sim 80''$. At 86 GHz, the full-width half-maximum of the main lobe is measured to be $36 \pm 3''$, shrinking to $33 \pm 2''$ at 115 GHz.

The efficiency of the main beam, $\eta_{\rm mb}$, was measured at several frequencies by comparing continuum observations of the planets Mars and Jupiter to empirical models of their brightness temperature. Values for $\eta_{\rm mb}$ range from 0.49 at 86 GHz to 0.42 at 115 GHz. Sources with angular extents greater than $80''$ couple to both the main beam and inner error beam, which in 2004 was found to contain 1/3 of the power present in the main beam. Values for the efficiency of this 'extended beam' ($\eta_{\rm xb}$) hence range from 0.65 to 0.55 over the same frequency range. Data calibrated onto the main beam or extended beam temperature scales (where appropriate) compare well to data from other international observatories.

In addition to the calibration work, a data reduction tool called 'Data From Mopra' (DFM) was developed to facilitate the reduction of simple position switched data. During the reduction process DFM automatically corrects for software bugs and calibration errors discovered during the commissioning work. All data for the HMC project was processed using this tool.

7-1.2 Future Work

As of the 2006 observing season, the correlator and receiver have been upgraded at Mopra and the beam re-characterised. With the advent of the new OTF-mapping mode, it is recommended that all observers map an SiO maser and a planet during the normal course of their observing run. Such data would be invaluable for the absolute calibration of the science data, but also to the ATNF for monitoring changes in the beam shape and efficiencies with time.

7-2 The Hot Molecular Cores survey

7-2.1 Summary

The Mopra telescope was used to survey for molecular emission towards 83 dusty clumps associated with CH_3OH masers. Targets were chosen from the source list of Walsh et al. (1998, 2003), which were themselves selected via the criteria of Wood & Churchwell (1989b) to have infrared colours indicative of UCHII regions.

Nine 3-mm transitions were observed towards each source: $CH_3CN\,(5-4)$, $CH_3CN\,(6-5)$, $CH_3OH\,(2-1)$, $^{13}CO\,(1-0)$, $N_2H^+\,(1-0)$, $HCO^+\,(1-0)$, $H^{13}CO^+\,(1-0)$, $HCN\,(1-0)$ and $HNC\,(1-0)$. To date this is the largest molecular line survey of its kind targeting CH_3OH masers. All but one of the targets are found to coexist with dense molecular gas.

The simple linear molecules ^{13}CO, N_2H^+, HCO^+, $H^{13}CO^+$, HCN and HNC were detected towards 82 targets (99 per cent) and beam-averaged column densities were derived for N_2H^+ and HCO^+.

CH_3CN, a tracer of warm and dense gas, was detected towards 58 sources (70 per cent), indicating the presence of a hot core within the $\sim 36''$ Mopra beam. 15 of these sources were previously known to harbour hot cores and the remaining 43 are new detections, effectively doubling the number of known hot cores.

Based on the 8 GHz continuum survey of Walsh et al. (1998), the sample may

be divided into masers associated with UCHII regions (radio-loud) and 'isolated' masers (radio-quiet). CH_3CN is detected towards both radio-loud and radio-quiet groups. That CH_3CN was detected towards 'isolated' masers strongly suggests that the powering source is internal.

The CH_3CN detection rate for radio-loud sources is 95 per cent compared to 63 per cent for radio-quiet sources. This result is consistent with the isolated maser sites being at a less advanced stage of evolution than the UCHII regions, i.e., the CH_3OH masers 'turn on' before the hot core becomes detectable and survive as the source evolves into a UCHII region. Based on 2-component greybody fits to the spectral energy distribution, the hot cores associated with the HII regions in the sample are found to be luminous and more massive, on average, than those associated with the isolated masers. Despite this, the CH_3CN detection rate remains higher towards UCHII regions when comparing luminosity matched samples, and the result still stands.

Rotational temperatures were derived for 38 sources where at least three CH_3CN lines were detected. Values range from 28 to 166 K, lower than previously published temperatures, derived from higher energy transitions. This supports the idea that in these observations, CH_3CN traces less dense gas further from the locus of the heating source.

CH_3OH is detected towards 78 sources (95 per cent). Rotational temperatures were derived for 71 sources and range from 3 K to 14 K, with a mean of 6.7 K. Considering that CH_3OH evaporates from icy grain mantles in warm gas (>90 K), these values are anomalously low implying that the transition is sub-thermally excited and that the rotational temperatures do not reflect the kinetic temperatures in the gas. Assuming the same excitation temperature, an average abundance ratio of 1.5 is derived between A- and E-type CH_3OH, consistent with previous observations in the literature.

By dividing the source-list into sub-samples associated with different tracers of age, it is possible to search for evidence of chemical evolution via a comparison between the median properties of the two groups. CH_3OH is found to be brighter

and more abundant in UCHII regions and in objects with detected CH_3CN, and may constitute a crude chemical clock in single dish observations. In contrast, despite being more luminous and easier to detect in UCHII regions, CH_3CN does not appear brighter or more abundant when compared to other lines.

Virial masses estimated from the N_2H^+ linewidths range from $40\,M_\odot$ to $2.5 \times 10^3\,M_\odot$. Values should be considered upper limits as the calculation does not take into account line-blending or magnetic support of clouds. Gas-masses derived from 1.2-mm emission Hill et al. (2005) range from $30\,M_\odot$ to $5 \times 10^3\,M_\odot$, consistent with having the same order of magnitude. The uncertainty associated with both calculations prevents the interpretation of individual clumps as gravitationally bound, although they are certainly consistent with being so.

A comparison of the optically thick HCO^+ line profile to its optically thin isotopomer, $H^{13}CO^+$, reveals blue- and red-skewed line profiles in 49 per cent of the sample. These profiles may be interpreted as signs of inward or outward gas-motions, respectively, and a statistical excess of either in a sample cannot be accounted for by rotation. Almost equal amounts of red and blue profiles are found in the source list, even when examining only a narrow cross-section (e.g., isolated masers only or UCHII regions only). The confused nature of these star-forming regions and the lack of spatial information means that these results are difficult to interpret.

The sample contains 12 infrared dark clouds (IRDCs), seen in absorption in the $8\,\mu$m MSX images. IRDCs are proposed to be the evolutionary precursors to hot cores (c.f. Rathborne et al. 2006), however, these clouds are found to contain a variety of objects with a wide range of properties, including one UCHII region. CH_3OH masers require high temperatures ($\sim 150\,K$, Sobolev et al. 1997) for excitation and clearly trace a later phase of star formation than the cold collapsing core. When searching for the earliest evolutionary phase of massive star formation, dark clouds associated with CH_3OH masers should be excluded.

The empirical mass-luminosity relation for the sample is found to be (weakly) $L \propto M^{0.68}$, compared to $L \propto M^3$ for evolved massive stars. In all cases, the mass of the gas in the clump is greater than the implied mass of the stellar content.

This is interpreted as a sign of the early evolutionary state of the maser-selected clumps, i.e., the embedded massive stars have not yet dispersed their natal molecular environment.

7-2.2 Future work

A number of the findings in this thesis require further investigation to eliminate systematic uncertainties.

The powering sources in our sample are biased towards being more luminous and more massive when associated with UCHII regions, compared to isolated masers. Bolometric and radio luminosity have been shown to be correlated (Beuther et al. 2002; Walsh et al. 1998), implying that the disparity in luminosity may be due to a sensitivity limit on the original radio-continuum survey. Hence, the division of the sample into objects with and without UCHII regions may be false. Recent continuum observations of 44 of these sources by Longmore et al. (*in preparation*) reveal that many isolated masers do in fact have detectable continuum emission at 22 GHz.

Some of the maser sites may also be associated with hyper-compact HII (HCHII) regions. This recently discovered class of HII region is typically less than 0.01 pc across (Avalos et al. 2006) and exhibits a free-free emission spectrum with a thick-thin turnover point at higher frequencies than typical UCHII regions. While little is known about HCHII regions to date, it is not necessarily correct to assume that the lifetime of HCHII regions will be negligible. Indeed, there is likely considerable overlap with the hot core phase. Keto (2003) has examined the possibility that accretion may continue despite the formation of an ionised HII region around the forming massive star or cluster. In this scenario the HII region begins quenched, evolves onto a long-lived (10^4-10^5 yr) 'trapped' phase and finally, as the accretion slows and the radiation pressure increases, expands rapidly. In order to correctly classify massive young stellar objects in the future, it is recommended that a sensitive survey is conducted for continuum emission at frequencies greater than 50 GHz, where the free-free emission is likely to be optically thin.

The eventual goal of this and similar work is to identify key species for use as a chemical clock. Comparing beam-averaged single dish observations to chemical models is often inconclusive. At early times the spatial extent of the gas containing high abundances of hot core molecules is expected to be small ($<20{,}000\,\mathrm{AU}$, Kurtz et al. 2000) and beam dilution factors act to smooth out the abundance differences. Rodgers & Charnley (2003), for example, present chemical models of hot cores convolved with the beam of a single dish telescope. While, beam-averaged abundances are predicted to change by an order of magnitude over the lifetime of the hot core ($10^5\,\mathrm{yrs}$), many of these species increase in step with each other. Candidate chemical clocks should ideally have abundance ratios which change by several orders of magnitude over the hot core lifetime. In this regard, esters and ethers formed through the reaction of alcohols may be particularly useful. Of these molecules methyl ethyl ether ($CH_3OC_2H_5$), dimethyl ether (CH_3OCH_3) and methyl formate (CH_3CHO) are predicted to have increasingly high abundances over time (Charnley et al. 1995).

Accurate abundance measurements are obviously essential when searching for chemical clocks. The unknown geometry of the emission within the beam adds an unknown uncertainty to single-dish measurements. Interpretation of observations in Chapters 4 and 5 suffer from the relatively low angular resolution of Mopra ($\sim 35''$). At a distance of 3 kpc the beam covers a physical size of $\sim 1\,\mathrm{pc}$ ($\approx 200{,}000\,\mathrm{AU}$) and likely samples emission from multiple discrete objects, which may be at very different stages of evolution (e.g., as in the case of G29.96−0.02, in Chapter 1). In order to disentangle emission from adjacent objects, and to correct for geometric effects, it is imperative to conduct observations at resolutions better than an arcsecond.

The accuracy of abundance measurements will also be limited by the number of transitions observed. Derivations of column density presented in this thesis rely on the assumption of local thermal equilibrium, which may not be valid in all cases. Non-LTE effects are much better identified when multiple transitions spanning a wide range of excitation conditions are measured. Future data should be analysed using the large velocity gradient technique, which takes into account radiative trap-

ping. In general, the greater the number of transitions measured, the smaller the absolute error on the derived abundance. High excitation transitions in the sub-millimetre bands exclusively trace dense and warm gas, giving access to the region adjacent to the powering sources. Correlators with bandwidths of several GHz are just now becoming available for the 3-mm band (e.g., the new MOPS correlator at Mopra, see http://www.narrabri.atnf.csiro.au/mopra/) which will allow simultaneous observations of multiple molecular lines.

The results presented in this work will form an excellent basis for future investigations of massive star-formation in the southern sky. Little is known about over two thirds of the HMC sample and the 43 newly detected hot cores are excellent candidates for further study with new high-resolution instruments, such as ALMA and the SMA. Of particular interest are the few very luminous sources without detected UCHII regions. These constitute the rarest and most massive stars, potentially at a stage of evolution prior to the development of a UCHII region. G6.54-0.11, G10.63-0.33, G24.79+0.08, G331.28-0.19 and G30.59-0.04 all have luminosities equivalent to single O7 type stars or earlier.

7-3 NGC 3576

7-3.1 Summary

A multi-wavelength study has been conducted of the giant HII region NGC 3576 and its environment. Recent 1.2-mm observations have revealed that the ionised gas is embedded in a larger filamentary structure of cool, dense dust, extending north east – south west. This thesis presents the first images of the entire complex made using the ATCA, Tidbinbilla and Mopra telescopes in ten molecular lines and 23 GHz continuum emission.

The ATCA interferometer was used to image the filament in the J K=(1,1), (2,2) and (4,4) transitions of NH_3, while the 70-m single-dish telescope at Tidbinbilla measured the total integrated flux density. The region was mapped in the 3-mm tran-

sitions of ^{13}CO (1 – 0), C^{18}O (1 – 0), HCO$^+$ (1 – 0), H^{13}CO$^+$ (1 – 0), N_2H^+ (1 – 0) and CS (1 – 0), using the new OTF mapping mode of the Mopra telescope. Observations were conducted with the aim of investigating if star-formation was taking place in the 'arms' of the filament.

Molecular emission was detected across the whole region. The dense gas tracers, N_2H^+ and CS, closely follow the 1.2-mm emission, except in the central HII region. The ATCA data was also used to image the 23 GHz continuum emission from the ionised gas. A comparison between the clumpy morphology of the molecular gas and the cometary morphology of the ionised gas reveals that the HII region is confined by the cloud on its western edge, while it has likely destroyed or dissipated much of the molecular gas on its eastern side.

Analysis of the NH_3 (1,1) and (2,2) data has shown that a clear temperature gradient exists in the western arm. Kinetic temperatures are highest adjacent to the boundary of the HII region ($\sim$30 K) and decrease to ambient values ($\sim$ 11 K) in the extremes, implying that the HII region is responsible for the heating. Gas in the inner part of the eastern arm is clumpy in nature and exhibits temperature 'hot spots', consistent with the interpretation that the gas is being swept away by supersonic winds or outflows from the HII region.

The NH_3 (1,1) emission has been decomposed into 37 individual clumps larger than the ATCA synthesised beam (11″) and their LTE masses have been calculated. Assuming an NH_3:H_2 abundance ratio of 1×10^{-8}, LTE masses range from 1 $M_\odot$ to 128 $M_\odot$. These values are comparable to the virial masses, also derived the NH_3 (1,1) data.

Column density maps have been made of CO, HCO$^+$, N_2H^+ and CS. A comparison between the maps reveals the SIMBA clump at $11^h11^m38.33^s$, $-61^d19^m53.9^s$ (J2000) has an overabundance of N_2H^+ and an under-abundance of CO, consistent with the chemistry of a cold, dense collapsing core. However, the kinetic temperature derived from NH_3 is $\sim$25 K, greater than typical temperatures of $\sim$ 10 K reported in the literature for similar objects. The NH_3 (1,1) line profiles were examined for signs of asymmetries indicating collapse, however, none are detected. Collapse cannot be

ruled out because the low optical depth of the NH_3 (1,1) transition means it is not sensitive to bulk motions in the gas.

The eastern arm of the filament is composed of two velocity-components, which merge adjacent to the central HII region. It is suggested that this morphology may be a telltale sign of a cloud-cloud collision. Two smaller velocity components are observed to merge into the SIMBA clump at the eastern extreme of the filament.

NGC 3576 was mapped for 22 GHz H_2O maser emission using the ATCA. Six new maser sites were detected in the arms of the filament, in addition to the three previously known masers in the central HII region. All maser sites are coincident with well defined clumps of NH_3 emission. Water masers are thought to be excited in outflows, indicating that star-formation is taking place in the clumps, however, it is not clear if massive stars are forming as no 23 GHz radio-continuum emission was detected towards the arms.

Any stars forming within the molecular clouds are likely young, as the positions of stars with infrared excess are anti-correlated with the molecular gas.

7-3.2 Future work

The results presented here demonstrate that stars are forming in the arms of the NGC 3576 filament. It is not yet clear, however, what their final masses will be or whether the star-formation has been triggered by the proximity of the HII region.

Further observations are needed to determine the masses and luminosities of the clumps detected via their 1.2-mm and NH_3 emission. One obvious route to take would be to measure the full SED of each clump. The data presented here clearly shows that the arms of the filament are seen in absorption in the near-infrared. Mid-infrared MSX data shows a similar picture, hence the SED must peak at longer wavelengths than 21 μm. The MIPSGAL Spitzer space telescope survey ($\lambda \sim 70\,\mu$m), will provide data on the Wiens side of the SED, however, new observatories such as the Herschel space telescope, which will operate from $60-600\,\mu$m, are necessary to constrain the peak. Herschel is due to launch in 2007. In the interim, the James

Clerk Maxwell Telescope (JCMT) could be used to obtain flux density points on the SED at 450 and 850 μm. The total bolometric luminosity and mass could then be determined using a simple greybody fit to these points.

If the SED fitting indicates that massive stars are indeed forming within the arms of the filament, then these objects are likely to be at a very early evolutionary state. A concerted effort should be made to search for inward gas motions at high resolution. Some of the more useful tracers in this respect would be the J = 2 – 1 transitions of CS and $C^{34}S$, however, the skewed profiles are only expected at high densities and small scales, and hence require arcsecond resolution observations. The newly upgraded ATCA would be an ideal instrument with which to pursue this study.

Evidence for outflow activity has been presented in the form of H_2O masers. To constrain the type of star formation taking place it is necessary to measure the mass loss rate from the velocity of the outflow. This could be easily achieved using the newly upgraded ATCA at 3-mm to observe SiO, which is preferentially enhanced in outflows. Data would also potentially reveal the orientation and extent of any outflow lobes, allowing a further study of sequential star formation in NGC 3576.

7-4 A vision for the future

This is an exciting time to study massive star formation. The capability to perform large scale multi-object and multi-transition spectral line surveys is truly new. Up until this year, the time necessary to observe large numbers (>50) of objects would have been prohibitively long for any single proposal. However, advances in sensor technology in 2005/2006 have changed the paradigm within which astronomers operate. For example, the new MOPS correlator installed on Mopra in 2006 is the first of a new generation of instruments which will be capable of recording hundreds of spectral lines simultaneously, over a continuous 8 GHz-wide band. The Mopra observations presented in Chapters 4 and 5 were conducted painstakingly over four years, measuring a single spectral line at a time. The new instrumentation would

allow the same body of data to be compiled within a few short weeks and with greater calibration accuracy. Similar advances are being made elsewhere, for example the SCUBA2 and HARP-B instruments on the JCMT. The speed and sensitivity of these instruments is such that it becomes extremely feasible to map large sections of the sky in reasonable times.

Chemical clocks have been the holy-grail of molecular surveys for decades. The ability to assign an age to a massive young stellar object based on its chemistry would have wide implications for all branches of astrophysics, from early galaxy formation to planet formation. However, to develop useful chemical clocks requires a statistical sample of massive young stellar objects, covering a range of luminosities and initial conditions. In late 2006 the JCMT will map the entire northern Galactic plane for thermal dust emission at 450 and 850 μm, using SCUBA2. A complimentary southern survey on APEX is also planned. These surveys will deliver an unbiased sample of the massive star forming clumps across the Galactic disk. To compare objects we need to normalise the sample by measuring their physical characteristics. Combining the data from the SCUBA2 Galactic Plane Survey with infrared data from the SPITZER surveys and sub-millimetre data from the upcoming Herschel satellite, will allow the determination of masses and luminosities for the whole sample. Further identification of massive star-forming regions at different evolutionary states will be achieved using the 6.67 GHz methanol maser multi-beam survey (currently underway), infrared selection criteria (e.g., from GLIMPSE, MIPSGAL, UKIDSS and the RMS survey) and free-free continuum surveys (e.g., the CORNISH survey). For the first time a representative sample of massive young stellar objects will be constructed, normalised by luminosity and mass.

In the latter half of the decade, using the new capabilities of Mopra, the JCMT and APEX (amongst others), astronomers will be able construct the first empirical models of chemistry in MYSOs. Through comparison of line intensities, and using statistical analysis techniques such as principal component analysis, they will identify trends in the abundance of key species. Such a result will drive the development of the next generation of chemical models and throw light on the complex early

evolution of massive stars. The SMA and IRAM (PdB) sub-millimetre interferometers will be used to image a select number of objects at sub-arcecond resolution and to investigate the trends in detail, so as to understand the underlying physics. High excitation spectral lines in the sub-millimetre regime trace the densest gas and probe the physical and chemical conditions close to the ignited star.

Looking further to the future, when the ALMA interferometer becomes operational in 2009 it will provide astronomers with a tool much more sensitive and with far greater resolving power than the current generation of telescopes. To make the most efficient use of ALMA careful consideration must be made of potential targets. Compared to their northern hemisphere counterparts, star forming regions in the southern hemisphere are relatively unknown. This thesis has identified an important set of southern hemisphere targets for future high resolution study with ALMA.

Appendix A

Determining kinematic distances

Measured values for the fundamental physical properties of a source, such as luminosity, size and mass, are dependent on the square of the distance to the source. In order to compare absolute values between sources, it is vital to obtain reliable distance estimates. Accurate distances to nearby sources have been found by measuring parallaxes (e.g., the Hipparcos mission, Perryman et al. 1995) but this technique is limited to sources within a few hundred parsecs. The easiest way to estimate a source's distance in the Galaxy is to measure its velocity along the line of sight via spectral line observations. The radial velocity of the source about the Galactic centre can then be determined using geometry and an estimate of source distance found assuming a Galactic rotation curve (e.g., Brand & Blitz 1993). Figure A.1 illustrates the geometry of this 'kinematic distance' technique. The following procedure was used to determine distances of all sources in Chapters 4 and 5.

The radial velocity of source with respect to sun is given by:

$$\mathrm{v_r} = \mathrm{V_s}\,\mathrm{Cos(m)} - \mathrm{V_O}\,\mathrm{Sin}(l), \tag{A.1}$$

where $\mathrm{V_s}$ is the radial velocity of the source, $\mathrm{V_0}$ is the radial velocity of the Sun in its orbit around the Galactic centre, and l is the galactic longitude of the source.

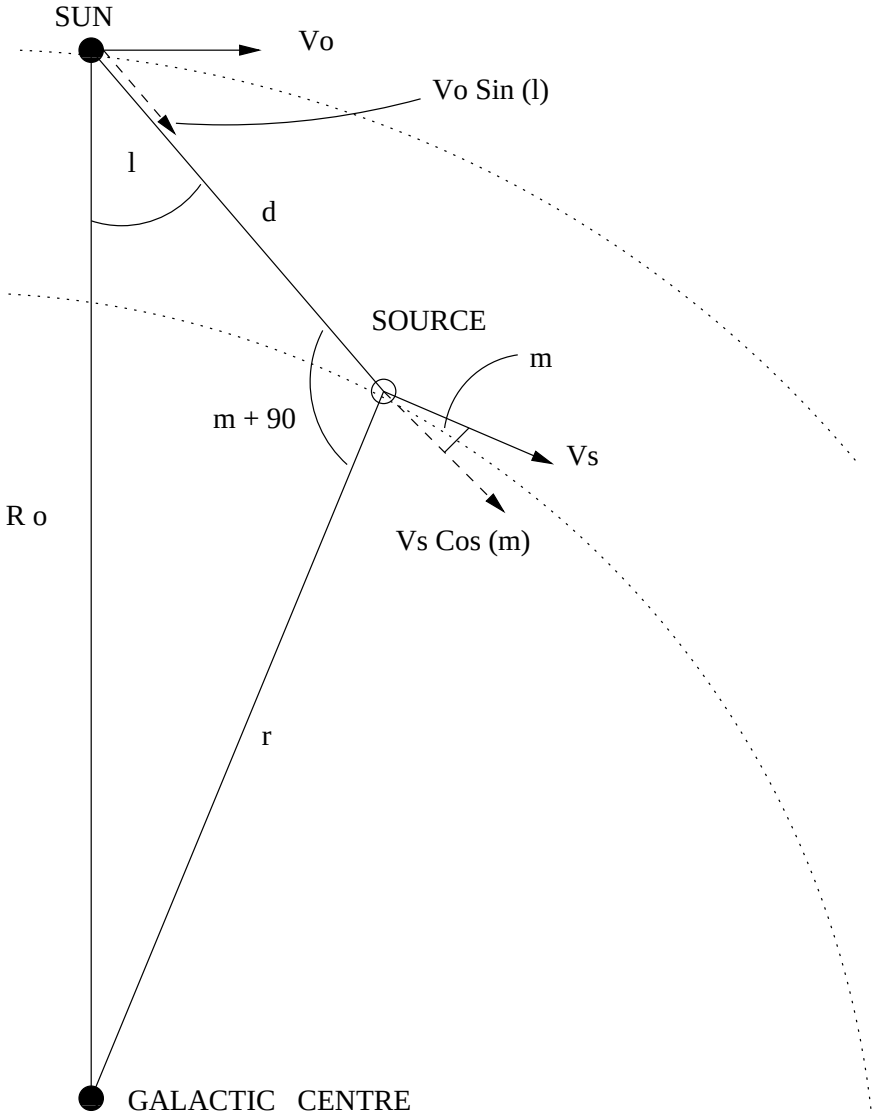

Figure A.1. Sketch showing the geometry of the kinematic distance problem.

Applying the sine-law to the sun-source-centre triangle we find

$$\frac{\mathrm{Sin}(l)}{\mathrm{r}} = \frac{\mathrm{Sin}(90^\circ + \mathrm{m})}{\mathrm{R_O}} = \frac{\mathrm{Cos(m)}}{\mathrm{R_O}}$$

$$=> \quad \mathrm{v_r} = \left(\frac{\mathrm{R_O V_s}}{\mathrm{r}} - \mathrm{V_O}\right) \mathrm{Sin}(l)$$

$$=> \quad \mathrm{V_s} = \frac{\left(\frac{\mathrm{v_r}}{\mathrm{Sin(l)}} + \mathrm{V_O}\right) \mathrm{r}}{\mathrm{R_O}}, \tag{A.2}$$

where $\mathrm{R_0}$ is the distance from the Sun to the Galactic centre. The Galactic rotation curve from Brand & Blitz (1993) is given by the empirical expression

$$\mathrm{V_s} = \mathrm{V_O} \left[\mathrm{a_1} \left(\frac{\mathrm{r}}{\mathrm{R_O}}\right)^{\mathrm{a_2}} + \mathrm{a_3}\right], \tag{A.3}$$

where $a_1 = 1.00767\,\mathrm{km\,s^{-1}}$, $a_2 = 0.0394$ and $a_3 = 0.00712\,\mathrm{km\,s^{-1}}$. Equations A.2 and A.3 are then combined to give an expression relating distance from the Galactic centre r and the measured radial velocity r_v

$$\frac{R_O V_O (a_1 \left(\frac{r}{R_O}\right)^{a_2} + a_3)}{\left(\frac{v_r}{\mathrm{Sin(l)}} + V_O\right) r} - 1 = 0 \tag{A.4}$$

Equation A.4 must be solved for r numerically, using the bisection method for example. Applying the Cosine-Law to Figure A.1 then gives:

$$\begin{aligned} & r^2 = d^2 + R_O^2 - 2R_O d\,\mathrm{Cos}(l) \\ => \quad & 0 = d^2 + (-2R_O \mathrm{Cos}(l))d + (R_O^2 - r^2) \end{aligned} \tag{A.5}$$

which is a quadratic and may be solved for d using the quadratic formula:

$$\frac{2R_O \mathrm{Cos(l)} \pm \sqrt{(-2R_O \mathrm{Cos(l)})^2 - 4(R_O^2 - r^2)}}{2}. \tag{A.6}$$

Outside the solar circle ($l > |90°|$) only one of the roots will be valid and a single kinematic distance exists. Inside the solar circle there will be two valid solutions: the near and far kinematic distances. Additional data is required to solve this 'distance ambiguity' (see Kolpak et al. 2003 and Jackson et al. 2002 for suggested methods.)

Appendix B

Greybody SED fits

Most of the thermal energy emitted by massive young stellar objects (MYSOs) is concentrated in the frequency range from $\sim 300\,\mathrm{GHz}$ (λ=1-mm) to $\sim 300\,\mathrm{THz}$ (λ=1 μm). The spectral energy distribution (SED) characterises the how the emission changes with frequency and can be a useful tool to reveal the nature and evolutionary state of MYSOs. Its shape is linked to the temperature and structure of the circumstellar material, and the total integrated intensity is directly proportional to the luminosity of the powering source.

Like their low-mass young cousins, MYSOs exhibit SEDs which differ substantially from a simple stellar blackbody. Sources in the Hot Molecular Cores project were fit with model SEDs representing emission from a warm and compact inner core, surrounded by a cool and extended dusty envelope. The function used was a sum of two blackbodies, modified by the dust optical depth:

$$\mathrm{F}_\nu = \mathrm{B}_\nu(\mathrm{T}_{\mathrm{cool}})\,\Omega_{\mathrm{envelope}}\,(1 - \mathrm{e}^{-\tau_\nu}) + \mathrm{B}_\nu(\mathrm{T}_{\mathrm{hot}})\,\Omega_{\mathrm{core}}. \tag{B.1}$$

In Equation B.1 τ_ν is the dust optical depth and Ω_{core} and $\Omega_{\mathrm{envelope}}$ are the solid angles subtended by the core and envelope. The optical depth is dependent on the frequency ν according to

$$\tau_\nu = \left(\frac{\nu}{\nu_0}\right)^\beta, \tag{B.2}$$

where ν_0 is the optical depth turnover frequency and β is the emissivity index of

the dust grains. The following pages present the results of our SED fits, which are analysed in section 4-2.2.

In the plots, MSX data points are plotted as circles, IRAS data points are plotted as squares, SCUBA data points are plotted as crosses and SIMBA data points are plotted stars. The solid line represents a two-component greybody fit to all data points, while the dashed line represents a fit to the SIMBA, SCUBA and MSX data only.

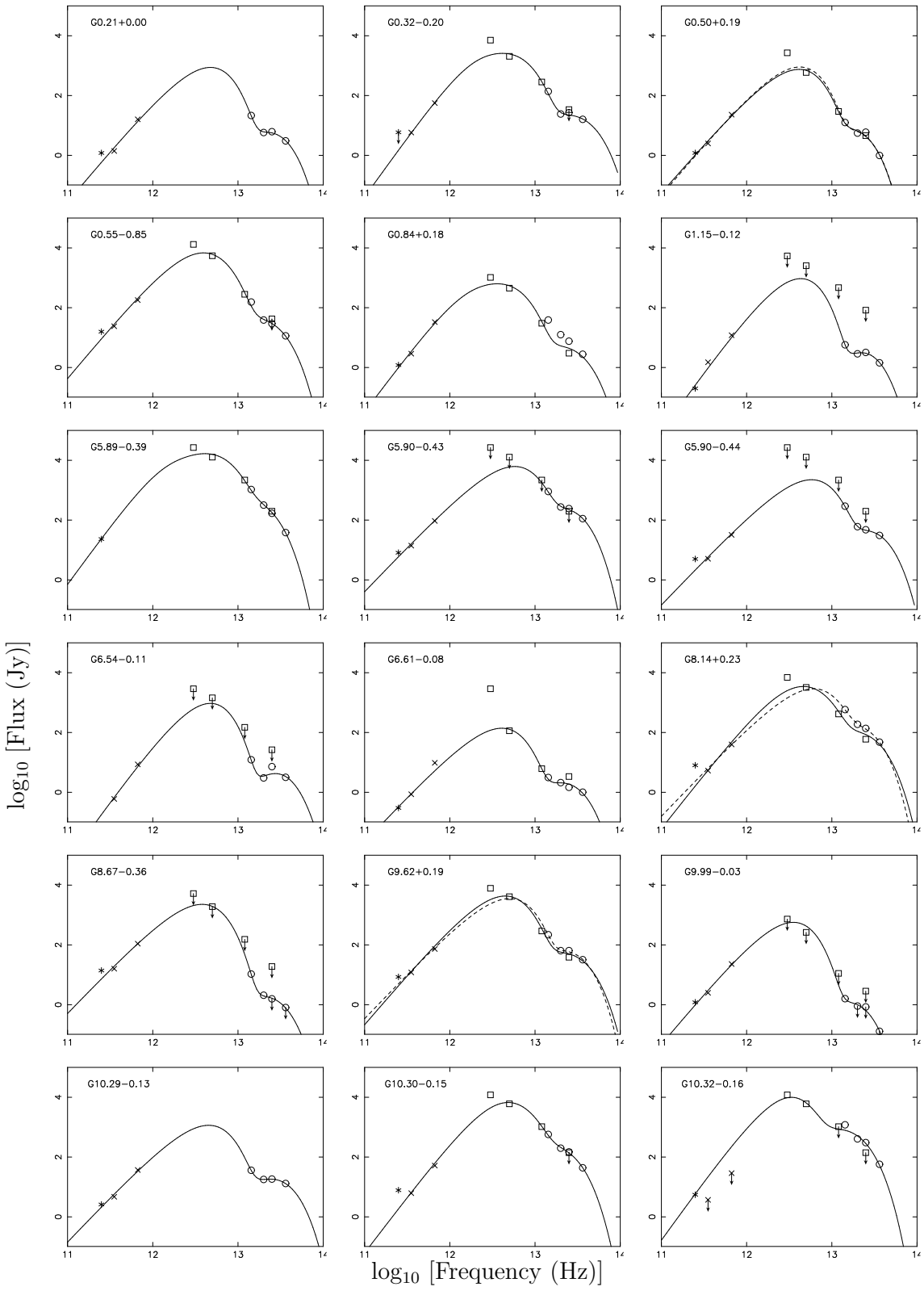

Figure B.1. Greybody fits to the SED of sources with near-IR and sub-millimetre data.

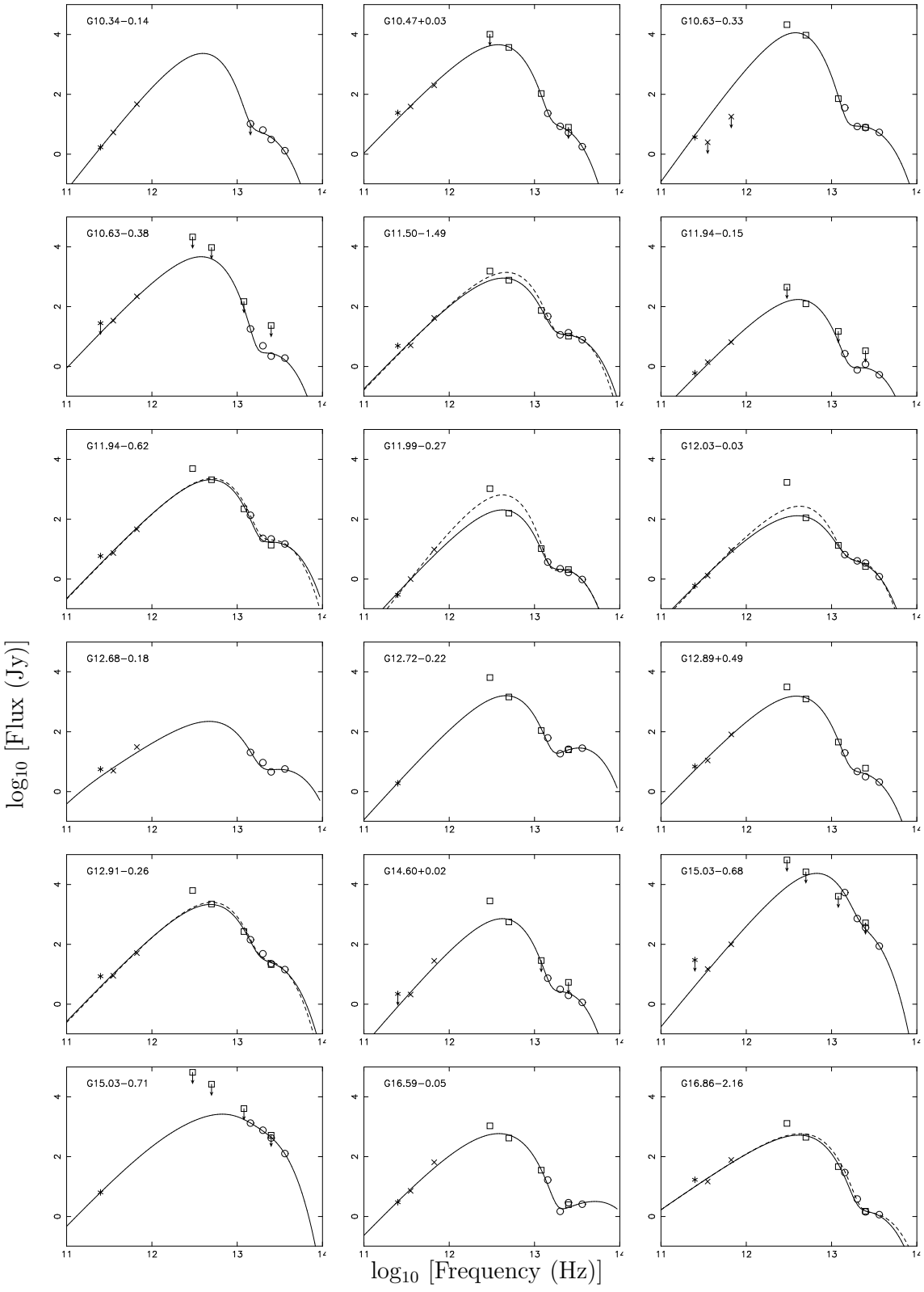

Greybody SED fits, – *continued.*

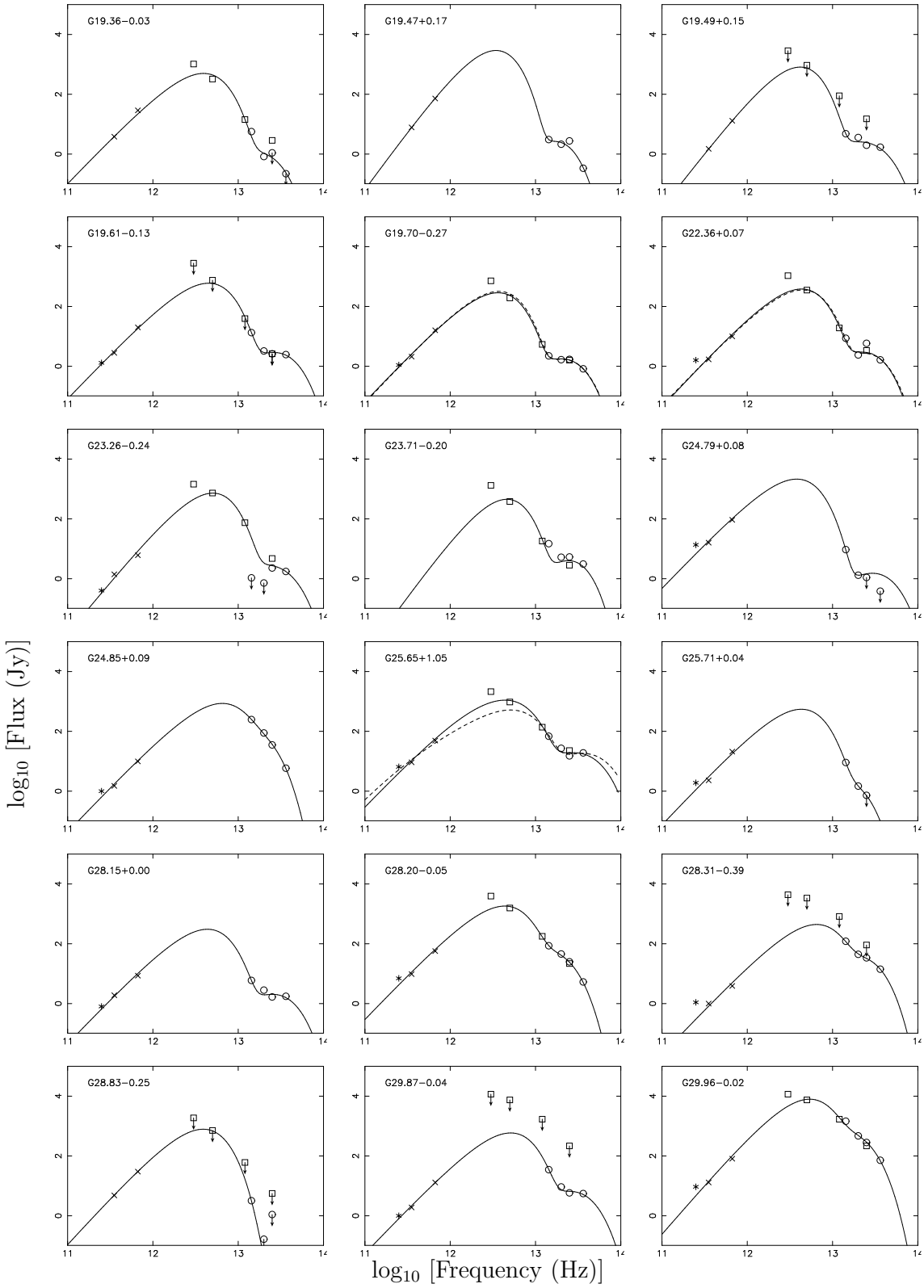

Greybody SED fits, – *continued.*

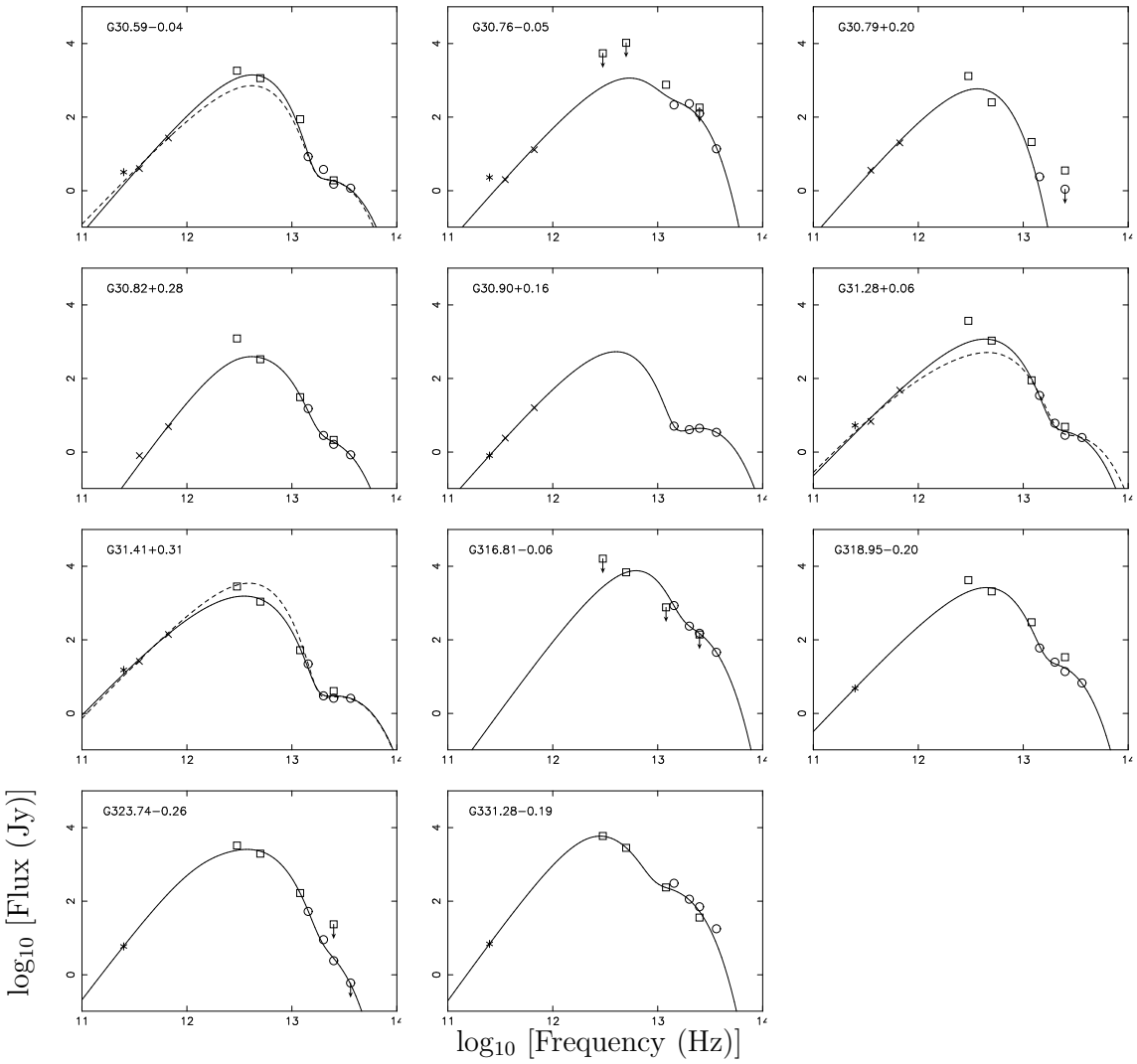

Greybody SED fits, – *continued.*

Appendix C

Mopra spectra

The following pages present the Mopra spectra, Gaussian fits and MSX-images for each of the 83 sources in the Mopra Hot Molecular Cores (HMC) survey (Chapters 4 and 5).

All spectra have been calibrated onto the main beam brightness temperature scale (T_{MB}) using the appropriate value of η_{mb} (see Table 3.4). Vertical dashed lines represent the systemic velocity of the source measured from the peak of the Gaussian fit to the $H^{13}CO^{+}$ line. Dotted lines represent the expected positions of other lines based on the systemic velocity. Gaussian lines were fit to all spectra except HCN, which exhibits complicated line profiles (see sections 4-4 and 5-3 for further details). Fits to individual components are plotted by a solid green line and the cumulative fit by a solid red line. Tables recording the parameters of the fits are presented in Appendix D.

The colour-scale plots present the 21 μm (E-band) 8 μm (A-band) MSX images, centred on the Mopra pointing position. Annotated on the images are the positions of the methanol masers (crosses) and the 36″ FWHM size of the Mopra beam at 86 GHz (circle). Squares mark the peaks of the compact 8 GHz continuum emission detected by Walsh et al. (1998). Colour versions all figures are available in the electronic version of this work.

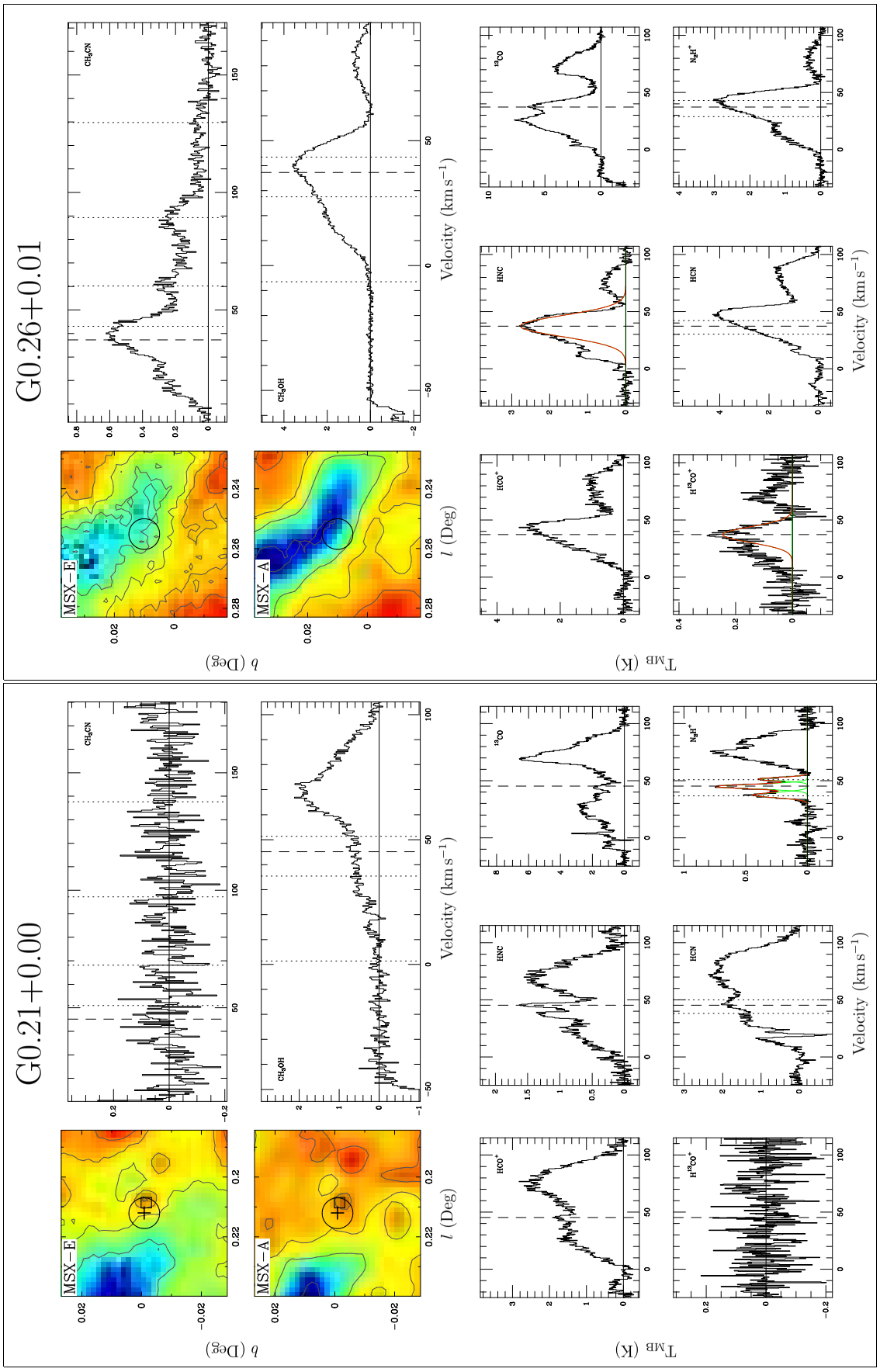

Figure C.1. Mopra spectra and near-infrared MSX-images for the HMC sources.

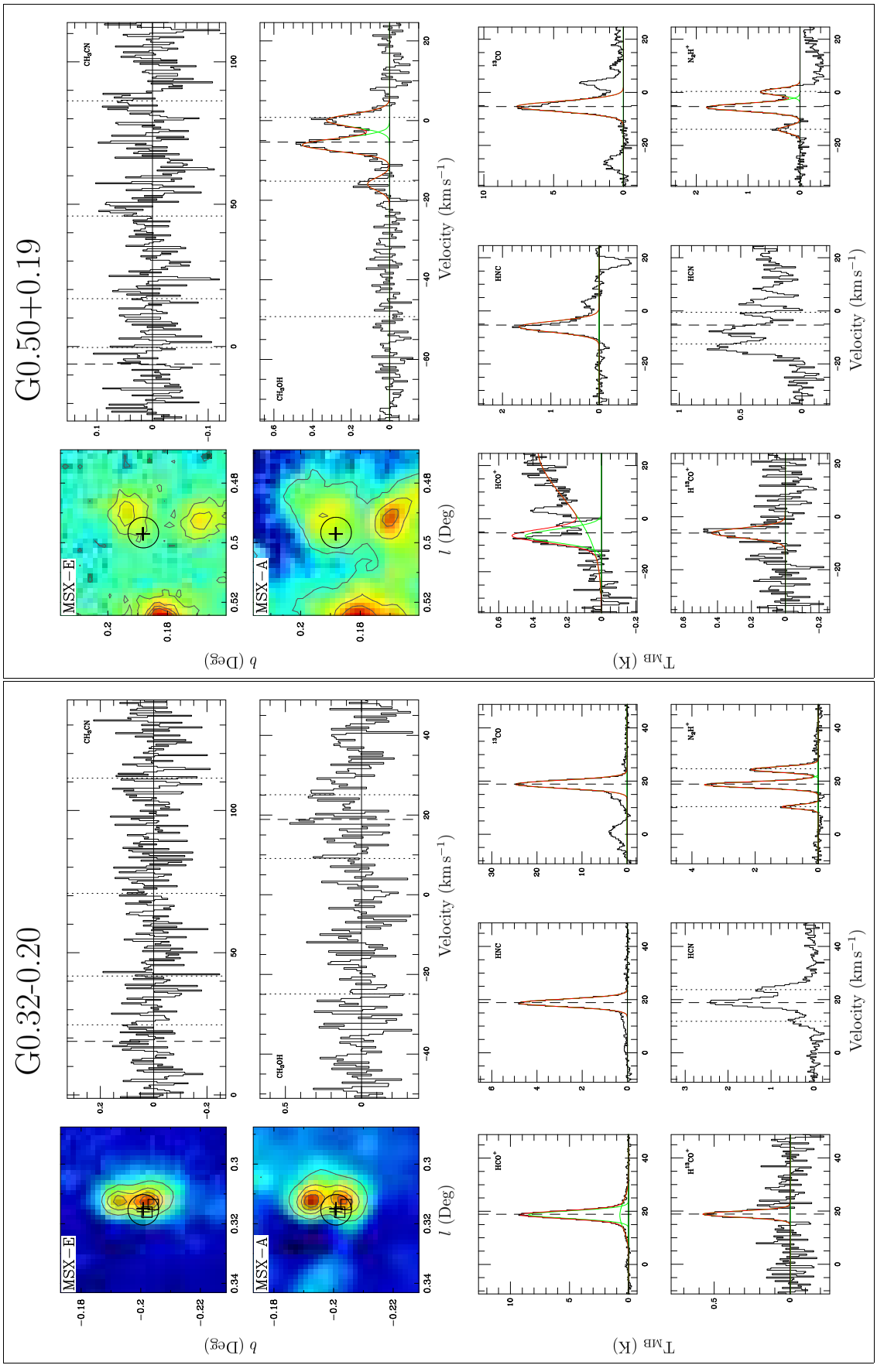

Mopra spectra and MSX images – *continued.*

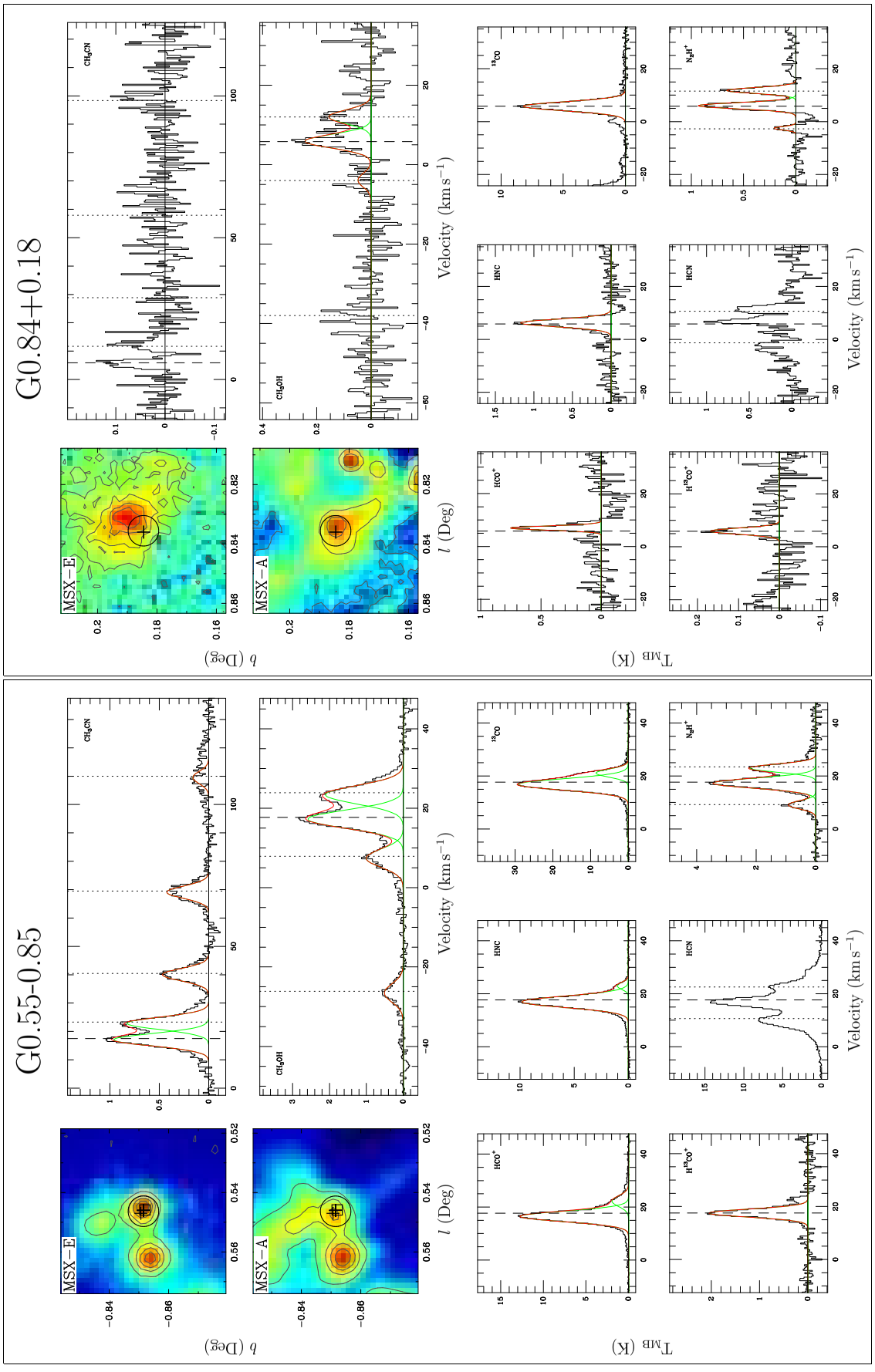

Mopra spectra and MSX images – *continued.*

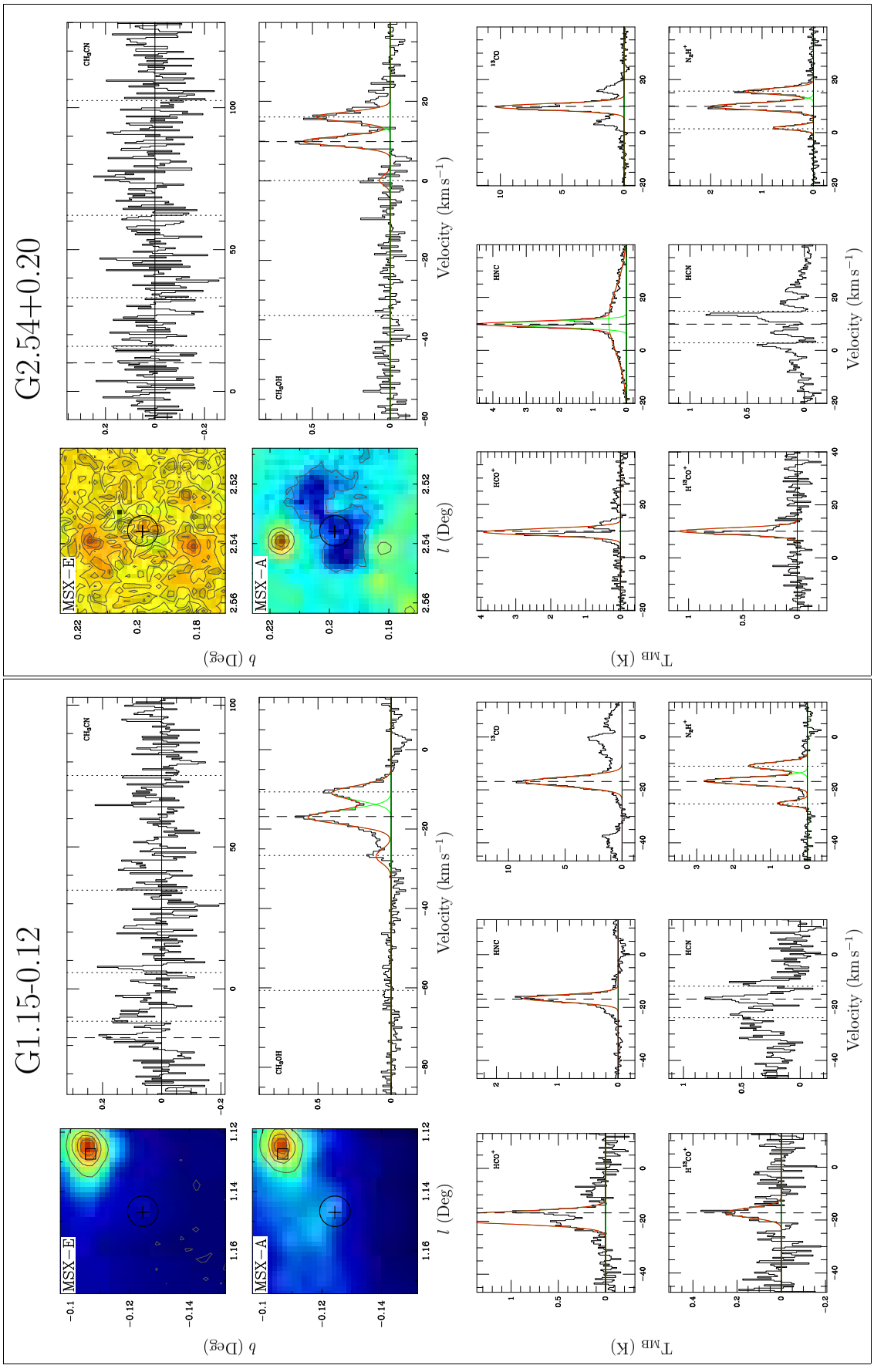

Mopra spectra and MSX images – *continued.*

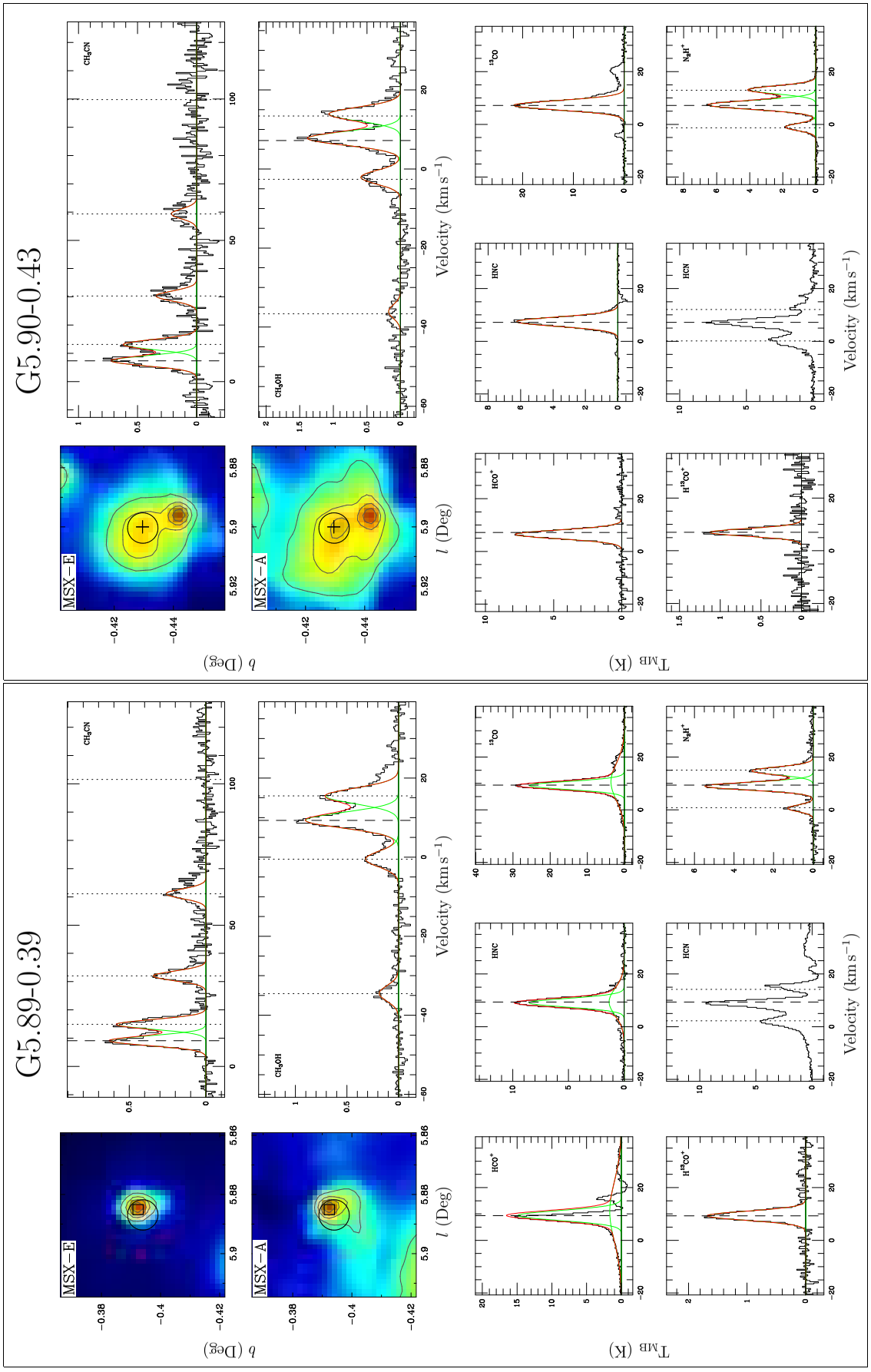

Mopra spectra and MSX images – *continued.*

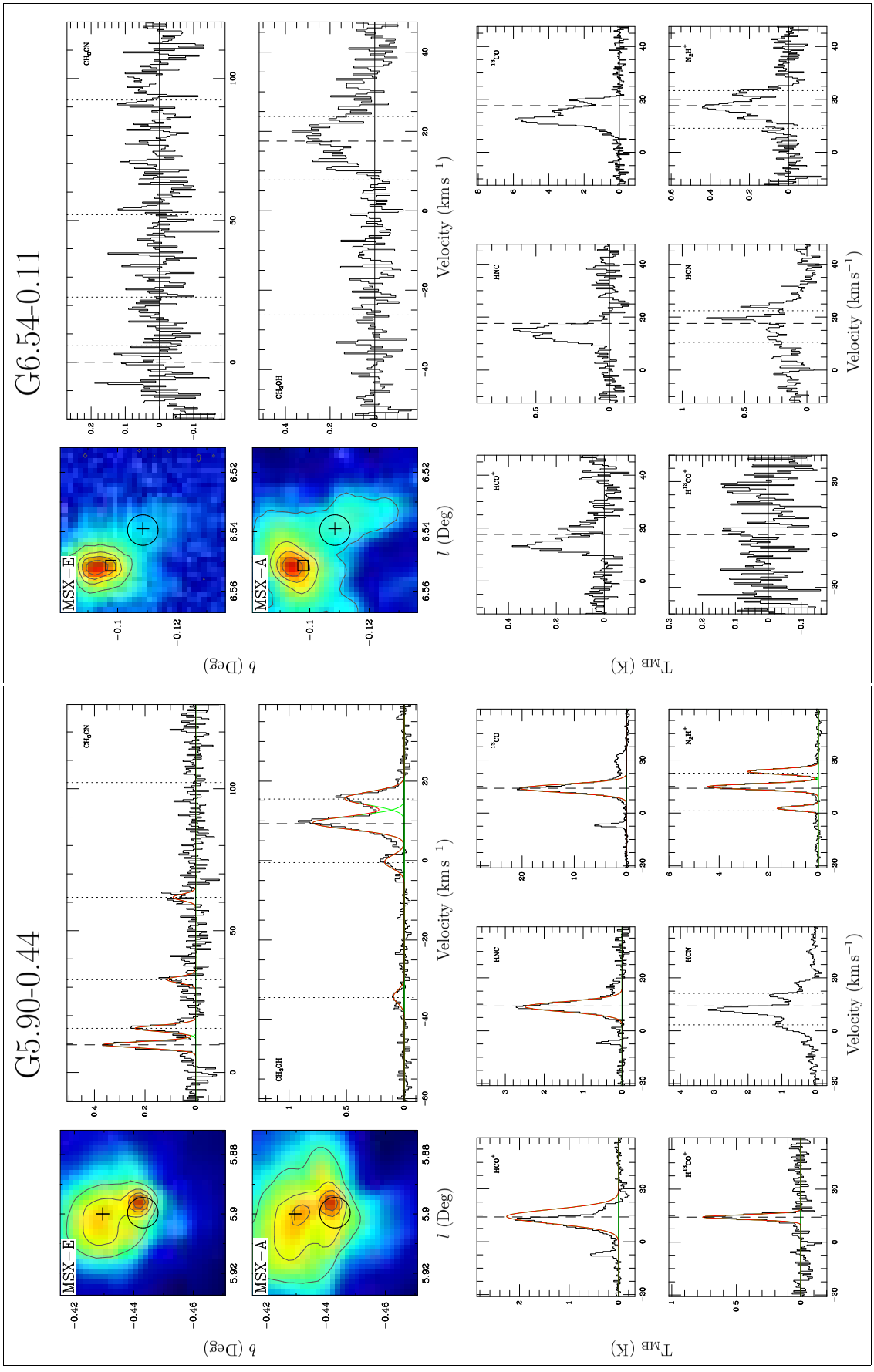

Mopra spectra and MSX images – *continued.*

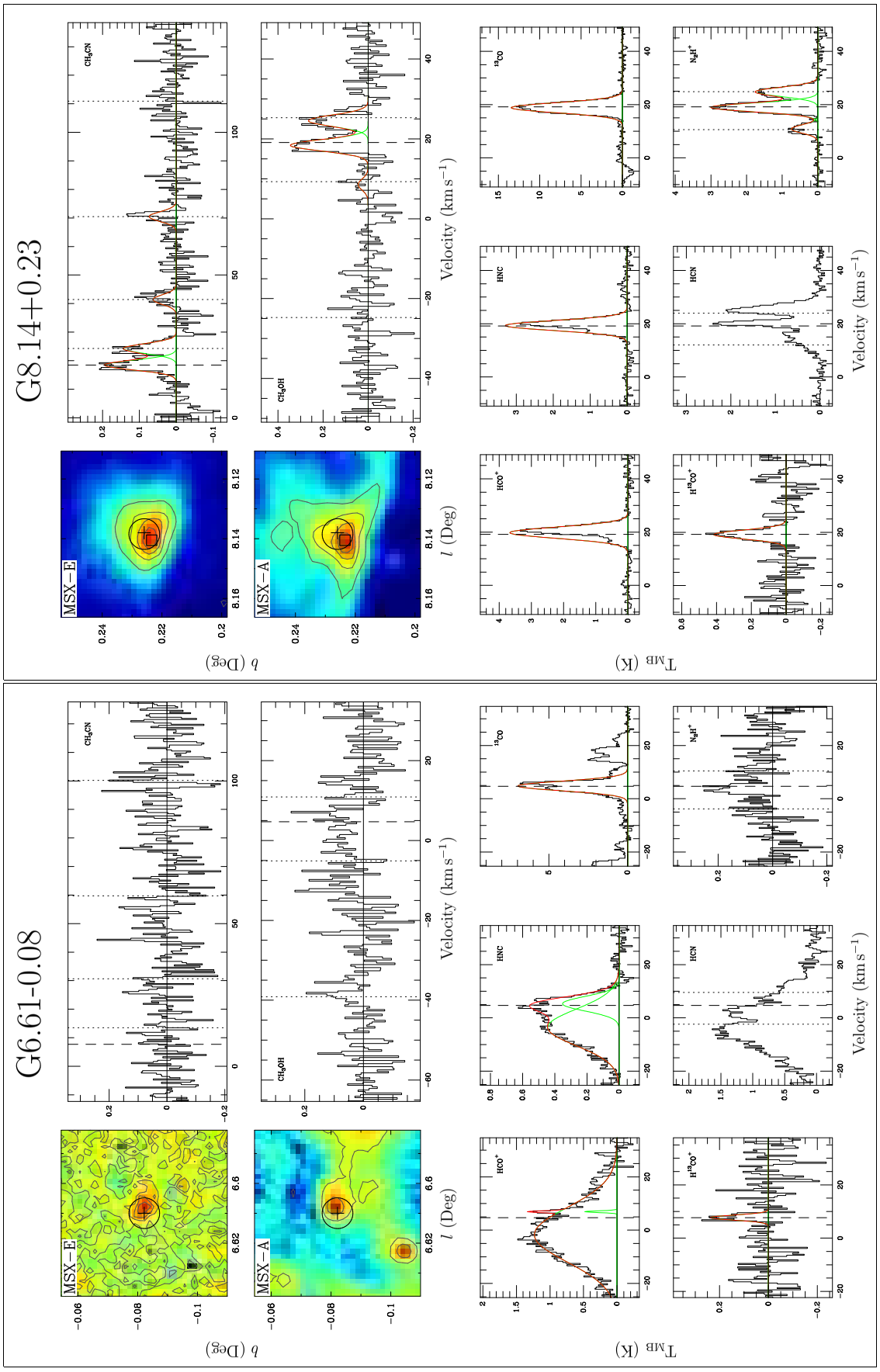

Mopra spectra and MSX images – *continued.*

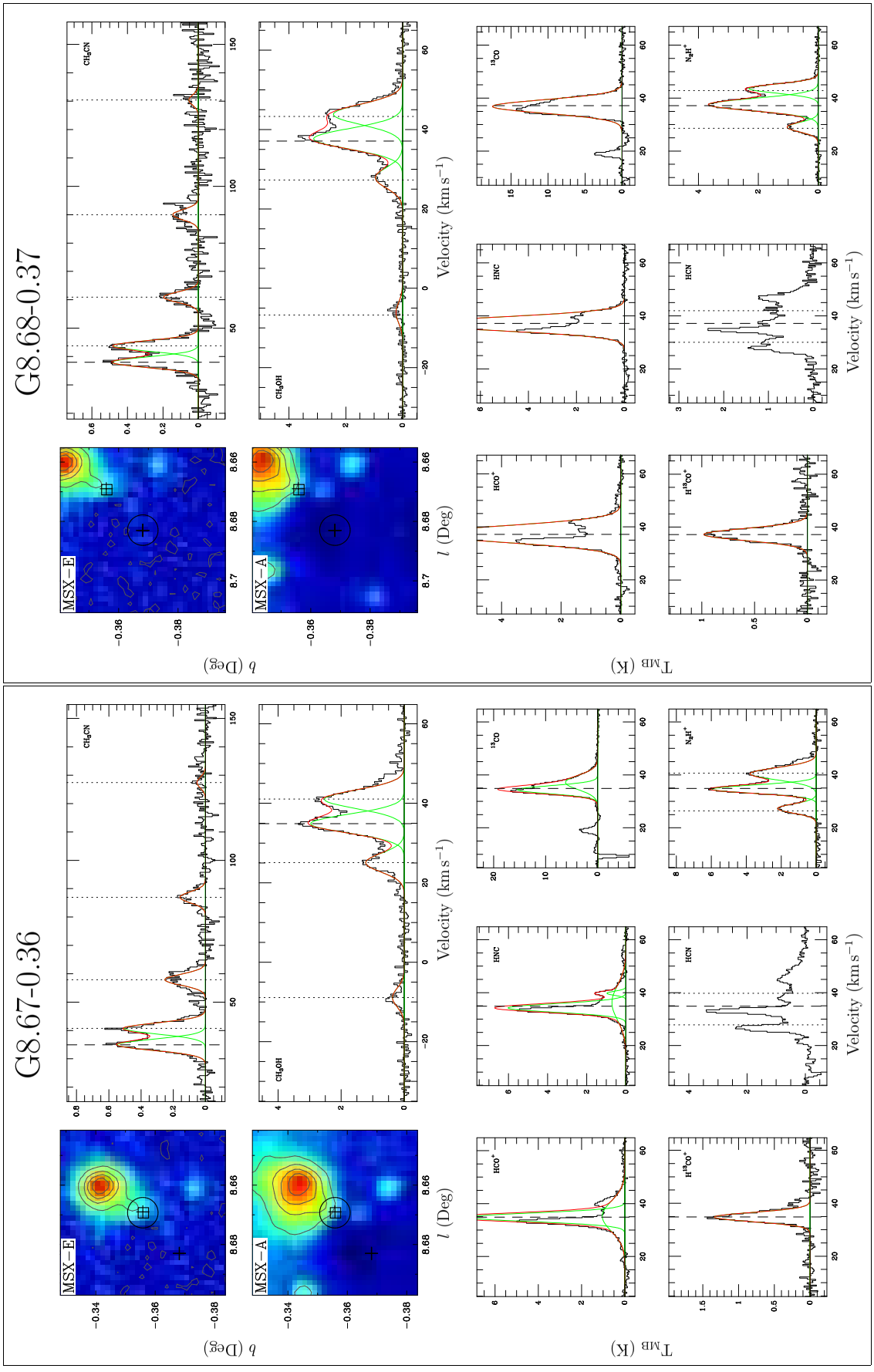

Mopra spectra and MSX images – *continued.*

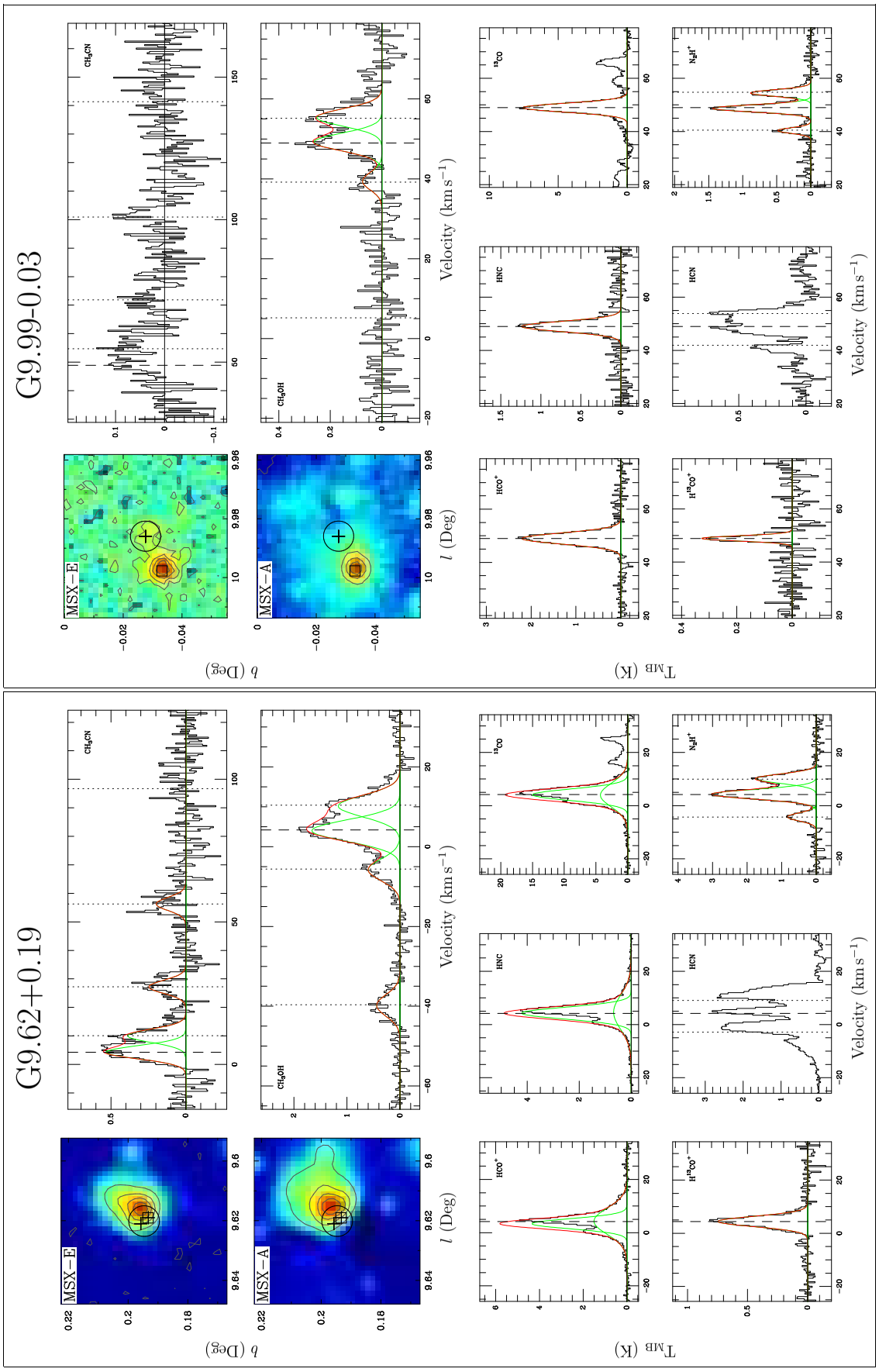

Mopra spectra and MSX images – *continued.*

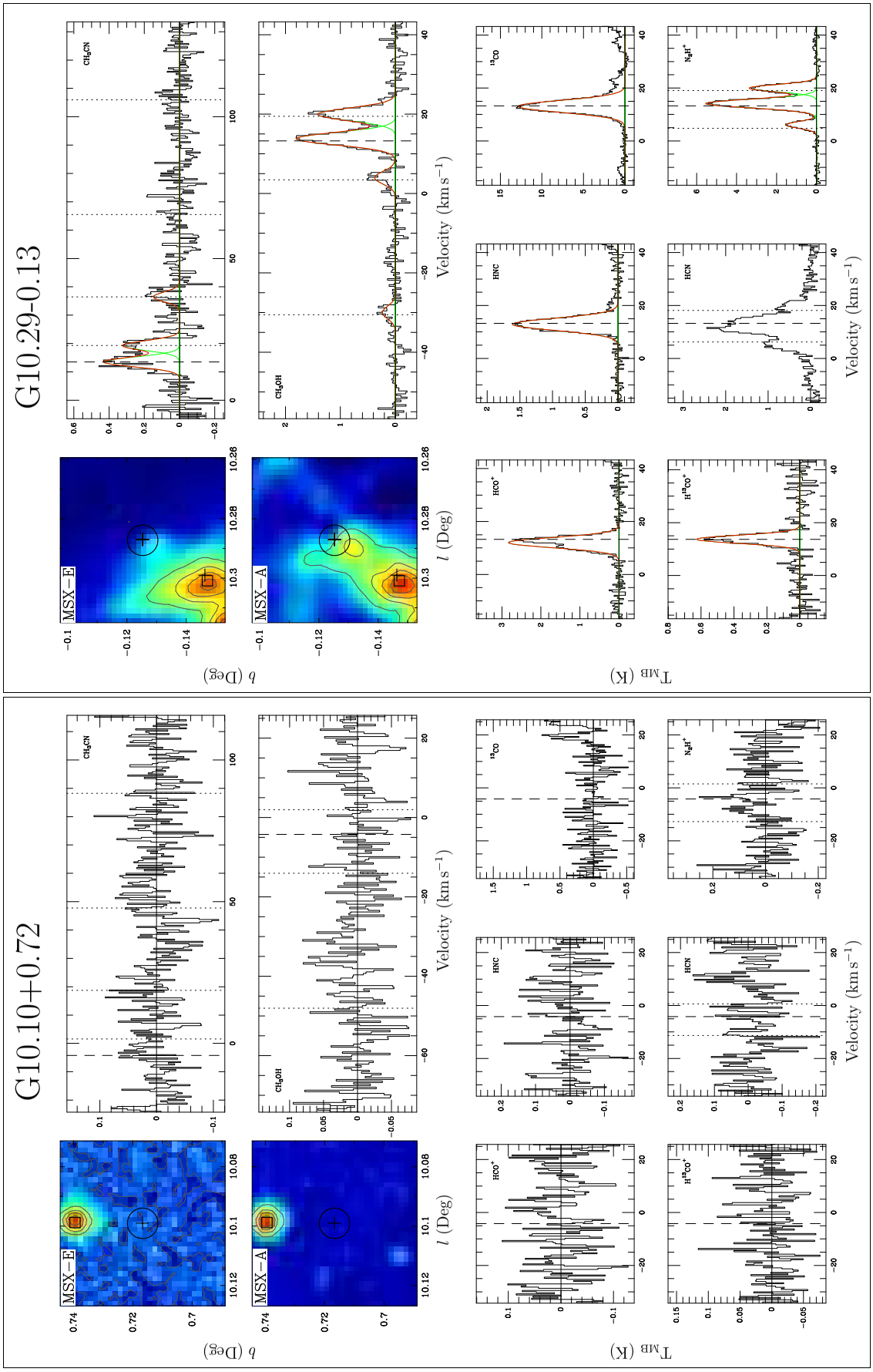

Mopra spectra and MSX images – *continued.*

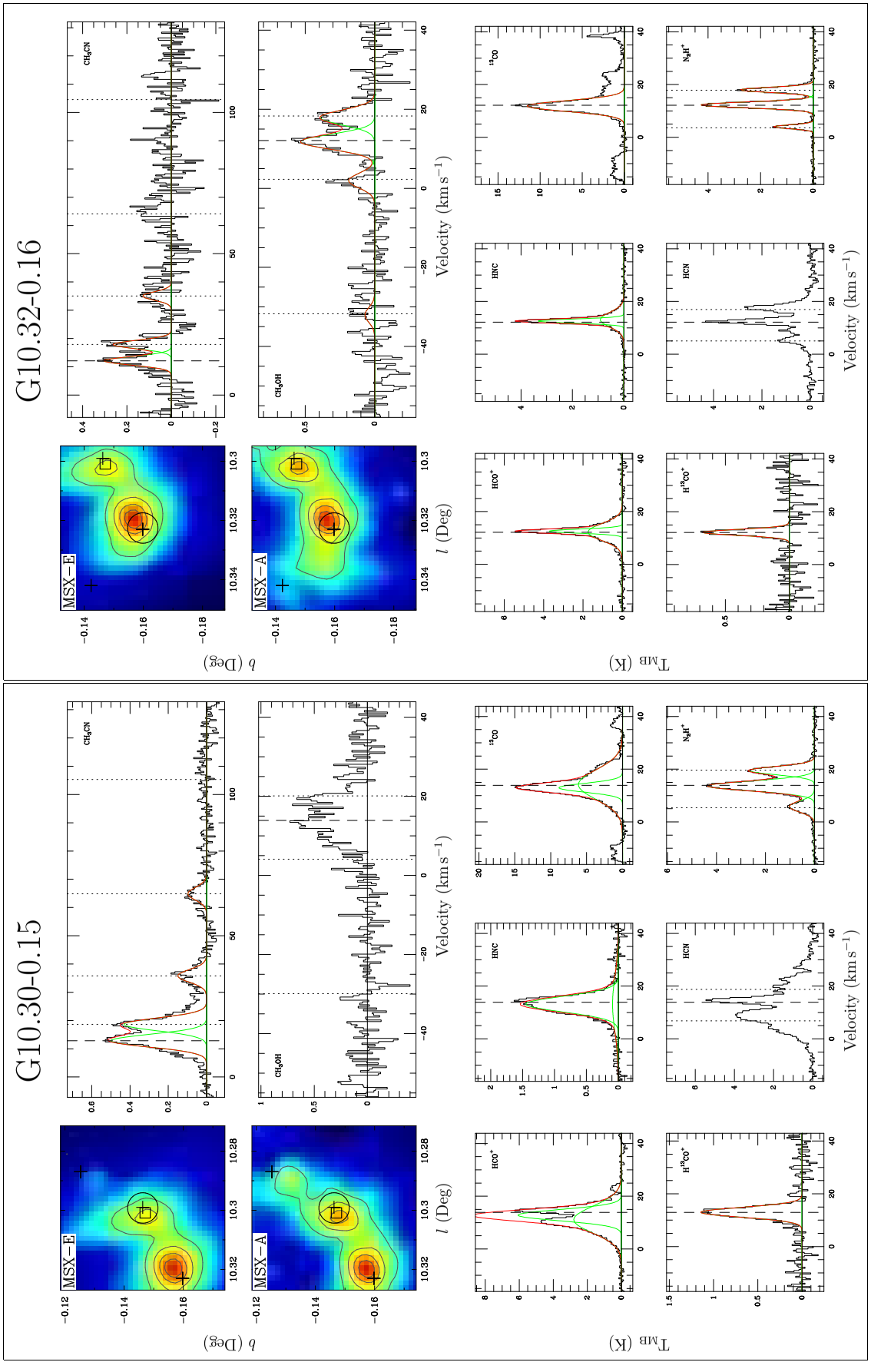

Mopra spectra and MSX images – *continued.*

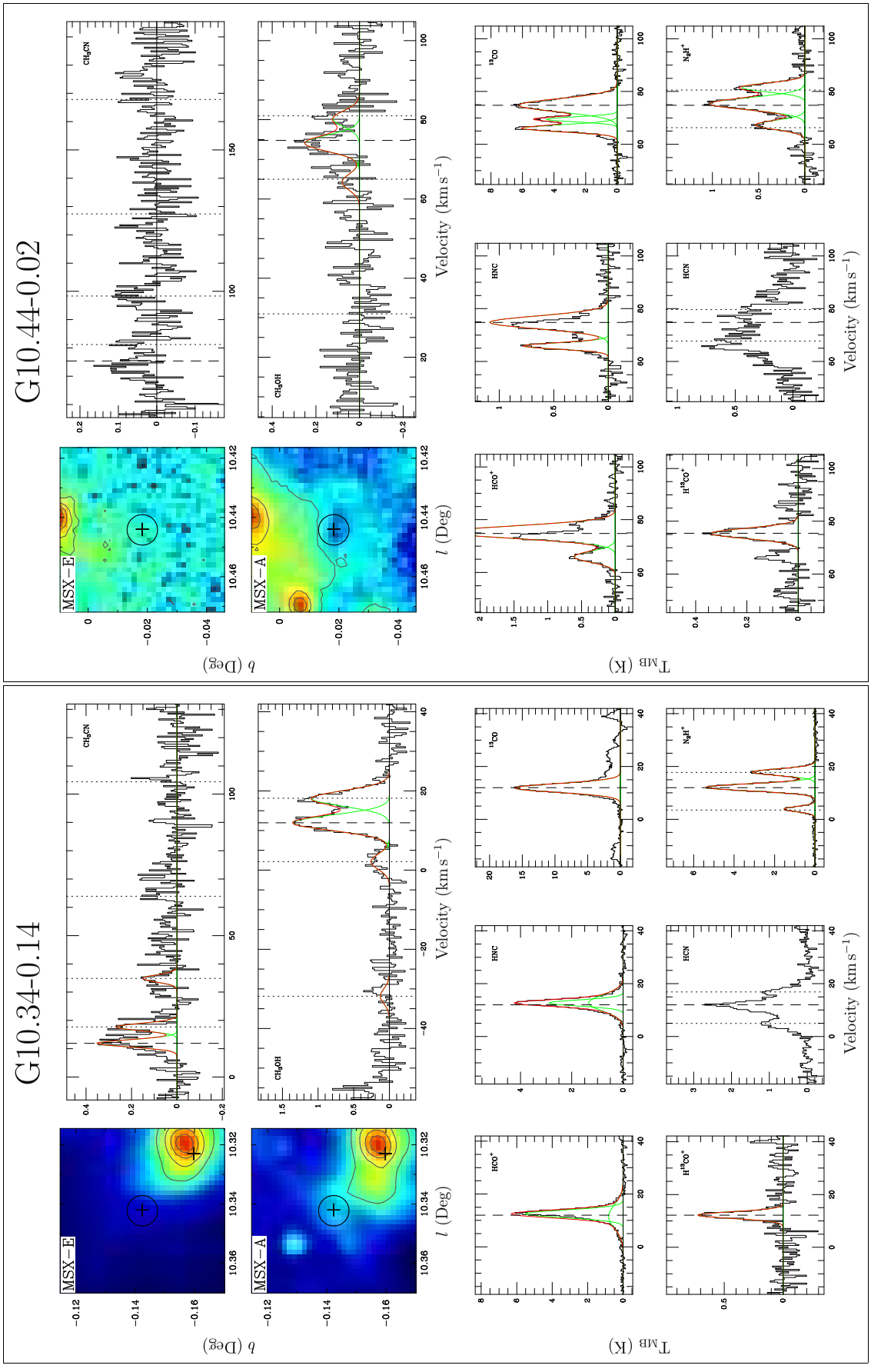

Mopra spectra and MSX images – *continued.*

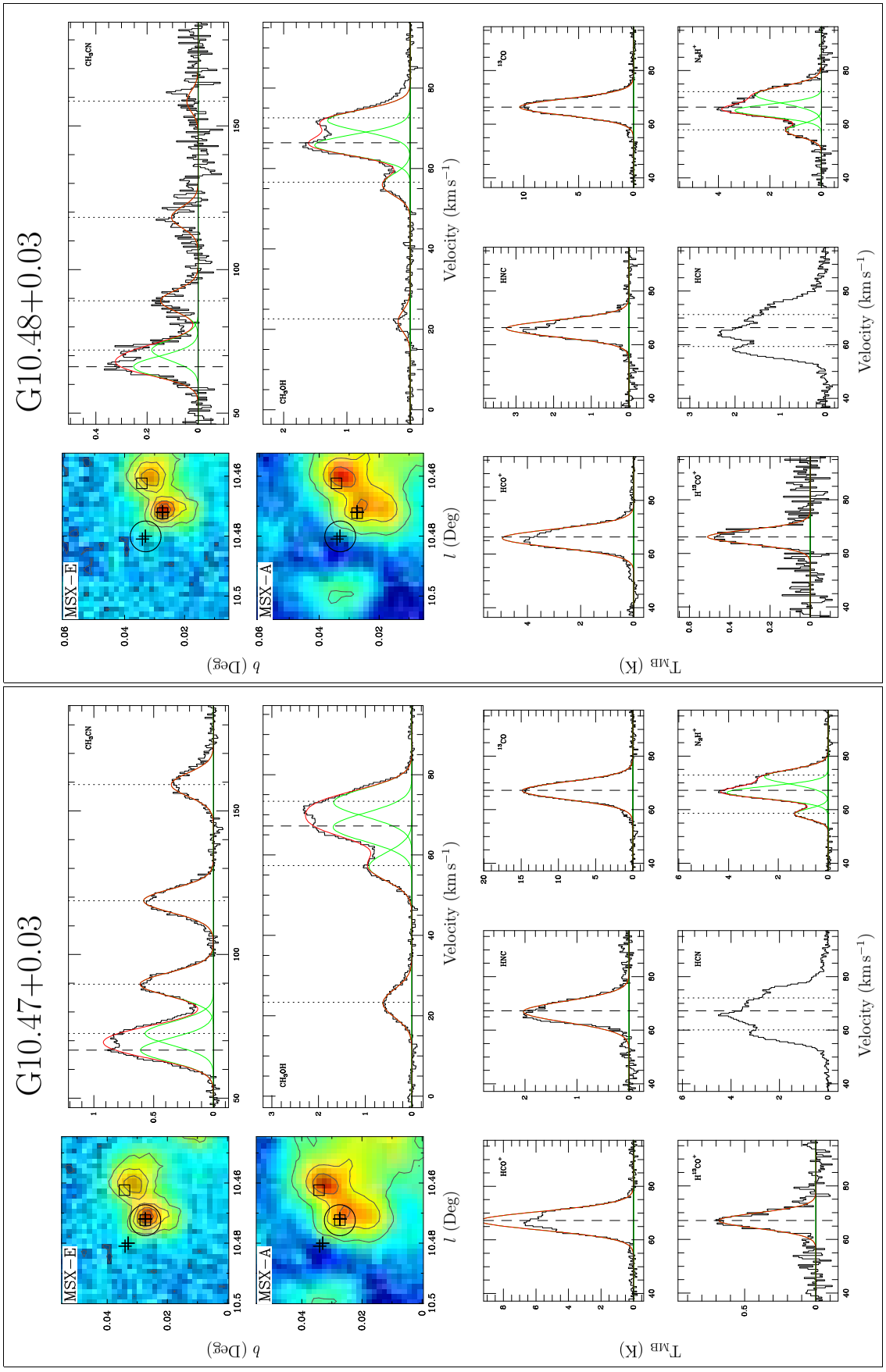

Mopra spectra and MSX images – *continued.*

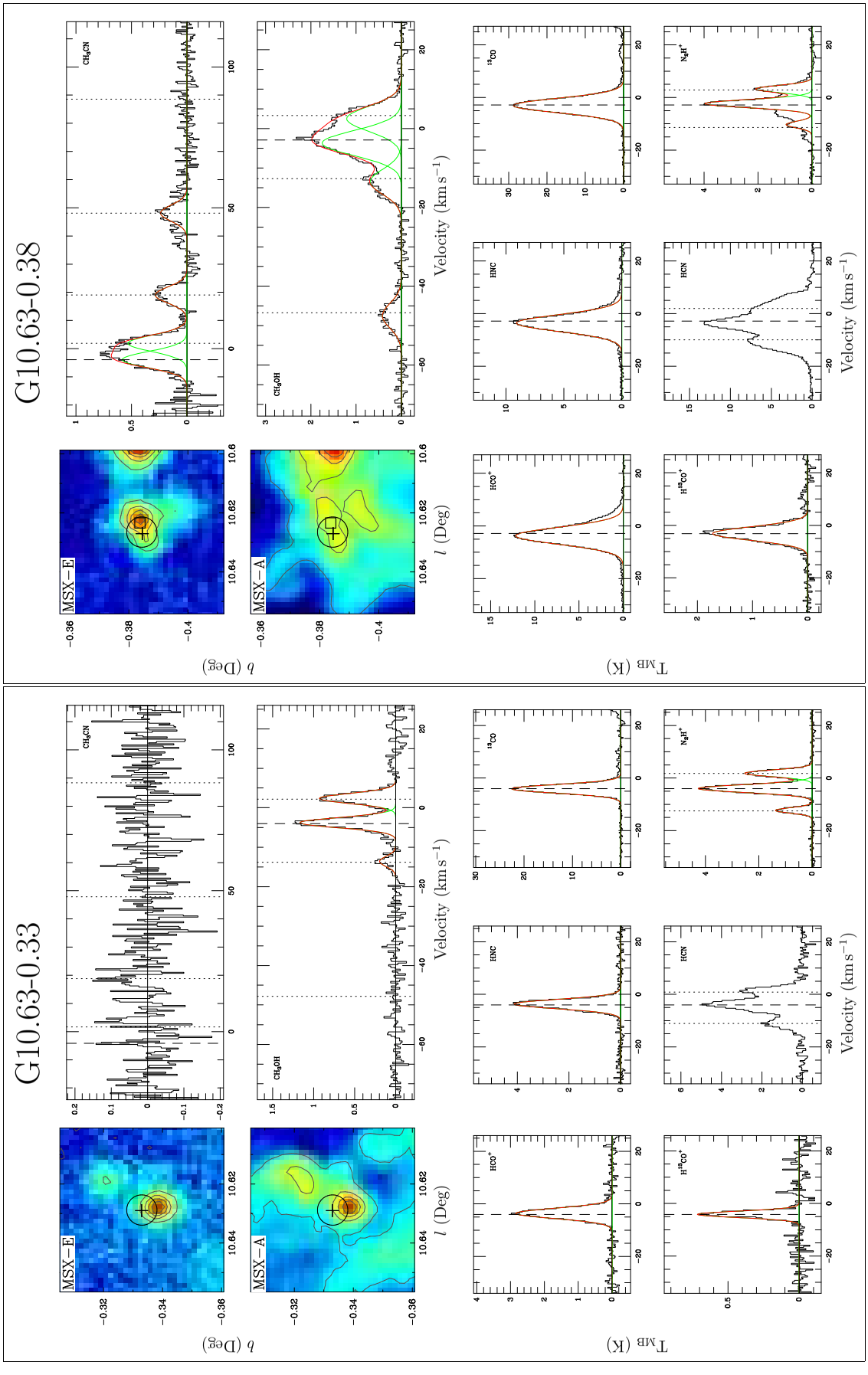

Mopra spectra and MSX images – *continued.*

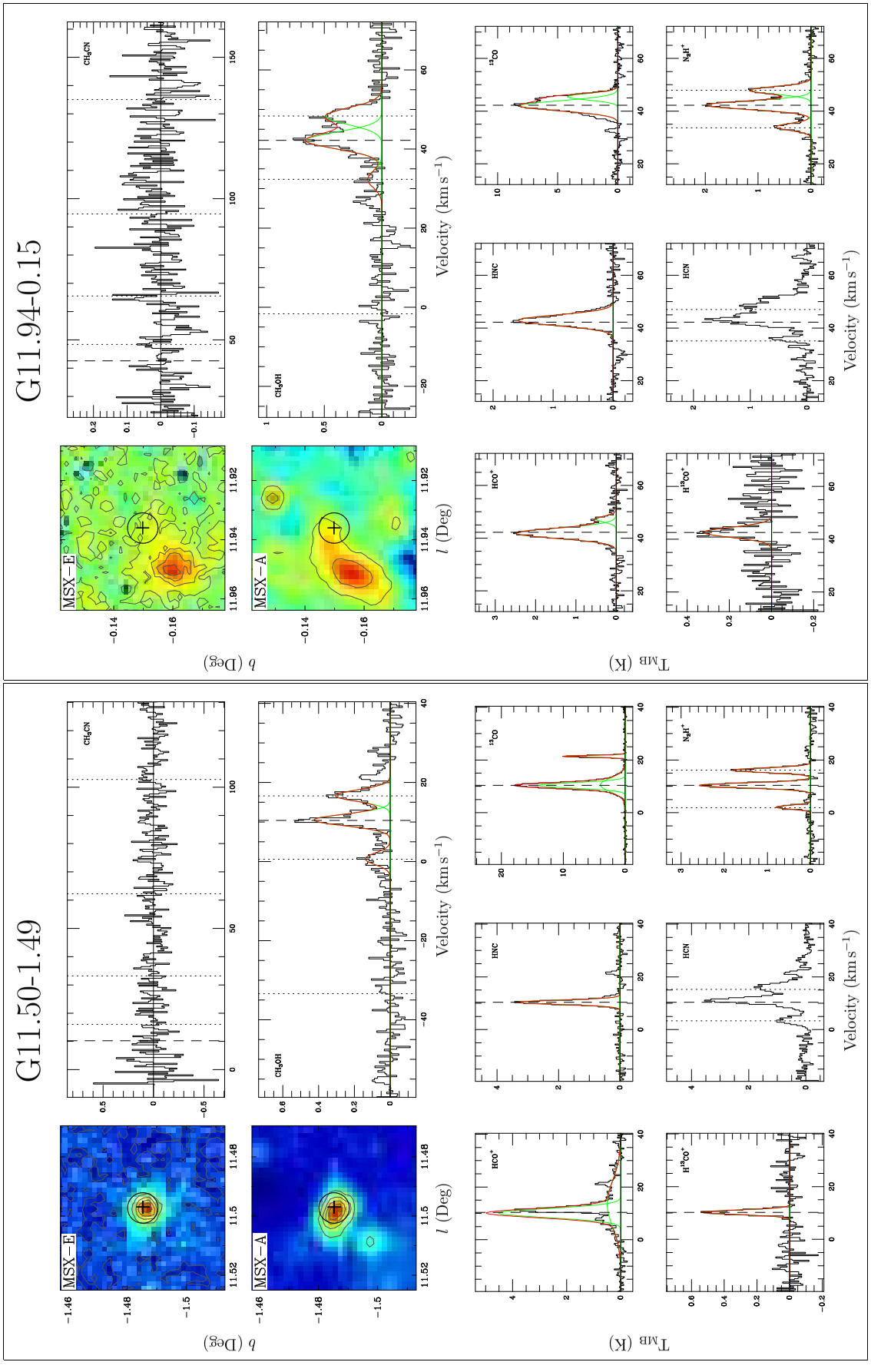

Mopra spectra and MSX images – *continued.*

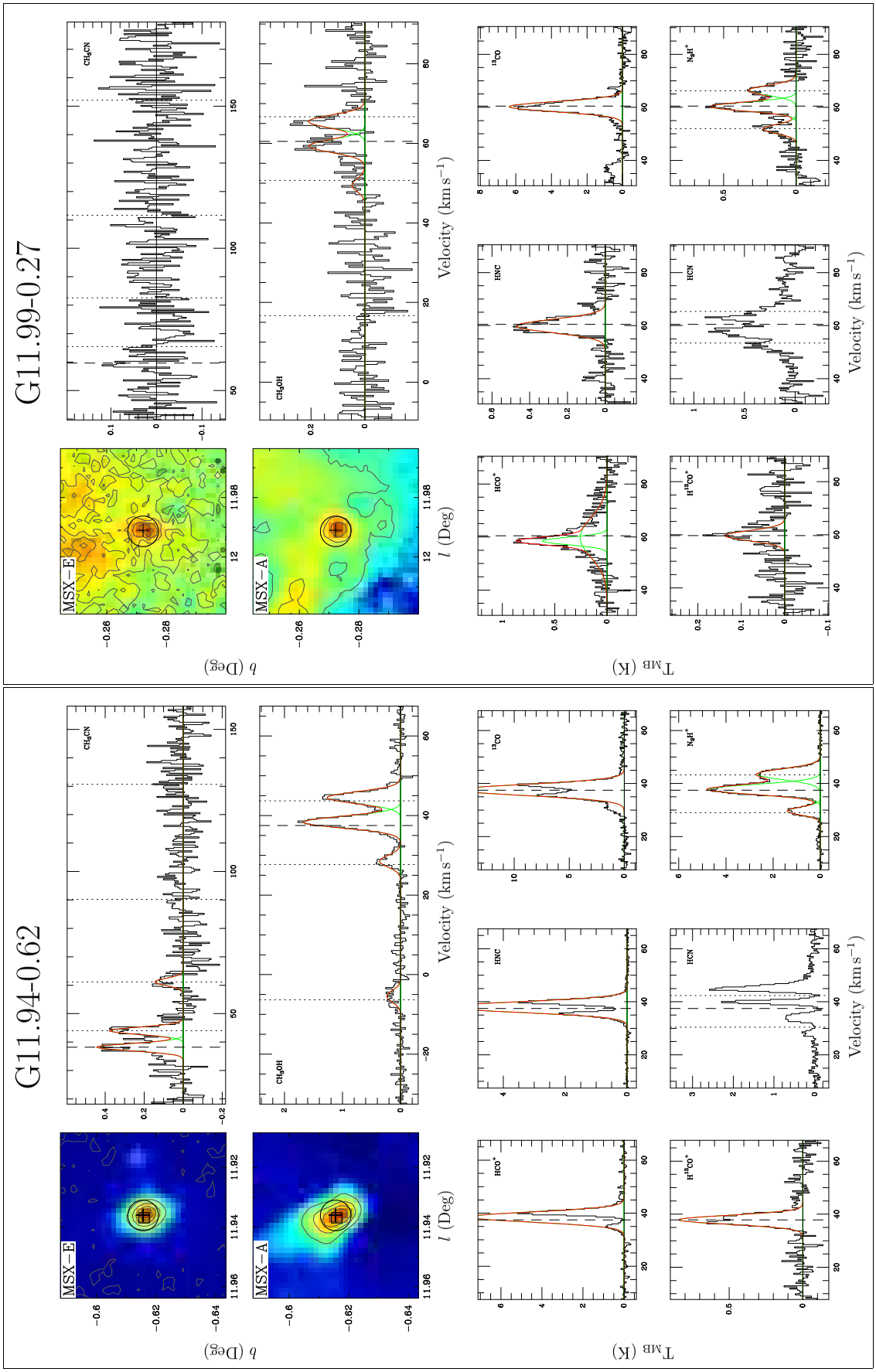

Mopra spectra and MSX images – *continued.*

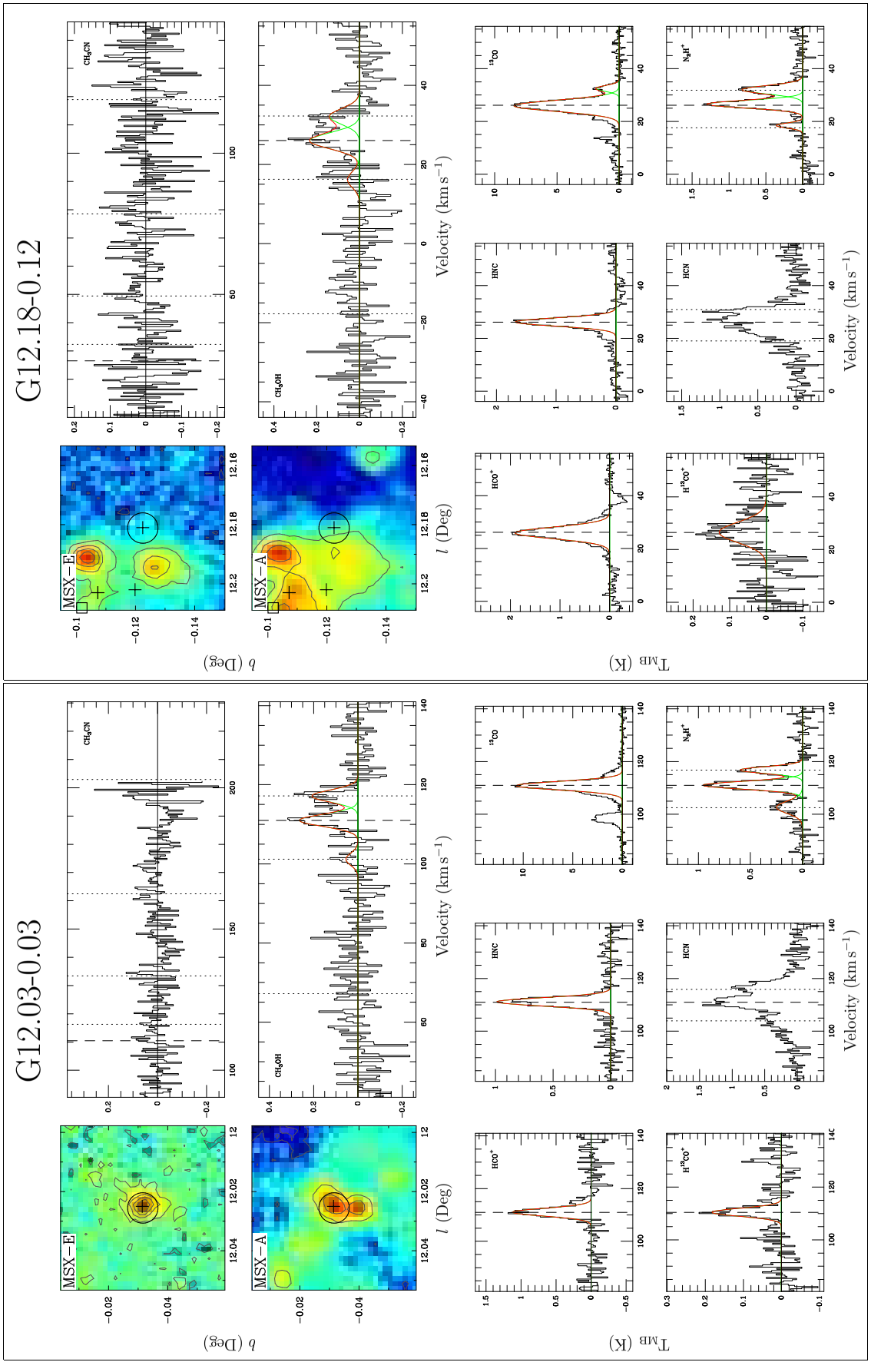

Mopra spectra and MSX images – *continued.*

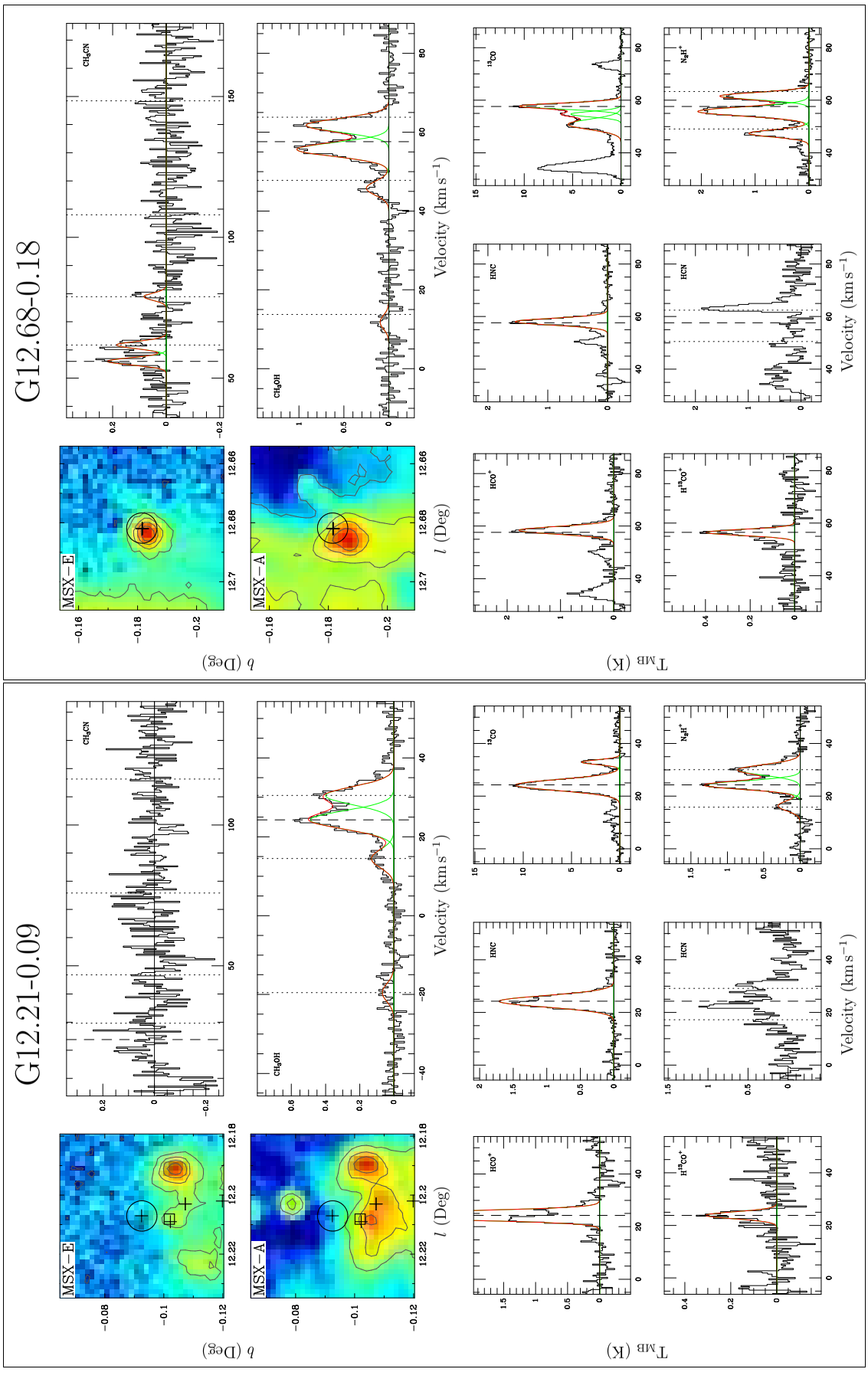

Mopra spectra and MSX images – *continued.*

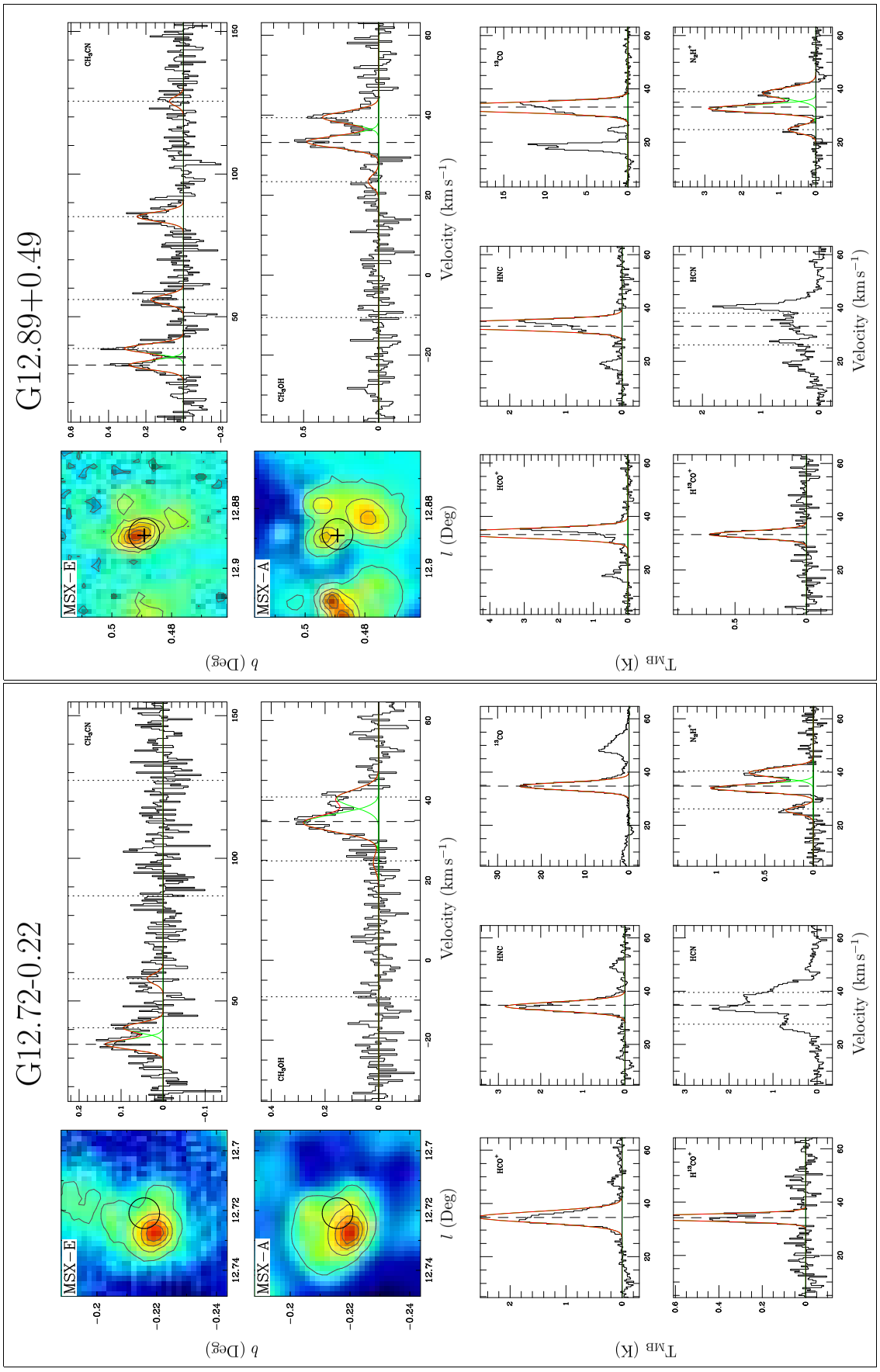

Mopra spectra and MSX images – *continued.*

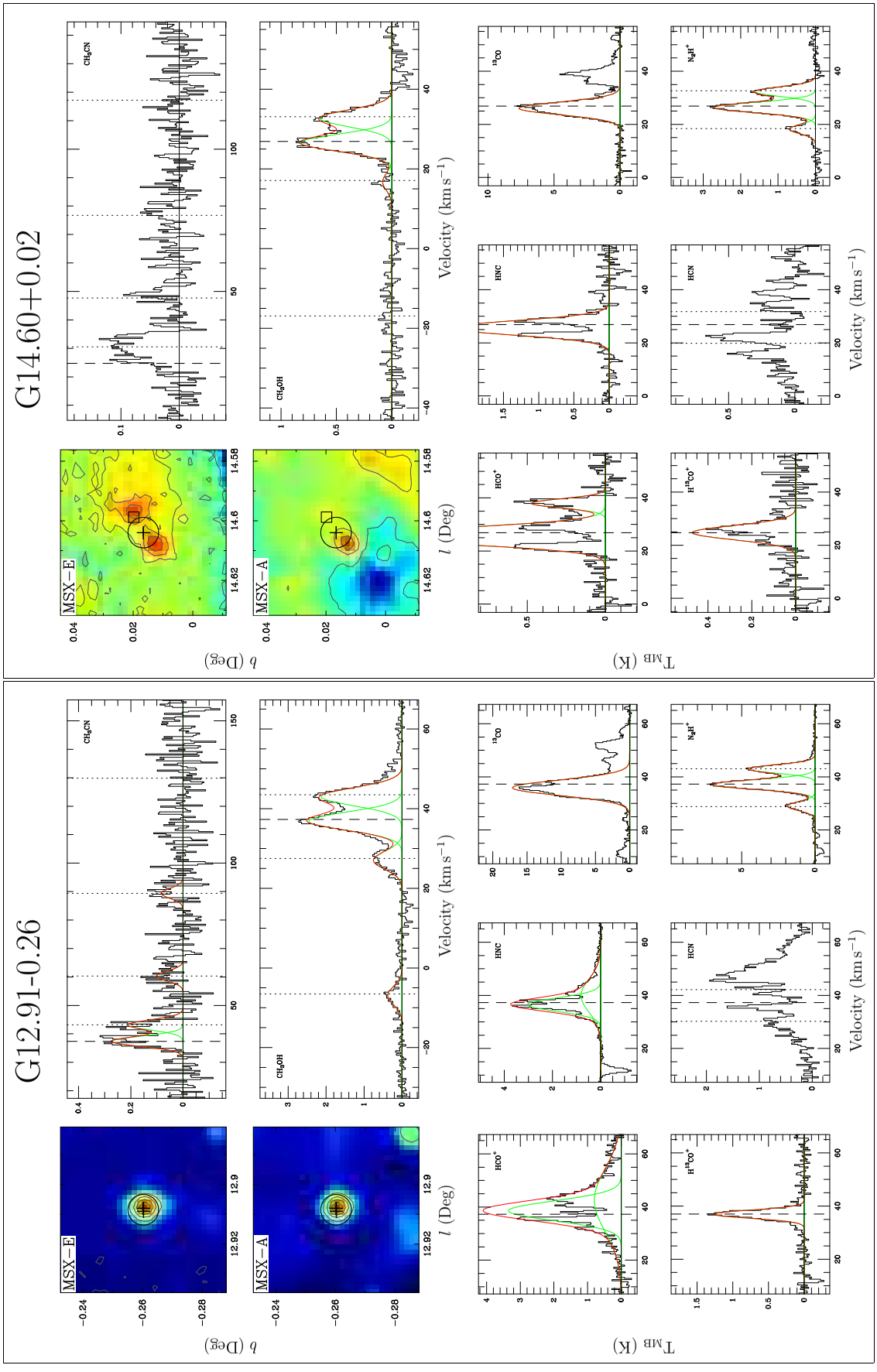

Mopra spectra and MSX images – *continued.*

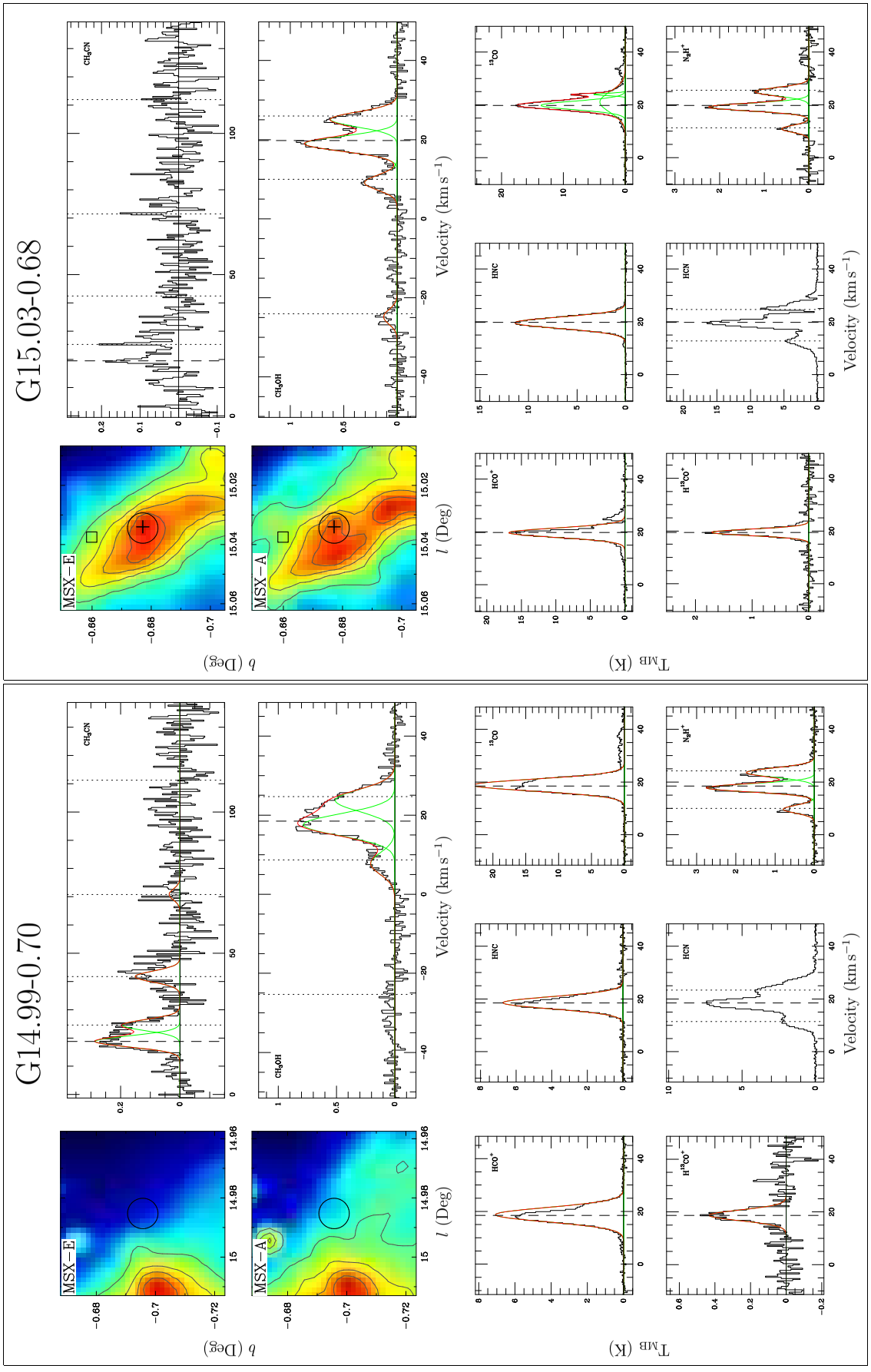

Mopra spectra and MSX images – *continued.*

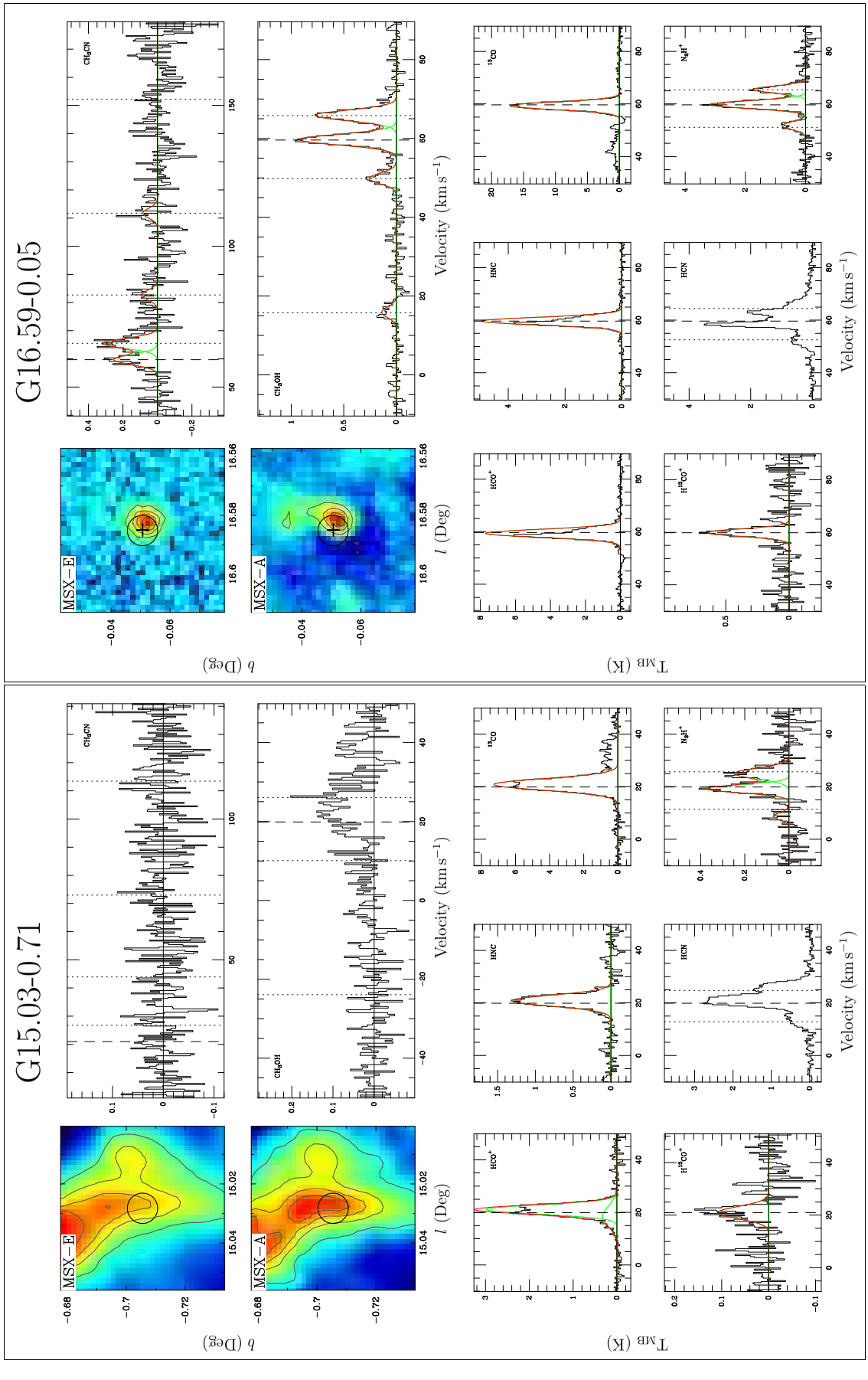

Mopra spectra and MSX images – *continued.*

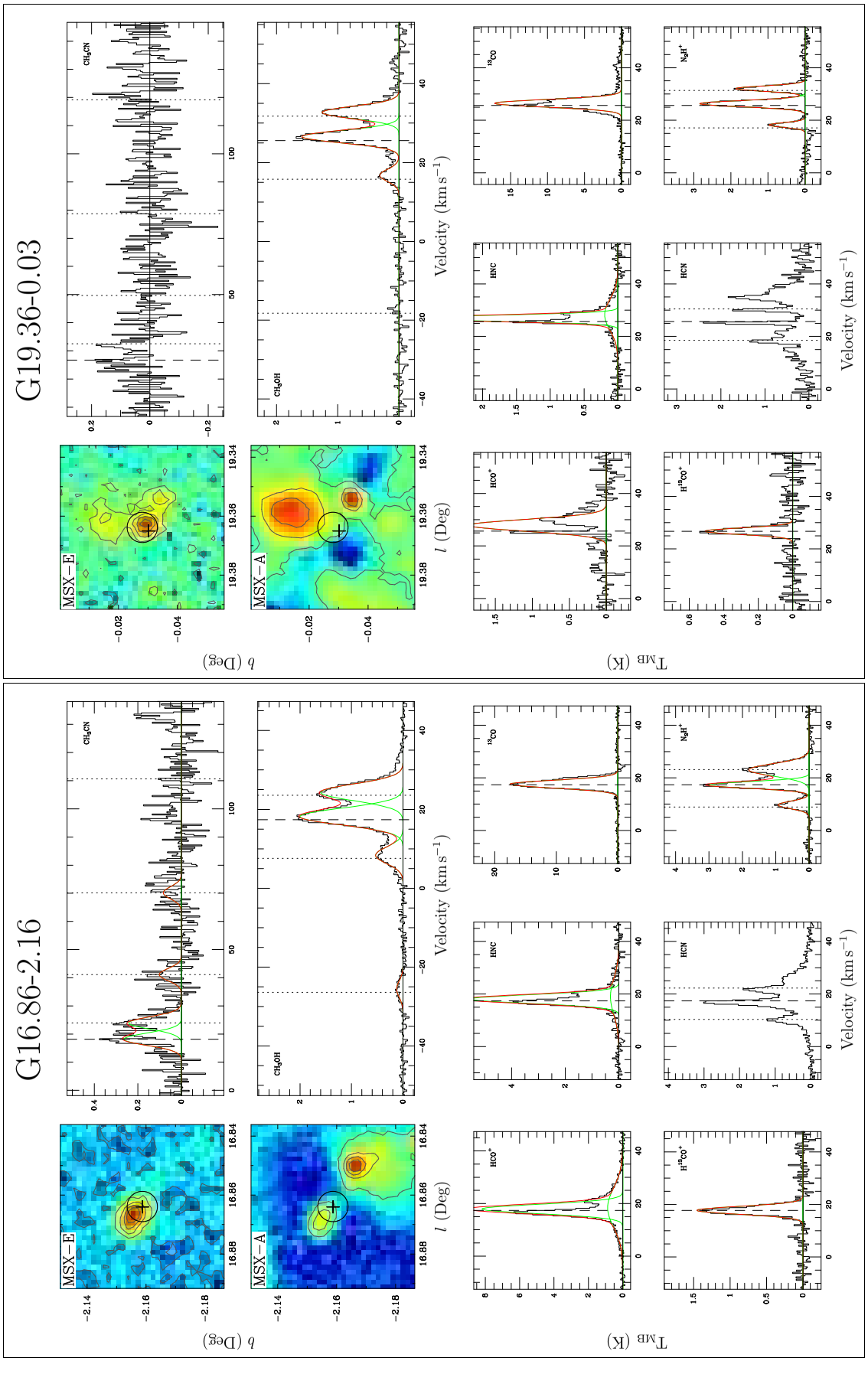

Mopra spectra and MSX images – *continued.*

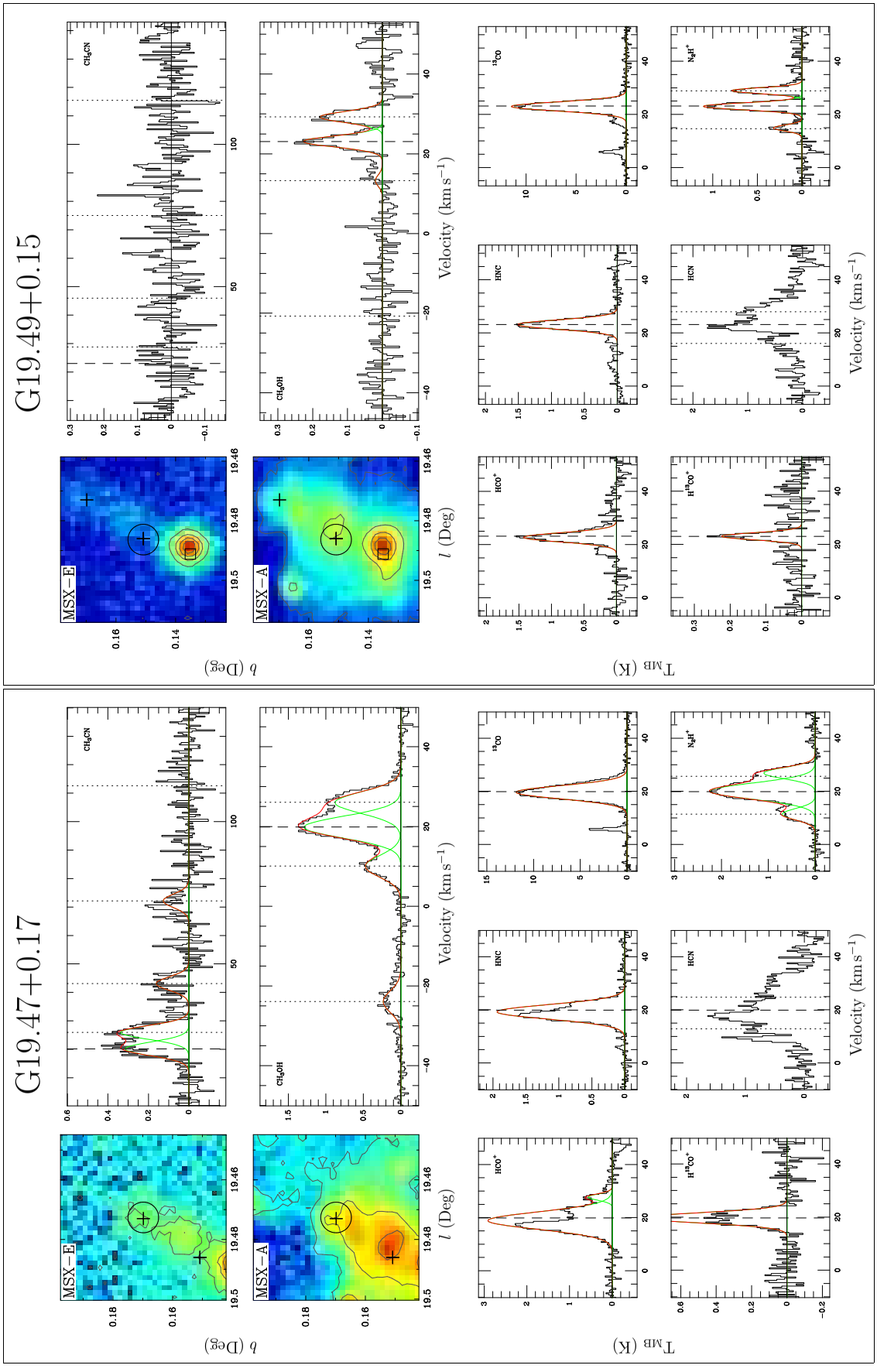

Mopra spectra and MSX images – *continued.*

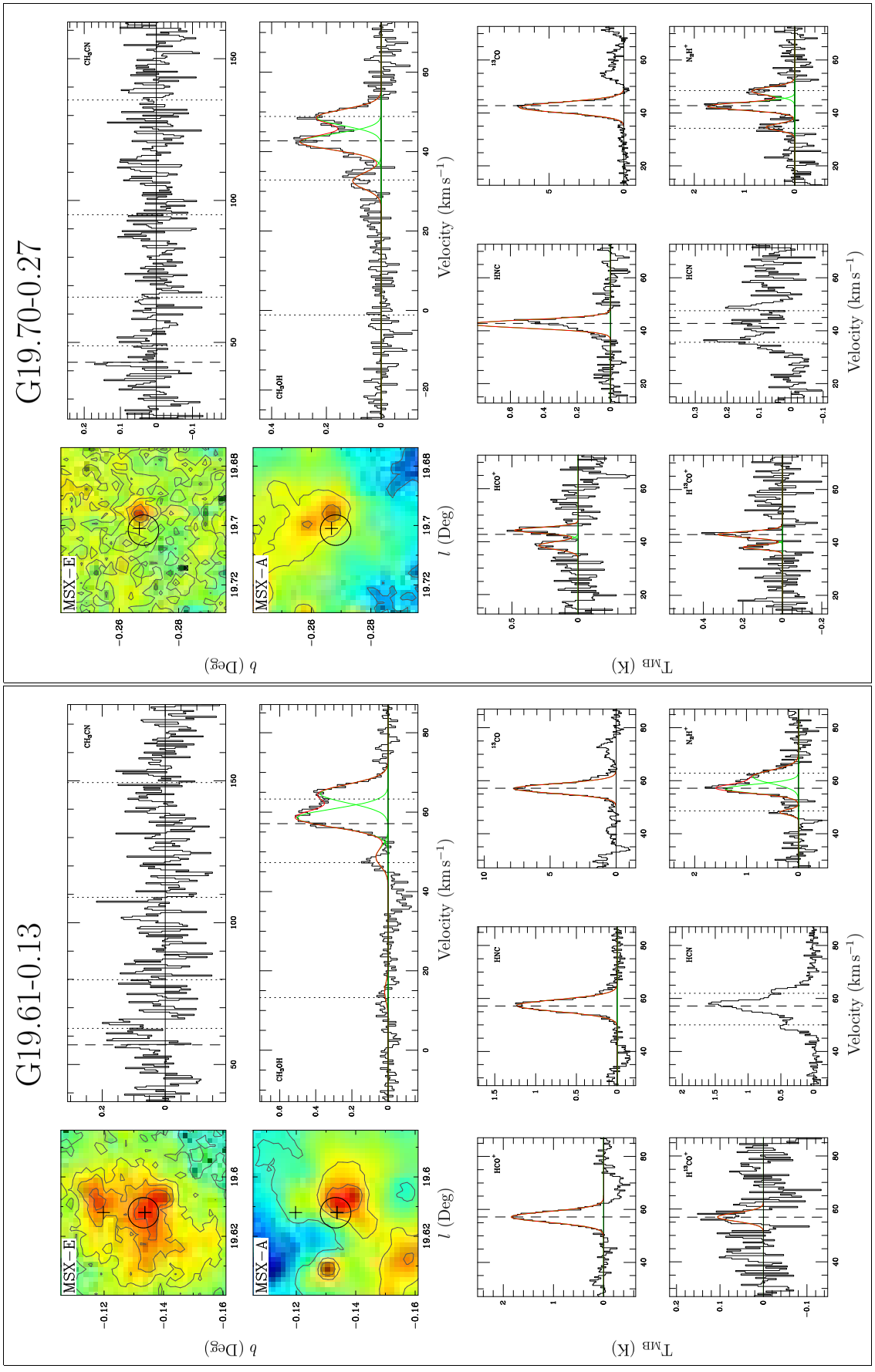

Mopra spectra and MSX images – *continued.*

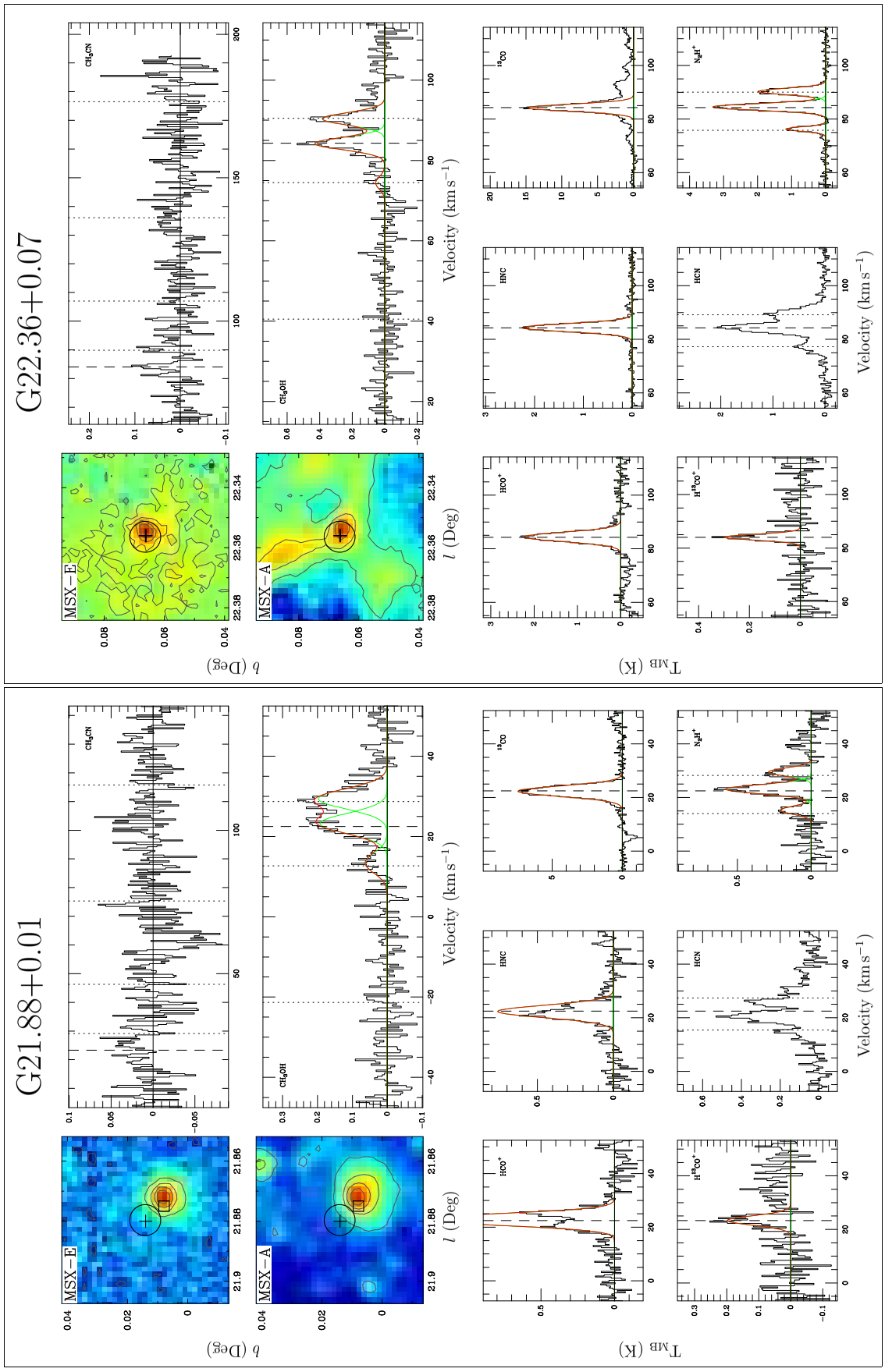

Mopra spectra and MSX images – *continued.*

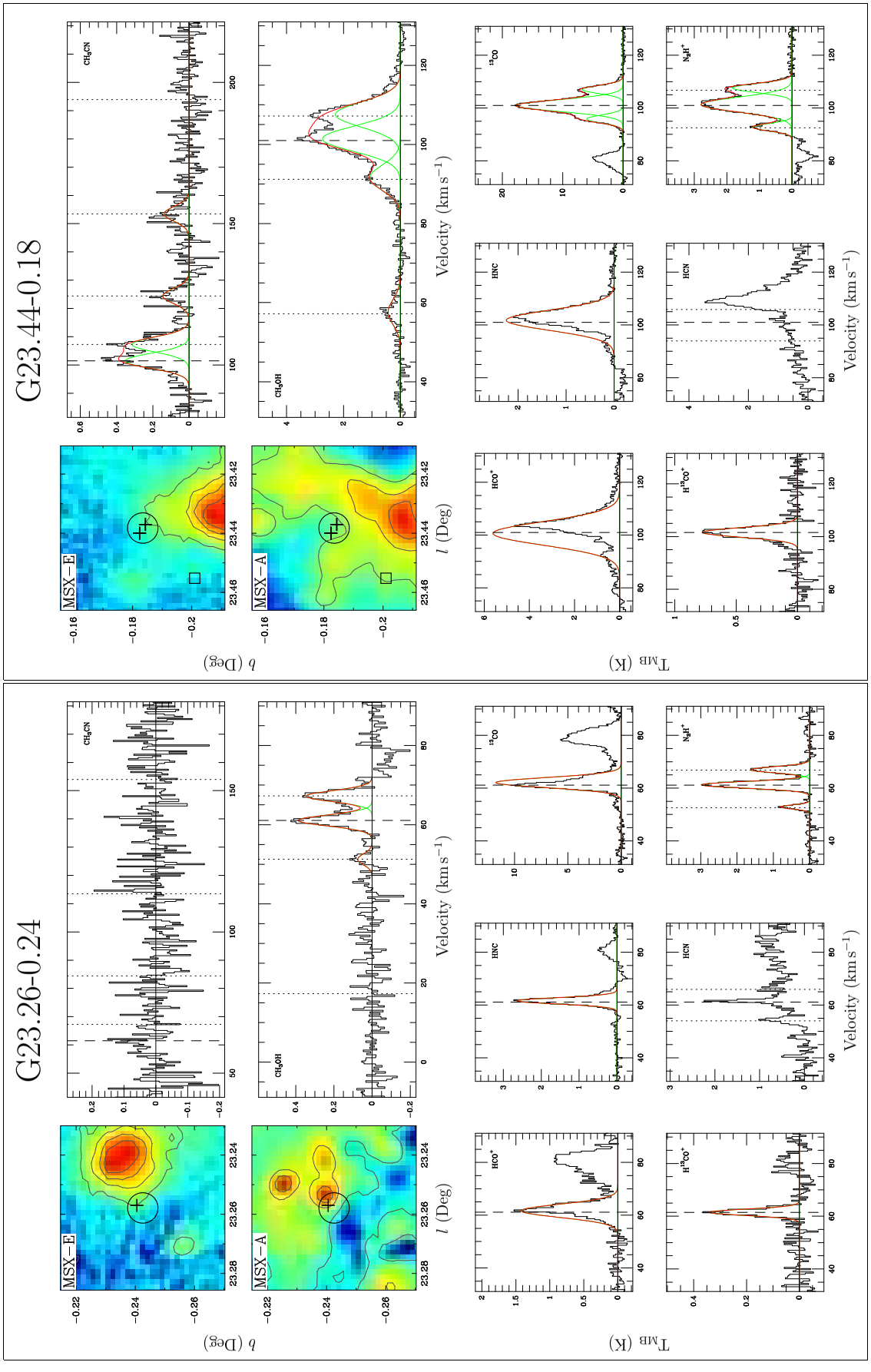

Mopra spectra and MSX images – *continued.*

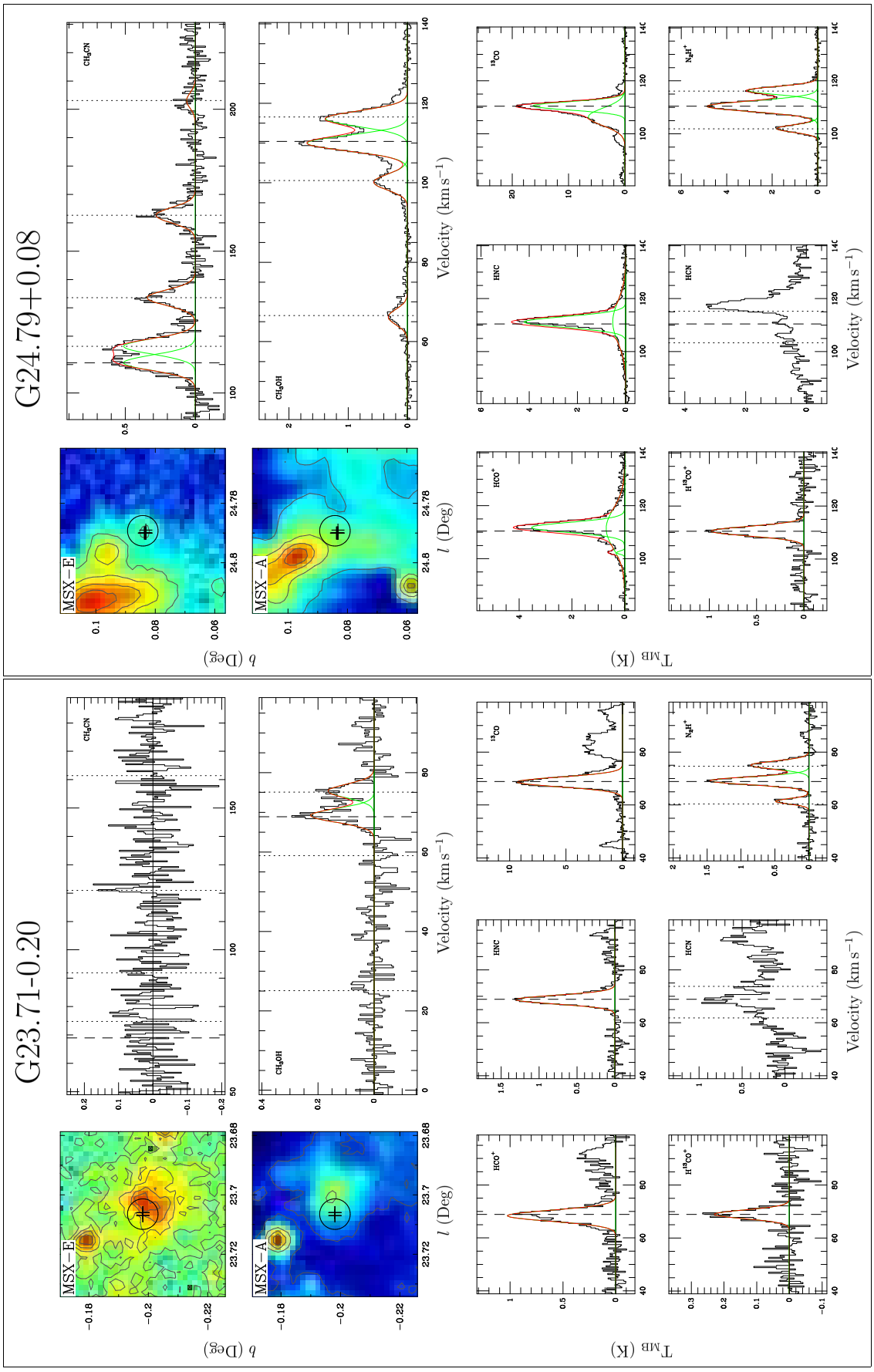

Mopra spectra and MSX images – *continued.*

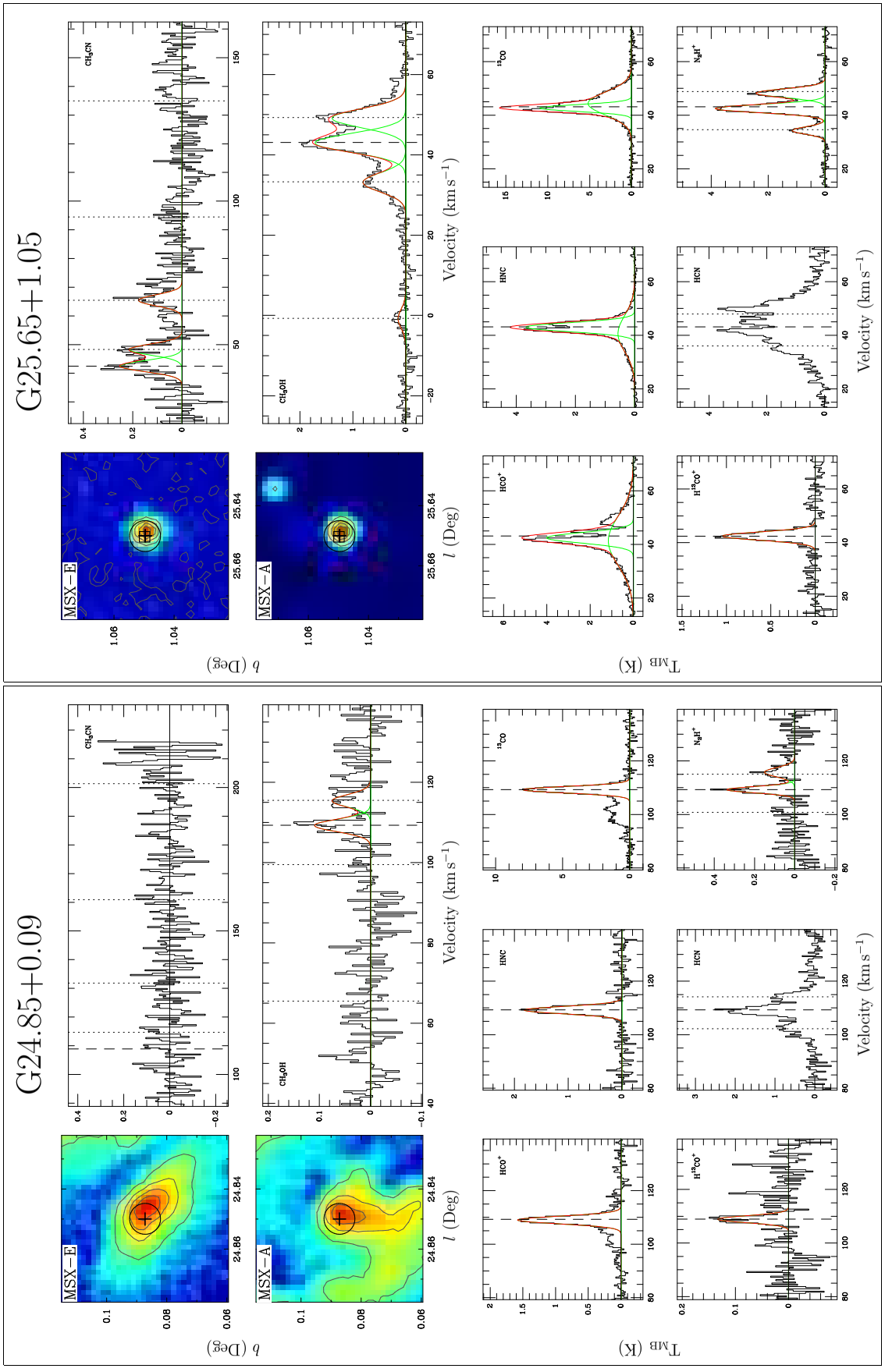

Mopra spectra and MSX images – *continued.*

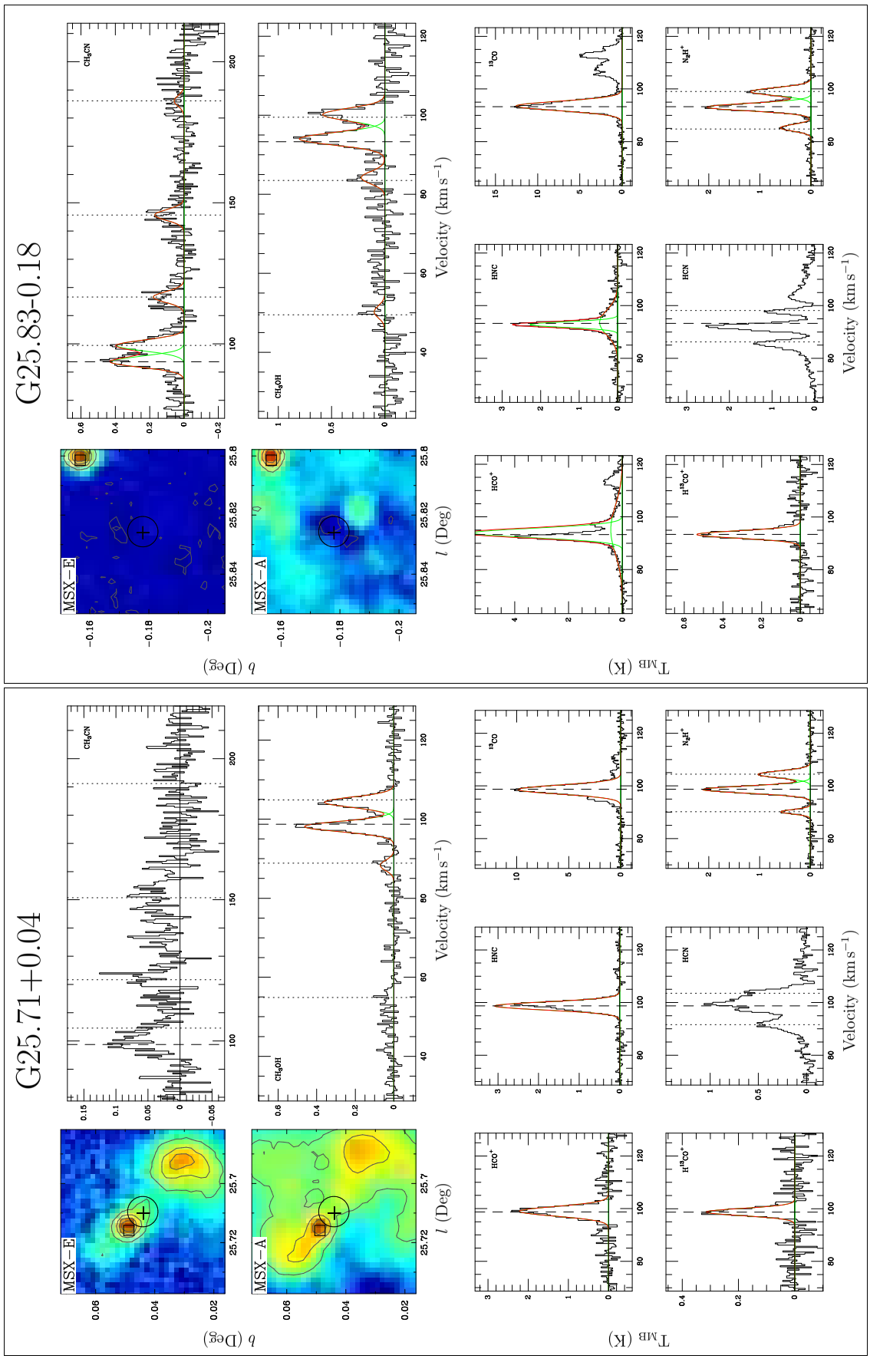

Mopra spectra and MSX images – *continued.*

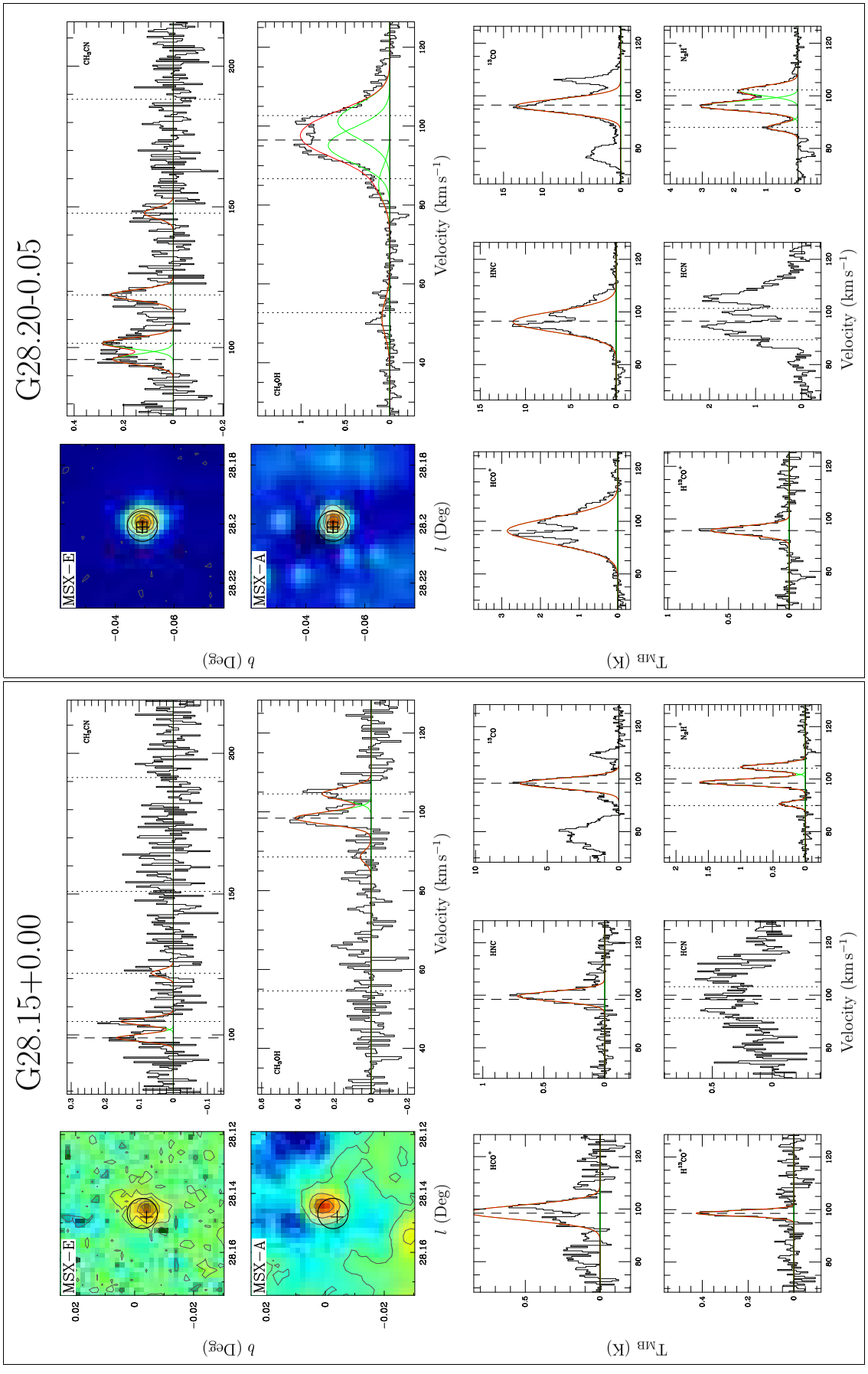

Mopra spectra and MSX images – *continued.*

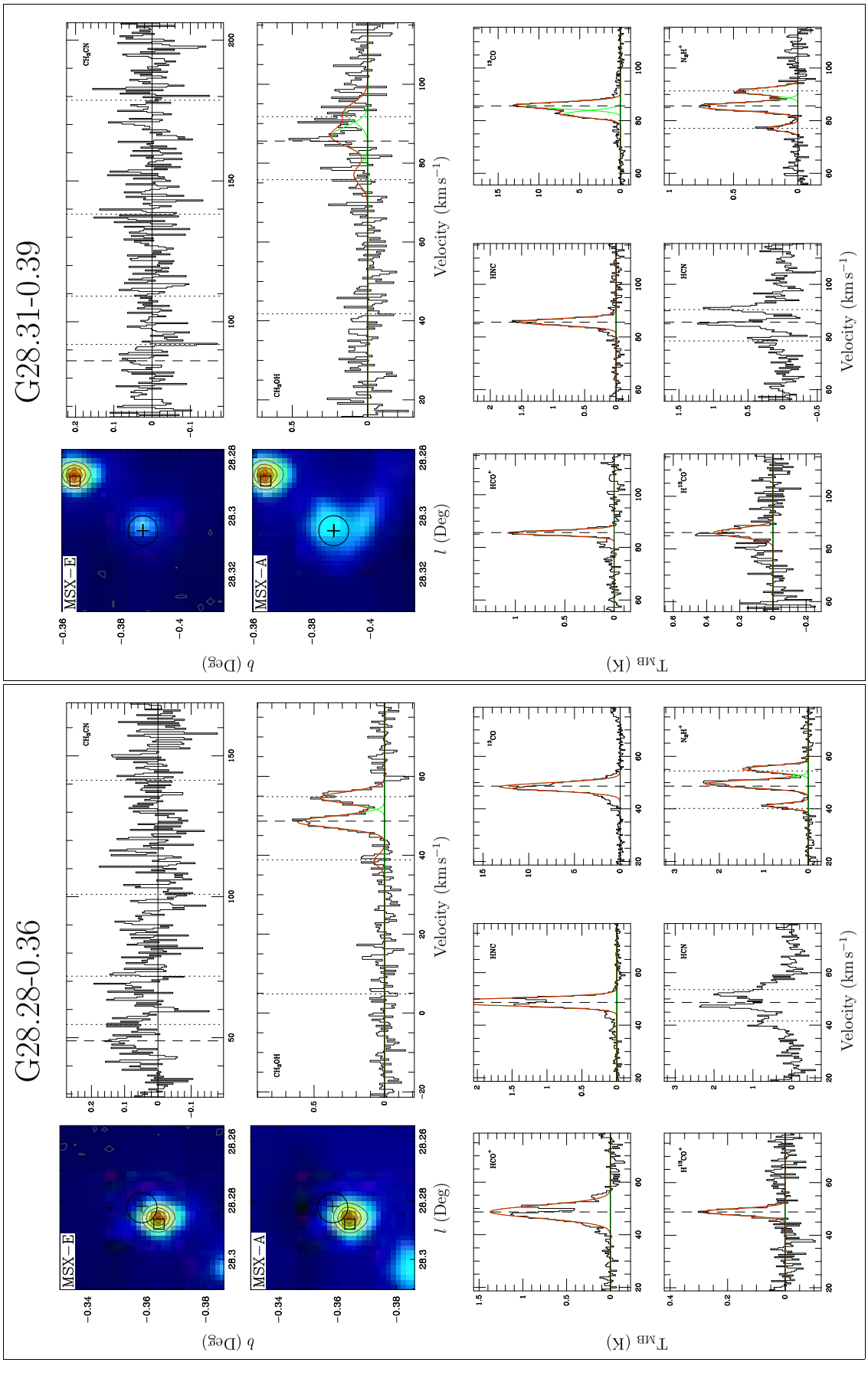

Mopra spectra and MSX images – *continued.*

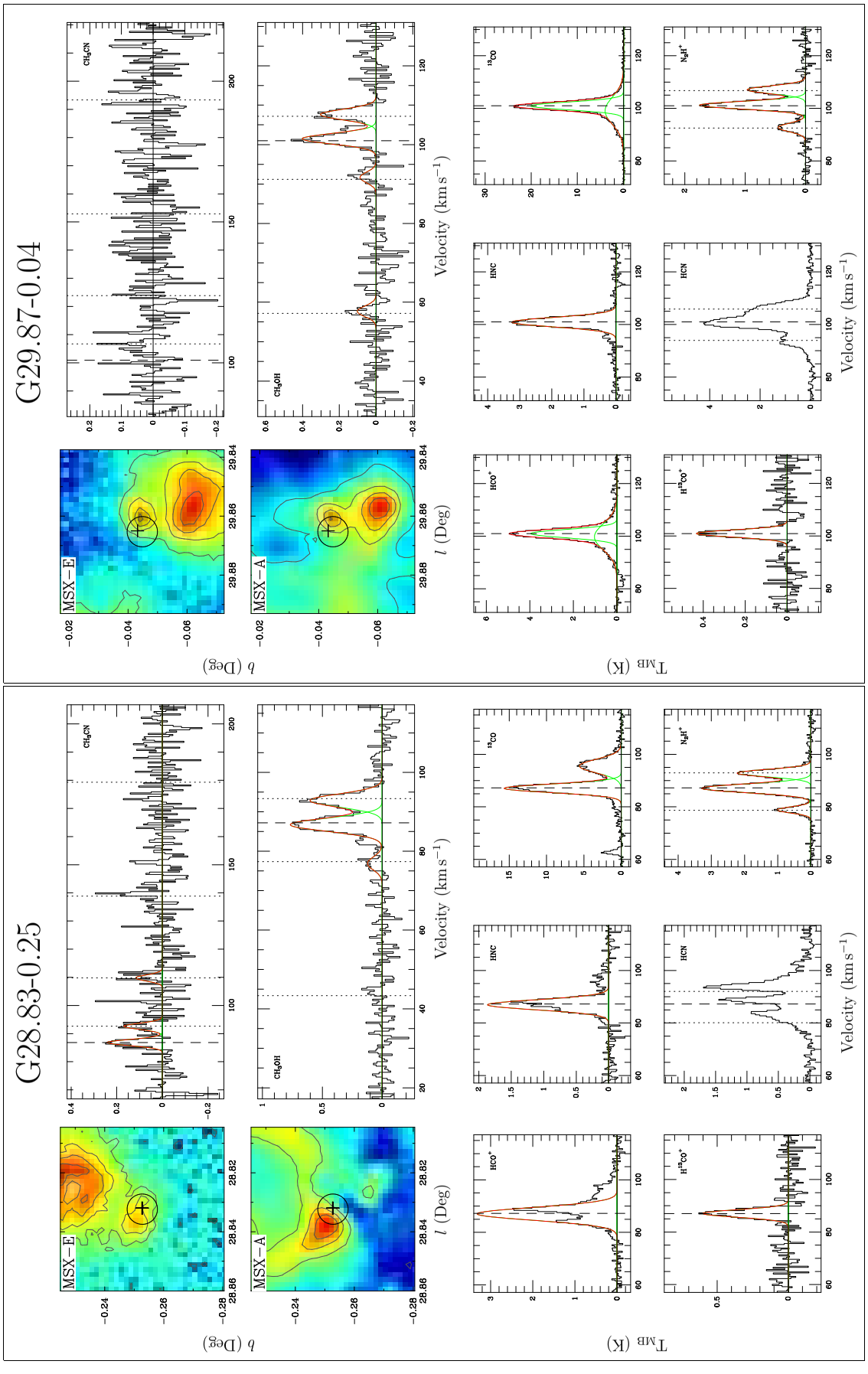

Mopra spectra and MSX images – *continued.*

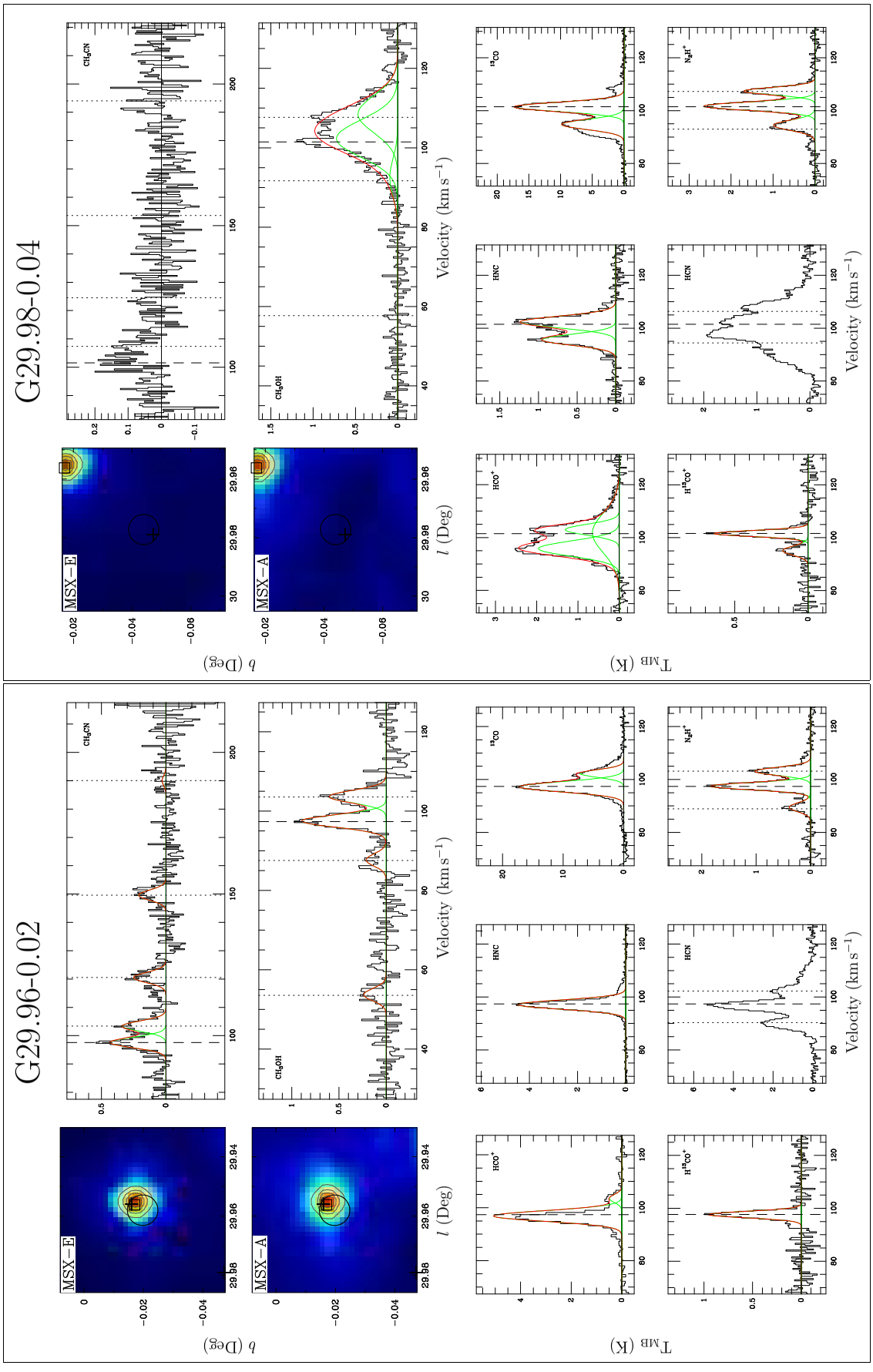

Mopra spectra and MSX images – *continued.*

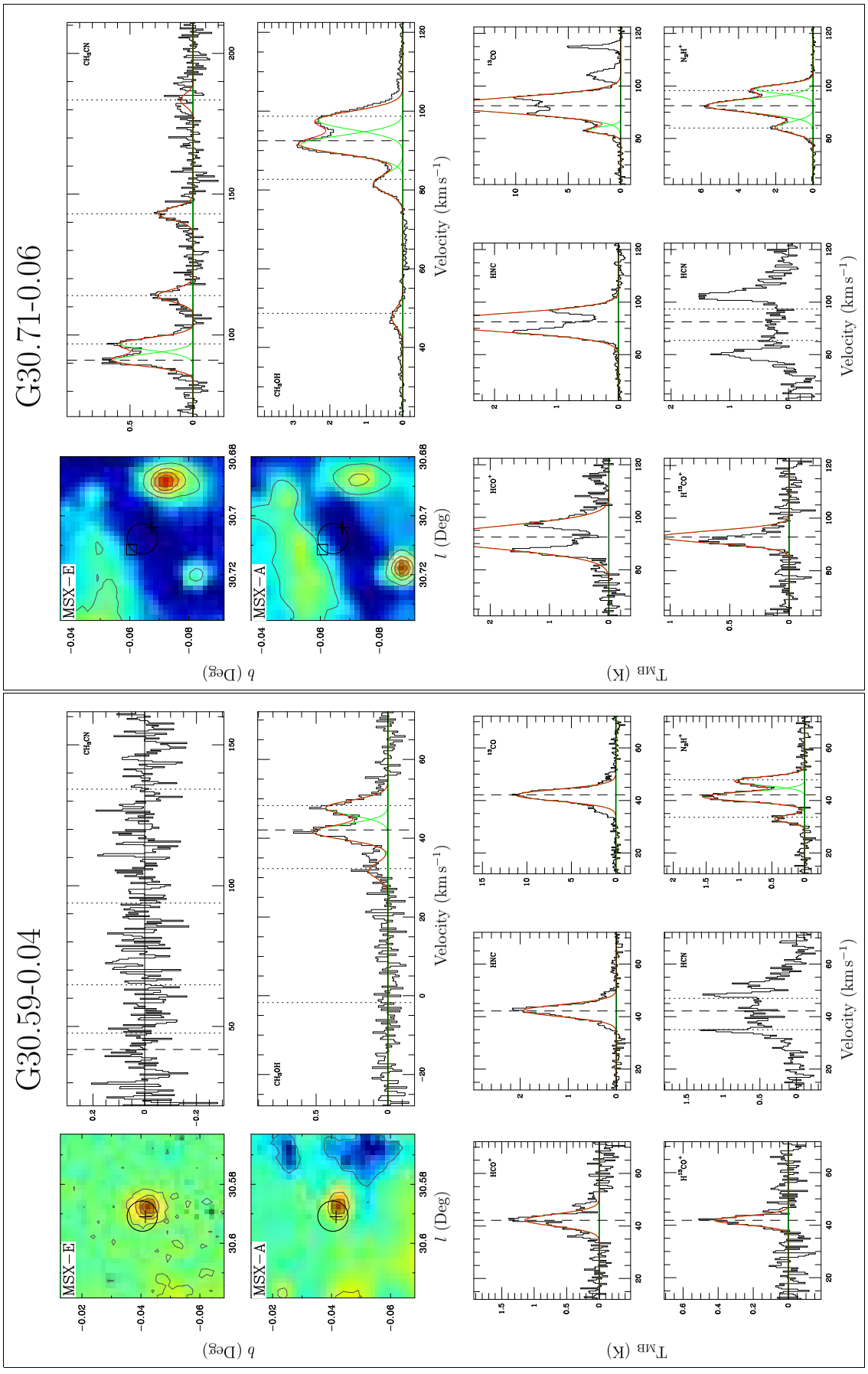

Mopra spectra and MSX images – *continued.*

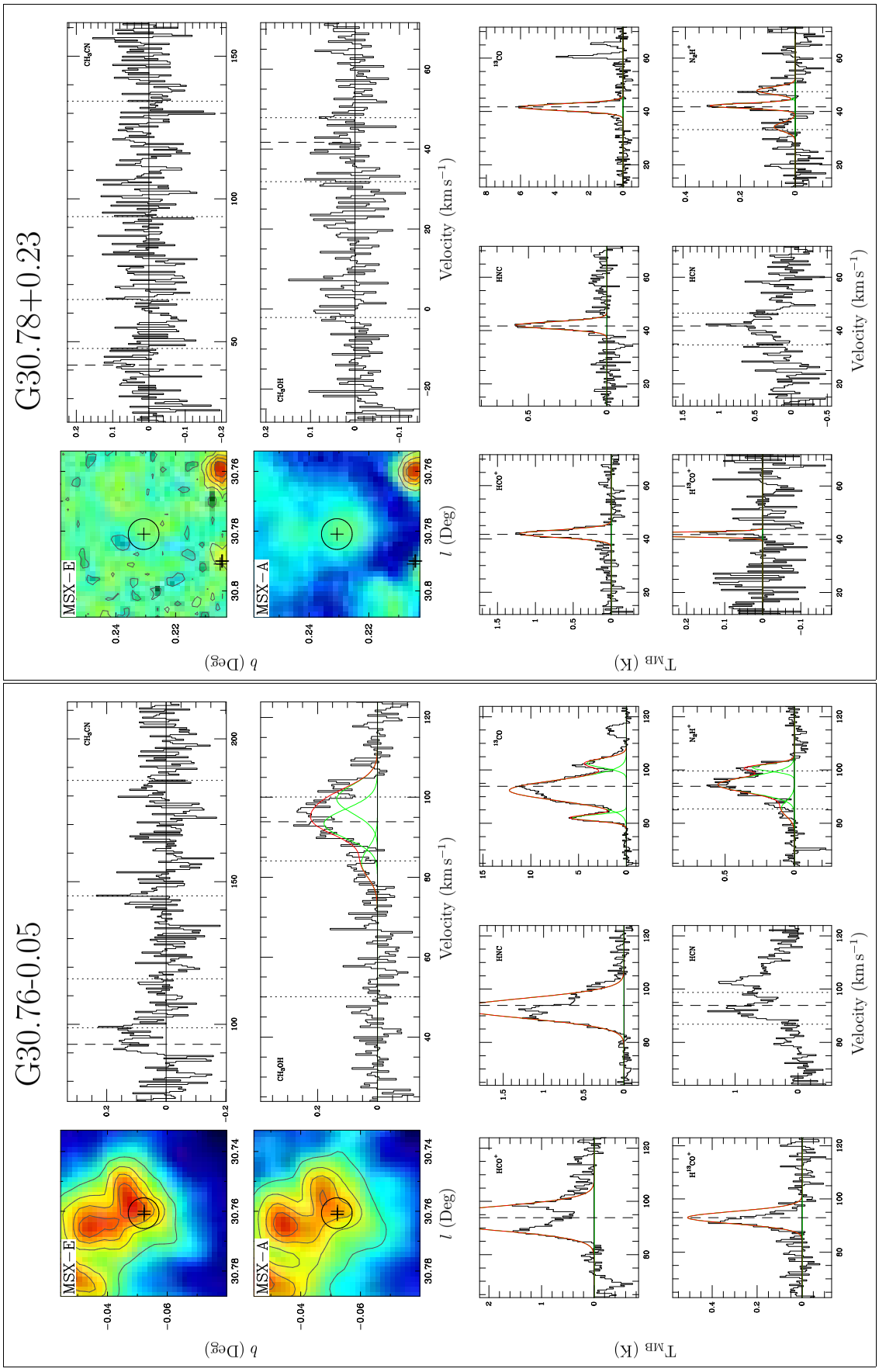

Mopra spectra and MSX images – *continued.*

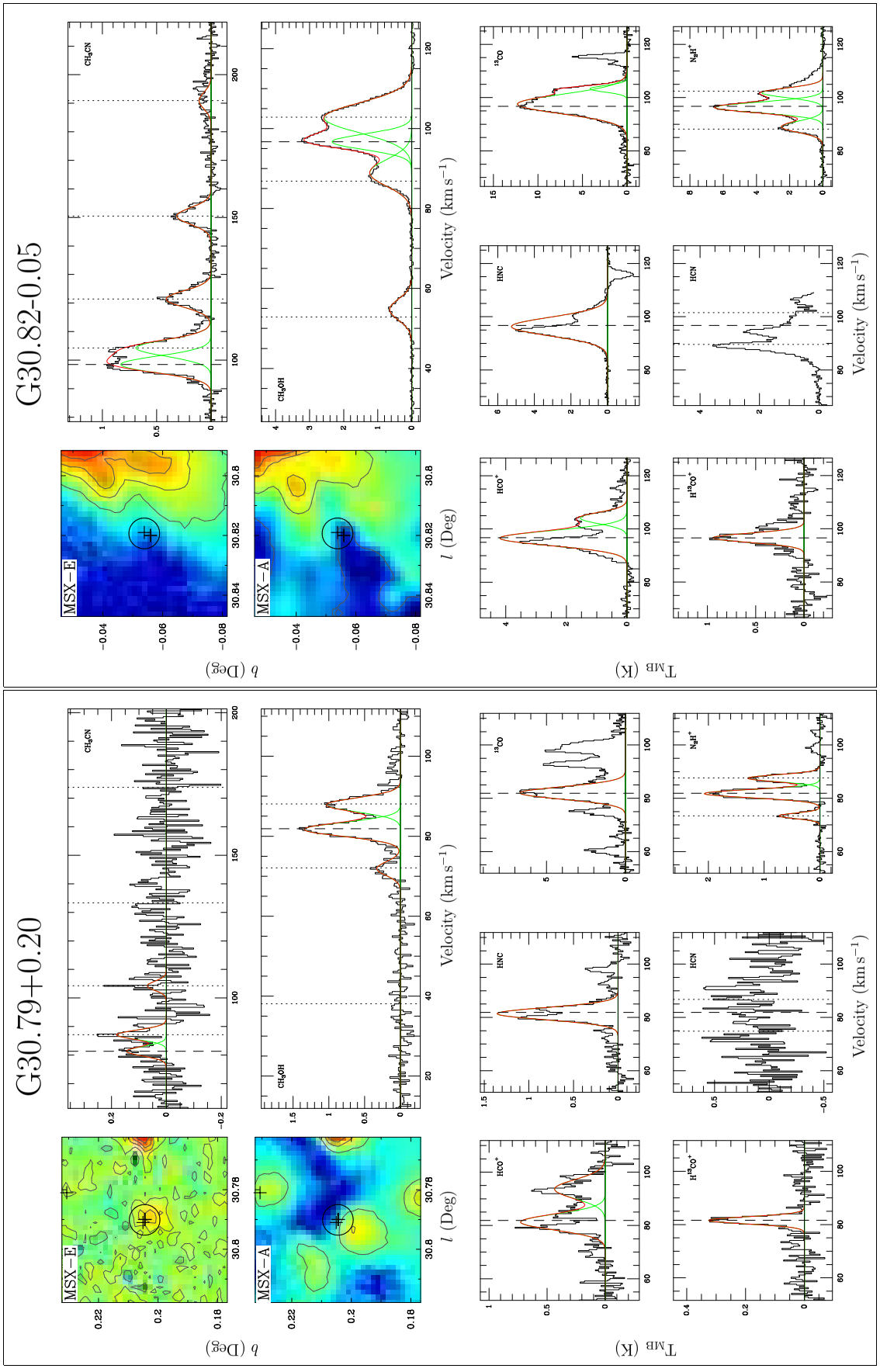

Mopra spectra and MSX images – *continued.*

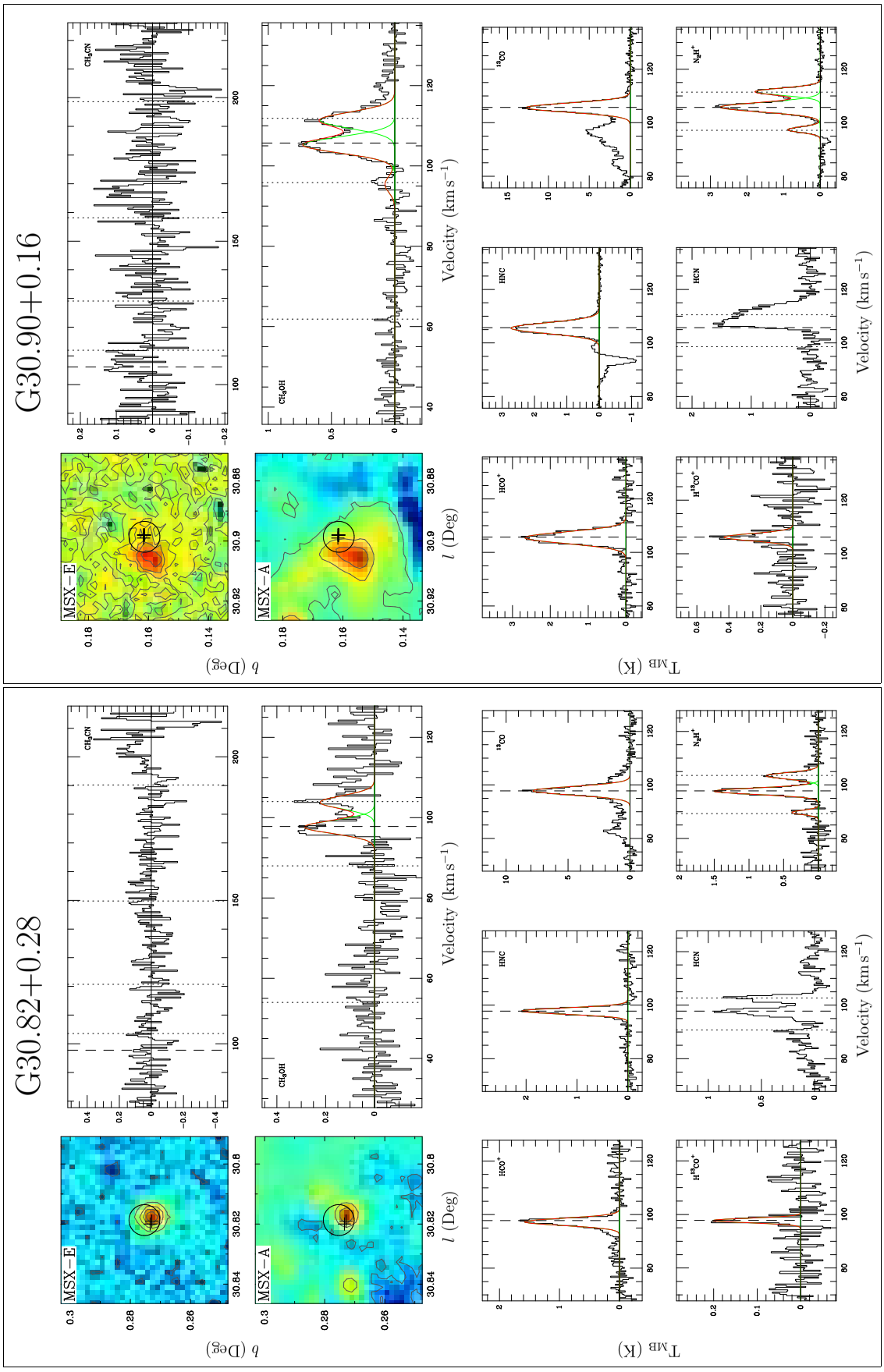

Mopra spectra and MSX images – *continued.*

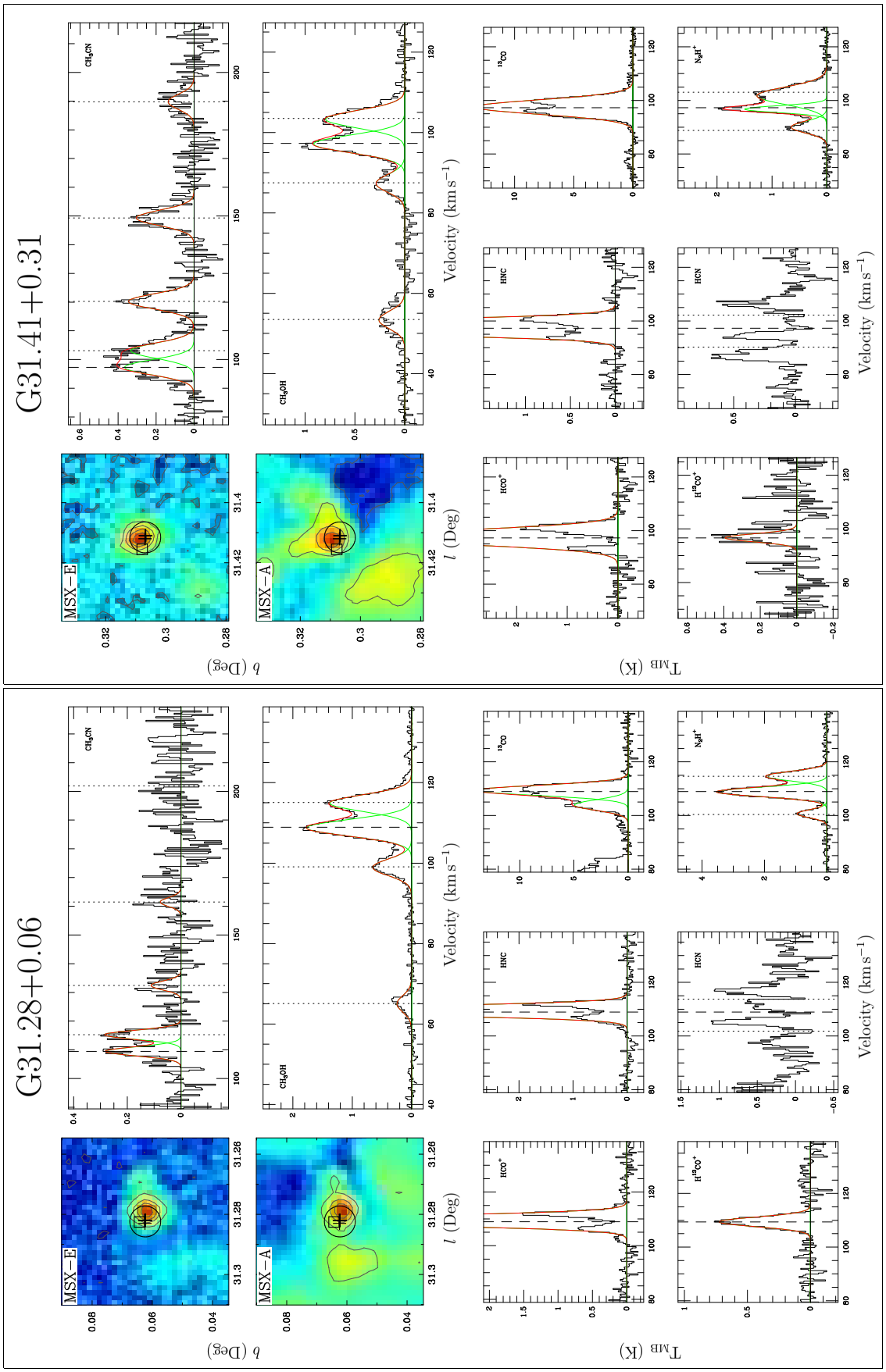

Mopra spectra and MSX images – *continued.*

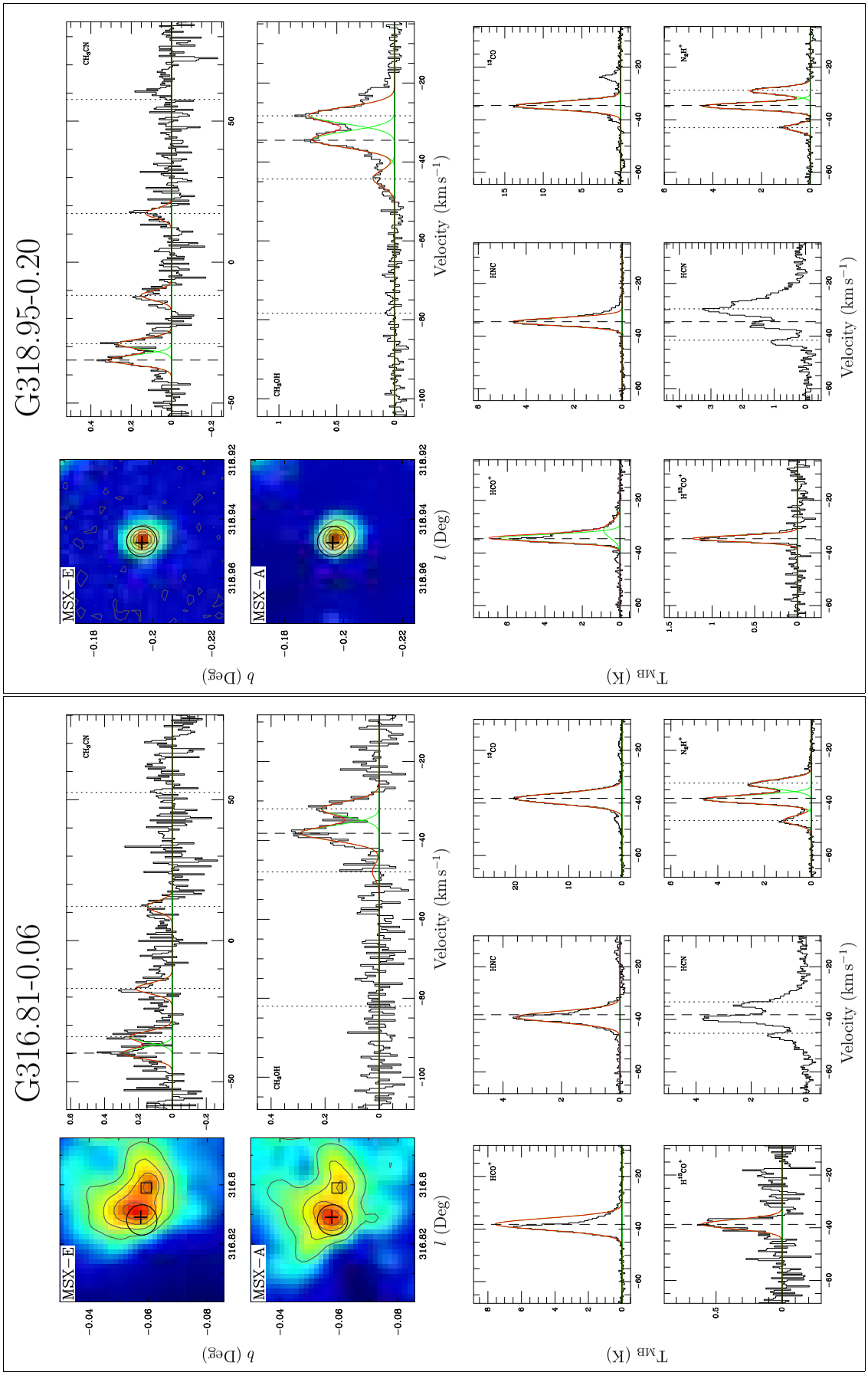

Mopra spectra and MSX images – *continued.*

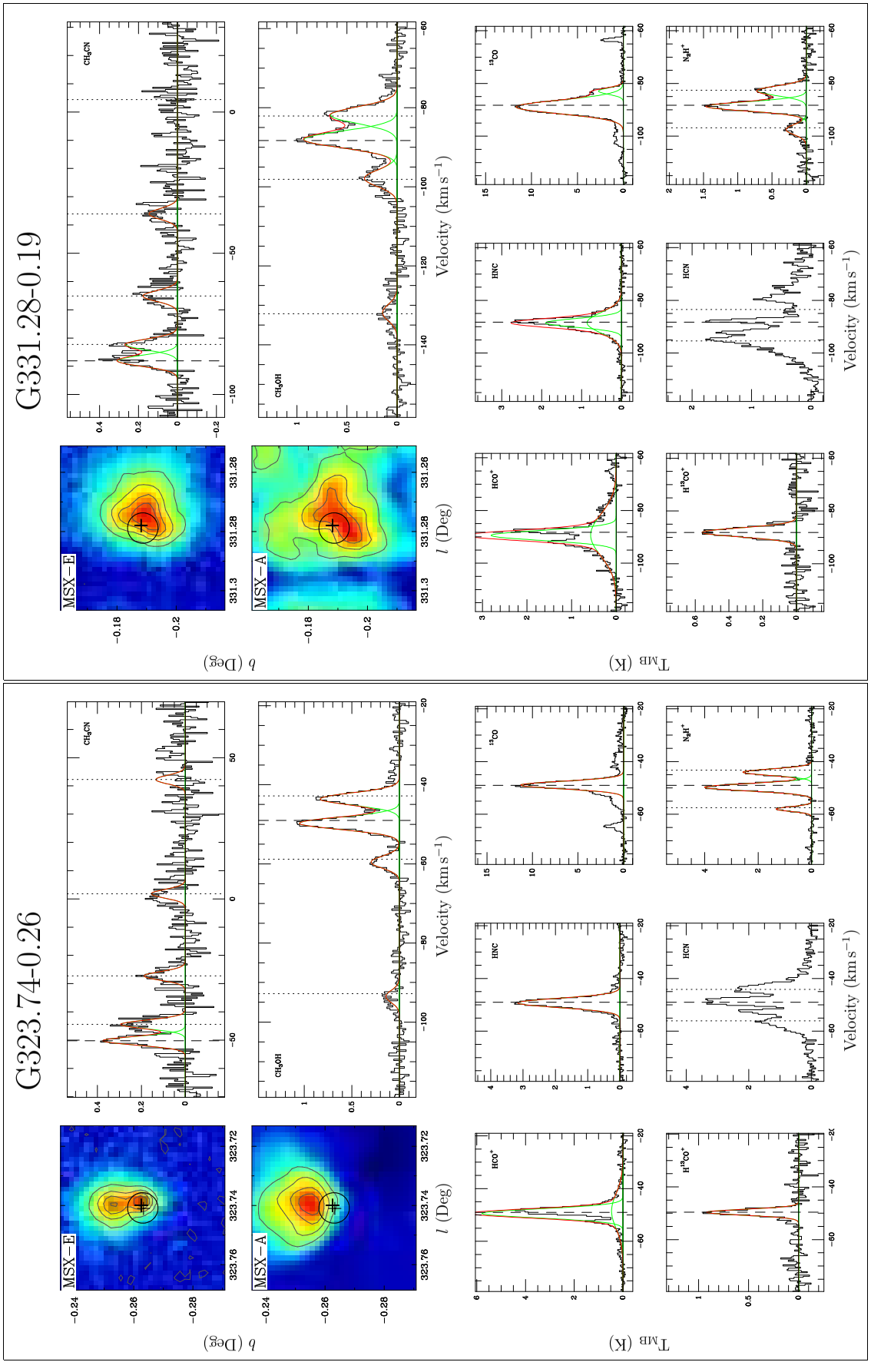

Mopra spectra and MSX images – *continued.*

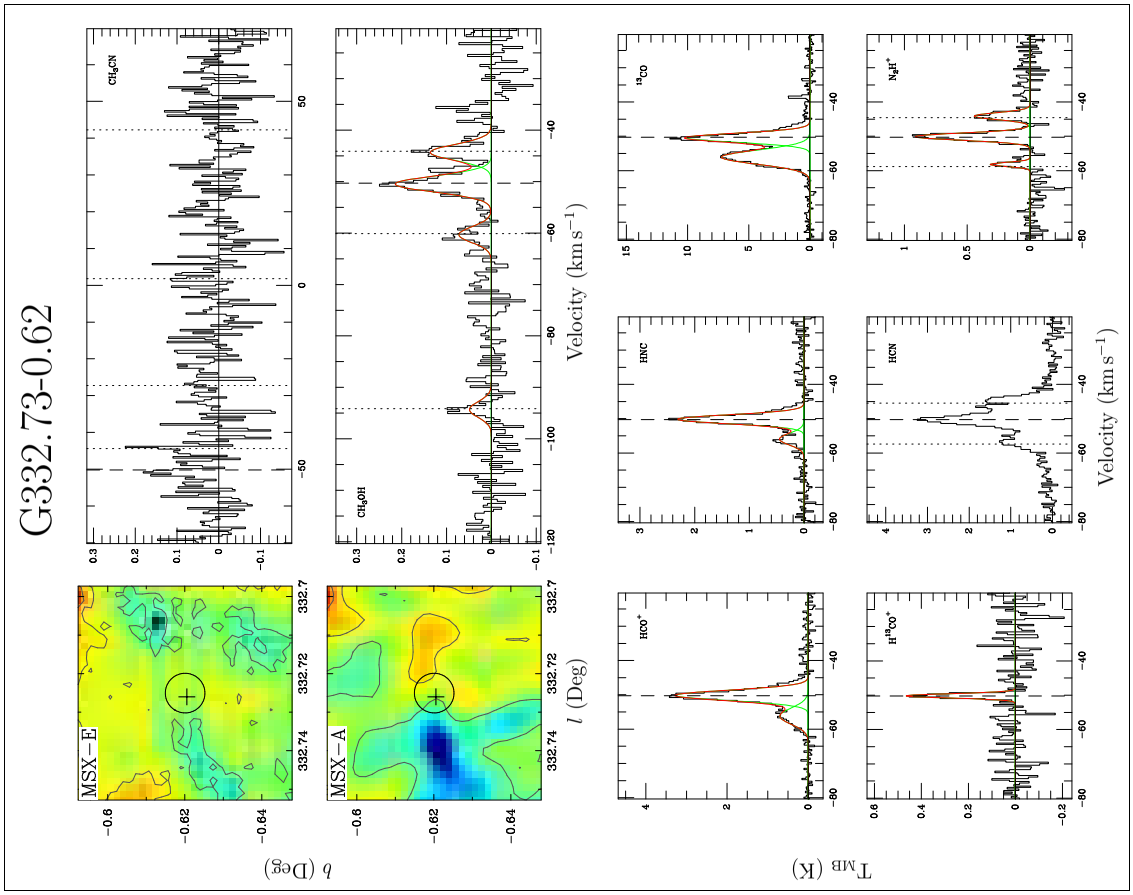

Mopra spectra and MSX images – *continued.*

Appendix D

Fitting parameters of the Mopra spectra

In this thesis we have used two methods to characterise the molecular emission: direct measurement from the line profiles and Gaussian fitting. The peak brightness temperature, area under the curve (integrated intensity) and equivalent width were measured directly from the HCO^+ and ^{13}CO and HCN lines, as all three species exhibit non-Gaussian line profiles (see sections 4-4 and 5-3). Multiple Gaussians were fit to all spectra except HCN, which exhibited very confused line profiles. The measured and fitted line parameters are tabulated in the following pages. Blended lines *not* associated with the main component are marked with a 'b' in the tables, similarly fits to high-velocity linewings are marked with a 'w'.

Table D.1: Parameters of the fits to the CH_3CN lines.

Source [α]	V_{LSR} [β] ($km\,s^{-1}$)	δV ($km\,s^{-1}$)	T_{MB} dv, K = 0 (K $km\,s^{-1}$)	T_{MB} dv, K = 1 (K $km\,s^{-1}$)	T_{MB} dv, K = 2 (K $km\,s^{-1}$)	T_{MB} dv, K = 3 (K $km\,s^{-1}$)	T_{MB} dv, K = 4 (K $km\,s^{-1}$)
G0.32−0.20	18.09	2.87	0.29 ± 0.13	0.25 ± 0.12	–	–	–
G0.55−0.85	17.22	5.66	5.47 ± 0.12	4.52 ± 0.11	2.73 ± 0.11	2.41 ± 0.12	0.90 ± 0.11
	18.32	7.87	2.56 ± 0.24	1.98 ± 0.23	1.87 ± 0.15	1.27 ± 0.15	–
G0.84+0.18	5.89	2.72	0.37 ± 0.06	0.24 ± 0.06	–	–	–
G1.15−0.12	−16.80	2.92	0.54 ± 0.12	0.46 ± 0.13	–	–	–
G5.89−0.39	9.20	4.54	2.73 ± 0.09	2.49 ± 0.09	1.48 ± 0.09	1.10 ± 0.09	–
G5.90−0.43	7.39	4.87	3.39 ± 0.30	2.80 ± 0.29	1.68 ± 0.30	1.01 ± 0.28	–
	7.23	5.12	2.75 ± 0.21	1.84 ± 0.21	1.25 ± 0.20	0.96 ± 0.19	–
G5.90−0.44	9.73	2.63	1.02 ± 0.08	0.66 ± 0.07	0.31 ± 0.07	0.22 ± 0.07	–
G8.14+0.23	18.60	4.34	0.91 ± 0.10	0.66 ± 0.10	0.32 ± 0.10	0.29 ± 0.10	–
G8.67−0.36	35.02	5.06	2.74 ± 0.10	2.48 ± 0.10	1.31 ± 0.10	0.76 ± 0.09	0.24 ± 0.09
G8.68−0.37	38.01	4.40	2.29 ± 0.09	2.25 ± 0.09	0.96 ± 0.09	0.72 ± 0.09	0.26 ± 0.09
G9.62+0.19	4.56	6.72	3.41 ± 0.27	2.13 ± 0.25	1.59 ± 0.19	1.39 ± 0.20	–
G9.99−0.03	49.56	4.48	0.34 ± 0.08	0.29 ± 0.08	0.13 ± 0.07	–	–
G10.29−0.13	13.40	4.81	2.01 ± 0.17	1.46 ± 0.17	0.68 ± 0.16	–	–
G10.30−0.15	12.88	5.39	2.80 ± 0.37	2.39 ± 0.36	0.85 ± 0.33	0.54 ± 0.32	–
	12.37	4.03	0.89 ± 0.14	0.77 ± 0.14	–	–	–
G10.34−0.14	12.07	4.55	1.24 ± 0.23	0.81 ± 0.22	0.37 ± 0.20	0.23 ± 0.20	–
	12.51	3.92	1.44 ± 0.13	1.31 ± 0.12	0.41 ± 0.12	–	–
G10.44−0.02	73.28	4.20	0.38 ± 0.09	0.15 ± 0.09	–	–	–
	75.56	5.49	0.72 ± 0.15	0.75 ± 0.20	–	–	–
G10.47+0.03	67.31	11.32	7.70 ± 0.48	5.02 ± 0.45	6.89 ± 0.28	6.53 ± 0.26	3.93 ± 0.25

Parameters of the fits to the CH_3CN lines – continued.

Source [α]	V_{LSR} [β] ($km\,s^{-1}$)	δV ($km\,s^{-1}$)	T_{MB} dv, K = 0 (K $km\,s^{-1}$)	T_{MB} dv, K = 1 (K $km\,s^{-1}$)	T_{MB} dv, K = 2 (K $km\,s^{-1}$)	T_{MB} dv, K = 3 (K $km\,s^{-1}$)	T_{MB} dv, K = 4 (K $km\,s^{-1}$)
G10.48+0.03	66.34	9.03	2.40 ± 0.33	1.59 ± 0.31	1.38 ± 0.18	1.00 ± 0.18	–
G10.63−0.38	−3.69	6.69	4.26 ± 0.25	3.59 ± 0.25	2.01 ± 0.18	1.62 ± 0.18	–
	−4.81	6.85	2.76 ± 0.27	3.17 ± 0.28	1.29 ± 0.17	1.50 ± 0.18	–
G11.94−0.62	38.11	4.24	1.74 ± 0.17	1.46 ± 0.16	0.58 ± 0.15	–	–
	38.11	3.83	0.64 ± 0.13	0.41 ± 0.12	0.27 ± 0.13	–	–
G12.68−0.18	55.99	4.13	0.86 ± 0.10	0.77 ± 0.10	0.37 ± 0.09	–	–
	56.73	4.89	0.92 ± 0.18	0.81 ± 0.19	0.85 ± 0.21	0.59 ± 0.19	–
G12.72−0.22	34.40	5.80	0.66 ± 0.13	0.44 ± 0.13	0.21 ± 0.12	–	–
G12.89+0.49	33.28	4.31	1.24 ± 0.16	1.32 ± 0.16	0.78 ± 0.17	1.05 ± 0.17	–
G12.91−0.26	37.40	4.18	1.07 ± 0.23	0.79 ± 0.21	0.33 ± 0.20	–	–
	37.47	5.03	2.22 ± 0.16	2.65 ± 0.16	1.56 ± 0.16	1.87 ± 0.17	–
G14.60+0.02	26.40	5.43	0.48 ± 0.05	0.67 ± 0.06	0.29 ± 0.05	0.26 ± 0.05	–
G14.99−0.70	19.09	6.51	1.61 ± 0.29	0.90 ± 0.27	0.94 ± 0.24	–	–
G15.03−0.68	19.99	4.38	0.67 ± 0.10	0.51 ± 0.10	0.11 ± 0.10	–	–
	19.65	3.42	0.86 ± 0.09	0.84 ± 0.09	0.60 ± 0.09	–	–
G16.59−0.05	59.91	5.00	1.21 ± 0.32	1.50 ± 0.33	0.53 ± 0.31	–	–
G16.86−2.16	18.14	5.79	1.41 ± 0.34	1.28 ± 0.33	0.49 ± 0.28	0.34 ± 0.30	–
	17.98	4.59	1.18 ± 0.17	1.66 ± 0.18	0.67 ± 0.17	0.40 ± 0.17	–
G19.36−0.03	25.83	3.87	0.55 ± 0.11	0.53 ± 0.10	–	–	–
G19.47+0.17	20.31	6.04	1.93 ± 0.25	2.01 ± 0.26	0.99 ± 0.24	0.81 ± 0.23	–
G19.61−0.13	57.07	5.68	0.43 ± 0.16	0.69 ± 0.17	–	–	–
G22.36+0.07	84.31	1.62	0.17 ± 0.04	0.11 ± 0.04	–	–	–

Parameters of the fits to the CH_3CN lines – continued.

Source [α]	V_{LSR} [β] (km s^{-1})	δV (km s^{-1})	T_{MB} dv, K = 0 (K km s^{-1})	T_{MB} dv, K = 1 (K km s^{-1})	T_{MB} dv, K = 2 (K km s^{-1})	T_{MB} dv, K = 3 (K km s^{-1})	T_{MB} dv, K = 4 (K km s^{-1})
G23.44−0.18	101.64	5.43	2.18 ± 0.17	1.88 ± 0.16	0.80 ± 0.15	0.83 ± 0.15	–
	102.48	5.45	2.45 ± 0.18	2.00 ± 0.18	0.89 ± 0.16	1.06 ± 0.17	–
G24.79+0.08	110.81	6.63	3.60 ± 0.22	3.42 ± 0.21	2.38 ± 0.20	1.92 ± 0.20	0.45 ± 0.18
	112.03	5.94	3.68 ± 0.22	3.58 ± 0.22	2.45 ± 0.21	2.55 ± 0.21	–
G25.65+1.05	42.55	4.55	1.11 ± 0.21	0.93 ± 0.21	0.78 ± 0.23	–	–
G25.71+0.04	99.01	5.26	0.45 ± 0.11	0.16 ± 0.11	0.19 ± 0.09	–	–
G25.83−0.18	93.81	5.25	2.13 ± 0.15	1.89 ± 0.15	0.92 ± 0.15	0.87 ± 0.14	0.33 ± 0.14
	94.38	5.27	1.84 ± 0.17	1.88 ± 0.17	0.96 ± 0.17	–	–
G28.15+0.00	98.95	3.22	0.54 ± 0.12	0.49 ± 0.12	0.20 ± 0.11	–	–
G28.20−0.05	95.86	5.83	1.19 ± 0.25	1.46 ± 0.26	1.31 ± 0.25	0.59 ± 0.22	–
G28.28−0.36	48.69	4.09	0.58 ± 0.11	0.41 ± 0.11	–	–	–
G28.83−0.25	86.83	2.70	0.67 ± 0.15	0.46 ± 0.14	0.32 ± 0.14	–	–
G29.96−0.02	97.75	5.02	2.02 ± 0.26	1.52 ± 0.24	1.24 ± 0.26	1.02 ± 0.26	0.24 ± 0.23
	97.12	6.53	2.21 ± 0.25	1.13 ± 0.22	1.50 ± 0.20	1.50 ± 0.23	–
G29.98−0.04	102.27	8.76	0.79 ± 0.10	0.46 ± 0.17	–	–	–
	100.49	3.02	0.71 ± 0.20	0.64 ± 0.20	–	–	–
G30.71−0.06	91.19	4.60	3.36 ± 0.29	3.03 ± 0.29	1.41 ± 0.28	1.35 ± 0.28	0.60 ± 0.27
	91.37	4.89	2.22 ± 0.22	1.98 ± 0.21	1.28 ± 0.23	1.43 ± 0.23	–
G30.76−0.05	92.65	4.18	0.67 ± 0.12	0.69 ± 0.12	0.15 ± 0.12	–	–
	98.26	2.15	1.35 ± 0.33	0.68 ± 0.22	–	–	–
G30.79+0.20	81.39	4.28	0.61 ± 0.26	0.76 ± 0.26	0.29 ± 0.25	–	–
G30.82−0.05	98.59	6.48	5.98 ± 0.44	4.82 ± 0.38	2.92 ± 0.33	2.18 ± 0.32	0.73 ± 0.31
	98.10	7.24	5.48 ± 0.33	3.88 ± 0.29	2.81 ± 0.23	3.36 ± 0.23	–

Parameters of the fits to the CH_3CN lines – continued.

Source [α]	V_{LSR} [β] ($km\,s^{-1}$)	δV ($km\,s^{-1}$)	T_{MB} dv, K = 0 (K $km\,s^{-1}$)	T_{MB} dv, K = 1 (K $km\,s^{-1}$)	T_{MB} dv, K = 2 (K $km\,s^{-1}$)	T_{MB} dv, K = 3 (K $km\,s^{-1}$)	T_{MB} dv, K = 4 (K $km\,s^{-1}$)
G30.90+0.16	105.62	4.19	0.43 ± 0.13	0.25 ± 0.12	–	–	–
G31.28+0.06	109.47	4.11	1.12 ± 0.29	1.13 ± 0.29	0.45 ± 0.28	–	–
	108.68	1.61	0.60 ± 0.12	0.32 ± 0.11	–	–	–
G31.41+0.31	97.64	7.44	2.64 ± 0.31	2.26 ± 0.29	2.56 ± 0.26	2.33 ± 0.29	1.04 ± 0.25
	98.11	7.33	3.83 ± 0.24	3.35 ± 0.23	3.02 ± 0.20	2.88 ± 0.21	–
G316.81−0.06	−39.69	3.70	0.99 ± 0.14	0.83 ± 0.14	0.67 ± 0.14	0.49 ± 0.14	–
	−43.70	7.44	0.24 ± 0.33	1.22 ± 0.36	–	–	–
G318.95−0.20	−34.68	4.47	1.48 ± 0.12	1.25 ± 0.12	0.76 ± 0.12	0.58 ± 0.12	–
G323.74−0.26	−50.11	4.30	1.55 ± 0.12	1.22 ± 0.11	0.82 ± 0.12	0.75 ± 0.12	–
	−48.73	2.90	0.85 ± 0.15	0.64 ± 0.14	–	–	–
G331.28−0.19	−87.85	5.36	1.60 ± 0.17	1.24 ± 0.16	0.94 ± 0.14	0.81 ± 0.14	–
G332.73−0.62	−50.74	2.55	0.37 ± 0.10	0.30 ± 0.09	–	–	–

[α] For each source the parameters of the $CH_3CN\,(5-4)$ fits are presented in the upper row and those of the $CH_3CN\,(6-5)$ fits are presented in the lower row.

[β] Quoted V_{LSR} is referenced to the K = 0 component.

Table D.2: Measured and fitted parameters of the HCO^+ and $H^{13}CO^+$ lines.

Source	HCO^+ Gaussian Fits [α]			HCO^+ Integrated Lines [β]			$H^{13}CO^+$ Gaussian Fits			Code [γ]
	T_{MB} dv (K km s^{-1})	V_{LSR} (km s^{-1})	δV (km s^{-1})	T_{MB} dv (K km s^{-1})	E-Width (km s^{-1})	T_{MB} (K)	T_{MB} dv (K km s^{-1})	V_{LSR} (km s^{-1})	δV (km s^{-1})	
G0.32-0.20	29.65 ± 0.59	18.71 ± 0.01	3.29 ± 0.04	29.63 ± 1.07	3.47	0.12	1.64 ± 0.15	18.85 ± 0.12	2.68 ± 0.29	
	9.31 ± 0.59	18.48 ± 0.01	11.88 ± 0.04							w
G0.50+0.19	2.77 ± 0.47	−6.52 ± 0.40	5.83 ± 0.55	1.46 ± 0.61	4.06	1.69	1.98 ± 0.21	−6.14 ± 0.22	4.27 ± 0.56	
	17.19 ± 0.59	26.37 ± 0.01	43.41 ± 0.04							b
G0.55-0.85	62.51 ± 0.49	16.44 ± 0.02	4.62 ± 0.04	67.09 ± 3.57	5.34	0.28	7.74 ± 0.23	17.52 ± 0.05	3.55 ± 0.13	
	9.84 ± 0.59	22.23 ± 0.01	4.77 ± 0.04							b
G0.84+0.18	1.50 ± 0.15	6.98 ± 0.09	1.86 ± 0.22	1.90 ± 1.01	3.39	1.80	0.49 ± 0.06	5.91 ± 0.17	2.74 ± 0.41	
G1.15-0.12	10.51 ± 2.44	−18.70 ± 0.10	4.50 ± 0.48	4.43 ± 1.08	5.30	1.29	1.11 ± 0.14	−17.23 ± 0.26	4.11 ± 0.61	
G2.54+0.20	12.42 ± 0.77	9.58 ± 0.05	2.97 ± 0.14	1.99 ± 0.49	1.13	0.28	3.26 ± 0.49	10.10 ± 0.17	2.82 ± 0.22	
G5.89-0.39	69.72 ± 0.42	9.40 ± 0.00	4.40 ± 0.03	43.75 ± 1.52	3.19	0.11	7.31 ± 0.16	9.31 ± 0.04	4.08 ± 0.10	
	47.45 ± 0.59	10.91 ± 0.01	26.75 ± 0.04							w
G5.90-0.43	32.27 ± 0.43	6.44 ± 0.03	3.88 ± 0.06	32.00 ± 2.35	4.14	0.30	4.09 ± 0.15	6.97 ± 0.06	3.41 ± 0.15	
G5.90-0.44	15.13 ± 0.22	9.50 ± 0.00	6.29 ± 0.09	10.06 ± 0.63	4.79	0.30	1.65 ± 0.08	9.46 ± 0.05	2.04 ± 0.11	
G6.61-0.08	0.37 ± 0.13	6.92 ± 0.13	0.73 ± 0.26	0.22 ± 0.80	0.77	2.78	0.58 ± 0.12	7.72 ± 0.23	2.24 ± 0.45	
	31.45 ± 0.59	−1.75 ± 0.01	23.98 ± 0.04							b
G8.14+0.23	19.53 ± 0.69	19.77 ± 0.07	5.00 ± 0.09	13.88 ± 1.08	4.26	0.33	1.53 ± 0.17	19.18 ± 0.20	3.60 ± 0.44	
G8.67-0.36	29.18 ± 0.55	34.80 ± 0.55	3.78 ± 0.06	10.76 ± 0.92	2.75	0.23	5.86 ± 0.15	34.80 ± 0.05	4.11 ± 0.13	
	14.61 ± 0.59	35.23 ± 0.01	13.20 ± 0.04							w
G8.68-0.37	51.08 ± 1.76	37.25 ± 0.05	7.33 ± 0.14	25.66 ± 1.06	7.57	0.31	5.58 ± 0.18	37.22 ± 0.07	5.35 ± 0.22	
G9.62+0.19	20.49 ± 0.62	3.35 ± 0.04	4.44 ± 0.08	10.99 ± 1.11	3.24	0.33	3.60 ± 0.10	4.45 ± 0.06	4.53 ± 0.15	
	18.37 ± 0.59	4.29 ± 0.01	11.47 ± 0.04							w
G9.99-0.03	11.48 ± 0.23	48.97 ± 0.05	4.88 ± 0.11	11.75 ± 1.28	5.26	0.57	0.80 ± 0.08	48.90 ± 0.11	2.29 ± 0.26	
G10.29-0.13	13.66 ± 0.57	12.04 ± 0.06	4.53 ± 0.25	12.64 ± 1.39	5.16	0.57	2.40 ± 0.34	13.70 ± 0.23	3.60 ± 0.27	
G10.30-0.15	31.97 ± 0.62	12.81 ± 0.03	4.95 ± 0.07	16.98 ± 2.03	4.26	0.51	5.33 ± 0.18	12.99 ± 0.07	4.38 ± 0.18	
	35.38 ± 0.59	11.11 ± 0.01	11.90 ± 0.04							w

Measured and fitted parameters of the HCO^+ and $H^{13}CO^+$ lines - *continued.*

Source	HCO^+ Gaussian Fits [α]			HCO^+ Integrated Lines [β]			$H^{13}CO^+$ Gaussian Fits			Code [γ]
	T_{MB} dv (K km s^{-1})	V_{LSR} (km s^{-1})	δV (km s^{-1})	T_{MB} dv (K km s^{-1})	E-Width (km s^{-1})	T_{MB} (K)	T_{MB} dv (K km s^{-1})	V_{LSR} (km s^{-1})	δV (km s^{-1})	
G10.32-0.16	7.16 ± 0.14	12.57 ± 0.02	1.81 ± 0.04	7.17 ± 0.96	1.94	0.26	1.89 ± 0.12	12.15 ± 0.09	2.63 ± 0.20	
	13.88 ± 0.59	12.23 ± 0.01	7.48 ± 0.04							w
G10.34-0.14	20.16 ± 1.00	12.46 ± 0.04	3.44 ± 0.10	15.73 ± 1.11	3.02	0.21	2.30 ± 0.16	12.22 ± 0.10	2.98 ± 0.25	
	9.15 ± 0.59	11.44 ± 0.01	10.49 ± 0.04							w
G10.44-0.02	14.79 ± 1.25	75.26 ± 0.12	5.59 ± 0.24	8.20 ± 1.14	5.45	0.76	1.66 ± 0.09	75.41 ± 0.12	4.58 ± 0.30	
	3.17 ± 0.59	65.92 ± 0.01	4.87 ± 0.04							b
G10.47+0.03	82.39 ± 1.56	67.13 ± 0.03	8.19 ± 0.12	66.60 ± 2.53	10.14	0.39	4.93 ± 0.17	67.05 ± 0.11	6.82 ± 0.28	
G10.48+0.03	42.33 ± 0.44	65.90 ± 0.03	8.04 ± 0.10	24.62 ± 1.02	8.36	0.35	3.40 ± 0.22	66.15 ± 0.17	6.26 ± 0.50	
G10.63-0.33	13.79 ± 0.22	−3.63 ± 0.04	4.55 ± 0.09	13.80 ± 1.21	4.78	0.42	2.17 ± 0.19	−4.14 ± 0.13	2.85 ± 0.18	
G10.63-0.38	98.30 ± 0.41	−3.74 ± 0.01	7.59 ± 0.04	95.57 ± 1.65	7.86	0.14	11.06 ± 0.26	−3.14 ± 0.05	6.04 ± 0.22	
G11.50-1.49	19.47 ± 1.72	10.11 ± 0.14	4.05 ± 0.14	9.26 ± 1.72	2.70	0.50	1.16 ± 0.08	10.26 ± 0.07	2.03 ± 0.16	
	10.89 ± 0.59	13.64 ± 0.01	20.46 ± 0.04							w
G11.94-0.15	11.95 ± 0.55	41.87 ± 0.07	4.52 ± 0.26	12.18 ± 1.40	4.73	0.54	1.53 ± 0.20	42.60 ± 0.29	4.46 ± 0.67	
	1.42 ± 0.59	47.18 ± 0.01	2.75 ± 0.04							b
G11.94-0.62	35.97 ± 0.94	38.54 ± 0.04	4.49 ± 0.06	15.97 ± 1.26	3.14	0.25	3.57 ± 0.24	37.89 ± 0.09	4.00 ± 0.28	
G11.99-0.27	2.18 ± 0.18	58.50 ± 0.13	3.33 ± 0.34	2.41 ± 1.02	4.48	1.89	0.66 ± 0.09	59.66 ± 0.26	4.47 ± 0.94	
	4.76 ± 0.59	59.83 ± 0.01	17.40 ± 0.04							w
G12.03-0.03	4.14 ± 0.26	111.04 ± 0.11	3.48 ± 0.25	4.49 ± 1.55	4.38	1.51	0.69 ± 0.09	110.47 ± 0.20	3.57 ± 0.55	
G12.18-0.12	10.42 ± 0.21	25.91 ± 0.04	5.13 ± 0.13	11.26 ± 0.75	5.92	0.39	1.25 ± 0.19	26.51 ± 0.67	9.12 ± 1.73	
G12.21-0.09	16.76 ± 4.94	24.24 ± 0.06	3.49 ± 0.38	7.26 ± 1.31	5.31	0.96	1.02 ± 0.13	23.82 ± 0.20	3.10 ± 0.50	
G12.68-0.18	6.55 ± 0.43	58.40 ± 0.10	3.46 ± 0.29	6.97 ± 1.14	3.93	0.64	1.15 ± 0.09	56.46 ± 0.10	2.70 ± 0.26	
G12.72-0.22	13.39 ± 0.51	34.87 ± 0.06	4.85 ± 0.14	10.31 ± 0.72	5.87	0.41	2.62 ± 0.36	34.19 ± 0.05	2.63 ± 0.21	
G12.89+0.49	23.06 ± 2.21	33.63 ± 0.10	3.83 ± 0.13	9.80 ± 1.25	3.26	0.42	2.23 ± 0.10	33.34 ± 0.07	3.09 ± 0.16	
G12.91-0.26	30.75 ± 1.27	38.57 ± 0.12	8.63 ± 0.28	12.79 ± 4.43	5.30	1.84	4.81 ± 0.14	36.95 ± 0.05	3.55 ± 0.12	
	23.45 ± 0.59	42.54 ± 0.01	27.54 ± 0.04							w

Measured and fitted parameters of the HCO^+ and $H^{13}CO^+$ lines - *continued.*

Source	HCO^+ Gaussian Fits [α]			HCO^+ Integrated Lines [β]			$H^{13}CO^+$ Gaussian Fits			Code [γ]
	T_{MB} dv (K km s^{-1})	V_{LSR} (km s^{-1})	δV (km s^{-1})	T_{MB} dv (K km s^{-1})	E-Width (km s^{-1})	T_{MB} (K)	T_{MB} dv (K km s^{-1})	V_{LSR} (km s^{-1})	δV (km s^{-1})	
G14.60+0.02	12.32 ± 4.70	25.64 ± 0.30	7.23 ± 1.41	4.93 ± 0.99	9.59	1.93	3.14 ± 0.67	24.74 ± 0.41	6.27 ± 0.74	
	2.04 ± 0.59	37.93 ± 0.01	4.05 ± 0.04							b
G14.99-0.70	47.84 ± 0.81	18.75 ± 0.04	6.35 ± 0.07	40.16 ± 1.20	6.74	0.20	2.19 ± 0.15	18.70 ± 0.16	4.75 ± 0.38	
G15.03-0.68	73.99 ± 0.70	19.68 ± 0.02	4.14 ± 0.03	64.16 ± 1.52	4.08	0.10	5.29 ± 0.13	19.50 ± 0.03	2.89 ± 0.09	
G15.03-0.71	12.97 ± 0.81	21.11 ± 0.04	4.08 ± 0.19	10.71 ± 0.80	5.23	0.39	0.63 ± 0.10	20.97 ± 0.45	5.44 ± 0.99	
	3.13 ± 0.59	18.50 ± 0.01	8.96 ± 0.04							w
G16.59-0.05	29.29 ± 0.57	59.34 ± 0.03	3.56 ± 0.05	21.53 ± 1.17	3.35	0.18	2.26 ± 0.17	59.86 ± 0.12	3.28 ± 0.30	
G16.86-2.16	36.43 ± 0.70	17.91 ± 0.03	4.17 ± 0.04	18.48 ± 1.03	3.42	0.19	5.48 ± 0.39	17.77 ± 0.12	3.54 ± 0.20	
	16.41 ± 0.59	18.44 ± 0.01	17.59 ± 0.04							w
G19.36-0.03	10.22 ± 0.93	27.85 ± 0.12	5.19 ± 0.43	5.76 ± 1.18	4.67	0.96	1.56 ± 0.09	26.73 ± 0.08	2.89 ± 0.19	
G19.47+0.17	23.68 ± 1.03	18.86 ± 0.12	7.64 ± 0.24	15.90 ± 1.63	7.25	0.74	3.96 ± 0.75	19.71 ± 0.13	4.49 ± 0.50	
	1.66 ± 0.59	27.70 ± 0.01	2.78 ± 0.04							b
G19.49+0.15	6.19 ± 0.23	22.70 ± 0.07	4.06 ± 0.20	6.07 ± 1.01	4.29	0.72	0.74 ± 0.07	23.03 ± 0.13	3.12 ± 0.37	
G19.61-0.13	9.32 ± 0.22	57.14 ± 0.06	4.75 ± 0.13	9.41 ± 1.10	5.30	0.62	0.42 ± 0.09	56.94 ± 0.45	3.77 ± 0.74	
G19.70-0.27	1.30 ± 0.21	44.28 ± 0.21	2.54 ± 0.49	1.56 ± 1.14	4.87	3.56	0.90 ± 0.15	42.99 ± 0.00	2.58 ± 0.52	
	1.05 ± 0.59	38.51 ± 0.01	3.32 ± 0.04							b
G21.88+0.01	7.22 ± 1.24	22.88 ± 0.09	4.96 ± 0.49	3.96 ± 0.97	6.70	1.64	0.87 ± 0.12	23.34 ± 0.27	4.16 ± 0.73	
G22.36+0.07	9.79 ± 0.23	84.39 ± 0.05	4.12 ± 0.12	10.54 ± 1.13	4.87	0.52	0.81 ± 0.08	84.07 ± 0.13	2.55 ± 0.28	
G23.26-0.24	8.90 ± 0.59	61.67 ± 0.19	5.89 ± 0.31	7.53 ± 1.13	5.11	0.77	1.02 ± 0.06	61.50 ± 0.08	2.81 ± 0.21	
G23.44-0.18	62.71 ± 1.99	100.62 ± 0.14	10.50 ± 0.16	37.47 ± 1.91	8.11	0.41	3.51 ± 0.17	101.59 ± 0.10	4.25 ± 0.24	
G23.71-0.20	5.33 ± 0.27	68.36 ± 0.11	4.89 ± 0.47	5.67 ± 1.15	6.44	1.31	0.95 ± 0.07	68.96 ± 0.13	3.86 ± 0.30	
G24.79+0.08	16.80 ± 2.07	111.79 ± 0.00	4.47 ± 0.34	14.46 ± 1.12	4.40	0.34	4.43 ± 0.16	110.51 ± 0.07	4.24 ± 0.18	
	13.17 ± 0.59	111.37 ± 0.01	17.71 ± 0.04							w
	0.43 ± 0.47	102.30 ± 0.40	1.35 ± 0.55							b
G24.85+0.09	5.60 ± 0.14	109.00 ± 0.04	3.32 ± 0.10	3.95 ± 0.72	3.48	0.63	0.43 ± 0.06	108.88 ± 0.22	3.01 ± 0.50	

Measured and fitted parameters of the HCO^+ and $H^{13}CO^+$ lines - *continued.*

Source	HCO^+ Gaussian Fits [α]			HCO^+ Integrated Lines [β]			$H^{13}CO^+$ Gaussian Fits			Code [γ]
	T_{MB} dv (K km s^{-1})	V_{LSR} (km s^{-1})	δV (km s^{-1})	T_{MB} dv (K km s^{-1})	E-Width (km s^{-1})	T_{MB} (K)	T_{MB} dv (K km s^{-1})	V_{LSR} (km s^{-1})	δV (km s^{-1})	
G25.65+1.05	19.53 ± 0.35	42.46 ± 0.04	4.58 ± 0.08	14.29 ± 1.43	3.68	0.37	4.04 ± 0.15	42.43 ± 0.06	3.63 ± 0.16	
	26.85 ± 0.59	41.34 ± 0.01	21.83 ± 0.04							w
G25.71+0.04	10.12 ± 0.33	98.97 ± 0.07	4.28 ± 0.16	10.17 ± 1.64	4.64	0.75	1.08 ± 0.07	98.73 ± 0.10	3.19 ± 0.22	
G25.83-0.18	25.00 ± 1.38	93.86 ± 0.07	4.24 ± 0.13	11.94 ± 1.32	3.42	0.38	1.89 ± 0.06	93.39 ± 0.06	3.32 ± 0.13	
	10.03 ± 0.59	95.08 ± 0.01	21.70 ± 0.04							w
G28.15+0.00	6.18 ± 1.20	98.70 ± 0.32	6.56 ± 0.61	3.47 ± 0.85	6.92	1.69	1.11 ± 0.07	98.59 ± 0.08	2.45 ± 0.18	
G28.20-0.05	35.26 ± 0.56	96.37 ± 0.07	11.59 ± 0.26	30.18 ± 1.41	11.21	0.53	2.71 ± 0.13	95.58 ± 0.09	3.93 ± 0.24	
G28.28-0.36	8.31 ± 0.22	48.73 ± 0.06	5.68 ± 0.23	7.53 ± 0.82	6.93	0.76	0.89 ± 0.07	48.87 ± 0.10	2.88 ± 0.26	
G28.31-0.39	2.49 ± 0.07	85.52 ± 0.03	2.17 ± 0.07	2.55 ± 0.29	2.42	0.28	1.50 ± 0.19	86.18 ± 0.23	3.92 ± 0.62	
G28.83-0.25	20.19 ± 0.60	87.06 ± 0.05	5.71 ± 0.19	6.10 ± 0.98	3.74	0.60	2.15 ± 0.14	87.06 ± 0.11	3.36 ± 0.23	
G29.87-0.04	15.44 ± 0.25	100.96 ± 0.03	3.67 ± 0.07	15.45 ± 1.18	4.20	0.32	1.47 ± 0.10	100.91 ± 0.10	3.20 ± 0.23	
	12.86 ± 0.59	99.72 ± 0.01	11.71 ± 0.04							w
G29.96-0.02	25.51 ± 1.43	96.86 ± 0.11	4.72 ± 0.15	14.50 ± 1.75	4.04	0.49	2.88 ± 0.14	97.63 ± 0.07	2.83 ± 0.17	
	1.86 ± 0.59	103.48 ± 0.01	3.59 ± 0.04							b
G29.98-0.04	6.72 ± 1.88	102.96 ± 0.19	4.83 ± 0.67	20.68 ± 1.55	10.55	0.79	1.80 ± 0.07	101.57 ± 0.05	2.63 ± 0.12	
	12.09 ± 0.59	101.74 ± 0.01	17.45 ± 0.04							w
	14.02 ± 0.47	95.81 ± 0.40	6.72 ± 0.55							b
G30.59-0.04	6.52 ± 0.30	42.21 ± 0.11	5.36 ± 0.33	6.99 ± 1.69	5.51	1.33	1.73 ± 0.13	41.81 ± 0.14	3.88 ± 0.34	
G30.71-0.06	33.30 ± 2.72	92.24 ± 0.12	9.96 ± 0.64	5.87 ± 1.51	4.68	1.20	6.40 ± 1.28	92.85 ± 0.34	5.53 ± 0.52	
G30.76-0.05	36.18 ± 2.71	93.58 ± 0.09	8.87 ± 0.38	8.46 ± 2.08	6.55	1.61	2.92 ± 0.33	93.00 ± 0.00	5.38 ± 0.73	
G30.78+0.23	4.22 ± 0.18	41.99 ± 0.07	3.29 ± 0.17	4.37 ± 1.00	3.82	0.88	0.90 ± 1.25	41.80 ± 0.00	1.55 ± 1.03	
G30.79+0.20	5.40 ± 0.44	81.25 ± 0.20	6.98 ± 0.93	3.94 ± 1.11	5.53	1.56	1.10 ± 0.07	81.59 ± 0.09	3.17 ± 0.23	
	3.87 ± 0.59	93.62 ± 0.01	8.34 ± 0.04							b
G30.82-0.05	29.34 ± 2.36	96.57 ± 0.23	6.58 ± 0.33	22.29 ± 1.50	6.56	0.44	4.09 ± 0.28	96.61 ± 0.12	4.08 ± 0.37	
	8.22 ± 0.59	104.12 ± 0.01	5.01 ± 0.04							b

Measured and fitted parameters of the HCO^+ and $H^{13}CO^+$ lines - *continued.*

Source	HCO^+ Gaussian Fits [α]			HCO^+ Integrated Lines [β]			$H^{13}CO^+$ Gaussian Fits			Code [γ]
	T_{MB} dv (K km s^{-1})	V_{LSR} (km s^{-1})	δV (km s^{-1})	T_{MB} dv (K km s^{-1})	E-Width (km s^{-1})	T_{MB} (K)	T_{MB} dv (K km s^{-1})	V_{LSR} (km s^{-1})	δV (km s^{-1})	
G30.82+0.28	5.33 ± 0.18	97.28 ± 0.05	3.16 ± 0.14	5.75 ± 1.16	3.73	0.76	0.42 ± 0.05	97.77 ± 0.12	1.98 ± 0.26	
G30.90+0.16	14.43 ± 0.33	105.53 ± 0.06	5.07 ± 0.13	14.02 ± 1.85	5.56	0.73	1.46 ± 0.21	106.17 ± 0.20	3.19 ± 0.61	
G31.28+0.06	23.88 ± 4.52	109.33 ± 0.06	4.38 ± 0.27	6.81 ± 0.90	4.38	0.58	3.23 ± 0.13	109.40 ± 0.08	4.18 ± 0.18	
G31.41+0.31	34.55 ± 4.10	97.50 ± 0.00	6.41 ± 0.37	10.04 ± 2.13	5.27	1.12	1.46 ± 0.20	96.66 ± 0.25	3.49 ± 0.53	
G316.81-0.06	42.43 ± 0.94	−38.16 ± 0.05	5.27 ± 0.06	29.12 ± 1.43	4.56	0.22	2.72 ± 0.24	−38.68 ± 0.20	4.21 ± 0.44	
G318.95-0.20	23.31 ± 1.13	−34.32 ± 0.04	3.38 ± 0.09	18.94 ± 1.14	3.72	0.22	3.57 ± 0.13	−34.53 ± 0.05	2.72 ± 0.10	
	6.26 ± 0.59	−31.33 ± 0.01	6.73 ± 0.04							w
G323.74-0.26	24.79 ± 1.13	−49.42 ± 0.06	4.02 ± 0.12	14.16 ± 1.26	3.71	0.33	2.56 ± 0.11	−49.65 ± 0.05	2.61 ± 0.13	
	7.64 ± 0.59	−48.52 ± 0.01	15.47 ± 0.04							w
G331.28-0.19	13.26 ± 0.71	−89.44 ± 0.05	4.44 ± 0.20	6.38 ± 1.30	3.84	0.78	2.39 ± 0.10	−88.11 ± 0.08	4.02 ± 0.20	
	11.29 ± 0.59	−89.34 ± 0.01	18.51 ± 0.04							w
G332.73-0.62	12.30 ± 0.29	−50.15 ± 0.03	3.55 ± 0.09	13.29 ± 1.30	4.01	0.39	0.72 ± 0.09	−50.20 ± 0.09	1.46 ± 0.20	
	4.14 ± 0.59	−56.21 ± 0.01	5.56 ± 0.04							b

[α] Gaussian fits to HCO^+ lines constrained by the sides of the line only. Any absorption dips were masked from the fitting routine.

[β] Integrated area under the line measured by summing the channels between suitable velocity limits.

[γ] 'w' denotes a fit to a high-velocity linewing while 'b' denotes a fit to a blended spectral line, assumed not associated with the source.

Table D.3: CH_3OH line parameters from Gaussian fits.

Source	V_{LSR} [α]	δV	T_{MB} dv, $J_{(k,k')} \rightarrow J'_{(k,k')}$, (K km s^{-1})			
	(km s^{-1})	(km s^{-1})	$2_{(-1,2)}\rightarrow1_{(-1,1)}$ E	$2_{(0,2)}\rightarrow1_{(0,1)}$ A+	$2_{(0,2)}\rightarrow1_{(0,1)}$ E	$2_{(1,1)}\rightarrow1_{(1,0)}$ E
G0.50+0.19	−6.12	3.76	1.31 ± 0.08	1.81 ± 0.08	0.46 ± 0.07	–
G0.55−0.85	17.23	5.40	12.11 ± 0.21	14.84 ± 0.21	5.77 ± 0.20	2.94 ± 0.20
G0.84+0.18	5.88	4.02	0.67 ± 0.10	1.04 ± 0.10	0.21 ± 0.09	–
G1.15−0.12	−17.02	4.18	1.80 ± 0.06	2.52 ± 0.06	0.46 ± 0.06	–
G2.54+0.20	9.97	2.88	1.46 ± 0.09	1.72 ± 0.09	0.21 ± 0.08	–
G5.89−0.39	9.32	4.62	3.48 ± 0.08	4.42 ± 0.08	1.57 ± 0.08	0.92 ± 0.08
G5.90−0.43	7.72	4.06	4.61 ± 0.13	5.98 ± 0.13	2.55 ± 0.13	0.77 ± 0.13
G5.90−0.44	9.48	3.86	2.12 ± 0.05	3.26 ± 0.05	0.70 ± 0.05	0.39 ± 0.04
G8.14+0.23	18.37	3.34	0.94 ± 0.10	1.23 ± 0.10	0.16 ± 0.09	–
G8.67−0.36	34.88	5.51	14.83 ± 0.28	17.39 ± 0.28	7.17 ± 0.27	2.19 ± 0.26
G8.68−0.37	37.66	6.04	15.64 ± 0.30	20.11 ± 0.31	6.15 ± 0.27	1.48 ± 0.27
G9.62+0.19	4.00	6.34	7.85 ± 0.31	11.21 ± 0.32	4.05 ± 0.28	2.97 ± 0.27
G9.99−0.03	49.23	5.12	1.37 ± 0.09	1.43 ± 0.09	0.41 ± 0.09	–
G10.29−0.13	13.82	3.70	5.56 ± 0.17	7.11 ± 0.18	1.49 ± 0.17	0.93 ± 0.17
G10.32−0.16	11.76	4.40	1.84 ± 0.16	2.49 ± 0.17	0.88 ± 0.15	0.33 ± 0.15
G10.34−0.14	11.97	4.57	5.31 ± 0.22	6.57 ± 0.23	1.26 ± 0.21	0.62 ± 0.21
G10.44−0.02	74.08	4.73	0.61 ± 0.14	1.26 ± 0.15	0.40 ± 0.15	–
G10.47+0.03	66.93	8.22	14.66 ± 0.18	14.75 ± 0.16	8.04 ± 0.10	5.43 ± 0.10
G10.48+0.03	65.78	6.16	8.55 ± 0.10	9.90 ± 0.10	2.88 ± 0.09	1.25 ± 0.09
G10.63−0.33	−3.78	3.01	2.98 ± 0.10	3.74 ± 0.10	0.63 ± 0.09	–
G10.63−0.38	−3.70	7.40	9.52 ± 0.28	13.78 ± 0.26	5.43 ± 0.19	3.31 ± 0.18
G11.50−1.49	10.50	3.42	1.11 ± 0.07	1.55 ± 0.08	0.51 ± 0.07	–

CH_3OH line parameters from Gaussian fits – *continued*.

Source	V_{LSR} [α]	δV	T_{MB} dv, $J_{(k,k')} \rightarrow J'_{(k,k')}$, (K km s^{-1})			
	(km s^{-1})	(km s^{-1})	$2_{(-1,2)}\rightarrow1_{(-1,1)}$ E	$2_{(0,2)}\rightarrow1_{(0,1)}$ A+	$2_{(0,2)}\rightarrow1_{(0,1)}$ E	$2_{(1,1)}\rightarrow1_{(1,0)}$ E
G11.94−0.15	42.18	4.98	2.56 ± 0.16	3.48 ± 0.16	0.65 ± 0.15	–
G11.94−0.62	38.33	3.46	4.67 ± 0.12	6.17 ± 0.12	1.33 ± 0.11	0.88 ± 0.11
G11.99−0.27	59.32	3.76	0.84 ± 0.10	0.83 ± 0.10	0.19 ± 0.09	–
G12.03−0.03	111.00	3.59	0.80 ± 0.13	1.01 ± 0.13	0.21 ± 0.12	–
G12.18−0.12	26.02	4.73	0.70 ± 0.20	1.17 ± 0.20	0.28 ± 0.16	–
G12.21−0.09	24.26	5.40	2.29 ± 0.07	2.81 ± 0.08	0.76 ± 0.07	0.39 ± 0.07
G12.68−0.18	55.60	4.11	4.02 ± 0.13	4.48 ± 0.14	1.10 ± 0.13	0.42 ± 0.12
G12.72−0.22	34.38	5.07	0.84 ± 0.09	1.51 ± 0.10	0.11 ± 0.08	–
G12.89+0.49	33.32	3.50	1.39 ± 0.12	1.79 ± 0.13	0.26 ± 0.12	–
G12.91−0.26	36.84	5.30	12.00 ± 0.21	13.85 ± 0.21	4.26 ± 0.20	2.15 ± 0.20
G14.60+0.02	26.53	4.96	3.42 ± 0.11	4.34 ± 0.11	0.43 ± 0.10	–
G14.99−0.70	17.55	6.48	3.52 ± 0.13	5.41 ± 0.13	1.42 ± 0.10	–
G15.03−0.68	18.96	4.43	2.94 ± 0.10	4.09 ± 0.10	1.44 ± 0.10	0.60 ± 0.10
G16.59−0.05	59.68	3.16	2.59 ± 0.08	3.11 ± 0.08	0.87 ± 0.08	0.46 ± 0.07
G16.86−2.16	18.18	4.94	8.41 ± 0.09	10.52 ± 0.09	2.80 ± 0.09	0.65 ± 0.09
G19.36−0.03	26.57	3.65	4.88 ± 0.11	6.16 ± 0.12	1.22 ± 0.11	–
G19.47+0.17	19.83	6.35	5.93 ± 0.12	8.71 ± 0.12	3.19 ± 0.10	1.59 ± 0.10
G19.49+0.15	23.10	3.28	0.62 ± 0.07	0.79 ± 0.08	0.07 ± 0.07	–
G19.61−0.13	58.49	5.43	2.17 ± 0.07	2.91 ± 0.07	0.39 ± 0.06	0.11 ± 0.06
G19.70−0.27	42.47	4.68	1.17 ± 0.07	1.47 ± 0.07	0.52 ± 0.07	–
G21.88+0.01	23.22	5.89	1.24 ± 0.08	1.21 ± 0.09	0.40 ± 0.07	–
G22.36+0.07	84.20	3.62	1.48 ± 0.10	1.65 ± 0.11	0.21 ± 0.10	–

CH_3OH line parameters from Gaussian fits – *continued*.

Source	V_{LSR} [α]	δV	T_{MB} dv, $J_{(k,k')} \rightarrow J'_{(k,k')}$, (K km s^{-1})			
	(km s^{-1})	(km s^{-1})	$2_{(-1,2)}\rightarrow1_{(-1,1)}$ E	$2_{(0,2)}\rightarrow1_{(0,1)}$ A+	$2_{(0,2)}\rightarrow1_{(0,1)}$ E	$2_{(1,1)}\rightarrow1_{(1,0)}$ E
G23.26−0.24	61.07	3.25	1.20 ± 0.09	1.34 ± 0.09	0.26 ± 0.08	–
G23.44−0.18	101.40	7.45	18.11 ± 0.45	21.71 ± 0.45	8.49 ± 0.34	3.41 ± 0.33
G23.71−0.20	69.20	4.02	0.70 ± 0.07	0.97 ± 0.07	–	–
G24.79+0.08	110.00	4.61	6.78 ± 0.09	8.30 ± 0.09	2.80 ± 0.09	1.60 ± 0.09
G24.85+0.09	109.21	3.63	0.29 ± 0.05	0.42 ± 0.05	–	–
G25.65+1.05	42.96	5.54	8.22 ± 0.16	10.11 ± 0.16	4.77 ± 0.16	0.84 ± 0.15
G25.71+0.04	98.15	3.08	1.18 ± 0.05	1.52 ± 0.05	0.23 ± 0.04	–
G25.83−0.18	94.01	3.64	2.26 ± 0.14	3.12 ± 0.15	0.86 ± 0.14	0.39 ± 0.14
G28.15+0.00	98.44	3.62	1.03 ± 0.11	1.61 ± 0.12	0.23 ± 0.11	–
G28.20−0.05	95.09	10.36	6.45 ± 0.43	7.65 ± 0.43	1.39 ± 0.19	0.98 ± 0.14
G28.28−0.36	48.47	3.43	1.67 ± 0.09	2.26 ± 0.10	0.27 ± 0.09	–
G28.31−0.39	86.80	5.82	0.94 ± 0.22	1.49 ± 0.27	0.56 ± 0.19	–
G28.83−0.25	86.75	3.92	2.51 ± 0.24	3.20 ± 0.25	0.51 ± 0.23	–
G29.87−0.04	101.48	3.12	1.01 ± 0.09	1.34 ± 0.10	0.29 ± 0.08	0.34 ± 0.08
G29.96−0.02	97.53	3.67	2.36 ± 0.15	3.50 ± 0.15	0.83 ± 0.14	0.93 ± 0.14
G30.59−0.04	41.56	4.40	2.02 ± 0.12	2.44 ± 0.13	0.63 ± 0.12	–
G30.71−0.06	91.48	5.47	13.51 ± 0.12	16.28 ± 0.12	4.70 ± 0.11	1.79 ± 0.11
G30.76−0.05	93.40	8.52	1.23 ± 0.22	1.62 ± 0.20	0.48 ± 0.10	–
G30.79+0.20	81.70	4.07	4.47 ± 0.14	5.82 ± 0.14	1.44 ± 0.13	–
G30.82−0.05	96.72	4.54	23.86 ± 0.28	11.32 ± 0.29	10.20 ± 0.15	4.26 ± 0.09
G30.82+0.28	97.66	3.84	0.91 ± 0.13	1.17 ± 0.13	–	–
G30.90+0.16	105.26	4.75	2.99 ± 0.12	3.65 ± 0.12	0.39 ± 0.11	–

CH_3OH line parameters from Gaussian fits – *continued*.

Source	V_{LSR} [α]	δV	T_{MB} dv, $J_{(k,k')} \rightarrow J'_{(k,k')}$, (K km s^{-1})			
	(km s^{-1})	(km s^{-1})	$2_{(-1,2)}\rightarrow1_{(-1,1)}$ E	$2_{(0,2)}\rightarrow1_{(0,1)}$ A+	$2_{(0,2)}\rightarrow1_{(0,1)}$ E	$2_{(1,1)}\rightarrow1_{(1,0)}$ E
G31.28+0.06	108.78	4.83	7.08 ± 0.08	9.07 ± 0.08	3.37 ± 0.08	1.27 ± 0.08
G31.41+0.31	97.14	5.11	4.32 ± 0.09	4.97 ± 0.09	1.57 ± 0.09	1.41 ± 0.09
G316.81−0.06	−38.20	4.40	1.00 ± 0.09	1.36 ± 0.10	0.12 ± 0.09	–
G318.95−0.20	−34.37	4.82	3.77 ± 0.09	3.61 ± 0.09	0.96 ± 0.09	–
G323.74−0.26	−49.74	3.62	3.21 ± 0.09	4.05 ± 0.09	1.15 ± 0.08	0.55 ± 0.08
G331.28−0.19	−88.05	4.90	3.46 ± 0.16	4.84 ± 0.17	1.70 ± 0.16	0.76 ± 0.16
G332.73−0.62	−50.50	3.60	0.52 ± 0.06	0.82 ± 0.06	0.28 ± 0.06	0.19 ± 0.06

[α] Quoted V_{LSR} is referenced to the $J_{(k,k')} = 2_{(0,2)}\rightarrow1_{(0,1)}$ A+ component.

Table D.4: N_2H^+ line parameters from CLASS HFS and Gaussian fits.

Source	CLASS hyperfine-splitting model		Gaussian fits [β]					
			Group-1		Group-2		Group-3	
	V_{LSR} [α] ($km\,s^{-1}$)	δV ($km\,s^{-1}$)	$\int T_{MB}\,dv$ ($K\,km\,s^{-1}$)	δV ($km\,s^{-1}$)	$\int T_{MB}\,dv$ ($K\,km\,s^{-1}$)	δV ($km\,s^{-1}$)	$\int T_{MB}\,dv$ ($K\,km\,s^{-1}$)	δV ($km\,s^{-1}$)
G0.21+0.00	–	–	2.49 ± 0.17	5.29 ± 0.45	3.76 ± 0.19	4.78 ± 0.30	1.49 ± 0.13	3.57 ± 0.34
G0.32−0.20	18.42 ± 0.01	1.88 ± 0.03	2.21 ± 0.10	1.82 ± 0.10	10.10 ± 0.12	2.63 ± 0.04	5.59 ± 0.12	2.46 ± 0.06
G0.50+0.19	−5.87 ± 0.03	2.82 ± 0.06	1.32 ± 0.15	2.92 ± 0.36	6.63 ± 0.18	3.45 ± 0.11	2.29 ± 0.17	2.81 ± 0.26
G0.55−0.85	16.99 ± 0.08	3.43 ± 0.15	3.54 ± 0.33	3.57 ± 0.47	16.36 ± 0.26	4.45 ± 0.09	8.37 ± 0.23	3.54 ± 0.11
G0.84+0.18	5.78 ± 0.03	2.09 ± 0.07	0.35 ± 0.07	1.55 ± 0.28	2.75 ± 0.10	2.77 ± 0.10	1.83 ± 0.10	2.60 ± 0.16
G1.15−0.12	−16.86 ± 0.04	2.47 ± 0.07	1.84 ± 0.15	2.12 ± 0.22	9.39 ± 0.18	3.14 ± 0.07	5.31 ± 0.18	3.12 ± 0.12
G25.65+1.05	42.33 ± 0.03	2.97 ± 0.06	3.98 ± 0.17	3.22 ± 0.17	14.67 ± 0.20	3.58 ± 0.06	9.83 ± 0.21	3.81 ± 0.10
G5.89−0.39	8.76 ± 0.03	2.79 ± 0.05	4.04 ± 0.19	2.95 ± 0.18	20.13 ± 0.22	3.46 ± 0.04	11.53 ± 0.23	3.50 ± 0.09
G5.90−0.43	7.13 ± 0.01	3.14 ± 0.03	6.23 ± 0.12	3.18 ± 0.07	27.81 ± 0.15	4.01 ± 0.03	15.44 ± 0.14	3.54 ± 0.04
G5.90−0.44	9.74 ± 0.01	1.76 ± 0.02	3.18 ± 0.09	1.80 ± 0.06	11.99 ± 0.10	2.50 ± 0.02	7.02 ± 0.10	2.31 ± 0.04
G8.14+0.23	18.79 ± 0.03	3.21 ± 0.04	2.88 ± 0.17	3.65 ± 0.21	12.45 ± 0.22	3.90 ± 0.08	7.54 ± 0.23	4.04 ± 0.14
G8.67−0.36	34.85 ± 0.03	3.81 ± 0.05	9.52 ± 0.24	4.04 ± 0.12	23.53 ± 0.53	3.71 ± 0.07	21.71 ± 0.79	5.39 ± 0.24
G8.68−0.37	37.20 ± 0.02	4.12 ± 0.02	4.64 ± 0.11	4.22 ± 0.11	21.22 ± 0.18	5.44 ± 0.06	10.01 ± 0.16	4.07 ± 0.06
G9.62+0.19	4.06 ± 0.03	3.44 ± 0.06	3.15 ± 0.20	3.56 ± 0.26	13.56 ± 0.29	4.21 ± 0.11	7.61 ± 0.29	4.09 ± 0.18
G9.99−0.03	48.50 ± 0.05	2.38 ± 0.10	1.28 ± 0.13	2.47 ± 0.35	4.82 ± 0.14	3.13 ± 0.11	2.77 ± 0.14	2.94 ± 0.19
G10.29−0.13	13.95 ± 0.01	2.88 ± 0.02	4.72 ± 0.14	2.89 ± 0.10	22.71 ± 0.16	3.85 ± 0.03	11.34 ± 0.15	3.17 ± 0.04
G10.30−0.15	13.37 ± 0.02	3.50 ± 0.04	5.34 ± 0.15	4.89 ± 0.18	20.50 ± 0.15	4.42 ± 0.04	10.34 ± 0.13	3.64 ± 0.05
G10.32−0.16	12.06 ± 0.02	1.81 ± 0.04	2.80 ± 0.08	1.75 ± 0.06	11.84 ± 0.10	2.60 ± 0.03	6.84 ± 0.10	2.32 ± 0.04
G10.34−0.14	11.90 ± 0.02	2.44 ± 0.04	3.79 ± 0.11	2.32 ± 0.08	18.44 ± 0.13	3.22 ± 0.03	9.67 ± 0.13	2.93 ± 0.05
G10.44−0.02	75.11 ± 0.09	3.80 ± 0.19	2.33 ± 0.13	4.14 ± 0.28	5.86 ± 0.21	5.34 ± 0.24	2.82 ± 0.17	3.89 ± 0.25

N_2H^+ line parameters from CLASS HFS and Gaussian fits – *continued*.

	CLASS hyperfine-splitting model		Gaussian fits [β]					
			Group-1		Group-2		Group-3	
Source	V_{LSR} [α] ($km\,s^{-1}$)	δV ($km\,s^{-1}$)	$\int T_{MB}\,dv$ ($K\,km\,s^{-1}$)	δV ($km\,s^{-1}$)	$\int T_{MB}\,dv$ ($K\,km\,s^{-1}$)	δV ($km\,s^{-1}$)	$\int T_{MB}\,dv$ ($K\,km\,s^{-1}$)	δV ($km\,s^{-1}$)
G10.47+0.03	66.40 ± 0.07	4.79 ± 0.11	6.51 ± 0.19	4.58 ± 0.15	24.09 ± 1.06	5.57 ± 0.15	17.17 ± 1.04	6.33 ± 0.27
G10.48+0.03	65.42 ± 0.09	5.36 ± 0.16	8.09 ± 0.77	5.55 ± 0.55	19.61 ± 4.03	5.49 ± 0.59	20.01 ± 3.68	7.36 ± 0.86
G10.63−0.33	−4.20 ± 0.02	2.60 ± 0.03	3.55 ± 0.09	2.42 ± 0.07	15.90 ± 0.10	3.49 ± 0.03	7.98 ± 0.10	2.96 ± 0.04
G10.63−0.38	−2.58 ± 0.01	2.84 ± 0.03	3.01 ± 0.17	2.97 ± 0.21	15.25 ± 0.15	3.61 ± 0.05	7.08 ± 0.15	3.19 ± 0.09
G11.50−1.49	10.17 ± 0.03	1.52 ± 0.06	1.48 ± 0.10	1.73 ± 0.13	6.18 ± 0.11	2.25 ± 0.05	3.96 ± 0.11	2.06 ± 0.07
G11.94−0.15	42.00 ± 0.06	2.97 ± 0.10	2.19 ± 0.13	3.13 ± 0.26	8.06 ± 0.15	3.82 ± 0.09	4.12 ± 0.14	3.34 ± 0.14
G11.94−0.62	37.63 ± 0.03	3.64 ± 0.04	5.21 ± 0.12	3.49 ± 0.09	22.04 ± 0.22	4.34 ± 0.04	13.59 ± 0.23	4.76 ± 0.09
G11.99−0.27	60.16 ± 0.10	3.56 ± 0.19	0.97 ± 0.16	3.99 ± 0.83	2.44 ± 0.16	3.90 ± 0.30	1.55 ± 0.16	4.42 ± 0.53
G12.03−0.03	110.79 ± 0.05	2.73 ± 0.09	1.43 ± 0.16	5.37 ± 0.81	3.54 ± 0.12	3.48 ± 0.14	1.94 ± 0.11	3.04 ± 0.19
G12.18−0.12	26.32 ± 0.05	2.89 ± 0.09	0.85 ± 0.15	2.23 ± 0.59	4.69 ± 0.19	3.40 ± 0.17	3.26 ± 0.20	3.72 ± 0.29
G12.21−0.09	24.07 ± 0.05	3.41 ± 0.09	1.46 ± 0.17	4.50 ± 0.65	5.29 ± 0.22	3.79 ± 0.18	4.24 ± 0.24	4.64 ± 0.34
G12.68−0.18	55.53 ± 0.03	2.57 ± 0.08	3.84 ± 0.16	3.24 ± 0.19	8.94 ± 0.18	4.07 ± 0.10	5.73 ± 0.16	3.27 ± 0.10
G12.72−0.22	33.93 ± 0.07	2.88 ± 0.12	0.95 ± 0.12	3.13 ± 0.44	3.67 ± 0.14	3.25 ± 0.13	2.89 ± 0.15	4.09 ± 0.26
G12.89+0.49	32.56 ± 0.07	3.00 ± 0.12	2.68 ± 0.22	3.35 ± 0.27	10.14 ± 0.29	3.30 ± 0.10	7.23 ± 0.34	4.74 ± 0.26
G12.91−0.26	36.91 ± 0.01	3.28 ± 0.02	7.87 ± 0.17	3.94 ± 0.11	31.36 ± 0.20	4.18 ± 0.03	17.56 ± 0.19	3.63 ± 0.05
G14.60+0.02	26.13 ± 0.04	3.64 ± 0.07	3.00 ± 0.19	4.05 ± 0.34	13.21 ± 0.25	4.57 ± 0.10	7.13 ± 0.23	4.10 ± 0.14
G14.99−0.70	17.70 ± 0.06	3.10 ± 0.10	2.98 ± 0.10	3.53 ± 0.13	10.64 ± 0.12	3.64 ± 0.05	7.58 ± 0.13	4.12 ± 0.08
G15.03−0.68	19.02 ± 0.06	2.86 ± 0.10	2.00 ± 0.17	3.09 ± 0.30	8.21 ± 0.20	3.43 ± 0.10	4.83 ± 0.20	3.75 ± 0.19
G15.03−0.71	19.07 ± 0.13	3.37 ± 0.23	0.25 ± 0.09	3.32 ± 1.12	1.40 ± 0.13	3.53 ± 0.36	1.23 ± 0.14	4.68 ± 0.66
G16.59−0.05	59.57 ± 0.06	2.66 ± 0.12	2.88 ± 0.31	3.50 ± 0.41	11.55 ± 0.32	3.40 ± 0.11	5.71 ± 0.32	3.08 ± 0.21

N_2H^+ line parameters from CLASS HFS and Gaussian fits – *continued*.

Source	CLASS hyperfine-splitting model		Gaussian fits [β]					
			Group-1		Group-2		Group-3	
	V_{LSR} [α] ($km\,s^{-1}$)	δV ($km\,s^{-1}$)	$\int T_{MB}\,dv$ ($K\,km\,s^{-1}$)	δV ($km\,s^{-1}$)	$\int T_{MB}\,dv$ ($K\,km\,s^{-1}$)	δV ($km\,s^{-1}$)	$\int T_{MB}\,dv$ ($K\,km\,s^{-1}$)	δV ($km\,s^{-1}$)
G16.86−2.16	17.48 ± 0.06	3.19 ± 0.10	3.32 ± 0.12	3.35 ± 0.15	9.55 ± 0.21	2.97 ± 0.06	10.64 ± 0.24	5.52 ± 0.16
G19.36−0.03	26.14 ± 0.03	1.97 ± 0.06	2.16 ± 0.12	2.09 ± 0.12	8.39 ± 0.14	2.77 ± 0.05	4.75 ± 0.13	2.39 ± 0.08
G19.47+0.17	19.52 ± 0.05	5.28 ± 0.08	3.75 ± 0.25	5.01 ± 0.31	16.92 ± 0.80	7.06 ± 0.35	5.84 ± 0.67	5.01 ± 0.37
G19.49+0.15	22.90 ± 0.04	2.21 ± 0.08	0.92 ± 0.13	2.69 ± 0.43	3.60 ± 0.13	3.05 ± 0.12	2.20 ± 0.13	2.62 ± 0.18
G19.61−0.13	56.88 ± 0.14	3.86 ± 0.19	0.88 ± 0.30	2.31 ± 0.97	6.04 ± 2.03	4.03 ± 0.62	5.50 ± 2.11	5.90 ± 1.76
G19.70−0.27	42.32 ± 0.10	2.80 ± 0.18	1.80 ± 0.39	2.96 ± 0.69	6.30 ± 0.46	3.41 ± 0.30	3.34 ± 0.45	3.68 ± 0.52
G21.88+0.01	23.10 ± 0.11	3.06 ± 0.20	0.78 ± 0.16	3.50 ± 0.97	2.47 ± 0.16	4.01 ± 0.31	1.07 ± 0.14	3.47 ± 0.53
G22.36+0.07	84.33 ± 0.04	2.20 ± 0.08	2.52 ± 0.10	2.02 ± 0.10	10.44 ± 0.13	2.96 ± 0.04	5.89 ± 0.12	2.79 ± 0.07
G23.26−0.24	61.05 ± 0.04	2.19 ± 0.07	1.56 ± 0.13	1.82 ± 0.18	9.44 ± 0.16	2.97 ± 0.06	4.77 ± 0.15	2.75 ± 0.10
G23.44−0.18	100.86 ± 0.08	4.37 ± 0.17	4.13 ± 0.16	3.23 ± 0.14	19.41 ± 0.39	6.52 ± 0.15	7.82 ± 0.34	4.03 ± 0.14
G23.71−0.20	69.06 ± 0.04	2.80 ± 0.07	1.25 ± 0.09	2.39 ± 0.22	5.43 ± 0.12	3.50 ± 0.09	3.23 ± 0.12	3.55 ± 0.16
G24.79+0.08	110.12 ± 0.03	3.49 ± 0.04	6.26 ± 0.14	3.26 ± 0.08	24.55 ± 0.20	4.74 ± 0.05	11.56 ± 0.18	3.52 ± 0.06
G2.54+0.20	9.70 ± 0.02	2.16 ± 0.06	1.52 ± 0.07	1.82 ± 0.10	6.45 ± 0.09	3.02 ± 0.05	3.79 ± 0.09	2.67 ± 0.08
G25.71+0.04	98.39 ± 0.02	2.47 ± 0.04	1.24 ± 0.08	2.01 ± 0.17	7.22 ± 0.10	3.20 ± 0.05	3.42 ± 0.10	3.11 ± 0.10
G25.83−0.18	93.01 ± 0.04	2.75 ± 0.08	1.89 ± 0.08	2.96 ± 0.15	7.30 ± 0.10	3.37 ± 0.06	4.45 ± 0.10	3.54 ± 0.10
G28.15+0.00	98.61 ± 0.03	2.14 ± 0.07	0.91 ± 0.08	2.11 ± 0.21	4.84 ± 0.09	2.78 ± 0.06	3.06 ± 0.10	2.86 ± 0.10
G28.20−0.05	95.96 ± 0.04	3.53 ± 0.07	3.34 ± 0.15	3.28 ± 0.18	14.02 ± 0.25	4.33 ± 0.09	8.48 ± 0.26	4.37 ± 0.15
G28.28−0.36	49.27 ± 0.03	2.48 ± 0.07	2.19 ± 0.12	2.17 ± 0.14	8.17 ± 0.14	3.31 ± 0.06	4.44 ± 0.12	2.82 ± 0.08
G28.31−0.39	85.17 ± 0.06	2.59 ± 0.11	0.61 ± 0.10	2.28 ± 0.45	2.86 ± 0.12	3.48 ± 0.17	1.54 ± 0.11	3.01 ± 0.24
G28.83−0.25	86.87 ± 0.04	2.97 ± 0.07	2.97 ± 0.12	2.73 ± 0.14	13.58 ± 0.16	3.87 ± 0.05	7.77 ± 0.14	3.29 ± 0.07

N_2H^+ line parameters from CLASS HFS and Gaussian fits – *continued*.

	CLASS hyperfine-splitting model		Gaussian fits [β]					
			Group-1		Group-2		Group-3	
Source	V_{LSR} [α] ($km\,s^{-1}$)	δV ($km\,s^{-1}$)	$\int T_{MB}\,dv$ ($K\,km\,s^{-1}$)	δV ($km\,s^{-1}$)	$\int T_{MB}\,dv$ ($K\,km\,s^{-1}$)	δV ($km\,s^{-1}$)	$\int T_{MB}\,dv$ ($K\,km\,s^{-1}$)	δV ($km\,s^{-1}$)
G29.87−0.04	101.02 ± 0.05	2.79 ± 0.08	1.81 ± 0.15	3.76 ± 0.36	6.44 ± 0.15	3.45 ± 0.09	3.59 ± 0.15	3.49 ± 0.17
G29.96−0.02	97.27 ± 0.03	2.70 ± 0.06	1.65 ± 0.47	3.94 ± 1.67	6.31 ± 0.39	3.22 ± 0.24	3.92 ± 0.42	3.61 ± 0.49
G29.98−0.04	101.53 ± 0.03	3.05 ± 0.05	4.73 ± 0.59	4.50 ± 0.69	10.53 ± 0.59	3.73 ± 0.26	6.03 ± 0.54	3.34 ± 0.36
G30.59−0.04	41.26 ± 0.03	3.28 ± 0.06	1.54 ± 0.11	3.16 ± 0.24	6.88 ± 0.16	4.16 ± 0.11	4.37 ± 0.16	3.86 ± 0.17
G30.71−0.06	91.91 ± 0.02	4.68 ± 0.04	10.81 ± 0.17	5.04 ± 0.10	37.12 ± 0.26	6.08 ± 0.05	13.00 ± 0.20	4.00 ± 0.05
G30.76−0.05	93.63 ± 0.13	4.99 ± 0.19	0.68 ± 0.25	6.80 ± 2.62	4.15 ± 0.32	7.07 ± 0.61	1.02 ± 0.15	3.19 ± 0.36
G30.78+0.23	41.90 ± 0.12	1.94 ± 0.23	0.32 ± 0.10	3.85 ± 1.57	0.73 ± 0.07	2.21 ± 0.24	0.47 ± 0.08	3.15 ± 0.57
G30.79+0.20	81.53 ± 0.03	2.69 ± 0.06	1.90 ± 0.08	2.43 ± 0.13	7.97 ± 0.10	3.61 ± 0.05	4.18 ± 0.09	3.04 ± 0.07
G30.82−0.05	96.14 ± 0.05	4.40 ± 0.09	13.02 ± 0.31	4.91 ± 0.14	32.25 ± 0.60	4.66 ± 0.09	16.45 ± 0.59	4.21 ± 0.15
G30.82+0.28	97.47 ± 0.05	2.14 ± 0.10	0.79 ± 0.14	1.93 ± 0.37	4.59 ± 0.17	2.86 ± 0.13	2.29 ± 0.18	2.86 ± 0.28
G30.90+0.16	105.55 ± 0.03	3.07 ± 0.05	2.40 ± 0.09	2.53 ± 0.11	12.10 ± 0.12	4.17 ± 0.05	6.01 ± 0.10	3.18 ± 0.06
G31.28+0.06	108.65 ± 0.02	3.38 ± 0.04	3.49 ± 0.14	3.42 ± 0.15	15.61 ± 0.20	4.15 ± 0.06	8.62 ± 0.21	4.16 ± 0.12
G31.41+0.31	97.30 ± 0.09	4.29 ± 0.15	3.53 ± 0.14	5.10 ± 0.26	4.76 ± 0.42	2.99 ± 0.16	10.24 ± 0.48	7.55 ± 0.35
G316.81−0.06	−38.73 ± 0.05	3.09 ± 0.09	4.94 ± 0.15	3.88 ± 0.15	17.53 ± 0.18	3.57 ± 0.04	11.39 ± 0.20	4.12 ± 0.09
G318.95−0.20	−34.95 ± 0.02	2.39 ± 0.03	3.35 ± 0.18	2.87 ± 0.18	14.44 ± 0.19	3.04 ± 0.04	8.13 ± 0.19	3.07 ± 0.09
G323.74−0.26	−49.96 ± 0.02	2.44 ± 0.03	2.96 ± 0.15	2.09 ± 0.12	14.02 ± 0.19	3.29 ± 0.05	7.84 ± 0.18	2.86 ± 0.07
G331.28−0.19	−88.88 ± 0.05	3.41 ± 0.07	1.43 ± 0.14	4.54 ± 0.49	6.35 ± 0.18	4.08 ± 0.13	3.33 ± 0.19	4.35 ± 0.28
G332.73−0.62	−50.21 ± 0.05	1.82 ± 0.12	0.48 ± 0.10	1.42 ± 0.33	2.38 ± 0.12	2.45 ± 0.15	1.11 ± 0.12	2.35 ± 0.27

[α] The V_{LSR} is referenced to the $F_1, F = 2,3 \rightarrow 1,2$, transition, i.e. the centre component of 'group-2'.

[β] The Gausian fits to the three groups are independant in all three variables; V_{LSR}, δV and T_{MB}.

Table D.5: HNC line parameters from Gaussian fits and direct measurement.

Source	Gaussian fits [α]			Integrated lines [β]			Code [γ]
	T_{MB} dv ($K\,km\,s^{-1}$)	V_{LSR} ($km\,s^{-1}$)	δV ($km\,s^{-1}$)	T_{MB} dv ($K\,km\,s^{-1}$)	Equivalent width ($km\,s^{-1}$)	Peak T_{MB} (K)	
G0.32−0.20	17.01 ± 0.17	18.73 ± 0.02	3.34 ± 0.04	17.08 ± 0.70	3.63	0.15	
G0.50+0.19	8.33 ± 0.20	−6.00 ± 0.00	4.72 ± 0.12	7.51 ± 0.71	4.15	0.39	
G0.55−0.85	52.64 ± 0.27	16.95 ± 0.01	5.03 ± 0.03	59.03 ± 1.23	5.83	0.12	
	3.41 ± 0.17	22.97 ± 0.02	3.08 ± 0.04				b
G0.84+0.18	4.25 ± 0.17	6.22 ± 0.07	3.41 ± 0.17	4.28 ± 0.90	3.44	0.72	
G1.15−0.12	5.34 ± 0.09	−16.59 ± 0.03	3.23 ± 0.06	6.60 ± 0.49	3.89	0.29	
G2.54+0.20	10.82 ± 0.62	9.86 ± 0.05	2.56 ± 0.12	19.45 ± 1.09	5.93	0.33	
	15.71 ± 0.17	11.30 ± 0.02	27.87 ± 0.04				w
G5.89−0.39	34.98 ± 1.36	9.06 ± 0.02	3.85 ± 0.08	52.53 ± 2.17	5.44	0.23	
	17.24 ± 0.17	9.41 ± 0.02	12.02 ± 0.04				w
G5.90−0.43	27.82 ± 0.11	7.43 ± 0.01	4.19 ± 0.02	28.57 ± 0.55	4.46	0.09	
G5.90−0.44	11.89 ± 0.29	9.07 ± 0.05	4.48 ± 0.14	13.46 ± 1.40	5.14	0.53	
G6.61−0.08	2.40 ± 0.28	5.31 ± 0.16	6.42 ± 0.43	9.83 ± 0.73	15.99	1.19	
	7.59 ± 0.17	−3.59 ± 0.02	16.07 ± 0.04				b
G8.14+0.23	15.45 ± 0.53	19.31 ± 0.07	4.41 ± 0.12	12.09 ± 0.97	4.29	0.34	
G8.67−0.36	24.52 ± 1.93	34.20 ± 0.07	3.82 ± 0.17	27.73 ± 1.11	4.98	0.20	
	11.67 ± 0.17	36.19 ± 0.02	15.35 ± 0.04				w
	1.88 ± 0.20	39.74 ± 0.00	1.82 ± 0.12				b
G8.68−0.37	56.10 ± 1.29	36.97 ± 0.03	6.00 ± 0.06	28.08 ± 1.17	6.12	0.26	
G9.62+0.19	23.53 ± 0.55	4.25 ± 0.03	5.25 ± 0.07	20.75 ± 0.42	4.92	0.10	
	10.84 ± 0.17	4.59 ± 0.02	15.05 ± 0.04				w

HNC line parameters from Gaussian fits and direct measurement – *continued*.

Source	Gaussian fits [α]			Integrated lines [β]			Code [γ]
	T_{MB} dv ($K\,km\,s^{-1}$)	V_{LSR} ($km\,s^{-1}$)	δV ($km\,s^{-1}$)	T_{MB} dv ($K\,km\,s^{-1}$)	Equivalent width ($km\,s^{-1}$)	Peak T_{MB} (K)	
G9.99−0.03	5.95 ± 0.55	48.98 ± 0.20	4.50 ± 0.50	6.51 ± 1.43	5.33	1.17	
G10.29−0.13	9.22 ± 0.14	12.90 ± 0.04	5.37 ± 0.09	9.09 ± 0.66	5.63	0.41	
G10.30−0.15	10.69 ± 0.42	13.15 ± 0.00	6.94 ± 0.17	12.39 ± 0.85	7.81	0.54	
	2.31 ± 0.17	13.15 ± 0.02	23.95 ± 0.04				w
G10.32−0.16	6.35 ± 0.20	12.54 ± 0.01	1.79 ± 0.04	12.75 ± 0.67	3.00	0.16	
	6.29 ± 0.17	13.09 ± 0.02	6.48 ± 0.04				w
G10.34−0.14	8.41 ± 0.73	12.66 ± 0.00	2.74 ± 0.11	18.21 ± 0.78	4.41	0.19	
	10.16 ± 0.17	12.66 ± 0.02	7.09 ± 0.04				w
G10.44−0.02	6.58 ± 0.40	74.79 ± 0.16	5.69 ± 0.28	4.94 ± 0.70	5.97	0.84	
	2.34 ± 0.17	65.86 ± 0.02	2.83 ± 0.04				b
G10.47+0.03	19.91 ± 0.85	66.91 ± 0.20	9.21 ± 0.45	19.43 ± 1.19	9.71	0.60	
G10.48+0.03	25.27 ± 0.43	66.04 ± 0.04	7.29 ± 0.13	22.87 ± 1.56	8.48	0.58	
G10.63−0.33	18.23 ± 0.22	−3.71 ± 0.02	4.15 ± 0.06	18.24 ± 1.08	4.56	0.27	
G10.63−0.38	72.36 ± 0.38	−3.60 ± 0.02	7.47 ± 0.05	74.20 ± 1.78	8.07	0.19	
G11.50−1.49	6.96 ± 0.13	10.34 ± 0.02	1.95 ± 0.04	7.53 ± 0.79	2.26	0.24	
G11.94−0.15	7.99 ± 0.15	42.94 ± 0.04	4.75 ± 0.11	8.04 ± 0.84	5.13	0.54	
G11.94−0.62	29.05 ± 0.29	37.99 ± 0.01	4.64 ± 0.03	14.51 ± 0.46	4.17	0.13	
G11.99−0.27	2.93 ± 0.13	59.84 ± 0.13	5.85 ± 0.30	2.89 ± 0.62	6.29	1.35	
G12.03−0.03	3.90 ± 0.13	111.13 ± 0.06	3.71 ± 0.16	3.86 ± 0.62	4.93	0.79	
G12.18−0.12	6.59 ± 0.16	26.21 ± 0.04	3.68 ± 0.11	7.67 ± 0.80	4.79	0.50	
G12.21−0.09	9.32 ± 0.17	24.22 ± 0.04	5.11 ± 0.11	8.56 ± 0.75	5.92	0.52	

HNC line parameters from Gaussian fits and direct measurement – *continued*.

Source	Gaussian fits [α]			Integrated lines [β]			Code [γ]
	T_{MB} dv ($K\,km\,s^{-1}$)	V_{LSR} ($km\,s^{-1}$)	δV ($km\,s^{-1}$)	T_{MB} dv ($K\,km\,s^{-1}$)	Equivalent width ($km\,s^{-1}$)	Peak T_{MB} (K)	
G12.68−0.18	5.02 ± 0.10	58.06 ± 0.03	3.05 ± 0.07	5.59 ± 0.51	3.47	0.32	
G12.72−0.22	11.62 ± 0.31	34.28 ± 0.04	3.84 ± 0.11	10.98 ± 0.91	4.57	0.38	
G12.89+0.49	16.23 ± 1.18	33.55 ± 0.04	3.67 ± 0.12	7.86 ± 0.70	4.46	0.40	
G12.91−0.26	19.02 ± 0.89	36.50 ± 0.06	5.88 ± 0.16	23.08 ± 1.07	6.55	0.30	
	12.48 ± 0.17	39.87 ± 0.02	14.38 ± 0.04				w
G14.60+0.02	15.15 ± 0.60	25.61 ± 0.06	6.35 ± 0.22	8.97 ± 1.29	7.38	1.06	
G14.99−0.70	38.62 ± 0.40	18.54 ± 0.03	5.39 ± 0.05	34.56 ± 1.56	5.80	0.26	
G15.03−0.68	61.32 ± 0.17	19.61 ± 0.01	5.05 ± 0.02	61.67 ± 0.86	5.46	0.08	
G15.03−0.71	6.88 ± 0.16	20.84 ± 0.06	4.92 ± 0.13	6.91 ± 1.01	5.49	0.80	
G16.59−0.05	17.98 ± 0.27	59.63 ± 0.02	3.42 ± 0.04	13.63 ± 0.75	3.47	0.19	
G16.86−2.16	23.05 ± 0.83	18.06 ± 0.04	3.92 ± 0.10	17.31 ± 1.29	4.61	0.34	
	5.36 ± 0.17	18.98 ± 0.02	16.07 ± 0.04				w
G19.36−0.03	8.85 ± 0.42	26.91 ± 0.03	2.69 ± 0.09	5.81 ± 0.61	3.66	0.38	
	2.87 ± 0.17	28.22 ± 0.02	13.77 ± 0.04				w
G19.47+0.17	13.17 ± 0.22	19.22 ± 0.04	6.38 ± 0.09	10.76 ± 0.68	6.88	0.43	
G19.49+0.15	6.68 ± 0.14	23.11 ± 0.04	4.15 ± 0.10	6.70 ± 0.62	4.66	0.43	
G19.61−0.13	6.92 ± 0.14	57.30 ± 0.05	5.28 ± 0.13	7.35 ± 0.70	5.97	0.57	
G19.70−0.27	3.31 ± 0.34	42.52 ± 0.12	3.72 ± 0.27	2.17 ± 0.60	4.19	1.15	
G21.88+0.01	4.38 ± 0.28	22.34 ± 0.12	5.40 ± 0.31	3.94 ± 0.87	7.01	1.55	
G22.36+0.07	8.49 ± 0.10	84.33 ± 0.02	3.54 ± 0.05	8.65 ± 0.56	3.92	0.25	
G23.26−0.24	7.91 ± 0.16	61.61 ± 0.03	2.82 ± 0.07	8.63 ± 0.52	3.23	0.19	

HNC line parameters from Gaussian fits and direct measurement – *continued*.

Source	Gaussian fits [α]			Integrated lines [β]			Code [γ]
	T_{MB} dv ($K\,km\,s^{-1}$)	V_{LSR} ($km\,s^{-1}$)	δV ($km\,s^{-1}$)	T_{MB} dv ($K\,km\,s^{-1}$)	Equivalent width ($km\,s^{-1}$)	Peak T_{MB} (K)	
G23.44−0.18	21.36 ± 1.65	101.76 ± 0.32	8.95 ± 0.41	17.27 ± 0.89	8.03	0.41	
G23.71−0.20	5.39 ± 0.15	68.73 ± 0.05	3.88 ± 0.13	5.45 ± 0.89	4.50	0.73	
G24.79+0.08	21.43 ± 0.88	111.18 ± 0.07	4.78 ± 0.11	24.50 ± 0.99	5.59	0.23	
	10.34 ± 0.17	111.23 ± 0.02	18.13 ± 0.04				w
G24.85+0.09	6.25 ± 0.23	109.17 ± 0.06	3.23 ± 0.13	6.22 ± 1.49	3.51	0.84	
G25.65+1.05	15.45 ± 0.19	43.02 ± 0.01	3.95 ± 0.05	22.11 ± 0.76	5.87	0.20	
	9.46 ± 0.17	40.63 ± 0.02	15.77 ± 0.04				w
G25.71+0.04	11.80 ± 0.36	98.70 ± 0.04	3.60 ± 0.08	9.67 ± 0.59	3.70	0.23	
G25.83−0.18	5.97 ± 0.30	92.79 ± 0.03	2.47 ± 0.09	11.44 ± 1.10	4.36	0.42	
	5.49 ± 0.17	93.56 ± 0.02	11.06 ± 0.04				w
G28.15+0.00	3.32 ± 0.12	99.62 ± 0.08	4.37 ± 0.20	3.69 ± 0.72	5.20	1.02	
G28.20−0.05	111.45 ± 1.44	96.26 ± 0.05	9.19 ± 0.12	98.09 ± 4.51	8.72	0.40	
G28.28−0.36	9.41 ± 0.25	48.85 ± 0.02	3.28 ± 0.07	6.89 ± 0.47	4.65	0.32	
G28.31−0.39	4.87 ± 0.10	85.70 ± 0.03	2.92 ± 0.07	5.29 ± 0.65	3.26	0.40	
G28.83−0.25	8.90 ± 0.39	86.94 ± 0.06	4.48 ± 0.19	7.77 ± 1.07	5.68	0.78	
G29.87−0.04	14.69 ± 0.22	100.88 ± 0.03	4.25 ± 0.07	15.72 ± 1.22	4.98	0.39	
G29.96−0.02	19.53 ± 0.18	97.12 ± 0.02	4.09 ± 0.03	19.69 ± 0.65	4.29	0.14	
G29.98−0.04	6.79 ± 0.55	102.31 ± 0.20	5.17 ± 0.40	12.34 ± 1.09	9.88	0.87	
	4.93 ± 0.17	95.61 ± 0.02	4.87 ± 0.04				b
G30.59−0.04	11.05 ± 0.18	42.26 ± 0.04	5.35 ± 0.11	11.97 ± 1.06	5.73	0.51	
G30.71−0.06	27.14 ± 0.46	92.14 ± 0.03	7.86 ± 0.08	13.10 ± 0.49	7.85	0.29	

HNC line parameters from Gaussian fits and direct measurement – *continued*.

Source	Gaussian fits [α]			Integrated lines [β]			Code [γ]
	T_{MB} dv ($K\,km\,s^{-1}$)	V_{LSR} ($km\,s^{-1}$)	δV ($km\,s^{-1}$)	T_{MB} dv ($K\,km\,s^{-1}$)	Equivalent width ($km\,s^{-1}$)	Peak T_{MB} (K)	
G30.76−0.05	19.33 ± 1.05	92.79 ± 0.10	8.76 ± 0.37	13.16 ± 1.00	10.87	0.83	
G30.78+0.23	1.95 ± 0.10	41.99 ± 0.08	3.13 ± 0.20	1.97 ± 0.57	3.37	0.97	
G30.79+0.20	7.72 ± 0.36	81.39 ± 0.07	5.35 ± 0.31	7.20 ± 0.99	7.17	0.98	
G30.82−0.05	45.65 ± 0.33	96.32 ± 0.03	8.16 ± 0.06	35.82 ± 0.99	7.33	0.20	
G30.82+0.28	6.11 ± 0.12	97.78 ± 0.03	2.76 ± 0.07	6.00 ± 0.77	3.04	0.39	
G30.90+0.16	13.65 ± 0.08	105.56 ± 0.01	4.70 ± 0.03	13.58 ± 0.49	5.30	0.19	
G31.28+0.06	29.33 ± 2.88	109.40 ± 0.00	4.11 ± 0.14	8.58 ± 0.81	4.61	0.44	
G31.41+0.31	34.71 ± 8.63	97.58 ± 0.05	5.07 ± 0.32	6.74 ± 0.99	7.06	1.04	
G316.81−0.06	18.68 ± 0.24	−39.09 ± 0.03	4.97 ± 0.06	17.49 ± 0.95	4.82	0.26	
G318.95−0.20	16.83 ± 0.12	−34.56 ± 0.01	3.48 ± 0.03	18.75 ± 0.86	4.23	0.19	
G323.74−0.26	13.92 ± 0.21	−49.28 ± 0.03	4.13 ± 0.08	14.87 ± 1.00	4.62	0.31	
G331.28−0.19	7.83 ± 1.39	−88.53 ± 0.10	3.87 ± 0.36	14.30 ± 0.99	5.53	0.38	
	8.31 ± 0.17	−88.49 ± 0.02	9.03 ± 0.04				w
G332.73−0.62	7.53 ± 0.22	−50.17 ± 0.04	3.06 ± 0.11	9.59 ± 1.30	4.02	0.55	
	1.89 ± 0.17	−55.95 ± 0.02	3.95 ± 0.04				b

[α] Gaussian fits to HNC lines constrained by the sides of the line only. Any absorption dips were masked from the fitting routine.

[β] Integrated area under the line measured by summing the channels between suitable velocity limits.

[γ] 'w' denotes a fit to a high-velocity linewing while 'b' denotes a fit to a blended spectral line, assumed not associated with the source.

Table D.6: ^{13}CO line parameters from Gaussian fits and direct measurement.

Source	Gaussian fits [α]			Integrated lines [β]			Code [γ]
	T_{MB} dv (K km s^{-1})	V_{LSR} (km s^{-1})	δV (km s^{-1})	T_{MB} dv (K km s^{-1})	Equivalent width (km s^{-1})	Peak T_{MB} (K)	
G0.32−0.20	92.78 ± 1.42	18.80 ± 0.03	3.52 ± 0.06	104.51 ± 3.73	4.25	0.15	
G0.50+0.19	37.66 ± 0.80	−5.33 ± 0.05	4.63 ± 0.12	37.09 ± 2.36	5.16	0.33	
G0.55−0.85	154.13 ± 3.24	16.79 ± 0.05	4.94 ± 0.09	190.88 ± 4.22	6.59	0.15	
	32.70 ± 1.42	21.08 ± 0.03	3.58 ± 0.06				b
G0.84+0.18	34.96 ± 0.81	5.81 ± 0.04	4.00 ± 0.11	38.47 ± 2.44	4.51	0.29	
G1.15−0.12	38.63 ± 0.89	−16.93 ± 0.05	4.24 ± 0.12	42.03 ± 2.32	4.58	0.25	
G2.54+0.20	31.85 ± 0.43	9.68 ± 0.01	2.88 ± 0.05	41.94 ± 2.71	4.75	0.31	
G5.89−0.39	96.59 ± 0.99	9.19 ± 0.01	3.55 ± 0.03	144.41 ± 6.71	5.11	0.24	
	62.47 ± 1.42	10.57 ± 0.03	16.26 ± 0.06				w
G5.90−0.43	97.97 ± 1.32	7.24 ± 0.03	4.24 ± 0.07	106.89 ± 3.44	5.04	0.16	
G5.90−0.44	80.10 ± 2.01	9.29 ± 0.04	3.70 ± 0.11	80.70 ± 2.82	3.92	0.14	
G6.61−0.08	31.35 ± 0.63	4.79 ± 0.04	4.22 ± 0.14	32.69 ± 2.67	4.94	0.40	
G8.14+0.23	62.83 ± 0.53	18.82 ± 0.02	4.38 ± 0.04	60.72 ± 3.15	4.88	0.25	
G8.67−0.36	57.90 ± 5.58	34.37 ± 0.05	3.53 ± 0.13	90.75 ± 4.25	5.70	0.27	
	41.93 ± 1.42	37.13 ± 0.03	6.37 ± 0.06				b
G8.68−0.37	111.63 ± 1.24	36.83 ± 0.03	5.99 ± 0.06	96.22 ± 3.56	6.73	0.25	
G9.62+0.19	80.76 ± 6.14	4.08 ± 0.03	5.06 ± 0.16	111.47 ± 4.10	6.68	0.25	
	47.60 ± 1.42	3.95 ± 0.03	10.42 ± 0.06				w
G9.99−0.03	31.51 ± 0.42	48.94 ± 0.03	3.91 ± 0.06	33.57 ± 2.28	4.46	0.30	
G10.29−0.13	73.09 ± 0.83	13.07 ± 0.03	5.34 ± 0.07	84.02 ± 3.77	6.57	0.29	

^{13}CO line parameters from Gaussian fits and direct measurement – *continued*.

Source	Gaussian fits [α]			Integrated lines [β]			Code [γ]
	T_{MB} dv ($K\,km\,s^{-1}$)	V_{LSR} ($km\,s^{-1}$)	δV ($km\,s^{-1}$)	T_{MB} dv ($K\,km\,s^{-1}$)	Equivalent width ($km\,s^{-1}$)	Peak T_{MB} (K)	
G10.30−0.15	36.70 ± 2.69	12.95 ± 0.06	3.90 ± 0.18	128.43 ± 4.18	8.74	0.28	
	85.65 ± 1.42	14.16 ± 0.03	13.12 ± 0.06				w
G10.32−0.16	58.18 ± 1.56	11.84 ± 0.06	4.73 ± 0.17	59.93 ± 2.49	4.81	0.20	
G10.34−0.14	67.04 ± 0.97	11.86 ± 0.02	3.90 ± 0.07	74.28 ± 2.85	4.73	0.18	
G10.44−0.02	38.64 ± 0.63	74.76 ± 0.04	5.81 ± 0.12	66.22 ± 3.81	10.68	0.61	
	10.54 ± 1.42	69.45 ± 0.03	2.21 ± 0.06				b
	19.75 ± 0.80	66.07 ± 0.05	3.06 ± 0.12				b
G10.47+0.03	121.94 ± 0.62	67.11 ± 0.02	7.71 ± 0.04	122.48 ± 4.05	8.31	0.28	
G10.48+0.03	80.04 ± 0.59	66.38 ± 0.03	7.24 ± 0.07	81.04 ± 3.66	8.36	0.38	
G10.63−0.33	91.25 ± 0.50	−4.11 ± 0.01	3.80 ± 0.02	91.27 ± 3.00	4.20	0.14	
G10.63−0.38	196.80 ± 0.82	−3.06 ± 0.01	6.42 ± 0.03	196.78 ± 3.77	7.03	0.14	
G11.50−1.49	36.66 ± 1.21	10.33 ± 0.01	2.47 ± 0.04	61.80 ± 1.83	3.50	0.10	
	26.08 ± 1.42	10.53 ± 0.03	6.12 ± 0.06				w
G11.94−0.15	38.46 ± 2.30	42.02 ± 0.11	4.44 ± 0.25	55.48 ± 2.96	6.54	0.35	
	12.92 ± 1.42	45.46 ± 0.03	2.89 ± 0.06				b
G11.94−0.62	78.81 ± 1.39	37.58 ± 0.02	4.91 ± 0.07	58.90 ± 3.12	6.31	0.33	
G11.99−0.27	30.17 ± 0.70	60.24 ± 0.05	4.44 ± 0.11	29.53 ± 2.34	5.22	0.41	
G12.03−0.03	43.34 ± 1.09	110.84 ± 0.04	3.81 ± 0.12	52.90 ± 3.20	4.94	0.30	
G12.18−0.12	44.67 ± 0.85	25.92 ± 0.04	4.96 ± 0.12	53.42 ± 4.03	6.60	0.50	
	5.18 ± 1.42	32.50 ± 0.03	2.65 ± 0.06				b
G12.21−0.09	56.58 ± 0.94	24.20 ± 0.04	4.92 ± 0.10	56.42 ± 3.20	5.37	0.30	

^{13}CO line parameters from Gaussian fits and direct measurement – *continued*.

Source	Gaussian fits [α]			Integrated lines [β]			Code [γ]
	T_{MB} dv (K km s^{-1})	V_{LSR} (km s^{-1})	δV (km s^{-1})	T_{MB} dv (K km s^{-1})	Equivalent width (km s^{-1})	Peak T_{MB} (K)	
G12.68−0.18	29.68 ± 1.22	57.79 ± 0.05	2.68 ± 0.10	70.22 ± 3.06	6.54	0.29	
	26.62 ± 1.42	50.82 ± 0.03	4.58 ± 0.06				b
	13.69 ± 0.80	54.72 ± 0.05	2.48 ± 0.12				b
G12.72−0.22	88.73 ± 2.16	34.70 ± 0.04	3.34 ± 0.10	96.98 ± 3.29	3.97	0.14	
G12.89+0.49	112.74 ± 6.21	33.03 ± 0.05	3.78 ± 0.09	63.74 ± 2.65	4.94	0.20	
G12.91−0.26	123.86 ± 1.31	35.89 ± 0.03	6.79 ± 0.08	110.62 ± 3.28	6.94	0.21	
G14.60+0.02	45.46 ± 2.63	26.01 ± 0.14	5.59 ± 0.51	45.18 ± 3.06	6.17	0.42	
G14.99−0.70	130.62 ± 1.52	18.81 ± 0.02	5.33 ± 0.06	110.18 ± 2.14	6.60	0.13	
G15.03−0.68	55.30 ± 2.62	19.77 ± 0.05	3.81 ± 0.07	99.53 ± 4.06	5.83	0.24	
	40.20 ± 1.42	21.06 ± 0.03	9.19 ± 0.06				w
	5.29 ± 0.80	23.92 ± 0.05	0.98 ± 0.12				b
G15.03−0.71	39.93 ± 0.96	20.83 ± 0.05	5.16 ± 0.17	37.68 ± 2.02	6.31	0.34	
G16.59−0.05	61.46 ± 0.96	59.27 ± 0.03	3.37 ± 0.06	60.82 ± 2.48	3.71	0.15	
G16.86−2.16	64.75 ± 0.54	17.59 ± 0.01	3.47 ± 0.04	69.71 ± 2.26	4.11	0.13	
G19.36−0.03	61.81 ± 0.81	26.45 ± 0.02	3.38 ± 0.07	60.04 ± 2.85	4.22	0.20	
G19.47+0.17	73.38 ± 1.57	19.64 ± 0.06	5.81 ± 0.15	76.53 ± 3.52	6.74	0.31	
G19.49+0.15	48.90 ± 0.94	22.98 ± 0.04	4.01 ± 0.10	51.53 ± 3.04	4.88	0.29	
G19.61−0.13	35.48 ± 0.91	57.01 ± 0.05	4.29 ± 0.14	38.14 ± 3.22	4.93	0.42	
G19.70−0.27	34.92 ± 0.90	42.07 ± 0.06	4.69 ± 0.15	34.60 ± 2.82	5.00	0.41	
G21.88+0.01	36.23 ± 0.60	22.34 ± 0.04	4.58 ± 0.08	35.90 ± 2.68	4.95	0.37	
G22.36+0.07	49.27 ± 0.82	84.21 ± 0.02	3.13 ± 0.07	58.71 ± 3.55	3.93	0.24	

^{13}CO line parameters from Gaussian fits and direct measurement – *continued*.

Source	Gaussian fits [α]			Integrated lines [β]			Code [γ]
	T_{MB} dv ($K\,km\,s^{-1}$)	V_{LSR} ($km\,s^{-1}$)	δV ($km\,s^{-1}$)	T_{MB} dv ($K\,km\,s^{-1}$)	Equivalent width ($km\,s^{-1}$)	Peak T_{MB} (K)	
G23.26−0.24	55.99 ± 5.42	62.11 ± 0.19	4.48 ± 0.38	44.14 ± 3.44	4.57	0.36	
G23.44−0.18	99.00 ± 6.92	100.92 ± 0.11	5.24 ± 0.41	149.75 ± 4.68	8.59	0.27	
	22.95 ± 1.42	95.81 ± 0.03	3.58 ± 0.06				b
	26.14 ± 0.80	107.03 ± 0.05	3.63 ± 0.12				b
G23.71−0.20	42.65 ± 2.14	68.70 ± 0.10	4.29 ± 0.26	48.89 ± 3.15	5.38	0.35	
G24.79+0.08	64.62 ± 0.23	110.56 ± 0.00	3.72 ± 0.02	129.56 ± 4.80	6.81	0.25	
	54.12 ± 1.42	106.39 ± 0.03	7.83 ± 0.06				w
G24.85+0.09	24.32 ± 0.44	109.22 ± 0.02	2.87 ± 0.06	25.35 ± 2.91	3.40	0.39	
G25.65+1.05	34.29 ± 1.87	42.67 ± 0.05	2.94 ± 0.11	79.69 ± 4.45	6.27	0.35	
	55.65 ± 1.42	44.37 ± 0.03	10.07 ± 0.06				w
G25.71+0.04	42.28 ± 0.75	98.61 ± 0.03	4.01 ± 0.09	48.61 ± 3.42	4.91	0.34	
G25.83−0.18	55.94 ± 2.67	93.53 ± 0.09	4.18 ± 0.25	54.80 ± 2.96	4.43	0.24	
G28.15+0.00	33.20 ± 1.52	98.34 ± 0.10	4.51 ± 0.25	36.92 ± 3.76	5.09	0.52	
G28.20−0.05	87.15 ± 0.65	96.20 ± 0.02	6.13 ± 0.07	91.28 ± 3.86	6.88	0.29	
G28.28−0.36	49.49 ± 0.58	48.42 ± 0.02	3.53 ± 0.06	53.15 ± 3.85	4.61	0.33	
G28.31−0.39	39.43 ± 1.47	85.85 ± 0.05	2.91 ± 0.10	63.77 ± 3.58	5.08	0.28	
	22.96 ± 1.42	82.47 ± 0.03	3.03 ± 0.06				b
G28.83−0.25	63.40 ± 0.81	87.07 ± 0.02	3.80 ± 0.07	62.74 ± 3.49	4.59	0.26	
	35.99 ± 1.42	95.55 ± 0.03	6.03 ± 0.06				b
G29.87−0.04	73.97 ± 0.20	100.90 ± 0.00	3.46 ± 0.01	123.64 ± 3.35	5.26	0.14	
	51.79 ± 1.42	99.06 ± 0.03	12.20 ± 0.06				w

^{13}CO line parameters from Gaussian fits and direct measurement – *continued*.

Source	Gaussian fits [α]			Integrated lines [β]			Code [γ]
	T_{MB} dv (K km s^{-1})	V_{LSR} (km s^{-1})	δV (km s^{-1})	T_{MB} dv (K km s^{-1})	Equivalent width (km s^{-1})	Peak T_{MB} (K)	
G29.96−0.02	83.11 ± 0.93	97.22 ± 0.02	4.52 ± 0.06	121.57 ± 4.54	6.83	0.26	
	26.08 ± 1.42	102.25 ± 0.03	3.41 ± 0.06				b
G29.98−0.04	76.53 ± 0.79	101.41 ± 0.02	4.15 ± 0.05	136.73 ± 5.11	8.02	0.30	
	46.66 ± 1.42	94.76 ± 0.03	4.47 ± 0.06				b
G30.59−0.04	61.72 ± 0.76	41.98 ± 0.03	5.18 ± 0.08	72.26 ± 4.96	6.41	0.44	
G30.71−0.06	132.02 ± 1.14	92.64 ± 0.01	7.35 ± 0.07	101.96 ± 3.31	10.28	0.33	
	9.95 ± 1.42	83.14 ± 0.03	2.98 ± 0.06				b
G30.76−0.05	115.49 ± 1.07	92.36 ± 0.04	8.87 ± 0.12	142.60 ± 5.32	12.82	0.48	
	16.33 ± 1.42	82.04 ± 0.03	2.72 ± 0.06				b
	18.32 ± 0.80	102.60 ± 0.05	4.19 ± 0.12				b
G30.78+0.23	19.22 ± 0.47	41.59 ± 0.04	2.96 ± 0.08	19.76 ± 3.40	3.31	0.57	
G30.79+0.20	39.04 ± 0.84	81.98 ± 0.05	5.49 ± 0.20	41.08 ± 3.74	6.54	0.59	
G30.82−0.05	111.01 ± 2.02	97.58 ± 0.07	8.49 ± 0.16	120.62 ± 5.09	10.16	0.43	
	12.62 ± 1.42	103.31 ± 0.03	2.86 ± 0.06				b
G30.82+0.28	31.11 ± 0.80	97.80 ± 0.04	3.73 ± 0.12	40.26 ± 4.16	4.94	0.51	
G30.90+0.16	54.63 ± 0.69	105.66 ± 0.03	4.03 ± 0.06	55.92 ± 3.53	4.27	0.27	
G31.28+0.06	65.91 ± 2.74	109.38 ± 0.09	4.42 ± 0.14	78.04 ± 4.33	8.34	0.46	
	24.47 ± 1.42	103.90 ± 0.03	4.65 ± 0.06				b
G31.41+0.31	89.04 ± 1.52	97.52 ± 0.03	6.25 ± 0.08	71.19 ± 3.55	8.04	0.40	
G316.81−0.06	104.04 ± 0.77	−38.34 ± 0.02	4.88 ± 0.04	107.15 ± 4.28	5.46	0.22	
G318.95−0.20	54.34 ± 0.38	−34.64 ± 0.01	3.76 ± 0.03	58.41 ± 3.17	4.29	0.23	

^{13}CO line parameters from Gaussian fits and direct measurement – *continued*.

Source	Gaussian fits [α]			Integrated lines [β]			Code [γ]
	T_{MB} dv ($K\,km\,s^{-1}$)	V_{LSR} ($km\,s^{-1}$)	δV ($km\,s^{-1}$)	T_{MB} dv ($K\,km\,s^{-1}$)	Equivalent width ($km\,s^{-1}$)	Peak T_{MB} (K)	
G323.74−0.26	40.78 ± 0.88	−48.93 ± 0.03	3.39 ± 0.09	50.24 ± 2.98	4.32	0.26	
G331.28−0.19	74.64 ± 1.13	−88.90 ± 0.04	6.00 ± 0.11	81.94 ± 2.68	7.20	0.23	
	8.24 ± 1.42	−82.90 ± 0.03	2.86 ± 0.06				b
G332.73−0.62	33.06 ± 0.72	−50.41 ± 0.03	3.07 ± 0.08	72.35 ± 3.84	6.46	0.34	
	36.80 ± 1.42	−56.07 ± 0.03	4.79 ± 0.06				b

[α] Gaussian fits to ^{13}CO lines constrained by the sides of the line only. Any absorption dips were masked from the fitting routine.

[β] Integrated area under the line measured by summing the channels between suitable velocity limits.

[γ] 'w' denotes a fit to a high-velocity linewing while 'b' denotes a fit to a blended spectral line, assumed not associated with the source.

Table D.7: HCN line parameters from direct measurement.

Source	T_{MB} dv ($K\,km\,s^{-1}$)	Equivalent width ($km\,s^{-1}$)	Peak T_{MB} (K)	RMS-noise (K)
G0.32−0.20	16.36 ± 1.30	2.32 ± 2.32	2.35	0.13
G0.50+0.19	8.00 ± 1.00	4.04 ± 4.04	0.66	0.10
G0.55−0.85	163.33 ± 2.37	3.80 ± 3.80	14.35	0.17
G0.84+0.18	6.94 ± 1.94	2.46 ± 2.46	0.94	0.18
G1.15−0.12	8.47 ± 1.91	3.52 ± 3.52	0.80	0.18
G2.54+0.20	3.60 ± 0.67	1.44 ± 1.44	0.83	0.07
G5.89−0.39	70.09 ± 1.49	2.52 ± 2.52	9.29	0.14
G5.90−0.43	53.90 ± 2.47	2.29 ± 2.29	7.85	0.22
G5.90−0.44	21.87 ± 1.15	2.35 ± 2.35	3.10	0.11
G6.54−0.11	5.49 ± 0.86	2.41 ± 2.41	0.76	0.09
G6.61−0.08	35.21 ± 3.04	7.72 ± 7.72	1.52	0.18
G8.14+0.23	19.95 ± 1.33	2.79 ± 2.79	2.39	0.12
G8.67−0.36	22.36 ± 1.36	2.23 ± 2.23	3.35	0.13
G8.68−0.37	26.20 ± 1.90	3.96 ± 3.96	2.21	0.16
G9.62+0.19	34.78 ± 0.74	4.19 ± 4.19	2.77	0.07
G9.99−0.03	7.26 ± 1.02	3.47 ± 3.47	0.70	0.10
G10.29−0.13	23.65 ± 2.10	3.41 ± 3.41	2.31	0.20
G10.30−0.15	64.75 ± 2.53	3.94 ± 3.94	5.48	0.19
G10.32−0.16	26.27 ± 1.67	2.05 ± 2.05	4.27	0.15
G10.34−0.14	21.40 ± 1.99	2.78 ± 2.78	2.57	0.19
G10.44−0.02	11.09 ± 2.32	4.85 ± 4.85	0.76	0.18
G10.47+0.03	74.27 ± 1.90	5.66 ± 5.66	4.38	0.14
G10.48+0.03	40.90 ± 1.54	6.05 ± 6.05	2.25	0.12
G10.63−0.33	43.70 ± 2.67	3.02 ± 3.02	4.82	0.24
G10.63−0.38	181.76 ± 3.40	4.71 ± 4.71	12.87	0.27
G11.50−1.49	21.10 ± 2.33	2.02 ± 2.02	3.48	0.24
G11.94−0.15	15.33 ± 1.64	3.24 ± 3.24	1.58	0.16
G11.94−0.62	14.31 ± 1.25	1.87 ± 1.87	2.54	0.11
G11.99−0.27	8.98 ± 1.54	3.85 ± 3.85	0.78	0.14
G12.03−0.03	15.46 ± 2.40	4.10 ± 4.10	1.26	0.20
G12.18−0.12	10.62 ± 2.03	3.01 ± 3.01	1.17	0.18
G12.21−0.09	8.24 ± 2.43	2.69 ± 2.69	1.02	0.23
G12.68−0.18	8.63 ± 3.21	1.95 ± 1.95	1.48	0.31
G12.72−0.22	22.72 ± 1.19	3.29 ± 3.29	2.30	0.11
G12.89+0.49	10.98 ± 1.25	2.18 ± 2.18	1.68	0.12
G12.91−0.26	32.60 ± 2.68	6.17 ± 6.17	1.76	0.18

HCN line parameters from direct measurement – *continued*.

Source	T_{MB} dv ($K\,km\,s^{-1}$)	Equivalent width ($km\,s^{-1}$)	Peak T_{MB} (K)	RMS-noise (K)
G14.60+0.02	5.61 ± 1.28	2.95 ± 2.95	0.63	0.11
G14.99−0.70	71.22 ± 1.19	3.20 ± 3.20	7.42	0.11
G15.03−0.68	117.99 ± 1.34	2.41 ± 2.41	16.30	0.12
G15.03−0.71	23.27 ± 1.11	2.93 ± 2.93	2.64	0.10
G16.59−0.05	23.21 ± 1.20	2.24 ± 2.24	3.45	0.10
G16.86−2.16	24.35 ± 1.43	2.69 ± 2.69	3.02	0.12
G19.36−0.03	22.93 ± 3.03	3.21 ± 3.21	2.38	0.23
G19.47+0.17	22.02 ± 3.18	5.13 ± 5.13	1.43	0.26
G19.49+0.15	17.43 ± 2.69	3.57 ± 3.57	1.63	0.24
G19.61−0.13	13.19 ± 1.09	2.93 ± 2.93	1.50	0.10
G19.70−0.27	2.12 ± 0.58	2.58 ± 2.58	0.27	0.06
G21.88+0.01	4.94 ± 0.64	3.42 ± 3.42	0.48	0.06
G22.36+0.07	16.01 ± 1.12	2.66 ± 2.66	2.01	0.10
G23.26−0.24	12.06 ± 3.03	1.79 ± 1.79	2.24	0.30
G23.44−0.18	42.51 ± 4.85	4.39 ± 4.39	3.23	0.28
G23.71−0.20	8.69 ± 2.85	3.35 ± 3.35	0.87	0.22
G24.79+0.08	33.81 ± 4.24	3.48 ± 3.48	3.24	0.29
G24.85+0.09	18.16 ± 3.15	2.72 ± 2.72	2.22	0.29
G25.65+1.05	59.43 ± 3.98	5.60 ± 5.60	3.54	0.26
G25.71+0.04	9.50 ± 0.66	3.26 ± 3.26	0.97	0.06
G25.83−0.18	16.97 ± 1.00	2.23 ± 2.23	2.54	0.10
G28.15+0.00	9.29 ± 2.86	4.74 ± 4.74	0.65	0.23
G28.20−0.05	19.09 ± 2.00	3.27 ± 3.27	1.95	0.22
G28.28−0.36	18.73 ± 3.85	2.84 ± 2.84	2.20	0.35
G28.31−0.39	6.35 ± 2.79	1.77 ± 1.77	1.19	0.26
G28.83−0.25	16.90 ± 1.27	3.37 ± 3.37	1.67	0.09
G29.87−0.04	39.72 ± 1.21	3.20 ± 3.20	4.13	0.10
G29.96−0.02	42.92 ± 1.93	2.77 ± 2.77	5.16	0.20
G29.98−0.04	32.03 ± 1.46	5.82 ± 5.82	1.84	0.11
G30.59−0.04	15.06 ± 2.75	3.80 ± 3.80	1.32	0.20
G30.71−0.06	16.46 ± 3.33	3.57 ± 3.57	1.54	0.25
G30.76−0.05	9.77 ± 2.30	2.22 ± 2.22	1.47	0.25
G30.78+0.23	6.83 ± 3.90	2.70 ± 2.70	0.84	0.38
G30.79+0.20	4.33 ± 3.75	1.73 ± 1.73	0.83	0.33
G30.82−0.05	30.14 ± 1.44	2.96 ± 2.96	3.40	0.14
G30.82+0.28	5.75 ± 0.96	2.11 ± 2.11	0.91	0.11
G30.90+0.16	11.76 ± 1.99	2.53 ± 2.53	1.55	0.22

HCN line parameters from direct measurement – *continued*.

Source	T_{MB} dv ($K\,km\,s^{-1}$)	Equivalent width ($km\,s^{-1}$)	Peak T_{MB} (K)	RMS-noise (K)
G31.28+0.06	10.52 ± 3.59	4.35 ± 4.35	0.81	0.31
G31.41+0.31	6.20 ± 1.49	3.39 ± 3.39	0.61	0.12
G316.81−0.06	32.79 ± 2.31	2.98 ± 2.98	3.66	0.20
G318.95−0.20	32.47 ± 2.45	3.44 ± 3.44	3.14	0.20
G323.74−0.26	36.72 ± 2.44	3.73 ± 3.73	3.28	0.22
G331.28−0.19	18.07 ± 1.96	3.50 ± 3.50	1.72	0.18
G332.73−0.62	27.55 ± 2.23	2.97 ± 2.97	3.10	0.19

Appendix E

Rotational diagram plots

The following pages present the CH_3CN and CH_3OH rotational diagrams. Rotational diagram plots made using CH_3CN are presented in Figure E.1 and utilise both the $J = 5 - 4$ (crosses) and $J = 6 - 5$ (squares) K-components. Error bars denote the 1-σ errors in the Gaussian fit to individual lines. The rotational temperature, T_{rot}, and total column density, N, may be found from the slope and y-axis intercept of a straight line fit to the data points. We fit the K-ladders separately (dashed lines) and in most cases took the weighted mean of the results as our final value for T_{rot} and N (solid line). The error in T_{rot} is dependant only on the relative calibration between lines in a single spectrum. The error in N is dependant on the absolute calibration, and is approximately 30 per cent.

The CH_3CN rotational diagrams are presented in Figure E.2 and were made using the $J = 2 - 1$ lines. In these plots the solid line is the fit to the E-type methanol only, while the dashed line is the fit to both the A and E-components. Error bars mark the 1-σ error in the column density of individual components, as determined by Gaussian fitting.

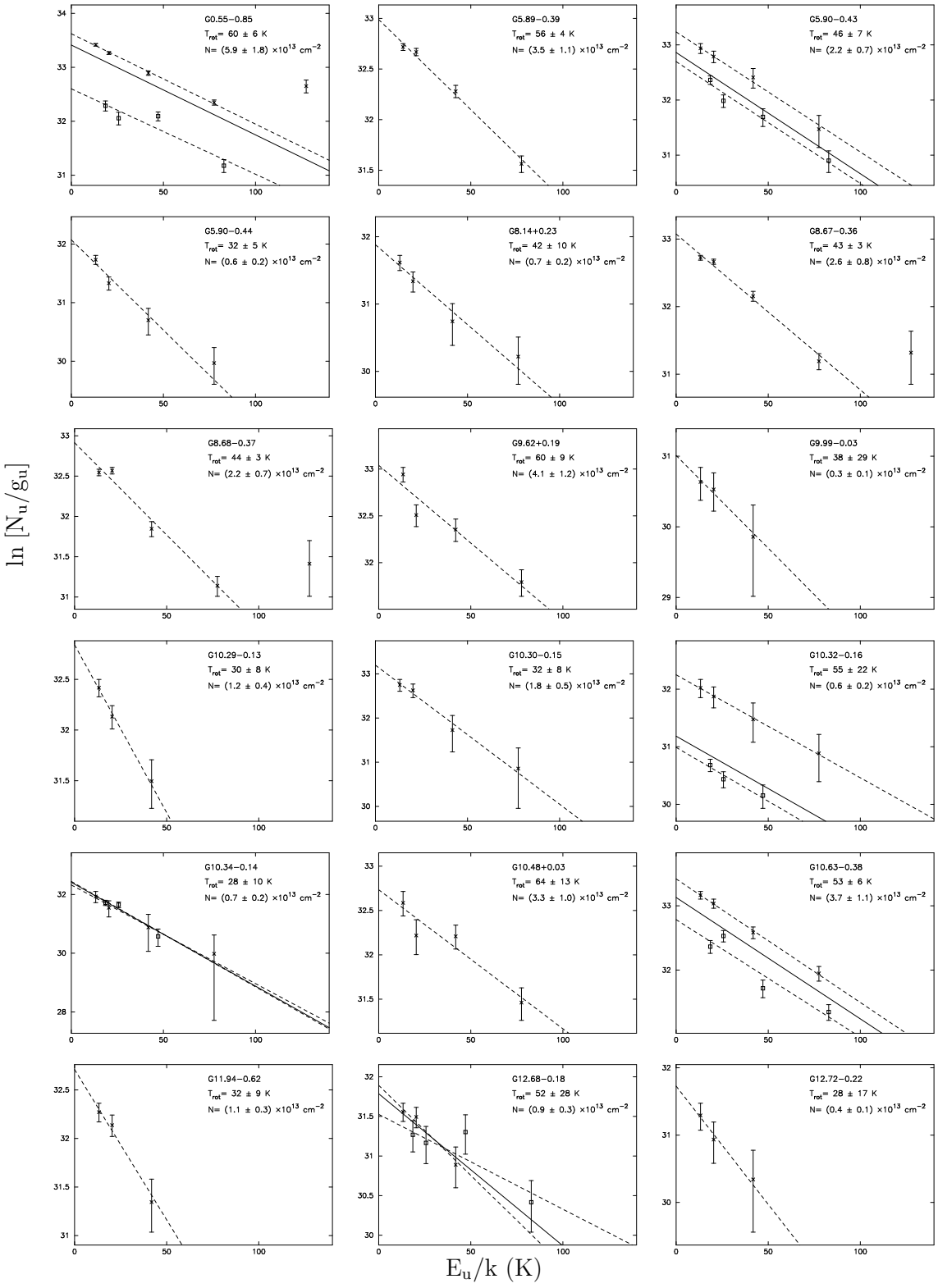

Figure E.1. CH_3CN rotational diagrams.

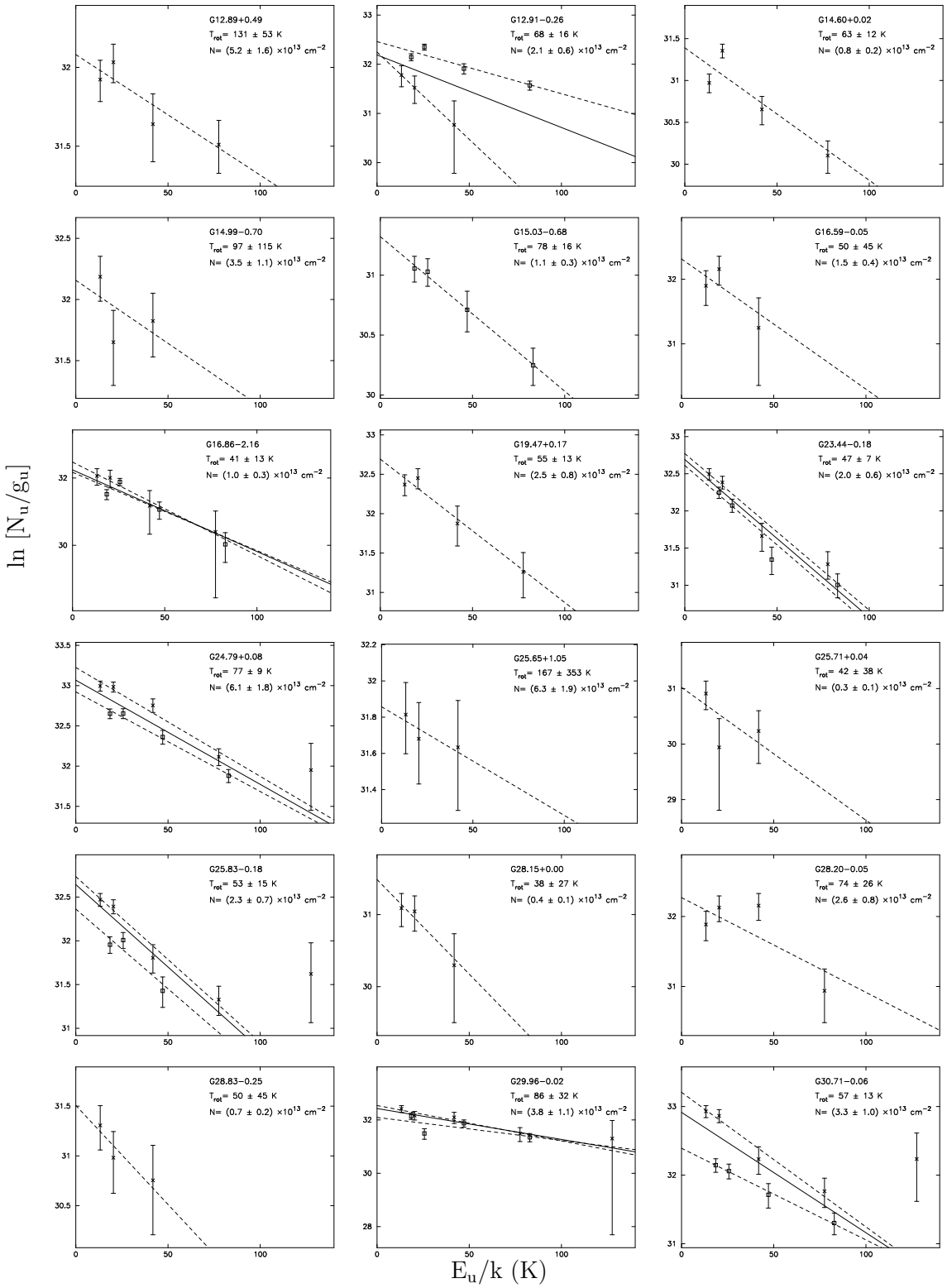

CH_3CN rotational diagrams – *continued*.

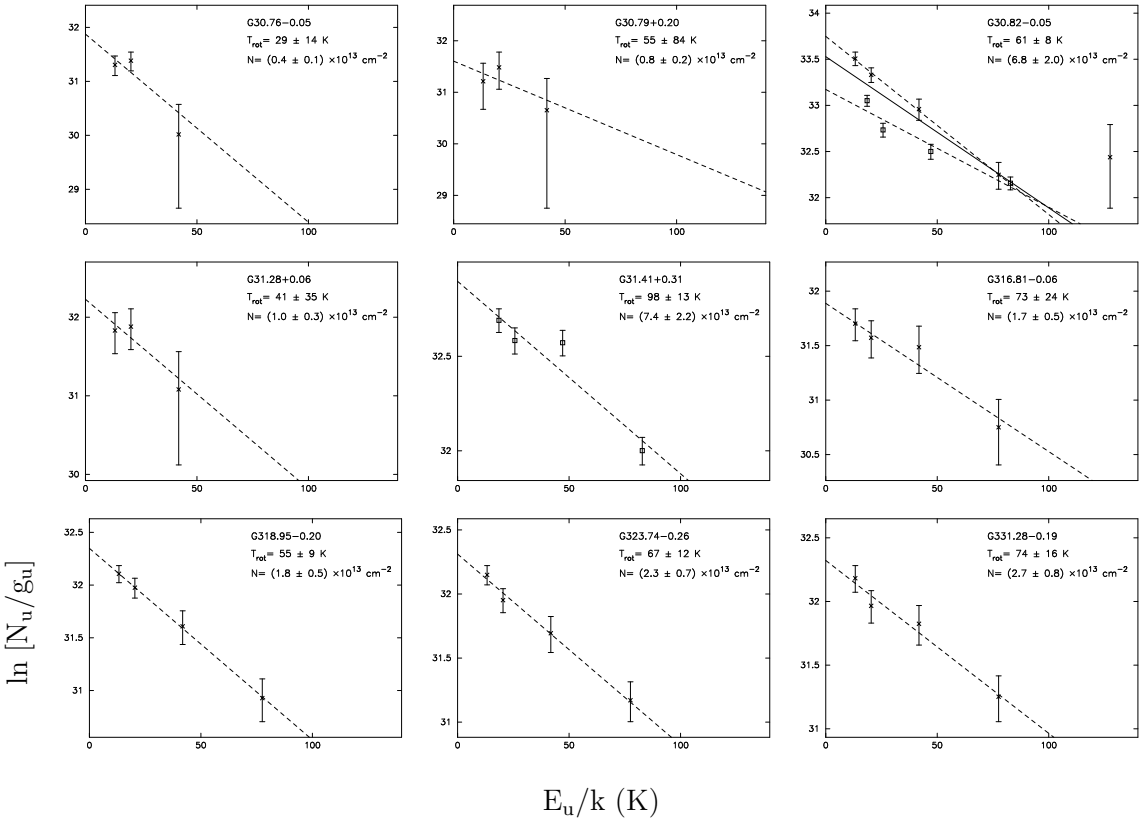

CH_3CN rotational diagrams – *continued*.

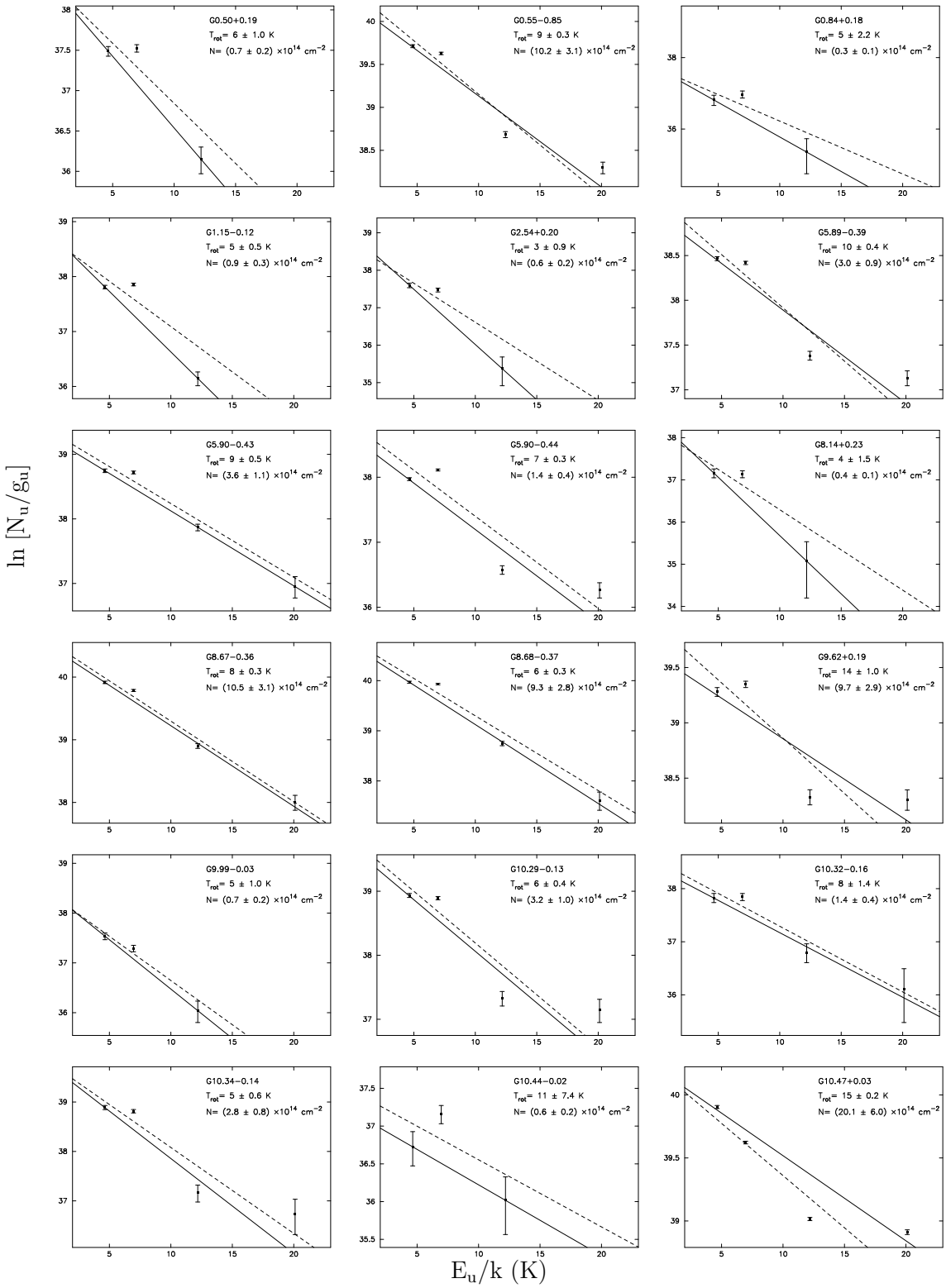

Figure E.2. CH_3OH rotational diagrams.

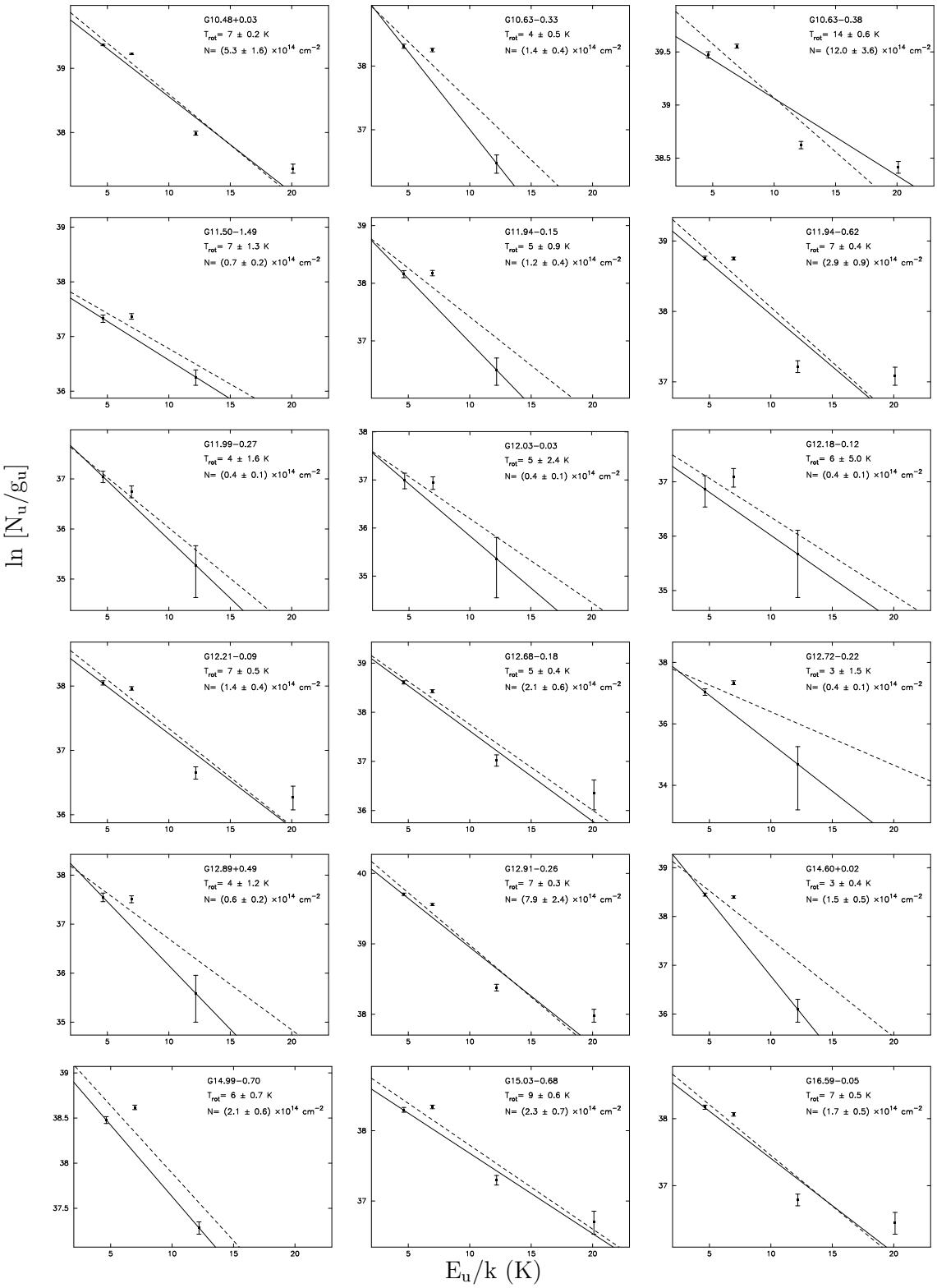

CH_3OH rotational diagrams – *continued*.

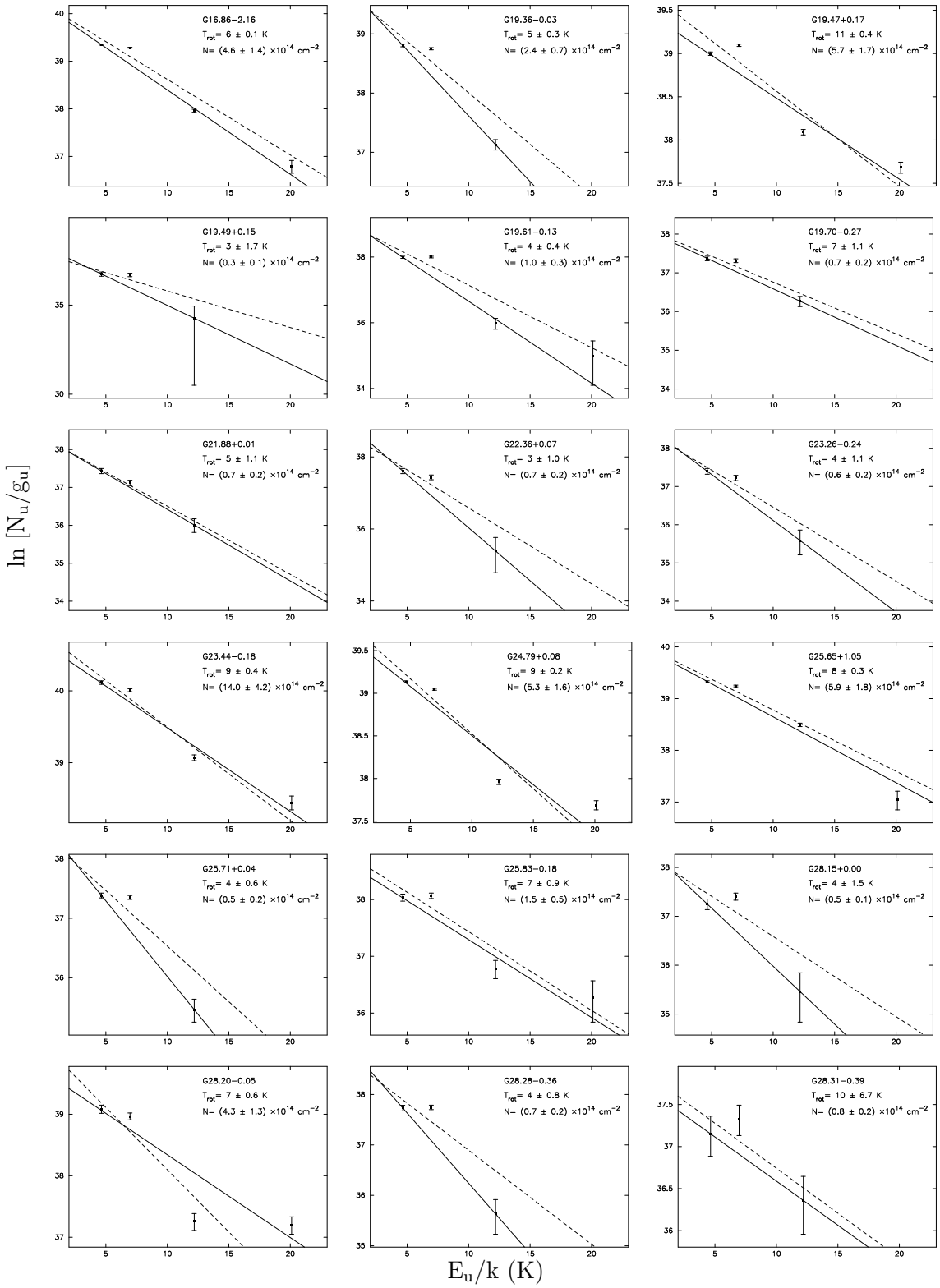

CH_3OH rotational diagrams – *continued*.

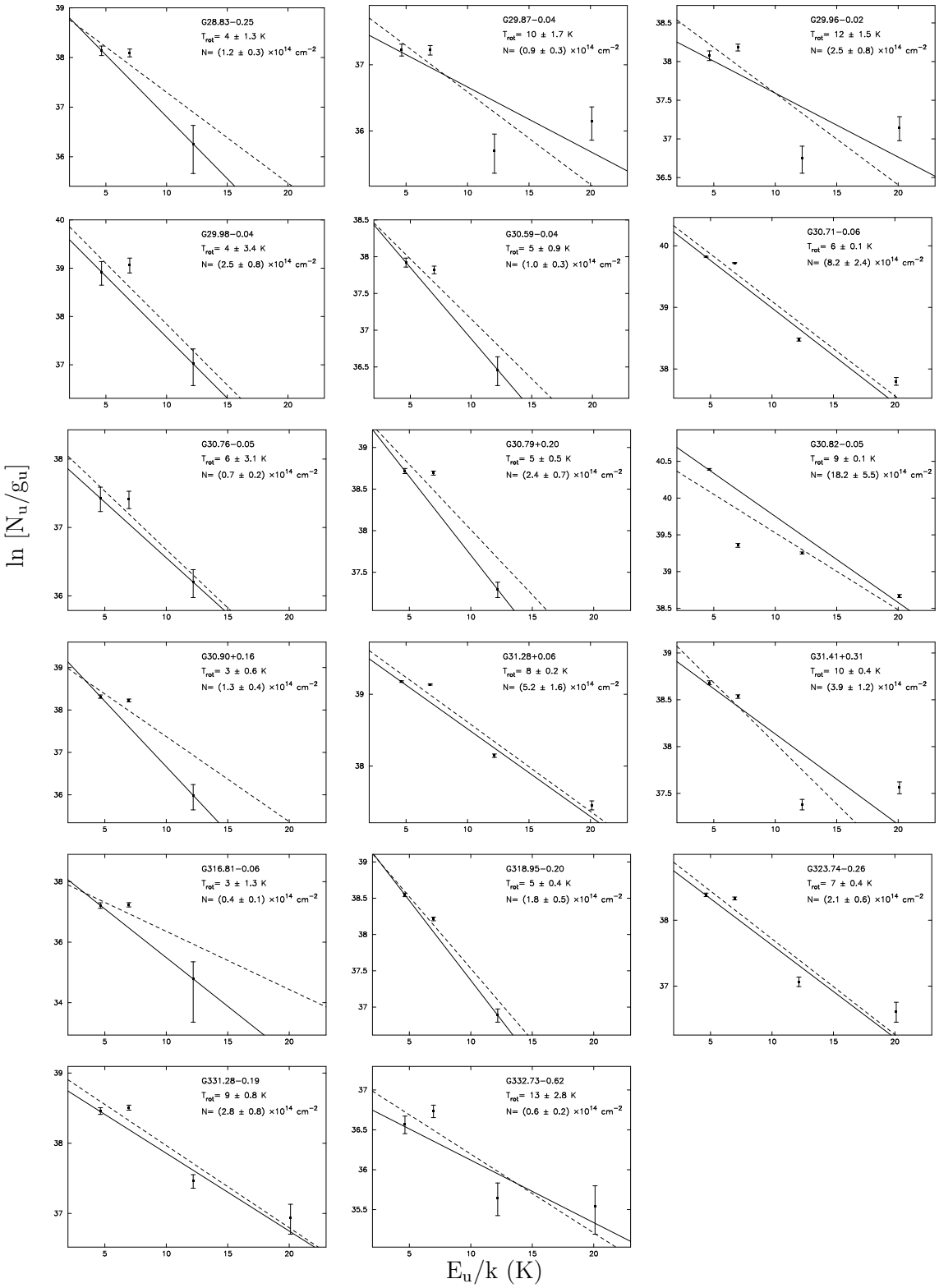

CH_3OH rotational diagrams – *continued.*

Appendix F

Einstein coefficients

Einstein coefficients are intrinsic properties of the molecule and transition being observed. The Einstein A coefficient is defined as the probability per second, per unit volume, of a spontaneous radiative transition from an upper to a lower energy level. It is essentially a measure of the intrinsic line strength of a transition. The values of A_{ul} used in this work were calculated from the empirical formula given in Pickett, et al. (1998):

$$A_{ul} = I_{ul}(T_0)\,\nu_{ul}\left(\frac{Q(T_0)}{g_u}\right) e^{\frac{E_u}{kT_0}} \times 1.748 \times 10^{-9}. \tag{F.1}$$

In Equation F.1:

- $T_0 = 300\,\mathrm{K}$, I_{ul} is the line intensity at 300 K in units of nm^2.MHz,
- ν_{ul} is the frequency of the transition in MHz,
- $Q(T_0)$ is the partition function evaluated at 300 K,
- g_u is the degeneracy of the upper level,
- E_u is the energy of the upper level,
- k is Boltzmann constant.

Table F.1 (overleaf) collects the molecular constants of the transitions observed in this thesis.

Table F.1: Molecular constants used in this thesis [α].

Species	Transition (J_K)	Frequency (GHz)	E_u/k (K)	A_{ul} (s^{-1})	n_{crit} [β] (cm^{-3})
CH_3CN	$5_0 \rightarrow 4_0$	91.987054	13.24	6.121×10^{-5}	6.0×10^{5} †
	$5_1 \rightarrow 4_1$	91.985284	20.39	5.875×10^{-5}	–
	$5_2 \rightarrow 4_2$	91.980000	41.82	5.139×10^{-5}	–
	$5_3 \rightarrow 4_3$	91.971374	77.53	3.913×10^{-5}	–
	$5_4 \rightarrow 4_4$	91.959206	127.51	2.200×10^{-5}	–
	$6_0 \rightarrow 5_0$	110.383494	18.54	10.895×10^{-5}	1.0×10^{6} †
	$6_1 \rightarrow 5_1$	110.381376	25.68	10.592×10^{-5}	–
	$6_2 \rightarrow 5_2$	110.374968	47.11	9.681×10^{-5}	–
	$6_3 \rightarrow 5_3$	110.364470	82.82	8.166×10^{-5}	–
	$6_4 \rightarrow 5_4$	110.349760	134.25	6.045×10^{-5}	–
HCO^+	$1 \rightarrow 0$	89.188526	4.28	3.020×10^{-5}	3.0×10^{5} †
$H^{13}CO^+$	$1 \rightarrow 0$	86.754330	4.16	2.800×10^{-5}	3.0×10^{5} †
CH_3OH	$2_{(-1,2)} \rightarrow 1_{(-1,1)}$ E	96.739390	4.642	2.495×10^{-6}	2.5×10^{5} †
	$2_{(0,2)} \rightarrow 1_{(0,1)}$ A+	96.741420	6.963	3.327×10^{-6}	–
	$2_{(0,2)} \rightarrow 1_{(0,1)}$ E	96.744580	12.188	3.327×10^{-6}	–
	$2_{(1,1)} \rightarrow 1_{(1,0)}$ E	96.755510	20.108	2.496×10^{-6}	–
^{13}CO	$1 \rightarrow 0$	110.210353	5.288	6.389×10^{-8}	6.5×10^{2} †
$C^{18}O$	$1 \rightarrow 0$	109.782173	5.267	4.961×10^{-7}	–
CS	$2 \rightarrow 1$	97.980950	7.052	1.703×10^{-5}	2.0×10^{5}
HNC	$1 \rightarrow 0$	90.663593	4.350	2.709×10^{-5}	2.5×10^{5} *sh*
HCN	$1_1 \rightarrow 0_1$	88.630416	4.253	2.444×10^{-5}	2.5×10^{5} *sh*
	$1_2 \rightarrow 0_1$	88.631847	–	–	–
	$1_0 \rightarrow 0_1$	88.633936	–	–	–
N_2H^+	$1_1 \rightarrow 0_1$	93.171880	4.471	3.654×10^{-5}	2×10^{5} *un*
	$1_2 \rightarrow 0_1$	93.173700	–	–	–
	$1_0 \rightarrow 0_1$	93.176130	–	–	–
NH_3	$1_1 \rightarrow 1'_{1'}$	23.694480	17.215	1.67×10^{-7}	2×10^{4} *sw*
	$2_2 \rightarrow 2'_{2'}$	23.722630	63.866	2.29×10^{-7}	

[α] Unless otherwise noted, all values quoted here are sourced from the NASA Jet Propulsion Lab (JPL) spectral line database (Pickett, et al. 1998).

[β] Critical density values marked with a † are calculated from the formula $n_{crit} = A_{ul}/\gamma_{H_2}$, where γ_{H_2} is the 'standard' collisional rate coefficient for H_2, assumed equal to 10^{10} molecules.s^{-1}.H_2-molecules^{-1}. Other values are referenced as follows: *sh* Schilke et al. (1992), *un* Ungerechts et al. (1997), *sw* Swade 1989.

References

Acord J. M., Churchwell E., Wood D. O. S., 1998, ApJ, 495, L107

Aikawa Y., Ohashi N., Inutsuka S.-i., Herbst E., Takakuwa S., 2001, ApJ, 552, 639

Allen C. W., 1973, Astrophysical quantities. London: University of London, Athlone Press, —c1973, 3rd ed.

Allen L. E., Burton M. G., Ryder S. D., Ashley M. C. B., Storey J. W. V., 1999, MNRAS, 304, 98

Andre P., Ward-Thompson D., Barsony M., 1993, ApJ, 406, 122

Araya E., Hofner P., Kurtz S., Bronfman L., DeDeo S., 2005, ApJS, 157, 279

Avalos M., Lizano S., Rodríguez L. F., Franco-Hernández R., Moran J. M., 2006, ApJ, 641, 406

Barbosa C. L., Damineli A., Blum R. D., Conti P. S., 2003, AJ, 126, 2411

Barrett A. H., Schwartz P. R., Waters J. W., 1971, ApJ, 168, L101+

Batrla W., Matthews H. E., Menten K. M., Walmsley C. M., 1987, Nat, 326, 49

Beltrán M. T., Cesaroni R., Neri R., Codella C., Furuya R. S., Testi L., Olmi L., 2005, A&A, 435, 901

Bergin E. A., Alves J., Huard T., Lada C. J., 2002, ApJ, 570, L101

Bergin E. A., Langer W. D., 1997, ApJ, 486, 316

Beuther H., Walsh A., Schilke P., Sridharan T. K., Menten K. M., Wyrowski F., 2002, A&A, 390, 289

Blake G. A., Masson C. R., Phillips T. G., Sutton E. C., 1986, ApJS, 60, 357

Bloemhof E. E., Reid M. J., Moran J. M., 1989, LNP Vol. 331: The Physics and Chemistry of Interstellar Molecular Clouds - mm and Sub-mm Observations in Astrophysics, 331, 228

Bockelee-Morvan D., Crovisier J., Colom P., Despois D., 1994, A&A, 287, 647

Bok B. J., 1956, AJ, 61, 309

Bok B. J., Reilly E. F., 1947, ApJ, 105, 255

Bonnell I. A., Bate M. R., 2006, MNRAS, 370, 488

Bonnell I. A., Bate M. R., Zinnecker H., 1998, MNRAS, 298, 93

Boogert A. C. A., Schutte W. A., Helmich F. P., Tielens A. G. G. M., Wooden D. H., 1997, A&A, 317, 929

Boogert A. C. A., Schutte W. A., Tielens A. G. G. M., Whittet D. C. B., Helmich F. P., Ehrenfreund P., Wesselius P. R., de Graauw T., Prusti T., 1996, A&A, 315, L377

Bourke T. L., Garay G., Lehtinen K. K., Koehnenkamp I., Launhardt R., Nyman L.-A., May J., Robinson G., Hyland A. R., 1997, ApJ, 476, 781

Bourke T. L., Hyland A. R., Robinson G., James S. D., Wright C. M., 1995, MNRAS, 276, 1067

Brand J., Blitz L., 1993, A&A, 275, 67

Brand J., Cesaroni R., Caselli P., Catarzi M., Codella C., Comoretto G., Curioni G. P., 12 others 1994, A&AS, 103, 541

Bromm V., Coppi P. S., Larson R. B., 1999, ApJ, 527, L5

Carr B. J., Bond J. R., Arnett W. D., 1984, ApJ, 277, 445

Caselli P., Benson P. J., Myers P. C., Tafalla M., 2002, ApJ, 572, 238

Caselli P., Hasegawa T. I., Herbst E., 1993, ApJ, 408, 548

Caselli P., Myers P. C., Thaddeus P., 1995, ApJ, 455, L77

Caselli P., Walmsley C. M., Zucconi A., Tafalla M., Dore L., Myers P. C., 2002, ApJ, 565, 331

Castor J., McCray R., Weaver R., 1975, ApJ, 200, L107

Caswell J. L., 1997, MNRAS, 289, 203

Caswell J. L., 2004, MNRAS, 351, 279

Caswell J. L., Batchelor R. A., Forster J. R., Wellington K. J., 1989, Australian Journal of Physics, 42, 331

Caswell J. L., Vaile R. A., Ellingsen S. P., Whiteoak J. B., Norris R. P., 1995, MNRAS, 272, 96

Ceccarelli C., Loinard L., Castets A., Tielens A. G. G. M., Caux E., 2000, A&A, 357, L9

Cernicharo J., 1991, in Lada C. J., Kylafis N. D., eds, NATO ASIC Proc. 342: The Physics of Star Formation and Early Stellar Evolution. p. 287

Cesaroni R., 2005, in IAU Symposium. p. 59

Cesaroni R., Churchwell E., Hofner P., Walmsley C. M., Kurtz S., 1994, A&A, 288, 903

Cesaroni R., Hofner P., Walmsley C. M., Churchwell E., 1998, A&A, 331, 709

Cesaroni R., Neri R., Olmi L., Testi L., Walmsley C. M., Hofner P., 2005, A&A, 434, 1039

Cesaroni R., Walmsley C. M., Churchwell E., 1992, A&A, 256, 618

Charnley S. B., 1997, ApJ, 481, 396

Charnley S. B., Kress M. E., Tielens A. G. G. M., Millar T. J., 1995, ApJ, 448, 232

Cheung A. C., Rank D. M., Townes C. H., Thornton D. D., Welch W. J., 1968, Physical Review Letters, 21, 1701

Cheung L. H., Frogel J. A., Hauser M. G., Gezari D. Y., 1980, ApJ, 240, 74

Churchwell E., 1999, in Lada C. J., Kylafis N. D., eds, NATO ASIC Proc. 540: The Origin of Stars and Planetary Systems. p. 515

Churchwell E., 2002, ARA&A, 40, 27

Churchwell E., Walmsley C. M., Cesaroni R., 1990, A&AS, 83, 119

Churchwell E., Walmsley C. M., Wood D. O. S., 1992, A&A, 253, 541

Codella C., Welser R., Henkel C., Benson P. J., Myers P. C., 1997, A&A, 324, 203

Crowther P. A., Conti P. S., 2003, MNRAS, 343, 143

Cummins S. E., Linke R. A., Thaddeus P., 1986, ApJS, 60, 819

Danby G., Flower D. R., Valiron P., Schilke P., Walmsley C. M., 1988, MNRAS, 235, 229

De Buizer J. M., Watson A. M., Radomski J. T., Piña R. K., Telesco C. M., 2002, ApJ, 564, L101

de Pree C. G., Nysewander M. C., Goss W. M., 1999, AJ, 117, 2902

De Vries C. H., Myers P. C., 2005, ApJ, 620, 800

de Zeeuw P. T., Hoogerwerf R., de Bruijne J. H. J., Brown A. G. A., Blaauw A., 1999, AJ, 117, 354

Dhendecourt L. B., Allamandola L. J., Baas F., Greenberg J. M., 1982, A&A, 109, L12

Dobbs C. L., Bonnell I. A., Clark P. C., 2005, MNRAS, 360, 2

Doty S. D., van Dishoeck E. F., van der Tak F. F. S., Boonman A. M. S., 2002, A&A, 389, 446

Downes D., Wilson T. L., Bieging J., Wink J., 1980, A&AS, 40, 379

Draine B. T., 1978, ApJS, 36, 595

Draine B. T., Lee H. M., 1984, ApJ, 285, 89

Dunne L., Eales S., Edmunds M., Ivison R., Alexander P., Clements D. L., 2000, MNRAS, 315, 115

Egan M. P., Price S. D., 1996, AJ, 112, 2862

Elitzur M., 1992, ARA&A, 30, 75

Elitzur M., de Jong T., 1978, A&A, 67, 323

Ellingsen S. P., Norris R. P., McCulloch P. M., 1996, MNRAS, 279, 101

Ellingsen S. P., von Bibra M. L., McCulloch P. M., Norris R. P., Deshpande A. A., Phillips C. J., 1996, MNRAS, 280, 378

Elmegreen B. G., 1979, ApJ, 231, 372

Elmegreen B. G., 1998, in Woodward C. E., Shull J. M., Thronson Jr. H. A., eds, ASP Conf. Ser. 148: Origins. p. 150

Emerson J. P., 1988, in NATO ASIC Proc. 241: Formation and Evolution of Low Mass Stars. p. 21

Estalella R., Mauersberger R., Torrelles J. M., Anglada G., Gomez J. F., Lopez R., Muders D., 1993, ApJ, 419, 698

Faúndez S., Bronfman L., Garay G., Chini R., Nyman L.-Å., May J., 2004, A&A, 426, 97

Figer D. F., Najarro F., Gilmore D., Morris M., Kim S. S., Serabyn E., McLean I. S., Gilbert A. M., Graham J. R., Larkin J. E., Levenson N. A., Teplitz H. I., 2002, ApJ, 581, 258

Frogel J. A., Persson S. E., 1974, ApJ, 192, 351

Fuente A., Neri R., Caselli P., 2005, A&A, 444, 481

Garay G., Lizano S., 1999, PASP, 111, 1049

Genzel R., 1986, in Masers, Molecules, and Mass Outflows in Star Formation Regions. p. 233

Genzel R., 1991, in Lada C. J., Kylafis N. D., eds, NATO ASIC Proc. 342: The Physics of Star Formation and Early Stellar Evolution. p. 155

Gibb A. G., Wyrowski F., Mundy L. G., 2004, ApJ, 616, 301

Gillespie A. R., White G. J., 1980, A&A, 91, 257

Girart J. M., Estalella R., Ho P. T. P., Rudolph A. L., 2000, ApJ, 539, 763

Goldsmith P. F., Bergin E. A., Lis D. C., 1997, ApJ, 491, 615

Goldsmith P. F., Langer W. D., 1999, ApJ, 517, 209

Goldsmith P. F., Langer W. D., Ellder J., Kollberg E., Irvine W., 1981, ApJ, 249, 524

Gomez Y., Garay G., Lizano S., 1995, ApJ, 453, 727

Greenberg J. M., Mendoza-Gomez C. X., Groot M. S. D., Breukers R., 1993. Dust and Chemistry in Astronomy, p. 271

Greenhill L. J., Booth R. S., Ellingsen S. P., Herrnstein J. R., Jauncey D. L., McCulloch P. M., Moran J. M., Norris R. P., Reynolds J. E., Tzioumis A. K., 2003, ApJ, 590, 162

Hanson M. M., Conti P. S., 1993, Bulletin of the American Astronomical Society, 25, 1456

Hanson M. M., Howarth I. D., Conti P. S., 1997, ApJ, 489, 698

Hatchell J., Thompson M. A., Millar T. J., MacDonald G. H., 1998, A&AS, 133, 29

Herbst E., Leung C. M., 1989, ApJS, 69, 271

Hildebrand R. H., 1983, QJRAS, 24, 267

Hill T., Burton M. G., Thompson M. A., Walsh A. J., Hunt-Cunningham M., Garay G., 2005, MNRAS, 363, 405

Hillenbrand L. A., 1997, AJ, 113, 1733

Hjellming R. M., 1966, ApJ, 143, 420

Ho P. T. P., Martin R. N., Myers P. C., Barrett A. H., 1977, ApJ, 215, L29

Ho P. T. P., Townes C. H., 1983, ARA&A, 21, 239

Hofner P., Kurtz S., Churchwell E., Walmsley C. M., Cesaroni R., 1994, ApJ, 429, L85

Hofner P., Kurtz S., Churchwell E., Watson A., 1996, Bulletin of the American Astronomical Society, 28, 848

Hogerheijde M. R., 2005, Ap&SS, 295, 179

Hogerheijde M. R., van Dishoeck E. F., Blake G. A., van Langevelde H. J., 1997, ApJ, 489, 293

Hollenbach D., 1997, in Reipurth B., Bertout C., eds, IAU Symp. 182: Herbig-Haro Flows and the Birth of Stars. p. 181

Hollenbach D. J., Tielens A. G. G. M., 1999, Reviews of Modern Physics, 71, 173

Hollis J. M., 1982, ApJ, 260, 159

Huard T. L., Sandell G., Weintraub D. A., 1999, ApJ, 526, 833

Jackson J. M., Bania T. M., Simon R., Kolpak M., Clemens D. P., Heyer M., 2002, ApJ, 566, L81

Jackson J. M., Rathborne J. M., Shah R. Y., Simon R., Bania T. M., Clemens D. P., Chambers E. T., Johnson A. M., Dormody M., Lavoie R., Heyer M. H., 2006, ApJS, 163, 145

James A., Dunne L., Eales S., Edmunds M. G., 2002, MNRAS, 335, 753

Jørgensen J. K., Schöier F. L., van Dishoeck E. F., 2004, A&A, 416, 603

Kandori R., Nakajima Y., Tamura M., Tatematsu K., Aikawa Y., Naoi T., Sugitani K., Nakaya H., Nagayama T., Nagata T., Kurita M., Kato D., Nagashima C., Sato S., 2005, AJ, 130, 2166

Karr J. L., Martin P. G., 2003, ApJ, 595, 900

Keto E., 2003, ApJ, 599, 1196

Kim H.-D., Balasubramanyam R., Burton M. G., 2002, Publications of the Astronomical Society of Australia, 19, 505

Kim H.-D., Cho S.-H., Chung H.-S., Kim H.-R., Roh D.-G., Kim H.-G., Minh Y. C., Minn Y.-K., 2000, ApJS, 131, 483

Kim H.-D., Cho S.-H., Lee C.-W., Burton M. G., 2001, Journal of Korean Astronomical Society, 34, 167

Kolpak M. A., Jackson J. M., Bania T. M., Clemens D. P., Dickey J. M., 2003, ApJ, 582, 756

Kramer C., Richer J., Mookerjea B., Alves J., Lada C., 2003, A&A, 399, 1073

Krumholz M. R., 2006, ApJ, 641, L45

Krumholz M. R., McKee C. F., Klein R. I., 2005, Nat, 438, 332

Kukolich S. G., 1967, Physical Review, 156, 83

Kurtz S., Cesaroni R., Churchwell E., Hofner P., Walmsley C. M., 2000, Protostars and Planets IV, p. 299

Kurtz S., Churchwell E., Wood D. O. S., 1994, ApJS, 91, 659

Kutner M. L., Ulich B. L., 1981, ApJ, 250, 341

Kylafis N. D., Pavlakis K. G., 1992, ApJ, 400, 344

Lada C. J., 1987, in IAU Symp. 115: Star Forming Regions. p. 1

Lada C. J., 1999, in Lada C. J., Kylafis N. D., eds, NATO ASIC Proc. 540: The Origin of Stars and Planetary Systems. p. 143

Lada C. J., Lada E. A., 2003, ARA&A, 41, 57

Lada C. J., Wilking B. A., 1984, ApJ, 287, 610

Ladd E. F., C. P., Purcell C. R., T. W., M. K., 2005, Technical report, Specification of frequency and velocity scales for Mopra spectra. ATNF

Ladd E. F., Heyer M. H., 1996, Technical report, FCRAO technical memorandum. Univ. of Massachusetts

Ladd E. F., Purcell C. R., Wong T., Robertson S., 2005, Publ. Astron. Soc. Austral., 22, 62

Larionov G. M., Val'tts I. E., Winnberg A., Johansson L. E. B., Booth R. S., Golubev V. V., 1999, A&AS, 139, 257

Lee J.-K., Walsh A. J., Burton M. G., Ashley M. C. B., 2001, MNRAS, 324, 1102

Leger A., Jura M., Omont A., 1985, A&A, 144, 147

Loren R. B., Mundy L. G., 1984, ApJ, 286, 232

Lumsden S. L., Hoare M. G., Oudmaijer R. D., Richards D., 2002, MNRAS, 336, 621

Mac Low M.-M., van Buren D., Wood D. O. S., Churchwell E., 1991, ApJ, 369, 395

MacDonald G. H., Gibb A. G., Habing R. J., Millar T. J., 1996, A&AS, 119, 333

Mackay D. D. S., 1999, MNRAS, 304, 61

MacLaren I., Richardson K. M., Wolfendale A. W., 1988, ApJ, 333, 821

MacLeod G. C., Gaylard M. J., 1992, MNRAS, 256, 519

Mader G. L., Johnston K. J., Knowles S. H., Mango S. A., Schwartz P. R., Waltman W. B., Moran J. M., 1975, ApJ, 200, L111

Maercker M., Burton M. G., Wright C. M., 2006, A&A, 450, 253

Mangum J. G., 1993, PASP, 105, 117

Mardones D., Myers P. C., Tafalla M., Wilner D. J., Bachiller R., Garay G., 1997, ApJ, 489, 719

Massi F., Codella C., Brand J., Di Fabrizio L., Wouterloot J., 2005, Memorie della Societa Astronomica Italiana, 76, 400

Mathis J. S., 1996, ApJ, 472, 643

McMullin J. P., Mundy L. G., Blake G. A., 1994, ApJ, 437, 305

Menten K., 1991a, in Haschick A. D., Ho P. T. P., eds, ASP Conf. Ser. 16: Atoms, Ions and Molecules: New Results in Spectral Line Astrophysics. p. 119

Menten K. M., 1991b, ApJ, 380, L75

Menten K. M., Walmsley C. M., Henkel C., Wilson T. L., 1988, A&A, 198, 253

Mezger P. G., Henderson A. P., 1967, ApJ, 147, 471

Millar T. J., Farquhar P. R. A., Willacy K., 1997, A&AS, 121, 139

Millar T. J., MacDonald G. H., Gibb A. G., 1997, A&A, 325, 1163

Minh Y. C., Irvine W. M., Ohishi M., Ishikawa S., Saito S., Kaifu N., 1993, A&A, 267, 229

Minier V., Burton M. G., Hill T., Pestalozzi M. R., Purcell C. R., Garay G., Walsh A. J., Longmore S., 2005, A&A, 429, 945

Minier V., Conway J. E., Booth R. S., 2001, A&A, 369, 278

Minier V., Ellingsen S. P., Norris R. P., Booth R. S., 2003, A&A, 403, 1095

Molinari S., Brand J., Cesaroni R., Palla F., 1996, A&A, 308, 573

Moneti A., 1992, A&A, 259, 627

Moorwood A. F. M., Salinari P., 1981, A&A, 102, 197

Morimoto M., Kanzawa T., Ohishi M., 1985, ApJ, 288, L11

Motte F., Schilke P., Lis D. C., 2003, ApJ, 582, 277

Norris R. P., Caswell J. L., Wellington K. J., McCutcheon W. H., Reynolds J. E., 1988, Nat, 335, 149

Norris R. P., Whiteoak J. B., Caswell J. L., Wieringa M. H., Gough R. G., 1993, ApJ, 412, 222

Nummelin A., Bergman P., Hjalmarson Å., Friberg P., Irvine W. M., Millar T. J., Ohishi M., Saito S., 2000, ApJS, 128, 213

Oka T., Shimizu F. O., Shimizu T., Watson J. K. G., 1971, ApJ, 165, L15+

Oliva E., Moorwood A. F. M., 1986, A&A, 164, 104

Olmi L., Cesaroni R., Hofner P., Kurtz S., Churchwell E., Walmsley C. M., 2003, A&A, 407, 225

Olmi L., Cesaroni R., Walmsley C. M., 1993, A&A, 276, 489

Olmi L., Cesaroni R., Walmsley C. M., 1996, A&A, 307, 599

Ossenkopf V., Henning T., 1994, A&A, 291, 943

Ott J., Weiss A., Henkel C., Walter F., 2005, ApJ, 629, 767

Panagia N., 1973, AJ, 78, 929

Pankonin V., Churchwell E., Watson C., Bieging J. H., 2001, ApJ, 558, 194

Park Y.-S., 2001, A&A, 376, 348

Penzias A. A., Burrus C. A., 1973, ARA&A, 11, 51

Perryman M. A. C., Lindegren L., Kovalevsky J., Turon C., Hoeg E., others) ., 1995, A&A, 304, 69

Persi P., Roth M., Tapia M., Ferrari-Toniolo M., Marenzi A. R., 1994, A&A, 282, 474

Pickett, H. M., Poynter R. L., Cohen E. A., Delitsky M. L., Pearson J. C., Muller, H. S. P., 1998, J. Quant. Spectrosc. Radiat. Transfer, 60, 883

Pillai T., Wyrowski F., Carey S. J., Menten K. M., 2006, A&A, 450, 569

Pirogov L., Zinchenko I., Caselli P., Johansson L. E. B., Myers P. C., 2003, A&A, 405, 639

Plambeck R. L., Menten K. M., 1990, ApJ, 364, 555

Plume R., Jaffe D. T., Evans N. J., 1992, ApJS, 78, 505

Pratap P., Megeath S. T., Bergin E. A., 1999, ApJ, 517, 799

Purcell C. R., 2006, MNRAS, 517, 799

Rathborne J. M., Jackson J. M., Simon R., 2006, ApJ, 641, 389

Rawlings J. M. C., Redman M. P., Keto E., Williams D. A., 2004, MNRAS, 351, 1054

Rawlings J. M. C., Taylor S. D., Williams D. A., 2000, MNRAS, 313, 461

Reid M. J., Haschick A. D., Burke B. F., Moran J. M., Johnston K. J., Swenson G. W., 1980, ApJ, 239, 89

Remijan A., Sutton E. C., Snyder L. E., Friedel D. N., Liu S.-Y., Pei C.-C., 2004, ApJ, 606, 917

Rodgers S. D., Charnley S. B., 2001, ApJ, 546, 324

Rodgers S. D., Charnley S. B., 2003, ApJ, 585, 355

Rohlfs K., Wilson T. L., 2004, Tools of radio astronomy. Tools of radio astronomy, 4th rev. and enl. ed., by K. Rohlfs and T.L. Wilson. Berlin: Springer, 2004

Rydbeck O. E. H., Hjalmarson A., Rydbeck G., Ellder J., Olofsson H., Sume A., 1981, ApJ, 243, L41

Rydbeck O. E. H., Sume A., Hjalmarson A., Ellder J., Ronnang B. O., Kollberg E., 1977, ApJ, 215, L35

Salvaterra R., Magliocchetti M., Ferrara A., Schneider R., 2006, MNRAS, 368, L6

Sandford S. A., Allamandola L. J., 1993, Icarus, 106, 478

Sault R. J., Teuben P. J., Wright M. C. H., 1995, in Shaw R. A., Payne H. E., Hayes J. J. E., eds, ASP Conf. Ser. 77: Astronomical Data Analysis Software and Systems IV. p. 433

Savage C., Apponi A. J., Ziurys L. M., Wyckoff S., 2002, ApJ, 578, 211

Schilke P., Groesbeck T. D., Blake G. A., Phillips T. G., 1997, ApJS, 108, 301

Schilke P., Walmsley C. M., Pineau Des Forets G., Roueff E., Flower D. R., Guilloteau S., 1992, A&A, 256, 595

Schöier F. L., Jørgensen J. K., van Dishoeck E. F., Blake G. A., 2002, A&A, 390, 1001

Schutte A. J., van der Walt D. J., Gaylard M. J., MacLeod G. C., 1993, MNRAS, 261, 783

Schutte W. A., Allamandola L. J., Sandford S. A., 1993, Icarus, 104, 118

Scott G. B. I., Freeman C. G., McEwan M. J., 1997, MNRAS, 290, 636

Shu F. H., Adams F. C., Lizano S., 1987, ARA&A, 25, 23

Shu F. H., Ruden S. P., Lada C. J., Lizano S., 1991, ApJ, 370, L31

Shull J. M., 1980, ApJ, 238, 860

Simon R., Jackson J. M., Bania T. M., Clemens D. P., Heyer M. H., Egan M. P., Price S. D., 2001, Bulletin of the American Astronomical Society, 33, 1450

Sobolev A. M., Cragg D. M., Godfrey P. D., 1997, A&A, 324, 211

Solomon P. M., Rivolo A. R., Barrett J., Yahil A., 1987, ApJ, 319, 730

Soria-Ruiz R., Alcolea J., Colomer F., Bujarrabal V., Desmurs J.-F., Marvel K. B., Diamond P. J., 2004, A&A, 426, 131

Stier M. T., Jaffe D. T., Rengarajan T. N., Fazio G. G., Maxson C. W., McBreen B., Loughran L., Serio S., Sciortino S., 1984, ApJ, 283, 573

Strömgren B., 1939, ApJ, 89, 526

Stutzki J., Winnewisser G., 1985, A&A, 144, 13

Sutton E. C., Jaminet P. A., Danchi W. C., Blake G. A., 1991, ApJS, 77, 255

Swade D. A., 1989, ApJ, 345, 828

Tan J. C., McKee C. F., 2004, ApJ, 603, 383

Testi L., Palla F., Prusti T., Natta A., Maltagliati S., 1997, A&A, 320, 159

Thompson M. A., MacDonald G. H., Millar T. J., 1999, A&A, 342, 809

Tielens A. G. G. M., Allamandola L. J., 1987, in Morfill G. E., Scholer M., eds, NATO ASIC Proc. 210: Physical Processes in Interstellar Clouds. p. 333

Townes C. H., Genzel R., Watson D. M., Storey J. W. V., 1983, ApJ, 269, L11

Townes C. H., Schawlow A. L., 1955, Microwave Spectroscopy. Microwave Spectroscopy, New York: McGraw-Hill, 1955

Turner B. E., 1974, ApJ, 193, L83

Turner B. E., 1989, ApJS, 70, 539

Turner B. E., 1991, ApJS, 76, 617

Turner B. E., 1996, ApJ, 468, 694

Ulich B. L., 1981, AJ, 86, 1619

Ungerechts H., Bergin E. A., Goldsmith P. F., Irvine W. M., Schloerb F. P., Snell R. L., 1997, ApJ, 482, 245

Ungerechts H., Walmsley C. M., Winnewisser G., 1980, A&A, 88, 259

Ungerechts H., Winnewisser G., Walmsley C. M., 1986, A&A, 157, 207

Urquhart J. S., Thompson M. A., Morgan L. K., White G. J., 2006, A&A, 450, 625

van der Tak F. F. S., 2004, in Burton M., Jayawardhana R., Bourke T., eds, IAU Symposium. p. 59

van der Tak F. F. S., 2005, in Cesaroni R., Felli M., Churchwell E., Walmsley M., eds, IAU Symposium. p. 70

van der Tak F. F. S., Boonman A. M. S., Braakman R., van Dishoeck E. F., 2003, A&A, 412, 133

van der Tak F. F. S., van Dishoeck E. F., Caselli P., 2000, A&A, 361, 327

van der Walt D. J., Gaylard M. J., MacLeod G. C., 1995, A&AS, 110, 81

van Dishoeck E. F., Blake G. A., 1998, ARA&A, 36, 317

van Dishoeck E. F., Glassgold A. E., Guelin M., Jaffe D. T., Neufeld D. A., Tielens A. G. G. M., Walmsley C. M., 1992, in Singh P. D., ed., IAU Symp. 150: Astrochemistry of Cosmic Phenomena. p. 285

van Dishoeck E. F., Jørgensen J. K., Maret S., Ceccarelli C., Caux E., Schöier F. L., Castets A., Tielens A. G. G. M., 2005, in Wilson A., ed., The Dusty and Molecular Universe: A Prelude to Herschel and ALMA. p. 191

Viti S., Caselli P., Hartquist T. W., Williams D. A., 2001, A&A, 370, 1017

Walsh A. J., Burton M. G., Hyland A. R., Robinson G., 1998, MNRAS, 301, 640

Walsh A. J., Burton M. G., Hyland A. R., Robinson G., 1999, MNRAS, 309, 905

Walsh A. J., Hyland A. R., Robinson G., Burton M. G., 1997, MNRAS, 291, 261

Walsh A. J., Macdonald G. H., Alvey N. D. S., Burton M. G., Lee J.-K., 2003, A&A, 410, 597

Wannier P. G., Lichten S. M., Morris M., 1983, ApJ, 268, 727

Watson C., Churchwell E. B., Zweibel E., Crutcher R. M., 2002, Bulletin of the American Astronomical Society, 34, 1135

Weidner C., Kroupa P., 2004, MNRAS, 348, 187

White G. J., Nelson R. P., Holland W. S., Robson E. I., Greaves J. S., McCaughrean M. J., Pilbratt G. L., Balser D. S., Oka T., Sakamoto S., Hasegawa T., McCutcheon W. H., Matthews H. E., Fridlund C. V. M., Tothill N. F. H., Huldtgren M., Deane J. R., 1999, A&A, 342, 233

Whitney B. A., Indebetouw R., Babler B. L., Meade M. R., Watson C., Wolff M. J., Wolfire M. G., Clemens D. P., Bania T. M., Benjamin R. A., Cohen M., Devine

K. E., Dickey J. M., Heitsch F., Jackson J. M., Kobulnicky H. A., six—others 2004, ApJS, 154, 315

Whittet D. C. B., 1992, Dust in the galactic environment. Dust in the galactic environment Institute of Physics Publishing, 306 p.

Williams D. A., 1993. Dust and Chemistry in Astronomy, p. 143

Williams J. P., de Geus E. J., Blitz L., 1994, ApJ, 428, 693

Wilner D. J., Wright M. C. H., Plambeck R. L., 1994, ApJ, 422, 642

Wilson T. L., Walmsley C. M., Jewell P. R., Snyder L. E., 1984, A&A, 134, L7

Wink J. E., Altenhoff W. J., Mezger P. G., 1982, A&A, 108, 227

Wood D. O. S., Churchwell E., 1989a, ApJ, 340, 265

Wood D. O. S., Churchwell E., 1989b, ApJS, 69, 831

Wu J., Evans N. J., 2003, ApJ, 592, L79

Wyrowski F., Schilke P., Walmsley C. M., Menten K. M., 1999, ApJ, 514, L43

Yorke H. W., Sonnhalter C., 2002, ApJ, 569, 846

Zavagno A., Deharveng L., Comerón F., Brand J., Massi F., Caplan J., Russeil D., 2006, A&A, 446, 171

Ziurys L. M., McGonagle D., 1993, ApJS, 89, 155